634

ARKIV FÖR FYSIK

UTGIVET AV

K. SVENSKA VETENSKAPSAKADEMIEN

Band 6

Med 49 avhandlingar

STOCKHOLM
ALMQVIST & WIKSELLS BOKTRYCKERI AB

LONDON
H. K. LEWIS & CO., LTD
136, GOWER STREET

1953

PARIS
LIBRAIRIE C. KLINCKSIECK
11 RUE DE LILLE

Häfte	1	innehållande	Nr 1— 9	utkom	den	23	jan. 1953
»	2	»	Nr 10—19	»	»	18	febr. 1953
»	3	»	Nr 20—28	»	»	27	april 1953
»	4	»	Nr 29—36	»	»	29	» 1953
»	5	»	Nr 37—45	»	»	5	aug. 1953
»	6	»	Nr 46—49	»	»	10	» 1953

SJÄTTE BANDETS INNEHÅLL

Sid.

1. Carlvik, I., Some measurements on the absorption of 75 – 200 keV electrons in aluminium . . . . . 1—16
2. Kleman, B., The intensity anomalies in the band-spectrum of CuH . . . . 17—24
3. Lundqvist, S. O., On the elastic constants of cubic ionic crystals . . . . . 25—38
4. Wiedling, T., Directional correlation measurements on successive nuclear gamma rays in Hf^{177} . . . . . 39—48
5. Malmfors, K. G., Nuclear resonance scattering of gamma-rays . . . . . . 49—56
6. Hellstrand, E. & Persson, R., Studies of the resonance absorption of neutrons in uranium with the time-of-flight method . . . . . 57—68
7. Erlandsson, G., Measurements on the microwave spectra of methyl alcohol and nitromethane . . . . . 69—72
8. Benedicks, C. & Ekelund-Kappeler, B., On the measuring of cohesional forces of solids, as influenced by liquids . . . . . 73—80
9. Slätis, H. & Zappa, L., The disintegration of Zr^{95} and Nb^{95} . . . . 81—93
10. Lagerqvist, Albin and Uhler, Ulla, The ultra-violet band-system of silicon monoxide . . . . . 95—112
11. Fröman, Per Olof, On the influence of spin and isotopes in the kinematical theory of neutron diffraction . . . . . 113—117
12. Svenonius, Per and Waller, Ivar, On the rôle of spin in the non-relativistic theory of the scattering of radiation . . . . . 119—121
13. Lindqvist, Torsten, Precision measurements of the gamma-radiation from $scandium^{46}$ . . . . . 123—126
14. Norinder, Harald and Siksna, Reinhards, Ions formed in a room by negative wire corona . . . . . 127—140
15. Lagerqvist, Albin, A band-system of radium chloride . . . . 141—142
16. Borelius, G., Berglund, Stig and Sjöberg, Sven, Measurements on the evolution of heat during the recovery of cold-worked metals . . . . 143—149
17. Norinder, Harald and Salka, Oskars, Screens in long discharge gaps . . 151—169
18. Brogren, Gösta and Haeggblom, Lars Erik, Some atomic planes in quartz suitable as lattices in X-ray spectroscopy . . . . . 171—176
19. Bruno, B. and Depken, S., Photodisintegration of the deuteron at high energies . . . . . 177—189
20. Borelius, G., On the solid-liquid transformation in metals . . . . 191—206
21. Borelius, G., On fusion as order-disorder transition . . . . 207—212
22. Alexopoulos, K. & Brogren, G., Evidence of a band structure in the Compton radiation from solids . . . . . 213—222
23. Lindholm, E., The vibrations and bending of pre-stressed circular plates . . 223—242
24. Holte, G., On the slowing down of neutrons in heavy water . . . . 243—254
25. Norinder, H. & Siksna, R., Ions formed in a room by positive wire corona 255—261
26. Wapstra, A. H., The decay energies of Pb^{209} and Si^{31} . . . . 263—267
27. Svenonius, P., On the coherent scattering of light by an electrostatic field according to the Dirac hole theory . . . . . 269—277
28. Siksna, R., Mobility spectra of ions formed by positive corona discharge 279—286

Sid.

29. Ingelstam, E., A phase contrast refractometer with high accuracy for gases and liquids . . . . . 287—316
30. Kristiansson, K., A radioactive altimeter for stratosphere balloons . . . . 317—319
31. Brogren, G., The X-ray diffraction from quartz and the influence of surface treatment . . . . . 321—334
32. Carlbom, L., Determination of the diffusion length of thermal neutrons in graphite . . . . . 335—348
33. Eriksson, H. A. S., Space reflection, time reversal and charge conjugation of spinor fields . . . . . 349—358
34. Kleman, B. & Werhagen, E., A $^2\Delta-^2\Pi$ system in germanium hydride (GeH) 359—367
35. Johansson, C. H. & Ljungberg, S., Influence of air pressure on the velocity of ejected explosion gases . . . . . 369—373
36. Pucher, W., Negativer Durchschlag von Luft in der Funkenstrecke Kugel–Platte bei Stosspannungen . . . . . 375—382
37. Pucher, W., Form der Negativen Vorentladung in Luft bei Atmosphärendruck für Stosspannungen . . . . . 383—393
38. v. Friesen, S. & Leide, G., A release mechanism for cosmic-ray-balloon experiments . . . . . 395—397
39. Kleman, B. & Werhagen, E., A $^4\Sigma^- - ^2\Pi$-system in germanium hydride (GeH) 399—406
40. Kleman, B. The 2700 Å-system in the band-spectra of AlH and AlD . . . 407—414
41. Slätis, H., A semicircular permanent magnet beta-ray spectrograph for photographic recording of conversion lines . . . . . 415—436
42. Vassy, A., Norinder, H. & Vassy, E., Etude spectrophotométrique d'étincelles de grande longueur dans l'air . . . . . 437—450
43. Hjalmar, E. & Slätis, H., A study of the (αp)-reaction in nitrogen by means of photographic emulsions . . . . . 451—462
44. Ingelstam, E. & Djurle, E., Phase contrast measurements of the ruling structure of optical gratings. II . . . . . 463—476
45. Erlandsson, G., Microwave spectrum of fluorobenzene . . . . . 477—478
46. Brogren, G., Concerning the possibility of using ground calcite crystals as X-ray gratings . . . . . 479—490
47. Erlandsson, G., Preliminary analysis of the microwave spectrum of formic acid 491—495
48. Sjöstrand, N. G., The influence of a cadmium sheet on the distribution of neutrons in graphite . . . . . 497—512
49. Nilsson, Å., A precision determination of the K excitation potential of some $3\,d$ elements . . . . . 513—592

ARKIV FÖR FYSIK Band 6 nr 1

Communicated 9 January 1952 by G. Borelius and H. Alfvén

Some measurements on the absorption of 75—200 keV electrons in aluminium

By Ingvar Carlvik

With 14 figures in the text

Abstract

Absorption curves in aluminium have been measured for monoenergetic electrons in the energy interval 75–200 keV, using mica-window G. M. counters as detectors. The measurements have been made with two different geometrical arrangements. The geometry does not seem to influence the general shape of the curves very much, except for the thinnest absorbers. The results are compared with existing range-energy relations.

1. Introduction

The range-energy relationship of β-rays in aluminium is given by the well-known equation of Feather for energies down to 0.7 MeV, but for lower energies it is less well established. Under 200 keV there are rather few measurements on the absorption of β-rays, and the range-energy relation is, in this region, mainly based on the practical ranges of Schonland (1) for homogeneous electrons. Schonland measured the electron currents with galvanometers. The present investigation was undertaken because it seemed interesting to make new measurements with G. M. counters on homogeneous electrons.

2. The accelerator

The electrons were accelerated in a small accelerator for 200 keV, which has been built at the Department I of Physics, Royal Institute of Technology, Stockholm.

A drawing of the acceleration tube is shown in Fig. 1 and a photograph of it in Fig. 2. The acceleration tube consists of four porcelain insulators with electrostatic lenses between them. It supports the high voltage electrode, which contains the electron gun, voltage sources for the electron gun, and variable transformers for varying the voltages. The transformers can be adjusted by means of cords from the control panel, and the power is supplied by an insulated transformer.

The electron gun consists of a tungsten filament, a first anode, which is at the same time a magnetic lens, and a second anode.

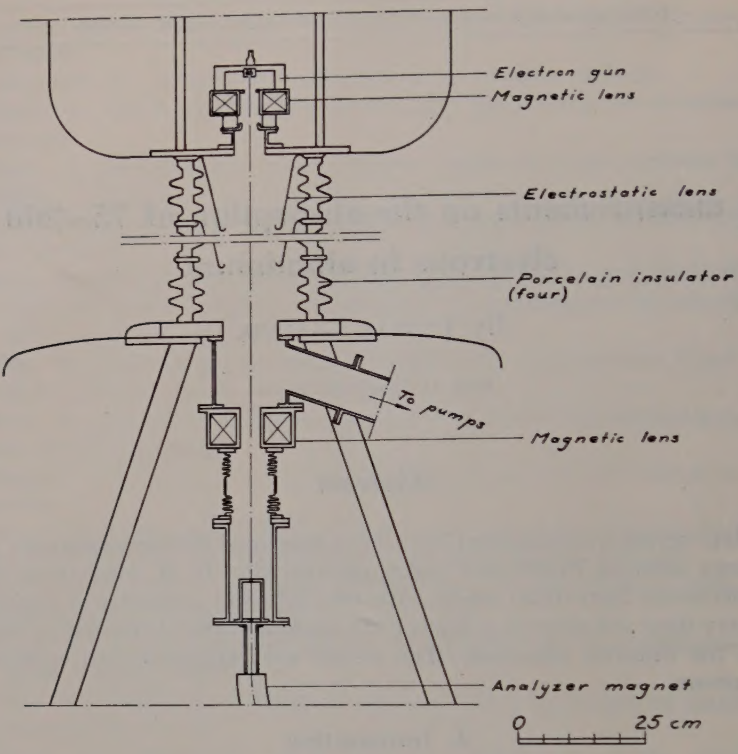

Fig. 1. The accelerator.

The high voltage is supplied by a Cockcroft and Walton set which gives 200 kV and a maximum current of 5 mA.

The acceleration tube is evacuated by a mechanical pump and an oil diffusion pump in series. A similar pair of pumps is used to evacuate the vacuum system after the analyzer, because of the low pumping speed through the analyzer deflection tube.

The voltage is not stabilized. It varied a little from time to time, so it had to be adjusted by hand throughout each measurement.

3. The resistor

The voltage is measured by means of a resistor consisting of 50 wire-wound resistors of 10 MΩ each, which are mounted in two identical tubes, with 25 resistors in each tube. The resistors are cooled by transformer oil, which is circulated through the tubes. The total resistance has been measured by using a bridge method, and referred to two standard instruments and two standard resistances (Fig. 3) at different temperatures. The resistance as a function of the temperature is plotted in Fig. 4.

When a voltage measurement is being made the temperature of the oil is measured before and after passing the resistor. The difference between the two temperatures

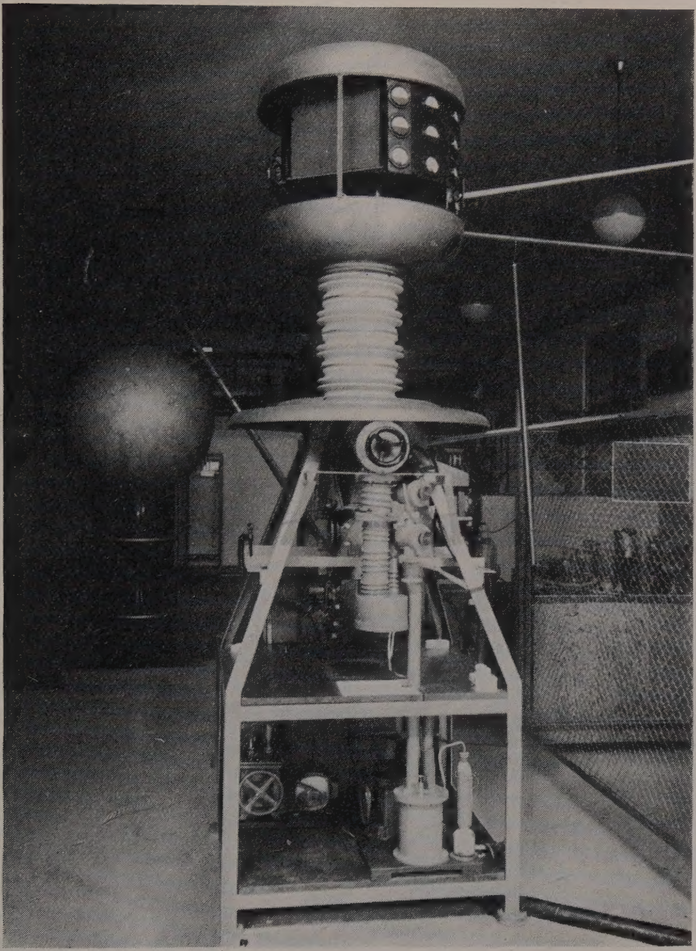

Fig. 2. General view of the accelerator.

s some tenths of one degree centigrade. The resistance is corrected for the change n temperature by means of the curve in Fig. 4.

The accuracy of the resistance measurement is about 1.0 MΩ (0.2 %) and the alibrated μA-meter is accurate to 0.5 μA. This gives a maximum error in the oltage measurement of 0.7 kV for 200 kV.

4. The analyzer

Since the voltage was not stabilized, and had a ripple which varied with the urrent, a 90° analyzer was used (Fig. 5 and 6) in order to get a well-defined nergy. It was built for a rather high resolution, because the intensity was expected o be sufficiently high.

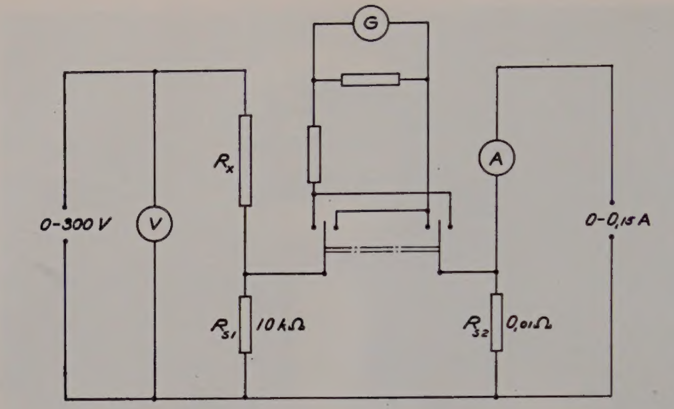

Fig. 3. The bridge for measuring the voltmeter resistor. If the current in the amp.meter is I and the voltage over the voltmeter is V the balance condition is

$$I \cdot R_{s2} = \frac{V \cdot R_{s1}}{R_x + R_{s1}} \approx \frac{V}{R_x} \cdot R_{s1}$$

which gives

$$R_x = \frac{V}{I} \cdot \frac{R_{s1}}{R_{s2}} = 10^6 \cdot \frac{V}{I}.$$

The galvanometer could be reversed to correct for any thermoelectric potential differences in the connections to the standard resistors.

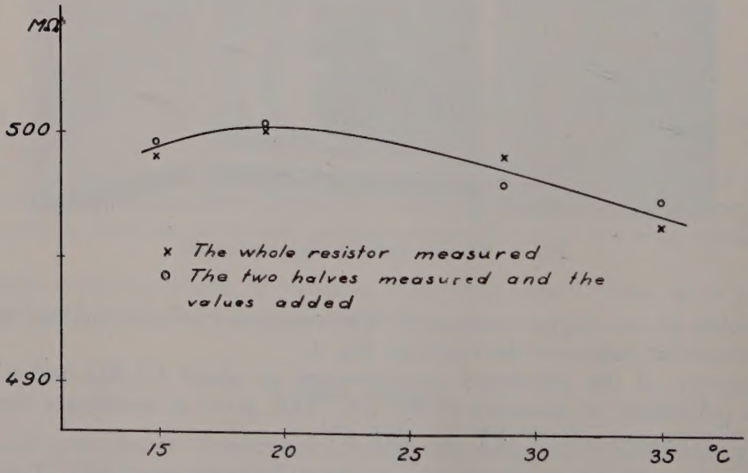

Fig. 4. The resistance of the voltmeter resistor versus temperature.

The radius of the electron path in the magnet is 300 mm, and the electron beam is defined by a collimator consisting of two circular apertures of graphite. They have a separation of 80 mm and the diameters are 0.5 and 1.0 mm. In the plane, where the image of the smaller aperture is formed, after the magnet, there is a hori-

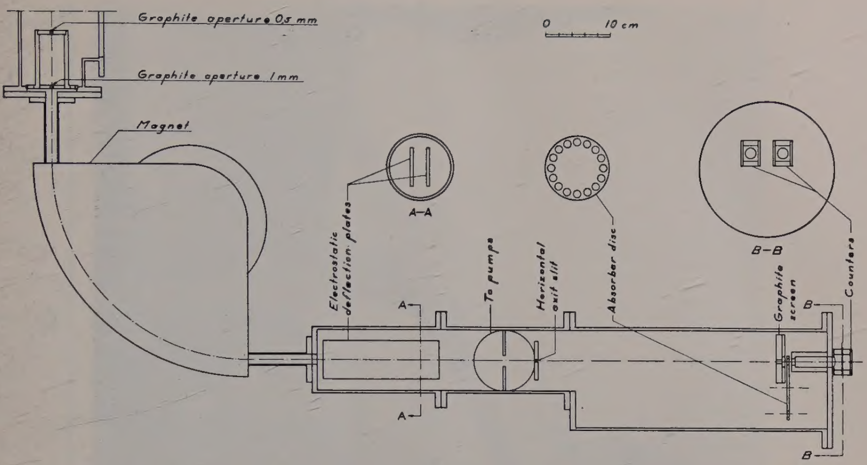

Fig. 5. The analyzer and the measuring arrangement. The absorber disk in front of the monitor is not shown.

zontal exit slit, 0.5 mm wide, which is also of graphite. The position of this slit is not very critical, since the distance between the holes defining the beam is so great.

This geometrical arrangement gives a theoretical energy spread of 0.3%.

With the radius of 300 mm the magnetic field necessary for 200 keV electrons is only 55 gauss. Although the magnet is made of iron of low remanence, the remanent field is quite noticeable in comparison with this weak field. To get a reproducible relationship between the energy and the current, when adjusting the current, it was necessary to follow a fixed scheme. The current was always increased from zero to the desired value. When the field was to be decreased, the current was first increased to 15 mA, then switched off and increased from zero again. This procedure was repeated several times if necessary to get reproducibility.

If the magnetic field strength is assumed to be

$$B = B_0 + k_1 \cdot i$$

where i is the current, and B_0 is the field strength when the current is zero, the connection between the energy of the electron and the magnetizing current should have the form

$$i = k \sqrt{W(W + 2W_0)} - i_0$$

where k and i_0 are constants, W is the kinetic energy and W_0 is the energy corresponding to the rest mass of the electron. In Fig. 7 the experimental values are plotted together with a curve calculated taking the values of the two constants which give the best fit. The curve shows that the equation assumed for the field strength is satisfactory.

A constant current was supplied to the analyzer coil from a storage battery.

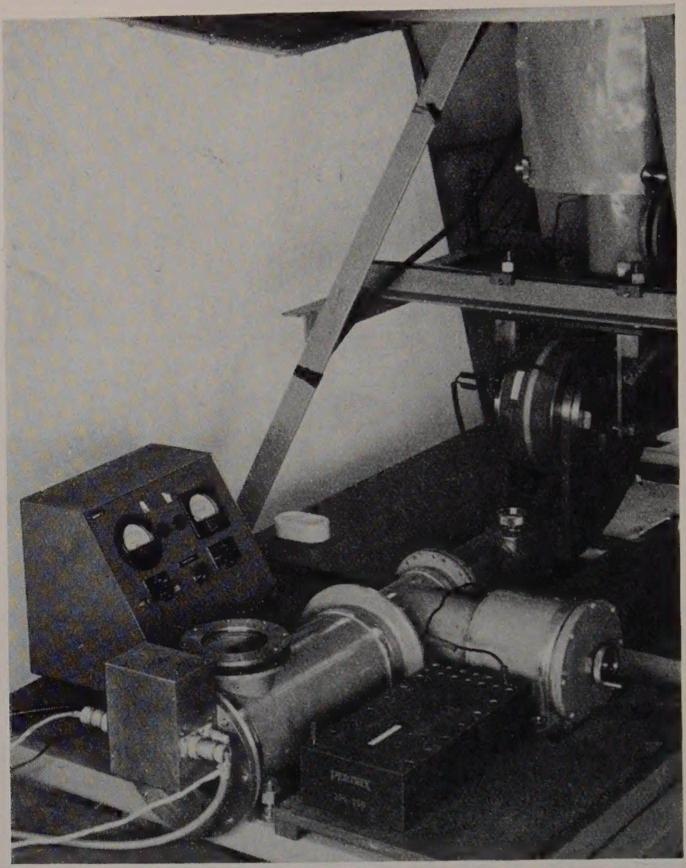

Fig. 6. The analyzer and the measuring arrangement.

5. The electrostatic deflection

To make the measurement independent of variations in the electron emission, or in the focusing, the electron beam was forced to oscillate between two counters, one of which was used as a monitor. The beam passed between two parallel vertical plates, to which convenient voltages could be given. One was coupled to a voltage which was adjusted so that the beam fell exactly midway between the two counters, and the other was given an alternating voltage from a specially built oscillator, giving a pure sinusoidal wave form. It had a frequency of about 185 p/s and its amplitude could be varied from 0 up to 2500 volts. The plates can be seen in Fig. 5.

The beam passed through the electrostatic deflecting field just after the magnet and before it came to the horizontal exit slit of the analyzer. The apparatus was built in this way so that it would not be too long. It was important with this design that the field and the exit slit should be exactly parallel. When making this adjustment the intensity variation with electron energy was studied, and the deflecting plates were adjusted until this variation was the same for the two counters. An example of this adjustment is shown in Fig. 8.

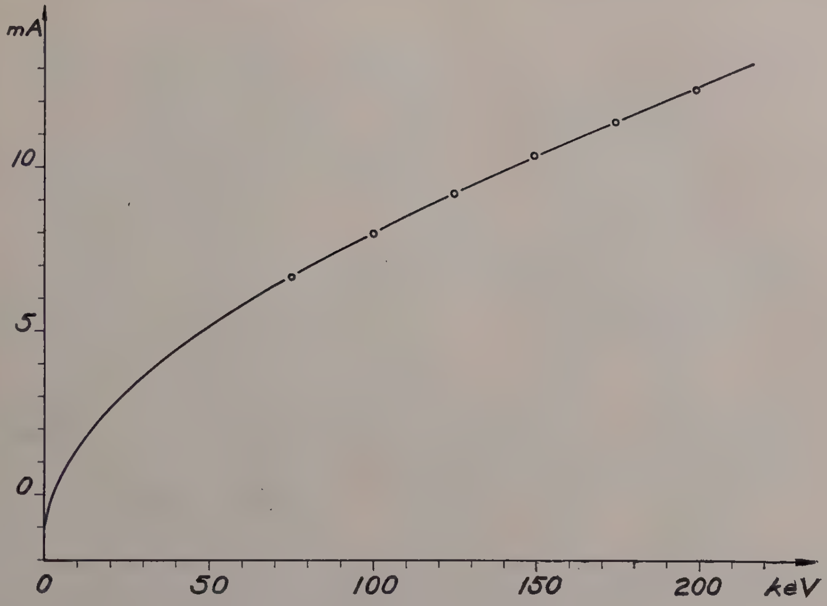

Fig. 7. The magnetizing current versus electron energy. The points are experimental. For calculation of the curve, see text.

6. The absorbers

As absorbers aluminium foils of different thicknesses were used. A set of absorbers was mounted over holes cut near the rim of a brass disk of 4 mm thickness (Fig. 5). Disks with different sets of absorbers were used for the different energies studied. The absorber thicknesses were chosen to give suitable points on the curves. The diameter of the absorbers was 10 mm. The thicknesses were determined by weighing. The absorbers were in general built up by mounting several thinner foils together.

Because the transmission variation was of the order of 10^6, it was necessary to vary the sensitivity of the monitor. This was done with another, smaller, disk with 6 different absorbers, mounted in front of the monitor. Three disks of this kind were used, each being suitable for a different range of energies.

Both the disks could be turned by means of shafts passing through ground joints in the walls of the vacuum system.

In front of the absorber disk a graphite screen was placed, provided with two holes of 6 mm diameter through which the beam passed to the absorbers. Behind this graphite screen was a shield of lead 2 mm thick to absorb any X-rays from the graphite screen, or from any other part of the analyzer.

7. The counters

After passing the absorber the electrons were counted in two cylindrical G. M. counters. These were made of brass and had glass ends (see Fig. 9), the gas filling being argon with 10% alcohol. The mica window and the glass plates in the ends were

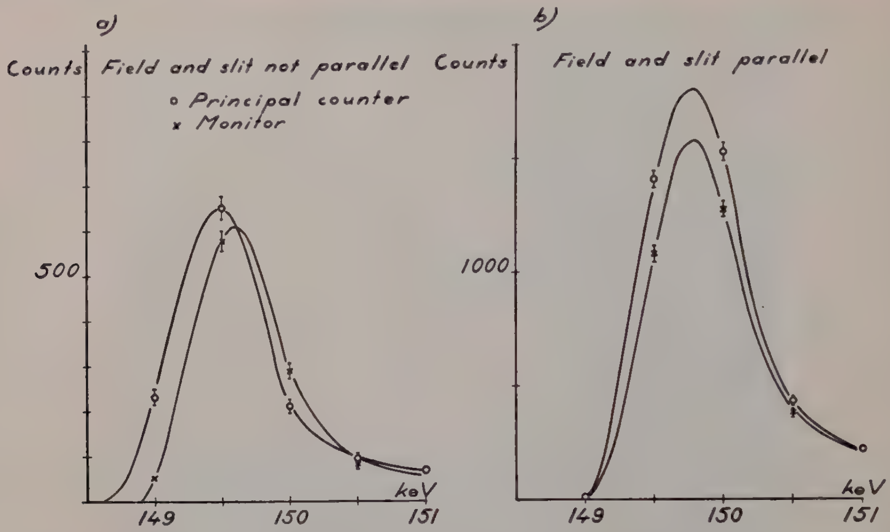

Fig. 8. Adjustment of the electrostatic deflection plates. The counting rate in each counter is plotted versus electron energy. In a) the deflecting field is not parallel with the exit slit but in b) the plates are adjusted to parallelism.

sealed to the brass tube with araldite. The same two counters (window thickness 2.9 mg/cm^2 for each) were used during the whole investigation.

The pulses were counted by two units, each of which consisted of a cathode follower, a scale-of-64, and a mechanical recorder.

8. Geometry

The absorption curves were measured with two different geometrical arrangements, which are shown in Fig. 9. In geometry I the distance beween the absorber and the counter is 75 mm and in geometry II this distance is 3 mm. The diameter of the counter window is 15 mm. These figures mean solid angles of about 0.5 % and 65 % of 2 π.

In geometry I, as can be seen in the figure, there was a graphite cylinder between the absorber and the counter, to prevent scattered electrons, which had not passed through the absorber, from being counted. The effect of this cylinder will be discussed in more detail later.

9. Measuring procedure

When an absorption curve was to be measured, the magnet current of the analyzer was first adjusted to the proper value for the energy chosen. The constant deflection voltage was then fixed so that the counting rate in the two counters varied quite symmetrically with the amplitude of the alternating deflection voltage. This meant that the deflection of the earth's magnetic field was compensated, and that the beam fell exactly between the two holes in the graphite screen. The amplitude

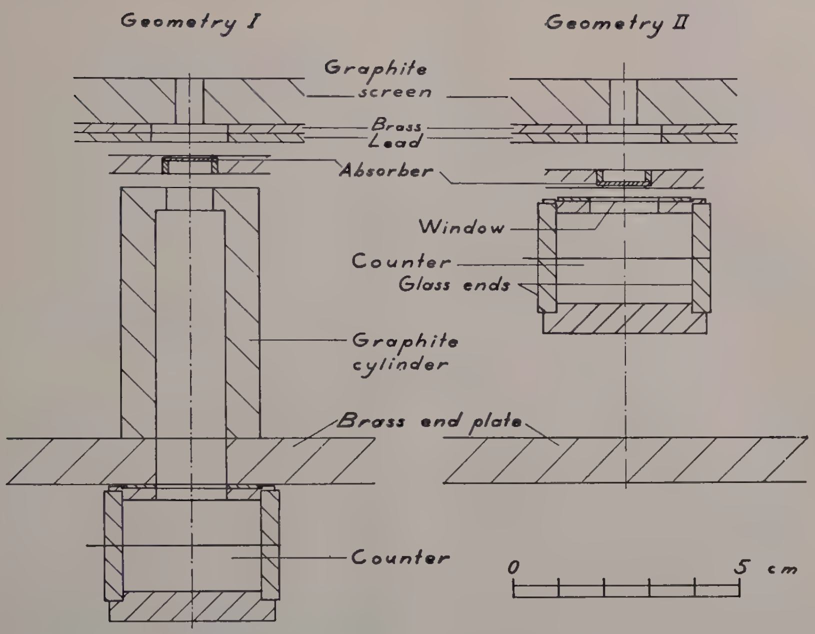

Fig. 9. The two geometries.

of the alternating voltage was then chosen so that the beam just crossed over each hole before it turned back.

The resolving time of the counters was about 200 μsec, but when correcting the counting rate for the resolving time, one had to take into account the fact that the beam did not fall on each counter more than during a part of the period, so that the true counting rate in the pulses was larger than the measured mean counting rate by a certain factor. This factor could be determined in two ways. One was to calculate it from a knowledge of the sweep amplitude and the geometry of the graphite screen. The other was to look at the pulses on an oscilloscope the sweep of which was synchronized to the oscillation frequency. It was then possible to determine the part of the period during which the pulses came. These two methods gave the same result. The correction for the resolving time was seldom more than 1 %, corresponding to a counting rate of about 500 c/min. The correction was of course applied, but as the beam intensity could vary during a measurement with one absorber it was better to avoid too high counting rates.

When the transmission was such that the counting rate of the main counter was about one tenth of that of the monitor, the absorber in front of the monitor was changed, and the beam intensity increased. The change-over points were measured especially carefully.

10. The resolution of the analyzer

To examine the resolution of an analyzer one measures the counting rate, either as a function of the magnet current at constant energy, or as a function of the energy with the magnet current held constant. It was a little laborious to vary

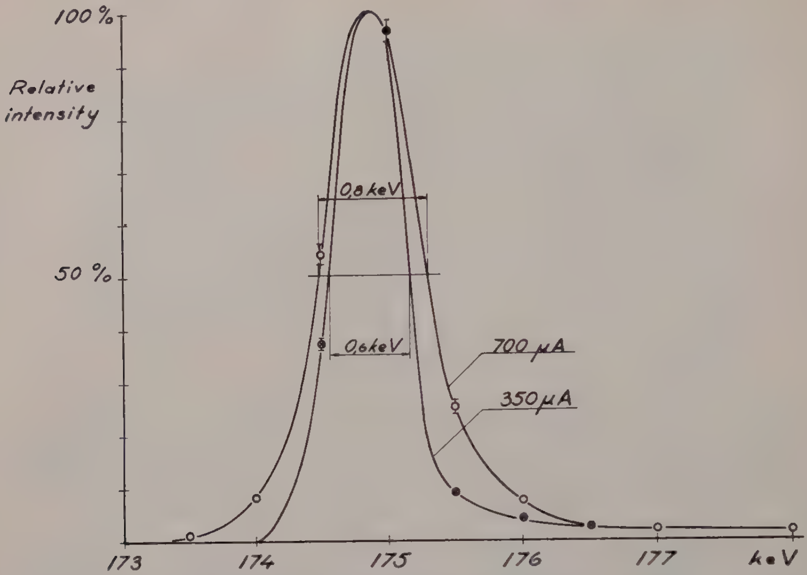

Fig. 10. The resolution of the analyzer. The counting rate (normalized to the same height for both curves) is plotted against electron energy for a constant magnetizing current. The curves are for two different load currents from the high-voltage generator, 350 µA and 700 µA.

the magnet current, for the scheme earlier described had to be followed, so the second method, with varying energy, was used. In Fig. 10 the counting rate is plotted against the voltage at a magnetic field corresponding to 175 keV. The beam intensity varied a little during the measurement, but it was verified that the variation was not excessive by measuring the counting rate first for increasing and then for decreasing voltage. Two curves are shown in the figure, corresponding to two different total currents from the high voltage source, 350 µA and 700 µA. At about 180 kV there is another peak in the two curves. At this voltage the first anode is at 175 kV, and the secondary electrons from it can pass the analyzer.

From the diagram, the half-widths of the two curves are about 0.35 % and 0.45 %. A simple calculation of the ripple, with a 0.01 µF output condenser, gives for the total ripple 0.4 % and 0.8 % respectively. Thus the ripple cannot be responsible for the whole width of the curves, but the resolution of the analyzer must also have an appreciable influence. The energy band from the accelerator may also have been broadened a little by collisions with gas molecules in the acceleration tube.

The energy band which could pass the analyzer at this energy had thus a half-width of at the most 0.3 %, and was probably smaller.

11. Results

Absorption curves were measured, with the two geometries, at 6 different energies: 74.9, 99.7, 124.4, 149.0, 173.9 and 198.8 keV. In the figures they are marked 75, 100, 125 and so on. Fig. 11 shows these twelve curves. The transmission (proportional to the ratio between the counting rates in the main counter and the monitor)

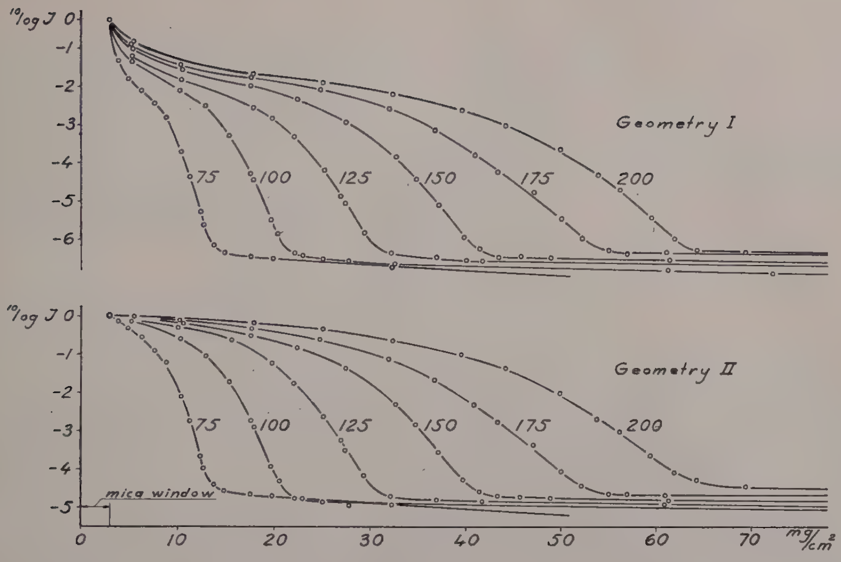

Fig. 11. Absorption curves. The counting rate is plotted in a logarithmic scale versus absorber thickness. There are one or two more points on each curve far to the right outside the range of the figure which give the slope of the right-hand parts of the curves. The statistical errors can hardly be seen on this logarithmic scale. For most values they are smaller than the circles marking the point.

has been plotted on a logarithmic scale against the absorber thickness. The window of 2.9 mg/cm^2 mica has been assumed to correspond to 2.9 mg/cm^2 Al, and has been included in the absorber thickness. The total variation in the intensity is seen to be of the order 10^6.

The intersection of the curves for 74.9 and 99.7 keV, with geometry II, is due to the window thickness. The transmission has arbitrarily been put equal to 1 for all energies, when there is no absorber except the window. In geometry II the absorber is very near the window, so that it can be assumed that the window has the same effect as if it were situated in the absorber position. The curves could thus be extrapolated back to zero and the transmission put equal to 1 in that point. In that case the intersection would disappear, as can easily be seen in the figure. This has not been done however, for it would be quite meaningless to extrapolate the curves with geometry I, and it was considered to be an advantage that the curves should be directly comparable.

The graphite cylinder in geometry I, which was mentioned earlier, was included to prevent scattered electrons from passing outside the graphite screen to the counters. Fig. 12 shows the effect of the cylinder. The upper three curves belong to the energy 99.7 keV and the lower curves to 198.8 keV, I and II mean geometry I and II, as before, and the curves III were measured with geometry I but with the graphite cylinder removed. The right parts of the curves are rather similar. There are, however, some more points to the right outside the range of the figure, the farthest at an absorber thickness of about ten times that marked R in the figure, and they show that curves I and II have a definite slope, the same for the same energy, but that this part of the curves III is horizontal.

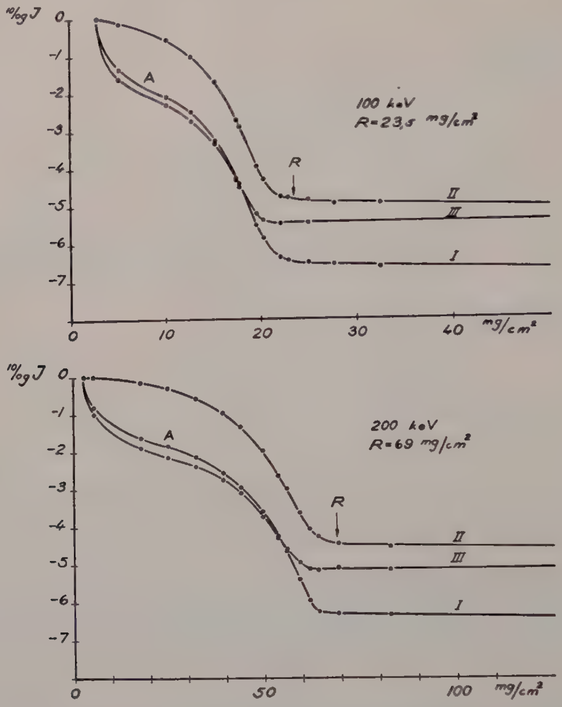

Fig. 12. Absorption curves for 99.7 and 198.8 keV, with counting rate plotted on a logarithmic scale. I: geometry I; II: geometry II; III: geometry I with the graphite cylinder removed.

It can be concluded that the horizontal part of curves III must be due to some radiation which had not passed the absorber. This might be X-rays, from the graphite screen for example, but as it could be reduced strongly by the cylinder it must have been scattered electrons which had passed outside the graphite screen.

The number of the scattered electrons can be estimated from curve III. The ratio between the counting rate for zero absorber and the constant counting rate for a thick absorber is between 10^5 and 10^6. This is the ratio between the number of electrons that pass the hole in the graphite screen and the number of scattered electrons that enter the counter. About one sixth of the total number of electrons incident upon the screen pass the hole. Thus for about 10^6 incident electrons one scattered electron enters the counter without passing the absorber.

There is still the question of whether any scattered electrons are counted when the cylinder is in position. Their number must be less than the counting rate for the thickest absorber used, i.e. at most of the order of one fifth of the counting rate at R in the figure. If there are any, they can have very little influence on the curves.

The cylinder had another influence which must also be considered. As well as preventing electrons which had not passed the absorber from being counted, it at the same time reflected back some electrons, which were scattered by the absorber out of the counter solid angle, in such a direction that they could still reach the counter. This explains why curve I lies a little above curve III in the beginning, although the difference grows smaller as the absorber thickness increases. Thus a curve, which follows curve III in the beginning and curve I in the end, would correspond best to the ideal geometry I.

The curves in Fig. 11 have not been corrected for this effect, the magnitude of which can be seen in Fig. 12. It does not influence the general shape of the curves very much, and in particular it does not affect the ranges that can be determined from the curves. It is only when the absolute intensities in the two geometries shall be compared that this correction has any importance.

12. Discussion

a) *The influence of the geometry*

The geometry dependence can be seen best in Fig. 12. If curve II in either of the two diagrams is compared with the combination of I and III mentioned above, it is evident that their shapes are rather similar. There is, however, a great difference at the lowest absorber thicknesses, where complete diffusion has not yet been reached. In geometry I the whole beam can enter the counter when there is no absorber. When the absorber thickness is increased the intensity falls very fast at first, because the electrons in the originally parallel beam are scattered, so that after a certain absorber thickness the counter receives a portion of the beam corresponding approximately to the solid angle subtended by its window. After that point (A in Fig. 12) the curves are almost parallel. They give the same range R (definition below).

The intensity ratio between the counting rates in geometry I and geometry II can be seen from Fig. 12 to be about 60. For the solid angles the corresponding ratio is about 130. The difference is probably due to an insensitive region in the counter just inside the window. Such a region round the window edge with a depth of one or two mm would lower the solid angle in geometry II sufficiently to give the observed difference. In geometry I there may also be some scattering into the counter by the brass end plate in the same manner as by the graphite cylinder.

b) *Comparison with range-energy relations.*

Several relations between range and maximum energy for β-rays have been proposed with the object of making it possible to determine the upper limit of β-spectra by absorption measurements. They are either quite empirical or are based on theoretical considerations and fitted to experimental values.

Some examples, valid in at least part of the energy range here considered, are:

FLAMMERSFELD $$E = 1.92\sqrt{R^2 + 0.22\,R}\quad (\text{MeV, g/cm}^2) \tag{2}$$

GLENDENIN $$R = 0.407 \cdot E^{1.38}\quad (\text{MeV, g/cm}^2)\quad 0.15 < E < 0.8 \tag{3}$$

LIBBY $$R = \frac{1}{150} \cdot E^{5/3}\quad (\text{keV, mg/cm}^2)\quad E < 200 \tag{4}$$

GLENDENIN has also given a curve, covering a wide region of energy. Another such curve and a discussion of the different kinds of ranges is given by GLOCKER (5).

Two of these relations have been plotted in Fig. 13. The difference between the curves has no significance, as the experimental material on β-rays in this region is not very large. For example FLAMMERSFELD uses the following points for nuclear

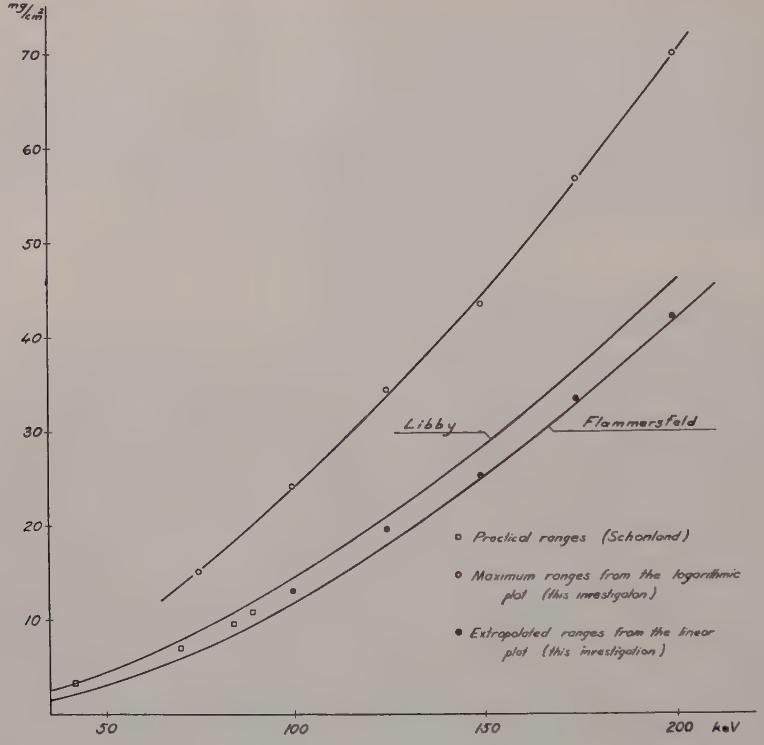

Fig. 13. Range-energy curves.

radiation under 200 keV: Ag^{109} and Ag^{107} (93.5 and 88.4 keV, 11 and 9 mg/cm²) and Br^{80} (47.2 keV, 2.7 ± 0.3 mg/cm²).

For determining the energy by a range measurement it is postulated that there is a certain quantity, for example the extrapolated range, that has a definite correlation with the mean range of electrons of a given energy. Only two kinds of ranges will be considered here.

Generally the maximum range, or end point, is used. It is defined as that point on the absorption curve at which there are no longer any particles observed above the background, or in other words that point, where the logarithmic absorption curve takes on the constant slope of the X-ray absorption. This point is marked R in Fig. 12.

For homogeneous electrons, e.g. internal conversion electrons, the plot should be linear in intensity, according to GLENDENIN, and the extrapolated range R_e should be used. GLENDENIN says that this method is applicable to energies above 0.2 MeV, but that the plot is too curved at lower energies for an extrapolation to be done.

The absorption curves for geometry II are plotted with a linear intensity scale in Fig. 14. It can be seen that they are rather straight over a considerable range, except for the lowest energy, 74.9 keV, and thus they show that extrapolation is possible down to 100 keV, if sufficient intensity is available.

Both kinds of ranges, maximum range from the logarithmic diagram (R) and

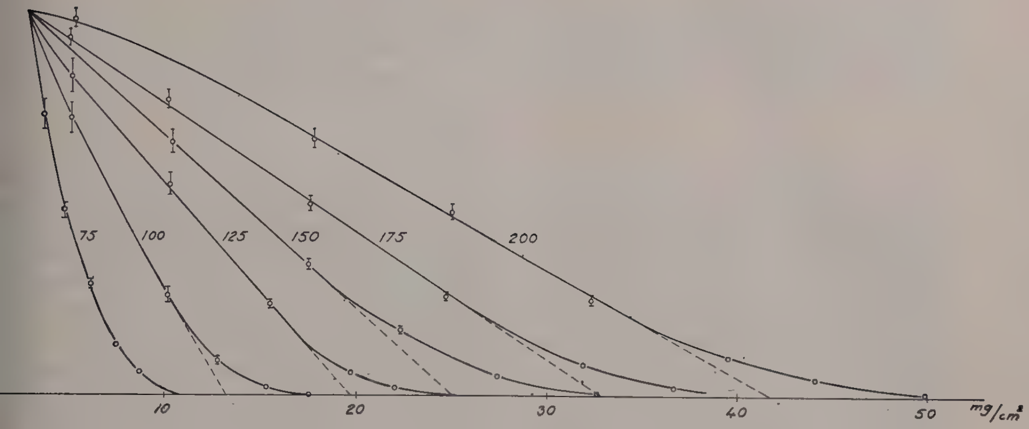

Fig. 14. Absorption curves for geometry II with linear scale for the counting rate.

Table 1

Energy keV	R_e mg/cm²	R mg/cm²
74.9		15
99.7	13	23.5
124.4	19.5	34
149.0	25	43
173.9	33	56
198.8	41.5	69

R_e: extrapolated range from the linear plot.
R: maximum range from the logarithmic plot.
R_e and R are determined to 0.5 mg/cm². The maximum error in the energy is 0.7 keV.

extrapolated range from the linear diagram (R_e), are given in Table I. They are plotted in Fig. 13.

The experimental points of SCHONLAND (1) in this energy interval are also plotted n Fig. 13. They are used as standard points for most range-energy relations. Schonand measured the currents that were reflected from the absorber, absorbed in it, and transmitted. From his diagram of the transmission as a function of the absorber thickness he determined the "practical range" by a straight line extrapolation.

It can be seen in the diagram (Fig. 13) that the measured R_e:s fall well on the curves. This means to begin with that they agree with the results of Schonland. They also verify the assumption that R_e for homogeneous electrons and R for nuclear β-rays (if the maximum energy of the β-rays is considered), are equal, in so far as the curves actually show the maximum range of β-rays.

The measured maximum ranges are longer by a factor of about 1.7, and that hey are so much longer shows that such ranges must be measured very carefully. The maximum range is dependent on the ratio of the number of electrons of the highest energies to the intensity of the X-ray background. For a β-spectrum this ratio must be dependent on the form of the spectrum.

In this investigation the ratio was very high, and the measurements show that under such conditions the measured maximum ranges can be very long.

13. Acknowledgements

This investigation was performed at the Royal Institute of Technology, Department I for Physics. The author wishes to express his gratitude to Professor GUDMUND BORELIUS, the director of the department, and to Dr. SIGVARD EKLUND, who suggested the subject and gave valuable advice throughout the experiment. His thanks are also due to Mr. PER ÖHNELL, who took part in the design of the accelerator, and to Mr. BERTIL HAGLUND, who assisted in the measurements.

The financial costs of this work were covered by the Swedish Atomic Energy Commission.

REFERENCES. 1. **Schonland B. F. J.,** Proc. Roy. Soc. (London) *A 104*, 235 (1923); *A 108*, 187 (1925). — 2. **Flammersfeld A.,** Z. Naturforschung *2 A*, 370 (1947). — 3. **Glendenin L. E.,** Nucleonics *2*, 12 (1948). — 4. **Libby W. F.,** Anal. Chem. *19*, No. 1, 2 (1947). — 5. **Glocker R.,** Z. Naturforschung *3 A*, 147 (1948).

Tryckt den 10 oktober 1952

Uppsala 1952. Almqvist & Wiksells Boktryckeri AB

ARKIV FÖR FYSIK Band 6 nr 2

Communicated 23 April 1952 by M. SIEGBAHN and E. HULTHÉN

The intensity anomalies in the band-spectrum of CuH

By BENGT KLEMAN

With 3 figures in the text

The band-spectrum of CuH has been photographed when excited at low pressure in a hollow cathode discharge. Intensity anomalies of the same type as was found in the (0–0) band of $^1\Sigma^* - {}^1\Sigma$ by SCHÜLER and GOLLNOW (1) are shown to be present in the bands belonging to the $^1\Sigma^* - {}^1\Sigma$ and $^1\Sigma^{**} - {}^1\Sigma$ systems. The anomalous intensity distribution in the bands of $^1\Sigma^* - {}^1\Sigma$ is interpreted as being due to a predissociation of $^1\Sigma^*$, and the distribution in $^1\Sigma^{**} - {}^1\Sigma$ as being due to accidental predissociations in $^1\Sigma^{**}$. The non-appearance in the hollow cathode discharge of the bands originating from the $^1\Pi$-states (of about equal energy with $^1\Sigma^*$ and $^1\Sigma^{**}$) is also assumed to be due to predissociation.

Introduction

Various types of cooled hollow cathodes have been used to investigate the band-spectra of metal hydrides, especially by SCHÜLER and co-workers (2, 3, 4). The intensity distribution in a water-cooled hollow cathode is normally found to correspond to a Boltzmann distribution of 700–900° K, and in a liquid air-cooled one to somewhat lower temperatures. In the (0–0) band (4280 Å) of the $^1\Sigma^* - {}^1\Sigma$ transition of CuH a curious intensity distribution was discovered by SCHÜLER and GOLLNOW (1). The first or second line in each branch proved to be the most intense, and the intensity then rapidly diminished for the higher rotation lines. At very low pressures (1/100 mm Hg) the intensity of the line P_1 was predominant in the band, while the intensity of higher members quickly disappeared with increasing rotation quantum-number.

This anomalous intensity distribution the discoverers interpreted as being due to a special mechanism for the molecular formation in the hollow cathode whereby the molecule is formed in the zero-level of the ground state. Thus, according to them, on excitation only the lower levels of the upper state are populated and consequently the intensity is concentrated to the beginning of the band. HERZBERG and MUNDIE (5) later put forward an entirely different explanation. According to this, the intensity anomaly is due to a predissociation of the upper Σ-state. They suggested that this predissociation might be caused by a continuous $^3\Sigma^+$-term arising from the H and Cu atoms in the ground-states. The assumption of a $^3\Sigma^+$-term as the perturbing term also explains the strength of the line P_1 at the lowest pressures, since this is the only line which does not predissociate according to the Kronig selection rules. The same holds for the assumption of a perturbing $^1\Pi$-term, but this leads to a value of the energy of dissociation which seems much too low. The changing appearence of the band at higher pressures towards a more normal intensity distribution is explained by the pressure-effect of predissociation, assuming the radiationless transition probability to be about as large as the probability for transitions with radiation.

HULTHÉN (6) presumed that the intensity anomaly was caused by a predissociation of the upper state into the continuum of the $^1\Sigma$-ground-state.

REINEBECK (7), in 1946, made a more thorough experimental investigation. Among her more important results may be mentioned her finding of the same anomalous intensity distribution in the (0–1) and (1–2) bands of a second electronic transition $^1\Sigma^{**}-{}^1\Sigma$. The deutride was also investigated, and here the intensity distribution was found to be normal. Reinebeck interpreted her results in favour of the Schüler theory of molecular formation, and in the light of some special experiments she discussed the ability of hydrogen to adhere to a copper surface, since this ability was assumed to be responsible for the special process of molecular formation.

In his dissertation in 1948 NILSSON (8) made a new experimental investigation. He found no deviations from the normal intensity distribution in the CuH-related spectra of CuD, AgH and AuH. He judged the intensity in the (0–1) band of the $^1\Sigma^{**}-{}^1\Sigma$ transition to be normally distributed. Both these results he finds contrary to the theory of Schüler. The first, since the related molecules may be expected to be formed in the same way and thus to show the same type of anomalous intensity distribution. The second, since, if the intensity anomaly is due to the process of formation in the ground-state, it should turn up in the bands of every electronic transition. Nilsson consequently supported the theory of a predissociation phenomenon.

Discussion of the investigations by Reinebeck and Nilsson

The conclusions and experimental results of Reinebeck and Nilsson will now be somewhat further discussed.

The fact that CuD shows a normal intensity distribution is interpreted by Reinebeck to imply that the anomalous intensity of CuH can not be caused by predissociation, since in that case the same type of anomaly should be present in the deutride. As is pointed out by Nilsson, the predissociation of the 2033–band in AlH (9) has no counterpart in the deutride. Especially when the predissociation is as weak as that presumed in CuH, it is not certain that it will turn up in the deutride in the same pressure-range.

On the contrary, it is not in accordance with practical experience that such a physical interaction as that supposed by Schüler and Reinebeck between copper and hydrogen should be so radically different in the case of copper and deuterium as to entail different mechanical processes of formation.

Reinebeck and Nilsson are of different opinions concerning the intensity distribution in the (0–1) band of the $^1\Sigma^{**}-{}^1\Sigma$ transition. An original photogram taken by REINEBECK (10) shows the same type of anomalous intensity distribution as is present in the (0–0) band of $^1\Sigma^{*}-{}^1\Sigma$.

The intensity distribution in the (0–1) band of $^1\Sigma^{**}-{}^1\Sigma$ in the exposures of Nilsson is more doubtful. The intensity maximum of the P-branch seems to fall in the same place as it would do in a Boltzmann distribution normal for the bands from a

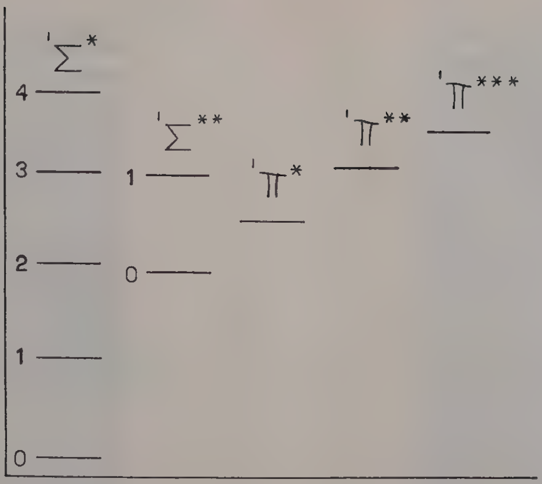

Fig. 1. The lower excited states of CuH.

hollow cathode discharge. As has been pointed out by SCHÜLER (10), however, it is necessary to take the whole branch into consideration in order to be sure that there is a normal intensity distribution, and not to judge too much from the first few lines. The later lines in the P-branch in the exposures of Nilsson seem to be too weak to correspond to a normal intensity distribution. In a normal Boltzmann distribution the lines up to P_{15}–P_{17} should be stronger than P_1.

The discrepancy in the appearance of the (0–1) band of $^1\Sigma^{**} - {}^1\Sigma$ in the exposures of Nilsson and Reinebeck may be explained by their different experimental conditions. Nilsson uses a water-cooled hollow-cathode with helium of the rather high pressure 2 mm as carrier gas, while Reinebeck uses a liquid air-cooled cathode with argon.

Reinebeck considers it unlikely that the same type of predissociation should occur in two different electronic states, and she regards her results as an important proof that the intensity anomaly is not caused by predissociation. It is not, however, improbable that $^1\Sigma^{**}$ is predissociated by the same continuous term that predissociates $^1\Sigma^*$. There are several excited states in CuH of about the same energy (Fig. 1) which perturb each other strongly. The level $v = 0$ of $^1\Sigma^{**}$, for instance, is perturbed by $v = 2$ of $^1\Sigma^*$ and also by a $^1\Pi$ term. A predissociation of $^1\Sigma^*$ and $^1\Sigma^{**}$ by the same continuous term is therefore not more improbable than a perturbation between $^1\Sigma^*$ and $^1\Sigma^{**}$. This point will be discussed more thoroughly later in this paper when the present experimental results have been described.

Experimental

A water-cooled hollow cathode of the Schüler—Gollnow type was used. As carrier gas helium, argon and neon were tried. With helium the hydride bands were weaker than with the other two gases, probably due to the less effective sputtering action of helium. The intensity anomaly seems also to be less pronounced with helium as carrier gas. With argon it was necessary to replace the liquid air-cooled charcoal

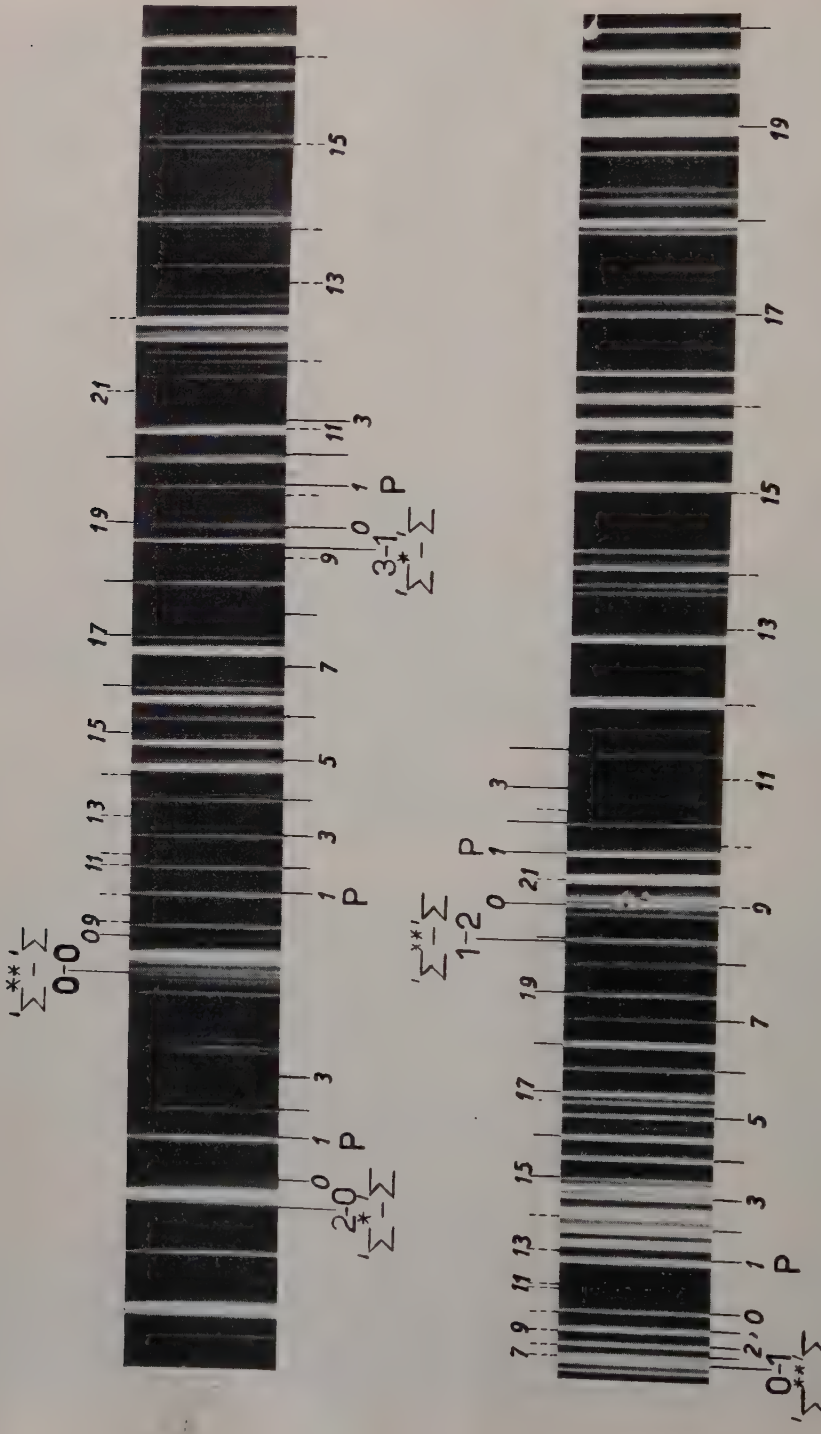
$'\Sigma^{**}-'\Sigma$ 0-0
$'\Sigma^{*}-'\Sigma$ 2-0
$'\Sigma^{*}-'\Sigma$ 3-1
$'\Sigma^{**}-'\Sigma$ 1-2
$'\Sigma^{**}-'\Sigma$ 0-1
P
0
1
3
5
7
9
11
13
15
17
19
21

Fig. 2. Part of the CuH spectrum from the hollow-cathode exposures in the one-meter concave grating. (With Ne of about 5/100 mm/Hg.)

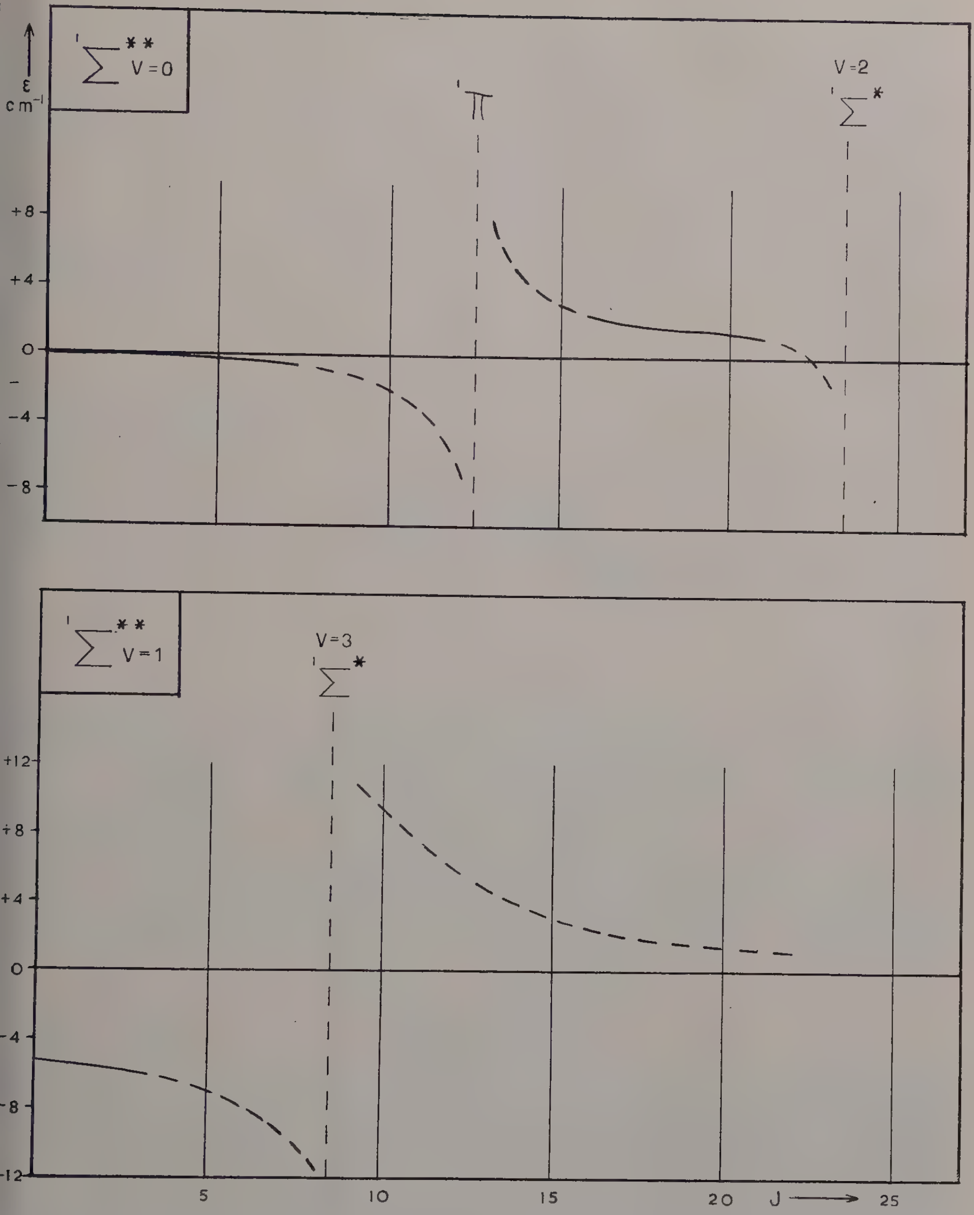

ig. 3. Perturbation figures after Heimer. The parts of the curves which contain levels giving ise to lines which appear at the lowest pressures in the hollow-cathode discharge have been drawn with full lines.

rap in the purifying circulation system with one cooled with dry ice. Because of this he exposures were not free from impurities. In the final exposures neon at a pressure f 1/100–5/100 mm Hg was used.

The voltage to the hollow cathode was supplied from a full-wave rectifier and was further smoothed out by a filter. The advantage of this arrangement as compared with the direct voltage from the line is that the voltage can easily be regulated to high values. When the discharge goes out the potential drop across the cathode increases greatly and consequently the ignition of the cathode is facilitated. This is of particular importance when low pressures are used.

Hydrogen was supplied from a bulb and the amount let in was 10–30 % of the carrier gas. The exposures were made on Ilford Zenith plates.

The spectrograph was a Zeiss glass spectrograph with three prisms. The spectrum was photographed from 3800 to 4700 Å. The dispersion around 4000 Å was about 6 Å/mm. On one of the strongest exposed plates the region between 3880–4250 Å was measured in a comparator and the wave-numbers calculated. The lines of CuH were identified by means of the measurements given by HEIMER and HEIMER (11, 12, 13).

On account of its mechanical construction it was not possible with this spectrograph to reach the region 3500–3800 Å, where the main $^1\Pi - ^1\Sigma$ bands are situated. The spectrum was therefore also photographed in a one-meter concave grating (dispersion 17 Å/mm, resolution 36 000). Ilford thin-film half-tone plates were used and the exposure times varied up to eight hours. The other experimental conditions were the same as when the glass-spectrograph was used. The wave-numbers for the lines in the region 3480–3890 Å were calculated.

$^1\Sigma^* - ^1\Sigma$

In this transition the bands (0–0), (1–0), (2–1), (2–0), and (3–1) can be identified on the plates. They all show the same type of intensity distribution with P_1 as the strongest line. In the weaker bands (2–1), (2–0), and (3–1) only the first 3–5 lines in each branch are to be seen. In the still weaker bands (3–2), (3–0), and (4–1) at least the line P_1 does seem to be present. It must, however, be said that the identification of a single line is rather uncertain on the strongly exposed plates.

It may be concluded that the bands emerging from the four or five lowest vibrational levels in the excited state $^1\Sigma^*$ all show the same type of anomalous intensity distribution.

$^1\Sigma^{**} - ^1\Sigma$

The bands (0–0), (0–1), and (1–2) have been identified. The intensity courses in (0–0), and (0–1) are similar. The first lines in the P and R branches are strong, but thereafter the intensity becomes weaker, and the lines R_7–R_{13} and P_9–P_{15} are extremely weak or completely missing. The lines R_{14}–R_{20} and P_{16}–P_{22} then turn up again with an intensity comparable to that of the first lines in the branches. The intensity then seems to drop again.

In the (1–2) band only the lines emerging from the first four rotational levels have been found. It shows the same falling curve in respect of intensity as the $^1\Sigma^* - ^1\Sigma$ bands with P_1 as the strongest line.

$^1\Pi - {}^1\Sigma$

There are three known $^1\Pi$-vibrational levels ($^1\Pi^*$, $^1\Pi^{**}$, and $^1\Pi^{***}$ of HEIMER (13)) situated in the term-scheme between $v = 2$ and $v = 4$ of $^1\Sigma^*$ (Fig. 1) which have not yet been satisfactorily related to electronic terms. No part of the five known bands emanating from these $^1\Pi$-terms has been identified with certainty on the hollow cathode exposures. A comparison between what is found of the $^1\Sigma - {}^1\Sigma$ bands on the present exposures and what has been registered by Heimer and Heimer in their exposures makes it probable that the $^1\Pi$-bands are weaker in the hollow cathode than in the arc.

Discussion

The observed intensity anomalies will now be explained from the assumption of a predissociation phenomenon.

We assume a low-lying continuous state, like the $^3\Sigma^+$ supposed by HERZBERG and MUNDIE (5), which goes beneath the level $v = 0$ of $^1\Sigma^*$. If a predissociation occurs in the level $v = 0$, it may be expected to occur also in the vibrational levels of $^1\Sigma^*$ lying nearest above it, in accordance with the observations.

As regards the other excited states of about the same energy, there is a great chance of their also being predissociated. The same selection rules as for a perturbation hold for predissociation, but the selection rule $\Delta J = 0$ can always be fulfilled in the continuous range. If it is known that $^1\Sigma^*$ is predissociated by a state which according to the selection rules may also predissociate the other states, there is a somewhat greater chance of finding a predissociation in a given one of these states than of finding a perturbation between this state and $^1\Sigma^*$.

From the analysis of the perturbations by Heimer (13) it is known that the two levels $v = 0$ and $v = 1$ of $^1\Sigma^{**}$ are perturbed by $^1\Sigma^*$. The level $v = 0$ of $^1\Sigma^{**}$ is also perturbed by a $^1\Pi$-state, probably a lower lying vibrational level of one of the directly observed Π-states.

There are therefore two predissociation-effects which may occur in $^1\Sigma^{**}$ and the Π-states. The whole vibrational levels may be predissociated as in $^1\Sigma^*$, or there may be an accidental predissociation in the regions of the perturbations. This latter effect is caused by the fact that in a perturbed region the eigen-functions of a state take on the properties of the perturbing state, and if this latter one is predissociated there will be a predissociation in the levels of the perturbation of the first state too.

The observations of the bands containing the vibrational level $v = 0$ of $^1\Sigma^{**}$ show that the state $^1\Sigma^{**}$ is not predissociated in the same way as $^1\Sigma^*$. Hence, since the strong interaction between $^1\Sigma^*$ and $^1\Sigma^{**}$ is known from the analysis of the perturbations, it is to be expected that the accidental predissociation between $^1\Sigma^*$ and $^1\Sigma^{**}$ in the regions of the perturbations should be shown in a loss of intensity. This seems to be established by the vanishing of practically the whole level $v = 1$ of $^1\Sigma^{**}$ and of the last rotational levels in $v = 0$.

The great reduction of intensity in the Π-perturbation in $v = 0$ of $^1\Sigma^{**}$ can be explained as an accidental predissociation if it is assumed that the Π-levels are predissociated.

This assumption seems to be strengthened by the non-appearance of the Π-bands in the hollow cathode discharge. It may be remarked that according to Heimer there is no visible reduction in intensity in the Π-perturbation when using an arc.

There is also another possible explanation of the intensity-reduction in the Π-perturbation. The extreme excitation-conditions may favour a transition to the $^1\Pi$-state. In this case the missing intensity should be found in transitions from this $^1\Pi$-state. It has not been found in the region of the (0–0), and (0–1) bands of $^1\Sigma^{**}$, but it cannot be stated with certainty that it is not there till the perturbation has been more fully analysed. In his analysis Heimer has not given any "extra lines." This latter explanation of the vanishing of the intensity seems, however, somewhat unlikely, since the known Π-bands do not appear, and it is more probable that this also is a case of accidental predissociation.

It is not possible on the basis of the existing experimental material to determine what state causes the predissociation, though the assumption of Herzberg and Mundie of a $^3\Sigma^+$ seems very plausible.

The work on the intensity anomalies of CuH will be continued when a current investigation of the spectrum of CuH from a King's furnace at this Institute is finished. It is especially hoped that this investigation will give fuller information about the perturbations and the Π-levels.

My thanks are due to Professor ERIK HULTHÉN and Docent BENGT E. NILSSON for placing at my disposal apparatus and experimental material used in earlier investigations of the same problem, and for helpful discussions.

Physical Institute, University of Stockholm, April 1952.

REFERENCES. 1. **Schüler, H., Gollnow, H.** Zeitsch. f. Physik, *108*, 714, 1938. — 2. **Schüler, H., Gollnow, H., Haber, H.** Zeitsch. f. Physik, *111*, 484, 1939. — 3. **Schüler, H., Gollnow, H., Fechner, E.** Ann. d. Physik, *36*, 328, 1939. — 4. **Schüler, H., Haber, H.** Zeitsch. f. Physik, *112*, 614, 1939. — 5. **Herzberg, G., Mundie, L. G.** Journ. Chem. Phys., *8*, 263, 1940. — 6. **Hulthén, E.** Ark. f. Mat. Astr. o. Fysik, *27B*, No. 5, 1940. — 7. **Reinebeck, L.** Zeitsch. f. Naturforschung, *2a*, 251, 1947. — 8. **Nilsson, B. E.** On the band spectra of the hydrides and deutrides of Cu, Ag, Au, Al. Dissertation, Stockholm 1948. — 9. **Grabe, B., Hulthén, E.** Zeitsch. f. Physik, *114*, 470, 1939. — 10. Private communication from Prof. H. Schüler to Prof. E. Hulthén. — 11. **Heimer, A., Heimer, T.** Zeitsch. f. Physik, *84*, 222, 1933. — 12. **Heimer, T.** Zeitsch. f. Physik, *95*, 321, 1935. — 13. —— Die Bandenspektren der Hydride und Deutride des Kupfers und Goldes. Dissertation, Stockholm, 1937.

Tryckt den 18 september 1952

Uppsala 1952. Almqvist & Wiksells Boktryckeri AB

ARKIV FÖR FYSIK Band 6 nr 3

Communicated 5 December 1951 by AXEL E. LINDH and I. WALLER

On the elastic constants of cubic ionic crystals

By STIG O. LUNDQVIST

The elastic constants c_{12} and c_{44} of cubic ionic crystals with ions having complete electron shells are investigated starting from the expression for the cohesive energy in the Heitler—London approximation. It is found that $(c_{44} - c_{12})$ is a function not only of the interionic distance and the overlapping but also of the relative size of the ions. For crystals with positive and negative ions of about the same size the deviations from the Cauchy relations must be expected to be very small. A new method of calculating c_{12} and c_{44} is developed and numerical applications have been carried out for NaCl.

In the classical theory of ionic crystals it was usually assumed that the ions have spherical symmetry and that the lattice energy can be expressed as a sum over the interaction energies between all pairs of ions in the lattice, the interaction between a pair of ions depending only on the distance between the nuclei. If this assumption were correct the three elastic constants c_{11}, c_{12} and c_{44} of a diatomic cubic lattice where each ion is a centre of symmetry would satisfy the Cauchy relation $c_{12} = c_{44}$. Accurate measurements on a number of ionic crystals have shown, however, that the Cauchy relations are actually not valid. A treatment of the elastic constants based on a general potential has been given by G. H. BEGBIE and M. BORN.[1] Later LÖWDIN[2] derived the expression for the cohesive energy in the Heitler—London approximation of an ionic crystal having complete electron shells and showed that because of the non-orthogonality of the atomic wave functions the interaction between the ions in the lattice is of a rather complicated many-body character.[3] He also computed the elastic constants of several alkali halides taking the non-orthogonality terms corresponding to many-body forces into account. The calculated values agree rather well with the empirical results; the deviations from the Cauchy relations have the correct sign but are too large. A comparison between the theoretical and the empirical values of the quantity $\frac{c_{44} - c_{12}}{\frac{1}{2}(c_{44} + c_{12})}$ for some alkali halides is given in the following table.

---

[1] G. H. BEGBIE, M. BORN, Proc. Roy. Soc., *188*, 179 (1947).

[2] P. O. LÖWDIN, Thesis, Uppsala 1948. Cf. also Arkiv f. mat. astr. o. fysik, 35 A, N:o 30, J. Chem. Phys., *18*, 365, (1950).

[3] Approximate expressions for the cohesive energy of ionic crystals, containing non-orthogonality terms formally corresponding to a many-body potential have earlier been derived by E. A. HYLLERAAS. Z. f. Phys., *63*, 771 (1930) and R. LANDSHOFF, Z. f. Phys., *102*, 201 (1936) but the importance of these terms for the elastic properties was not discussed by these authors.

Table of $2(c_{44} - c_{12})(c_{44} + c_{12})^{-1}$

Crystal	Theoretical value	Experimental value
LiF	0.41	0.32
LiCl	0.29	—
NaCl	0.43	0.29
KCl	0.45	0.11

The discrepancy between the theoretical and empirical values seems to be more pronounced as the positive ion increases in size. Supplementing Löwdin's discussion this paper presents some further considerations of the elastic constants as regards the deviations from the Cauchy relations. A new method of calculating the contributions to c_{12} and c_{44} from the terms corresponding to many-body forces will be described.

The elastic contants c_{ij} at absolute zero are defined by the formula

$$c_{ij} = \frac{1}{V_0}\left(\frac{\partial^2 E_{\text{coh}}}{\partial x_i \delta x_j}\right)_{x_i = x_j = 0}. \tag{1}$$

Here V_0 is the molar volume of the crystal under no stress, E_{coh} is the cohesive energy per mole of the strained crystal, and x_i, x_j $(i, j = 1 \ldots . 6)$ are the components of the strain.

Löwdin's expression for the cohesive energy of an ionic solid with ions having complete electron shells can, after some elementary transformations and summations over the spin coordinates, be written[1]

$$E_{\text{coh}} = E_1 + E_2 + E_3 + E_4 \tag{2}$$

$$E_1 = \frac{e^2}{2}\sum_g \sum_{g'}{}^{(g)} \left\{\frac{\varepsilon_G \varepsilon_{G'}}{r_{GG'}} + \varepsilon_G \frac{\omega_{g'}(r_{GG'})}{r_{GG'}} + Z_{G'} \frac{\omega_g(r_{GG'})}{r_{GG'}} - 2(g' g g')_\omega\right\} \tag{2a}$$

$$E_2 = -e^2 \sum_g \sum_{g'}^{(g)} (g g' g' g) \tag{2b}$$

$$E_3 = 2e^2 \sum_g \sum_{g'} \sum_{g''}^{(g)} p_{gg'} \{\varepsilon_{G''}(g' G'' g) + (g' g'' g)_\omega + (g' g'' g'' g)\} \tag{2c}$$

$$E_4 = e^2 \sum_g \sum_{g'} \sum_{g''} \sum_{g'''} p_{gg''} p_{g'g'''} \{2(g'' g''' g g') - (g'' g''' g' g)\}. \tag{2d}$$

The symbols used here have the following meaning. Z_G is the atomic number of the nucleus at a certain lattice point G, ε_G denotes the valency of the ion at the lattice point G, and e is the electron charge. The index $g = (G, \mu)$ refers to a certain electron orbital μ with the quantum numbers (n, l, m) of an ion at a certain lattice point G. $\sum\limits_g$ means a summation over all electron orbitals and lattice points and may be written $\sum\limits_g = \sum\limits_G \sum\limits_\mu^G$, where the suffix G indicates a summation over orbitals associated with the ion at the lattice point G. $\sum\limits_g^{(g')}$ means a summation over all orbitals except those associated with the ion at the lattice point G'. We will introduce the further convention $\sum\limits_g f(G) = \sum\limits_G f(G)$.

---

[1] Cf. S. O. LUNDQVIST–P. O. FRÖMAN, Arkiv f. fysik, *2*, 431 (1950).

The bracket symbols are defined by

$$(g\,G'\,g'') = \int \psi_g^*(\boldsymbol{r}) \frac{1}{|\boldsymbol{r} - \boldsymbol{r}_{G'}|} \psi_{g''}(\boldsymbol{r})\, d\boldsymbol{r}$$

$$(g\,g'\,g''\,g''') = \int\!\!\int \psi_g^*(\boldsymbol{r}_1)\, \psi_{g'}^*(\boldsymbol{r}_2) \frac{1}{|\boldsymbol{r}_1 - \boldsymbol{r}_2|} \psi_{g''}(\boldsymbol{r}_1)\, \psi_{g'''}(\boldsymbol{r}_2)\, d\boldsymbol{r}_1\, d\boldsymbol{r}_2$$

$$(g\,g'\,g'')_\omega = \int \psi_g^*(\boldsymbol{r}) \frac{\omega_{g'}(|\boldsymbol{r} - \boldsymbol{r}_{G'}|)}{|\boldsymbol{r} - \boldsymbol{r}_{G'}|}\, \psi_{g''}(\boldsymbol{r})\, d\boldsymbol{r}$$

$\psi_g(\boldsymbol{r})$ are the one-electron wave functions for the free ions and have the well known form

$$\psi_{n\,l\,m}(\boldsymbol{r}) = \frac{f_{n\,l}(r)}{r} S_{l\,m}(\vartheta, \varphi)$$

$S_{l\,m}(\vartheta, \varphi)$ are the normalized spherical harmonics.
$\omega_g(r)$ is defined by

$$\omega_g(r) = 2\left\{\int_r^\infty f_g^2(x)\, dx - r \int_r^\infty \frac{f_g^2(x)}{x}\, dx\right\}.$$

The quantities $p_{g\,g'}$ are the elements of a matrix $\boldsymbol{p}$ given by

$$\boldsymbol{p}\,(\boldsymbol{1} + \boldsymbol{s}) = \boldsymbol{s} \tag{3}$$

where $\boldsymbol{s}$ is the Hermitian matrix formed by the overlap integrals

$$s_{g\,g'} = \int \psi_g^*(\boldsymbol{r})\, \psi_{g'}(\boldsymbol{r})\, d\boldsymbol{r} - \delta_{g\,g'}. \tag{4}$$

In the expression (2), E_3 and E_4 correspond to a many-body potential of a ather complicated form. Therefore Löwdin introduced certain approximations nto his calculations. The overlap integrals $s_{g\,g'}$ associated with ionic crystals are n general rather small quantities and under certain conditions[1] it is possible to expand the matrix $\boldsymbol{p}$ in the series

$$\boldsymbol{p} = \frac{\boldsymbol{s}}{\boldsymbol{1} + \boldsymbol{s}} = \boldsymbol{s} - \boldsymbol{s}^2 + \boldsymbol{s}^3 - + \ldots \tag{5}$$

---

[1] Lundqvist–Fröman, l. c. p. 434.

Neglecting terms of third and higher orders in the $s_{gg'}$, LÖWDIN obtained an approximate expression for E_3 and E_4, which in our notation reads[1]

$$E_3 = 2e^2 \sum_{g} \sum_{g'}^{(g)} s_{gg'} \left\{ \sum_{g''}^{(g)} \left[\varepsilon_{G''} (g' G'' g) + (g' g'' g)_\omega \right] + (g' g' g' g) \right\} -$$

$$- 2e^2 \sum_{g} \sum_{g'}^{(g)} (\mathbf{s}^2)_{gg} \left\{ \frac{\varepsilon_{G'}}{r_{GG'}} - \varepsilon_{G'} \frac{\omega_g (r_{GG'})}{2 r_{GG'}} + (g g' g)_\omega \right\} \qquad (2c')$$

$$E_4 = - e^2 \sum_{g} \sum_{g'}^{(g)} s_{gg'} s_{gg'} (g g' g g'). \qquad (2d')$$

Here $(\mathbf{s}^2)_{gg}$ means the gg-element of the matrix $\mathbf{s}^2$.

In this paper we shall use the approximate expressions (2c′) and (2d′) instead of (2c) and (2d) and we will show that even this first approximation will give results for the deviations from the Cauchy relations that are at least qualitatively in agreement with the empirical results. For our purpose it is convenient to divide the various interaction terms in E_{coh} into three distinct parts:

1. The electrostatic part of E_1 (2a)

$$E^{\text{elstat}} = \frac{e^2}{2} \sum_{G} \sum_{G'}^{(G)} \frac{\varepsilon_G \varepsilon_{G'}}{r_{GG'}}. \qquad (6)$$

The contribution from this term to c_{12} and c_{44} for a crystal of the NaCl-type is given by the expression

$$c_{12}^{\text{elstat}} = c_{44}^{\text{elstat}} = \frac{3\, e^2\, \varepsilon^2}{2\, a_0^4}\, 0.2318. \qquad (7)$$

Here $\varepsilon = |\varepsilon_G|$, and a_0 is the interionic distance in the unstrained lattice.

2. All other parts of E_{coh} the terms of which are functions only of the distance between two neighbouring lattice points, that is: E_2, E_4 (2d′) the last three terms in E_1 and part of E_3 (2c′). The interaction between nearest unlike neighbours in a lattice of the NaCl-type will give no contributions to c_{12} and c_{44}, and the interaction between neighbours of higher orders will give the same contribution to c_{12} and c_{44}. As we are mainly interested in the deviations from the Cauchy relations we do not need to take these terms into account in the following.

3. That part of E_3 which corresponds to a many-body potential. We shall introduce the notation E^* for this part.

$$E^* = 2e^2 \sum_{g} \sum_{g'}^{(g)} \sum_{g''}^{(gg')} s_{gg'} \left\{ \varepsilon_{G''} (g' G'' g) + (g' g'' g)_\omega \right\} -$$

$$- 2e^2 \sum_{g} \sum_{g'}^{(g)} (\mathbf{s}^2)_{gg} \left\{ \frac{\varepsilon_{G'}}{r_{GG'}} - \varepsilon_{G'} \frac{\omega_g (r_{GG'})}{2 r_{GG'}} + (g g' g)_\omega \right\}. \qquad (8)$$

---

[1] Löwdin, l. c. p. 38.

We will now introduce some further approximations. The quantities $(g'g''g)_\omega$ are as a rule very small and will therefore be neglected. Similarly the last two terms on the second line are small but not definitely negligible. Their contributions to c_{12} and c_{44} are probably small and we shall neglect these terms in order to simplify our discussion. Neglecting these terms altogether we are left with the following simple expression for E^*[1]

$$E^* = 2e^2 \sum_{g} \sum_{g'}^{(g)} \left\{ \sum_{G''}^{(G\,G')} s_{gg'}\,\varepsilon_{G''}\,(g'\,G''\,g) - (\mathbf{s}^2)_{gg}\,\frac{\varepsilon_{G'}}{r_{G\,G'}} \right\}. \tag{9}$$

The problem of calculating the contribution from E^* to the elastic constants c_{12} and c_{44} of a cubic lattice is essentially a problem of finding a suitable approximation for the first sum in (9). This will necessarily involve certain series expansions, the terms of which must be evaluated by numerical methods; so the results will be restricted to those crystals for which the computations have been performed. Therefore we have chosen first to consider two idealized limiting cases, where certain results can be obtained without numerical work. In the first case we consider crystals having very small positive ions, in the second case crystals where the positive and negative ions are assumed to be of the same size.

Crystals with very small positive ions

We shall assume that the amplitudes of the radial wave functions $f_{nl}(r)$ associated with the positive ion are large only in the closest neighbourhood of the nucleus and vanishingly small for $r \geq R$, where R is small compared with the interionic distance a. Only overlap effects between nearest neighbours will be considered. Since the sum $\sum_{g}^{G} (\mathbf{s}^2)_{gg}$ will have the same value for both kinds of ions the second sum in (9) will be identically zero for crystals where each ion is a centre of symmetry. Using the symmetry in g and g' and summing over all lattice points G belonging to the positive ions we get

$$E^* = 4Le^2 \sum_{g}^{G(-)} \sum_{g'}^{(G)} \sum_{G''}^{(G\,G')} s_{gg'}\,\varepsilon_{G''}\,(g'\,G''\,g) \tag{10}$$

where g now runs over the orbitals of a certain positive ion with the nucleus at the lattice point G and g' over the orbitals of its nearest negative neighbours G'. L denotes the Avogadro number. According to our assumptions, we can get a simple approximate expression for the integral $(g'G''g)$ by replacing the denominator $|\mathbf{r} - \mathbf{r}_{G''}|$ by $r_{GG''}$:

$$(g'\,G''\,g) = \frac{s_{g'g}}{r_{G\,G''}}$$

---

[1] Note that (9) is simply an approximate expression for the first sum in (2c) and is obtained from this sum by replacing $p_{gg'}$ and p_{gg} by $s_{gg'}$ and $-(\mathbf{s}^2)_{gg}$ respectively and putting $(g\,G'\,g) = \dfrac{1}{r_{G\,G'}}$.

and

$$E^* = 4\,L e^2 \sum_{g}^{G(-)} \sum_{g'}^{(G)} s_{g\,g'} s_{g'\,g} \sum_{G''}^{(G\,G')} \frac{\varepsilon_{G''}}{r_{G\,G''}}. \tag{11}$$

Following Löwdin we shall introduce the notation

$$c_{ij}^{*} = \frac{1}{V_0}\left(\frac{\partial^2 E^*}{\partial x_i\, \delta x_j}\right)_0. \tag{12}$$

From (11) and (12) we can derive the expressions for c_{12}^* and c_{44}^* for a crystal of NaCl-type, which will be a first approximation of Löwdin's formulae

$$c_{12}^{*} = \frac{18\, e^2 \varepsilon}{a_0^4}\left(0.2318\, F + 0.1295\, a\, \frac{d\,F}{d\,a}\right)_0 \tag{13a}$$

$$c_{44}^{*} = \frac{18\, e^2 \varepsilon}{a_0^4}\, 0.2318\,(F)_0 \tag{13b}$$

$$c_{12} - c_{44} = c_{12}^{*} - c_{44}^{*} = \frac{18\, e^2 \varepsilon}{a_0^3}\, 0.1295\left(\frac{d\,F}{d\,a}\right)_0 \tag{13c}$$

$$F = 2 \sum_{g}^{G} \sum_{g'}^{G'} s_{g\,g'} s_{g'\,g}; \quad a = r_{G\,G'}.$$

For interionic distances and overlap integrals of ordinary magnitude the deviations from the Cauchy relations will be considerable.

As has been pointed out by Löwdin, the neglect of overlap effects between nearest negative neighbours might not be justified for crystals where the positive ion is small. If the overlapping between nearest negative neighbours is taken into account we have to add to (11) the expression

$$E^{*\prime} = 2\,L e^2 \sum_{g}^{G\,(-)} \sum_{g'}^{(G)} \sum_{G''}^{(G\,G')} \left\{ s_{g\,g'}\, \varepsilon_{G''} (g'\,G''\,g) - s_{g\,g'} s_{g'\,g} \frac{\varepsilon_{G''}}{r_{G\,G''}} \right\}.$$

Here g runs over the orbitals of a certain negative ion and g' over the orbitals of its nearest negative neighbours. We define a new quantity F' by

$$F' = 2 \sum_{g}^{(-)\,G} \sum_{g'}^{(-)\,G'} s_{g\,g'} s_{g'\,g}; \quad G \neq G'.$$

As $(g'\,G''\,g)$ is of the order $\frac{s_{g'\,g}}{r_{G\,G''}}$, $E^{*\prime}$ is the difference between two expressions of the second order in $s_{g\,g'}$ and we might expect the contributions to $c_{12} - c_{44}$ to be small — at least, as long as the ratio F'/F is small.

Crystals with positive and negative ions of the same size

We shall investigate this case under the idealized assumption that the structure of the outer electron shells is the same for both kinds of ions and that he radial wave functions $f_{nl}(r)$ for corresponding orbitals of the two kinds of ons are the same. The overlap effects associated with the inner shells are of econdary importance and will be neglected. To make a simple treatment posible we shall regard the positive and negative ions as completely identical exept for their nuclear charges. It is immaterial for our result wether we use he expression (9) or the first sum in (2c), of which (9) is a first approximaion, so in this section we put E^* = the first sum in (2c).

We consider now a large crystal under a homogenous strain, a crystal where ach ion is a centre of symmetry. Introducing the abbreviation

$$B_{g\,g'\,G''} = p_{g\,g'}(g'\,G''\,g)$$

ve get

$$E^* = 2\,e^2 \sum_{g} \sum_{g,} \sum_{G''}^{(G)} \varepsilon_{G''} B_{g\,g'\,G''} = e^2 \sum_{g} \sum_{g'} \sum_{G''}^{(G)} \{\varepsilon_{G''} B_{g\,g'\,G''} + \varepsilon_{\bar{G}''} B_{\bar{g}\,\bar{g}'\,\bar{G}''}\} \tag{14}$$

vhere the summations are to be performed over quantities both with and withut $^-$.

Let g and g' refer to two ions at the mutual distance $r_{G\,G'} = R$ and G'' to certain lattice point determined by its coordinates relative G and G'. Also, et $\bar{g}$ and $\bar{g}'$ refer to two ions of opposite sign to g and g' respectively, at the ame mutual distance $r_{\bar{G}\,\bar{G}'} = R$; and $\bar{G}''$ to a certain lattice point with the same oordinates relative $\bar{G}$ and $\bar{G}'$ as G'' relative G and G'. We now make use of ur assumption, and let g and $\bar{g}$, g' and $\bar{g}'$ denote corresponding orbitals of the wo kinds of ions, so that

$$B_{g\,g'\,G''} = B_{\bar{g}\,\bar{g}'\,\bar{G}''}.$$

urthermore, since g and g' refer to ions of opposite signs, we obtain the aditional relation $\varepsilon_{\bar{G}''} = -\varepsilon_{G''}$ which leads to

$$E^* = e^2 \sum_{g} \sum_{g'} \sum_{G''}^{(G)} (\varepsilon_{G''} - \varepsilon_{G''}) B_{g\,g'\,G''} \equiv 0. \tag{15}$$

his result holds in the homogeneously strained as well as in the unstrained tate. We note that overlap effects between neighbours of arbitrary orders are ncluded, and that in the simple case where only overlapping between nearest nlike neighbours is taken into account the result (15) will still hold. From 15), (12) and our arguments on pp. 28 and 29 we get the following result for he elastic constants c_{12} and c_{44} of a cubic crystal where each ion is a centre f symmetry

$$c_{12} = c_{44} \tag{16}$$

The results obtained by studying these two limiting cases can be summarized s follows: We consider a large crystal of cubic structure, keep the interionic istance and the overlap integrals fixed and vary the relative size of the ions. eglecting the overlapping between neighbours of orders higher than the first e might expect the deviations from the Cauchy relations to be comparatively rge as long as the positive ion is comparatively small, but that a succesive decrease in E^*, c_{12}^* and c_{44}^* will occur as we gradually increase the size of the positive ion. The same will probably apply if in (9) we replace $s_{gg'}$ and $-(\boldsymbol{s}^2)_{gg}$ by $p_{gg'}$ and p_{gg} respectively. The fact that the energy expression contains a terms which in this way depends on the size of the positive ions, is rather satisfactory as the empirical results indicate that such a dependence actually exists. For LiF and MgO, where the positive ions are very small the values of c_{44}/c_{12} are 1.4 and 1.8 respectively. On the other hand for a number of crystals where the radial wave functions of the positive ions have an extension comparable with those of the negative ions, the values of c_{44} and c_{12} are roughly equal (e.g. KCl, KBr, KI, RbCl, CsBr). Because of the variations in the interionic distance and the overlapping for real crystals, we cannot draw any decisive conclusions about the variations in the deviations from the Cauchy relations for different crystals, but anyhow we must expect the deviations to be small for crystals where the ions are of about the same size.

In a note on the deviations from Cauchy relations in NaCl- and CsCl-type crystals[1], E. Burstein, P. L. Smith and D. L. Arenberg say that the overlapping is larger in LiF and MgO than in other crystals where the ratio c_{44}/c_{12} is smaller and that these large overlap effects would be responsible for the large deviations from the Cauchy relations for these crystals. We wish to point out that the overlapping (measured e.g. by the quantity F (14)) seems to increase with increasing size of the positive ion, and is in fact smaller in LiF than in NaF and KF. The same thing is also true for the alkali chlorides.[2]

From this preliminary investigation it seems rather clear that the elastic constants c_{12} and c_{44} in this approximation must be a function of the relative size of the positive and negative ion as well as of the overlapping and the interionic distance. Löwdin's method of expanding the denominator in $(g'G''g)$ in spherical harmonics with the origin at the lattice point of a positive ion is very useful when applied to crystals where the positive ion is comparatively small, but for crystals containing heavier positive ions a decrease in E^*. c_{12}^* and c_{44}^* must be entirely due to the higher terms in the expansion, which would make an accurate calculation of these quantities rather unwieldy. In the following part of this paper it will be shown how the calculations can be performed taking the relative size of the ions into account in a more direct way. Only overlap effects between nearest unlike neighbours will be considered.

Calculation of the non-orthogonality term E^*

The integral $(g'G''g)$ is given by

$$(g'G''g) = \int \psi_{g'}^*(\boldsymbol{r}) \frac{1}{|\boldsymbol{r}-\boldsymbol{r}_{G''}|} \psi_g(\boldsymbol{r})\, d\boldsymbol{r}. \tag{17}$$

In the case where this integral depends on the relative positions of three distinct lattice points G, G' and G'', it can only be evaluated in terms of certain series expansions, unless the atomic wave functions are of a very simple orm.[1] Instead of expanding the denominator in (17) in spherical harmonics with he origin at a lattice point we intend to make a corresponding expansion with he origin at the geometrical centre of mass $\xi_{g g'}$ of the quantity

---

[1] Phys. Rev., *87*, 314 (1951).

[2] P. O. Löwdin: Thesis, l. c. pp. 77–93.

$$s_{g' g} = \int \psi^*_{g'}(\boldsymbol{r})\, \psi_g(\boldsymbol{r})\, d\boldsymbol{r}.$$

Before proceeding further we shall introduce certain approximations which re by no means essential for this method but which are introduced only in rder to simplify the calculation. Following Löwdin, we shall assume that the adial wave functions $f_{n l}(r)$ associated with the positive ions satisfy the condition

$$f_{n l}(r) = 0 \quad r > r_{G G'}.$$

his condition is in actual fact only approximately fulfilled, but the contribuion to the integrals from the region $r > r_{G G'}$ will in most applications be small ompared with that from the region $r < r_{G G'}$. We shall further assume that the unction $\psi^*_{g'}(\boldsymbol{r})\, \psi_g(\boldsymbol{r})$ vanishes outside a sphere with its centre at the geometical centre of mass $\xi_{g g'}$ and radius $R_{\xi G''}$, where $R_{\xi G''}$ denotes the distance beween $\xi_{g g'}$ and the nearest of the lattice points G''. According to these assumpions we can omit the limits of integration in the following and make a simple ransformation of our integrals to a coordinate system with the lattice point f the positive ion at the origin.

The geometrical centre of mass is given by

$$s_{g' g}\, \xi_{g g'} = \int \psi^*_{g'}(\boldsymbol{r})\, \psi_g(\boldsymbol{r})\, \boldsymbol{r}\, d\boldsymbol{r}. \tag{18}$$

ince the elements $s_{g g'}$ (and also $p_{g g'}$) vanish unless g and g' refer to orbitals vith the same magnetic quantum number m, we need only calculate $(g' G'' g)$ n the case where the function $\psi^*_{g'}(\boldsymbol{r})\, \psi_g(\boldsymbol{r})$ has rotational symmetry with repect to the axis $\boldsymbol{r}_{G G'}$.

We now introduce a system of spherical coordinates (r, ϑ, φ) with the origin t $\xi_{g g'}$ and the polar axis along the vector $\boldsymbol{r}_{G G'}$. Putting the well known exansion

$$\frac{1}{|\boldsymbol{r} - \boldsymbol{r}_{G''}|} = \sum_{h=0}^{\infty} \sum_{m=-h}^{+h} \frac{4\pi}{2h+1} \frac{r^h}{r_{\xi G''}^{h+1}} S_{h m}(\vartheta, \varphi)\, S^*_{h m}(\vartheta_{G''}, \varphi_{G''}), \quad r < r_{\xi G''}$$

vhere $\vartheta_{G''}$ and $\varphi_{G''}$ are the angle coordinates of the lattice point G'', into (17) ve get, after some simplifications

$$(g' G'' g) = \sum_{h=0}^{\infty} \frac{P_h(\cos \vartheta_{G''})}{r_{\xi G''}^{h+1}} I_{h, g' g} \tag{19}$$

vhere

$$I_{h, g' g} = \int \psi^*_{g'}(\boldsymbol{r})\, \psi_g(\boldsymbol{r})\, r^h P_h(\cos \vartheta)\, d\boldsymbol{r}$$

nd $P_h(\cos \vartheta)$ are the Legendre polynomials.

---

[1] In the special case where $\psi_g(\boldsymbol{r})$ and $\psi_{g'}(\boldsymbol{r})$ are $1s$ hydrogen-like functions with the same creening constant, the integration can be carried out in terms of elliptical coordinates. Cf. A. SCHUCHOWSKY, Acta Physicochimica U.S.S.R., *1*, 901 (1934); G. GORDADSE, Z. f. Phys., 6, 542 (1935).

Transforming the integrals $I_{h,g'g}$ to another system of spherical coordinates (r', ϑ', ψ') with the origin at G, the lattice point of the positive ion, we get the following results for $h = 0, 1, 2$.

$$\begin{aligned} I_{0,g'g} &= s_{g'g} \\ I_{1,g'g} &= 0 \\ I_{2,g'g} &= I'_{2,g'g} - s_{g'g}\,\xi^2_{gg'} \end{aligned} \tag{20}$$

where

$$I'_{2,g'g} = \int \psi^*_{g'}(\mathbf{r}')\,\psi_g(\mathbf{r}')\,r'^2 P_2(\cos\vartheta')\,d\mathbf{r}'.$$

Introducing the abbreviations

$$F_{h,gg'} = s_{gg'} I_{h,g'g} \tag{21}$$

and

$$A_h(\xi_{gg'}) = \sum_{G''}^{(GG')} \frac{\varepsilon_{G''} P_h(\cos\vartheta_{G''})}{r^{h+1}_{\xi G''}} \tag{22}$$

we get the following expression for E^*.

$$E^* = 2e^2 \sum_g \sum_{g'}^{(g)} \sum_{h=0}^{\infty} A_h(\xi_{gg'})\,F_{h,gg'}. \tag{23}$$

We now consider a large crystal of NaCl-type under no stress. In a system of Cartesian coordinates with its axes parallel to the edges of the cube, two arbitrary lattice points will have the relative coordinates $(l_1 a_0, l_2 a_0, l_3 a_0)$, where the possible values of l_1, l_2, l_3 are all integers between $-\infty$ and $+\infty$. Similarly, the vector $\mathbf{r}_{\xi G''}$ has the components $((l_1 - \eta_{gg'})a_0, l_2 a_0, l_3 a_0)$, provided $\mathbf{r}_{GG'} = (a_0, 0, 0)$. The new quantity $\eta_{gg'}$ appearing here is defined by

$$\xi_{gg'} = \eta_{gg'} r_{GG'}. \tag{24}$$

The lattice sums A_h can now be written

$$A_h(\eta) = \frac{\varepsilon}{a_0^{h+1}} \sum_{l_1 l_2 l_3}'' \frac{(-1)^{l_1+l_2+l_3}}{\{(l_1-\eta)^2 + l_2^2 + l_3^2\}^{\frac{h+1}{2}}} P_h\left(\frac{l_1-\eta}{\{(l_1-\eta)^2 + l_2^2 + l_3^2\}^{\frac{1}{2}}}\right). \tag{25}$$

$\sum''$ means that the points $(0,0,0)$ and $(1,0,0)$ are to be omitted. In order to treat the lattice sums $A_h(\eta)$, we shall introduce the notations

$$S_n^{(0)}(\eta) = \sum_{l_1 l_2 l_3}'' (-1)^{l_1+l_2+l_3} \frac{1}{\{(l_1-\eta)^2 + l_2^2 + l_3^2\}^{\frac{n}{2}}} \tag{26}$$

$$S_n^{(4)}(\eta) = \sum_{l_1 l_2 l_3}'' (-1)^{l_1+l_2+l_3} \frac{(l_1-\eta)^4 + l_2^4 + l_3^4}{\{(l_1-\eta)^2 + l_2^2 + l_3^2\}^{\frac{n}{2}}} \tag{27}$$

$$T_n(\eta) = \sum_{l_1 l_2 l_3}'' (-1)^{l_1+l_2+l_3} \frac{l_2^2}{\{(l_1-\eta)^2 + l_2^2 + l_3^2\}^{\frac{n}{2}}}. \tag{28}$$

In most applications it ought to be sufficient to take only the first two non-vanishing terms in (23) into account. For $h = 0$ and $h = 2$ we get

$$A_0(\eta) = \frac{\varepsilon}{a_0} S_1^{(0)}(\eta)$$

$$A_2(\eta) = \frac{\varepsilon}{a_0^3} (S_3^{(0)}(\eta) - 3\,T_5(\eta)). \tag{29}$$

We note that for sufficiently small ions our expression (23) becomes equiv-alent to (11), and from the simple symmetry properties of the lattice sums A_n we can easily see that every term in our expansion of E^* will be identically zero if the positive and negative ions are supposed to be identical, so this method will obviously give results in complete agreement with those we have already obtained.

The elastic constants c_{12} and c_{44}

The elastic constants c_{12} and c_{44} are in our approximation given by

$$c_{12} = c_{12}^{\text{elstat}} + \overset{*}{c}_{12}$$

$$c_{44} = c_{44}^{\text{elstat}} + \overset{*}{c}_{44}. \tag{30}$$

We shall now derive the expressions for $\overset{*}{c}_{12}$ and $\overset{*}{c}_{44}$.

If $(l_1\,a_0, l_2\,a_0, l_3\,a_0)$ are the relative coordinates of the two lattice points G and G'' and $(a_0,\ 0,\ 0,)$ are the relative coordinates of G and G' in the unstrained lattice, the distance $r_{\xi G''}$ in the strained lattice will be given by

$$r_{\xi G''} = a_0 \{ (l_1 - \eta_{g g'})^2 (1 + 2 x_1) + l_2^2 (1 + 2 x_2) + l_3^2 (1 + 2 x_3) + + 2 l_2 l_3 x_4 + 2 l_3 (l_1 - \eta_{g g'}) x_5 + 2 (l_1 - \eta_{g g'}) l_2 x_6 \}^{\frac{1}{2}}. \tag{31}$$

Because of the symmetry in the indices g and g', our formula (23) can be written

$$E^* = 4 e^2 \sum_{g}^{(+)} \sum_{g'}^{(-)} \sum_{h=0}^{\infty} A_h (\eta_{g g'}) F_{h, g g'} \tag{32}$$

Each positive ion has six nearest negative neighbours but the lattice symmetry reduces the number of possibilities to three, namely when the relative coordi-nates of G and G' in the undeformed lattice are

(1) $(\pm a_0,\ 0,\ 0)$
(2) $(0,\ \pm a_0,\ 0)$
(3) $(0,\ 0,\ \pm a_0)$.

Performing the summation over the six neighbouring lattice points G' of a cer-tain positive ion G and then over all lattice points G, we get

$$E^* = 8\,L e^2 \sum_{g}^{G} \sum_{g'}^{G'} \sum_{h=0}^{\infty} \{A_h^{(1)}(\eta_{g g'})\,F_{h,g g'}^{(1)} + A_h^{(2)}(\eta_{g g'})\,F_{h,g g'}^{(2)} + A_h^{(3)}(\eta_{g g'})\,F_{h,g g'}^{(3)}\} \quad (33)$$

where the figures (1), (2), and (3) imply that we have to substitute the corresponding expressions for $r_{G G'}$, $r_{\xi G''}$ and $\cos \vartheta_{G''}$ in $A_h(\eta)$ and $F_{h,g g'}$. It is convenient to introduce the abbreviation

$$\Gamma_h(\eta) = A_h^{(1)}(\eta) + A_h^{(2)}(\eta) + A_h^{(3)}(\eta).$$

From (34) and (12) we get the following formulae for $\overset{*}{c}_{12}$ and $\overset{*}{c}_{44}$

$$\overset{*}{c}_{12} = \frac{4\,e^2}{a_0^3} \sum_{g}^{G} \sum_{g'}^{G'} \sum_{h=0}^{\infty} \Bigg\{ F_{h,g g'} \frac{\partial^2 \Gamma_h(\eta_{g g'})}{\partial x_1 \delta x_2} + a \frac{d F_{h,g g'}}{d a} \left(\frac{\partial A_h^{(1)}(\eta_{g g'})}{\partial x_2} + \frac{\partial A_h^{(2)}(\eta_{g g'})}{\partial x_1} \right) +$$

$$+ a F_{h,g g'} \frac{d \eta_{g g'}}{d a} \left[\frac{d}{d\eta} \left(\frac{\partial A_h^{(1)}(\eta)}{\partial x_2} + \frac{\partial A_h^{(2)}(\eta)}{\partial x_1} \right)_0 \right]_{\eta = \eta_{g g'}} \Bigg\}_0 \quad (34\,\text{a})$$

$$\overset{*}{c}_{44} = \frac{4\,e^2}{a_0^3} \sum_{g}^{G} \sum_{g'}^{G'} \sum_{h=0}^{\infty} \left\{ F_{h,g g'} \frac{\partial^2 \Gamma_h(\eta_{g g'})}{\partial x_4^2} \right\}_0 . \quad (34\,\text{b})$$

Here the symbols $\left(\frac{\partial^2 \Gamma_h(\eta_{g g'})}{\partial x_1 \delta x_2}\right)_0$, $\left(\frac{\partial^2 \Gamma_h(\eta_{g g'})}{\partial x_4^2}\right)_0$, $\left(\frac{\partial A_h^{(1)}(\eta_{g g'})}{\partial x_2}\right)_0$ and $\left(\frac{\partial A_h^{(2)}(\eta_{g g'})}{\partial x_1}\right)_0$ denote certain lattice sums. For the sake of brevity we give the results only for $h = 0$.

$$\left(\frac{\partial^2 \Gamma_0(\eta)}{\partial x_1 \delta x_2}\right)_0 = \frac{3\,\varepsilon}{2\,a_0} \{S_1^{(0)}(\eta) - S_5^{(4)}(\eta)\}$$

$$\left(\frac{\partial A_0^{(1)}(\eta)}{\partial x_2}\right)_0 = \left(\frac{\delta A_0^{(2)}(\eta)}{\delta x_1}\right)_0 = -\frac{\varepsilon}{a_0} T_3(\eta) \quad (35)$$

$$\left(\frac{\partial^2 \Gamma_0(\eta)}{\partial x_4^2}\right)_0 = \frac{3\,\varepsilon}{2\,a_0} \{S_1^{(0)}(\eta) - S_5^{(4)}(\eta)\}.$$

For numerical applications of our formulae (23) and (34 a, b), we must know the values of the lattice sums for a number of values of the parameter η. We have calculated the sums for $h = 0$ and $h = 2$, using the rapidly convergent method developed by EVJEN[1]. We note that for $h = 0, 2, 4 \ldots$ the lattice sums $A_h(\eta)$ and their derivatives with respect to the components of the strain appearing in (34) satisfy the relations

$$A_h(1-\eta) = -A_h(\eta), \quad 0 \leq \eta \leq 1; \quad A_h(\tfrac{1}{2}) = 0. \quad (36)$$

We have performed the calculation for $\eta = 0$, 0.1, 0.2, 0.3, 0.4, the values for $\eta = 0.5$, 0.6, 0.7, 0.8, 0.9, 1.0 are obtained from (36). The final results are given in the following table.[2]

---

[1] H. M. EVJEN, Phys. Rev., *39*, 675 (1932).

[2] As the summations have been performed over a cube whose side is only three times the lattice parameter, not more than the first two figures given in the table are reliable.

$\eta =$	0.0	0.1	0.2	0.3	0.4
$\frac{a_0}{\varepsilon} A_0(\eta)$	-0.748	-0.636	-0.503	-0.348	-0.178
$\frac{a_0^3}{\varepsilon} A_2(\eta)$	$+1.000$	$+1.159$	$+1.065$	$+0.800$	$+0.424$
$\frac{a_0}{\varepsilon}\left(\frac{\partial^2 \Gamma_0(\eta)}{\partial x_1 \delta x_2}\right)_0$	$+2.086$	$+1.969$	$+1.642$	$+1.166$	$+0.600$
$\frac{a_0}{\varepsilon}\left(\frac{\partial A_0^{(1)}(\eta)}{\partial x_2}\right)_0$	$+0.583$	$+0.560$	$+0.468$	$+0.338$	$+0.177$
$\frac{a_0}{\varepsilon}\left(\frac{\partial^2 \Gamma_0(\eta)}{\partial x_4^2}\right)_0$	$+2.086$	$+1.969$	$+1.642$	$+1.166$	$+0.600$
$\frac{a_0^3}{\varepsilon}\left(\frac{\partial^2 \Gamma_2(\eta)}{\partial x_1 \delta x_2}\right)_0$	0.000	$+0.560$	1.516	2.079	1.461
$\frac{a_0^3}{\varepsilon}\left(\frac{\partial A_2^{(1)}(\eta)}{\partial x_2}\right)_0^*$	-2.974	-2.724	-2.279	-1.576	-0.794
$\frac{a_0^3}{\varepsilon}\left(\frac{\partial^2 \Gamma_2(\eta)}{\partial x_4^2}\right)_0$	-11.900	-10.595	-7.601	-4.224	-1.713

Application to sodium chloride

The quantities $F_{h,gg'}$, $\eta_{gg'}$ and their derivatives can be calculated using well known methods. We have computed E^*, c_{12}^* and c_{44}^* for NaCl according to our formulae (23) and (35 a, b) neglecting the contributions from the terms for which $h \geq 3$. $F_{h,gg'}$ and $\eta_{gg'}$ were calculated for NaCl from LÖWDIN's numerical tables. The values of the lattice sums were obtained from the table by interpolation. The convergency of our series expansion in h seems quite good, the contribution from the term $h = 2$ was only a few per cent of the total. The results of our calculation are given below.[1]

E^* kcal/mol

a_0 a.u.	Calc.	Löwdin
5.20	— 6.7	— 10.9

---

* Note that $\left(\frac{\partial A_2^{(1)}(\eta)}{\partial x_2}\right)_0 = \left(\frac{\partial A_2^{(2)}(\eta)}{\partial x_1}\right)_0$.

[1] The contribution from the overlapping between the 2p orbitals of Na^+ and the 3s orbitals of Cl^- could not be calculated because the quantities necessary to compute η and F_2 were not tabulated. By putting $\eta = 0$ we have estimated the values -0.4, -0.028 and $+0006$ as an upper limit for the contributions to E^*, c_{12}^* and c_{44}^* respectively.

10^{11} dyne/cm^2

	Calc.	Löwdin	Emp.
c_{44}^*	+ 0.116	+ 0.126	–
c_{12}^*	– 0.367	– 0.417	–
$c_{44}-c_{12}$	+ 0.483	+ 0.543	+ 0.341

Adding the contribution from the electrostatic part, given by (7), we finally get

10^{11} dyne/cm^2

	Calc.	Löwdin	Emp.[1]
c_{44}	1.515	1.525	1.327
c_{12}	1.032	0.982	0.986

$2\,(c_{44}-c_{12})\,(c_{44}+c_{12})^{-1}$

Calc.	Löwdin	Emp.
0.38	0.43	0.29

The calculated values agree very closely with Löwdin's results; the improvement in the value of $(c_{44}-c_{12})$ is too small to be of significance. The agreement between the calculated and the observed deviation from the Cauchy relation must be considered as rather satisfactory in view of the various approximations introduced. We have neglected the contributions from all higher order effects in the cohesive energy, e.g. the zero point oscillations and the effects depending on the mutual deformations of the ions in the lattice and instead of calculating the elastic constants from (2) we have used an expression correct only to the second order in the overlap integrals and have taken only the overlapping between nearest unlike neighbours into account. For KCl, however, the table of $2\,(c_{44}-c_{12})\,(c_{44}+c_{12})^{-1}$ given on p. 26 shows a large discrepancy between the observed value and the theoretical value calculated by Löwdin. We intended to calculate c_{12} and c_{44} for KCl according to our method, but certain of the quantities η and F_2 necessary for the computation could not be calculated from Löwdin's tables. The neglect of the higher terms in the overlap integrals is not justified to the same extent for KCl as for NaCl and it is possible that these terms as well as the other higher order effects mentioned above must be taken into consideration in order to get a better agreement with the experimental results.

I wish to express my gratitude to Professor I. Waller for suggesting this investigation and for many valuable discussions on these matters. I am also indebted to Fil. mag. G. Hagevall for helpful assistance with the numerical calculation.

Institute of Mechanics and Mathematical Physics, University of Uppsala.

---

[1] W. C. Overton, R. T. Swim, Phys. Rev. *84*, 758 (1951).

Tryckt den 25 oktober 1952

Uppsala 1952. Almqvist & Wiksells Boktryckeri AB

ARKIV FÖR FYSIK Band 6 nr 4

Communicated 14 November 1951 by G. DE HEVESY and ERIK HULTHÉN

Directional correlation measurements on successive nuclear gamma rays in Hf^{177}

By T. WIEDLING

With 7 figures in the text

1. Introduction

In his now classical work on the use of the coincidence method in the investigation of disintegration schemes of radioactive nucleus, DUNWORTH (1) mentioned that there might be an angular correlation between two γ-quanta successively emitted from two excited states in a nucleus. A theoretical treatment of the problem was first made by HAMILTON (2) who performed a quantum-mechanical investigation of the case when the radiation emitted was pure, i.e. there was no mixture of magnetic and electric radiation. Further he made the assumption that the intermediate excited level of the nucleus had a short lifetime compared to the time required for the nuclear spin to precess. YANG (3) extended the calculations to the more general case when the latter assumption was not valid. The theory of angular correlation in a form applicable to the successive emission of any nuclear radiation was given by FALKOFF and UHLENBECK (4). FIERZ (5) gave general equations for γ-γ-angular correlations. Correlation functions were given by LING and FALKOFF (6) when one of the gamma rays was a mixture of magnetic dipole and electric quadrupole radiation and the other either a pure dipole or a pure quadrupole. This problem is discussed by LLOYD (7), too.

The effect of the extra-nuclear electrons on the angular correlation was calculated by GOERTZEL (8) who also discussed the effect of an external magnetic field. This last effect has also been discussed by SPIERS (9) who has as well published theoretical investigations on directional effects at low temperatures. BIEDENHARN *et al.* (10) have presented a theory of angular correlation in triple cascade transitions.

LLOYD (11) and FALKOFF (12) have given tables for higher multipole-gamma-correlations. Furthermore LLOYD (13) has made theoretical investigations of delayed coincidence angular correlations.

The experimental investigations hitherto performed are, with two exceptions, made on nuclei of the even-even type, where it is supposed that the ground state of the nucleus has zero spin. The exceptions are Cu^{65} (14) and Cd^{111} (15, 16, 17, 18) with the ground state spins 3/2 and 1/2 respectively.

FRAUENFELDER *et al.* (17, 18) have shown the effect of the external electron-configuration on angular correlation.

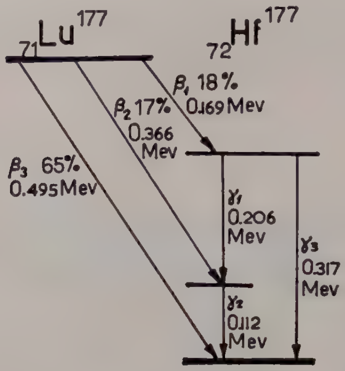

Fig. 1. Disintegration scheme of Lu^{177} proposed by DOUGLAS (20).

2. Statement of problem

The present gamma-gamma-angular correlation measurements are performed on Hf^{177}.

Lu^{177}, which has a halflife (19) of 6.9^d, has the decay scheme (20) given in Fig. 1. BUNYAN *et al.* (21) have searched for a metastable state in the interval $3 \cdot 10^{-7} - 10^{-3}$ seconds but with negative results.

RASMUSSEN (22) has made spectroscopic fine structure measurements and has reported a ground state spin of $\leq 3/2$ in Hf^{177}.

LLOYD (23) and RACAH (24) have given the general γ-γ-angular correlation function in the form of a Legendre series

$$W(\Theta) = 1 + \Sigma A_L P_L (\cos \Theta)$$

where the sum is taken for even L-values. The coefficients A_L are functions of the angular momenta $J - \Delta i$, J, and $J + \Delta J$ for the second excited, the first excited, and the ground state, and also of the multipole order of the emitted γ-radiation.

With the spin of the ground state limited to Rasmussen's values there would be a certain possibility to determine this spin with correlation measurements and at the same time to get information as to the character of the gamma-radiation. Furthermore one would also get information about the β-spectrum of Lu^{177}.

3. Apparatus

Scintillation counters consisting of 1P21 photomultipliers and NaI(Tl) crystals were used as γ-detectors. Multipliers and crystals were mounted in small light-tight houses which were water cooled. The water was cooled down to a temperature of about 2° C in a deep-freezer and pumped through a closed system. In this way the photomultipliers got a rather constant temperature and low dark-current.

The counters were placed on a board covered with aluminum, 2 mm thick. One counter was fixed and the other one revolving, both at the same distance from the sample holder.

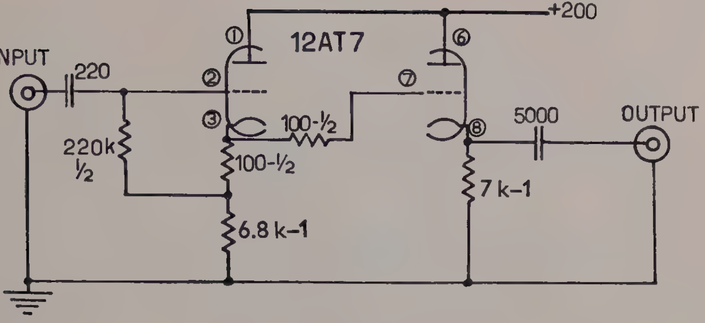

Fig. 2. The pre-stage.

The pre-amplifiers were coupled directly to the photomultipliers with very short vires. The pre-stages (Fig. 2) consisted of the double triode 12AT7. One half of the ube was used as impedance transformer from the photomultiplier anode and the ther as driver of the coaxial cable to the main amplifiers. These were of the type lescribed by JORDAN and BELL (25). From the amplifiers the pulses were fed to fast liscriminators and from those to the coincidence circuit.

A diagram of the coincidence circuit is seen in Fig. 3. The first two tubes T_1 and $_2$ form with the transformer (type: Utah 9318; winding ratio 1 : 1 : 1) the blocking scillator which is triggered with positive pulses on the grid of tube T_1. This way f triggering requires short rise-time of the trigger pulse. Here this is reached by sing the fast discriminator pulses. This method of triggering also permits the disriminator pulses to be relatively long without the occurrence of multiple triggering. n order to get pulses with relatively flat top, a resistance of 150 ohms is connected vith the control-grid of tube T_2. The cathode resistance of T_2 is 100 ohms in one hannel and 240 ohms in the other. The pulses on the cathode of T_2 have a positive ign and have a length at the base of approximately 0.4 μs. The rise time is approxiately 0.05 μs. If the resistance of 150 ohms in the grid circuit of T_2 is disconnected, arrower pulses with a length of approximately 0.25 μs are received. The blocking scillator transformer of the type used here sets, however, a lower limit for the ngth of the pulses.

The coincidence tube was of the type 6AS6 where the normal control-grid and the uppressor-grid were used as control electrodes. To get a compensation for the ifference between mutual conductances of the grids used, the cathode resistances n the blocking oscillators were 100 ohms and 240 ohms respectively for the conrol- and suppressor-grids.

The coincidence pulses are amplified with T_5 and have now sufficient amplitude o trigger the following discriminator of conventional type (26).

The resolving time of the coincidence circuit is changed either by changing the egative voltage on the control-grids of the coincidence tube or the voltage on the rid of tube T_6.

The positive and negative power supplies of the coincidence circuit have been very vell stabilized. The filaments of the tubes have been stabilized by a constant voltage ransformer (Advance Components Ltd., type MT 262A).

The high degree of stability and constant resolving time of the coincidence circuit re indicated in Table I. The measurements are performed in five following days nd with conventional methods.

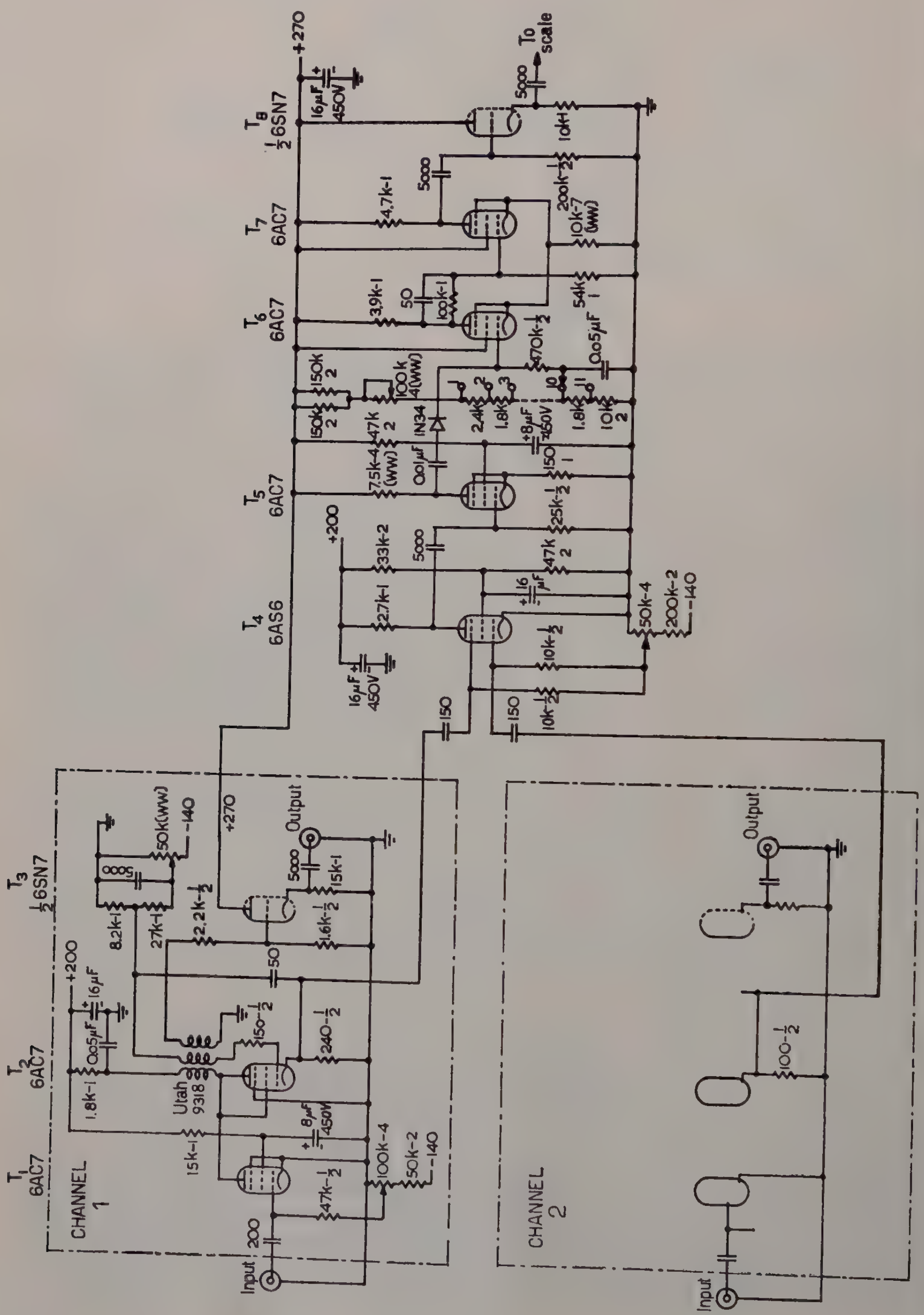

Fig. 3. The coincidence circuit

Table I

Day	Resolving time, μs
1	0.264
2	0.259
3	0.263
4	0.264
5	0.267

4. Experimental

Lu^{177} was obtained by irradiation of "spec-pure" lutecium-oxide[1], Lu_2O_3, with low neutrons during three weeks in Harwell[2]. In this way a very high specific activty was obtained which made it possible to use small sources. To get minimum cattering around the source the sample holder was made of thin aluminum.

Fig 4 shows the spectrum of Hf^{177} taken with a scintillation spectrometer. The eft top is a 65-kev K x-ray, the other two are the γ-energies of 112 and 206 kev. small peak is seen at a dial of about 215. This is the weak cross-over-gamma of 18 kev. The intensity of the latter is about 10^{-2} of the intensity[3] of the 206-ev gamma (no correction for internal conversion). This spectrometer recording hows that if any other γ-transitions exist they are of a low intensity if they are ot wholly converted.

In this investigation of Hf^{177} the energy discriminating ability of the scintillation ounter was only partly used. By using single-channel differential discriminators after ach amplifier it would be possible, in the cases of more complicated disintegration chemes, to investigate the angular correlation between different energy components. he K x-ray line of Hf^{177} (65 kev) was partly discriminated against, partly absorbed n tin. Fig. 5 shows the absorption-curves of the counters used. It is seen that the 5 kev x-ray quanta are fully absorbed to a high degree at approximately 0.1 cm in. (It will be remarked here that the radiation also had to pass a 0.002 cm thick u-foil).

A possible and serious source of error in experiments of this kind is scattering of amma radiation between the counters and resulting false coincidences. In the presnt experiment the circumstances were the following: If the angle between the rimary and Compton scattered quanta is 180° the latter has an energy of approxiately 120 kev if the primary energy is 206 kev (γ_1 in Hf^{177}) and 80 kev if it is 112 ev (γ_2 in Hf^{177}). When a quantum has been registered in one counter and scatters 80°, it must pass through the Sn-absorbers of both counters. Thus the probability hat it will be absorbed is large. When the counters were oriented 90° in relation to ach other they were screened with lead, approximately 0.8 cm.

An experimental investigation of the angular resolution of the counters was erformed by counting the number of coincidences as a function of the angle between he counters. This investigation was made on annihilation radiation from Na^{22} Fig. 6).

---

[1] From Johnson, Matthey and Co.

[2] The author is indebted to Dr. G. W. WELLS for this irradiation.

[3] This will later be investigated with higher accuracy.

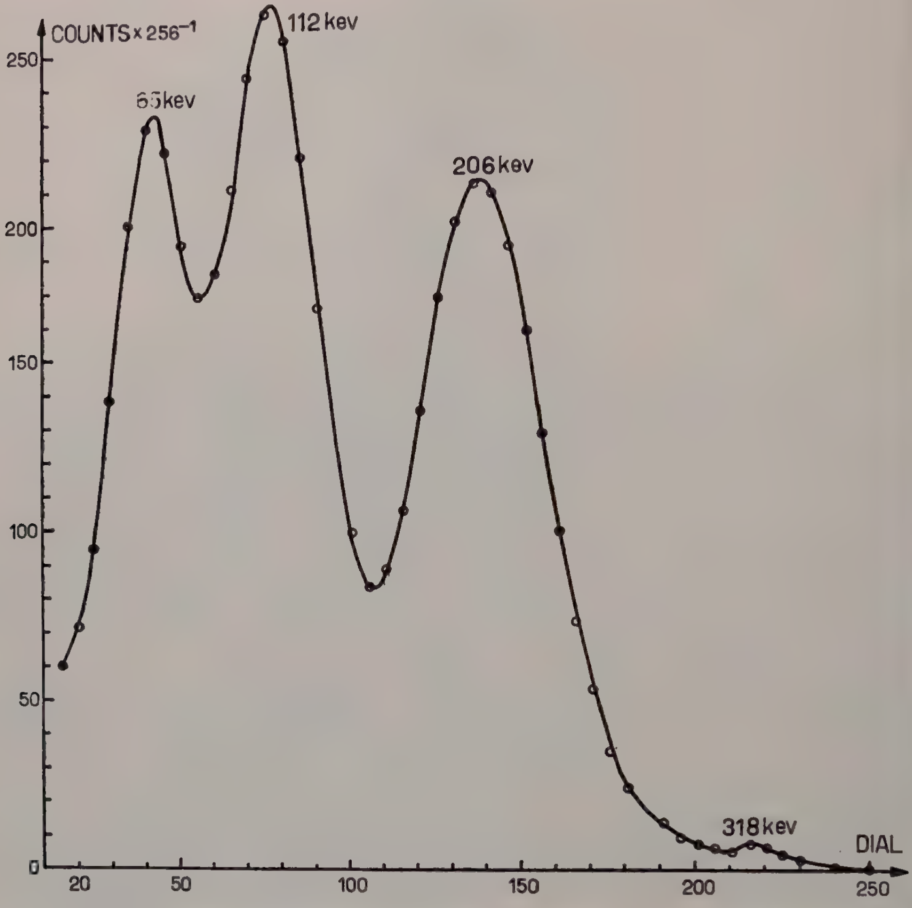

Fig. 4. Pulse height distribution from Hf^{177} showing the 65-kev x-ray, the 112-kev, the 206-kev and 318-kev gamma-rays.

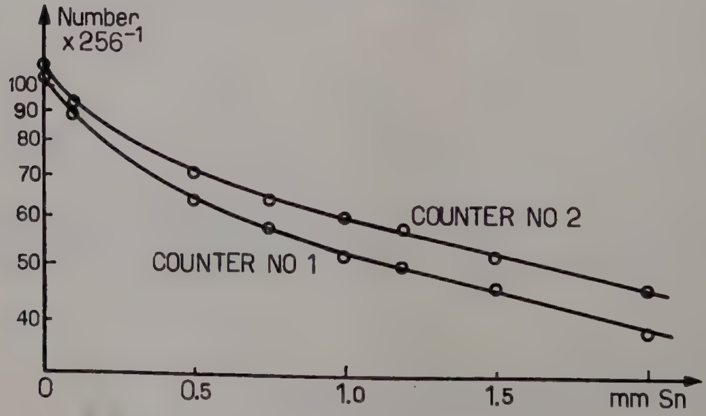

Fig. 5. Absorption in tin of x-rays and γ-rays of Hf^{177}.

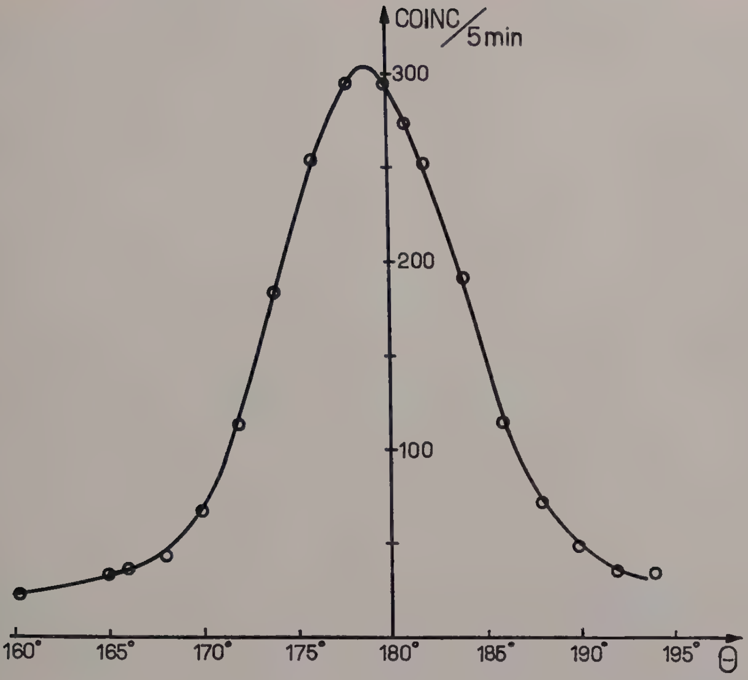

Fig. 6. Angular distribution of coincidences from annihilation radiation.

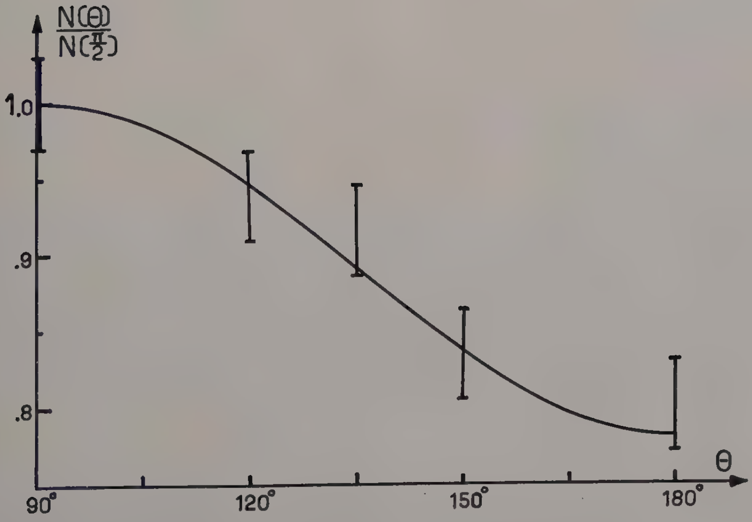

Fig. 7. Correlation of γ-rays from Hf^{177}.

Two different measurements were performed, one with 0.10 cm Sn-absorbers, the other with 0.13 cm absorbers, giving $\frac{N_{\gamma\gamma}(180°)}{N_{\gamma\gamma}(90°)} = 0.80$ and 0.81 respectively ($N_{\gamma\gamma}$ = the number of coincidences in the 180° and 90° directions). It is seen that the 65-kev x-ray cannot appreciably have effected the results. The values above are corrected for the finite angular resolution of the counters. Fig. 7 gives the distribution of the experimental points for different angles Θ.

5. Results and discussions

The hitherto published theoretical investigations (27, 28) on pure radiation of dipole-dipole, quadrupole-dipole, quadrupole-quadrupole and of higher multipole orders give, if the spin (29) of the ground state of Hf ^{177} is 1/2 or 3/2, the values of $\frac{W(180°)}{W(90°)} - 1$ shown in Table II. In all the cases mentioned in the table we have

$$W(\Theta) = 1 - A_2 \cos^2 \Theta.$$

Table II

Multipoles	Spin	$1 - \frac{W(180°)}{W(90°)}$
Dipole-Quadrupole	$5/2 \to 7/2 \to 3/2$	0.217
Dipole-Quadrupole	$3/2 \to 5/2 \to 1/2$	0.273
Quadrupole-Dipole	$1/2 \to 5/2 \to 3/2$	0.273
Dipole-2^3-pole	$9/2 \to 7/2 \to 1/2$	0.177
Dipole-2^3-pole	$11/2 \to 9/2 \to 3/2$	0.177
Dipole-2^4-pole	$11/2 \to 9/2 \to 1/2$	0.216
Dipole-2^4-pole	$13/2 \to 11/2 \to 3/2$	0.216
Quadrupole-Quadrupole	$5/2 \to 3/2 \to 1/2$	0.246

If γ_2 was a 2^3-pole or 2^4-pole the first excited state of Hf^{177} would have a halflife of a magnitude counted in seconds (30, 31). Thus dipole-2^3-pole and dipole-2^4-pole transitions are impossible.

The quadrupole-dipole transitions 1/2→5/2→3/2 and 3/2→5/2→1/2 and the quadrupole-quadrupole transition 5/2→3/2→1/2 are excluded for two reasons: the theoretical values are too small compared with the experimental ones. Further the quadrupole-quadrupole transition mentioned is not very likely for another reason. AUSTERN and SACHS (32) have shown that all magnetic multipole transitions show interactioneffects and they have made estimates of the influence of these effects on magnetic dipole transition probabilities. When selection rules allow both magnetic dipole and electric quadrupole, magnetic dipole is favoured over electric quadrupole. The $\left[1 - \frac{W(180°)}{W(90°)}\right]$-value is, however, calculated for pure radiation.

The last cases we have to discuss are the two dipole-quadrupole transitions 5/2→7/2 →3/2 and 3/2→5/2→1/2. The first of these transitions has a $\left[1 - \frac{W(180°)}{W(90°)}\right]$-value hich fits the experimental one rather well. Fig. 7 gives the experimental points nd the theoretical curve $W(\Theta)=1-0.217\cos^2(\Theta)$. However, according to GOERTZEL 31) the masking of the angular correlation is small if

$$\tau_B \leq \frac{1}{20\,\pi\,c\cdot\Delta\,\nu}$$

here τ_B is the halflife of the intermediate nuclear state and $\Delta\,\nu$ is the fine-structure plitting of the atom. Nor do we have any masking if the magnetic moment of the lectrons in the atom is zero in the ground state. If, however, the atom is excited he magnetic moment will differ from zero and thus the angular correlation may be nfluenced.

Thus it is not absolutely excluded[1] that the correlation has been disturbed and hat the correct spins of the states are 3/2, 5/2, and 1/2 instead of 5/2, 7/2, and 3/2.

Earlier measurements (34) of the $\frac{K}{L}$-ratio of the 112-kev gamma have given $=0.5$. According to Goldhaber's *et al.* empirical curves over $\frac{K}{L}$ as a function of ($E=$the γ-energy, $Z=$the proton number) this gamma-ray has $\Delta I=2$ and is an lectric quadrupole, E2. This is consistent with our results but contrary to HEBB nd NELSON's (35) theoretical estimates.

Table III gives the log $(f\,t)$ values computed by FEINGOLD (36).

Table III

Component	Energy, kev	log $(f\,t)$	Nature (37, 38)
β_1	169	5.86	Allowed
β_2	366	6.95	First forbidden
β_3	495	6.80	First forbidden

As for allowed β-transition the parity change is "no" and for first forbidden transi-ons "yes" the β-spectrum would give a parity change between the first and second xcited states and between the ground state and second excited state of Hf^{177} but change between the ground state and first excited state. Thus we may conclude nat the 206-kev gamma ray is an electric dipole, E1, the 112-kev gamma ray an ectric quadrupole, E2, and the cross-over gamma ray an electric dipole, E1. If, owever, γ_1 and γ_3 have the same character, γ_3 would, according to the theory, ave a higher transition probability than γ_1 which is in contradiction to this xperiment.[2]

---

[1] Note added in proof: MCGOWAN et al. have reported a halflife of the intermediate state orter than 10^{-10} sec, Phys. Rev. *85*, 152 (1951).

[2] Note added in proof: F. K. MCGOWAN, E. D. KLEMA, and P. R. BELL have published me results which are consistent with ours, Phys. Rev. *85*, 152 (1951).

Acknowledgements

I wish to express my gratitude to Professor ERIK HULTHÉN, Director of the Institute of Physics, for his encouraging interest in this work and for valuable discussions. I also wish to thank the Swedish Atomic Committee for financial support and Graham Brothers AB for letting me use one of their deep-freezers.

Physical Institute, University of Stockholm.

REFERENCES. 1. **J. V. Dunworth,** Rev. Sci. Inst., *11,* 167 (1940). — 2. **D. R. Hamilton,** Phys. Rev. *58,* 122 (1940). — 3. **C. N. Yang,** Phys. Rev. *74,* 764 (1948). — 4. **D. L. Falkoff** and **G. E. Uhlenbeck,** Phys. Rev. *79,* 323 (1949). — 5. **M. Fierz,** Helv. Phys. Acta *22,* 489 (1949). — 6. **D. S. Ling** and **D. L. Falkoff,** Phys. Rev. *76,* 1639 (1949). — 7. **S. P. Lloyd,** Phys. Rev. *81,* 161 (1951). — 8. **G. Goertzel,** Phys. Rev. *70,* 897 (1946). — 9. **J. A. Spiers,** Nat. Res. Coun. Can. Publ. Nr. 1925 (1949). — 10. **L. C. Biedenharn, G. B. Arfken,** and **M. E. Rose,** Phys. Rev. *83,* 586 (1951). — 11. **S. P. Lloyd,** Thesis, University of Illinois (1951). **S. P. Lloyd,** Phys. Rev. *83,* 716 (1951). — 12. **D. L. Falkoff,** Phys. Rev. *82,* 98 (1951). — 13. **S. P. Lloyd,** Phys. Rev. *82,* 277 (1951). — 14. **T. Wiedling** and **Allan Carlsson,** Phys. Rev. *83,* 181 (1951). — 15. **F. Boehm** and **M. Walter,** Helv. Phys. Acta *22,* 378 (1949). — 16. **D. M. Roberts** and **R. M. Steffen,** Phys. Rev. *82,* 332 (1951). — 17. **H. Frauenfelder,** Phys. Rev. *82,* 548 (1951). — 18. **H. Aeppli, H. Frauenfelder,** and **M. Walter,** Helv. Phys. Acta *24,* 335 (1951). — 19. **K. Way** *et al.*, Nuclear Data, Circular of the National Bureau of Standards 499 (1950). — 20. **D. G. Douglas,** Phys. Rev. *75,* 1960 (1949). — 21. **D. E. Bunyan, A. Lundby,** and **D. Walter,** Proc. Phys. Soc. *62 A,* 253 (1949). — 22. **E. Rasmussen,** Naturw. *23,* 69 (1935). — 23. **S. P. Lloyd,** Phys. Rev. *81,* 307 (1951). — 24. **G. Racah,** Phys. Rev. *82,* 309 (1951). — 25. **W. H. Jordan** and **P. R. Bell,** Rev. Sci. Inst. *18,* 703 (1947). — 26. **W. C. Elmore** and **M. Sands,** Electronics p. 202. National Nuclear Energy Series, Manhattan Project Technical Section, Division V — Volume I, McGraw-Hill (1949). — 27. **R. D. Hamilton,** Phys. Rev. *58,* 122 (1940). — 28. **S. P. Lloyd,** Phys. Rev. *83,* 716 (1951). — 29. **E. Rasmussen,** Naturw. *23,* 69 (1935). — 30. **V. F. Weisskopf,** Phys. Rev. *83,* 1073 (1951). — 31. **M. Goldhaber** and **A. W. Sunyar,** Phys. Rev. *83,* 906 (1951). — 32. **N. Austern** and **R. G. Sachs,** Phys. Rev. *81,* 710 (1951). — 33. **G. Goertzel,** Phys. Rev. *70,* 897 (1946). — 34. **K. Way** *et al.*, Nuclear Data. — 35. **M. H. Hebb** and **E. Nelson,** Phys. Rev. *58,* 486 (1940). — 36. **A. M. Feingold,** Rev. Mod. Phys. *23,* 10 (1951). — 37. **E. J. Konopinski,** Rev. Mod. Phys. *15,* 209 (1943). — 38. **L. W. Nordheim,** Phys. Rev. *78,* 294 (1950).

Tryckt den 25 oktober 1952

Uppsala 1952. Almqvist & Wiksells Boktryckeri AB

ARKIV FÖR FYSIK Band 6 nr 5

Communicated 4 June 1952 by Erik Hulthén

Nuclear resonance scattering of gamma-rays

By K. G. Malmfors

With 2 figures in the text

Introduction: In the visible region of the spectrum resonance scattering of otons is an effect which is easily observable. In 1929, Kuhn (1) draw the ention to the fact that an analogous process is to be expected in the region gamma-rays in which case the absorption and the reemission of the gamma-anta is associated with the excitation of a *nucleus* identical with that emitting primary ray. Several attempts have been made to demonstrate the effect -6). The reason why such experiments have given no positive result is that, e to the high energy of the gamma-rays, the emitting and the scattering clei recoil with an energy which is much greater than the width of the nuclear citation levels.

Moon (7, 8) has analyzed the situation and arranged an experiment in which recoil is compensated by mechanically moving the gamma-source with a h velocity (~700 m/sec.) towards the scatterer. Moon's experiments with 411 keV gamma-radiation from Au^{198} scattered in mercury gives the first lication of a positive result, though the effect is very small and just outside erimental errors. A repetition of these experiments with an improved ap-atus was recently reported by Storruste (9).

The aim of the present investigation is to show that in certain cases nuclear onance scattering can be made observable by increasing the temperature of gamma-source or of the scatterer. The condition for a resonance effect is filled in those cases when the thermal velocity component in the direction vards the scatterer is such that the recoil is compensated.

Theory. By using the following expression for the cross-section of resonant ttering

$$\sigma_{\text{res}} = \frac{\lambda^2}{8\pi} \cdot \frac{\Gamma^2}{(E-E_0)^2 + \frac{1}{4}\Gamma^2} \tag{1}$$

ere λ is the wavelength, Γ the resonance width, E the energy of the gamma- and E_0 the resonance energy, and by supposing that the thermal velocities the source and the scatterer are distributed as in a gas at temperature T, on has deduced the following expression for the effective cross-section of onance scattering, taking into account the energy shift due to the recoil and thermal motion

$$\sigma_T = \frac{\lambda^2 \cdot \Gamma}{4\sqrt{\pi}} \cdot \sqrt{\frac{M c^2}{E^2 \cdot 4 k T}} \cdot e^{-\frac{M\left(\frac{E}{Mc} - u\right)^2}{4kT}} \tag{2}$$

M is the nuclear mass, k and c are Boltzmann's constant and the velocity of light respectively. u represents the mechanical velocity applied to the gamma-source in Moon's experiments. In the following the case is considered where $u = 0$. Formula (2) is deduced with the assumption that the emitter and the scatterer have the same temperature. If the temperatures are T_1 and T_2 respectively, the above expression is modified to

$$\sigma = \frac{\lambda^2 \cdot \Gamma}{4\sqrt{\pi}} \cdot \sqrt{\frac{M c^2}{E^2}} \cdot \frac{1}{\sqrt{2k(T_1 + T_2)}} \cdot e^{-\frac{\frac{E^2}{Mc^2}}{2k(T_1+T_2)}} \tag{3}$$

or by putting

$$\frac{E^2}{Mc^2} \cdot \frac{1}{2k(T_1 + T_2)} = g^2 \tag{4}$$

and

$$\lambda = \frac{hc}{E}$$

$$\sigma = \frac{h^2 c^4}{4\sqrt{\pi}} \cdot \frac{M}{E^4} \cdot \Gamma \cdot g \cdot e^{-g^2}. \tag{5}$$

In the following we consider the cross-section in the special case where 411 keV gamma-radiation from Au^{198} is scattered in mercury of which only the 10 % aboundant isotope Hg^{198} is effective as resonance scatterer. By taking this fact into account and by inserting numerical values into (5) one obtains:

$$\left\{ \begin{aligned} \sigma &= 8.8 \cdot 10^{-10} \cdot \Gamma \cdot g \cdot e^{-g^2} && (6) \\ g &= \frac{73.3}{\sqrt{T_1 + T_2}} && (7) \end{aligned} \right.$$

Table I shows how the factor $g \cdot e^{-g^2}$ depends on the gold temperature while the scatterer is supposed to be at room temperature.

Table I.

T_1 (C°)	$g \cdot e^{-g^2}$
20°	0.0003
100°	0.0006
300°	0.0050
500°	0.014
700°	0.030
900°	0.048
1 100°	0.071
1 300°	0.096
1 500°	0.118

At the melting point of gold (1 063°) the factor is about 0.065. (The cor-esponding factor in Moon's case is about 3.0 when the gamma-source has the deal velocity.

The cross-section for resonant scattering should be compared with that of Rayleigh scattering, since both processes give elastically scattered quanta which annot be separated from each other by filtering or other energy discrimination. The angular distribution of resonantly scattered radiation is assumed not to deviate much from the isotropic distribution. For the cross-section of Rayleigh cattering (10) we have used the value $1.2 \cdot 10^{-25}$ cm². If gold an mercury are held at room temperature the resonantly scattered radiation gives a very small ontribution, but if the gold temperature is increased to the melting point the elative increase of the elastically scattered radiation is

$$\frac{\sigma}{\sigma_R} = 4.8 \cdot 10^{14}\, \Gamma. \tag{8}$$

The energy width and the mean life of the excited level are connected by the elation $\tau \cdot \Gamma \approx \frac{h}{2\pi}$ and since coincidence experiments (11) have shown that $\tau < 10^{-10}$ sec there follows $\Gamma > 10^{-17}$ and consequently the relative increase will be of the order 0.5 % or larger.

Experimental arrangement

So far two series of experiments have been performed. In the first 0.1 g gold was used which had been irradiated in the Harwell reactor to an activity of 0 mC. This was placed in a cavity of a graphite resistance oven and could be heated above the melting temperature. In the second series the gold sphere 0.2 g, 120 mC) was placed in a small evacuated quartz tube which was heated

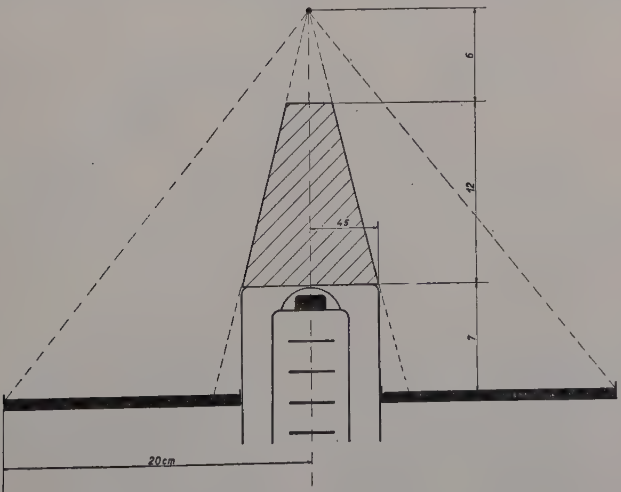

Fig. 1. Arrangement for the scattering experiments.

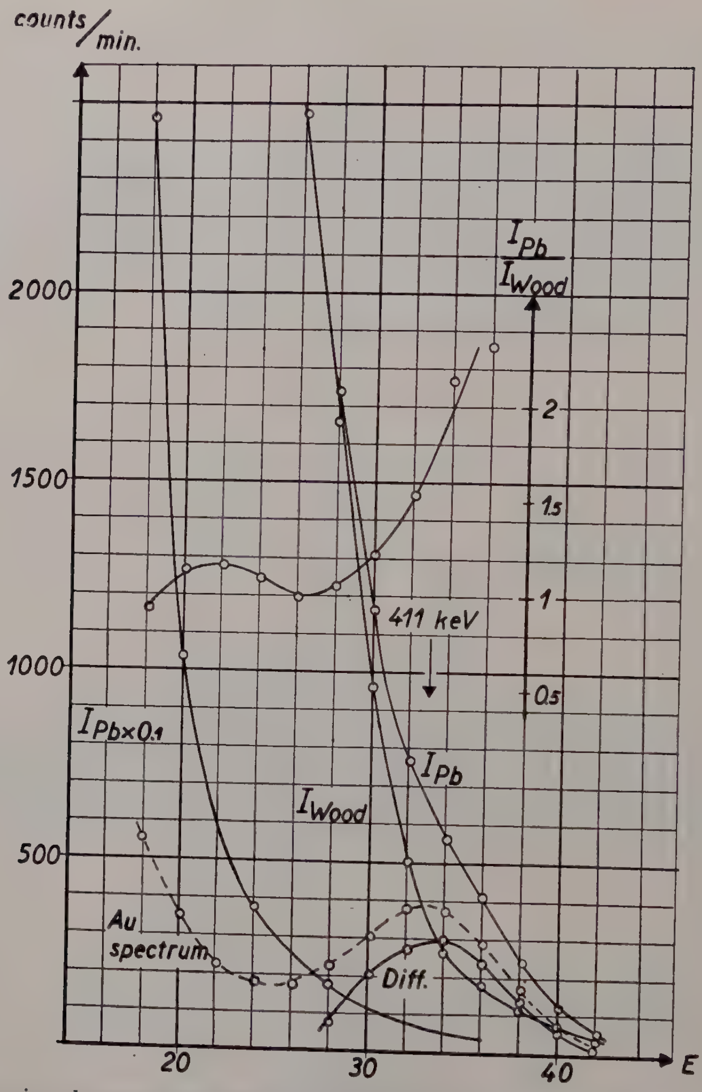

Fig. 2. Comparison between the spectrum of gamma-radiation scattered in lead and in wood. The dotted curve shows the spectrum of the direct radiation.

with a welding flame. The gold temperature was measured with an optical pyrometer.

The gamma-radiation was scattered from a horizontal surface as is seen in Fig. 1. The scatterer was liquid mercury (depth 6 mm) or alternatively a lead plate of the same dimensions. In the case of lead no effect of resonance scattering is to be expected. The detector was a 1 cm³ NaI (Tl) crystal and photomultiplier. The pulses were analyzed by means of a channel-discriminator with variable channel width. A lead cone shielded the detector from direct radiation.

Table II

	Hg		Pb
A1	6.9 ± 1.3	A4	1.4 ± 1.3
A2	2.0 ± 0.5	A6	5.3 ± 1.7
A3	5.9 ± 0.9	A7	0.6 ± 1.3
A5	3.8 ± 1.6	A9	1.3 ± 0.7
A8	5.5 ± 0.9	A10	1.0 ± 0.8
A12	5.1 ± 0.6	A11	1.9 ± 0.9

Fig. 2 shows the energy spectrum of the radiation scattered from lead and the radiation scattered from wood. The idea of this experiment was to distinguish Compton-scattered radiation from elastically scattered radiation. Since the Rayleigh scattering is proportional to the third power of atomic number its contribution should be negligible in the case of wood. The wood curve was normalized to give the best fit with the lead curve in the Compton region. The corresponding curve for mercury coincides with that of lead within the experimental errors. It is evident from this figure that the curves have different character at the high energy end and since the difference curve coincides with the 411 keV line in the spectrum of the direct radiation from gold (the dotted curve in Fig. 2) it seems likely that the difference curve is due to elastically scattered radiation. In the following experiments the spectrometer was adjusted so that only the high energy end of the spectrum was recorded where about 50 % of all quanta are assumed to be scattered elastically.

During the first series of measurements (denoted by A) the spectrometer was held at a fixed position ($E > 32$) and the gold was heated above the melting temperature. This experiment included 6 series with mercury and 6 with lead. In each run the gold was alternatingly cold and warm for periods of some minutes' length. In all cases the counting rate increased when the gold source was heated. The relative increase in percent is given in Table II. The probable errors, $\frac{1}{\sqrt{N}}$, are based on the number of counts.

Table III

	Temp.	Energy	Hg	Pb	Diff.
B1	~1 000°	32>E>34	2.45 ± 0.35	0.91 ± 0.34	1.54 ± 0.49
B2	»	»	2.88 ± 0.35	1.69 ± 0.34	1.19 ± 0.49
B3	»	34>E>36	2.79 ± 0.48	1.71 ± 0.47	1.08 ± 0.67
B4	»	28>E>29	1.48 ± 0.35	0.31 ± 0.34	1.17 ± 0.49
B5	»	24>E>25	1.48 ± 0.36	1.36 ± 0.35	0.12 ± 0.50
B6	»	30>E>32	2.51 ± 0.60	0.75 ± 0.57	1.76 ± 0.83
B7	»	40>E>42	4.09 ± 1.00	2.25 ± 0.95	1.84 ± 1.38
B8	»	37>E	1.14 ± 0.70	−0.03 ± 0.69	1.17 ± 1.00
B9	»	34>E>36	2.43 ± 0.64	1.98 ± 0.61	0.45 ± 0.89
B10	~1 100°	34>E>37	3.37 ± 0.58	1.21 ± 0.56	2.16 ± 0.81
B11	»	»	4.63 ± 0.60	3.24 ± 0.56	1.39 ± 0.82
B12	»	32>E>35	3.42 ± 0.70	1.03 ± 0.64	2.39 ± 0.95
B13	»	»	3.29 ± 0.69	1.86 ± 0.75	1.43 ± 1.02
B14	»	»	4.56 ± 0.74	3.57 ± 0.69	0.99 ± 1.02

In the second series (denoted by B), measurements were made with different adjustment of the spectrometer as indicated in Table III. (The energy scale refers to Fig. 2.) Nine runs were performed at ~ 1 000° C and five runs at ~1 100° C. Each run included about 10 cold and 10 warm measuring periods. In this experiment the mercury and lead scatterers were interchanged regularily, so that each run with mercury was followed by one with lead under identical conditions.

Temperature effect in the gamma-source

In all measurements (except one) the counting rate was higher with a hot emitter than with a cold one and this was the case also when the radiation was scattered in lead. In Table IV some data are given which show than even the direct radiation increases with the temperature of the gold source. Measurements were performed in three perpendicular directions in order to ascertain that the increase is not due to an asymetrical deformation of the gold sphere. As the following calculation shows, the effect is due to the thermal expansion of the gamma-source, a result which at first sight seems somewhat surprising.

Let us consider the absorption of the gamma-rays in the gold sphere itself. If the radius of the sphere is R and the absorption obeys the relation $I = I_0 \cdot e^{-\frac{x}{\xi}}$, the following expression gives that fraction of all emitted quanta which leave the gold sphere

$$\frac{1}{\frac{4}{3}\pi R^3}\cdot\int_0^R 2\pi r\,dr \int_{-\sqrt{R^2-r^2}}^{\sqrt{R^2-r^2}} e^{-\frac{\sqrt{R^2-r^2}+y}{\xi}}\,dy \tag{9}$$

or integrated

$$\frac{3}{a^3}\left[\frac{a^2}{2} - 1 + (a+1)\,e^{-a}\right] \tag{10}$$

or approximately, if $a \ll 1$

$$1 - \tfrac{3}{8}\,a + \tfrac{1}{10}\,a^2 + \cdots \tag{11}$$

where a is written for $\frac{2R}{\xi}$.

If the linear expansion coefficient of gold is $\varkappa$ the density varies by a factor $(1 - 3\varkappa \cdot \varDelta T)$ when the temperature is increased by $\varDelta T$. At the same time

Table IV

	Temp.	Position	Direct radiation
B15	~1 000°	Vertical	1.03 ± 0.35
B16	»	Horizontal	0.85 ± 0.35
B17	»	» (turned 90°)	0.98 ± 0.35
B18	~1 100°	Vertical	1.29 ± 0.28

all gamma-paths within the gold increase by the factor $(1+\varkappa\cdot\Delta T)$. The net result is that $\frac{R}{\xi}$ varies by a factor $(1-2\varkappa\cdot\Delta T)$. If this correction is applied to formula (10) one obtains for the temperature influence on the rate of emission from the gold sphere the factor:

$$1+2\varkappa\cdot\Delta T\cdot\frac{\frac{a^2}{2}-3+(a^2+3a+3)e^{-a}}{\frac{a^2}{2}-1+(a+1)\cdot e^{-a}}. \tag{12}$$

A determination of ξ by absorption in a gold foil under the actual conditions gave $\xi=3.5$ mm and since the radius of the 0.2 g gold sphere is 1.35 mm one obtains $a=0.77$ and for (12):

$$1+2\varkappa\cdot\Delta T\cdot 0.255.$$

As $\varkappa\simeq 17\cdot 10^{-6}$ and $\Delta T\simeq 1000°$ the increase in counting rate will be 0.9 %. If the melting point of gold is passed, the volume change during the melting (12) $\frac{\Delta V}{V}=5.2$ % will give nearly the same contribution so that the total effect when heating the gold above the melting point will be 1.8 %. The corresponding figures with the smaller, 0.1 g, gold sample are 0.7 % and 1.4 % respectively. Table V shows a comparison between the observed and the calculated values.

Table V

	Temp.	Exp.	Theor.
A	>1 100°	1.5±0.5	1.4
B	~1 000°	1.3±0.3	0.9
	~1 100°	2.2±0.2	1.8
Direct	~1 000°	1.0±0.2	0.9
	~1 100°	1.3±0.3	1.8

Resonance scattering

Tables II and III show that in every measurement the temperature influence is greater with mercury as scatterer than with lead. In Table VI all measurements are taken together in four groups. The first group represents the first

Table VI

	Temp.		Hg	Pb	Diff.
I	>1 100°	Hg: A1, 2, 3, 5, 8, 12 Pb: A4, 6, 7, 9, 10, 11	4.2 ±0.4	1.5 ±0.5	2.7 ±0.7
II	~1 100°	B 10, 11, 12, 13, 14	3.85±0.19	2.17±0.18	1.68±0.26
III	~1 000°	B 1, 2, 3, 6, 7, 8, 9	2.59±0.31	1.31±0.32	1.28±0.45
IV	»	B 4, 5	1.48±0.25	0.82±0.25	(0.66±0.35)

experiment A which was performed above the melting temperature. The second group contains those series B where the gold was heated to ~1100°, the third group those with heating to ~1000° except two series (B 4 and B 5) which are added up in the fourth group. The reason is that the latter were measured at such a low energy that the elastically scattered radiation contributed only by a small fraction to the intensity measured. It is worth noticing that a temperature increase by 100° increases the percentage by a factor 1.7/1.3 in good agreement with what is to be expected from Table I. On the average elastically scattered radiation is responsible for about 50 % of the measured intensity, except for the fourth group, which is not included in the mean value. With this fact taken into consideration one obtains for the relative increase of elastically scattered radiation

$$\frac{\sigma}{\sigma_R} = 3.0\ \%$$

and consequently, according to (8)

$$\Gamma = 6.3 \cdot 10^{-17}\ \text{ergs or } 3.9 \cdot 10^{-5}\ \text{eV}.$$

The application of Heisenberg's relation gives for the mean life

$$\tau \approx 1.6 \cdot 10^{-11}\ \text{sec.}$$

This value is in good agreement with Moon's result but is about 20 times smaller than the value reported by Storruste. In the latter case, however, the main part of the discrepancy is due to the fact that Storruste has taken into account the different statistical weights of the ground state and the excited state in Hg^{198} by multiplying the expression given in formula (1) by $\frac{1+2\,j_a}{1+2\,j_g}$. With respect to the spins of the levels this factor is 5. From the theoretical point of view it is not clear whether this factor shall enter into the formula or not.

In the experiments reported here the resonance scattering cross-section has been determined relative to the Rayleigh scattering cross-section, while in the other two cases Compton scattered radiation is only partially filtered out. The difficulties involved in the estimation of the remaining Compton radiation may well account for the discrepancy.

LITTERATURE: (1) **Kuhn, W.,** Phil. Mag. *8*, 625, 1929. — (2) **Goldhaber, M.** *et al.* Phys. Rev. *55*, 57, 1939. — (3) **Zuber, K.,** Helv. Phys. Acta, *16*, 407 and 429, 1945. — (4) **Schiff, L. I.,** Phys. Rev. *70*, 761, 1946. — (5) **Pollard, E.** and **Alburger, D. E.,** Phys. Rev. *74*, 926, 1948. — (6) **Gaertner, E. R.** and **Yeater, M. L.,** Phys. Rev. *76*, 363, 1949. — (7) **Moon, P. B.,** Proc. Roy. Soc. *63*, 1189, 1950. — (8) ——, Proc. Roy. Soc. *64*, 76, 1951. — (9) **Storruste, A.,** Investigation of gamma-rays by the scintillation method. Meddelelse nr. 185 fra Universitetets Fysiske Institutt, Oslo 1951. — (10) ——, Proc. Roy. Soc. *63*, 1197, 1950. — (11) **Bell, R. E.** and **Graham, R. L.,** Phys. Rev. *78*, 490, 1950. — (12) **Endo,** Journal of the Inst. of Metals, *30*, 121, 1923.

Tryckt den 25 oktober 1952

Uppsala 1952. Almqvist & Wiksells Boktryckeri AB

ARKIV FÖR FYSIK Band 6 nr 6

Communicated 10 September 1952 by MANNE SIEGBAHN and G. BORELIUS

Studies of the resonance absorption of neutrons in uranium with the time-of-flight method

By E. HELLSTRAND and R. PERSSON

With 12 figures in the text

Manuscript received 27 June 1952

Introduction

The values given by MEITNER *et al.* [1], ANDERSON [2] and SAUERWEIN [3] of the resonance absorption of neutrons in uranium were all obtained with the well-known boron- and self-absorption method. This method will give accurate results only when there is one single resonance, and in uranium there are certainly more than one.

As a part of the neutron physics program of this institute a time analyzer specially designed for time-of-flight spectrometry has been constructed by Techn. lic. G. von DARDEL [4], and by his courtesy has been available for studies of the resonance absorption in uranium. As a neutron source we first used a 2 MeV van de Graaff machine at the Research Institute for National Defence in Stockholm, but the neutron intensity was found to be too low. By kind permission of Professor MANNE SIEGBAHN we were allowed to use the 7 MeV cyclotron of the Nobel Institute in Stockholm.[1]

Theoretical considerations

Many experiments have been made using the time-of-flight method, and detailed treatments of the theory and method have already been given by many authors [5], [6], [7]. We therefore restrict ourselves to a short summary.

To determine the neutron absorption of a sample as a function of energy, its transmission for neutrons of different times-of-flight is measured. This is done in the following way. During a short time interval a neutron burst is produced at a well-defined place. Neutrons with their velocity vector within a certain solid angle are allowed to enter a detector, after traversing a certain flight path. By selecting groups of neutrons arriving at the detector after times $t, t + \Delta t, \ldots$ from their birth, the energy distribution of the neutron pulse can be determined with and without the sample in front of the detector, and thus the transmission at different neutron energies can be found.

---

[1] We wish to express our thanks to the cyclotron group at the Nobel Institute for the continuous help they have given us.

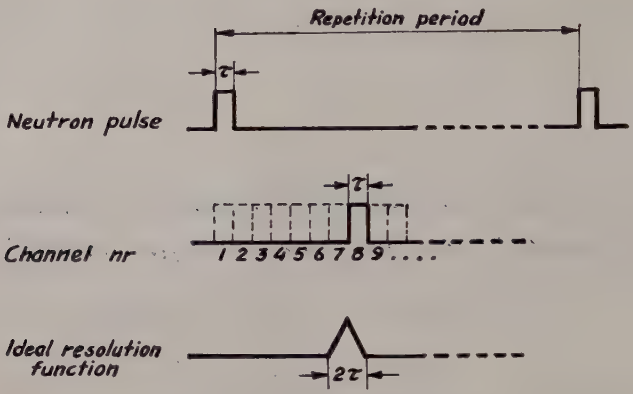

Fig. 1. Relation between the resolution function and the neutron pulse and channel widths.

The transmission for monoenergetic neutrons of a sample containing n atoms/cm^2 and with a total cross section σ_{tot} cm^2 can be written

$$T_0 = e^{-n\,\sigma_{\text{tot}}}. \tag{1}$$

In the resonance region σ_{tot} can be written as the sum of a constant cross section σ_{const} and a resonance cross section σ, which obeys the Breit-Wigner one-level formula if the resonances are not too closely spaced. Thus we have (resonance scattering neglected)

$$\sigma(E) = \left(\frac{E_0}{E}\right)^{\frac{1}{2}} \frac{\sigma_0\,\Gamma^2}{4(E-E_0)^2+\Gamma^2}, \tag{2}$$

where E_0 = resonance energy,
σ_0 = resonance cross section,
and Γ = total width of resonance,

or, written as a function of the time-of-flight Λ (Λ in μs/m and Γ in eV),

$$\sigma(\Lambda) = \sigma_0 \frac{\Lambda/\Lambda_0}{1+\left(\frac{5220}{\Gamma}\right)^2\left(\frac{1}{\Lambda^2}-\frac{1}{\Lambda_0^2}\right)^2}. \tag{3}$$

The ideal transmission curve (1) corresponds to perfect resolution and cannot be obtained experimentally. With a given resolution function $f(\lambda)$, one gets instead (assuming negligible variation of the neutron intensity within a channel width)

$$\begin{gathered} T(\Lambda) = \int_{-a}^{b} f(\lambda)\cdot T_0(\Lambda+\lambda)\,d\lambda, \\ f(\lambda)\neq 0 \text{ for } -a<\lambda<b; \int_{-a}^{b} f(\lambda)\,d\lambda = 1. \end{gathered} \tag{4}$$

Thus the shape of the measured transmission curve depends on the resolution function. This is mainly determined by the duration and shape of the neutron pulse and the channel width. To give maximum counting rate for a given resolution the length of the pulse modulating the ion source in the cyclotron and the channel width are chosen equal, giving a triangular resolution function (Fig. 1), which, however, will in reality be somewhat smeared out and broadened by the spread in acceleration time of the ions in the cyclotron, by the length of the detector, which causes an uncertainty in the flight path of the neutrons, and by the finite rise-time of the pulses in the electrical circuits.

To avoid the need of knowing the exact form of the resolution function, we define, following RAINWATER and HAVENS [6], the *"absorption integral"*

$$A = \int_{\Lambda_1}^{\Lambda_2} [1 - T(\Lambda)]\, d\Lambda, \tag{5}$$

where Λ_1 and Λ_2 are the limits of the resonance region. A is equal to the area between the line representing unity transmission and the measured transmission curve, normalized in such way that $T = 1$ far from the resonance. Expanding $T_0\ (\Lambda + \lambda)$ in a Taylor series around the point Λ, A can be written in the following form

$$A = \int_{\Lambda_1}^{\Lambda_2} [1 - T_0(\Lambda)]\, d\Lambda + [\overset{\Lambda_2}{\underset{\Lambda_1}{I}} T_0] \int_{-a}^{b} f(\lambda)\, \lambda\, d\lambda + \cdots \tag{6}$$

where we remember that T_0 is the transmission at perfect resolution. Thus the integral is independent of the resolution if $\overset{\Lambda_2}{\underset{\Lambda_1}{I}} T_0 = \overset{\Lambda_2}{\underset{\Lambda_1}{I}} T_0' = \cdots = 0$, which is approximately the case.

The experimentally found value of A should be compared with the theoretical value $A = \int (1 - T_0(\Lambda))\, d\Lambda$, using (1) and (3). The integral cannot be evaluated analytically, but for two special cases we can get a useful approximate result. Supposing $\Gamma \ll E_0$ and $\left(\frac{E_0}{E}\right)^{\frac{1}{2}} \approx 1$ we have for

1) $n\sigma_0 \gg 1$, representing a thick sample,

$$A_{\text{thick}} = \frac{\Lambda_0}{2E_0} \sqrt{\pi n \sigma_0 \Gamma^2} \tag{7}$$

which gives

$$\sigma_0 \Gamma^2 = \frac{4}{\pi} \left(\frac{E_0}{\Lambda_0}\right)^2 \frac{A_{\text{thick}}^2}{n}.$$

2) $n\sigma_0 \ll 1$, representing a very thin sample,

$$A_{\text{thin}} = \frac{\pi}{4} \frac{\Lambda_0}{E_0} n \sigma_0 \Gamma$$

which gives

$$\sigma_0 \Gamma = \frac{4}{\pi} \left(\frac{E_0}{\Lambda_0}\right) \frac{A_{\text{thin}}}{n}.$$

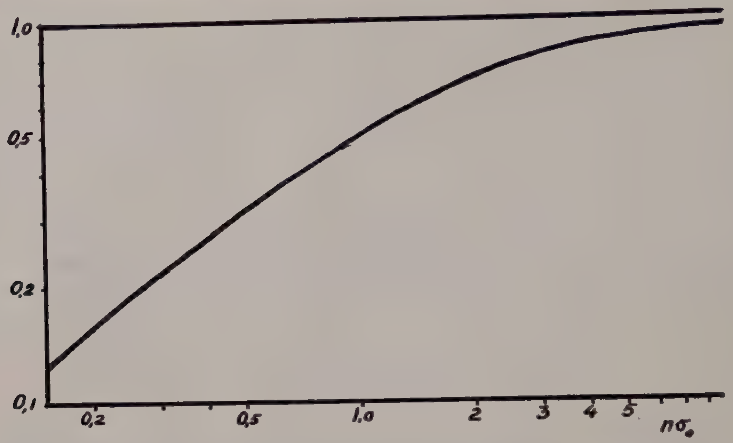

Fig. 2. The deviation of the quantity $\left(\frac{4}{\pi}\left(\frac{E_0}{\Lambda_0}\right)^2 \frac{A^2}{n\sigma_0\Gamma^2}\right)$ from unity for $0.1 < n\sigma_0 < 10$. [8]

Thus by determining A_{thick} and A_{thin} it is in principle possible to get $\sigma_0\Gamma^2$ and $\sigma_0\Gamma$, from which σ_0 and Γ can be calculated separately.

A slightly different approach specially suitable for cases when Γ is much less than the resolution width is given by RAINWATER and HAVENS [8]. From Eq. (7) we form the expression

$$Z = \frac{4}{\pi}\left(\frac{E_0}{\Lambda_0}\right)^2 \frac{A^2}{n\sigma_0\Gamma^2},$$

which for thick samples is equal to 1, but decreases as n decreases. By numerical integration of (5) the real value of Z can be obtained, and is plotted as a function of $n\sigma_0$ in Fig. 2. To find σ_0 and Γ two samples are used, one thick and one thin, and the areas are determined. Putting $Z = 1$, one gets $(\sigma_0\Gamma^2)_{\text{thick}}$, $(\sigma_0\Gamma^2)_{\text{thin}}$ and the ratio $(\sigma_0\Gamma^2)_{\text{thin}} / (\sigma_0\Gamma^2)_{\text{thick}}$, which is less than 1, and by means of Fig. 2 yields an approximate value of $n\sigma_0$ for the thin sample. Knowing n, σ_0 can be determined, and thus also Γ, from the value of $\sigma_0\Gamma^2$ for a thick sample.

Apparatus

Fig. 3 gives a view of the experimental arrangement and in Fig. 4 a block diagram is shown of the electrical circuits. The neutron source is a 7 MeV cyclotron with an internal Be-target [9]. The ion beam is pulsed by means of a set of 8 parallel-coupled 6Y6G tetrodes in series with the arc. These valves, ordinarily cut off, are opened by pulses from the time analyzer, resulting in the generation of the desired ion pulses.

The neutrons generated at the target are slowed down in a paraffin moderator outside the cyclotron, and a beam within a certain solid angle is allowed to enter the detector, situated about 6 m from the front surface of the paraffin.

The neutron beam is shielded from stray neutrons by means of a cylindrical collimator consisting of paraffin and boron trioxide arranged as shown in Fig. 5. The thermal neutrons from the paraffin are captured by a cadmium sheet 2 mm thick.

The detector consists of three ionization chambers of total volume about 1500 cc filled with purified BF_3 of natural isotopic composition at a pressure of 600 mm Hg. The high tension used is 3400 V, which is enough to give a good discriminator plateau without risk of breakdown.

The pulses from the BF_3 chambers are amplified in a conventional amplifier and led via a discriminator to the time-analyzer and a scale of 64. As the time-analyzer will be described in detail elsewhere we give only some information of interest for the present investigation. It has 20 channels, each with a scale of four and a register, the smallest channel width being 2 μs. The repetition rate can be varied in four steps, giving an operating cycle period of 20, 40, 100 or 200 times the channel width τ, and the twenty channels, covering a time interval of $20 \times \tau$, can be distributed in various ways over the whole range. As the neutron pulse must be synchronized with the time measuring equipment the time-analyzer also delivers the pulses modulating the arc in the cyclotron. These pulses, the length of which is usually chosen

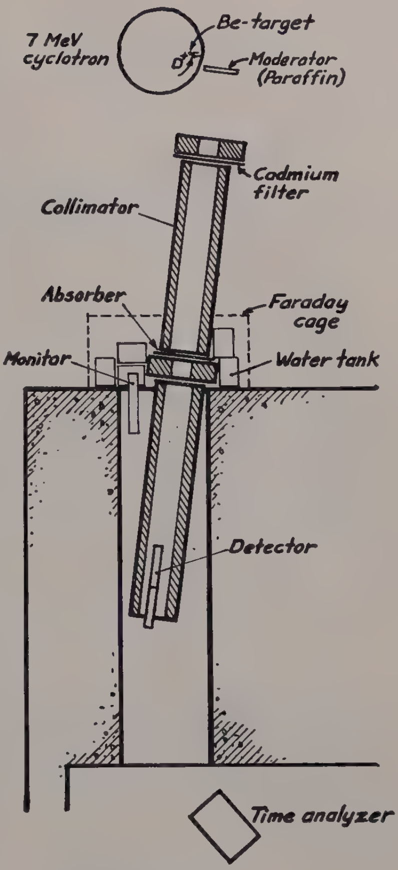

Fig. 3. General view.

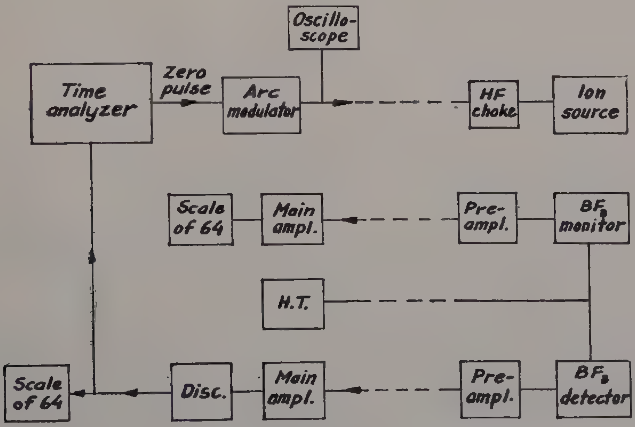

Fig. 4. Block diagram of electrical circuits.

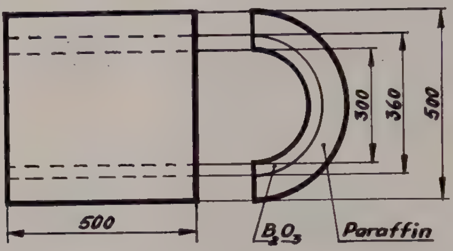

Fig. 5. Segment of collimator.

equal to the channel width, will be called the "zero-pulses" in the discussion below.

An extra BF_3 chamber with amplifier and scale is used as a monitor and all results are normalized to the same number of monitor counts.

The electrical circuits are shielded from the high frequency field of the cyclotron by a sort of Faraday cage, and the pulse to the ion source is fed through a high-frequency filter.

Experimental procedure

On account of the 2 mm thick cadmium filter only neutrons of times-of-flight less than about 120 μs/m, or 735 μs for a flight path of 6.15 m, reach the detector. Thus the repetition period ought to be longer than 735 μs to avoid overlapping. For a pulse width of 4 μs, which according to RAINWATER and

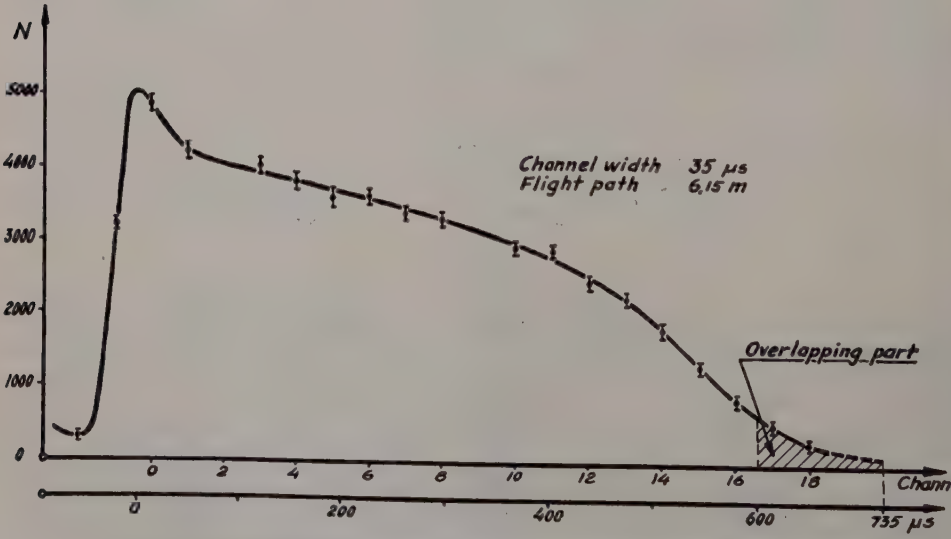

Fig. 6. The epicadmium neutron intensity as a function of time-of-flight.

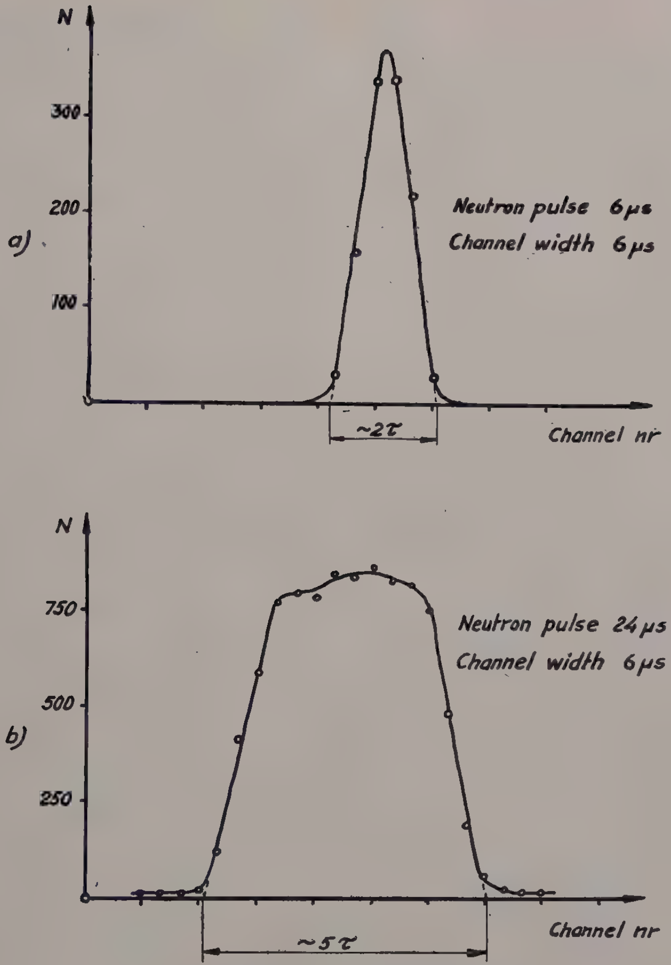

Fig. 7. Measured resolution functions.

Havens [8] is about the lower limit for an arc-modulated cyclotron, this implies a repetition period of $200 \times 4 = 800$ μs. Because of geometrical inconveniences at the cyclotron (only internal target, no space available in the forward direction of the neutron bursts), the intensity was not high enough to allow a duty ratio larger than 100. We thus had to make a compromise between using a rather large channel width (8 μs), giving bad resolution, and a short one, causing overlapping over a long energy region. We chose a repetition period of 600 μs, corresponding to a channel width of 6 μs, which gives overlapping for neutron times-of-flight less than about 22 μs/m or, in energy units, above 11 eV. As seen from Fig. 6 the overlapping part of the intensity decreases rapidly with energy, and is at most only 15 % of the very fast neutron intensity. As the resolution is rather bad in the high energy region, we have neglected the influence of the overlapping.

In order to determine the resolution function we replaced the BF_3 detector by a pentane chamber which, detecting recoil protons, is only sensitive to high energy neutrons [7]. By means of a delay line the relative time positions of the zero-pulse and the channels could be changed in steps of 2 μs, and thus a rather precise curve could be obtained (Fig. 7). Fig. 7 a is the curve obtained with the neutron pulse equal to the channel width and Fig. 7 b with the neutron pulse four times the channel width. The latter arrangement was used for the thinnest absorbers to increase the counting rate, the better statistical accuracy more than compensating for the decrease in resolution.

The base of the resolution function in Fig. 7 a is about 2τ, with a small tail on either side. The tail caused by incomplete quenching of the arc in the ion source reported by RAINWATER and HAVENS [8] was not found. The curve mentioned above was determined once and for all, and in order to check the apparatus from time to time we instead used the method described by RAINWATER and HAVENS in [8]. They used the highly energy-dependent transmission of a 2.89 g/cm^2 thick paraffin layer to determine the resolution. It can be shown that at neutron energies as high as 10^4 eV, corresponding to a time-of-flight of 0.7 μs/m, the transmission only amounts to 0.4 %. Thus only the highest energy neutrons are transmitted without suffering collisions. This method has the advantage that the BF_3 chambers in their normal positions may be used as detector, and thus it gives the resolution function under working conditions, and the real time-lag between the zero-pulse and neutrons detected after a negligible time-of-flight. This delay was found to be 16 μs. The curve as a whole will, however, be less exact than that obtained with the pentane chamber, because of the high background of diffused neutrons.

Five samples were used as absorbers, four consisting of uranium trioxide, UO_3, thicknesses 5.46 g/cm^2, 3.45 g/cm^2, 0.27 g/cm^2 and 0.092 g/cm^2 and one of U_3O_8, thickness 0.67 g/cm^2. All were made of fine powder compressed in cylindrical boxes with aluminium walls, except the thinnest, which was slurried in a solution of polyvinyl acetate. They were mounted at equal distances from the target and the detector.

As the neutron intensity was fairly low the experiments had to be made over a long time interval. In order to reduce errors caused by various drifts in the apparatus a long run was divided into intervals with and without sample. To give the best statistical accuracy the ratio t_{in}/t_{out} was chosen equal to $\sqrt{\frac{N_{out}}{N_{in}}}$, where t_{in} (N_{in}) and t_{out} (N_{out}) are the counting intervals (rates) with the sample in and out respectively [10].

Results

In the region above 16 eV only the thickest absorber was used. There are rather strong indications of resonances at about 20 and 38 eV, as may be seen from Fig. 8. The curves are normalized in such a way that $T = 1$ far from the resonances. Assuming single resonances, and $n\,\sigma_0 \gg 1$, we obtain the following values for the energies and the "strengths" of the resonances:

$$E_0 = 20 \pm 2 \text{ eV}; \quad \sigma_0 \Gamma^2 = 4.5 \pm 2 \quad b\,(\text{eV})^2.$$
$$E_0 = 38 \pm 4 \text{ eV}; \quad \sigma_0 \Gamma^2 = 6.5 \pm 4 \quad b\,(\text{eV})^2.$$

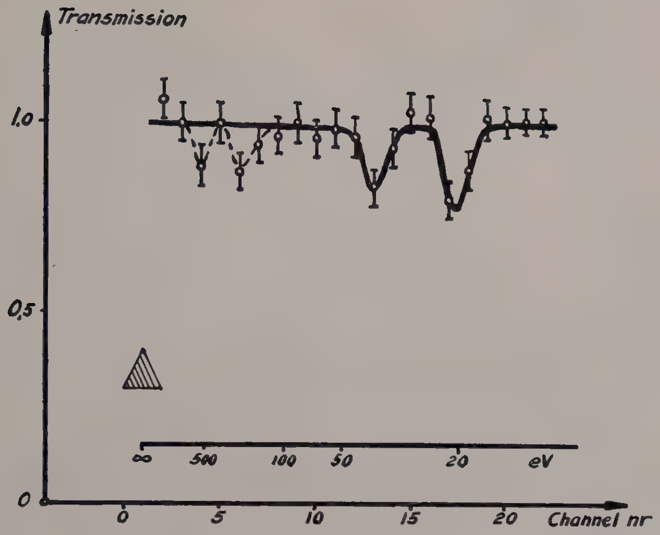

Fig. 8. Normalized transmission curve for 5.46 g/cm² UO_3. ($E > 16$ eV.)

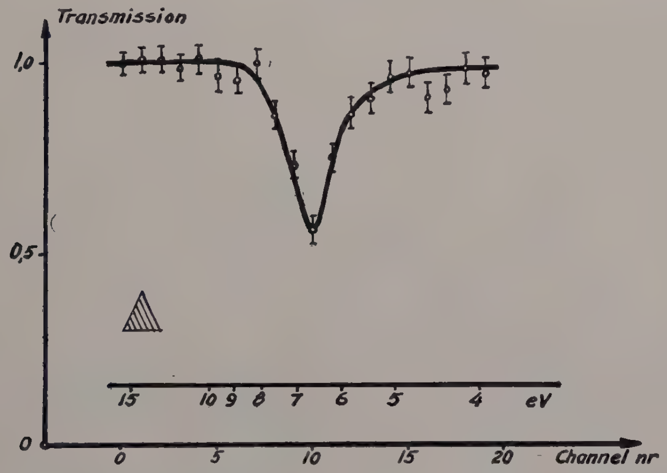

Fig. 9. Normalized transmission curve for 5.46 g/cm² UO_3. (16 eV $> E >$ 3.7 eV.)

There may also be resonances at about 200 and 600 eV, but the resolution does not allow any certain determination. A control measurement was made with a channel width of 7 μs and the transmission curve obtained had the same appearance as Fig. 8.

In the region between 3.7 and 16 eV all the five absorbers were used. The results with 5.46 g/cm², 0.67 g/cm² and 0.092 g/cm² are shown in Figs. 9, 10 and 11. We have only found one certain resonance in this region, and the energy value is determined to

$$E_0 = 6.6 \pm 0.2 \text{ eV}.$$

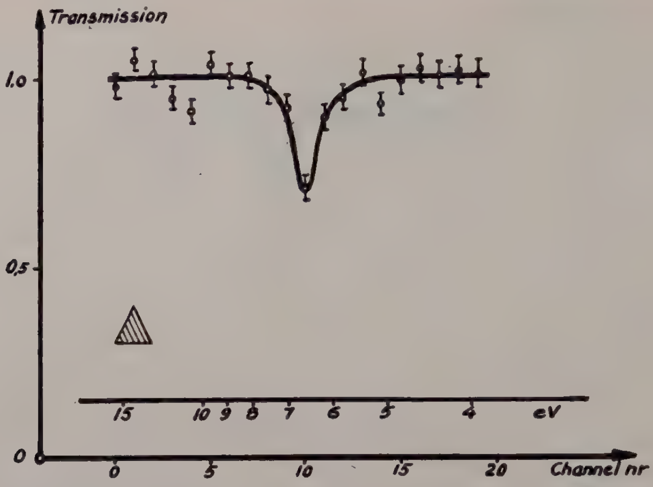

Fig. 10. Normalized transmission curve for 0.67 g/cm² U_3O_8. (16 eV $> E >$ 3.7 eV.)

Table 1

Sample		A µs/m	$\sigma_0\,\Gamma^2$
No.	g/cm²		
I.	5.46	1.42±0.10	12.4±1.8
II.	3.45	1.19±0.07	13.7±1.8
III.	0.67	0.57±0.06	15.4±3.6
IV.	0.27	0.36±0.05	16.4±4.2
V.	0.092	0.14±0.02	7±2
Weighted mean for I—III			13.5±1.5

The area A as a function of $\sqrt{n}$ is given in Fig. 12. All the values except that for the thinnest absorber lie rather well on a straight line through the origin and from the slope of this line we obtain $\sigma_0\,\Gamma^2$ (see Eq. (7) and Table 1)

$$\sigma_0\,\Gamma^2 = 13.5 \pm 1.5\, b(\mathrm{eV})^2.$$

Moreover the deviation from the straight line for the thinnest absorber indicates that this absorber is not a "thick" one, and thus from Fig. 2 a rough value for σ_0 can be estimated. This gives

$$\sigma_0 = 5400^{+3500}_{-2200} \text{ barns},$$

from which follows

$$\Gamma = 0.050 \pm 0.015 \text{ eV}.$$

As the Debye temperature of UO_3 is 140° K [11], the formula for the doppler width $\Delta = 2\sqrt{\frac{m}{M}E_0\,kT}$ is valid [12]. With $E_0 = 6.6$ eV and $T = 300°$ K we

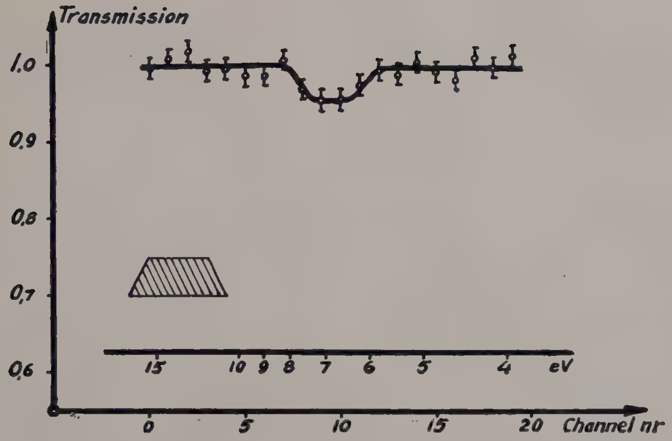

Fig. 11. Normalized transmission curve for 0.092 g/cm^2 UO$_3$. (16 eV $> E >$ 3.7 eV.)

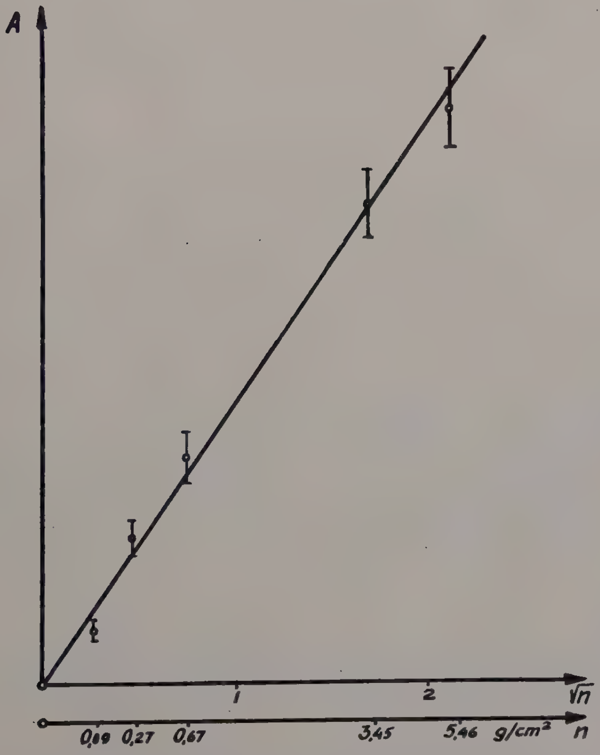

Fig. 12. The absorption integral as a function of $\sqrt{n}$.

obtain $\Delta = 0.052$ eV. Therefore the doppler effect cannot be neglected as is tacitly assumed above and the area A will be too large and thus also the value of σ_0. Further calculations on the influence of the doppler effect [15] give the more accurate results:

$$\sigma_0 \Gamma^2 = 12.4 \pm 1.3\, b(\text{eV})^2$$

$$\sigma_0 = 5000^{+2000}_{-1500} \text{ barns}$$

$$\Gamma = 0.050 \pm 0.010 \text{ eV}$$

These values of the parameters for the main resonance are to be compared with the values obtained with the boron- and self-absorption method. SAUERWEIN [3] found $E_0 = 7.5 \pm 1.5$ eV, $\Gamma = 0.0075$ eV, $\sigma_0 = 40\,000$ barns (corrected for the doppler effect = 4700 barns), giving $\sigma_0 \Gamma^2 = 2.2\, b$ (eV)^2. ANDERSSON [2] found $E_0 < 11$ eV, $\Gamma = 0.20$ eV and $\sigma_0 = 4600$ barns, giving $\sigma_0 \Gamma^2 \approx 180\, b$ (eV)^2. Thus our value for $\sigma_0 \Gamma^2$ lies between these values but does not agree with either of them.

To check the energy calibration we made a measurement of the 5 eV resonance of silver, for which we got

$$E_0 = 5.1 \pm 0.2 \text{ eV}$$

in good agreement with the more precise value, $E_0 = 5.17 \pm 0.08$ eV, found by SELOVE [13]. From our measurement we could also roughly estimate the value of $\sigma_0 \Gamma^2 \approx 250$ for silver, which does not disagree too much with SELOVE's value $\sigma_0 \Gamma^2 = 365 \pm 30\, b(\text{eV})^2$ and RAINWATER's $300 \pm 50\, b(\text{eV})^2$ [14]. Thus it is not probable that there is any great systematic error in our measurement.[1]

Acknowledgement

We wish to express our sincere thanks to the Director of the physical department, Dr SIGVARD EKLUND, for his encouraging interest, and to Techn. lic. GUY VON DARDEL, leader of the neutron physics group, who has closely followed every step of the work and made many valuable suggestions.

REFERENCES: [1] **L. Meitner, O. Hahn** and **F. Strassman,** Z. Phys. *106,* 249 (1937). — [2] **H. L. Andersson,** Phys. Rev. *57,* 566 (1940) and *80,* 499 (1950). — [3] **K. Sauerwein,** Z. Naturforschung *2a,* 73 (1947). — [4] **G. F. von Dardel,** Arkiv för fysik *2,* 337 (1950). — [5] **C. P. Baker** and **R. F. Bacher,** Phys. Rev. *59,* 332 (1941). — [6] **L. J. Rainwater** and **W. W. Havens, Jr,** Phys. Rev. *70,* 136 and 154 (1946). — [7] **W. B. Jones, Jr,** Phys. Rev. *72,* 362 (1947). — [8] **W. W. Havens, Jr** and **L. J. Rainwater,** Phys. Rev. *83,* 1123 (1951). — [9] **H. Atterling,** K. Sv. Vetensk. Årsbok (1945). — [10] **M. E. Rose** and **M. M. Shapiro,** Phys. Rev. *74,* 1853 (1948). — [11] **J. J. Katz** and **E. Rabinowitch,** The Chemistry of Uranium, p. 278, McGraw-Hill (1951). — [12] **W. E. Lamb, Jr,** Phys. Rev. *55,* 190 (1939). — [13] **W. Selove,** Phys. Rev. *84,* 869 (1951). — [14] **L. J. Rainwater** *et al.,* Phys. Rev. *71,* 65 (1947). — [15] **G. von Dardel** and **R. Persson** to be published.

AB Atomenergi, Department of Physics, Stockholm, Sweden.

---

[1] *Note added in proof:* During the printing of this manuscript curves of the neutron cross section for natural uranium have appeared in AECU-2040, Neutron Cross Sections, 1952. These curves are consistent with ours within the error limits. The values of $\sigma_0 \Gamma^2$, σ_0 and Γ are not given.

Tryckt den 15 november 1952

Uppsala 1952. Almqvist & Wiksells Boktryckeri AB

ARKIV FÖR FYSIK Band 6 nr 7

Communicated 28 May 1952 by Erik Hulthén

Measurements on the microwave spectra of methyl alcohol and nitromethane

By Gunnar Erlandsson

A Stark-effect modulation microwave spectrometer has been built at this institution. The instrument, which will be described in more detail later on (when the equipment is more complete), has been tried on methyl alcohol and nitromethane (CH_3NO_2).

Two klystrons type 2K33 have been used to cover the region 16.3—25.7 kMc/s. The absorption cell is 3 m long and consists af a 3 cm wave-guide with central steel electrode. A National HRO7-receiver is used as spectrum amplifier tuned to the modulation frequency 100 kc/s. Sine-wave modulation biased to ground has been used with maximum field intensity of about 600 volts/cm.

Frequencies have been measured with a TE_{01}-cavity wave-meter of the type described by Bleany, Loubser and Penrose (1). The output from the wave-meter is mixed with the spectrum signal in a difference amplifier and thus presented on the same oscilloscope screen as the absorption lines. One single wave-meter has been used to cover the entire frequency region investigated. The average error in the freqency measurements on ammonia lines between 19.5—25 kMc/s has been about ± 2 Mc/s. Below 19.5 kMc/s the accuracy is slightly worse because here only two resonances can be used instead of three resonances above 19.5 kMc/s. Most frequency values presented below are, however, believed to be good to ± 5 Mc/s.

Table 1

Methyl alcohol spectrum

Frequency value found here	Frequency according to (2)	Stark-effect order	Estimated relative intensity
16390	—	1	S
16556	—	—	W
16937	16941,6	—	W
17507	—	2	W
17906	17911,1	1	S
17944	—	1	S
18159	—	1	M
19139	—	—	M
19386	19390,18	1	M
19964	—	1	M

Table 2

CH_3NO_2 spectrum

Frequency	Stark-effect order	Estimated relative intensity	Frequency	Stark-effect order	Estimated relative intensity
16342	—	M	20405	2	W
16414	2	S	21190	—	W
16522	2	W	21500	—	W
16556	2	S	22054	2	S
16689	—	W	22068	1	W
16727	2	W	22267	2	W
16807	2	M	22332	2	W
16823	—	W	22370	1	W
16915	—	W	22391	2	W
16948	2	W	22418	1	W
17053	2	W	22478	2	M
17228	—	W	22489	2	M
17365	—	W	22528	2	W
17462	—	W	22536	2	W
17513	2	W	22628	2	M
17530	—	W	22651	2	W
17618	1	M	22701	2	S
17864	—	W	22820	2	S
17900	1	M	23004	2	M
17968	2	S	23330	—	M
18068	2	W	23455	2	S
18102	—	W	23499	2	W
18112	—	W	23594	2	W
18136	—	W	23661	1	M
18172	—	W	23700	2	W
18239	—	W	23744	2	M
18256	—	W	23754	1	W
18574	—	W	23782	2	W
18609	—	W	23798	—	W
18665	—	W	23896	—	W
18810	2	W	23939	—	W
18938	—	W	24140	2	W
19025	—	W	24286	2	W
19055	—	M	24338	2	W
19233	—	W	24386	1	W
19370	2	W	24420	—	W
19420	—	W	24433	2	S
19576	—	W	24506	2	W
19617	—	W	24589	2	M
19719	—	W	24658	1	W
19794	—	W	24959	—	W
19828	—	W	25224	—	W
20026	—	W	25373	1	M
20079	—	M	25394	2	S
20188	—	W	25405	2	S
20260	—	W	25684	2	W
20291	2	S	25701	2	W

The results obtained on methyl alcohol agree well with the results of HUGHES, GOOD and COLES (2) as far as the frequency regions of good instrument sensitivity are overlapping. Between 16.3–20.0 kMc/s, however, ten lines have been found, only three of which are reported in (2). The frequency values found here are listed in Table 1 together with estimated relative intensities and Stark-effect order. The line at 19964 Mc/s has a linear Stark-effect such as displayed in Fig. 2 b of Ref. (2) and is thus expected to have $\Delta J/=1$. Only two components on each side have been seen, whence the lower J-value should be 2. The Stark-effects of the other lines cannot be resolved with the sine wave modulation used.

Nitromethane has been investigated previously by DAILEY and WILSON (3) (4) and by BAK *et al.* (5) who have reported some 15 lines. In the present investigation 94 lines were measured. The agreement with previous measurements is good for some lines. For other lines, however, there are deviations of as much as 15 Mc/s. Two lines reported in (3) and (5) have not been found here (23250 and 24017 Mc/s). The results are listed in Table 2.

I wish to express my thanks to Professor ERIK HULTHÉN for extending to me the facilities of this institution and for his interest in the work, to Dr. phil. Börge Bak in Copenhagen for a highly purified sample of nitromethane and for much helpful advice and to Försvarets Forskningsanstalt for the loan of some microwave components. The work has been economically supported by Svenska Atomkommittén and by Statens Naturvetenskapliga Forskningsråd.

Stockholm, May 15, 1952.
University of Stockholm, Department of Physics.

REFERENCES: (1) (**B. Bleany, J. H. N. Loubser** and **R. P. Penrose,** Proc. Phys. Soc. *59,* 185 (1947). — (2) **R. H. Hughes, W. E. Good** and **D. K. Coles,** Phys. Rev. *84,* 418 (1951). — (3) **B. P. Dailey** and **E. B. Wilson Jr.,** Phys. Rev. *72,* 522 (1947). — (4) **P. Kisliuk** and **C. H. Townes,** Journ. of Research NBS *44,* 611 (1950). — **B. Bak, E. Stenberg Knudsen** and **E. Madsen,** Phys. Rev. *75,* 1622 (1949).

Tryckt den 15 november 1952

Uppsala 1952. Almqvist & Wiksells Boktryckeri AB

ARKIV FÖR FYSIK Band 6 nr 8

Read 14 May 1952

On the measuring of cohesional forces of solids, as influenced by liquids

By C. BENEDICKS and B. EKELUND-KAPPELĖR

With 2 figures in the text

Contents

1. Introduction 73
2. Method developed 74
3. Experimental results 75
    I. Pressure $\leqq$ 2.7 g 75
        a. Dry air 75
        b. Two organic liquids 75
        c. Distilled water containing air 75
        d. Water out-gassed 75
        e. Water containing a wetting agent 76
    II. Pressure = 15.4 g 76
        f. Water out-gassed 76
        g. Water containing a wetting agent 77
    III. Pressure = 32.2 g 77
        h. Water containing a wetting agent 77
4. Further remarks: repolishing, surface tension 77
5. Conclusion 77
Summary 78

1. Introduction

The cohesional forces between solid particles ("coherescence" according to A. ATTERBERG[1]) are of a great importance, theoretically as well as technologically.

V. S. VESELOVSKIJ and I. A. SELYAEV[2] have studied the mechanical properties of wet clay balls; P. A. ILMONI and M. TIGERSCHIÖLD[3] those of pellets of ore concentrates ("slig"). In both papers it is maintained, that the main reason for the cohesional forces observed is the occurrence of contracting menisci in the very surface layer of the wet pellet, surrounded by air.

It is evident, however, that consideration must be given to the cohesional forces (S_0) acting between the particles when dry — though being extremely small — and

---

[1] Int. Mitt. d. Bodenkunde Vol. *2*. 14 g. 1912—13.
[2] *Colloid J.*, U. S. S. R., *2*, 417, 1936.
[3] Jernk. Ann. *134*, 135, 1950.

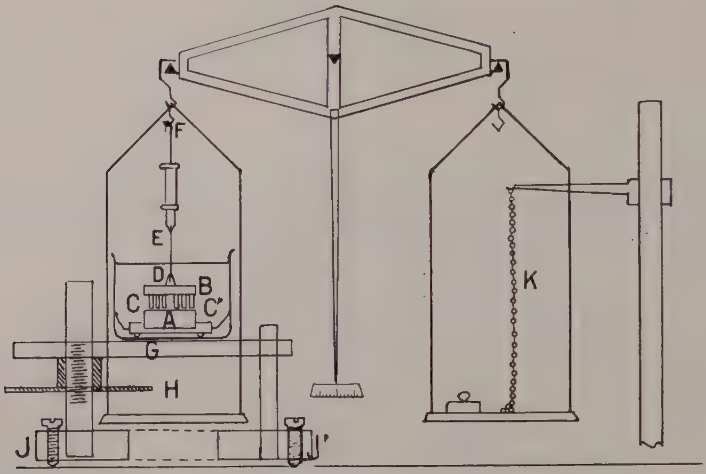

A	Brass disc	*G*	Micrometer table
BCC'	Brass "brush"	*H*	Graduated circular disc
DE	Tungsten wire	*JJ'*	Levelling screws
EF	Coarse adjusting device	*K*	Loading chain

Fig. 1.

also, in particular, to the *cohesional forces* (S_L) *acting between the particles when wet* — in which case the attraction may be expected to be considerably greater than in a dry condition.

This has actually been pointed out by C. Benedicks and P. Sederholm[1], when discussing "the influence of a liquid on the occurrence of fissures and on the attraction between two plane surfaces". There (fig. 2) two curves were sketched to illustrate the relative magnitudes of the dry attraction S_0 and the wet attraction S_L, the latter presumed to be appreciably greater, at a constant distance d.

The scope of the present investigation is to bring forth an experimental method for the evaluation of S_0 and S_L.

2. Method developed

As primary material commercial brass was chosen (~ 33% Zn). *A* (Fig. 1) is a carefully planed and polished disc (15 × 5.5 mm); *B* is a disc (15 × 2 mm) provided with about 80 regularly spaced 0.3 mm holes, each containing a brass pin *C*, *C'* (free length 5 mm; tin soldered). The carefully polished lower ends of the pins thus constituted a comparatively well defined plane area (the "brush" was embedded in sealing wax during shaping); the resulting contact area may be estimated to, say, 4 mm^2.

By means of a centric holder *D*, *B* was suspended by a very thin tungsten wire (0.017 mm), the upper end of which was attached to an adjustable holding device *EF*, where *F* is a hook, suspended from the lower hook of an analytical precision balance (Sartorius).

---

[1] Jernk. Ann. *129*, 107, 1945 (Swed.).

The disc A is rigidly mounted in a glass beaker (150 cm^3), which is supported by a micrometer table G, adjustable by a graduated disc H and adjustable also by the levelling screws J, J' and free from any contact with the balance pan. On the other pan, a very fine chain K of Ag (1 mm = 0.0022 g) could be loaded (mm-reading).

The entire apparatus was standing on a rigid marble table.

The function of the tungsten wire was to reduce as far as possible the influence of the surface tension of the liquid when used. The general run of an experiment was the following.

1. Out-gassing of test bodies submerged in the liquid, comprizing vigorous boiling, and cooling 45 mins.
2. Inserting beaker in the balance house; after having counterbalanced the brass "brush" (weight P) — so as to be freely suspended in the liquid — the micrometer table was adjusted to zero position of balance pointer.
3. Arresting balance so that A is loaded with the weight P for a given length of time.
4. Disarresting balance; lowering chain successively until the "brush" comes loose from the disc A; the value of cohesion p is then obtained.

3. Experimental results

The main point of interest would have been to know the mean free distance between the two surfaces (of A and of CC'). Since this variable is scarcely available for direct computation, the experiments were made using a few different contact pressures P, and varying the time of observation, so that the free distance should vary in a given direction. The results are to be seen in Fig. 2.

I. Pressure (approximately) $P = 2.7$ g

a) *Dry air.* — $P = 2.7$ g.

The observations *a* show no appreciable cohesional effect at shorter periods of time, but after 12 (1.5 mg), 24 and 36 hours resp. an increasing value is obvious. Some part of the observed effect, however, might be due to an incomplete removal of humidity.

b) *Two organic liquids.* — $P = 2.5$ g (corrected!).

A plain but modest effect was also observed — as indicated by the points b and b' — when using benzine (ligroin) and ethanol. Their relative positions indicate that ethanol exerts a slightly stronger influence than benzine.

c) *Water containing air.* — $P = 2.4$ g.

As shown by the observations c, a regular, continuous increase in cohesional force with time was obtained, up to 14 mg.

d) *Water out-gassed.* — $P = 2.4$ g.

The cohesional increase takes place at a considerably accelerated rate, reaching a maximum near 28 mg after about 20 hours. The accelerated rate may be attributed to the absense of air (no air precipitation being possible). In a similar way, the

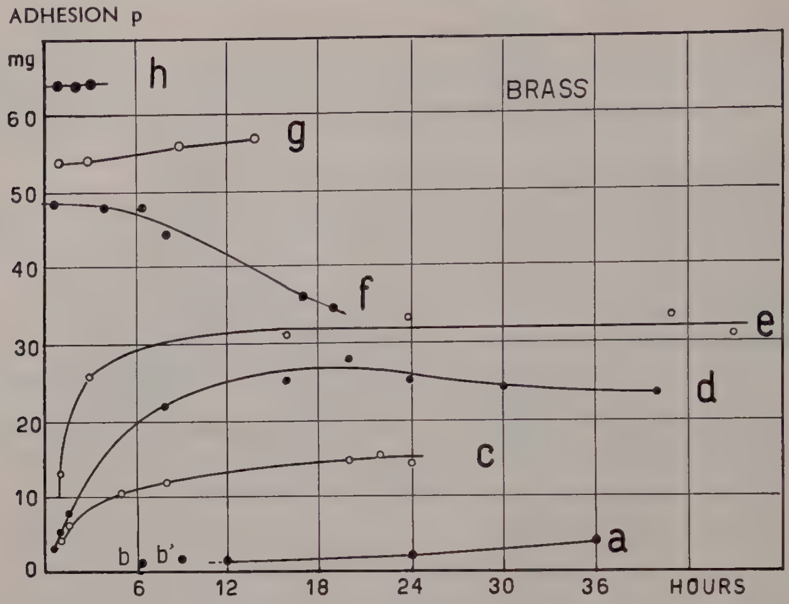

	P gram
a Dry	2.7
b Benzine. *b'* Ethanol	2.5
c Water containing air	2.4
d Water out-gassed	2.4
e Water containing a wetting agent	2.4
f Water out-gassed	15.4
g Water containing a wetting agent	15.4
h Water containing a wetting agent	32.2

Fig. 2.

final decrease may be explained by a successive absorption of air, giving an air content of the water as in *c*, with an enrichment at the contact surface.

e) *Water containing a wetting agent.* — *P* = 2.4 g.

The curve *e* illustrates the effect of using a 0.01% aqueous solution of a wetting agent, dodecyl amine acetate. It will be seen that the increase in cohesional effect in this case is *greatly accelerated and strengthened:* after 12 hours, a value of about 30 mg is reached, remaining almost constant for a long period (48 hours).

II. Pressure *P* = 15.4 g

f) *Water out-gassed.*

The increased load causes a remarkably high cohesional effect: after 1 hour the high value of 48 mg was obtained. Curve *f* further reveals a plain decrease. This might appear strange, but it may be due to the same cause as that of the decreasing curve *d:* the out-gassed water successively reabsorbs air, concentrating at the contact surface. The strong influence of a thin gas layer on the cohesional forces has been experimentally proved.[1]

g) *Water containing a wetting agent.*

By the use of the wetting agent, the cohesional effect is furthermore increased (up to a value of 54 mg for 1 hour's contact; curve *g*). Further, we see that with increasing time the cohesional effect steadily increases. This is what we may expect from the excellent wetting of the liquid: a good wetting signifies the absence of a gaseous interphase and causes, as already pointed out, strong cohesional forces.

III. Pressure $P = 32.2$ g

h) *Water containing a wetting agent.*

The fine tungsten wire did not allow the application of a substantially increased pressure. A few check trials, however, were made using the higher pressure 32.2. It will be seen that the values obtained (*h*) exhibit an appreciable increase, reaching 64 mg. *This is about 43 times the dry value observed in a.*

4. Further remarks: repolishing, surface tension

Preliminary tests had shown that it was essential for a satisfactory reproducibility, that the brass test bodies were freshly repolished before each series of tests (the polishing was made on soft endwood (alder), using stearine oil and freshly ignited Vienna-chalk (910° C); after the polishing, careful washing with benzine).

The surface tension of the liquids used was determined using the method of capillary rise. The values obtained were the following:

	dyne/cm
Water, pure	72.9
water + 0.01% dodecyl amine acetate	45.0
ethanol	21.2
benzine (ligroin)	20.8

Thus, the maximum cohesional attraction observed cannot be interpreted as being merely a function of the liquid surface tension — as had been supposed. If this assumption were true, one would expect a much lower cohesional value in the case of the dodecyl addition (surface tension 45.0 dyne/cm) than in the case of pure water (72.9). The experiments show the contrary to be the case.

5. Conclusion

The above experiments were made on a solid metal, brass (in the form of a "brush" placed on a brass disc — preventing too great an influence of the viscosity of the liquid — as would be the case if the brush had been placed on another plane disc).

---

[1] C. Benedicks a. P. Sederholm, Experiments regarding the influence of an adsorbed layer on cohesion and coalescence in liquids and in solids. Arkiv f. Mat., Astr. o. Fysik *30 A*, No. 6, p. 1—34, 1943. — Adsorption as the cause of the phenomenon of the "floating drop", and foam consisting solely of liquids. Nature *153*, 80, 1944. — Further experiments regarding the phenomenon of floating drops. Arkiv f. Mat., Astr. o. Fysik *30 B*, No. 5, p. 1—8, 1944. Corroborating results were obtained by I. N. Plaksin and S. W. Bessonow, Veränderungen der Benetzbarkeit der Metalle und Sulphidmineralien bei der Einwirkung verschiedener Gase. Doklady Akademii Nauk SSSR *61*, 865, 1948 (in Russ.).

While the cohesional forces in a dry condition are very small (say 1.5 mg; Fig. 2 *a*), the attraction when totally immersed in ordinary distilled water was found to be about 9 times greater (*c*). Water to which a wetting agent (0.01% dodecyl amine acetate) had been added, gave a cohesional attractive force 21 times greater (*e*). This at a load of $P = 2.4$ g. At $P = 15.4$ g it started by giving a value 37 times the primary one (*f*). At $P = 32.2$ g the action was found to be 43 times greater than the dry value (*h*).

The fact that an increased pressure gives a higher cohesional value, is obviously due to a decreased distance between the solid surfaces.

The fact that, in general, the cohesion increases with time may be referred to the fact that, when under pressure, the distance successively decreases.

Out-gassed water giving successively a decrease in cohesion (*d*, *f*) must be due to a successive air absorption of the liquid with concentration in the boundary, resulting in an increased distance (this fact e.g. causes that the curve *d* successively approaches the curve *c*).

These preliminary experimental results are of a special interest for the formation of pellets of ore concentrates as well as for the pressing of tablets in general and for similar questions.

Many problems present themselves for further investigation. In the first place, some pure noble metals, say Ag, Au, Pt — possibly by means of a simplified contact device — may be investigated, and also several minerals.

The influence of an increased pressure ($P > 40$ g) naturally demands further investigation. The behaviour of quite a number of different liquids must obviously be followed up; interesting is also the question whether the addition of very fine powders to the liquids would noticeably alter their influence.

Cordial thanks are expressed to M. O. Tenow, Fil. Lic., for useful collaboration.

SUMMARY

1. A method has been elaborated permitting the determination of cohesional[1] forces by means of an analytical balance. The attracting objects were of brass: a "brush" and a disc, possessing plane, polished surfaces. The former was suspended by a 0.017 mm tungsten wire, permitting submersion in a liquid, without any appreciable disturbance caused by the surface tension of the liquid (Fig. 1). The cohesional forces after different times are to be seen in Fig. 2.

2. In a dry condition, the cohesive forces observed are rather small, but increasing with time (curve *a*).

3. Distilled water containing air showed first (during about 10 hours) a considerable increase, approaching then an asymptotic value (*c*).

4. Out-gassed distilled water shows a still greater increase up to a maximum (after 20 hours; *d*). The following decrease implies an asymptotic approaching to the curve *c* for water containing air already at the beginning.

5. The addition of a wetting agent (*e*) causes an accelerated increase of the cohesional force, up to a rather high asymptotic value (about 33 mg; for water containing air the value was 14 mg).

---

[1] The word "additional" might appear preferable to "cohesional" (used here in order to point out the close relation to the inner forces of the solids).

6. The above figures were obtained when using a load near $P=2.7$ g. $P=15.4$ g gave a considerably higher initial value (49 mg). The subsequent decrease may be attributed to a successive absorption of air (*f*).

7. The addition of the wetting agent, for $P=15.4$ g, gave a value up to 54 mg after 1 hour, showing a successive linear increase (*g*). This is in accordance with the characteristic property of a wetting agent to prevent the presence of a gaseous interface.

8. The highest load used, $P=32.2$ g, gave a still higher cohesional value, 64 mg.

The method, thus, has given several elucidating results. The cohesional forces between two solids immersed in a liquid were measured, at least relatively; they have been found to assume considerable values (p), at least when using a high load (P), and excluding any precipitation of a gaseous phase in the boundary.

Stockholm, Labor. C. Benedicks
May 1952.

Tryckt den 17 november 1952

Uppsala 1952. Almqvist & Wiksells Boktryckeri AB

ARKIV FÖR FYSIK Band 6 nr 9

Communicated 28 May 1952 by MANNE SIEGBAHN and ERIK HULTHÉN

The disintegration of Zr^{95} and Nb^{95}

By HILDING SLÄTIS and LUISA ZAPPA[1]

With 10 figures in the text

1. Introduction. According to Nuclear Data (30) the Zr^{95} nucleus disintegrates to Nb^{95} ($=Cb^{95}$) and Nb^{95} to Mo^{95} in accordance with the following scheme.

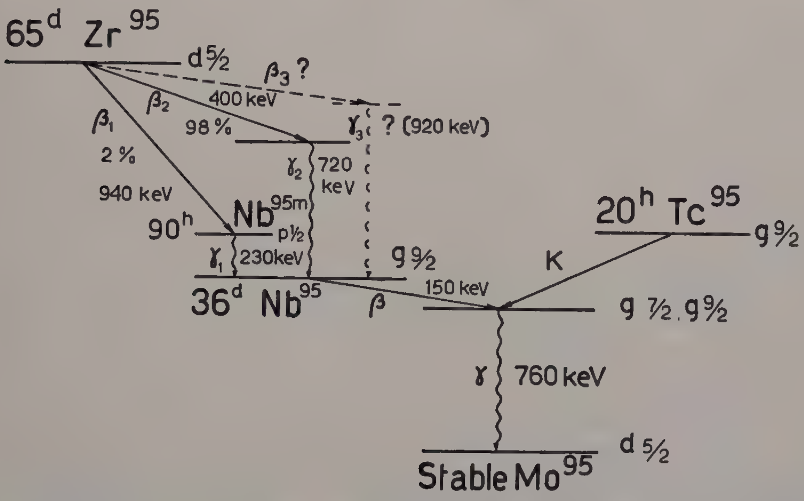

Fig. 1. Decay scheme for Zr^{95} and Nb^{95} according to LEVINGER (18) and NEDZEL (28). The decay of 20^h Tc^{95} is part of a scheme given by MEDICUS *et al* (25). Compare Nuclear Data (30).

Zr^{95} is obtained either as a fission product (GOLDSCHMIDT and PERLMAN (11), see also 13, 12, 32, 36, 9) or by bombarding Zr^{95} with slow neutrons (35). The half-life is about 65 days (35, 14, 31, 12, 1). Zr^{95} decays by beta emission to Nb^{95}. This nucleus decays according to GRUMMITT and WILKINSON (12) with a half-life of 33 days to Mo^{95}, the upper energy limit of the electrons being 150 keV. The most probable half-life is 36 days (4, 31, 16). The 90 hours beta particle activity, already observed in 1940 (35), was assigned by ENGELKEMEIR, BRADY, and STEINBERG (2) in 1943 to niobium, and by STEINBERG (39) and by HUDGENS and LYON (16) to an isomeric state of Nb^{95}. JACOBSON and OVERSTREET (17) give the half-life 73–78 hours for this activity. The part of the decay scheme in Fig. 1 which belongs to Zr^{95} was proposed by LEVINGER (18), and the Nb–Mo-decay by NEDZEL (28). The values for the energies are means of earlier spectrometer measurements.

---

[1] Temporarily absent from Istituto di Fisica, Politecnico, Milano.

The decay scheme $Zr^{95} \rightarrow Nb^{95} \rightarrow Mo^{95}$ does not seem to need much improvement, only the question about a third β-γ-transition and the classification of the 720 keV level in zirconium remaining unsolved. We had, however, already started an investigation of these disintegrations before the scheme in Fig. 1 was published. Though our results are mostly in agreement with those given in Fig. 1, our independent investigation may be of some value. We have found slightly different energy values, made measurements on the half-life of the niobium isomer, calculated internal conversion coefficients, and proposed the parity and spin of the 720 keV level.

We have on two different occasions irradiated ZrO_2 in the Harwell pile. Besides the zirconium and niobium activities there was a very strong activity of Hf^{181} (46 days). The upper energy limits of Zr^{95} and Hf^{181} are almost the same, and the half-lives are of the same order of magnitude. The hafnium activity had therefore to be removed, which was not possible by customary chemical methods. Mag. W. FORSLING (8) of our institute, using the ion exchange method, succeeded in making pure samples of zirconium oxide.[1]

2. Earlier measurements. The results previously obtained are summarized for convenience in Table 1.*)

The indications for a third decay component in zirconium are very weak. NEDZEL (28) found by spectrometer measurements a gamma line of 920 keV energy. The existence of the ray is, however, according to NEDZEL, "somewhat doubtful". The value 910 keV, given by MANDEVILLE and SCHERB (20), does not belong to this "third line". Although it was first related to Zr^{95}, it was later assigned to Nb^{95} (21), because coincidence measurement showed (22) that the 910 keV gamma ray followed the 130 keV beta radiation from Nb^{95}. The energy value 910 keV was obtained by coincidence absorption techniques and obviously belongs to the 760 keV radiation.

The spin for the Mo^{95} nucleus has been found by hyperfine structure measurements to be 5/2 (MACK, see FEENBERG, 7 b).

3. The zirconium and niobium sources. For investigating beta spectra, some mgs of ZrO_2, purified by the ion exchange method as mentioned above, were mounted on "Glasan" films of 3 mg/cm² thickness and covered with a 0.1 mg/cm² thick zapon foil. The niobium samples (Nb_2O_5) were separated chemically according to a method used in Berkeley[2] and mounted on backing films in the same way as the zirconium samples. The diameter of the samples was 6 mm and the thickness 2–6 mg/cm². When the energy of the gamma lines was determined from the photoelectrons in lead, some hundreds of mgs of the radioactive material was enclosed in a small brass cylinder, the wall thickness of which was 1 mm. On the base of the cylinder a lead foil of 0.03 mm thickness served as a radiator for the photoelectrons.

4. The beta-spectrum of Zr^{95}. The high-transmission intermediate image beta spectrometer (37, 38) was used for investigating the beta-spectra. The baffles

---

[1] We are deeply indebted to Mag. W. FORSLING for all the separations made in the present investigations. We also thank Dr LARS MELANDER for many chemical separations of Zr and Nb.

[2] W. WAYNE MEINKE, Chemical Procedures Used in Bombardment Work at Berkeley, UCRL–432, Sep. 41–1. Compare the preceding foot-note.

*) *Note added in proof:* C. Y. FAN (Phys. Rev. *87*, 252, 1952) found the following results for Nb^{95}: Beta-ray end-point energy 160 ± 3 keV, gamma-ray energy 770 ± 10 keV, total internal conversion coeff. 0.0016 ± 0.00016.

Table 1

Earlier investigations of Zr^{95} and Nb^{95}

References	Energy in keV							% β_1/β_2	Half-lives			Remarks	
	Zr^{95}		Nb^{95}				Mo^{95}		days	hours	days	*a* = absorption method *s* = beta spectrometer α = internal conversion coefficient	
	β_1	β_2	γ_1	γ_2	γ_3	β	γ		Zr^{95}	Nb^{95m}	Nb^{95}		
35									63				
12, 14, 1									65				
31									65.5		38.7		
17										73–78			
5										80–85			
39			240[1]					2		90		*a*	[1] almost completely converted
12, 1, 4											35		
26	880	400		600			580					*a*	β–γ coincidences
20, 21, 22		400		3–400		140	920[2]					*a*	[2] coinc. absorption
1	1 000	420		880				2				*a*	
28	1 000	394	234[3]	730[4]	920 ?[5]			2				*s*	[3] α = 0.002, [4] 0.001, [5] 0.0007
19	887	400		708				2				*s*	
18			242[6]			156	776	0.15–1.4		90		*s*	[6] almost completely converted
16			216[7]			146	758[8]	1.4		90	35	*s*	[7] compl. converted, [8] α = 0.0024
2			240[9]			150	820	2		82	35	*a*	[9] almost compl. converted
3						150						*a*	
29			233			154	776[10]					*s*	[10] $\alpha_K = 0.004$, $\alpha_L = 0.0003$
33							750					*s*	
25							762					*s*	follows the K-capture in Tc
6						163	771					*s*	α = 0.0018, K/L ~ 2.3
40						[11]	[11]						[11] no β–γ angular correlation
	940	400	230	720	920 ?	150	762	1.9	65	84	35.7		Mean of earlier measurements (for the energies, only spectrometer measurements are used).
Present paper	840 ±80	371 ±10	231* ±10	721** ±10	1 070 ?	159 ±10	745*** ±10	1.0 ±0.1		84 ±2		*s*	* α = ∞, ** α = 0.0024, *** α = 0.0024 no γ–γ-coincidences

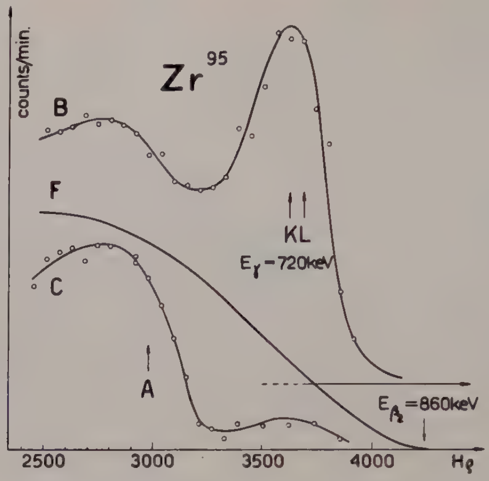

Fig. 2. *B*. The hard beta component and the 720 keV internal conversion line in the beta spectrum of Zr^{95}. *C*. Distribution of Compton electrons released in inactive ZrO_2 by the 720 keV gamma radiation of active zirconium. *F*. Ideal allowed beta spectrum with maximum energy 860 keV.

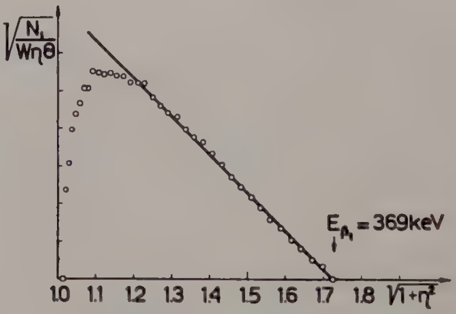

Fig. 3. Fermi plot for the weak component in the beta spectrum of Zr^{95}.

in the spectrometer were adjusted for a resolving power of 4 per cent. When the main component β_2 was studied, using thin sources, this resolving power was achieved. However, as the specific activity of the zirconium was low, thick samples had to be used when the hard beta component β_1 of low intensity (1%) was investigated. This circumstance introduced a broadening of the conversion lines (the half-width of the KL-line in Fig. 2 is for instance 9 per cent).

We found two beta components in the beta radiation from Zr^{95}, in agreement with earlier results. Fig. 3 shows the Fermi plot of the weaker component β_2, the maximum energy of which was found to be 369 keV. Another series gave 373 keV. The Fermi plot is linear. In Fig. 2 the curve B consists of the harder beta component β_1 and a conversion line KL, corresponding to the gamma ray energy 720 keV. This conversion line conceals the high energy part of β_1. Thus only a small part of the spectrum β_1 is free, since the softer beta component masks the low energy part of the spectrum.

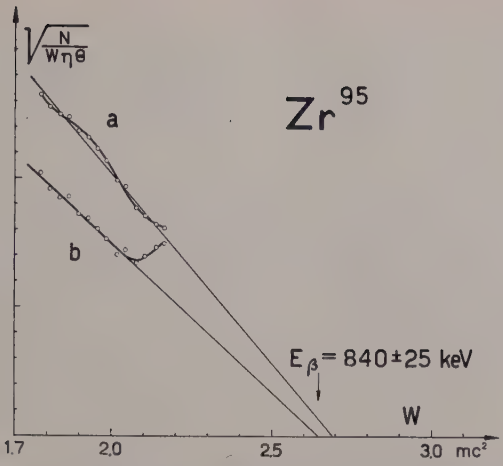

Fig. 4. *a*. Fermi plot for the hard electron distribution in the beta spectrum of Zr^{95}. *b*. Fermi plot of the hard electron distribution in the beta spectrum of Zr^{95}, from which a Compton electron distribution has been subtracted (compare curve *C* in Fig. 2). If the α-factor (reference 41) is used, the upper energy limit is reduced by 80 keV.

The Fermi plot of β_1 is given in Fig. 4, curve *a*. This should be a straight line (or, as we shall find later from the *ft*-values, show the characteristic "α" type forbidden spectrum (41), which, however, in the short interval considered cannot be distinguished from a straight line). The deviation of the curve from the straight line shows some kind of systematic error. This is caused by Compton electrons released in the sample itself by the strong 720 keV gamma radiation. In order to study the influence of the Compton electrons the spectrum of these electrons was recorded. The curve C in Fig. 2 shows the momentum distribution obtained when a disk of inactive ZrO_2 1.5 mm thick was used as a radiator in front of a sample of active zirconium. This active zirconium was enclosed in a brass capsule, the walls of which were thick enough to absorb all beta particles from the active zirconium.

A beta spectrum which is not influenced by Compton electrons should have the form F in Fig. 2. The influence of Compton electrons on the shape of the spectrum B is obvious. If we assume that 50 per cent of the electrons at $H\varrho = 3\,000$ are Compton electrons, and subtract the corresponding C-spectrum from B, we get a Fermi distribution shown by the curve *b* in Fig. 4. The Fermi plot is now linear, if we exclude the part through the last three points, which are obviously influenced by the 720 keV K-conversion line (the peak of this line should be at W = 2.35 in Fig. 4). For the maximum energy of the β_1-component we find 840 ± 25 keV. If, however, the α-factor is used, the upper energy limit is reduced by about 80 keV.

The occurrence of these Compton electrons makes it difficult to determine the beta transition ratio β_1/β_2 from the shape of the beta spectrum. We found, indeed, that the ratio obtained depended on the thickness of the zirconium sample, going from 3.2 per cent for thicker samples to 2.4 per cent for thinner ones. Because of the granular structure of the sample the weight of the sample per square cm is not a measure of the thickness, and hence it was not possible to extrapolate the value for the ratio to zero sample thickness. The ratio was therefore determined from other considerations (§ 9).

In zirconium samples of the age of a week or more there is a second conversion line, which belongs to the isomer Nb^{95m}. The momentum of the electrons is about 1 700, corresponding (if K-electrons) to a transition of energy 231 keV. As the line rises only a few per cent over the β_2 spectrum, good statistical accuracy is necessary in order to record the line. Fig. 9 shows the line separated from the beta spectrum background.

No conversion line corresponding to a gamma ray energy of 920 keV was found (28). There was however a weak conversion line corresponding to 1070 keV gamma ray energy. The half-life of the line was the same as for Zr^{95}. The intensity of the line compared with the intensity of the 720 keV line was, however, quite different (20% and 2%, respectively) in two different samples which had been irradiated at Harwell at different times. The 1070 keV gamma radiation may therefore originate in some contamination. A special investigation of this question will be made in the future (see § 6 and 10).

5. The beta-spectrum of Nb^{95}. Fig. 5 shows the beta spectrum of Nb^{95}. The Fermi plot of the continuous beta spectrum is presented in Fig. 6. The form of the plot is linear, the upper energy limit being 159 keV. The dashed line in Fig. 5 corresponds to the straight line in the Fermi plot and may be considered as the beta spectrum corrected for the absorption in the GM-window. There is a conversion line corresponding to a gamma radiation of 745 keV energy (other measurements gave 745, 747 and 747 keV, respectively) and a second one, corresponding to 231 keV (mean of 231, 232, 232 and 229 keV). The half-widths are 5 and 7.5 per cent respectively. The second conversion line belongs to the so-called 90^h isomer of Nb^{95}, found by ENGELKEMEIR, BRADY and STEINBERG (2). We have followed the decay of this activity very thoroughly (over a period of more than four half-lives) and found a half-life of 84 ± 2 hours (Fig. 7).

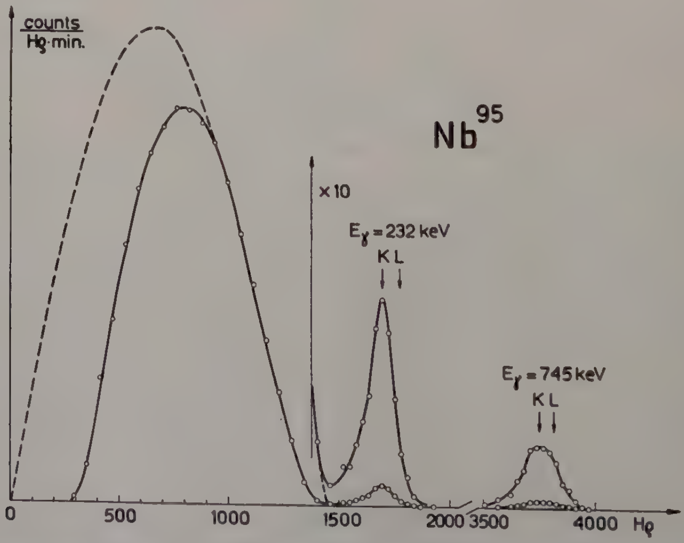

Fig. 5. The beta spectrum of Nb^{95}. The dashed curve corresponds to an ideal, allowed, Fermi distribution. The 232 keV internal conversion line belongs to the 84^h Nb^{95} isomer.

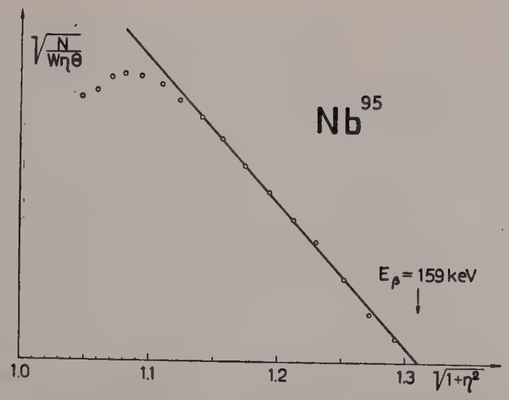

Fig. 6. Fermi plot for the beta spectrum of Nb^{95}.

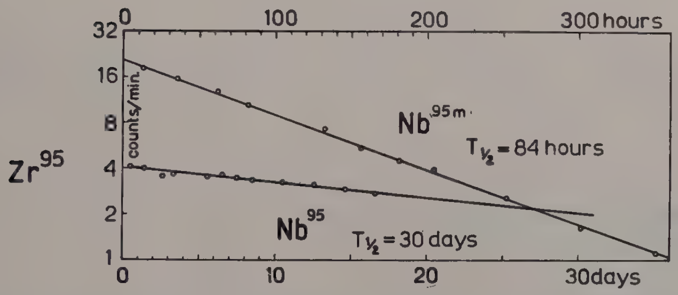

Fig. 7. Decay curve for the 84^h Nb^{95} isomer. An approximate value (30 days) for the half-life of Nb^{95} is sufficient for a calculation of the half-life of the 84^h isomer.

The decay of Nb^{95} resembles the main decay of Zr^{95}. In both cases the beta emission is followed by a gamma ray of almost the same energy, 745 and 720 keV, respectively. It was therefore interesting to see if there was a Compton distribution of electrons released from the niobium sample by the 745 keV gamma radiation, similarly to that in the case of zirconium. Fig. 8 shows that this does in fact happen. The curve *B* obviously consists of such a Compton distribution and the internal conversion line. The Compton electron distribution curve *C* was obtained in a way similar to that for zirconium: a 1.5 mm thick disk of inactive Nb_2O_3 was irradiated by the 745 keV gamma radiation emerging from some hundreds of mgs of active Nb_2O_3 enclosed in a brass capsule, the walls of which were thick enough to absorb all beta particles from the active niobium. The curve *C* shows in addition the external conversion line of the 745 keV gamma radiation.

In the case of niobium there is no risk of confusing the Compton distribution in the curve *B* (Fig. 8) with a possible harder beta component, because the beta spectrum of niobium does not hide the Compton distribution. If we take only that part of the curve *B* which lies between the $H\varrho$-values 2 500 and 3 000 (as in the case of zirconium), and consider this part as part of a harder beta component of upper energy

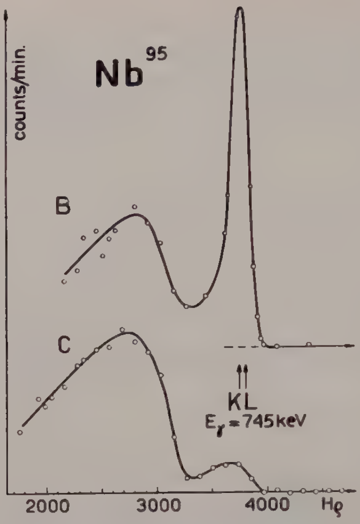

Fig. 8. *B*. The internal conversion line of the 745 keV gamma radiation together with the spectrum of the Compton electrons released in the sample itself. *C*. Distribution of Compton electrons released in inactive Nb_2O_5 by the 745 keV gamma radiation of active niobium.

limit 860 keV, then we find that this component should amount to about 1.4 per cent of the real beta spectrum.

This circumstance shows that in the case of zirconium the harder beta component possibly amounts only to $2.4 - 1.4 = 1$ per cent. We will see below (§ 9) that this in fact the case.

6. The photo spectrum of Zr^{95}. The secondary electron spectrum from a lead converter of thickness 0.03 mm was investigated. Besides the Compton edge there was a strong photo line corresponding to a gamma ray energy of 722 keV (mean of 719, 722 and 726 keV). No photo line corresponding to the 231 keV transition was found, which agrees with the supposition that the transition is completely converted.

Particular care was devoted to the search for a gamma line (28) in the vicinity of 920 keV. No such line was found, however, but the K, L photo line belonging to the 1070 keV gamma radiation was recorded (compare § 4 and 10).

7. The photo spectrum of Nb^{95}. Only one conversion line was recorded, the unresolved group of K-, L- . . . lines corresponding to the gamma ray of energy 744 kev (mean of 752, 743 and 738 keV).

8. Conversion coefficients. We have measured the total conversion coefficients ($\alpha_K + \alpha_L + \cdots$) of the internal conversion lines. The result is seen in Table 2.

The theoretical K-shell internal conversion coefficients (34) for the Zr^{95} 721 keV and Nb^{95} 745 keV transitions are given in Table 3.

Table 2

Experimental values for the total conversion coefficients

γ-ray	$\alpha_{K+L+\dots}$
Zr^{95} 721 keV	0.0024
Nb^{95} 745 keV	0.0024
Nb^{95m} 231 keV	∞

Table 3

Theoretical values for the K-conversion coefficients, Rose *et al.* (32)

γ-ray	α_1	α_2	α_3	β_1	β_2
Zr^{95} 721 keV	0.00055	0.00148	0.0035	0.0014	0.0038
Nb^{95} 745 keV	0.00051	0.00132	0.0031	0.0013	0.0035

We have measured the total conversion coefficients. The K-conversion coefficients are at least 12% smaller than the total conversion coefficients. We thus get the upper limit 0.0021 for the K-conversion coefficients, and conclude that the gamma radiations considered must be electric quadrupole or magnetic dipole.

9. Determination of the ratio β_1/β_2 for Zr^{95}. We have used three different methods to determine the ratio β_1/β_2 between the hard and the soft beta components in the beta spectrum of Zr^{95}. The three methods are:

1) Calculation of the areas under the ideal β_1 and β_2 components, constructed by means of the Fermi plots.

2) The β_1 component is followed by the completely converted 231 keV transition. The ratio of the area of this conversion line to the area of the whole beta spectrum of Zr^{95} thus gives the ratio β_1/β_2 (provided the 84^h Nb^{95} isomer is in equilibrium with the Zr^{95}).

3) After the separation of Nb^{95} from the active zirconium the 231 keV transition conversion line and the continuous beta spectrum of niobium are recorded. The area of the line and that of the beta spectrum are measured and the size of these areas at the time of the separation calculated. The amount of niobium 95 which has grown during the time from the irradiation of the zirconium in the pile until the separation can easily be calculated, and hence the ratio β_1/β_2 determined.

The application of the first method has already been described. It was found that the 720 keV gamma radiation introduced Compton electrons which masked the true form of the β_1-spectrum. By estimating the size of this disturbance, the ratio β_1/β_2 was estimated to be of the order of one per cent.

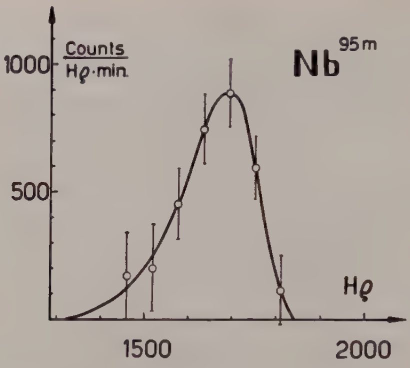

Fig. 9. Internal conversion line of the 84h Nb^{95} isomer, separated from the beta spectrum of Zr^{95}.

The second method is laborious, because the conversion line rises only a few per cent over the continuous β_2-spectrum. We have made several runs in order to get a statistical accuracy of 1% for the points investigated. Fig. 9 shows the conversion line obtained when the difference between the counts measured and the counts computed from the Fermi distribution is plotted as a function of the momentum of the electrons. The value obtained in this way for the ratio β_1/β_2 is 1.0 ± 0.2 per cent.

When the third method was used, it was found that the area of the 231 keV conversion line was 1.37 per cent of the area of the niobium continuous beta spectrum at the time of separation. Considering that the amount of niobium was, at the time of separation, 73 per cent of that of zirconium, we get for the ratio β_1/β_2 the value 1.00 ± 0.1 per cent.

We thus find by three different methods the value 1% for the ratio β_1/β_2.

10. Scintillation spectrometer measurements.[1] No γγ-coincidences were found. As well as the 720 keV line, the gamma spectrum of Zr^{95} showed the already mentioned gamma line of 1070 keV energy. The intensity was about 2% of that of the 720 keV line. These measurements were made 6 and 8 months after the beta spectrometer measurements, and showed that the half-life of the 1 070 keV radiation was the same as that of Zr^{95} (see § 4 and 6).

11. The *ft*-values for the beta transitions. From the relative intensities of the beta components in the beta spectrum of Zr^{95}, we found, using the *f*-values computed by FEENBERG and TRIGG (7 a), the following *ft*-values (Table 4).

The classification of beta decay according to MAYER, MOSZKOWSKI and NORDHEIM (23) is given in the last column.

---

[1] We are greatly indepted to Civiling. BJÖRN ÅSTRÖM, who kindly made these measurements. Details of the scintillation spectrometer will soon be published by ÅSTRÖM in Arkiv för Fysik.

Table 4

Data for the beta transitions

Nucleus	Maximum β-energy keV	log ft	Classification of β-decay
Zr^{95}	860	9.75	(c) $\Delta I = 2$. Yes, first forbidden
»	371	6.47	(b) $\Delta I = 0,1$. Yes, first forbidden or (d) $\Delta I = 1$. No, $\Delta l = 2$, l-forbidden
Nb^{95}	159	5.09	(a) $\Delta I = 0,1$. No, allowed.

12. The decay scheme. The classification of the levels in Fig. 1 are in accordance with the spin orbit coupling scheme (15, 24). Nuclear isomerism is to be expected for the niobium levels $g_{9/2}$ and $p_{1/2}$ and the classification of the 860 keV beta transmission (Table 4) shows that the ground state of Zr^{95} is a $d_{5/2}$-level, as proposed by Mayer, Moszkowski, and Nordheim (23). The isomeric state is fed by the 860 keV beta transition and deexcited by the completely converted 231 keV transition. This level must therefore be a $p_{1/2}$-level. Beta transitions to the $g_{9/2}$-level should give $\Delta I = 2$, no, and be second or higher forbidden.

The ft-value for the main beta decay gives a choice between (b) ($\Delta J = 0,1$, yes, first forbidden) or (d) ($\Delta J = 1$, no, $\Delta l = 2$, l-forbidden). The first possibility (b) involves $p_{3/2}$ or $f_{5/2}$ for the 721 keV level. Both possibilities should, according to the γ-selection rules of Dancoff and Morrison (1 b) (or in the form given by Goldhaber and Sunyar (10)) give rise to a strong gamma ray to the $p_{1/2}$-level and no observable transition to the ground level, quite contrary to the experimental facts. An $f_{7/2}$-level should indeed give the 721 keV gamma transition to the ground level $g_{9/2}$, but this ray should be electric dipole, in contradiction with the measurements.

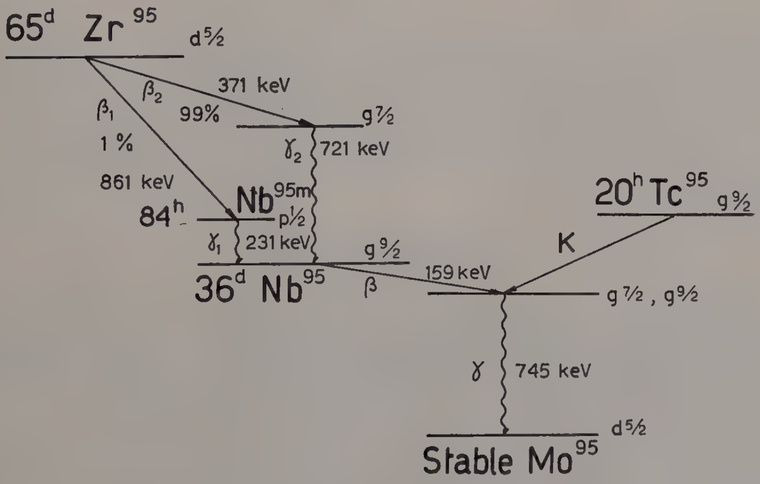

Fig. 10. Decay scheme of Zr^{95} and Nb^{95}, with data measured in the present work.

Thus there remains the possibility (d), that the 371 keV beta spectrum is l-forbidden with $\Delta I=1$, no, $\Delta l=2$, which gives $g_{7/2}$ for the 721 keV-level.

Fig. 10 gives the decay scheme of Zr^{95} and Nb^{95} with the data obtained in the present work. The assumption of $g_{7/2}$ for the keV level explains the fact that there is no observable gamma-transition to the $p_{1/2}$-level ($\Delta I=3$, yes, E 3, transition order $=3$), but only a transition to the ground level ($\Delta I=1$, no, M 1, transition order $=2$). The internal conversion coefficient measured agrees with this explanation (§ 8).

The excited 745 keV level of Mo^{95} may be a $g_{7/2}$-level, as proposed by FAN (6), or a $g_{9/2}$-level, as suggested by MEDICUS *et al.* (25). In both cases the β-spectrum has the allowed form with no parity change, and the gamma radiation will be magnetic dipole or electric quadrupole, respectively. The transition orders are in both cases 2, and the conversion coefficients are almost exactly the same.

SUMMARY

1. Zirconium oxide was irradiated by neutrons in the Harwell pile and the active zirconium separated from impurities (mostly Hf) by means of the ion exchange method (separation performed at this institute by W. Forsling).

2. The beta and gamma radiations from Zr^{95}, Nb^{95}, and $\mathrm{Nb}^{95\mathrm{m}}$, were investigated by means of the intermediate image beta spectrometer as well as by means of a crystal scintillation spectrometer (the scintillation spectrometer of B. Åström).

3. The half-life of the Nb^{95}-isomer was found to be 84 ± 2 hours.

4. The ft-values for the beta transitions and the internal conversion coefficients for the gamma radiations were determined.

5. The decay scheme for Zr^{95} and $\mathrm{Nb}^{95\mathrm{m}}$ proposed by LEVINGER (18) and the decay scheme for Nb^{95} suggested by NEDZEL (28), were confirmed. The slightly different energy values and other data found are given in Table 1 and in the decay scheme of Fig. 10.

6. The doubtful 920 keV gamma radiation observed by NEDZEL (28) in the decay of Zr^{95} was not found, but a 1070 keV gamma radiation was recorded. The half-life of the radiation was the same as for Zr^{95}, but the intensity compared with that of the 721 keV line was not the same in two samples irradiated at different times at Harwell. The 1070 keV gamma ray may therefore originate in some contamination.

7. The experimental results agree with the supposition that the 721 keV level of Nb^{95} is a $g_{7/2}$-level.

Acknowledgements

It is a pleasure for one of the authors, Luisa Zappa, to express her gratitude to Professor Manne Siegbahn and the Nobel Institute of Physics for the hospitality extended to her during her stay in Stockholm. She is also indepted to the Italian Research Council for enabling her to take part in this research.

Nobel Institute of Physics, Academy of Sciences, Stockholm 50.

REFERENCES: 1. **E. L. Brady, D. W. Engelkemeir** and **E. P. Steinberg,** NNES (= National Nuclear Energy Series) 9, paper 85, 1951. — 1 b. **S. Dancoff** and **P. Morrison,** Phys. Rev. *55,* 122, 1939. — 2. **D. W. Engelkemeir, E. L. Brady** and **E. P. Steinberg,** NNES 9, paper 88, 1951. — 3. **D. W. Engelkemeir,** NNES 9, paper 89, 1951. — 4. **D. W. Engelkemeir** and **E. L. Brady,** Plutonium Project Report CC-418 A, 9, 1943. — 5. —— NNES 9, paper 92, 1951. — 6. **C. Y. Fan,** Phys. Rev. *81,* 300, 1951. — 7 a. **E. Feenberg** and **G. Trigg,** Rev. Mod. Phys. *22,* 399, 1950. — 7 b. **E. Feenberg,** Phys. Rev. *77,* 771, 1950. — 8. **W. Forsling,** Arkiv för Kemi (in print, 2 papers). — 9. **R. H. Goeckermann** and **I. Perlman,** Phys. Rev. *76,* 628, 1949. — 10. **M. Goldhaber** and **A. W. Sunyar,** Phys. Rev. *83,* 906, 1951. — 11. **B. L. Goldschmidt** and **I. Perlman,** NNES 9, paper 84, 1951. — 12. **W. E. Grummitt** and **G. Wilkinson,** Nature *158,* 163, 1946. — 13. **O. Hahn** and **F. Strassmann,** Naturw. *31,* 499, 1943. — 14. —— Z. f. Ph. *121,* 729, 1943. — 15. **O. Haxel, J. H. D. Jensen** and **H. E. Suess,** Phys. Rev. *75,* 1766, 1949; Z. f. Phys. 128, 295, 1950. — 16. **J. E. Hudgens, Jr** and **N. S. Lyon,** Phys. Rev. *75,* 206, 1949. — 17. **L. Jacobson** and **R. Overstreet,** NNES 9, paper 91, 1951. — 18. **J. S. Levinger,** NNES 9, paper 94, 1951. — 19. **W. S. Lyon, J. Hudgens, Jr,** see reference 30, (49L17). — 20. **C. E. Mandeville** and **M. V. Scherb,** Phys. Rev. *73,* 1434, 1948. — 21. **C. E. Mandeville, M. V. Scherb** and **W. B. Keighton,** Phys. Rev. *74,* 888, 1948. — 22. **C. E. Mandeville** and **M. V. Scherb,** *74,* 1248, 1266, 1948. — 23. **M. G. Mayer, S. A. Moszkowski** and **L. W. Nordheim,** Rev. Mod. Phys. *23,* 315, 1951. — 24. **M. G. Mayer,** Phys. Rev. *75,* 1969, 1949. — 25 a. **H. Medicus, A. Mukerji, P. Preiswerk** and **G. de Saussure,** Phys. Rev. *74,* 839, 1948. — 25 b. **H. Medicus, P. Preiswerk** and **P. Scherrer,** Helv. Phys. Acta *23,* 299, 1950. — 26. **A. C. G. Mitchell** and **L. J. Brown,** NNES 9, paper 86, 1951. — 27. **W. N. Moquin** and **M. L. Pool,** Phys. Rev. *65,* 60, 1944. — 28. **V. A. Nedzel,** NNES 9, paper 87, 1951. — 29. —— NNES 9, paper 90, 1951. — 30. Nuclear Data, NBS Circular 499, United States Department of Commerce, National Bureau of Standards, Sept. 1950, April 1951 and Nov. 1951. — 31. **M. L. Pool** and **J. E. Edwards,** Phys. Rev. *67,* 60, 1945. — 32. Plutonium Project Nuclei Formed in Fission, Rev. Mod. Phys. *18,* 513, 1946. — 33. **W. Rall** and **R. G. Wilkinson,** Phys. Rev. *71,* 321, 1947. — 34. **M. E. Rose, G. H. Goertzel** and **C. L. Perry,** K-shell internal conversion coefficients, Revised Tables, Oak Ridge 1951. — 35. **R. Sagane, S. Kojima, G. Miyamoto** and **M. Ikawa,** Phys. Rev. *57,* 1179, 1940. — 36. **G. T. Seaborg** and **I. Perlman,** Rev. Mod. Phys. *20,* 585, 1948. — 37. **H. Slätis** and **K. Siegbahn,** Phys. Rev. *75,* 1955, 1949. — 38. —— Arkiv för Fysik, *1,* 339, 1949. — 39. **E. P. Steinberg,** NNES 9, paper 93, 1951. — 40. **R. Stump** and **S. Frankel,** Phys. Rev. *79,* 243, 1950. — 41. **C. S. Wu,** Rev. Mod. Phys. *22,* 386, 1950.

Tryckt den 25 november 1952

Uppsala 1952. Almqvist & Wiksells Boktryckeri AB

ARKIV FÖR FYSIK Band 6 nr 10

Communicated 27 February 1952 by MANNE SIEGBAHN and ERIK HULTHÉN

The ultra-violet band-system of silicon monoxide

By ALBIN LAGERQVIST and ULLA UHLER

With 3 figures in the text

Abstract

The ultra-violet bands of SiO, which consist of a single $^1\Pi - {}^1\Sigma$ system, designated $A \rightarrow X$, have been the object of a new rotational analysis, in which the following bands have been examined: 0,4, 0,3, 0,2, 0,1, 1,0, 1,1, 1,5, 2,0 and 2,6. The constants derived are:

$B_v'' = 0.7272_9 - 0.0050_8\,(v'' + \frac{1}{2})\ \mathrm{cm}^{-1}$	$B_v' = 0.6312_8 - 0.0069_5\ (v' + \frac{1}{2})$
$D'' = 1.02 \times 10^{-6}$	$D' = 1.43 \times 10^{-6}$
$r_e'' = 1.509 \times 10^{-8}\mathrm{cm}$	$r_e' = 1.620 \times 10^{-8}\ \mathrm{cm}$
$\omega_e'' = 1241.4_4$	$\omega_e' = 852.7_1$
$\omega_e'' x_e'' = 5.9_2$	$\omega_e' x_e' = 6.4_4$

In the upper state several perturbations have been found. They appear to arise from interactions with four electronic states. Three of the perturbing states are singlets, one is a $^1\Sigma^-$, the other two $^1\Pi$ or $^1\Delta$, the fourth one is a $^3\Sigma^-$ state. The analogy with the spectra of CO and SiS is striking. A fair amount of information has been obtained for the $^3\Sigma^-$ state. We have $\omega_{^3\Sigma^-} \sim 700$ and $B_{^3\Sigma} \sim 0.52$.

§ 1. Introduction

SiO is allotted a band-system in the ultra-violet region from about 2 000 Å to about 3 000 Å. The spectrum is obtained in flames into which $SiCl_4$ is introduced, in discharge tubes with $SiCl_4$ and oxygen and very strongly in arcs. Head measurements have been performed by JEVONS (1924) and SHARMA (1944). A rational analysis has been carried out by SAPER (1932). His analysis shows that the spectrum consists of a band-system of singlet structure, the transition $^1\Pi - {}^1\Sigma$. This system reminds one of the corresponding systems in CO (fourth positive system, CAMERON, 1927) and in SiS (BARROW, 1946). SAPER notes that the upper levels are perturbed. He does not, however, make a complete investigation of the nature of the perturbing states. The perturbations in the corresponding states in CO and SiS have been rather carefully investigated (CO: COSTER and BRONS, 1934, SCHMID and GERÖ, 1935, BUDÓ and KOVÁCS, 1938; SiS: LAGERQVIST, NILHEDEN and BARROW, 1952). Thus it seemed to us to be of interest to re-analyse the SiO spectrum with special attention to the perturbations.

§ 2. Experimental

The SiO bands were obtained by using an arc burning between two carbon electrodes, the lower one positive, the upper one negative. The lower electrode was filled with small crystals of silicondioxide. The voltage was 440 D. C. and the current about 5 A. The bands appeared with good intensity. They were photographed in the first and second orders of a 21 ft. Wood grating with 165 000 lines. The dispersion in the first order is about 1.3 Å/mm and in the second order 0.6 Å/mm. When taking the second order plates we used a liquid filter consisting of nickel and cobalt sulphate (BÄCKSTRÖM 1940) to get rid of the first-order lines between 4 000 and 5 000 Å. This solution absorbs almost all of the blue light but transmits the ultra-violet part of the spectrum. The exposure-time on Ilford-Zenith plates was 2.5 hours in the first and 10 hours in the second order. The first-order plates were over-exposed in order to obtain a measurable plate of the 2,0 band, which was too weak in the second order. Iron lines served for comparison. (The M. I. T. Tables 1939.)

§ 3. Structure of the bands

The appearance of the structure of some of the bands is shown in the reproductions in Fig. 1. The band-origins are given in Table 1. The wave-numbers of the band-lines will be found in Tables 2–4. Overlapped lines are indicated with an asterisk. All bands except the 2,0 band were measured from second-order plates. The accuracy in the line measurements is estimated as 0.05 cm^{-1}. The measurements of the first-order plate are less accurate. To designate the perturbations two types of printing are used in Tables 2–4.

Table 1

Band-origins

The differences between calculated and observed values are given in brackets.

6			37 107.58 (−0.36)
5		37 450.81 (−0.14)	
4			
3	38 987.04 (+0.12) 1 206.18		
2	40 193.22 (−0.14) 1 217.51		
1	41 410.73 +0.11		
0		43 480.14 826.77 (+0.13)	44 306.91 (+0.31)
v'' / v'	0	1	2

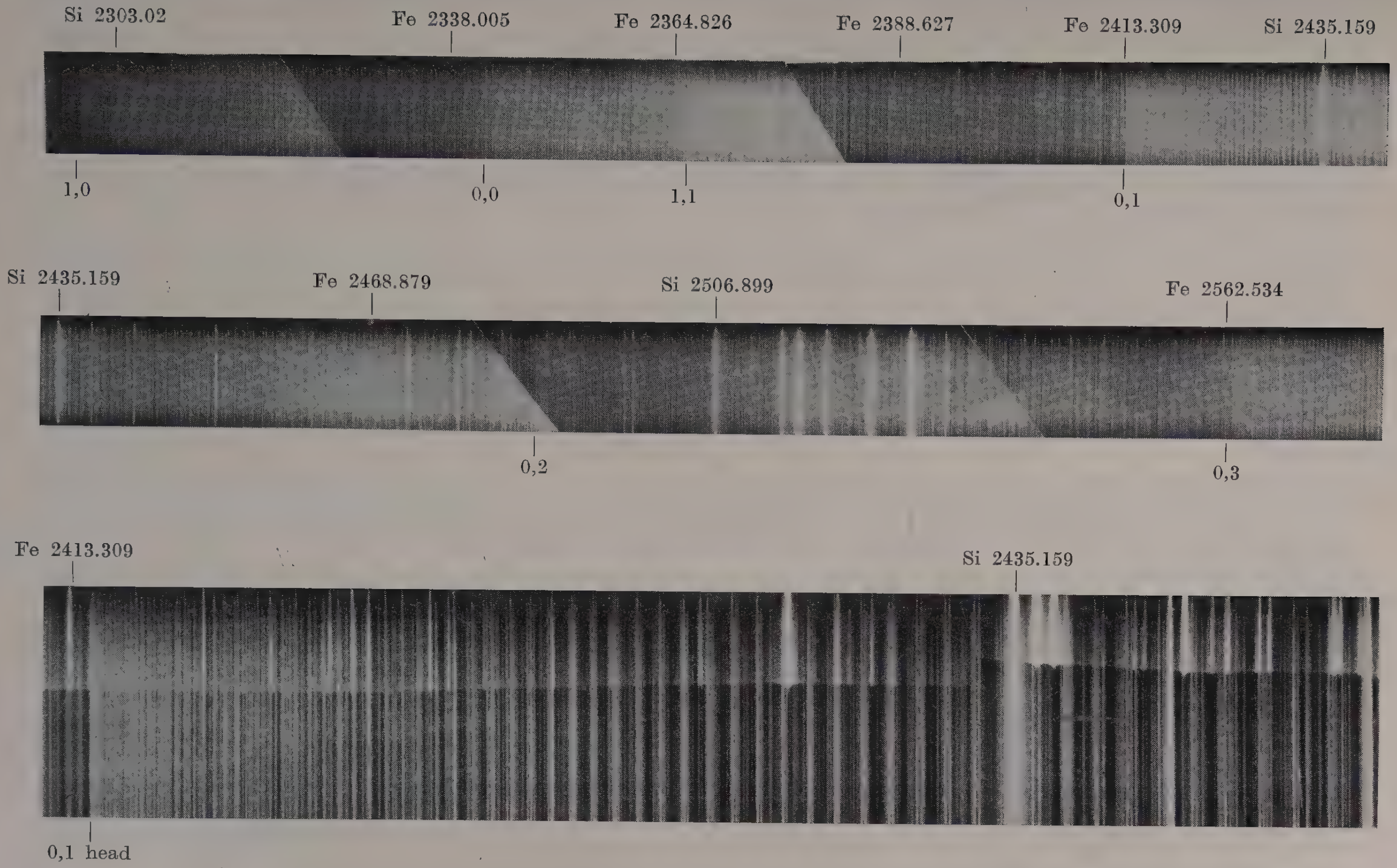

Fig. 1. Reproductions of the SiO band-spectrum. The magnifications are 1·5 and 7·1 respectively.

Table 2

Wave-numbers for the 0,1, 0,2 and 0,3 bands

J	*Q*(0,1)	*R*(0,1)	*P*(0,1)	*Q*(0,2)	*R*(0,2)	*P*(0,2)	*Q*(0,3)	*R*(0,3)	*P*(0,
6			41 398.38*						
7			96.32*						
8			94.08*	40 188.76					
9	41 402.94*		91.42*	86.87					
10	00.64*	41 414.34	88.03	84.97*					
11	398.38*	13.44	84.87	82.40*			38 976.23*		
12	96.32*	12.62*	81.44	80.16*			74.15*		
13	94.08*	11.57	77.64	77.38*			72.02		
14	91.42*	10.17	73.92	74.77*		40 156.40*	69.78		38 952.
15	88.72	08.76	69.95	72.16*		52.66*	67.27		48.
16	85.74	06.98	65.76	69.41*		48.85*	64.71		44.
17	82.55	05.05	61.44	66.39*		44.90*	61.73		40.
18	79.22	02.94*	56.89	63.15*		40.59*	58.91		36.
19	75.93*	00.68*	52.13	159.66*	40 184.97*	36.05*	55.74	38 980.89	32.
20	72.18	398.38*	47.18	56.40*	82.40*	31.25	52.49*	78.74	27.
21	68.39	95.65	42.05	52.66*	80.16*	26.30	49.12*	76.23*	22.
22	64.25	92.96	36.82	48.85*	77.38*	21.26	45.55*	74.15*	17.
23	60.06	89.90	31.28	44.90*	74.77*	15.91	41.76	71.48	12.
24	55.66	86.65	25.58	40.59*	72.16*	10.49	37.73	68.85	07.
25	50.97	83.32	19.38	36.05*	68.67	04.87	33.47	65.95	02.
26	46.17	79.68	13.48*	31.79	65.46	099.16	29.26	62.92	896.
27	41.18	75.93*	07.23*	27.01	61.91	93.12	24.89	59.71	91.
28	35.98	72.18*	00.91*	22.05	58.16	86.92	20.25	56.28	85.
29	30.57	67.85*	294.27*	17.11*	54.40	80.55	15.30	52.69*	79.
30	25.05	63.55	87.52*	11.71*	50.38	73.90	10.55	49.12*	72.
31	19.38*	59.05	80.53	06.19*	46.18	67.26	05.31	45.27*	66.
32	13.48*	54.41	73.37	00.43*	41.70	60.52	00.04	41.03	59.
33	07.23*	49.40	65.94	094.82	37.03	53.46	894.47	36.58	53.
34	00.91*	44.10	58.35	88.73	32.23	46.26	88.82	32.11	46.
35	294.27*	_39.77_	50.55	82.51	28.17	38.66	82.83	32.11	39.1
36	_88.46*_	_34.00_	42.49	_76.95_	_28.17_	38.66	82.83	_28.41_	39.1
37	_81.19_	_28.17_	_35.19_	_70.05_	_22.74_	30.83	_77.74_	_23.43_	31.8
38	_74.07_	_22.40_	_26.46_	_63.26_	_17.11*_	_atom line_	_71.17_	_18.39_	25.1
39	_66.77_	_16.30_	_17.98_	_56.48_	_11.71*_	_15.80*_	_64.82_	_13.31_	_17.3_
40	_59.28_	_10.11_	_09.29_	_49.32_	_06.19*_	_07.56*_	_58.30_	_08.01_	_09.6_
41	_51.64_	_03.70_	_00.39_	_42.15_	_00.43_	_39 999.25*_	_51.67_	_02.52*_	_01.6_
42	_43.76_	_297.05_	_191.27_	_34.63_	_094.17_	_90.92_	_44.79_	_896.88*_	_793.6_
43	_35.73*_	_90.21_	_82.03_	_27.03_	_87.86_	_82.26*_	_37.81_	_91.06*_	_85.3_
44	_27.51_	_83.24_	_72.58_	_19.25_	_81.61_	_73.33_	_30.64_	_85.28*_	_76.9_
45	_19.05_	_76.03_	_62.95_	_11.29_	_75.02_	_64.35_	_23.33*_	_79.02*_	_68.3_
46	_10.41_	_68.59_	_53.06_	_03.14_	_68.25_	_55.18_	_15.79*_	_72.75*_	_59.7_
47	_01.56_	_61.02_	_42.97_	_39 994.80_	_61.29_	_45.75_	_08.12*_	_66.47*_	_50.7_
48	_192.61*_	_53.17_	_32.74_	_86.17_	_54.18_	_36.17_	_00.27*_	_59.57_	_41.7_
49	_83.38*_	_45.09_	_22.25_	_77.51_	_46.98_	_26.46_	_792.17*_	_52.68_	_32.4_
50	_74.07*_	_37.03_	_11.65_	_68.63_	_atom line_	_16.37_	_83.97_	_45.62_	_23.1_
51	_64.41*_	_28.57*_	_00.81_	_59.54_	_31.66_	_06.35_	_75.63_	_38.53_	_13.3_
52	_54.53*_	_20.09_	_089.75*_	_50.25_	_atom line_	_896.06_	_67.05_	_31.24_	_03.4_
53	_44.58_	_11.21_	_78.69*_	_40.86_	_15.80*_	_85.49_	_58.29_	_23.53*_	_693.6_

Table 2 (cont.)

J	Q(0,1)	R(0,1)	P(0,1)	Q(0,2)	R(0,2)	P(0,2)	Q(0,3)	R(0,3)	P(0,3)
4	_34.49_	_02.27_	_67.06*_	_31.21_	_39 999.25*_	_63.97_	_40.34_	_08.12*_	_73.32_
5	_24.06_	_193.04_	_55,61*_	_21.36_	_90.36_	_53.02_	_31.08_	_799.92*_	_62.69_
6	_13.44_	84.55	_43.66_	_11.34_	82.26*	_41.84_	_21.54_	92.42*	_52.02_
7	_02.60_	74.07*	_31.62_	_01.13_	72.64	_30.34_	_11.91_	83.32	_41.19_
8	_091.59_	64.41*	20.29	_890.63_	63.34	19.47	_02.10_	74.74	30.79
9	_80.35_	54.53*	07.15	_atom line_	53.93	07.16	_692.22_	65.93	
0	_68.90_	44.11	40 994.69	_69.24_	44.33	795.09	_81.90_	56.89	
1	_57.11_	33.68	81.89	_58.09_	34.58	83.01	_71.32_	47.68	
2	46.12	23.10	68.96	47.77	24.63		61.45	38.35	
3	33.76	12.31	55.76	36.12	14.47		50.54	28.91	
4	21.50	01.13	42.36	24.46	04.02		39.53	19.01	
5	09.05	089.75*	28.81*	12.76	893.60		28.34	08.79	
6	40 996.52	_78.69*_	15.35*	00.76	_82.91_			699.30	
7	83.67	_67.06*_	00.56	788.68	_71.93_			88.89	
8	70.64	_55.36*_	_887.00_	76.30	_60.70_			78.37	
9	57.53	_43.01_	_72.40_		_49.36_			67.84	
0	44.12	_30.70_	_57.75_		_37.79_			56.97	
1	30.49	_18.07_	_43.02_		_26.14_			45.88	
2	16.58	_05.48_	_27.98_		_14.14_				
3	02.53	_atom line_	_12.75_		_01.94_				
4	888.17	_40 979.67*_	_797.31_		_789.64_				
5	73.50	_66.33_	_81.63_		_77.03_	_592.43_			
6	58.85	_52.85_	_65.73_			_77.36_			
7	42.50	_38.96*_	_49.64_			_61.98_			
8	_29.77_	_25.21_	_33.55_			_46.61_			
9	_14.15_	_10.90_	_16.76_			_30.98_			
0	_798.47_	_896.52_	_00.02_			_15.19*_			
1	_82.62_	_81.82_	_683.22*_	_39 598.16_		_498.89*_			
2	_66.56_	_67.02_	_66.17_	_82.91_		_82.68_			
3	_50.34_	_51.70_		_67.51_		_66.14_			
4	_33.55*_	37.55		_51.77*_		_49.38_			
5	_15.70_	21.40		_atom line_		_32.33_			
6	00.59	05.66		20.62		16.24			
7	683.22	789.59		04.32*		398.28			
8		73.42		487.86*	594.93	80.67			
9		56.98		71.20	79.42	62.88			
0		40.32		54.38*	63.78	44.92			
1		23.46		37.41	47.86	26.76			
2		06.29		20.08*	31.84	08.35			
3		689.04		02.58	15.19*	289.70			
4		71.28		384.83	498.89*	70.95			
5				66.95	81.91	51.99			
6				48.77	64.88	32.79			
7				30.52	47.64	13.36			
8				{ 10.53 _12.63_	30.15	193.73			
9				_293.16_	12.37	73.81			
0				_74.17_	394.46	53.79			
1				_54.89_	76.30	33.37			
2				_35.50_	58.06	12.83			
3				_15.78_	39.35	092.12			

Table 2 (cont.)

J	$Q(0,1)$	$R(0,1)$	$P(0,1)$	$Q(0,2)$	$R(0,2)$	$P(0,2)$	$Q(0,3)$	$R(0,3)$	$P(0$
104				*195.86*	20.48	71.10			
105				*75.67*	01.37	50.05*			
106				*55.22*	282.10	28.58			
107				*34.23*	62.56	06.71			
108				14.42	42.72				
109				293.17	22.68				
110				71.82	02.64				
111				50.05*	181.70				
112				28.05	*61.53*				
113				*09.48**	*40.44*				
114					*19.12*				
115					*97.66*				
116					*75.99*				
117					*53.90*				
118					*31.83*				
119					*09.48**				

All the perturbations are rather faint and only in a few cases have extra lines been found.

Not all lines in the 0,2 band were measured. This does not, however, influence the analysis, because the part omitted in the 0,2 band is analysed in the 0,1 band. As a rule the first 60–70 lines in a branch of a band are situated before the next band-head in the same sequence. Owing to the great number of lines, we have concentrated our measurements to a selection of bands most convenient for the analysis and representing the levels $v' = 0$, 1, and 2. In these bands we were able to pick out the Q-branch of the 0,4 band and the three branches of the 1,1 band for lines with higher J-values. This was valuable as a check on the analysis.

Silicon has three isotopes. Attention has been paid only to the most abundant one ^{28}Si (92.2 %).

§ 4. Determination of rotational constants

The rotational constants for the lower unperturbed v''-levels have been determined with the weighted centre-of-gravity method (see LAGERQVIST, LIND and BARROW, 1950).

The rotational constants of the upper perturbed v'-levels have been determined in a different way. The method introduced by GERÖ (1935) for detecting perturbations in the upper state was used. The following expressions are formed

$$\frac{R(J-2)-R(J-1)+P(J)-P(J+1)}{4J} = B'' - B'_d + 6D' - 2J^2(D''-D') \qquad (1)$$

$$\frac{Q(J-1)-Q(J)}{2J} = B'' - B'_c - 8J^2(D''-D'). \qquad (2)$$

Plotting the left-hand-side expressions against J^2, one obtains ΔB as the intercept at $J=0$. ΔD is obtained from the slope. As B'' and D'' have already

Table 3

Wave-numbers for the 0,4 and 1,1 bands

J	$Q(0,4)$	$Q(1,1)$	$R(1,1)$	$P(1,1)$
65	37 455.93*			
66	45.27*			
67	34.36*			
68	23.50*			
69	12.39			
70	01.09			
71	389.59			
72	77.95			
73	66.11			
74	53.98			
75	41.66			
76	29.14			
77	15.43 _19.36_			
78	_04.83_			
79	_291.69_			
80	_78.28_			
81	_65.01_			
82	_51.46_			
83	_37.60_			
84	_22.96*_			
85	10.63			
86	195.69*			
87	81.32			
88	66.59			
89	51.92			41 328.76
90	36.79	41 416.31		08.71
91	21.62	396.85		288.46*
92	06.11*	78.24		67.88
93	090.58*	58.50		47.17
94	74.90*	38.72		25.52
95	58.96*	18.49		03.58
96	42.69	298.19	41 412.62*	180.59
97	26.25	77.53	392.96*	_62.95*_
98	08.23* _10.29_	56.48	73.39	_39.69_
99	_36 992.94_	35.73*	53.43	_17.65_
100	_75.94_	14.74	33.16	_095.18_
101	_58.71_	192.61*	12.69	_72.41_
102	_41.35_	_76.32_	291.89	_49.47_
103	_23.67_	_53.06*_	70.78	_26.06_
104	_05.88_	_30.22_	49.12	_02.74_
105	_887.82_	_07.25_	_28.57*_	_40 978.99_
106	_69.46_	_083.54_	_04.87_	54.74
107	_50.59_	_58.47_	_183.38*_	31.68
108	33.03	34.92	_61.90_	06.25
109	13.98*	11.06		881.82
110	794.70	40 987.30		
111	75.37	63.09		
112	55.57*	38.78*		
113	_38.70_	13.85		
114	_16.25_	889.09		
115	_696.05_	63.85		
116	_75.64_	38.35		
117	_55.05*_			
118	_33.91*_	_786.81_		
119		_60.28_		
120		_33.55*_		
121		_06.29_		
122		_679.18_		

been obtained with the method, as mentioned above, it was possible to determine B' and D'. The B-values B_c and B_d from the two Λ-type doubled terms do not differ in any higher degree, so we have taken their mean as an effective B'-value. When forming the combination defect

$$R(J) - Q(J) - Q(J+1) - P(J+1) \sim 2(B_d - B_c)(J+1)^2$$

we obtain $B_d - B_c = -0.0000_7$ for $v' = 0$, and -0.0000_9 for $v' = 1$.

The error in the B-values is roughly of the magnitude ± 0.0002.

The rotational constants are given in Table 5.

The calculated values are found from the expressions:

$$B''_v = 0.7272_9 - 0.0050_8\,(v + \tfrac{1}{2})$$
$$B'_v = 0.6312_8 - 0.0069_5\,(v + \tfrac{1}{2}).$$

The mean of the observed D''-values is 1.02×10^{-6}, of the observed D'-values 1.43×10^{-6}.

Table 4

Wave-numbers for the 1,0, 1,5, 2,2 and 2,0 bands

J	$Q(1,0)$	$R(1,0)$	$P(1,0)$	$Q(1,5)$	$R(1,5)$	$P(1.5)$	$Q(2,6)$	$R(2,6)$	$P(2,6)$	$Q(2,0)$	$R(2,0)$	$P(2,0)$
5							37 104.91					
6							03.88*					
7							02.86*					
8							01.62					
9				37 443.61*			00.13			44 297.96*		
10				42.10		37 429.67	098.49			95.51*		
11				40.33		26.66*	96.83*			92.92*		
12				38.44		23.50	94.76*	37 112.54		90.11*		
13	43 460.98			36.39		20.23	92.72*	10.69		87.00		
14	58.07			34.36*		16.85	90.58*	09.29		84.16		
15	55.01			31.76*		13.21	88.04	07.86	37 070.46*	80.96		44.262.12
16	51.71			29.29		09.87	85.48*	06.55	66.54*	77.48		57.67
17	48.43*			26.66*		06.11	82.76	04.91*	62.34*	73.93		52.67
18	44.56*	43 468.25*		23.81*		02.04	79.88	02.86*	57.90*	69.58	44 292.92*	47.91*
19	40.76*	65.36	43 417.43	20.91	37 445.27*	397.33	76.77	01.08	53.62	65.35*	90.11*	42.54*
20	36.46	62.47	11.78	17.69	43.61*	92.84	73.52*	099.14	49.05	61.16*	86.40	36.67*
21	31.91	59.32	06.00	14.38	41.55	88.28	70.10	96.83*	44.34	56.32	82.94	30.76*
22	atom line	55.94	00.33	10.87	39.29	83.58	66.54*	94.32	39.56*	51.46	79.38	24.44*
23	atom line	52.49	394 36	07.25	36.94	78.66	62.79	91.69*	34.44	46.17	75.65	17.80*
24	18.11	48.43*	88.18	03.38	34.36*	73.75	58.96*	88.96	29.45	40.88	71.09	11.38
25	12.76	44.56*	81.72	399.46	31.76*	68.46	54.80	85.48*	24.11*	35.12	66.41	04.49
26	07.35	40.76*	75.02	95.40*	28.66	63.07	50.62*	_86.32_	18.17	29.41	61.16* _65.35*_	197.27
27	01.61	35.97	68.05	91.17	25.63	57.61	46.08	_81.78*_	12.21	23.17	_59.06_	89.37
28	395.74	atom line	61.04	86.67	22.43	52.00	41.35*	_77.94_	_09.81_	16.84	_53.46_	80.99 _85.19*_
29	89.70	atom line	53.75	82.06	19.05	46.08	36.31	_74.27_	_02.70*_	10.25	_47.91*_	_75.94*_
30	83.38	atom line	46.27	77.30	15.52	40.21	30.76*	_70.46*_	36 996.34	03.00	_42.54*_	_67.83*_
31	77.13*	16.51	38.57	72.30	11.72	34.05	24.11* _33.47_	_66.54*_	_89.91*_	194.53	_36.67*_	_59.77*_
32	70.27	10.86	30.60	67.36	07.98	27.76	15.30* _25.30*_	_62.34*_	_83.62*_	_93.42_	_30.76*_	_51.40_
33	63.38	05.19	22.56	62.09	03.98	21.31	_18.74_	_57.90*_	_76.82_	_85.19*_	_24.44*_	_42.59*_
34	56.06	399.33	14.08	56.65	00.04	14.74	_12.77_	_53.20_	_69.61*_	_77.25_	_17.80*_	_33.62*_
35	48.89	93.06	05.53	51.12	395.40*	07.84	_06.68_	_48.73_	_62.50*_	_68.78_	_10.92_	_24.65*_

38	25.66	73.55	78.47	33.40	81.32	86.32*	_88.22_	35.91	40.08* 43.86	_43.68_	91.27	098.41
39	17.46	66.49	68.84	27.23*	76.27	78.83*	_81.85_	30.76*	34.84	_35.01_	83.47	87.77*
40	09.00	59.28	59.59*	20.76	71.01	71.22*	_75.30_	25.30*	26.76	_25.97_	75.94*	77.65*
41	00.41	51.78	49.72	14.21	65.65	63.62	_68.53_	19.73*	18.78	_16.80_	67.83*	67.22*
42	291 62	44.11	39.75*	07.47	59.99	55.58	_61.68_	14.07	10.61	_07.27_	59.77*	56.54*
43	82.50	35.20 _39.88_	29.36	00.57	53.15 _58.00_	47.44	_54.55_	08.23*	02.41	_097.46_	51.40*	45.92*
44	73.19	_28.89_	18.63	293.61*	_49.36_	39.01	_47.30_	02.01	894.00	_87.77*_	42.59*	34.62*
45	63.76	_20.51_	06.85 _11.57_	86.32*	_43.04_	29.50 _34.16_	_40.08*_	36 995.93	85.36	_77.65*_	33.62*	23.40*
46	53.82	_11.89_	_197.90_	78.83*	_36.78_	_22.96*_	_32.45*_	89.91*	76.59	_67.22*_	24.65*	11.84*
47	43.74	_03.06_	_86.57_	71.22*	_30.37_	_13.73_	_24.71*_	83.62*	67.66	_56.54*_	15.19*	43 999.69*
48	33.05	_294.20_	_75.12_	62.86	_23.83_	_04.80_	_16.71*_	76.82	58.54*	_45.92*_	05.67*	87.96*
49	20.96 _25.99*_	_84.98_	_63.50_	52.71 _58.29_	_17.15_	_195.69*_	_08.59_	69.61*	49.32	_34.62*_	095.92	75.27*
50	_14.04_	_75.57_	_51.65_	_48.62_	_10.17_	_86.35*_	_00.38_	62.50*	39.81	_23.40*_	85.71	63.09
51	_02.87_	_65.78_	_39.59_	_40.14_	_02.95_	_76.88*_	_891.89_	55.23*	30.30	_11.84*_	75.47	50.27
52	_191.74_	_55.43_ 59.59*	_27.45_	_31.60_	_295.28_ 99.35	_67.23*_	_83.13_	47.81*	20.51	_43 999.69*_	64.68	37.38
53	_80.47_	47.12	_14.75_	_22.96*_	89.64	_57.25*_	_74.22_	40.08*	10.57	_87.96*_	54.00	24.42
54	_68.96_	36.36	_01.62_ 105.69*	_14.16_	81.52	_46.92*_ 51.08	_64.74_	32.45*	00.54	_75.27*_	43.00	11.09
55	_57.18_	25.99*	090.58	_05.26*_	73.72*	38.50	_54.14*_	24.71	790.26	_61.52_	31.76	897.37
56	_45.31_	15.06	76.94	_196.23_	65.67	27.66*	51.99	16.71*	79.83	55.85	20.46	83.50
57	_33.21*_	03.90	63.42	_86.84_	57.62	16.93*	40.28	08.05	69.12	40.66	08.62	69.45
58	_20.84*_	192.90	49.82	_77.48_	49.34	06.11*	29.84	899.65	58.33	26.98	43 996.64	55.03
59	_08.22*_	81.61	36.11	_67.80_	40.93	095.61	19.74	90.95	47.33	13.23	84.37	40.53
60	_095.34*_	69.83	22.13	_57.98_	32.31*	84.72	09.49	81.81	36.30	899.13	71.32	25.84*
61	_82.25*_	58.04	07.95	_48.05_	23.65	73.52*	_799.80_	_73.14_	24.78	_85.52_	_59.01_	10.62
62	_69.13*_	45.82	42 993.39	_37.81_	14.66	62.34*	_88.73_	_63.77_	12.84	_71.07_	_46.07_	94.94
63	_55.53*_	33.25*	78.85	_27.66*_	05.67*	50.62*	_78.03_	_54.14*_	_01.67*_	_56.44_	_32.40_	_79.97_
64	_41.77_	20.84*	63.87	_16.93*_	196.23*	39.03	_67.02*_	47.55	_689.55*_	_41.53_	22.55	_64.16_
65	_27.68_	08.22*	48.80	_06.11*_	86.35*	27.48*	_55.57*_	37.13	_76.96_	_25.84*_	07.97	_47.68_
66	_13.04_	095.34*	33.47	_094.68*_	76.88*	15.30*	_41.70*_ 51.03	26.61*	68.32*	_09.24_ 17.72	893.63	35.36
67	_42 996.61_ 43 004.10	82.25*	17.95	_81.78*_	67.23*	03.11	36.30*	16.33*	55.05*	798.75	79.00	17.52*
68	42 987.17	69.13*	02.21	75.74	57.25*	36 990.66	23.85	05.98	41.82	82.40	64.52	00.52*
69	71.24	54.81	886.18	63.27	46.92*	78.10	12.11	795.60	28.71	66.30	49.83	683.50*
70	55.80	40.96	69.88	51.45	36.35	65.26	00.29	84.77		50.43	34.83	66.48
71	40.36	26.65	53.27	39.56*	25.78	52.47*	688.22	74.07		33.99	19.77	48.88*
72	24.66	12.32	36.71	27.48*	14.97	39.23	76.09	62.88		17.52*	04.36	31.24*

Table 4 (cont.)

J	$Q(1,0)$	$R(1,0)$	$P(1,0)$	$Q(1,5)$	$R(1,5)$	$P(1,5)$	$Q(2,6)$	$R(2,6)$	$P(2,6)$	$Q(2,0)$	$R(2,0)$	$P(2,0)$
73	08.88	42 997.46	19.77	15.30*	03.88*	26.24	63.67	51.72*		700.52*	788.73	13.14*
74	892.56	81.38	02.54	02.70*	091.69 _96.83_	12.68	51.19*	40.35		683.50*	72.74	595.12*
75	74.92 _81.49_	_69.80_	784.96	36 988.66 _95.19_	_883.75_	898.86	38.34	28.71		66.48	56.78	76.44*
76	_62.03_	_53.25_	66.26	_79.70_	_71.16_	84.42*		16.88		48.88*	40.22	57.75*
77	_44.20_	_37.75_	_51.79_	_65.76_	_58.96*_	_73.46_		04.52*		31.21*	23.34	38.47*
78	_27.08_	_21.56_	_32.68_	_52.47*_	_47.15_	_58.54*_		_693.50_		13.14*	_07.50_	19.57
79	_09.70_	_05.53_	_14.05_	_39.23*_	_35.07_	_43.49_		_80.81_		595.12*	_690.14_	499.75
80	_792.47*_	_889.21_	_695.34_	_25.72_	_22.77_	_28.82_		_68.32*_		76.44*	_72.63_	_80.91*_
81	_74.63_	_72.75_	_76.70_	_12.09_	_10.29_	_13.98*_		_55.41_		57.75*	_55.05_	
82	_56.69_	_55.95_	_57.36_	_898.31_	_997.56_	_799.11_		_42.41_		38.47*	_37.27_	
83	_38.49_	_38.82_		_84.42*_	_84.65_	_83.98*_		_29.29_		15.87 _22.68_	_18.93_	
84	_20.12_	_21.53_		_70.26_	_71.60_	_68.50*_				_00.81_	_00.63_	
85	_01.47_	_03.79_		_55.90_	58.15	_53.19_				_480.34*_	_581.31_	
86	_682.65_	786.55		_41.32_	45.21	_37.60_				_60.28_	_62.52_	
87	_63.40_	68.35		_26.61_	31.47	_21.49_				_39.73_	44.59	
88		50.13		_11.63_	17.72	05.71*				_19.54_	24.90	
89		31.63		_796.48_	03.58	689.55*				_398.50_	04.99	
90		12.90		_81.03_	889.37*	73.11				_77.13*_	484.73	
91		693.86		_64.99_ 67.02	74.99	56.48				_56.06_		
92		74.57		50.20	60.35	39.69				_33.64*_		
93		55.14		34.25	45.56	22.60				_10.11_		
94				18.10	29.84*					295.25		
95				01.67*	_16.90_					71.43		
96				685.12	_799.80*_					48.36		
97				68.32*	_83.98*_					25.01		
98				51.19*	_68.50*_					01.58*		
99				33.91*						177.73		
100										_54.65_		
101										_30.23_		
102										_05.69*_		
103										_081.06_		
104										_56.40_		
105										_31.09_		
106										_05.67_		
107												

J	$Q(2, 0)$
110	_01.26_
111	_873.76_ 76.13
112	47.94
113	20.49
114	792.47*
115	64.71
116	36.35

Table 5

Rotational constants for the $A\ ^1\Pi$ and $X\ ^1\Sigma$ states

v	$B''_{\text{obs.}}$	$B''_{\text{calc.}}$	$D''_{\text{obs.}}$	$B'_{\text{obs.}}$	$B'_{\text{calc.}}$	$D'_{\text{obs.}}$
0	0.7247	0.7247_5	1.04×10^{-6}	0.6278	0.6278	1.43×10^{-6} (from 7 observations)
1	0.7195	0.7197	0.99	0.6209	0.6209	1.42 (from 4 observations)
2	0.7149	0.7146	1.03	0.6139	0.6139	1.46 (» 3 »)
3	0.7095	0.7095	(1.10)			
4		0.7044				
5	0.6992	0.6994	1.00			
6	0.6943	0.6943	1.06			

The internuclear distances are:
$r_e'' = 1.509 \times 10^{-8}$ cm and $r_e' = 1.620 \times 10^{-8}$ cm.
Kratzer's relation ($D_e = 4\,B_e^3/\omega_e^2$) gives $D_e'' = 1.00 \times 10^{-6}$ and $D_e' = 1.38 \times 10^{-6}$.

§ 5. Determination of vibrational constants

The origins of the bands, calculated in the usual way, have already been given in Table 1. The upper-state vibrational constants ω_e' and $\omega_e' x_e'$ have been computed from the origins. As the lower state is unperturbed, it is possible to use a more accurate method for the determination of ω_e'' and $\omega_e'' x_e''$. The following expression is formed for the Q-branches of two bands with the same upper level but with different lower lewels (i and k),

$$A = Q(J)_{v' v_i''} - Q(J)_{v' v_k''} = \nu_0(v' v_i'') - \nu_0(v', v_k'') + (B_k'' - B_i'')\,J(J+1).$$

If one plots A against $J(J+1)$, the difference $\nu_0(v', v_i'') - \nu_0(v', v_k'') = G''(v_i'') - G''(v_k'')$ is graphically obtained. All possible combinations have been treated. This method is not convenient for perturbed levels. The constants derived are:

$$\omega_e' = 852.7_1 \qquad \omega_e'' = 1241.4_4$$
$$\omega_e' x_e' = 6.4_4 \qquad \omega_e'' x_e'' = 5.9_2$$
$$\nu_e = 42834.9_3$$

§ 6. Perturbations

Saper (1932) reported in his paper that the Q-branches are perturbed owing to interactions of the upper levels with unknown electronic states. He dit not, however, make a complete investigation of the perturbations, doubtless for the simple reason that good methods for the treatment of perturbations had at that time not yet been worked out.

We have found many perturbations in the upper-state levels in the Q-branches and in the R and P branches. The lower levels are unperturbed. The perturbations were detected by forming the expressions (1) and (2) and plotting them against J (Fig. 2). Information on the perturbations is summarized in Table 6 and in Fig. 3. The figure shows the upper vibrational levels plotted against $J(J+1)$. In the diagram, circles, triangles, squares and crosses indicate the positions where the perturbations culminate.

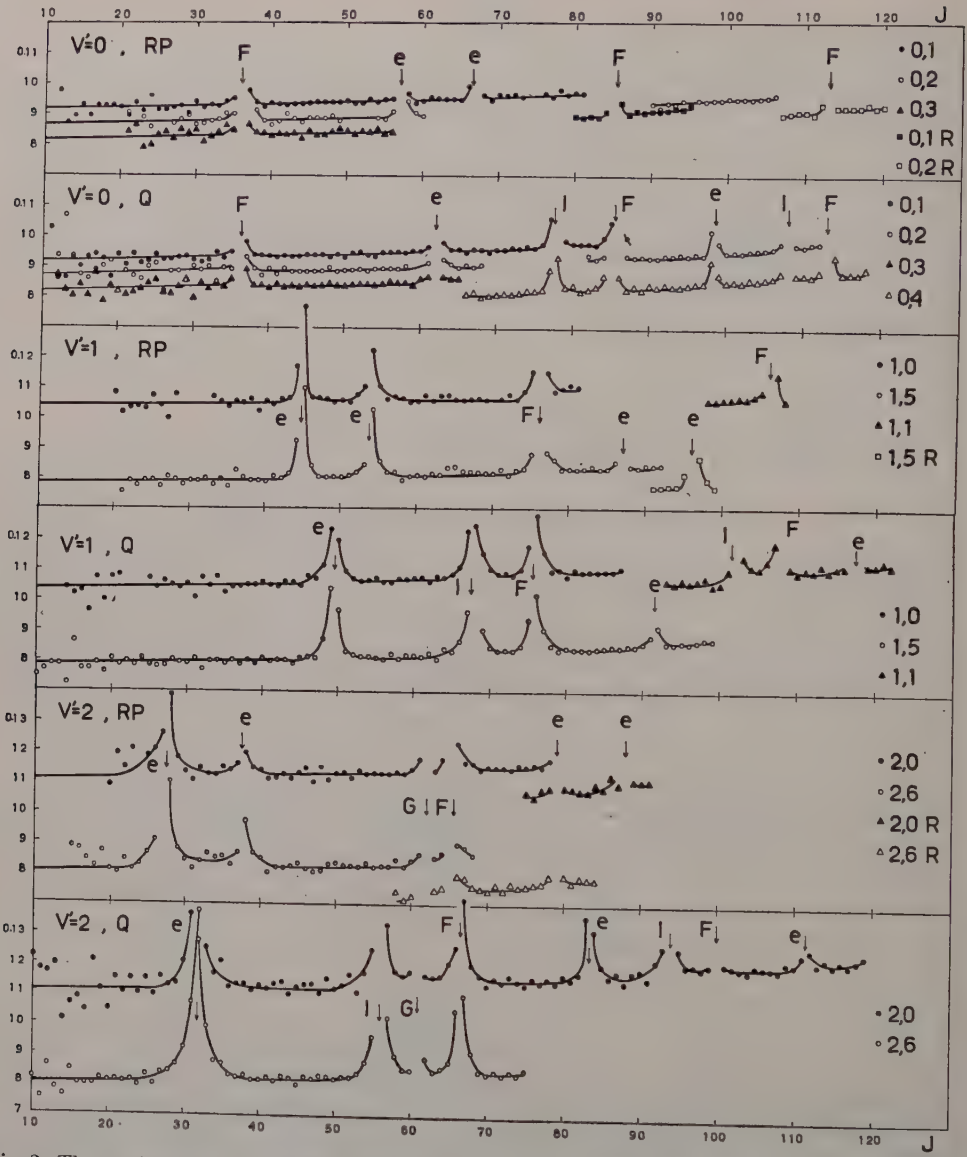

Fig 2. The variation of ΔB with J. For the R and P branches $[R(J-2) - R(J-1) + P(J) - P(J+1)]/4J$ is plotted against J. In certain regions, where the P-branch is not analysed, $[R(J-2) - R(J-1)]/2J$ is used. This is in the figure indicated by an R; 0,1 R, 0,2 R etc. For the Q-branches $[Q(J-1) - Q(J)]/2J$ is plotted against J.

a. The perturbing states

The perturbations found may be explained by the interaction of four perturbing states, a triplet one and three singlet ones. These states are here called e, F, I and G. Three of them seem to lie lower than the $A\,^1\Pi$ state. State e is probably $^3\Sigma^-$, as in the CO and SiS spectra (Coster and Brons 1934, Budó and Kovács 1938, Lagerqvist, Nilheden and Barrow 1952). At a $^3\Sigma^-{}^1\Pi$ perturbation there are three interactions: the $^3\Sigma_J^-$ component perturbs the c-terms in $^1\Pi$ and the $^3\Sigma_{J-1}^-$ and $^3\Sigma_{J+1}^-$ components perturb the d-terms. In this way the spectrum shows a perturbation in the Q-branch at a certain J-value and two perturbations in the R and P branches, situated one at a higher and one at a lower J-value than that for the Q-branch. The state F is a $^1\Pi$ or a $^1\Delta$ state. As both the Λ-type terms of $A\,^1\Pi$ are perturbed, it cannot be a $^1\Sigma$ state. The state F is also found in SiS. The state G is of the same type as F. Only two GA-interactions are found, one in the Q-branch and the other in the R and P branches of $v'=2$ in A. The I-state must be described as a $^1\Sigma^-$ state, as only the c-terms of $A\,^1\Pi$ are perturbed. The same state is discussed in CO and an extension of the analysis of the SiS spectrum shows the same in $D\,^1\Pi$ of SiS (Nilheden, private communication).

Table 6

Summary of the perturbations

v'	J^*			B_s	ν_s	$C_s + \nu_0$	Perturbing state
	RP	Q	RP				
0	36.1	36.3	—	—	f	~ 42 800	F $^1\Pi$ or $^1\Delta$
0	57	62	66.5	0.519	e	43 068	e $^3\Sigma^-$
0	—	77.5	—	—	i	~ 43 300	I $^1\Sigma^-$
0	85.5	85.3	—	—	$f+1$	—	F
0	not found	98.5	not found	0.511	$e+1$	43 751	e
0	—	108	—	0.514	$i+1$	—	I
0	113	113	—	0.514	$f+2$	—	F
1	44.6	49.5	53.6	0.511	$e+1$	43 744	e
1	—	67.5	—	0.514	$i+1$	—	I
1	75.8	75.6	—	0.514	$f+2$	—	F
1	87	91.5	96	0.509	$e+2$	44 409	e
1	—	101.5	—	0.509	$i+2$	—	I
1	106.5	107.5	—	0.508	$f+3$	—	F
1	—	117.5	—	0.505	$e+3$		e
2	27.5	31.8	37.5	0.509	$e+2$	44 412	e
2	—	56.3	—	0.509	$i+2$	—	I
2	62	61	—	—	g	—	G $^1\Pi$ or $^1\Delta$
2	65.5	66.5	—	0.508	$f+3$	—	F
2	79	83.5	88	0.505	$e+3$	45 054	e
2	—	94	—	—	$i+3$	—	I
2	—	100	—	—	$f+4$	—	F
2	—	111.5	—	—	$e+4$	—	e

In Fig. 3 the eA-interactions are indicated by circles, FA-interactions by squares, IA-interactions by crosses and GA-interactions by triangles. Filled tokens are used for perturbations in the Q-branches, open tokens for those in the R and P branches.

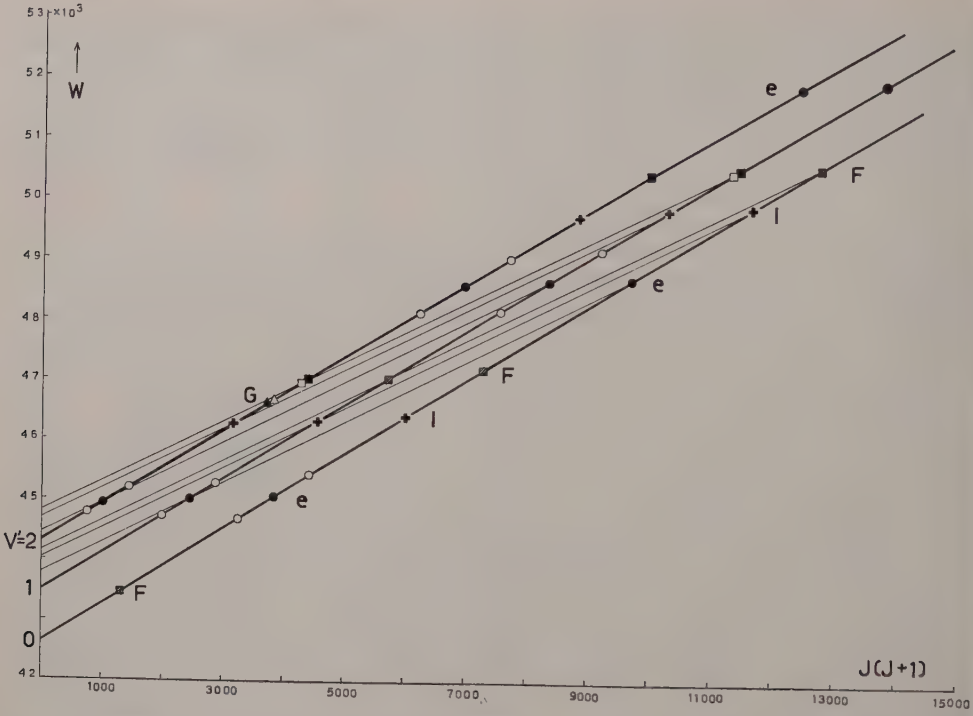

Fig. 3. Perturbations in SiO-term-values plotted against $J(J+1)$. For the sake of clarity, only a few of the perturbing levels are drawn. Perturbations with $e\,^3\Sigma^-$ are indicated with circles, $I\,^1\Sigma^-$ perturbations with crosses, $F\,^1\Pi$ perturbations with squares and $G^1\,\Pi$ interactions with triangles. Filled tokens are used for interactions in the Q-branches, open tokens for those in the R and P-branches. Half-filled tokens where Q interactions coincide with RP interactions.

b. Determination of constants for the perturbing states

The $e\,^3\Sigma^-$ *state*

Kovács (1950) has developed the method for determining B and C values for perturbing states if at least two extra lines at consecutive J-values are known. Only in one case in the present analysis have we found two extra lines, namely in the Q-branch of the 2,6 band at $J=31$ and 32. Kovács has shown that it is possible to treat a $^3\Sigma$ $^1\Pi$ perturbation in the Q-branch as a singlet-singlet ($^1\Sigma\,^1\Pi$) interaction. The $B_{^3\Sigma^-}$ value may be computed from

$$\frac{f_1+f_2}{2}=\frac{B'_\Pi+B_{^3\Sigma^-}}{2}-B''_\Sigma,\ \text{where}\ f=\frac{\Delta Q}{2J} \tag{3}$$

and the indexes 1 and 2 indicate the two interacting levels.

Another method for obtaining the $B_{^3\Sigma}$-value at a $^3\Sigma$ $^1\Pi$ perturbation is the following. The terms of $^1\Pi$ and $^3\Sigma$ may be written approximately

$$
\begin{aligned}
F_J^{\Pi} &= B_{\Pi} J(J+1) \\
F_{J+1}^{3\Sigma} &= C + B_{3_\Sigma}(J+1)(J+2) \\
F_J^{3\Sigma} &= C + B_{3_\Sigma} J(J+1) \\
F_{J+1}^{3\Sigma} &= C + B_{3_\Sigma}(J-1)J.
\end{aligned}
$$

We assume that the interactions of the three $^3\Sigma^-$ components culminate at the J-values J_1, J_2 and $J_3 (J_3 > J_1)$ in the $^1\Pi$ levels. From the expressions of the terms at the perturbations in the R and P branches at J_1 and J_3 we get

$$B_{3_{\Sigma^-}} = B_{\Pi} \frac{J_3(J_3+1) - J_1(J_1+1)}{(J_3+1)(J_3+2) - (J_1-1)J_1}. \tag{4}$$

This method is in the following called the J_1, J_3 method.

According to a third method one calculates the perturbing B-value from the slope of the energy-level curve (se Fig. 3). At two consecutive Π vibrational levels the perturbations (in the Q-branch) occur at $J = J_2$ in $(v'+1)$ and at J_2' in v'. If one neglets the effect of the D-values the perturbing B-value is

$$B_{3_\Sigma} = \frac{B_v' J_2'(J_2'+1) - B_{v+1}' J_2(J_2+1) - [G_\Pi(v'+1) - G_\Pi(v')]}{J_2'(J_2'+1) - J_2(J_2+1)}, \tag{5}$$

where G_Π is the vibrational energy of Π. This method is here referred to as the slope-method.

Some B-values of the perturbing $e\,^3\Sigma^-$ state are determined with these three methods. The lowest vibrational $e\,^3\Sigma^-$ level found (at $J \sim 62$ in $v' = 0$) is given the vibrational quantum number e, the others $(e+v)$. The B^{e+v} values obtained are given in Table 7.

Table 7

The observed B-values of the $e^3\Sigma^-$ state

v in $e^3\Sigma^-$	B^{e+v} with »the extra line» method	B^{e+v} with the J_1, J_3 method	B^{e+v} with the slope-method	B^{e+v} mean
e		0.51_{86}		0.519
$e+1$		0.50_{80}	0.51_{41}	0.511
$e+2$	0.509_3	0.51_{16} 0.50_{80}	0.50_{95}	0.509
$e+3$		0.50_{23}	0.50_{77}	0.505

The observed B-values follow approximately the equation

$$B^{e+v} = 0.517 - 0.004\ v.$$

The C-values given in Table 6 are determined with the approximate equation

$$C = (B^{\Pi} - B^{e+v})\ J^{*2}, \tag{6}$$

where J^* is the J-value obtained from Fig. 2.

In one case (from the perturbation in the 2,6 band at $J=31$ and 32) the following more accurate equation was also used

$$C=\nu_0+B^{\Pi}+\tfrac{1}{2}\{(J-1)[Q(J)+Q'(J)]-(J+1)[Q(J-1)+Q'(J-1)]\}.$$

The calculations show that $\omega_e^e \geq 686$ and that $\omega_e x_e \sim 4$.

The F ($^1\Pi$ or $^1\Delta$) *state*

The magnitudes of the observed B and C values are of the same order as those for $e\,^3\Sigma^-$. The B-values are obtained with the slope method. It is impossible to decide the absolute numbering of the vibrational levels.

The $I\,^1\Sigma^-$ state

The B-values, determined from the slope, are of the same magnitude as those for e and F. The absolute vibrational quantum number cannot be stated.

The G ($^1\Pi$ *or* $^1\Delta$) *state*

Only one perturbation in $v'=2$ is found. Nothing can be said about the B-value. As the G-state does not perturb $v'=1$ and 0, it is not quite out of the question that the perturbation found emanates from $v=0$ in G. It is, however, impossible to be sure of this. It may happen that the perturbing matrix elements for interactions between lower G-levels and A-levels are too small to produce observable perturbations.

Comparison of SiO with CO and SiS

The data abtained about the electronic states in SiO are given in Table 8. A comparison between SiO, CO and SiS will be found in Table 9. As for CO and SiS, it is most likely that $A\,^1\Pi$ and $X\Sigma$ dissociate into the ground-states of the atoms, Si (^{3}P) + O (^{3}P). The dissociation energies in Table 8 are obtained with a Birge-Sponer linear extrapolation.

Table 8

Summary of constants for SiO

State	T_0	ω_e	$\omega_e x_e$	B_e	α_e	$D_e \times 10^6$	$r_e \times 10^8$	D(e.v.)
$G\,^1\Pi$ or $^1\Delta$	$\leq \sim 44\,700$	—	—	—	—	—	—	—
$I\,^1\Sigma^-$	$\leq \sim 43\,300$	~ 680	—	≥ 0.517	~ 0.006	—	< 1.79	—
$e\,^3\Sigma^-$	$\leq 43\,068$	≥ 684	~ 4	≥ 0.519	~ 0.004	—	< 1.79	—
$F\,^1\Pi$ or $^1\Delta$	$\leq \sim 42\,800$	~ 660	—	≥ 0.517	~ 0.005	—	< 1.79	—
$A\,^1\Pi$	42 640.4	852.7_1	6.4_4	0.6313	0.0069_5	1.43	1.620	3.5
$X\,^1\Sigma$	0	$1\,241.4_4$	5.9_2	0.7273	0.0050_8	1.02	1.509	8.1

As may be seen from Table 9, the three molecules have five corresponding states. Further, the state $G\,^1\Pi$ or $^1\Delta$ in SiO may have its counterpart in CO: $F\,^1\Pi$. In the term-scheme for CO we have called the perturbing $^1\Pi$ state in the $A\,^1\Pi$ state of CO F'. This perturbing state was found in the beginning of the level $v=1$ by GERÖ and later published among the perturbing states in CO

Table 9

States of SiO compared with those of SiS and the lowest states of CO

CO			SiO				SiS			
T_0	ω/ω_x	B/B_x	State	T_0	ω/ω_x	B/B_x	State	T_0	ω/ω_x	B/B_x
$\leq$ 64 800	$\geq$ 0.49	$\geq$ 0.64	$e\ {}^3\Sigma^-$	$\leq$ 43 070	$\geq$ 0.55	$\geq$ 0.71	$e\ {}^3\Sigma^-$	$\geq$ 35 140	$\geq$ 0.55	$\geq$ 0.70
61 785	0.52	0.65								
55 900	0.56	0.69								
48 688	0.80	0.87								
							E ?	41 751	0.54	—
99 730	0.97	—	$G\ {}^1\Pi$ or ${}^1\Delta$	$\leq$ 44 700	—	0.87				
92 923	0.98	—								
91 926	0.98	—								
86 918	0.96	1.02								
$\leq$ 66 380	$\geq$ 0.48	$\geq$ 0.75	$I\ {}^1\Sigma^-$	$\leq$ 43 300	$\geq$ 0.55	$\geq$ 0.71	$I\ {}^1\Sigma^-$	—	—	> 0.88
$\leq$ 66 230	—	< 0.83	$F\ {}^1\Pi$ or ${}^1\Delta$	$\leq$ 42 800	$\geq$ 0.53	$\geq$ 0.71	$f\ {}^1\Pi$ or ${}^1\Delta$	$\leq$ 37 000	$\geq$ 0.60	$\geq$ 0.79
64 747	0.70	0.83	$A\ {}^1\Pi$	42 640	0.69	0.87	$D\ {}^1\Pi$	34 910	0.68	0.88
							(a) ?	(15 000)	(0.87)	—
0	1.00	1.00	$X\ {}^1\Sigma^+$	0	1.00	1.00	$X\ {}^1\Sigma^+$	0	1.00	1.00

by GERÖ and SCHMID (1935). COSTER and BRONS (1934), with less to go upon, incorrectly presumed that the beginning of the level $v=0$ in A is perturbed by a ${}^1\Pi$ state. A corresponding transition to EX in SiS is not found in SiO. If it is present, it ought to be situated in the extreme ultra-violet region.

Thus, the analogy between the spectra of the three molecules is very great.

February 1952. Physics Department, The University, Stockholm.

REFERENCES: **Bäckström, H.**, 1940, Ark. f. Kem. Min. o. Geol. *13A*, Nr. 24. — **Barrow, R. F.**, 1946. Proc. Phys. Soc., *58*, 606. — **Lagerqvist, A.**, **Nilheden, G.**, and **Barrow, R. F.** 1952, Proc. Phys. Soc. A, *65*, 419. — **Budó, A.** and **Kovács, I.**, 1938, Zeit. f. Phys., *109*, 393. — **Cameron, W. H. B.**, 1927, Phil. Mag. (7) *3*, 110. — **Coster, D.** and **Brons, F.**, 1934, Physica, *1*, 634. — **Gerö, L.**, 1935, Zeit. f. Phys., *93*, 669. — **Jevons, W.**, 1924, Proc. Roy. Soc. London, *106*, 174. — **Kovács, I.**, 1950, Acta Phys. Hung. *1*, 97. — **Lagerqvist, A.**, **Lind, E.** and **Barrow, R. F.**, 1950, Proc. Phys. Soc. A, *63*, 1132. — M. I. T. Wave-length Tables, 1939. (London: Chapman and Hall.) — **Saper, P.**, 1932, Phys. Rev., *42*, 498. — **Schmid, R.** and **Gerö, L.**, 1935, Zeit. f. Phys., *94*, 386. — **Sharma, D.**, 1944. Proc. Nat. Acad. India, *14A*, 37.

Tryckt den 17 november 1952

Uppsala 1952. Almqvist & Wiksells Boktryckeri AB

ARKIV FÖR FYSIK Band 6 nr 11

Communicated 4 June 1952 by IVAR WALLER

On the influence of spin and isotopes in the kinematical theory of neutron diffraction

By PER OLOF FRÖMAN

Although many papers[1] have been written before about the subject treated here no complete treatment has been given. The purpose of the present paper is to derive a formula more general than those derived up to now which takes into account the effects of temperature, spin, and isotopic disorder on the diffraction of slow neutrons by single crystals in which the magnetic interaction between the neutron and the scattering nuclei can be neglected. The treatment is closely connected with that in a previous paper by the present author.[2] As regards the notations and the basic equations we refer to that paper, which will be called II in the following.

The spin vector of the nucleus l is denoted by $\boldsymbol{s}_l$ (the angular momentum is $\hbar\,\boldsymbol{s}_l$), and its spin state is characterized by the normalized ket vector $|j_l, m_l)$, where j_l is the nuclear spin and m_l its component in a fixed direction. The corresponding symbols for the neutron are the spin vector $\boldsymbol{S}$, the angular momentum $\hbar\,\boldsymbol{S}$ and the normalized ket vector $|\frac{1}{2}, M)$, where M can take the two values $\pm\frac{1}{2}$. (The neutron spin is $\frac{1}{2}$.)

The possible wave functions of the crystal are $\Phi_n(q)\,|j, m)$, where $\Phi_n(q)$ is the function defined on p. 191 in II and $|j, m)=\prod_l |j_l, m_l)$. Here $q=(q_1, q_2, \ldots, q_{3N})$, $n=(n_1, n_2, \ldots, n_{3N})$, $j=(j_1, j_2, \ldots, j_N)$ and $m=(m_1, m_2, \ldots, m_N)$. When the magnetic interaction is neglected the scattering cross section for slow neutrons can be calculated from the pseudopotential

$$V=-\frac{2\pi\hbar^2}{\mu}\sum_l \{a_l(j_l)+b_l(j_l)\,\boldsymbol{S}\cdot\boldsymbol{s}_l\}\,\delta(\boldsymbol{r}-\boldsymbol{r}_l)$$

by means of Born's approximation. The constants a_l and b_l are closely connected with the scattering lengths in the singlet and triplet states for the nucleus l.[3] Hence they depend on which one of the possible isotopes that is situated at the place l. This is indicated by writing a_l and b_l as functions of the nuclear spin j_l. We hope that it will cause no confusion to use this notation even if there are different isotopes with the same spin j_l, which can be situated at the place l.

---

[1] J. SCHWINGER and E. TELLER, Phys. Rev. 52, 286 (1937); I. POMERANTSCHUK, Phys. Zs. Sow. 13, 65 (1938); O. HALPERN and M. H. JOHNSON, Phys. Rev. 55, 898 (1939); H. HAMERMESH and J. SCHWINGER, Phys. Rev. 69, 145 (1946); E. FERMI and L. MARSHALL, Phys. Rev. 71, 666 (1947); M. E. ROSE, Nucleonics Dec. 1948, p. 23, and AECD 2183; W. G. POLLARD, not published.

[2] P. O. FRÖMAN, Arkiv för Fysik, Band 4 nr 6.

[3] L. ROSENFELD, Nuclear Forces, p. 106.

The wave function of the incident neutron is

$$e^{i\boldsymbol{k}\cdot\boldsymbol{r}}\sum_M c_M\,|\tfrac{1}{2}, M)$$

where the c_M are supposed to be normalized so that

$$\sum_M |c_M|^2 = 1. \tag{1}$$

The polarization of the incident neutron is

$$f = |c_{+\frac{1}{2}}|^2 - |c_{-\frac{1}{2}}|^2. \tag{2}$$

Solving (1) and (2) for $|c_M|^2$, we get

$$|c_M|^2 = \tfrac{1}{2} + Mf, \quad M = \pm\tfrac{1}{2}. \tag{3}$$

We shall now calculate the matrix element of V for the transition

$$\boldsymbol{k},\ \underbrace{c_{+\frac{1}{2}},\ c_{-\frac{1}{2}}}_{f};\quad n,\ m \rightarrow \boldsymbol{k}'_\nu,\ M';\quad n+\nu,\ m'$$

where $\boldsymbol{k}'_\nu$ is defined on p. 192 in II. Using the definitions of $\boldsymbol{B}_{ls}$ and $A_{\alpha\beta}(x)$ on p. 192 in II and well-known properties of the angular momentum, we get[1]

$$(\boldsymbol{k}'_\nu, M';\ n+\nu, m'\,|V|\,\boldsymbol{k}, c_{+\frac{1}{2}}, c_{-\frac{1}{2}};\ n, m) =$$
$$= -\frac{2\pi\hbar^2}{\mu}\sum_l (j, m'\,|O_l|\,j, m)\, e^{-i(\boldsymbol{k}_\nu - \boldsymbol{k})\cdot\boldsymbol{R}_l}\prod_s A_{n_s+\nu_s,\, n_s}(-(\boldsymbol{k}'_\nu - \boldsymbol{k})\cdot\boldsymbol{B}_{ls}) \tag{4}$$

where

$$O_l = \sum_M c_M(\tfrac{1}{2}, M'\,|a_l + b_l\,\boldsymbol{S}\cdot\boldsymbol{s}_l|\,\tfrac{1}{2}, M) = c_{M'}(a_l + M' b_l s_{lz}) +$$
$$+ \tfrac{1}{2}\,\delta_{M', +\frac{1}{2}}\, c_{-\frac{1}{2}}\, b_l(s_{lx} - i s_{ly}) + \tfrac{1}{2}\,\delta_{M', -\frac{1}{2}}\, c_{+\frac{1}{2}}\, b_l(s_{lx} + i s_{ly}). \tag{5}$$

If the initial state of the crystal is a definite one (n, m) but its final state any one, the differential scattering cross section for the transition of the neutron from the state with the wave vector $\boldsymbol{k}$ and the polarization f to a state with the wave vector in the direction $\boldsymbol{K}$ and with the spin component M' is according to (4)

$$\sum_\nu\sum_{m'}\frac{\mu^2}{4\pi^2\hbar^4}\,\frac{k'_\nu}{k}\,|(\boldsymbol{k}'_\nu, M';\ n+\nu, m'\,|V|\,\boldsymbol{k}, c_{+\frac{1}{2}}, c_{-\frac{1}{2}};\ n, m)|^2 =$$
$$= \sum_\nu \frac{k'_\nu}{k}\sum_{ll'}(j, m\,|O_l^* O_{l'}|\,j, m)\, e^{i(\boldsymbol{k}_\nu' - \boldsymbol{k})\cdot(\boldsymbol{R}_l - \boldsymbol{R}_{l'})}\,\cdot$$
$$\cdot\prod_s A_{n_s+\nu_s,\, n_s}((\boldsymbol{k}'_\nu - \boldsymbol{k})\cdot\boldsymbol{B}_{ls})\, A_{n_s+\nu_s,\, n_s}(-(\boldsymbol{k}'_\nu - \boldsymbol{k})\cdot\boldsymbol{B}_{l's}), \tag{6}$$

---

[1] Notice that the index s in $\boldsymbol{B}_{ls}$ and n_s refers to the enumeration of the lattice vibrations but has nothing to do with the spin vectors $\boldsymbol{s}_l$.

O_l^* denoting the operator which is Hermitian conjugated to O_l. Of course the summation over ν in (6) is restricted to those ν that make k'_ν real. For the quantity $(j, m \,|\, O_l^* O_{l'} \,|\, j, m)$ in (6) we get from (3), (5) and well-known properties of the angular momentum

$$(j, m \,|\, O_l^* O_{l'} \,|\, j, m) = (\tfrac{1}{2} + M' f)\,(a_l + M' m_l b_l)^*\,(a_{l'} + M' m_{l'} b_{l'}) + \\ + \tfrac{1}{4}\,(\tfrac{1}{2} - M' f)\,|b_l|^2\,\{j_l\,(j_l + 1) - m_l\,(m_l - 2\,M')\}\,\delta_{ll'}. \tag{7}$$

In accordance with the principles of statistical mechanics we obtain the physically measurable differential scattering cross section by averaging (6) over all possible initial states of the crystal. The probability that the isotope with the spin j_l is at the place l in the lattice and that its spin component in the preferred direction is m_l is called $P_l(j_l, m_l)$. We suppose that the probabilities $P_l(j_l, m_l)$ and $P_{l'}(j_{l'}, m_{l'})$ are statistically independent if $l \neq l'$ and that the vibration states of the crystal are statistically independent of the isotope-distribution in the crystal[1] and of the spin states of the nuclei. Then the probability that the crystal at the temperature T has the isotope-distribution j and the quantum state n, m is $\prod_l P_l(j_l, m_l) \prod_s (1 - \alpha_s)\,\alpha_s^{n_s}$, α_s being defined on p. 193 in II. Performing the averaging of (6) over all possible initial states of the crystal and taking account of (7), we get the following expression for the differential scattering cross section for the transition of the neutron from the initial state with the wave vector $\boldsymbol{k}$ and the polarization f to a final state with the wave vector in the direction $\boldsymbol{K}$ and with the spin component M'

$$\sigma(\boldsymbol{k}, f;\ \boldsymbol{K}, M') = (\tfrac{1}{2} + M' f) \sum_\nu \frac{k'_\nu}{k} \sum_{ll'} F_l^*(M')\,F_{l'}(M')\,e^{i\,(\boldsymbol{k}_\nu{}' - \boldsymbol{k}) \cdot (\boldsymbol{R} - \boldsymbol{R}_{l'})}\,\cdot \\ \cdot \prod_s \sum_{n_s} (1 - \alpha_s)\,\alpha_s^{n_s}\,A_{n_s+\nu_s,\,n_s}((\boldsymbol{k}'_\nu - \boldsymbol{k}) \cdot \boldsymbol{B}_{ls})\,A_{n_s+\nu_s,\,n_s}(-(\boldsymbol{k}'_\nu - \boldsymbol{k}) \cdot \boldsymbol{B}_{l's}) + \\ + \sum_l G_l(f, M') \sum_\nu \frac{k'_\nu}{k} \prod_s \sum_{n_s} (1 - \alpha_s)\,\alpha_s^{n_s}\,|A_{n_s+\nu_s,\,n_s}((\boldsymbol{k}'_\nu - \boldsymbol{k}) \cdot \boldsymbol{B}_{ls})|^2 \tag{8}$$

where

$$F_l(M') = \overline{a_l + M' m_l b_l} \tag{8'}$$

and

$$G_l(f, M') = (\tfrac{1}{2} + M' f)\,\left(|\overline{a_l + M' m_l b_l}|^2 - \overline{|a_l + M' m_l b_l|^2}\right) + \\ + \tfrac{1}{4}\,(\tfrac{1}{2} - M' f)\,\overline{|b_l|^2\,\{j_l\,(j_l + 1) - m_l\,(m_l - 2\,M')\}}, \tag{8''}$$

the bars on the right-hand sides of (8′) and (8″) meaning averaging with respect to the probability $P_l(j_l, m_l)$. (It should be observed that a_l and b_l are functions of j_l). As expression (8″) is a sum of two non-negative terms, we have

---

[1] The distribution of the isotopes in the crystal has in reality some influence on the lattice vibrations because the masses of the isotopes are different. Neglecting this influence we suppose that the $\boldsymbol{B}_{ls}$ are independent of the isotope-distribution.

$G_l(f, M') \geq 0$. The sums over n_s on the right-hand side of (8), which are extended from $n_s = \frac{1}{2}(|\nu_s| - \nu_s)$ to $n_s = \infty$, can be evaluated by means of the formula which was derived in the appendix of II.

The right-hand side of (8) is the sum of two expressions of quite different kinds. The first one is of the same form as the expression for the differential scattering cross section of a single crystal without isotopic disorder and without spinning nuclei.[1] For the further treatment of it we refer to II. The second one represents purely diffuse scattering. For cubic crystals it can be estimated numerically by the use of Debye's approximation for the lattice vibrations. We remark that it is always independent of the temperature if the energy of the incident neutron is so large compared with the energies of the heat vibrations of the crystal that it is allowed to approximate $\boldsymbol{k}'_\nu$ by $\boldsymbol{K}$ everywhere. Using the formula which was derived in the appendix of II and the formula

$$\sum_{\nu=-\infty}^{+\infty} J_\nu(z)\,\zeta^\nu = e^{\frac{z}{2}\left(\zeta - \frac{1}{\zeta}\right)}$$

we get in fact

$$\sum_{\nu} \prod_{s} \sum_{n_s} (1-\alpha_s)\,\alpha_s^{n_s}\,|A_{n_s+\nu_s,\,n_s}((\boldsymbol{K}-\boldsymbol{k})\cdot\boldsymbol{B}_{ls})|^2 = 1.$$

If the atomic nuclei of the crystal are unpolarized we have

$$P_l(j_l, m_l) = \frac{1}{2\,j_l+1}\,p_l(j_l),$$

where

$$p_l(j_l) = \sum_{m_l=-j_l}^{j_l} P_l(j_l, m_l)$$

is the probability that the nucleus l be the isotope j_l. In this case the formulae (8′) and (8″) become

$$F_l = \bar{a}_l \tag{8′ a}$$

$$G_l = (\tfrac{1}{2} + M' f)\,\{(\overline{|a_l|^2} - |\bar{a}_l|^2) + \tfrac{1}{12}\,\overline{j_l(j_l+1)\,|b_l|^2}\} + \tfrac{1}{4}(\tfrac{1}{2} - M' f)\,\tfrac{2}{3}\,\overline{j_l(j_l+1)\,|b_l|^2} =$$

$$= \{\tfrac{1}{2}(\overline{|a_l|^2} - |\bar{a}_l|^2) + \tfrac{1}{8}\,\overline{j_l(j_l+1)\,|b_l|^2}\} + \{(\overline{|a_l|^2} - |\bar{a}_l|^2) - \tfrac{1}{12}\,\overline{j_l(j_l+1)\,|b_l|^2}\}\,M' f \tag{8″ a}$$

the bars meaning now averaging with respect to the probability $p_l(j_l)$, i.e. averaging over the possible isotopes that can be situated at the place l in the lattice. From (8″ a) it is immediately seen that for unpolarized nuclei G_l can be equal to 0 only if $a_l(j_l)$ is independent of j_l and $b_l(j_l) = 0$ for all possible values of j_l. We remark further that if both the atomic nuclei of the crystal and the incident neutrons are unpolarized the scattered neutrons are also unpolarized. This is easily seen from (8), (8′ a) and (8″ a).

---

[1] See (5) on p. 193 in II.

In the limiting case when the nuclei of the crystal are infinitely heavy (i.e. all $\boldsymbol{B}_{ls}=0$ and all $\omega_s=0$) the differential scattering cross section (8) becomes

$$\sigma(\boldsymbol{k}, f;\ \boldsymbol{K}, M')_{\text{infinitely heavy nuclei}} =$$

$$= (\tfrac{1}{2}+M'f)\,\Big|\sum_l F_l(M')\,e^{-i(\boldsymbol{K}-\boldsymbol{k})\cdot\boldsymbol{R}_l}\Big|^2 + \sum_l G_l(f, M').$$

I wish to express my gratitude to Professor IVAR WALLER for suggesting that I do this investigation and for the valuable discussions I have had with him.

Tryckt den 17 november 1952

Uppsala 1952. Almqvist & Wiksells Boktryckeri AB

ARKIV FÖR FYSIK Band 6 nr 12

Read 12 March 1952 by IVAR WALLER

On the rôle of spin in the non-relativistic theory of the scattering of radiation

By PER SVENONIUS and IVAR WALLER

Several authors[1] have treated the problem of multipole radiation in atomic spectra. They all seem to have followed the same theoretical lines. Starting from the non-relativistic quantum-mechanical charge and current densities derivable from the Pauli equation, they obtain the corresponding radiation field by using the retarded potentials. In this way, dependence on spin is lost, and difficulties arise in accounting for the complete dependence on spin in the non-relativistic case.[2] The reason why this method of calculation is incomplete has been pointed out by PAULI.[3] In the non-relativistic approximation of the relativistic current density, there is a spin-dependent term, but this term having zero divergence, it can not be directly derived from the non-relativistic wave equation.

We will here undertake a purely quantum-mechanical, non-relativistic treatment of scattering problems with regard of spin. According to PAULI, the non-relativistic Hamiltonian H of an electron (mass m, charge ε) moving in an electromagnetic field $\boldsymbol{A}$ and electrostatic field V can be written

$$H = \frac{1}{2\,m}\left(\boldsymbol{p} - \frac{\varepsilon}{c}\boldsymbol{A}\right)^2 + \varepsilon\,V - \frac{\hbar}{m\,c}\,\boldsymbol{S}\cdot\boldsymbol{H},$$

where

$h = 2\pi\hbar$ = Planck's constant,

c = the velocity of light in vacuo,

$\boldsymbol{p}$ = the operator $-i\hbar$ grad,

$\boldsymbol{S} = \frac{1}{2}\hbar\,\boldsymbol{\sigma}$,

$\boldsymbol{\sigma}$ = the Pauli spin matrices,

$\boldsymbol{H}$ = rot $\boldsymbol{A}$ = the magnetic field vector.

---

[1] See A. RUBINOWICZ: Rep. on progr. in physics XII (1948—49) p. 233 and J. Phys. Radium 10 (1949) p. 33 D where extensive bibliographies are given.

[2] *Cf. e.g.* H. C. BRINKMAN: Physica I (1934) p. 97.

[3] W. PAULI: Handb. d. Physik XXIV/1 (1933) p. 239 eq. (96).

The whole system is supposed to be enclosed in a cube of periodicity L^3. The electromagnetic field A then may be expanded according to the theory of second quantization:

$$A = \sum_s \sum_{\lambda=1}^{2} \varkappa_s \, \boldsymbol{e}_{s\lambda} (a_{s\lambda} e^{i\boldsymbol{k}_s \cdot \boldsymbol{x}} + \overset{*}{a}_{s\lambda} e^{-i\boldsymbol{k}_s \cdot \boldsymbol{x}})$$

where

$$\varkappa_s = (\hbar c / L^3 k_s)^{\frac{1}{2}},$$

and $\sum_s$ indicates summation over all values of $\boldsymbol{k}_s$ satisfying the condition $2\pi \boldsymbol{k} = L \boldsymbol{n}$, $\boldsymbol{n}$ being any vector with integer components

λ runs over two indices, numbering two orthogonal directions of polarization $(\boldsymbol{e}_{s\lambda})$ satisfying the conditions $\boldsymbol{k}_s \cdot \boldsymbol{e}_{s\lambda} = 0$ and $|\boldsymbol{e}_{s\lambda}| = 1$.

Any photon $(\boldsymbol{k}_s, \boldsymbol{e}_{s\lambda})$ is thus characterized by the indices s and λ. The operators of absorption or emission of this kind of photon are denoted by $a_{s\lambda}$ and $\overset{*}{a}_{s\lambda}$ respectively.

We shall now regard

$$H_0 = \frac{1}{2m} \boldsymbol{p}^2 + \varepsilon V$$

as the unperturbed Hamiltonian of the electron. The Hamiltonian of our system can then be written

$$H_0 + \sum_s N_s \hbar c k_s + W$$

where

$$W = -\frac{\varepsilon}{mc} (\boldsymbol{p} \cdot \boldsymbol{A} + \boldsymbol{S} \cdot \boldsymbol{H}) + \frac{\varepsilon^2}{2mc^2} \boldsymbol{A}^2$$

and N_s denotes the number of photons with momentum $\boldsymbol{k}_s$. W will be treated as a perturbation operator. We obviously have

$$\boldsymbol{p} \cdot \boldsymbol{A} = \sum_{s\lambda} \varkappa_s \, \boldsymbol{e}_{s\lambda} \cdot \boldsymbol{p} \, (a_{s\lambda} e^{i\boldsymbol{k}_s \cdot \boldsymbol{x}} + \overset{*}{a}_{s\lambda} e^{-i\boldsymbol{k}_s \cdot \boldsymbol{x}})$$

and

$$\boldsymbol{S} \cdot \boldsymbol{H} = \sum_{s\lambda} \varkappa_s \, \boldsymbol{e}_{s\lambda} \cdot i \, \boldsymbol{S} \times \boldsymbol{k}_s \, (a_{s\lambda} e^{i\boldsymbol{k}_s \cdot \boldsymbol{x}} - \overset{*}{a}_{s\lambda} e^{-i\boldsymbol{k}_s \cdot \boldsymbol{x}}).$$

From the last equations we conclude that the perturbation matrix, the scattering amplitudes, etc., directly follow from the corresponding expressions in the non-relativistic theory excluding spin ($\boldsymbol{S} = 0$) by the substitution

$$\boldsymbol{p} \, e^{i\boldsymbol{k} \cdot \boldsymbol{x}} \to (\boldsymbol{p} + i \, \boldsymbol{S} \times \boldsymbol{k}) \, e^{i\boldsymbol{k} \cdot \boldsymbol{x}}$$

in every matrix element of the operator $\boldsymbol{p}$.

This result may be compared with the corresponding conclusions from the non-relativistic approximation to the Dirac theory. WALLER[1] has shown *e.g.* that some matrix elements become proportional to[2]

$$\int \{ \overset{*}{\psi}_n \boldsymbol{e} \cdot \boldsymbol{p}\, \psi_m + \boldsymbol{e} \cdot \operatorname{rot} (\overset{*}{\psi}_n \boldsymbol{S}\, \psi_m) \}\, e^{-i \boldsymbol{k} \cdot \boldsymbol{x}}\, d\tau.$$

Integrating the second member by parts, we see that the matrix elements turn into

$$\int \overset{*}{\psi}_n \boldsymbol{e} \cdot (\boldsymbol{p} - i\, \boldsymbol{S} \times \boldsymbol{k})\, e^{-i \boldsymbol{k} \cdot \boldsymbol{x}}\, \psi_m\, d\tau.$$

The connection with the spinless, non-relativistic expression is the same as above. Our non-relativistic treatment thus is equivalent to the non-relativistic approximation to the Dirac theory.

We turn now to the case of spontaneous emission. The probability that a photon $\boldsymbol{k}, \boldsymbol{e}$ will be emitted within the element of solid angle $d\,\Omega$ when the electron state changes from n to m is evidently[3]

$$d\,\Omega \frac{k\, \varepsilon^2}{h\, m^2 c^2} \,|\, A_{mn} \,|^2,$$

where

$$A_{mn} = \int \overset{*}{\varphi}_m \boldsymbol{e} \cdot (\boldsymbol{p} - i\, \boldsymbol{S} \times \boldsymbol{k})\, e^{-i \boldsymbol{k} \cdot \boldsymbol{x}}\, \varphi_n\, d\tau.$$

It is interesting to compare this result with BRINKMAN's[4], whose spin-magnetic dipole terms are immediately obtainable from A_{mn}.

So far we have treated only the case of a one-electron atom. The calculation is easily extended to include any number N of electrons, and the earlier conclusions remain valid if we now make the substitutions

$$\boldsymbol{p}_j\, e^{i \boldsymbol{k} \cdot \boldsymbol{x}_j} \rightarrow (\boldsymbol{p}_j + i\, \boldsymbol{S}_j \times \boldsymbol{k})\, e^{i \boldsymbol{k} \cdot \boldsymbol{x}_j} \qquad (j = 1, 2, \ldots N)$$

in the matrix elements of $\boldsymbol{p}_j$ in the spinless, non-relativistic theory. Here $\boldsymbol{p}_j$ is the momentum operator and $\boldsymbol{S}_j$ the spin angular momentum operator of the j^{th} particle. Thus we have a simple rule for introducing spin dependence into the non-relativistic dispersion formula of a many-electron problem.[5]

A report of this paper was given at the Conference of the Swedish National Committee for Physics in 1951 by the first-named author and is published in Arkiv för fysik.

---

[1] I. WALLER: Zs. f. Ph. 61 (1930) p. 837 eq. (13).

[2] The notations are slightly changed.

[3] φ_m denotes the eigenfunctions of H_0.

[4] *Loc. cit.* eq. (13).

[5] *Cf. e.g.* I. WALLER: Zs. f. Ph. 51 (1928) p. 213.

Tryckt den 9 december 1952

Uppsala 1952. Almqvist & Wiksells Boktryckeri AB

ARKIV FÖR FYSIK Band 6 nr 13

Communicated 8 October 1952 by Erik Hulthén and Axel E. Lindh

Precision measurements of the gamma-radiation from scandium^{46}

By Torsten Lindqvist

With 2 figures in the text

Introduction. The present investigation of the gamma-radiation from Sc^{46} was carried out with a two-directional focusing betaspectrometer, recently constructed at the Physics Laboratory in Uppsala. The spectrometer is of the type described by Hedgran, Siegbahn and Svartholm (1). The construction was made possible by financial support from the Swedish Atomic Committee. The mounting of the spectrometer and the arrangements for measurement of the field were entrusted to the author.

Adjustments. The magnetic field was measured against a calibrated reference field in a Helmholtz coil. The voltages from two pick-up coils, one in each field, were taken out by brushes and led to a detector. "Balance" was said to be obtained when the reference field was so adjusted that the detector indicated a minimum. Fig. 1 shows the sensibility of balancing. The minimum can be located with a precision of 1 in $5 \cdot 10^3$.

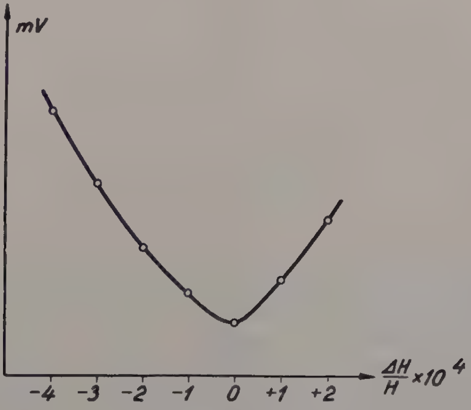

Fig. 1.

The positions of the source and the GM-counter were adjusted by means of the photographic method. (For all the adjustments ThB was used.) It was found that the image of the source was situated in a plane 16 mm below that of the source.[1] This means that the horizontal plane of symmetry for the geometrical arrangements does not coincide with that for the magnetic field. The effect is probably due to the iron feet supporting the magnet. When the source was lowered 8 mm the image fell in the same plane.

The resolving power $\frac{\Delta H}{H}$ for different solid angles Ω and different source widths d_p was investigated. In all cases the GM-slit was equal to d_p. For the result see Table 1.

Table 1

d_p mm	Ω %	Resolving power %	
		Theoretical	Experimental
2	0.5	0.35	0.50
2	1.1	1.00	0.80
4	0.5	0.45	0.60
4	1.1	1.10	1.20
8	0.5	0.65	0.95
8	1.1	1.30	1.35

The $H\varrho$-values of the conversion-lines (in gauss. cm) were determined from the equation (I).

$$H\varrho = \text{const.}\ (R - R_e) \qquad \text{(I)}$$

where R is the potentiometer reading corresponding to the current through the Helmholtz coil when the conversion-line is focused. R_e is for compensating the earth's field. For the calibration certain conversion-lines from Th active deposite were used (see Table 2).

Table 2

Conversion-line	Energy		Reference
	$H\varrho$	keV	
F	1388	148	G. LINDSTRÖM (2)
I	1754	222	»
L	2607	422	»
X	9988	2531	W. L. BROWN (3)

The constant in (I) was determined by several runs and the values differed no more than 3 parts in 10^3. The mean value for each conversion-line seemed to drop with increasing energy, probably due to a systematic error in the arrangements. In order to obtain the highest accuracy in the measurements it is therefore adviseble always to use a reference line of small energy difference.

In view of what has been said above, when using a reference line the accuracy at present in determining the energies of the conversion-lines is 1 in 10^3.

Measurements of Sc^{46}. The beta-disintegration of Sc^{46} is followed by the emission of two gamma-rays, here called γ_1 and γ_2. The half life of the isotope is 85 days.

---

[1] I am indebted to Dr. A. HEDGRAN for suggesting this investigation.

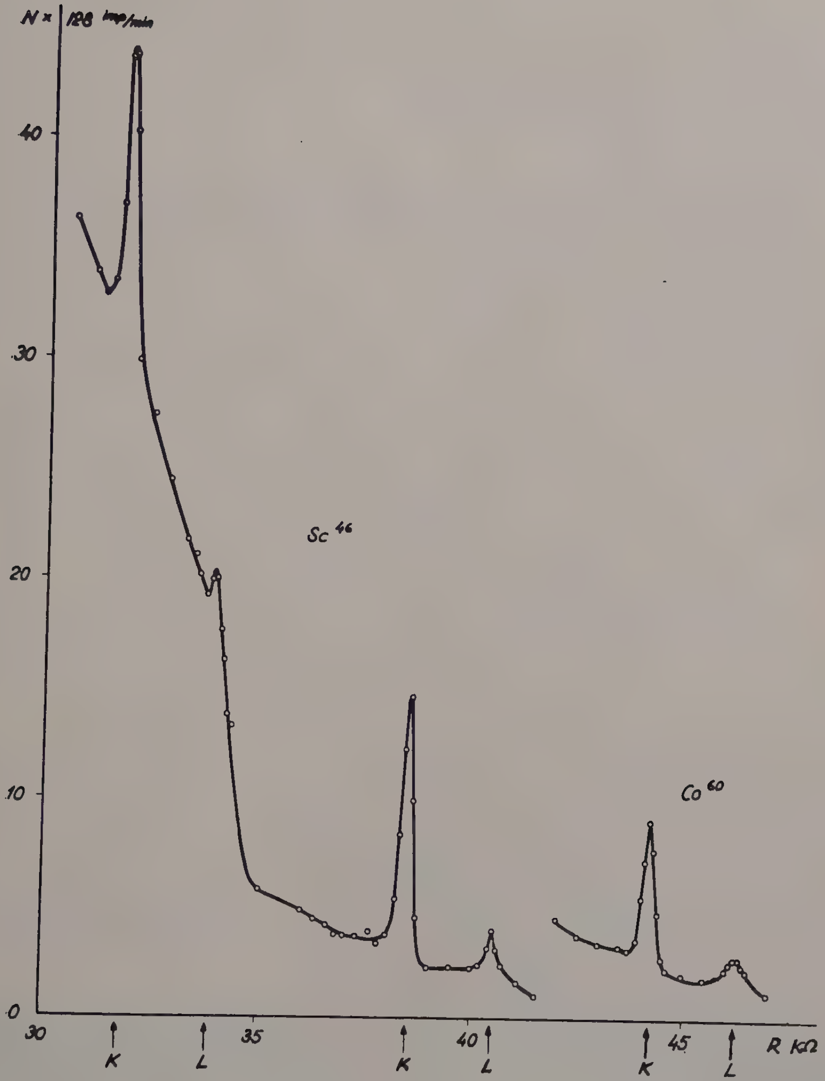

Fig. 2.

Table 3

Author	Year	γ_1MeV	γ_2MeV	Reference
1. H. Walke.	1939	—	1.25 ± 0.1	(4)
2. L. Meitner	1945	—	1.25	(5)
3. Miller, Deutsch.	1947	0.90 ± 0.02	1.12 ± 0.02	(6)
4. Peacock, Wilkinsson	1947	0.88 ± 0.02	1.12 ± 0.02	(7)

Table 3 shows the previous results of the measurements of these gamma-energies. The first two authors used the method of absorption and their results are therefore not of high accuracy. The other results were obtained by beta-spectroscopy methods and agree well with the results obtained here.

The isotope Sc^{46} was obtained from the Atomic Energy Establishments at Harwell. The target material was Sc_2O_3.

The gamma-rays were recorded with high resolution (5–$7 \cdot 10^{-3}$) by means of their external photo-lines. The radioactive material, Sc_2O_3, was contained in a brass capsule of 3 mm diameter in order to cut out all the beta-particles from the source. The converters were thin lead foils. The reference line used was the external photo-line from Co^{60} gamma-ray of energy 1.3316 MeV, measured with the crystal spectrometer by LIND, BROWN and DU MOND (8). Both K-photo-lines and L-photo-lines have been used as well. Fig. 2 shows the photo-lines from Sc^{46} and Co^{60}.

The following energies have been used for the absorption edges in lead (9).

$$K - \text{abs.} = 87.6 \text{ keV}$$
$$L - \text{abs.} = 15.8 \text{ keV}.$$

Table 4 shows the result.

Table 4

Run	Converter thickness mg/cm²	Resolution %	γ_1-energy MeV		γ_2-energy MeV	
			K-line	L-line	K-line	L-line
1	5.5	0.7	0.884	0.884	1.119	1.116
2	5.5	0.7	0.886	0.886	1.123	1.119
3	7.5	0.4	0.884	0.884	1.118	1.119
Mean value			0.8847		1.1190	

We thus obtain the values

$$\gamma_1 = 0.885 \pm 0.002 \text{ MeV}$$
$$\gamma_2 = 1.119 \pm 0.002 \text{ MeV}$$

for the energies of the scandium gamma-rays.

The result above, the first obtained by our spectrometer, is to be considered as a preliminary proof of the spectrometer working well.

Acknowledgements. The author wish to thank the manager of this laboratory professor AXEL E. LINDH and professor PER OHLIN for their great interest in the construction work. In particular I am indebted to professor KAI SIEGBAHN and to Dr. ARNE HEDGRAN of the Nobel Institute for Physics for giving me a great deal of advice. I also wish to thank Mr. JOHN AMBERNTSSON in the laboratory workshop for his skilful work, which made the trimming fairly easy.

Physics Laboratory, University of Uppsala, September 1952.

REFERENCES

1. Proc. Phys. Soc. *63*, 960 (1950). — 2. Phys. Rev. *83*, 465 (1951). — 3. Phys. Rev. *83*, 271 (1951). — 4. Phys. Rev. *57*, 163 (1940). — 5. Ark. f. Mat., Astr. o. Fys. Bd 32 A, no. 6 (1945). — 6. Phys. Rev. *72*, 527 (1947). — 7. Phys. Rev. *72*, 251 (1947). — 8. Phys. Rev. *76*, 1838 (1949). — 9. M. SIEGBAHN, Spektroskopie der Röntgenstrahlen.

Tryckt den 9 december 1952

Uppsala 1952. Almqvist & Wiksells Boktryckeri AB

ARKIV FÖR FYSIK Band 6 nr 14

Read 5 February 1952

Ions formed in a room by negative wire corona

By Harald Norinder and Reinhards Siksna

With 13 figures in the text

Within the scope of the investigation of ions produced by different ionizers in the air of a closed room, recently carried out at this Institute [7], [8], ions formed by corona discharge have been included. Results of the *measurements of the ions formed by a negative wire corona* will be given here.

1. Experimental arrangement

The arrangement of the used experimental devices is shown in Fig. 1.

1.1. The room in which the ions were produced

The room, T, in which the ions were produced, was the one used earlier for investigation of ions from other producers [7], [8]. It is a room in a wagon used at the movable field stations for other purposes. The dimensions of the floor of the room are shown in Fig. 1 in cm. The volume of the room was 16.5 m³. The wooden walls and the ceiling of the room were covered inside with rather thick pasteboard and the floor with linoleum. All splits, also at the doors and the windows, were stopped up by strips of pasted paper.

1.2. The corona wire

A stage was built by fastening three heavy brass wires of 5 mm diameter on the circumference of a 16 cm circle on two circular bakelite plates. Through the centres of the circles two small porcelain bushings were arranged. Between the ends of the metal rods of the bushings a 0.25 mm thick kanthal wire was held. This wire was connected with the used high tension source and so the corona wire was built. The length of the corona wire was c. 2 m. The heavy brass wires of the stage were earthed. The stage with the corona wire was put up in the test-room by the aid of three bands at each end in a mode shown in Fig. 1 at a distance of 1.15 m from the floor.

1.3. The high tension equipment

A high tension equipment for the corona was set up in the small side-room of the wagon. This equipment consisted of an ordinary rectifier R as shown in the figure.

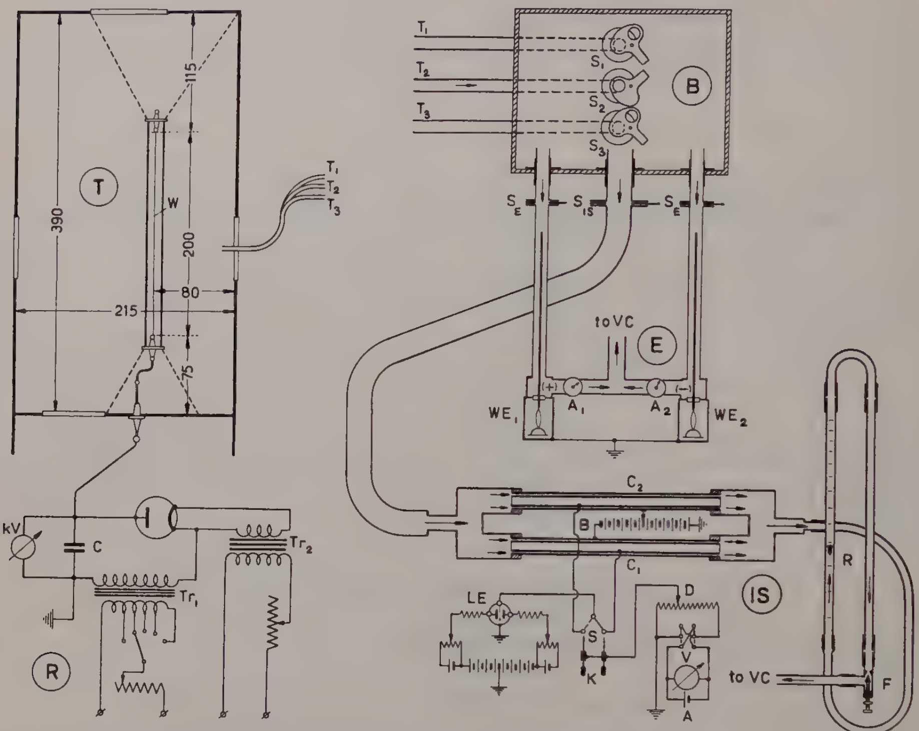

Fig. 1. Schematic diagram of the used experimental arrangement.
(T) test-room, W corona wire; (R) rectifier, Tr_1 high tension transformer, Tr_2 heating transformer, kV Starke-Schröder high tension voltmeter; (B) suction box, T_1, T_2, T_3 suction tubes from the test-room, S_1, S_2, S_3 slides of the suction tubes, S_E slides to Ebert ion-counters, S_{IS} slide to the Israël large-ion counter; (E) Ebert ion-counters, WE Wulf bifilar electrometers, A anemometers; (IS) Israël large-ion counter, C_1, C_2 cylindrical condensers, LE Lindemann electrometer, S switch of the condensers, D calibration device of the electrometer, K keys to the calibration device, R rotameter, F valve to adjust the air-flow.

The capacity of the condenser of the rectifier $C = 0.22$ μF. A Starke-Schröder high-tension voltmeter was used to measure the high tension applied to the corona wire. One terminal of the condenser was connected with the corona wire through a bushing in the wall to the test-room, the other was earthed. Control of the high tension was carried out by switching on the high tension transformer in steps on the net-side and varying the heating current of the rectifier tube by variation of a resistance in the primary circuit of the heating transformer. The highest potential applied to the corona wire was c. 15 kV.

1.4. Removal for test of the ionized air of the room

The test of the ionic state of the air from the surroundings of the corona wire was realised by suction of the air into the ion-counters. For this purpose three brass tubes of 30 mm diameter were installed in one of the side-walls of the test-room. The ion-counters were placed in an observation hut beside the wagon of the test-room, and the three openings in the side-wall of the wagon were connected through c. 0.6 m long flexible metal tubes, T_1, T_2 and T_3 of 33 mm diameter, with a suction box, B, installed in the observation hut. These connection tubes from the test-room had been made tight by wrapping with an isolation tape. By this arrangement it was possible to suck the air from the room in the wagon to the suction box and into the ion-counters in the observation hut. Mostly only one of the connection tubes was used.

1.5. The suction box

As mentioned, the suction of the air into the ion-counters followed through the suction box B. This box was connected through three side-slides, S_1, S_2 and S_3 of a construction shown in the figure, with the tubes, T_1, T_2 and T_3, to the test-room. The dimensions of the box were $48 \times 44 \times 32.5$ cm. The slides S_E and S_{IS} were installed on the bottom of the box, which was connected with the ion-counters.

1.6. The ion-counters

We used two Ebert ion-counters, E, one charged for positive ions, the other for negative ions, and an Israël large-ion counter, Is.

1.6.1. The Ebert ion-counter

As known the Ebert ion-counter consists of a cylindrical condenser with the inner electrode connected with a Wulf bifilar electrometer WE and charged to a potential of c. 200–300 volts. Ions of sign opposite to that of the charge on the inner electrode are collected by that electrode *discharging* the electrometer. The number of ions, or rather the number of elementary charges in cm³ of the air aspirated through the counter is calculated from the formula

$$n = \frac{C\,\delta V}{300\, e\Phi t}$$

where C is the measured capacitance of the apparatus, δV the voltage drop, $e = 4.80 \times 10^{-10}$ ESU the elementary charge, Φ the air-flow through the apparatus in sec^{-1} and t the duration of an observation. In the Ebert counter the air-flow Φt during an observation is measured by the anemometer A. The suction of the air is made by a vacuum cleaner.

1.6.2. The Israël large-ion counter

In the Israël large-ion counter [1] the "charging" method is applied, i.e. the air is drawn through two cylindrical type condensers, the outer cylinders of which are maintained at a constant potential while at the beginning of an observation the inner cylinders are near earth's potential. Ions which are well within these condensers and of the same sign as the potential of the outer cylinders are driven towards the inner cylinders. All ions of a mobility greater than a certain value and a fraction of the ions of lower mobilities reach these cylinders and impart a charge to them. This charge is measured with a Lindemann electrometer. A schematic diagram of the Israël large-ion counter with the used accessories is given in Fig. 1. C_1 and C_2

are the two cylindrical condensers; the outer cylinders are connected with one terminal of the battery B, whose other terminal is grounded; with the aid of a switch S the inner cylinders may alternately be connected with the needle of the LINDEMANN electrometer LE; the calibrating device of the electrometer is shown by D, with keys, K, it is possible to connect one terminal or the other of the switch S with the calibrating circuit and by this with the needle of the electrometer.

For the purpose of suction the condensers may be connected in series or in parallel. The series-connection is used by ISRAËL to determine the spectral distribution of the ions with respect to the mobilities. Using the parallel connection, as shown in the figure, one condenser can be charged to count positive ions, the other to count negative ions. Using the parallel connection with charge of the same sign on both condensers, but of different values of the applied potential, one may count ions with different limit mobilities. The air-stream through the condensers is measured with a rotameter R, a graduated glass tube in which a small ebonite or aluminium body can rotate; this rotor remains in a state of equilibrium at a certain height in the glass tube under given flow conditions. The velocity of the air-stream or the air-flow can be adjusted with the aid of the valve F. The suction of the air is made by a vacuum cleaner. VC shows the tube of the latter.

One of the advantages of the ISRAËL counter is the convenient manner to determine the drawn air-stream by using the rotameter. A necessary condition to catch the large ions in the apparatus is a high voltage applied to the outer cylinder of the condenser, or using a slow air-flow. The voltage is limited by the dielectric disturbances which arise when the voltage is too high. By using a slow air-flow difficulties as to measure it arise. With the used rotameter it was possible to measure an air-flow down to 0.03 l/sec. Another advantage of the rotameter is the possibility to measure the momentary values of the air-flow, while with an anemometer, for instance, we can only determine the value of the air volume drawn through the apparatus during a certain time interval, for which determination it is necessary to read off the scale twice.

2. Arrangement of the measurements

2.1. With Ebert ion-counters

It is evident that using EBERT counters one can expect to obtain only a general insight into the ionic conditions because of the variation of the limit mobility of these apparatuses, especially if the distribution of the ions with respect to the mobilities is one with mobilities below that of small ions. For example, during our measurements of ions formed by ultra-violet light [7] and produced by the electric heater [8], the following property of the number of ions counted with EBERT counters was inferred: the number of counted ions was dependent on the potential applied at the inner electrode of the counter — an indication that the apparatuses counted also larger ions (intermediate) present in a greater amount. In the present case the conditions were of another feature. The dependence of the number of counted ions on the potential was not so marked, thus it might be concluded that the present counted ions were mostly real small ions and therefore the number of ions counted with the EBERT counter could in this case be regarded as more representative of the small ions than during earlier measurements. The measurements with the ISRAËL counter confirmed also the presence of a greater amount of small ions in this case. To avoid disturbances which might be caused by the variation of the applied potential the measurements with the EBERT counter were carried out with the same potential at the beginning of each measuring period. The average limit mobility of the used EBERT counters was c. 0.05 cm sec^{-1} : Volt cm^{-1}.

There were no chances to determine the composition of the ions with respect to the mobilities using EBERT counters.

2.2. The method of a periodical alternation of chosen adjusted limit mobilities by using the Israël large-ion counter

In order to obtain an insight into the distribution of the present ions with respect to the mobilities the measurements with the ISRAËL counter were carried out at different adjusted limit mobilities k_* of the condensers. The variation of the limit mobility is generally meant to be carried out by variation of the potential applied to the outer cylinder of the condenser. It is obvious that such a variation of the potential is not possible to apply to the ISRAËL counter, when the sensitive LINDEMANN electrometer is used, because of the dielectrical disturbances, which arise when the applied potential is changed. But the ISRAËL counter possesses another possibility to vary the limit mobility, viz. by means of the variation of the air-flow through the measuring condensers; adjustment of the air-flow and the reading off of the momentary value of the air-flow is also possible to carry out very speedily. Series of measurements with the ISRAËL counter were carried out alternately changing chosen adjusted limit mobilities of the counter by variation of the air-flow through the condensers. In such a way the trends of the number of ions caught at several adjusted limit mobilities k_* were obtained. Both condensers of the large-ion counter were connected in parallel for the air-flow. Except the first series of measurements, where ions of both polarities were measured, only negative ions were measured in all the others. In some cases only 4 adjusted limit mobilities were chosen using a constantly applied potential of c. 130 V at one of the condensers, in some cases 8 adjusted limit mobilities were chosen using also the other condenser with an applied potential of c. 9.3 V. The used limit mobilities k_* are denoted in Fig. 2 and 3.

3. Phenomena observed

3.1. Corona wire switched on suddenly to a comparatively high voltage

The highest voltage used was c. 15 kV. If such a negative potential was switched on suddenly to the corona wire the following phenomena were observed (Fig. 2 and 3):

(1) A sudden increase of the number of negative ions measured with the EBERT counter up to comparatively high values. Some variations also occur.

(2) The number of ions measured with the large-ion counter also increases but not so much. Some variations occur also here.

(3) Only one enormous increase of negative ions was established with the EBERT counter and the large-ion counter.

After switching off the potential and discharging the condenser of the rectifier:

(1) The number of negative small ions measured with the EBERT counter decreases almost suddenly.

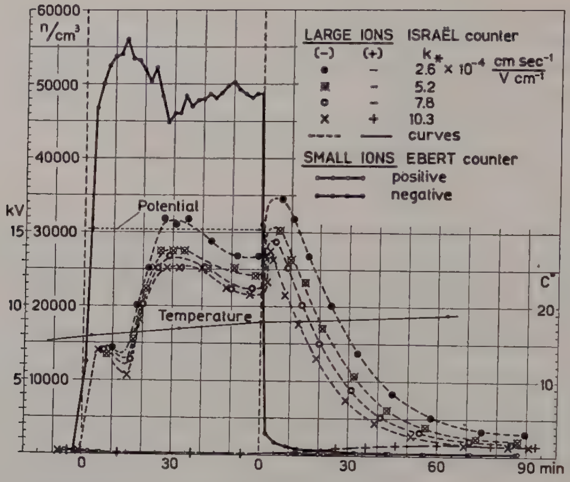

Fig. 2. Number of ions measured with EBERT ion-counters and the ISRAËL large-ion counter adjusted at different limit mobilities k_*. The present ions were formed by corona discharge in a room when a sufficiently high potential was switched on to a thin wire.

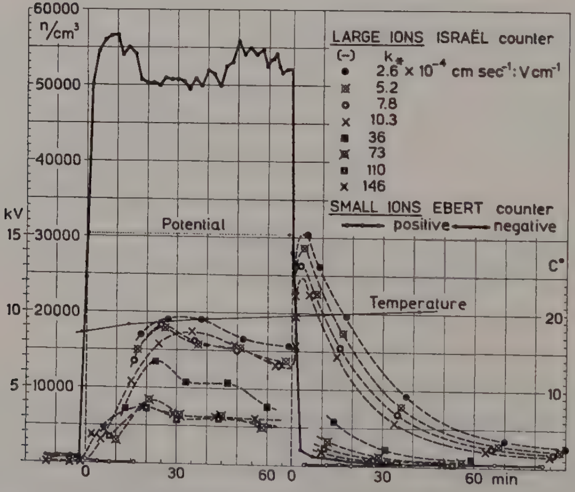

Fig. 3. Number of ions measured with the EBERT ion-counter and the ISRAËL large-ion counter adjusted at 8 different limit mobilities k_*. Corona wire switched on suddenly to a comparatively high negative voltage.

(2) The number of negative large ions, on the contrary, increases already from the beginning in order to decrease gradually after that.

(3) The number of positive small and large ions increases gradually after the switching off of the potential and reaches after a time the level of the decreased number of negative ions.

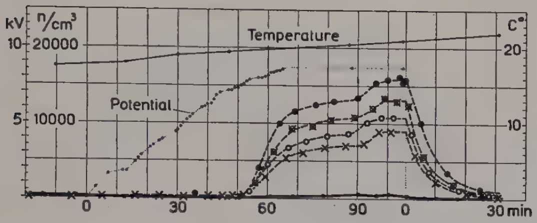

Fig. 4. Number of ions measured when corona wire was switched on at gradually increased negative voltage which was not sufficient for production of small ions.

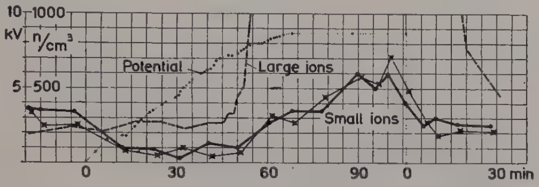

Fig. 5. Variation of the number of ions measured with two EBERT ion-counters (both charged for negative ions) when the applied negative potential was not sufficient for producing of small ions. Data shown in Fig. 4 in a larger vertical scale.

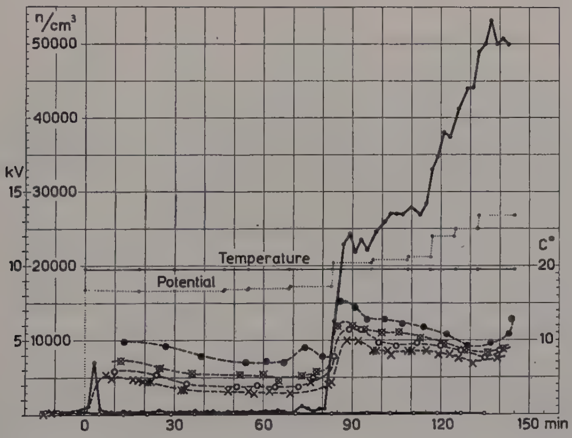

Fig. 6. Number of ions measured when corona wire was switched on at different negative voltages.

3.2. Corona wire at gradually increased high voltage

In order to clarify the dependence of the concentration of ions on the potential applied to the corona wire, the voltage was increased gradually. The following phenomena were observed, if the applied tension increased comparatively slowly:

(1) Only the number of large ions increases at the beginning starting at a tension of c. 8 kV (Fig. 4). (Attention must be paid to the comparatively equal distances between the curves of different adjusted limit mobilities).

(2) Simultaneously, the number of small ions decreases starting from the point of

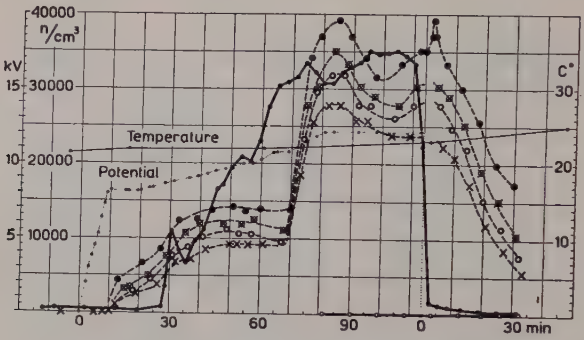

Fig. 7. Number of ions measured at comparatively slow increase of the applied negative potential.

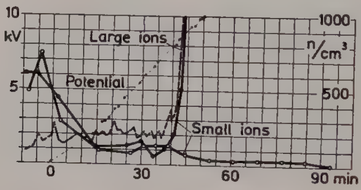

Fig. 8. Variation of the number of positive and negative ions measured with EBERT ion-counters at the beginning of the series of measurements shown in Fig. 9.

time at which the potential is applied, in order to increase somewhat, when it reaches the potential at which the rapid increase of the number of large ions began. This event is also shown in Fig. 5 using a larger vertical scale. This decrease at the beginning is observed in all cases, and it might be explained by a transport of the small ions, normally present in the test-room by the electric field, to the earthed cage of the corona device.

(3) After switching off the potential the number of large ions decreases starting from the levels reached by the used potential without any temporary increase as in the first case considered in 3.1.

(4) A similar trend may be seen also in Fig. 6, where it is also shown that by increasing the potential still more a rapid increase of the number of small ions follows. The same feature is shown in Fig. 7 and in a smaller scale in Fig. 10.

(5) The eruption of the number of small ions near the starting point must be marked in Fig. 6. A similar event may be established also in Fig. 7 and 11. Reduction of the steepness of the curves of the number of small ions after the rapidly starting increase (Fig. 9, 10, 11) may be a revelation of the same event.

3.3. Corona wire at potentials with different increases

Series of measurements at increased potentials with different steepnesses are shown in Fig. 7, 9, 10, 11. The following conclusions may be drawn from these curves:

(1) Generally the curves of the number of ions are of the same feature, only with different rapidity of the variations and of different heights of the reached values.

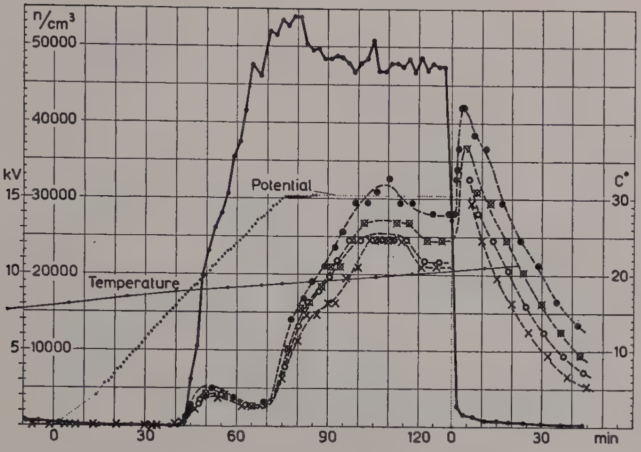

Fig. 9. Number of ions measured at a gradual increase of the applied negative potential.

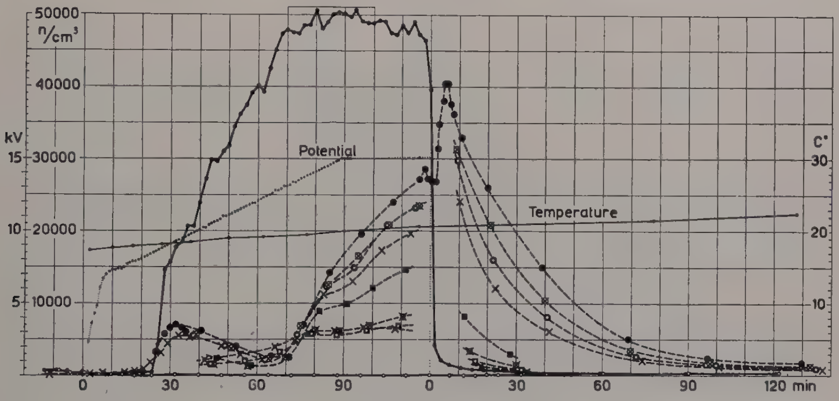

Fig. 10. Number of ions measured at a gradual increase of the applied negative potential.

(2) The number of large ions decreases after reaching the first lower maximum in order to increase rapidly to a higher second maximum, after reaching it a low decrease follows in some cases.

(3) It seems, that a lower number of large ions corresponds to a higher number of small ions. The reason of this correlation is not clarified. May it be so that a lower number of small ions corresponds to higher temperature (lower density of air)?

(4) Increase of the large ions after switching off the potential is higher if the number of small ions present is higher and the number of present large ions lower.

3.4. Curves of the number of ions caught at different adjusted limit mobilities k_*

The shapes of the curves obtained at different adjusted limit mobilities k_* are different, but it is significant that apart from the different heights of the corre-

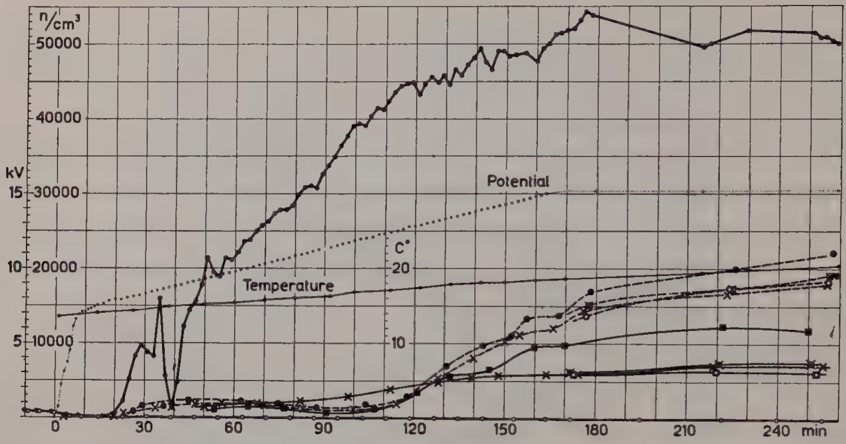

Fig. 11. Number of ions measured at a gradual increase of the applied negative potential.

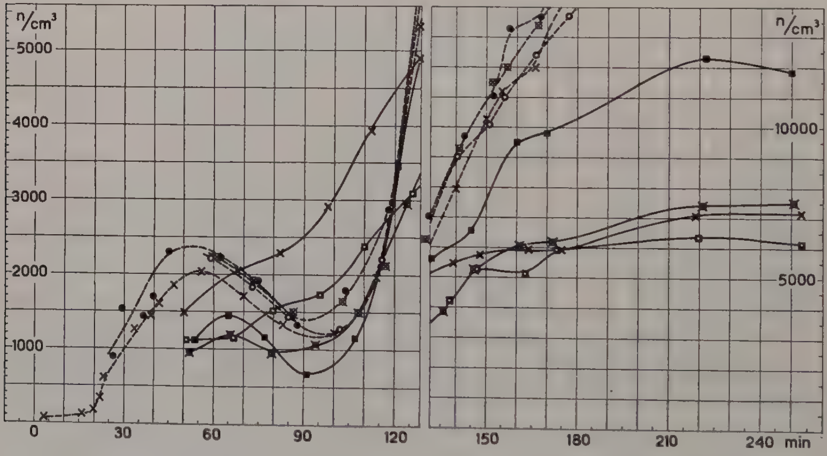

Fig. 12. Number of ions shown in Fig. 11 in a larger vertical scale.

sponding levels the general shape of curves corresponding to a definite k_* remains the same during all the series of measurements. It must be pointed out here that the properties of the curves which will be given in the following, may be established more or less markedly in all the obtained series of measurements. Therefore these properties must be regarded as typical under given experimental conditions. May be that it is of advantage to use the curves obtained with a slower increase of the potential, if we want to follow the feature of the mentioned properties of the curves.

By measuring the number of ions caught at different adjusted k_* the intention was to attempt a calculation of the distribution of the present ions with respect to the mobilities. The results of this attempt will be given in another place, but we will consider here the corresponding things without ready characteristics which are necessary for calculation of the ionic mobility spectra. But it was established that

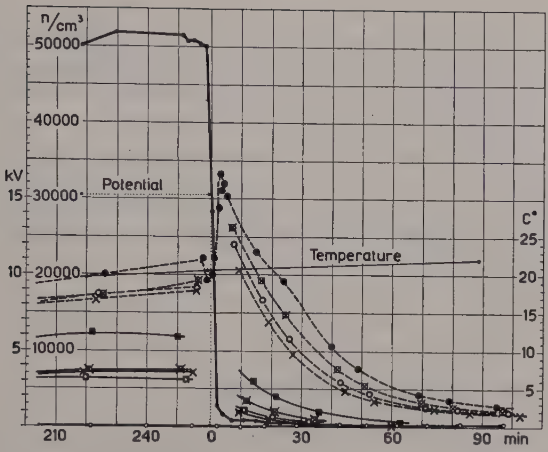

Fig. 13. Number of ions after switching off corona potential. Continuation of the curves shown in Fig. 11 and 12.

the curves of the number of ions caught at different adjusted k_* are of such an unexpected characteristic shape that from those alone it is possible to obtain certain information about the distribution of the ions with respect to the mobilities.

The characteristic properties of the curves at different k_* are as follows:

(1) At the beginning when the presence of the small ions is not yet revealed the curves of different k_* are arranged in comparatively equal distances from one another so that the curves of a lower k_* are situated at a higher level than those of a higher k_* (Fig. 4, 6, 7). This fact indicates that ions with lower mobilities are predominant. In this case there are Langevin- and ultra-large ions.

(2) During a stage of the processes the curves of the highest adjusted $k_* = 146 \times 10^{-4}$ exceed all the other curves in order to return below the curves with lower k_* (Fig. 10, 11). This event is also shown in a larger scale in Fig. 12. The same thing less marked is also shown in Fig. 3. Prevalence of ions with higher mobility is indicated here.

(3) The curves of the four highest adjusted $k_* = 146, 110, 73, 36 \times 10^{-4}$ are of a different behaviour in dependence on the value of k_*. The curves with the lowest of these mobilities $k_* = 36 \times 10^{-4}$ have a shape similar to that of the curves with the four lowest adjusted mobilities $k_* = 10.3, 7.8, 5.2, 2.6 \times 10^{-4}$ (Fig. 10, 11, 12). On the other hand, the shapes of the curves with the three highest $k_* = 146, 110, 73 \times 10^{-4}$ are of the same feature and in some cases the curves crowd together. This crowdedness corresponds to a state of saturation of the ion-number — reciprocal mobility characteristics.

(4) A similar phenomenon of curves with the lower adjusted $k_* = 10.3, 7.8, 5.2, 2.6 \times 10^{-4}$ may be stated. During some stages of the processes all the lowest levels $k_* = 7.8, 5.3, 2.6 \times 10^{-4}$ have crowded together. (Fig. 11, 12, during the time interval between 60 and 90 minutes, when the first decrease of the large ions is present, and during the time interval between 120 and 140 minutes, when the second rapid increase of the large ions is present). A saturation state must be concluded here, and the absence of ions with mobilities lower than a certain value may be expected in this case. During other stages of the processes the curves of the second and the

third $k_* = 7.8$, 5.3×10^{-4} crowd together (Fig. 10), in some cases the last curve of $k_* = 10.3 \times 10^{-4}$ joins these (Fig. 11 during the last period before the switching off).

(5) The order of the curves changes completely after switching off the potential. Instantly after the switching off the curves arrange themselves below one another in the sequence of the adjusted limit mobilities k_* with the lowest k_* at the highest level and the highest k_* at the lowest level. Attention must be paid to the curvature of the curve of the lowest $k_* = 2.6 \times 10^{-4}$ at the beginning of the decrease. The mentioned order of the curves indicates that a transformation of the ions present at the moment of the switching off of the potential occurs during this stage of the processes in a way by which ions with higher mobilities will be transformed into ions with lower mobilities.

4. Discussion

It must be pointed out once again that all the events mentioned in the previous paragraph may be stated more or less markedly in all the presented curves. Therefore it may be assumed that if a variation of the feature of a curve or the sequence of the curves above one another occurs, a process of production or transformation of ions obtains the leading rôle.

According to this assumption it may be concluded that:

(1) Because of the prevalence of the small ions (measured with the EBERT counter) it must be assumed that these are dominant and primary.

(2) But at the beginning of the formation of ions by negative corona a process by which large ions will be produced, must also be present (Fig. 4, 6). This process acts also during the further development of the phenomenon besides the small-ion process, and if the small ions break down under certain conditions of the dominant rôle (for example the first eruption of the small ions before the rapid increase) they will be brought down by the large-ion process. Only later, when the small-ion process has much increased, the large-ion process is put back to a secondary rôle.

(3) A separate process must be accepted for the second increase of the large ions.

(4) A new process occurs after switching off the potential. Increase of the number of large ions and arrangement of the curves in sequence of the mobilities k_* must be caused by this process.

(5) Variations of the spectral composition with respect to the mobilities might also be regarded as an indication of the presence of some processes.

From the obtained curves of the variation of the number of ions it could be concluded that the phenomena in the space around a corona wire must be characterized as such, the state of which is not determined only by the conditions present at this moment (for example, by the potential applied to the corona wire, this potential is one of the important factors, which determine these conditions), but also by the way in which the present state is reached, for example, how rapidly the increase of the potential followed, how long the constant state lasted etc. In other words, the present ionic state around the corona wire at a definite applied potential is without doubt dependent on this potential, but it is as much dependent on the prehistory of the corona discharge.

We have no evidences now to explain the mentioned processes indicated by the measuring curves.

As the cause of the large-ion processes ultra-violet light or chemical reactions produced by the corona discharge might be mentioned. By these processes condensation nuclei may be produced, and by electric charging of the nuclei large ions could be formed. But the possibility, pointed out by NOLAN and O'KEEFFE [4], [5], [6] that ions produced by corona discharge from a water drop may have charges of the order of one hundred electrons, must also be considered. This possibility could be clarified by simultaneous measurements of the trend of the concentration of nuclei besides the ionic measurements.

We will not compare here our results with those of other authors [2], [3], [4], [5], [6], who have investigated the ions produced by corona discharge, because the prevailing conditions were different, but we will return to this question later.

In the end it may be noted here that the test sample of the air was taken from a volume of the air around the corona wire definite by the location of the inlet of the suction tube in relation to the corona wire. By using additional tubes to the inlet of the suction tubes it is possible to suck the air samples from any part of the test-room. By preliminary measurements with such additional tubes arranged in the test-room at different heights and at different distances from the corona wire it is shown that the concentration of definite ions is not equal at different points in the test-room, but the general behaviour of the curves obtained at a definite adjusted limit mobility is of the same feature as shown in this article. Therefore the events considered here must be regarded as representative of all the processes around a corona wire, although the concentration of ions in a definite region of mobilities may be different in dependence on the distance from the corona wire.

Acknowledgements

The Swedish Natural Science Research Council deserves to receive thanks for placing means at the disposal of the Institute to perform this investigation. Mr. A. METNIEKS who assisted in the measurements and calculations deserves appreciation.

SUMMARY

Ions formed in a room by negative wire corona were measured with EBERT ion-counters and with an ISRAËL large-ion counter adjusted at chosen limit mobilities. Only negative ions were established in a prevailing quantity during corona discharge. Characteristic shapes of the curves of the concentration of ions measured at the chosen adjusted limit mobilities may be inferred during corona discharge and after switching off the corona potential. These characteristic properties of the mentioned curves were more pronounced when the corona voltage increased gradually. Certain processes of the formation and transformation of ions might be imagined to be the cause when a definite shape of the curves occurs or when there is shown a definite relation between the order of the curves in dependence on the adjusted limit mobilities.

Institutet för högspänningsforskning vid Uppsala Universitet, October 1951.

REFERENCES. [1] **Israël, H.**: Ein transportables Messgerät für schwere Ionen. *Z. Geophys., 5,* 342–350, 1929. — [2] —— und **Schulz, L.**: Das Ionengerät der AEG. *Der Balneologe, 1,* 503–506, 1934. — [3] **Koller, L. R.**: Ionization of the atmosphere and its biological effects. *J. Franklin Inst., 214,* 543–568, 1932. — [4] **Nolan, J. J.** and **O'Keeffe, J. G.**: The ions produced by discharge at liquid surfaces. *Proc. Roy. Irish Acad.* (A) *39,* 21–30, 1929. — [5] ——: Electric discharge from water drops. *Proc. Roy. Irish Acad.* (A) *40,* 86–98, 1932. — [6] ——: Multiply charged large ions. *Proc. Roy. Irish Acad.* (A) *41,* 26–40, 1933. — [7] **Norinder, H.** and **Siksna, R.**: Ions produced in the air at atmospheric pressure by ultra violet light from a quartz-mercury arc. *Ark. Fys., 5,* 23, 471–491, 1952. — [8] **Siksna, R.**: Positive ions formed by an open electric heater. *Ark. Fys., 5,* 25, 531–543, 1952.

Tryckt den 22 december 1952

Uppsala 1952. Almqvist & Wiksells Boktryckeri AB

ARKIV FÖR FYSIK Band 6 nr 15

Communicated 8 October 1952 by ERIK HULTHÉN

A band-system of radium chloride

By ALBIN LAGERQVIST

No band-spectrum allotted to a molecule including Ra has hitherto been known. In 1933 E. RASMUSSEN (1933, 1934) investigated the atomic spectrum of radium. He used a hollow cathode containing some mg radium chloride in a helium atmosphere. Some time ago RASMUSSEN told me that on his radium plates from 1933 he remembered some band-heads. He allowed me to borrow his plates for a band-spectroscopic examination.

The spectrograms were taken with a 4 m Rowland grating in a Paschen mounting. The band-spectrum consists of two very intense red-shaded sequences, one at 6 763 Å, the other at 6 498 Å. Just in front of the stongest sequence — that at 6 498 Å — some rather faint bands are visible beginning at 6 489 Å. Besides the two strong sequences there is another very weak one beginning at 6 607 Å. The structure of the 6 498 sequence shows clearly that we have a $\Pi-\Sigma$ transition, with the R-heads beginning at 6 489 and the Q-heads at 6 498 Å. The most likely interpretation is that the three sequences belong to a $^2\Pi-^2\Sigma$ transition, with the sequences 6 498 and 6 763 Å as the $\Delta v=0$ transition from the two sub-levels in $^2\Pi$ to the normal state $^2\Sigma$. The bands beginning at 6 607 then form the $\Delta v=-1$ sequence from the upper $^2\Pi$ sub-level. The system shows a very narrow Condon parabola. Owing to strong helium lines and other disturbances it is impossible to detect the other sequences. The band-heads are given in Table 1. The vibrational analysis gives the following two head-equations for the $^2\Pi-^2\Sigma$ transition.

$$\nu_{v',\,v''}=15\,386.5+252.9\,(v'+\tfrac{1}{2})-0.72\,(v'+\tfrac{1}{2})^2-256.2\,(v''+\tfrac{1}{2})+0.71\,(v''+\tfrac{1}{2})^2$$

$$\nu_{v',\,v''}=14\,782.1+253.8\,(v'+\tfrac{1}{2})-0.71\,(v'+\tfrac{1}{2})^2-256.2\,(v''+\tfrac{1}{2})+0.71\,(v''+\tfrac{1}{2})^2.$$

The different alkaline earth halides have very similar molecular term-schemes. The ground state X is a $^2\Sigma$, the first excited state A is a $^2\Pi$, the next B is a $^2\Sigma$ and the following C a $^2\Pi$. The system of RaCl corresponds to the transition CX. The vibrational constants, the $^2\Pi$-splittings and the force constants of the chlorides are given in Table 2. The successive alteration of the magnitudes of the constants is striking. An approximate value of the dissociation energy for the ground state in RaCl can be obtained from the equation $D=\omega^2/4\,\omega\,x$. One obtains $D=2.9$ e.v.

Table 1

Q and R heads of the system $C\,^2\Pi$–$X\,^2\Sigma$ of RaCl

v', v''	Q_1 in Å	in cm^{-1}	Q_2 in Å	in cm^{-1}	R_2 in Å	in cm^{-1}	v', v''	Q_2 in Å	in cm^{-1}
0,0	6 763.3	14 781.0	6 498.1	15 384.9	6 489.2	15 406.0	0,1	6 607.6	15 129.9
1,1	64.7	78.6	99.6	81.3	90.6	02.6	1,2	08.4	28.1
2,2	65.8	76.1	500.9	78.2	92.1	399.1	2,3	09.2	26.3
3,3	66.9	73.7	02.4	74.7			3,4	10.1	24.2
4,4	68.0	71.3	03.8	71.4			4,5	11.0	22.1
5,5	69.0	69.2	05.2	68.1			5,6	11.8	20.3
6,6	70.2	66.5	06.6	64.8			6,7	12.7	18.5
7,7	71.3	64.1	08.1	61.2			7,8	13.5	16.4
8,8	72.5	61.5	09.7	57.5			8,9	14.4	14.4
9,9	73.6	59.1	11.2	53.9					
10,10	74.7	56.7	12.7	50.4					
11,11	75.8	54.3	14.3	46.6					
12,12	77.1	51.5	15.7	43.3					
13,13	78.1	49.3	17.3	39.5					
14,14	79.2	46.9	18.8	36.0					
15,15			20.3	32.5					

Table 2

Constants for the $C\,^2\Pi$ and $X\,^2\Sigma$ states of the alkaline-earth chlorides

Molecule	T_e	$^2\Pi$ splitting	ω''	$\omega'' x''$	ω'	$\omega' x'$	$k_{2\Sigma}$ in dyne/cm
BeCl			846.58	5.11			$3.02 \cdot 10^5$
MgCl			465.4	2.05			1.82 ·
CaCl	26 574.7 26 498.9	75.8	369.8	1.31	336.0	1.4	1.54
SrCl	25 401.7 25 245.5	156.2	302.3	0.95	279.9	0.68	1.35
BaCl	19 450.1 19 062.9	387.2	279.3	0.89	285.0 280.2	0.79 0.79	1.28
RaCl	15 386.5 14 782.1	604.4	256.2	0.71	252.9 253.8	0.72 0.71	1.17

I must record my thanks to Professor Rasmussen for his generosity in putting his plates at my disposal.

September, 1952. Physics Department, The University, Stockholm.

REFERENCES

Rasmussen, E., 1933, Zeits. für Physik, *86*, 24.
——, 1934, Zeits. für Physik, *87*, 607.

Tryckt den 22 december 1952
Uppsala 1952. Almqvist & Wiksells Boktryckeri AB

ARKIV FÖR FYSIK Band 6 nr 16

Read 10 September 1952

Measurements on the evolution of heat during the recovery of cold-worked metals

By G. Borelius, Stig Berglund and Sven Sjöberg

With 4 figures in the text

The recovery of metals after cold-working as a function of time and temperature has been studied by many investigators, by following the variations of the mechanical, resistometric, or magnetic properties. As it should be expected that the evolution of heat during the recovery should be particularly simply related to the atomic rearrangement, we have tried to measure this small evolution of heat by methods of isothermal calorimetry developed in our laboratory and used so far for the study of precipitation and order-disorder phenomena.

A preliminary report on such calorimetric measurements on aluminium and copper recovering at 60 to 130° C was given at the Solvay Conference 1951 (1). These preliminary measurements had shown that the evolution of heat was of a measurable magnitude and on the whole decreased with time in a hyperbolic way. A certain deviation of the curves first obtained from the simple hyperbolic form has later been studied thoroughly and traced to an unexpected source of error, so that the present results are simpler than the earlier ones. Our new measurements are so far confined to the recovery of Al, Cu and Zn at 100° C.

The experimental arrangements have been very much the same as those described in recent papers on the precipitation of nitrogen (2) and carbon (3) from α-iron. The specimen was placed in a vertical glass tube of 18 mm inner diameter. The glass tube was mounted in the centre of a copper tube of 50 mm diameter, forming the inner wall of a double-walled vapour thermostat kept at an extremely constant temperature. Between the glass tube and the wall of the thermostat was a series of thermocouples, which were connected over a commutator to a galvanometer, the deflection of which under ideal conditions is proportional to the heat evolved in the specimen per unit of time.

The specimens were made from moulded (Al, Zn) or turned and annealed (Cu) rods of the pure metals with an initial diameter of about 8 mm. They were cold-worked at room temperature by rolling to double length, and cut into pieces of 40 mm length. These pieces were put into a container of copper, shown in fig. 1, fitting into the glass tube of the measuring apparatus. A copper-constantan thermocouple was introduced into a copper tube at the centre of the container for the production of Peltier heat for calibration purposes.

As the rate of recovery increases very rapidly with increasing temperature, and, at constant temperature, decreases rapidly with time, it is necessary in order to

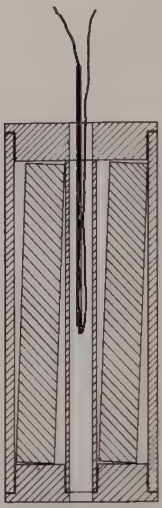

Fig. 1. Specimens and copper container.

measure as much as possible of the heat evolved, to start the measurements quickly. The specimen was heated up to the measuring temperature, in this case 100° C, in an oven, the temperature of which was appreciably above 100°, and the rise of the temperature was followed by means of the thermocouple attached to the specimen. The moment the temperature reached 100° C the specimen was transferred to the thermostat. Here it was first held for some time in the upper part of the glass tube, where the space between the glass tube and the wall of the thermostat was filled by a copper block in order to bring the temperature of the specimen nearer to that of the thermostat before moving the specimen to its proper place for measurements. These preliminary manipulations require a lot of practice, but even so it always takes some time (of the order of half an hour) before the after effects of the initial temperature differences have disappeared. During this period of disturbances, in which there is also a rapid decrease in the rate of recovery, the heat evolved per unit time, the power P, is not proportional to the galvanometer deflection s but has to be calculated, as described in earlier papers (2) from

$$P = a s + b \frac{ds}{dt} \qquad (1)$$

where a and b are constants and t the time variable. The constants a and b can both be determined from the calibration with Peltier heat, a from the constant steady galvanometer deflection for a given power P, and b/a from the exponential variation of the deflection s with the time t after breaking the current and thereby making $P = 0$.

Another source of error, well-known from our earlier measurements, is the electromotive forces in the leads from the thermocouples in the apparatus to the commutator. In our case we had on these leads a temperature difference from 100° C to room temperature, and although the leads are copper wires taken from the same reel, they are always thermoelectrically different enough to cause electromotive

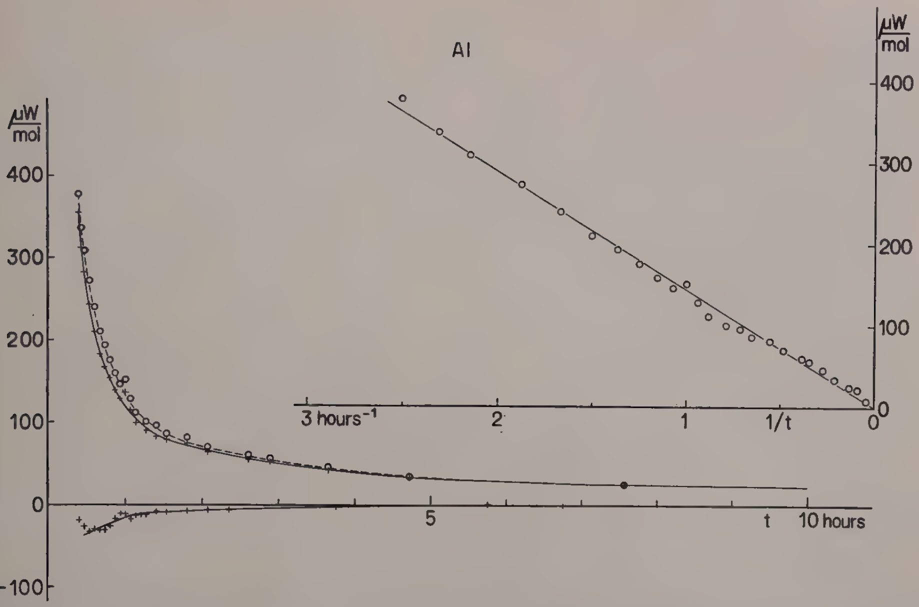

Fig. 2. Rate of evolution of heat in Al rolled to double length, measured at 100° C immediately after rolling.

forces that cannot be neglected. Each series of measurements has therefore to be continued until the evolution of heat has practically disappeared, and only the constant galvanometer deflection from the disturbing thermoelectric forces remain. This constant deflection has to be deducted from all the readings of the series.

In search of further possible sources of error we have made rather extensive measurements on samples of pure un-worked metals. Though in these cases no effect was to be expected, we found repeatedly that samples that were taken from room temperature up to 100° C. showed an appreciable absorption of heat during the first hours. Samples that were heated above 100° C and then measured at that temperature showed a small evolution of heat. If the sample was kept at room temperature in a dessicator before the measurements at 100°, or if the relative humidity in the room was lowered, the effect was decreased. We therefore concluded that the effect was due to variations of the adsorbed layer of moisture on the surface of the sample. Somewhat to our surprise, we found that the heat effect corresponded to calculated variations in the thickness of the adsorbed layer of the order of 100 Ångström. Similar variations have however been found previously (4) by other methods. This source of error probably played a certain role in the measurements reported at the Solvay conference (1). In order to avoid them, we have in the present investigation tried to keep the samples as dry as possible while at room temperature. As a further check, after each series of measurements on the cold-worked samples, we made a new series of measurements on the same sample (without renewed cold-working) under as far as possible similar conditions.

The present investigation comprises measurements at 100° C on Al, Cu and Zn immediately after rolling, and on Al and Cu after rolling and a preliminary recovery

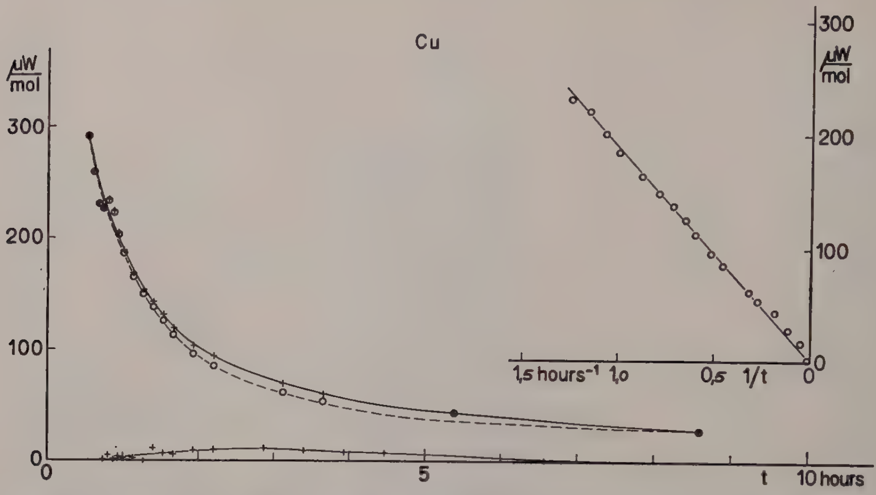

Fig. 3. Rate of evolution of heat in Cu rolled to double length, measured at 100° C immediately after rolling.

during 41 and 45 hours, respectively, at 60° C. The samples were of the purest available metals, Al from the laboratories of Finspongs Metallverk, Cu from Ädelmetallaktiebolaget in Malmö, and Zn from A.B. Kebo in Stockholm.

Earlier comparative measurements on this very pure Al and technically pure Al seem to indicate, however, that the purity does not greatly influence the recovery phenomena.

Some results are shown in figures 2 to 4, and in table 1. In the diagram to the left in the figures, the crosses indicate the measurements of the main series and of the control series during the first ten hours, as function of the time t. The main series were continued for three or four days in order to obtain reliable final values of the zero points. The control series give rather small values. Though we do not understand them in all details, we have thought it best to take them as corrections throughout. The corrected values are marked by circles. The rate of evolution of heat is given in microwatt per mol. The diagrams to the right show heating power of recovery against the reciprocal of time. The diagrams in fig. 2 and 3 indicate that the power P is a simple hyperbolic function of the time t if the measurements are performed immediately after the cold-working. We then have

$$P=\frac{a}{t} \tag{2}$$

where a is a constant. If the sample has partly recovered at a lower temperature before the measurements at 100°, the rate of evolution of heat seems to be described by

$$P=\frac{a}{t+t_0} \tag{3}$$

where t_0 is a constant depending on the temperature and duration of the preliminary

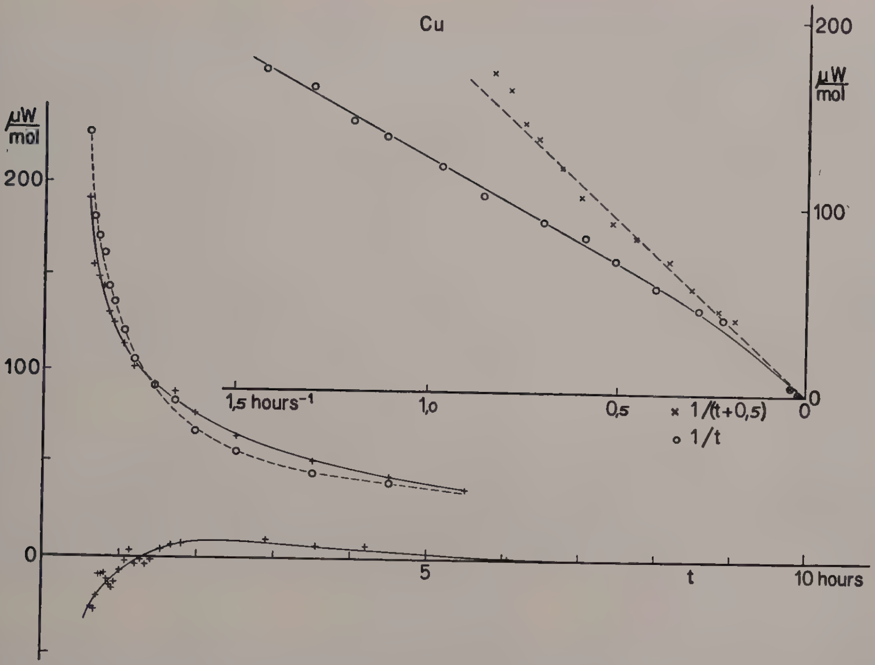

Fig. 4. Rate of evolution of heat in Cu rolled to double length, aged at 60° C for 45 hours, measured at 100° C.

Table 1

Results for measurements at 100° C

Metal	Preceding recovery	a Ws/mol	t_0 hours	b
Al	none 41 hours at 60° C	0.53 0.43	 1.0	5900 7100
Cu	none 45 hours at 60° C	0.67 0.68	 0.5	4600 4600
Zn	none	0.32		9700

recovery. From the results collected in table 1 it seems likely or at least possible, that the constant a is the same whether or not there is any preliminary heating.

Earlier theoretical attempts to describe the recovery can be summarized by the formula

$$P = -\frac{dQ}{dt} = cQe^{-\frac{E-bQ}{RT}} \tag{4}$$

where P is the rate of heat evolution, Q the heat per mol still to be given off for full recovery, t the time, c a constant of the order of the frequency of the atomic vibrations, E the activation energy at the end of the recovery process, b a constant with the dimension of a number, R the gas constant and T the absolute temperature. In the formula first proposed by VAN LIEMPT (5) the activation energy was assumed to be constant throughout the recovery process. This leads, however, to an exponential decrease of Q and P with the time, which is not in agreement with the experimental facts. The linear increase of the activation energy with decreasing Q was introduced by KUHLMANN (6) and seems to give an adequate description of the phenomena as they are known at the present time. The constant c is of the order 10^{13} cycles per second. An estimation of E for aluminium made by KUHLMANN, MASING and RAFFELSIEPER (7) gives a value of $E = 48\,000$ calories per mol.

A mathematical analysis of the differential equation (4) shows that within the wide limits of time

$$\frac{1}{c} \ll t \ll \frac{1}{c} e^{\frac{E}{RT}} \tag{5}$$

which for instance in the case of aluminium at 100° C means a time well above 10^{-13} and well below 10^{16} seconds, the power P is approximately given by

$$P = \frac{RT}{b} \cdot \frac{1}{t}. \tag{6}$$

Here t is the time from a moment when the extrapolated value of the power P would be infinite. In reality, of course, P starts at a finite value, but as this value must be expected to be very high, t is practically equal to the time from the start of recovery. Equation (6) thus corresponds to the empiric formula (2), the empiric constant being

$$a = \frac{RT}{b}. \tag{7}$$

The results of the measurements at a higher temperature (100° C) after a preceding recovery at a lower temperature (60° C) are what could be expected if the structural result of the recovery during a long time at a lower temperature is the same as that during a shorter time t_0 at a higher temperature. At the time t after the increase of temperature we should then expect the power

$$P = \frac{RT}{b} \frac{1}{t_0 + t} \tag{8}$$

which is consistent with the empirical formula (3), the constant a having again the value given by equation (7).

The values of b obtained from the empiric values of a by means of equation (7) are given in the last column of Table 1.

With the value of $b = 6\,000$ obtained for Al and the value of $E = 48\,000$ calories per mol given by KUHLMANN, MASING and RAFFELSIEPER, we find that already an energy of $Q = 48\,000 : 6\,000 = 8$ calories per mol introduced in the specimen by coldworking makes the activation energy in equation (4) zero. This means such a rapid initial rate of recovery that there will be, if equation (4) is valid, no practical possibility and even no physical meaning to try strictly to divide the energy taken up by the sample during cold-working in a purely thermal part, directly occuring as atomic vibrations, and a structural part gradually transformed into heat by the process of recovery.

The questions of practical interest are how much structural energy there is still left in the specimen after recovery during a given time at a given temperature, and how long time will be necessary for practically full recovery at a given temperature. Probably these questions will be answered by continued measurements of the heat evolved during recovery at a number of successively increased temperatures up to a temperature where full recovery is reached in a reasonable time.

The investigation has been supported by a grant from the Swedish Council for Technical Research.

Stockholm, Royal Institute of Technology, Department of Physics.

LITERATURE: (1) **G. Borelius,** L'état solide, Inst. Solvay, Bruxelles 1952, p. 427. — (2) **G. Borelius, S. Berglund,** and **O. Avsan,** Arkiv för Fysik *2* (1951), 551. — (3) **G. Borelius** and **S. Berglund,** Arkiv för Fysik *4* (1951), 173. — (4) **R. Strömberg,** Vetenskapsakademiens Handlingar, Stockholm, *6,* nr 2 (1928). — (5) **J. A. M. van Liempt,** Z. anorg. allg. Chemie *195* (1931), 366. — (6) **Doris Kuhlmann,** Zeitschr. f. Physik *124* (1947), 468. — (7) **D. Kuhlmann, G. Masing,** and **J. Raffelsieper,** Metallkunde *40* (1949), 241.

Tryckt den 22 december 1952

Uppsala 1952. Almqvist & Wiksells Boktryckeri AB

ARKIV FÖR FYSIK Band 6 nr 17

Read 14 May 1952

Screens in long discharge gaps

By Harald Norinder and Oskars Salka

With 15 figures in the text

Contents

1. Development hitherto 151
2. Screens in positive discharges 153
   a. The corona 153
   b. The bundle of rays 154
   c. The anode plasma channels 156
3. Screens in negative discharges 156
   a. The screen in the corona region 156
   b. The screen in the glowing-cloud 158
   c. The effect of the screen on the plate stem 159
   d. The screen and the plasma channels 159
   e. Figures on the screen 160
4. Lichtenberg figures on the screen 161
5. Discussion 165
   a. General 165
   b. The screen in positive discharges 166
   c. The screen in negative discharges 166
   d. Concluding remarks 167
6. Summary 168

1. Development hitherto

When a screen is placed in the spark gap of an inhomogeneous electrical field, it exerts a considerable influence on the electrical condition of the gap, and this affects in particular the value of the breakdown voltage. The early experiments of Steinmetz (1) in this field have been supplemented by the work of Marx (2), Buchwald (3), Roser (4) and some Russian experiments (5, where other Russian references are also given). The alteration of the breakdown voltage may be explained by the change in the field brought about by the introduction of the screen. Layers of opposite charge appear on the surface of the screen, and the distribution may be taken to be nearly uniform. The screen thus becomes a plate electrode, so to speak, above the earthed plate electrode so that the screen transforms the sphere-plate arrangement in part to a homogenous parallel plate arrangement. Such screens only serve a purpose in the case of curved electrodes at positive potential with respect to the plane electrode. The breakdown voltage is then raised considerably if the screen is placed near (some cm from) the positive point. If the screen is placed near to the plate electrode it has practically no effect. The effect of the screen is quite different with negative electrodes. In this case, the breakdown voltage is lowered, and the effect is particularly marked when the screen is in the lower part of the gap. Thus, by correct installation of a screen, the breakdown voltage may be raised as much as three times for strongly inhomogeneous fields, whereas the breakdown voltage may be reduced by as much as one half if the screen is set up incorrectly.

The effect of the screen may be explained as follows, after MARX (2 b). The breakdown discharge for positive polarity follows discharge channels which proceed outwards from the anode (the point). Thsee channels are developed by electrons, which are drawn to the anode along the field lines. If some of these electrons are obstructed by a screen, the development of the channels is stopped, and the breakdown voltage correspondingly raised. With negative discharges, the channels appear on both sides of the screen, and this effect is inoperative.

Screens have recently attained a new significance, in that they may be employed to explain the mechanism of discharges across long gaps. In two earlier publications (6, 7) we have presented new experimental material relevant to the problem of the evolution of the discharge across a long gap. Since the present investigation was largely based on the mechanism of discharge outlined in the two previous papers, we will briefly mention the conclusions reached there. In (6)—*positive impulse voltages*—it was shown that the development of the discharge passes through three main stages with the sphere-plate arrangement: corona, plasma channel, and main flash. The corona, consisting of a stem and crown, does not reach the plate. The plasma channel begins at the anode and develops towards the plate along diffuse luminous bundles of rays. The positive plasma channel bridges the entire gap; there is no observable negative channel meeting it from the plate.

The development of the discharge is quite different from *negative impulse voltages* (7). There are three stages of development in this case as well; corona, plasma channel, and main flash—but the process is different in many important respects from that occurring with the sphere positive. The corona, with its crown, bridges the whole gap—in one or more stages. The consecutive stages are formed with the help of a luminous glowing cloud, which bridges the preceding stage, and from whose surface the following stage develops. When the tip of the last corona stage reaches the plate, near to the plate (at a maximum measured distance of 13 cm) appear sharp bright channels, called plate stems; they originate in the final glowing cloud, and they grow towards the plate. When the glowing cloud has achievel contact with the plate, a plasma channel begins to form at the plate. This plasma channel begins by returning along the same course as the plate stem, but in its later development it is preceded by several brush-shaped luminiscences. The plasma channel develops stage by stage towards the sphere cathode. At about the same time, cathode plasma channels of several stems commence at the sphere. Both the anode and cathode plasma channels develop entirely within the glowing cloud which bridges the gap. The meet somewhere in the middle or in the upper half of the gap, and the meeting is often accompanied by the formation of complicated loops. Thus, the preliminary plasma channel for a negative discharge also begins at the anode (the plate in this case).

It is important to stress the differences between the plasma channels for positive and negative sphere electrodes: for the *positive* polarity, the plasma channel commences at the anode sphere, where the necessary field intensity may be attained at a smaller voltage. The less intense field near the cathode plate does not suffice for the formation of plasma channels there, so the gap is bridged completely by the anode channel. The primary plasma channel for *negative polarity* also begins at the anode, which is the plate in this case, of course. It is obvious that the necessary field intensity is only attained here at a much higher voltage. The neighbourhood of the cathode is therefore subjected to a much more intense field than in the positive case, and this is sufficient for the formation of a cathode plasma channel. The gap is thus bridged simultaneously by plasma channels from the anode and the cathode.

The purpose of the experiments described in this paper was to investigate the effect of a screen on the stages of the spark process outlined above, to investigate how the phenomena observed accord with the current theoretical explanation, and lastly, to endeavour to find new experimental bases for the study of the discharge mechanism.

The experimental method used, and the lay-out of the apparatus, was the same as in the two preceding series or experiments (6, 7). The screen materials used were cellophane (0.02 mm thick), drawing paper (0.05 mm), pressboard (0.1 and 2 mm), bakelite (6.5 mm) and ebonite (3 mm). The spark-gap was on an average about 1 m long. The ratio of the screen thickness to the length of the gap indicates that the state of the field was not essentially altered by the interposition of a screen.

2. Screens in positive discharges

The sequence of positive pre-breakdown discharges (6) consists of the following idividual phenomena: a. corona, with stem and crown of threads, b. bundle of rays, c. anode plasma channel (at the sphere). Since the conditions for the occurrence of the three stages and their physical aspects are quite different, it is to be expected that the effect of the screen will be quite different for the three stages. The tests with different screen materials has shown that the material itself has little or no influence. But the thickness of the screen certainly had some influence.

a. The corona. The corona has a certain length, depending on the spherical electrode used and on the voltage, and therefore covers only a part of the gap, there being no luminous phenomenon in the rest of the gap. In order to test the effect of the screen when in the dark region of the gap, the corona was photographed for different screen distances and its length measured. A voltage of 214 kV was applied to the spark-gap (the sphere being 6.2 cm in diameter, and the gap 124 cm long), which voltage was somewhat more than the onset voltage for the corona. The external appearance of the corona remained the same during these experiments, although its length changed a little, as shown in the following table.

Table 1

Distance of the screen from the plate cm	0	42	83	106	without screen
Length of the corona cm	14.5	14	13	13	14.5

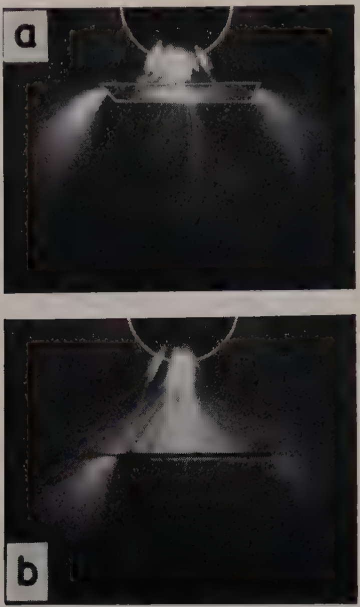

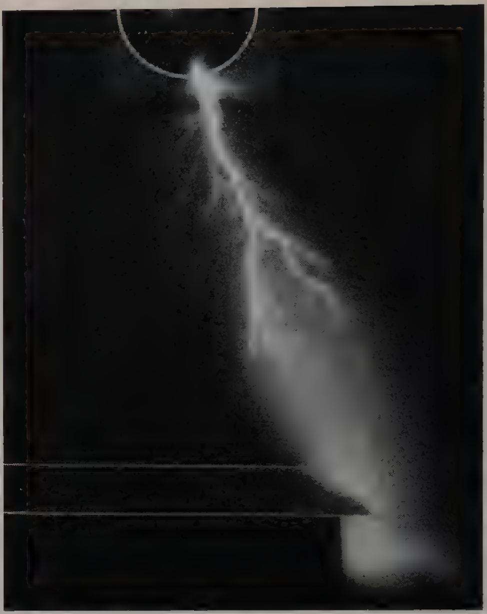

Fig. 1. Screen (0.02 mm cellophane) in the corona crown of a positive discharge: a. in the upper part, b. in the middle. Each figure represents the superposed photographs of 30 consecutive coronae.

Fig. 2. The screen is impassable for the bundle of rays of a positive discharge. The bundle tends to make its way round the screen. Screen material: 2 mm pressboard.

The change is not marked, but there is a tendency for the corona to shrink when the screen is in the dark region. This effect increases as the screen approaches the sphere. When the screen lies on the plate, it has no observable effect.

Though the effect on the corona of a screen placed in the dark region is slight, the interposition of the screen in the visible region of the corona produces a strong effect. Both the threads of the crown and the stem are halted at the screen, although it is possible that a new corona develops from its lower surface. If the screen is in the stem region this is always observable; when in the crown region, only in the upper part of the crown (Fig. 1 a), never in the lower part (Fig. 1 b). The new corona growing out from the screen is not of the same appearance as the ordinary corona coming from the electrode, the difference being that the former has no stem. Close examination of the photographs shows that the lower corona cannot be regarded as extensions of the upper ones.

b. The bundle of rays. As already mentioned (6), the bundle of rays commences at the same time as the anode plasma channel, and its diffusely luminous branches reach to the plate. The photographs show that the screen is impassable for these bundles, whatever its distance, so that the thickness of the screen is immaterial; even the thinnest screen—0.02 mm cellophane—stopped the bundle of rays completely. The branches of the bundle tended to go round the screen to reach the plate below (Fig. 2). If the screen is effective in closing

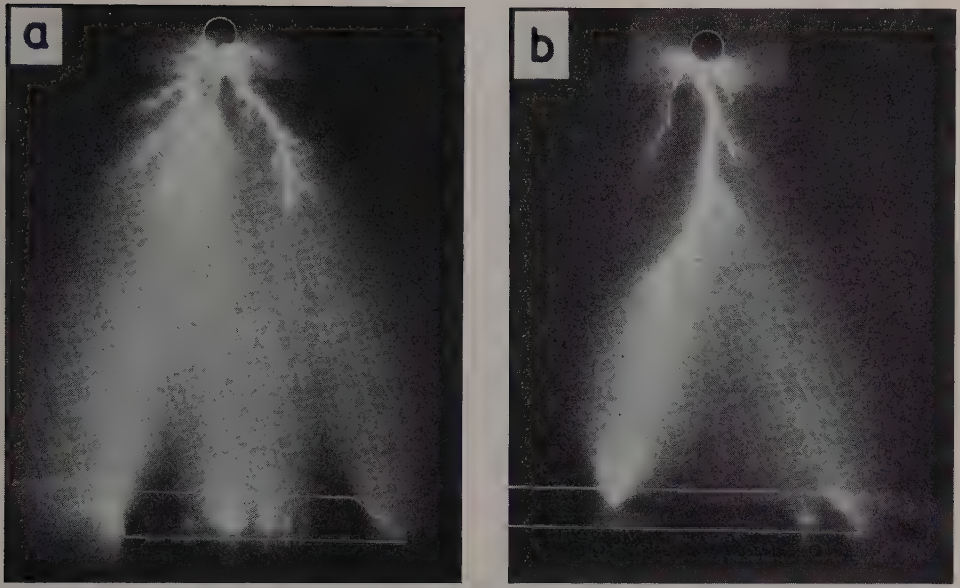

Fig. 3. A screen near to the plate electrode leads to cathode plasma channels with positive discharges. a. 0.02 mm cellophane screen at a distance of 1.5 cm from the plate; b. 0.1 mm pressboard screen at a distance of 5 cm from the plate. The small sparks between the screen and the plate should be noticed.

this way to the bundle, it can only develop in the upper part of the gap. If there is a hole in the screen, the bundle makes its way through this hole, and is thereby much constricted, after which is once more spreads out in the lower part of the gap.

What has been described above applies only when the screen is not near to the plate. When the screen is only some cm from the plate, a new phenomenon occurs: one or more sparks bridge the space between screen and plate. The sparks have not sufficient energy to break through the screen; they leave no holes behind them in the screen. On the upper surface of the screen, directly above the point where the spark strikes it, a luminous point appears, and a part of the bundle of rays in that region joins on to it. The plasma channels develop from the luminous point at the screen and grow towards the anode. It is in this way that the cathode plasma channels originate (Fig. 3).

When the screen is laid upon the plate electrode, the luminous points in general appear—and with them the cathode plasma channels—only with the thicker screens. Fig. 4 a shows the beginning of a plasma channel at a screen of pressboard 2 mm thick. With the thinner screens, however, the upper (anode) plasma channel reaches the cathode without the cathode plasma channel commencing (Fig. 4 b). In these cases the bundle flows into the screen in the same way as it does into a metal electrode. It should be added that when there is a hole in the screen and at the same time a luminous point at the screen, the further development process always takes the easier course, that is to say, the upper (anode) plasma channel grows to meet the cathode channel which orig-

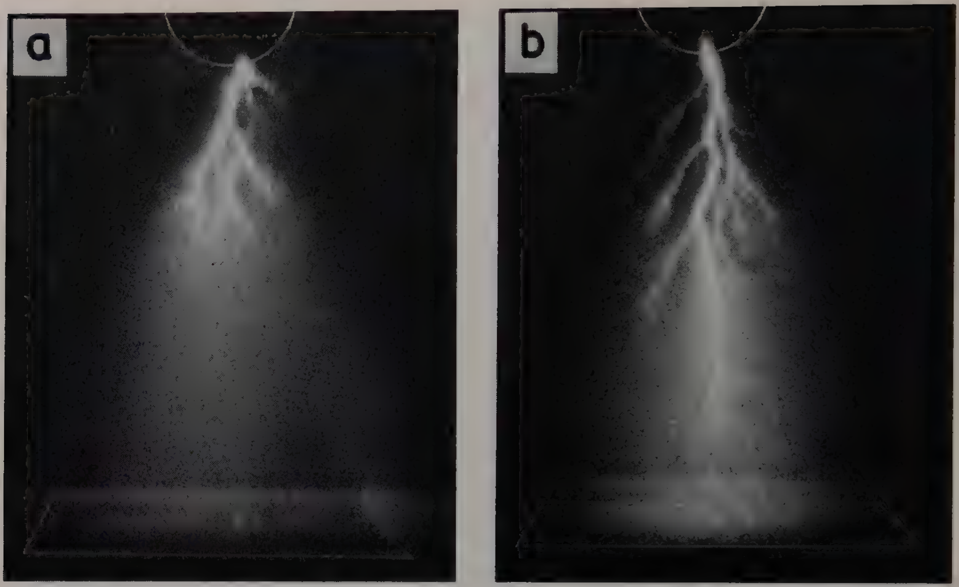

Fig. 4. The screen resting directly on the earthed plate, with a positive discharge. Cathode plasma channels occur only when the screen is thick. Screen material: a. 2 mm pressboard; b. 0.05 mm drawing paper.

inates at the luminous point, and does not go through the hole to the plate electrode.

c. The plasma channels. In order to investigate the influence of the screen on the development of the plasma channels, it was placed in the upper half of the gap, in the region where the thread-crown of the corona would normally have been. The photographs show that the plasma channel "passes through" the screen (Fig. 5 a). It may be seen from Fig. 5 b that a high energy is necessary for this penetration—one plasma channel takes a longer path around the edge of the screen instead of the shorter way through the screen. Since the "passage" of a half-developed plasma channel through the screen left no hole (the subsequent spark did leave a hole), we may conclude that two separate processes are involved here, an upper—between the sphere and the screen—and a lower—from the lower surface of the screen. This conclusion is borne out by the fact that the photographs show a kink or other irregularity in the path of the plasma channel where it meets the screen. It not seldom happens that a plasma channel appears from the lower surface of the screen without an upper plasma channel; it suffices if a bundle of rays reaches the screen (Fig. 5 c).

3. Screens in negative discharges

a. The screen in the corona region. A screen placed in the stem region of the corona does not hinder the propagation of the stem. In Fig. 6 b, only the left-hand side is screened, the right being free. The picture shows that the

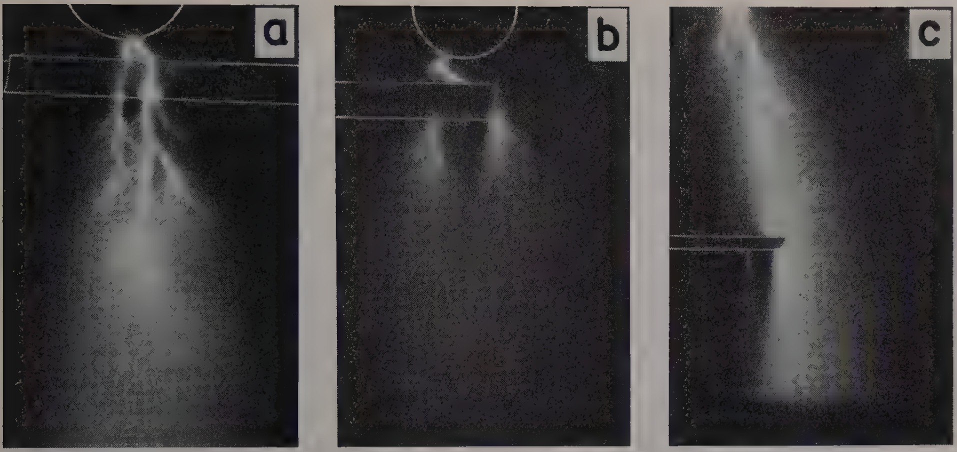

Fig. 5. The screen is no barrier for an anode plasma channel in the case of positive discharges. Screen material: a. 0.02 mm cellophane, b. 0.05 mm drawing paper. An anode plasma channel may also develop from the screen: c. Screen: 0.05 mm drawing paper.

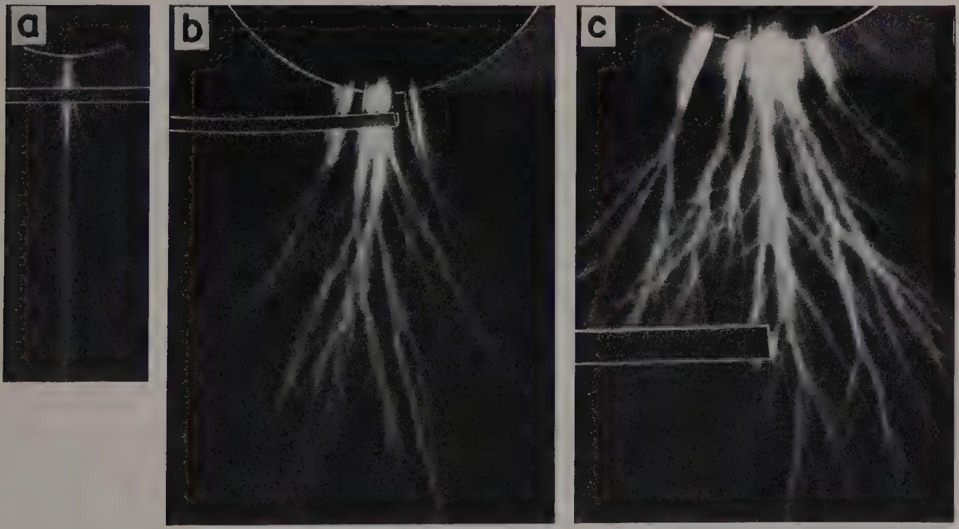

Fig. 6. Screen in negative discharges at the corona-onset voltage (a), and for higher voltages (b, c). The screen does not retard the stem (a, b), though the crown threads are stopped (c). Screen material: 2 mm pressboard.

screen is no obstacle to the stem. Indeed, it seems that the stem even prefers to develop in the screened part. The stem exhibits the same property even in the initial stage of its development, that is, at the onset voltage of the corona (Fig. 6 a). Although there is visible luminescence on both sides of the screen, giving the impression that the discharge passes through the screen, there is actually no hole in the screen.

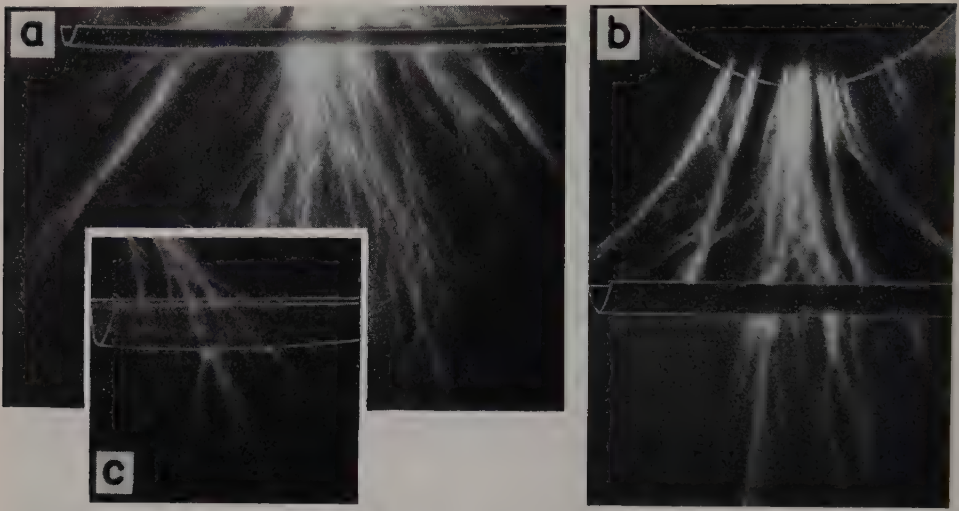

Fig. 7. The formation of a new corona on the lower surface of the screen with negative discharges, with the aid of a luminous spot (c), stem-like channels (b), and diffuse threads or space stems (a). Screen material: a, b. 2 mm pressboard, c. 0.02 mm cellophane.

The screen was next placed in the crown region of the corona. In this position it exerted a marked influence on the development of the corona, and the threads of the crown were cut off. This suppression was more complete the thicker the screen (Fig. 6 c). When the screen was thin, a new corona easily developed from its lower surface (Fig. 7 c). For this to happen with thicker screens, it was necessary for the corona crown to be more strongly developed, that is, the corona voltage had to be higher (Fig. 7 b). The formation of the new corona may take place in one of three different ways: 1) The threads begin from a luminous spot on the upper surface of the screen (Fig. 7 c); 2) concentrated, strongly luminous channels form on the lower side of the screen (Fig. 7 b); 3) the new threads commence from a diffuse luminescence, like a glowing cloud, which develops from a large patch on the screen, and they soon converge into a stem, which may be called the space stem (Fig. 7 a).

b. The screen in the glowing cloud. On account of its diffuse luminosity, the glowing cloud of the negative discharge might be compared to the bundle of rays in the positive discharge. But what happens when the glowing cloud encounters the screen indicates that this comparison is not justified. The glowing cloud penetrates a screen without any great difficulty (Fig. 8 a). It shows no tendency to go round the screen, in the way that the bundle of rays with positive discharges does. It has been shown (7) that the glowing cloud never joins a metal anode plate in its diffuse form; there is always a plate stem between them. It was found that this was not the case when a screen was laid on the plate electrode. There is then no plate stem, but instead very short stemlike channels. A similar phenomenon is observed when the screen is in the gap (Fig. 8 a). Finally, Fig 8 c shows clearly that the penetration of the screen by the

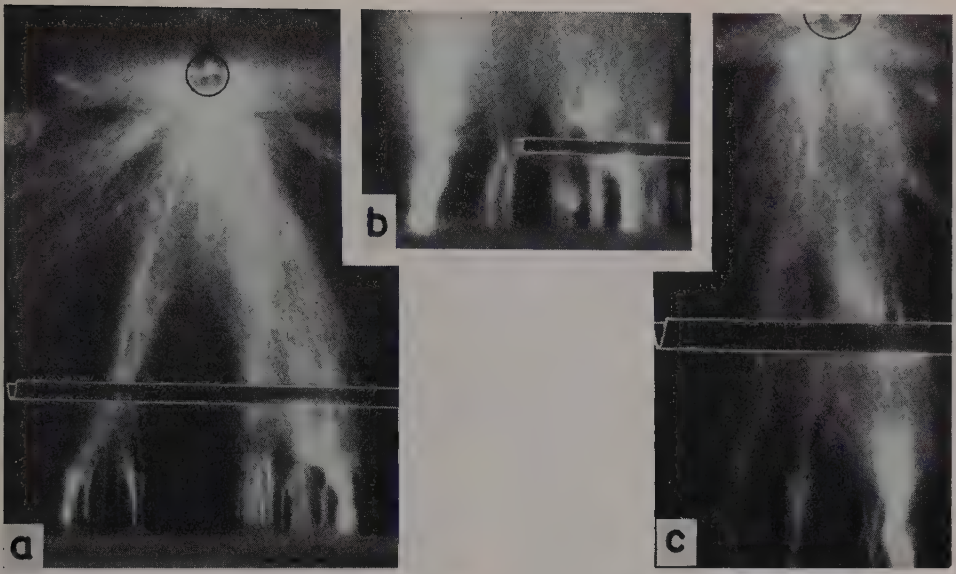

Fig. 8. Effect of the screen on the glowing cloud and the anode plasma channels with negative discharges. Screen: 2 mm pressboard.

glowing cloud is only apparent. In actual fact, there are two separate processes involved—one above and one below the screen.

c. The effect of the screen on the plate stem. The development of the plate stem was in no case disturbed by the interposition of the screen; the lenght, appearance and formation of the plate stem remained unchanged (Fig. 8 a). This was true when the screen was not too near to the plate (more than 15 cm distant). If the screen was nearer to the plate, the plate stem was obliged to develop only in the space between the screen and the plate. There was also a noticeable tendency for the plate stem to form more irregularly when the screen was very near to the plate.

d. The screen and the plasma channels. As mentioned in the introduction, the negative discharge may develop by means of both cathode (upper) plasma channels and anode (lower) plasma channels. If the screen is placed at the beginning of the crown, then—as will be seen from the photograph—the *cathode plasma channel* grows out from the electrode as if there were no screen. The plasma channel in this case therefore has the same properties as when there is no screen: 1) it exists only in the upper half of the gap, where there is a strong field; 2) it is unable to penetrate to the region where the field is weaker, and consequently, 3) the gap can only be bridged if the field is not too inhomogeneous, i. e. if the gap is small. When the gap is larger, the process is the same with a screen as without it: the first corona stage is bridged by a glowing cloud, whereupon a second stage develops with new stem and crown. The cathode plasma channel so-to-speak awaits the arrival of the anode plasma channel from below.

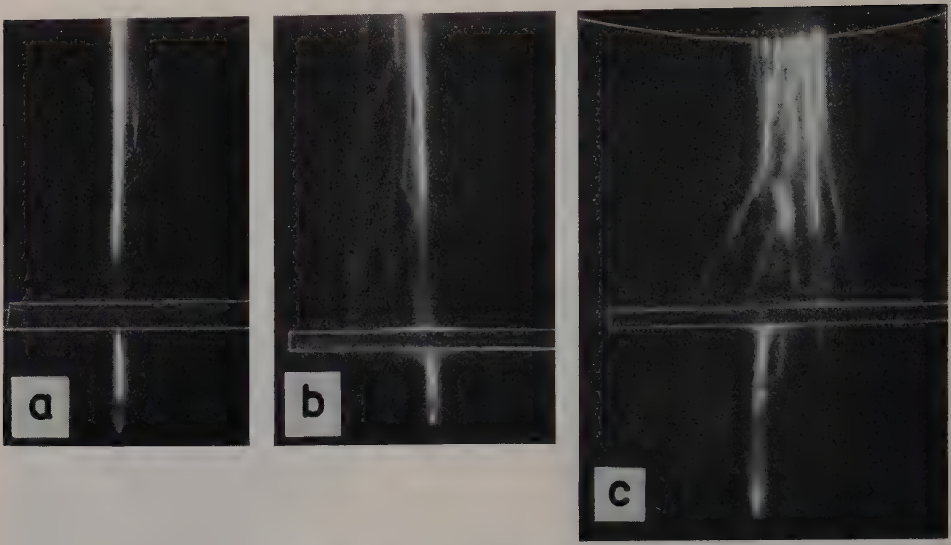

Fig. 9. Screen in a narrow discharge gap (field not too inhomogeneous). Sphere diameter 50 cm, gap 18.1 cm. Screen material: a. 2 mm pressboard, b, c. 6.5 mm bakelite.

Neither is the *anode plasma channel* altared in its development by the interposition of the screen. It commences in the usual fashion from the plate stem, and proceeds in the direction of the screen. The glowing cloud which is necessary for its development comes from the lower surface of the screen (Fig. 8 c). Besides this plasma channel (below the screen), a plasma channel above the screen may often be observed, growing in the direction of the cathode. There is no immediate connection between the two processes; it may happen that they develop in different ways, so that the lower one may occur by itself, for instance, and the upper one begin only when the other has reached the screen (Fig. 8 b). This continues to grow upwards until it meets the cathode plasma channel. However, there are also cases where both processes begin simultaneously or after a short delay, Fig. 8 c shows such a case.

It was also interesting to investigate the effect of the screen on the development of the plasma channel for narrow spark-gaps. With these, the gap is bridged by the upper plasma channel alone in the absence of the screen. Figs. 9 a, b show that in this case the screen does not change the process; the plasma channel begins at the electrode and at the screen simultaneously, and both channels move in the direction of the plate electrode. Both channels are therefore of a cathode character. The lower channel cannot be regarded merely as a continuation of the upper (Fig. 9 c), so we must conclude that two separate processes are involved.

e. Figures on the screen. The examination of the photographs obtained shows that large patches appear where the threads of the preliminary discharge processes arrive at or leave the screen, these patches often being strongly luminous, like the threads associated with them (Figs. 10 a; c). It is clear from many of the photographs that these patches are in the form of patterns. In those cases

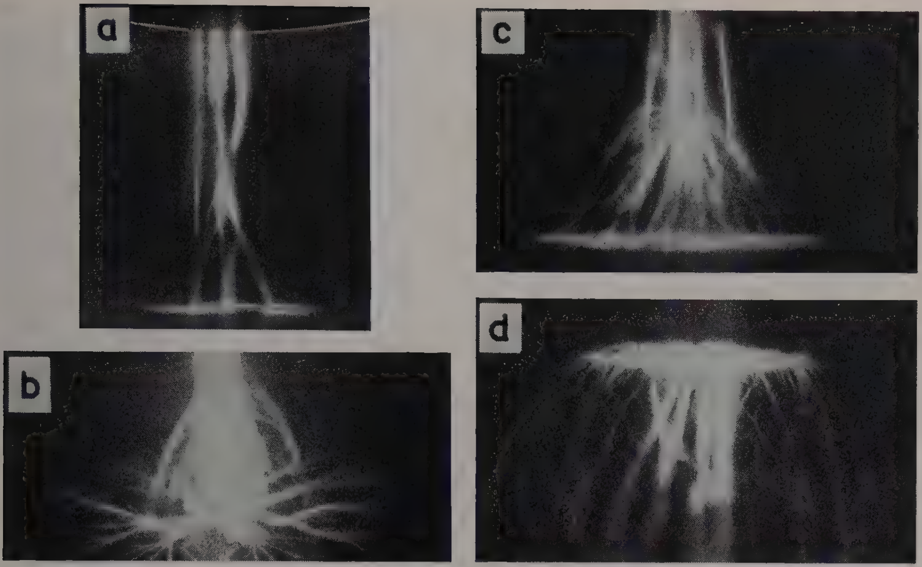

Fig. 10. Photographs of the screen surface show the existence of Lichtenberg figures. a, c. the upper surface for a pre-discharge, b. the same for a plasma channel, d. the lower screen surface for a pre-discharge. Screen: 6.5 mm bakelite. Polarity: negative.

where a plasma channel commences at the electrode and moves toward the screen, it can be observed that there is a Lichtenberg spark-figure on the screen (Fig. 10 b). This leads to an important conclusion: the visible threads and channels of the pre-discharge form Lichtenberg figures where they strike the surface of the screen, and conversely, the growth of a thread or channel from the screen begins with Lichtenberg figures. (Fig. 10 d.)

4. Lichtenberg figures on the screen

We wish to point out that the present experiments are only regarded as preliminary, as a more detailed investigation will be described in a later publication.

Although Lichtenberg figures on photographic film have a finer and more detailed form, it was not possible to use them in the experiments referred to here. Film is sensitive not only to the phenomena in the immediate neighbourhood of the surface which are our main interest here, but also to all luminous phenomena in the gap, particularly at the spherical electrode and the plate, and is usually over-exposed in consequence. The Lichtenberg figures referred to are therefore powder figures, i. e. of the original Lichtenberg type. Many of the details are thus lost, but it is nevertheless possible to carry out convenient measurements of the polarity and potential of the charge on the figures. The most important result of the experiments was that the Lichtenberg figures appear only for *visible* preliminary discharges. If the gap remains dark during the application of the impulse, there are no figures on the screen. This rule also

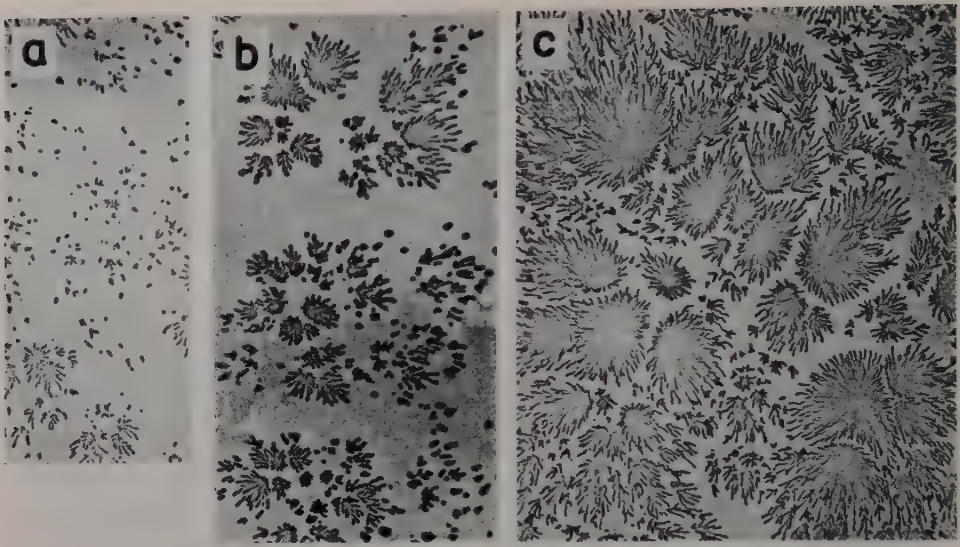

Fig. 11. Lichtenberg powder figures on the upper screen surface with a positive discharge.

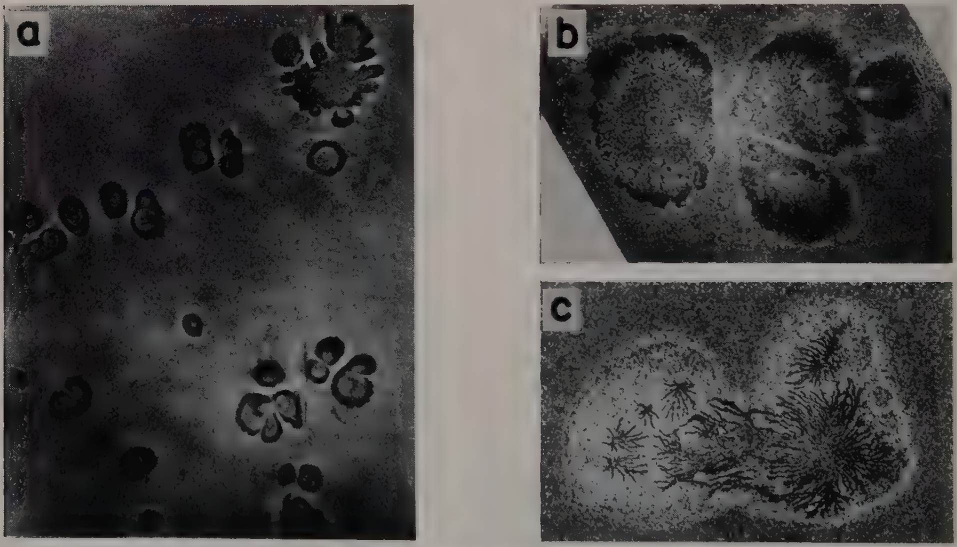

Fig. 12. Lichtenberg dust figures on the screen with a negative discharge. a. general view of the upper screen surface, b. separate picture of the upper negative Lichtenberg figures, c. corresponding lower positive Lichtenberg figures.

applies one-sidedly, i. e. when there is a luminous pre-discharge in the upper part of the gap, but none in the lower, the figures appear only on the upper side of the screen.

Since no discharge threads develop below the screen for *positive discharges,*

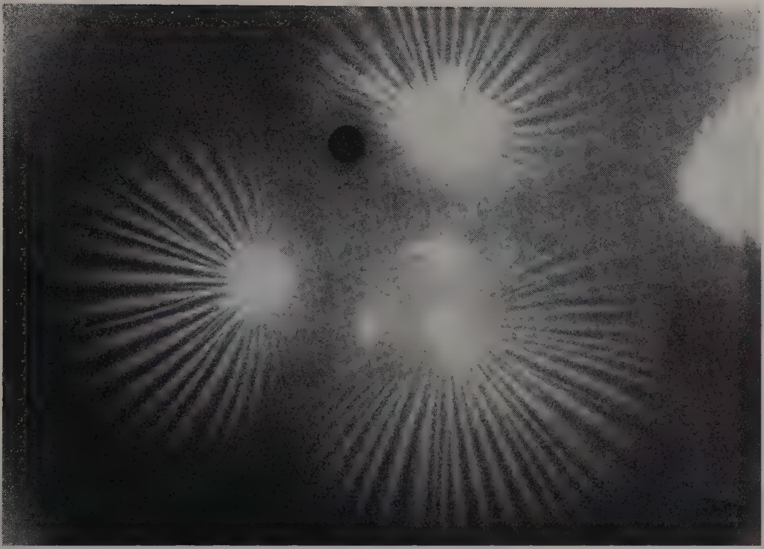

Fig. 13. A group of upper Lichtenberg figures produced by negative discharge. The film itself was used as screen. The black ring visible in the picture is due to a hole perforated in the film.

no Lichtenberg figures then appear on the lower surface of the screen. They appear only on the upper surface, and their shape has the positive character of the primary Lichtenberg figures, i. e. the charge moves in single sharply-defined branches. The figures vary in dimensions, and to some extent in shape, according to the conductance of the space-threads which arrive at the screen. Thus, if the screen conveys away only a little charge, we have something like that shown in Fig. 11 a (the screen lies on the plate, and is touched only by a weak bundle of rays), where the positive figures shrink to small V-shaped hooks, which may even degenerate into small streaks or points. A crown which strikes the screen gives rise to far larger figures (Fig. 11 b). When the bundle of rays is strongly developed, the figures are particularly large and distinct, and the branches are very close to each other (Fig. 11 c).

With *negative discharge*, in contrast to the positive, Lichtenberg figures were observed on both sides of the screen. Every thread of the corona crown meeting the screen forms a negative figure at the meeting point (Fig. 12 a). Such a powder figure is irregular, seldom round in form, usually without discernible sectors such as are characteristic of negative figures. However, there are figures in which the formation of sectors is clearly observable (Fig. 15 a, b). Of course, these sectors are always present, but the powder figures do not always allow us to observe them. The figures are easily descernible when taken on photographic film (Fig. 13). The larger powder figures are of a form which indicates that they are built up in steps (Figs. 12 b, 15 b). The negative powder figures are either purely negative in form, or there may be small positive figures within the figure area. These positive decorations vary from small points (Fig. 12 b) to small stars (Fig. 14 a). If there is a glowing cloud in the crown region, the positive decorations appear in the outer part of the figure, and are in the form

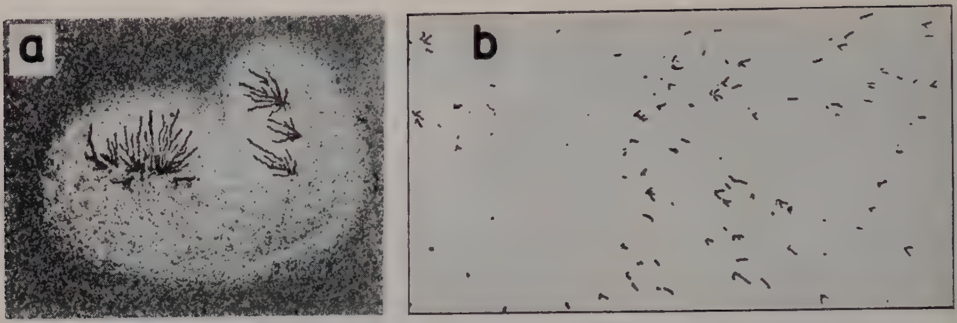

Fig. 14. Back-discharge figures with negative discharges. a. negative Lichtenberg figure with positive back-discharge figures, b. the upper screen surface when struck by the glowing cloud.

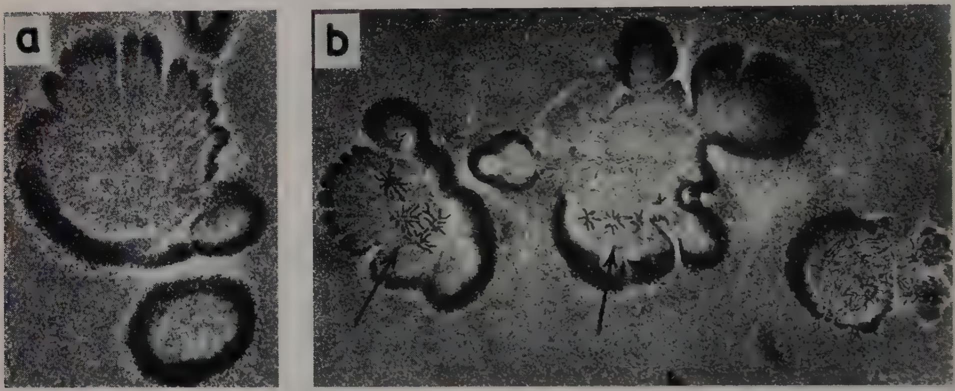

Fig. 15. Production of positive Lichtenberg figures within the area of the main negative figure by means of a proof sphere. a. negative figure with no blemishes, b. the arrows indicate the positive back-discharge artificially produced figures.

of points or V-shaped hooks (Fig. 14 b). So much for the figures on the upper surface of the screen, but the negative figures which we have hitherto been considering are not the only ones occurring. If a new corona develops from the lower surface of the screen, Lichtenberg figures appear there too. On the lower surface of the screen, opposite the upper negative Lichtenberg figures (Fig. 12 b), there is often a similar area marked in the powder, though the lower figure is *always* positive in form (Fig. 12 c). The branches of these figures often extend beyond the marked area.

As regards the *polarity* of the charge of the Lichtenberg figures, their denotations correspond, that is to say, a negative figure is associated with negative charge, a positive with positive. Measurements were carried out with the help of a sphere of 2 cm diameter attached to the end of an amber rod, a point 1 cm long (0.7 mm wire) being fixed to the sphere. This point facilitated the picking up of charge from a point of the figure. The polarity of the charge thus taken up was determined with an electrometer. It was found that the potential of the proof sphere was larger for negative figures than for positive. An interesting phenomenon was observed during the course of these measurements of polarity. We chose a negative Lichtenberg figure of pure negative form, that is, without any of the above-mentioned positive decorations (Fig. 15 a). When the area was touched with the point, a small positive figure appeared at the place where contact had been made. It is obvious that the proof sphere had collected the charge from the place where the positive figure appeared, and we may therefore conclude that when charge is removed from the area of the negative Lichtenberg figure, a positive figure results. If charge is taken up from several places in a negative Lichtenberg figure by a sphere which is neutralised each time, several small positive figures will appear, as shown in Fig. 15 b, where the Lichtenberg figure to the left was touched five times, the middle one four, while the positive figures in the right-hand figure were produced spontaneously. Each contact gave the proof sphere a charge of about $2 \cdot 10^{-9}$ coulombs, and a potential of about 2 kV. It should also be mentioned that it is not necessary to touch the screen with the point to produce the small positive figures. They appear even before contact is made, probably to the accompaniment of a small spark. This explains the fault in the centre of the small positive figure in Fig. 15 b.

5. Discussion

a. General. We will endeavour to explain the effect of a non-conducting screen on a discharge on the basis of the results obtained. The effects of a screen on positive and negative discharges are fundamentally different. The channels of the pre-discharge are completely halted by the screen when the spherical electrode is positive, but with negative polarity they are transmitted. There is a certain discernible retardation in the latter case, but only when the corona crown is faint. However, the passage of the channels through the screen is only apparent. It is conceivable that electrons or radiation might effect a penetration. Wynn-Williams (8) assumes that certain stages of the discharge emit radiation of wavelength between 13 and 1 000 Å, which penetrate air at ordinary pressure to a distance of some centimetres. If we attribute to such radiation the power to penetrate an ebonite screen 3 mm thick so that it retains sufficient energy to start a new corona in the lower gap, the lower process would be a continuation of the upper. This is not borne out by experiment, and moreover, it is improbable that such radiation—even if it occurs—could penetrate a screen 3 mm thick; so the process of "penetration" cannot be explained by radiation. The idea that it is electrons which penetrate the screen also encounters great difficulties, and this too must be regarded as improbable. The energy required for an electron to penetrate a layer of ebonite 3 mm thick would be of the order of Mev, and there can be no question of such energies in our discharge space. Consequently the "passage" of the channels of negative discharge through the screen must be explained in some other way. We are concerned here with two processes: the screen constitutes an intermediate object, which receives charge upon its upper surface and from the lower surface of which new threads develop. The link between the two processes is purely electrostatic, that is to say, due to the electrical field. It is thus comprehensible that no hole is left in the screen by the pre-discharge channel, no hole appearing until the final stage, the main discharge.

b. Positive discharges. Following these lines, the effect of the screen on a positive discharge may be explained as follows. The corona collects from its crown region the free electrons already present, and those released by itself, and they are conducted to the spherical electrode by the corona threads. A thread which touches the screen acts like a positive electrode at the screen, though its conductance is somewhat limited. The positive Lichtenberg figure at the contact point of the thread indicates that the thread conducts away some of the electrons from the ionised surface of the screen, leaving a positive charge in the branches of the figure. The bundle of rays which subsequently arises obviously involves a movement of electrons upward, since it gives rise to positive Lichtenberg figures where it is connected with the screen. Whether the upper surface of the screen was previously ionised uniformly (by photo-ionisation, for instance), or whether the ionisation was local, following the growth of figure branches, remains an open question. In either case, a positive Lichtenberg figure appears on the screen in a positive discharge. The figure has a positive charge, of insufficient density to start a new crown from the lower surface of the screen. This accounts for the total screening for crown-threads and bundles of rays—even when the screen is very thin—and the corresponding raising of the breakdown voltage brought about by a screen suitably placed. The fact that the presence of a screen near the plate lowers the breakdown voltage a little (4) may be explained thus: the positive charge on the upper surface screen causes a spark breakdown to the plate, on account of the short distance and the correspondingly intense field, and this gives rise to the anode (lower) plasma channel (Fig. 3). But if the stem meets the screen, i. e. if the screen is near the anode sphere, the screen receives more charge, sufficient to produce a new corona from the lower surface of the screen. As a consequence, the effect of the screen is also slight in this region [cf. (4)]. When the voltage has collapsed and electrons cease to be conducted away from the screen, the electrons in the channels exercise no retro-effect on the screen surface, so there are no figures due to back-discharge in the positive Lichtenberg figures, such as there are with the negative.

c. Negative discharges. Let us now consider the observations of the screen effect for negative discharges. In this case, the electrons in all the channels move downward towards the plate electrode. If such a channel ends in mid-air, the electrons have been captured by gas molecules (such is the case with crown threads, for instance). A thread that encounters the screen "sprays" some of this free charge over the surface, leading to the formation of a negative Lichtenberg figure. The charge on a negative figure is considerably denser than that on a positive figure, and it is at a higher potential. The downward effect of the charge is similar to that of a charged electrode, and leads without difficulty to new channels proceeding from the lower surface of the screen. The screen facilitates the development of the discharge across wide gaps because of charge accumulation, which cannot occur to a comparable extent when only air is present in the gap. Contrary to the case with positive discharge "back figures" of positive type do occur. When the impulse voltage collapses, the potential of the sphere falls, the field between sphere and screen is reversed, and the electrons on the screen and in the channels tend to return to the sphere, so that with negative figures some of the electrons are conducted away from the figure. Since this process, which was mentioned above, is accompanied by the formation of positive figures, positive back-discharge figures appear on the main negative Lichtenberg figure, these positive figures having nothing to do with positive charge in this case.

Under the influence of the negative charge on the upper (negative) Lichtenberg figure, a new corona begins from the lower surface, and the transfer of charge to the plate thus continues. This process takes place more or less as follows: the negative charge on the upper surface of the screen gives rise to a field between the screen and the plate, and the electrons which happen to be on the lower surface of the screen ionise the nearby gas by collision, under the influence of this field, whereupon a new corona begins, which presumably ionises the screen surface. The stem of the corona collects some of the electrons from the ionised patch, and a positive Lichtenberg figure appears on the lower surface of the screen in consequence, with a positive charge upon it.

This explanation is in full conformity with experiment (2). The breakdown voltage is in general lowered with negative discharges, especially when the screen is placed in the lower half of the gap, not too near to the plate.

d. Concluding remarks. The accumulation of electrons on the screen, and their conducting away, are from the statistical standpoint such that the breakdown voltage may take widely spread values without variation of the experimental conditions. It is therefore impossible to determine the effect of the screen exactly. The current idea (4) that there is uniform distribution of charge on the screen is contradicted by the fact that the screen acquires an arbitrary distribution of charge concentrated in the Lichtenberg figures.

We have already referred to the intimate relation which may be supposed to connect the pre-discharge in air and the Lichtenberg figures (6). The present work confirms this view. The basic conception of the breakdown mechanism for wide gaps in air is still deficient, however, and further investigation is needed. One thing may nevertheless be taken as generally valid: the transport of electrical particles in air at atmospheric pressure proceeds along narrow channels—when it is accompanied by visible phenomena, at least. If such charge in motion strikes the surface of a semi-conducting or non-conducting plate, its movement continues along the branches of primary Lichtenberg figures, or spark figures derived from them. There are many well known examples of this. To take a few of them: 1) A spark which strikes the surface of a semi-conducting plate forms there a spark figure of polarity corresponding to the electrode of origin (9). 2) So-called lightning figures appear on the skin of a person struck by lightning (12). 3) An electron beam emitted by a glowing wire in air at atmospheric pressure forms Lichtenberg figures where it strikes an insulating surface, and these may be rendered visible by subsequent dusting (10). 4) A pre-discharge striking an oil surface sets it in motion—with positive polarity the surface is slightly rippled, whereas with negative the oil surface is struck in several places, from which circular waves are propagated (11). 5) If a discharge encounters an oil drop on the surface of a non-conductor, it scatters the oil in a radial pattern, giving rise to Aldini oil figures (12). 6) Lichtenberg figures have been obtained where the electrode is not in contact with the film, but at a certain distance from it (13, 14, 15). Lichtenberg made his original discovery in a way similar to this. He observed that the dust on the resin cake of an electrophorus arranged itself in the form of little stars (for positive polarity) or circular spots (for negative). He attributed the figures to the impact of the luminous discharge on the surface of the resin (12).

We attach particular importance to the explanation of the conditions for the occurrence of the lower (cathode) plasma channel with positive discharges. No such channel occurs in laboratory experiments if the plate electrode is of metal, unless there is a screen near to it or a more or less insulating layer covers it. The lower part of the discharge is in the latter case similar to that for negative discharges. An important conclusion may be drawn from this: that the determination of the polarity of a lightning flash from the manner in which its lower channels behave should be undertaken with great care, since the electrical properties of the zone struck by the lightning exert a very considerable influence on the form of the channels. Other factors than the screening effect mentioned above also play a part. Neither do photographs of a lightning flash provide an unambiguous indication of the polarity of a charged cloud, as the branching and spark channels are not in conformity with those which indicate the polarity of spark discharges produced in the laboratory.

6. SUMMARY

The individual stages of the pre-discharge lead to movement of the electrons. With positive discharges, the electrons are drawn upward toward the anode sphere, and with negative discharges they are spouted into the gap. Therefore, the upper surface of a screen of insulating material is subjected either to a "suction" or to a jet of electrons, according to the respective case. Both give rise to Lichtenberg figures. The charge which is thus drawn from the screen or imparted to it is localised in these figures, and the polarity of the figures depends on the way in which the charge moves.

Positive discharges impart positive charge to the screen, of a low density, which is not sufficient to start a new pre-discharge from the lower surface of the screen. The screen thus checks the development of the discharge and raises the breakdown voltage in this case. When the screen is near the upper electrode, the density of the charge on it is so high that this effect is insignificant. A screen placed near to the plate gives rise to a spark between the plate and the screen, and this starts a cathode plasma channel.

With negative discharges, the screen is sprayed with charge, and acquires a charge of such high density that it acts like an advanced electrode. New pre-discharges arise without difficulty from the lower surface of the screen. The screen aids the development of the discharge, and the breakdown voltage is usually lowered.

The form of the Lichtenberg figures is determined by the direction of the movement of the electrons on the surface of the screen. The positive figures appear when electrons are drawn away and the negative figures when electrons are deposited.

Institutet för högspänningsforskning vid Uppsala Universitet, Maj 1952.

LITERATURE: 1. **Roth, A.:** Hochspannungstechnik, p. 178, Verlag Springer, Berlin 1927. — 2. **Marx, E.:** a) Der Durchschlag der Luft im unhomogenen elektrischen Felde bei verschiedenen Spannungsarten. Elektrotechnische Zeitschr. Vol. 51, p. 1161, Berlin 1930. b) Lichtbogen-Stromrichter für sehr hohe Spannungen und Leistungen. Verlag Springer, Berlin 1932. — 3. **Buchwald, H.:** Dissertation. T. H. Braunschweig 1930. — 4. **Roser, H.:** Schirme zur Erhöhung der Durchschlagsspannung in Luft. Elektrotechnische Zeitschr. Vol. 53, p. 411, Berlin 1932. — 5. **Komelkov, V. S.** and **Lifshits, A. M.:** Influence of barriers on the development of the electric discharge in long gaps. Izv. Akad. Nauk. SSSR, Otdel Tekn. Nauk, No. 10, p. 1463, Moscow 1950. — 6. **Norinder, H.** and **Salka, O.:** Mechanism of positive spark discharges with long gaps in air at atmospheric pressure. Arkiv för Fysik, Band 3, No 19, p. 347, Stockholm 1951. — 7. —— Mechanism of negative spark discharge with long gaps in air at atmospheric pressure. Arkiv för Fysik, Band 5. — 8. **Wynn–Williams, C. E.:** An investigation into the theory of the "three-point gap". Phil. Mag. Vol. 1, p. 353, London 1926. — 9. **Merrill, F. H.** and **von Hippel, A.:** The Atomphysical Interpretation of Lichtenberg Figures and their Application to the Study of Gas Discharge Phenomena. Journal of Applied Physics, Vol. 10, p. 873, New York 1939. — 10. **Selenyi, P.:** On the electrographic recording of fast electrical phenomena. Journal of Applied Physics, Vol. 9, p. 637, New York 1938. — 11. **Weber, W.:** Durchschlag des geschichteten Dielektrikums Öl—Luft bei Stoss- und Wechselspannung. Archiv für Elektrotechnik, Vol. 31, p. 197, Berlin 1937. — 12. Handbuch der Physik, Geiger und Scheel. Vol. 14, p. 391, 392, Verlag Julius Springer, Berlin 1927. — 13. **Morris, Thomas, A.:** "Heat developed" and "powder" Lichtenberg figures and the ionization of dielectric surfaces produced by electrical impulses. British Journal of Applied Physics, Vol. 2, p. 98, London 1951. — 14. **Lord Armstrong, C. B.:** Electric Movement in air and water. Fig. 9, 10, 30 and 31. Smith, Elder and Co, London 1897. — 15. **Yoshida, U.** and **Tanaka, S.:** The secondary and the tertiary figures produced on photographic plates by electric discharges. Mem. Coll. Sci. Kyoto Imp. Univ. Vol. 5, p. 145 (Fig. 10), Kyoto 1921/1922.

Tryckt den 24 januari 1953

Uppsala 1953. Almqvist & Wiksells Boktryckeri AB

ARKIV FÖR FYSIK Band 6 nr 18

Communicated 8 October 1952 by AXEL E. LINDH and IVAR WALLER

Some atomic planes in quartz suitable as lattices in X-ray spectroscopy

By GÖSTA BROGREN and LARS ERIK HAEGGBLOM

In an earlier communication (1) one of us pointed out the possibility of using some atomic planes in quartz as X-ray lattices. We have now investigated the atomic planes $11\bar{2}2$, $20\bar{2}3$, $30\bar{3}1$, and $22\bar{4}3$ with a tube spectrometer.[1] The methods of adjustment and measurement are described previously (2). The quartz plates used were cut and ground with the surfaces parallel to the actual planes. The slit width was 0.015 mm. Double exposures were made with the Cu $K\alpha_1$- or Mo $K\alpha_1$-line. The tube length was not the same in all recordings, so it is given beneath the tables.

The temperature corrections were calculated from the values of the linear expansion coefficient parallel to the axis, $\alpha_{11} = (7.161 + 0.0160\ t) \cdot 10^{-6}$, and that perpendicular to the axis, $\alpha_{\perp} = (13.255 + 0.0223\ t) \cdot 10^{-6}$, given by BENOIT (3). These are more accurate than those determined by JAY (4) with a Debye-Scherrer camera. The linear expansion coefficients perpendicular to the different atomic planes are all calculated at 20° C.

The results are given in Tables 1–4. In these the following designations are introduced:

t is the temperature in °C,
$2\,\varphi_0$ is the angle obtained from the readings on the angular scale,
a is the distance between the $K\alpha_1$-lines of the double exposures in mm,
$2\,\Delta\varphi$ is the angle computed from a and the length of the tube,
$\varphi_t = \varphi_0 + \Delta\varphi$ is the glancing angle at t° C,
$\Delta\varphi_t =$ is the temperature correction of the glancing angle,
φ_{18} is the glancing angle at 18° C.

The spacings are calculated by inserting the wave-length values $\lambda = 1537.399$ (5) X.U. for Cu $K\alpha_1$, and $\lambda = 707.831$ (3) X.U. for Mo $K\alpha_1$. The real interatomic distances were obtained from the relation

$$d_n = d\left(1 - \frac{4\,d^2}{n^2}\,\frac{\delta}{\lambda^2}\right),$$

where d_n is the lattice constant of the nth order,
$\delta = 1 - \mu$,
$\mu =$ the refractive index,
$\frac{\delta}{\lambda^2} = 3.64 \cdot 10^{-12}$ (6).

---

[1] The luminosity of the different planes, the nature of the quartz crystal and the influence of the surface treatment on the resolving power are the objects of another investigation to be published in the near future.

Table 1

Determination of the spacing of plane $11\bar{2}2$ with Cu Kα_1 in the first order

Plate No.	$2\varphi_0$	a mm	$2\Delta\varphi$	φ_t	t	$\Delta\varphi_t$	φ_{18}
1	50° 6′ 54″.8	+ 0.1900	1′ 45″.4	25° 4′ 20″.1	22°.3	4″.6	25° 4′ 24″.7
2	10 24 4	− 0.1900	1 45 4	19 5	22 6	4 8	24 3
3	10 1 1	− 0.1364	1 15 8	22 7	20 4	2 5	25 2
4	6 35 0	+ 0.2312	2 8 3	21 7	20 8	1 9	24 6
5	10 27 3	− 0.1814	1 40 7	23 3	20 2	2 3	25 6
6	6 52 7	+ 0.2019	1 52 1	22 4	20 6	2 8	25 2
7	6 52 6	+ 0.2022	1 52 3	22 5	20 1	2 2	24 7
8	9 56 5	− 0.1269	1 10 5	23 0	19 9	2 0	25 0
9	9 15 1	+ 0.2719	2 31 0	23 1	19 8	1 9	25 0
10	10 16 0	− 0.1649	1 31 6	22 2	20 9	3 0	25 2
11	10 10 1	− 0.1522	1 24 8	22 8	19 8	1 9	24 7
12	6 35 6	+ 0.2350	2 10 5	23 1	20 0	2 1	25 2
13	10 23 4	− 0.1771	1 38 4	22 5	20 3	2 5	25 0
						Mean value:	25° 4′ 25″.0

Tube length = 371.52 ± 0.05 mm
Linear expansion coefficient $\alpha = 10.9 \cdot 10^{-6}$
$\Delta\varphi_t'' = 2.25\,(t - 18)\,\mathrm{tg}\,\varphi$
$d_1 = 1813.902$ X.U.
$d_\infty = 1813.989$ X.U.
$d_{\mathrm{calc}} = 1813.99$ X.U.

Table 2

Determination of the spacing of plane $20\bar{2}3$ with Cu Kα_1 in the first order

Plate No.	$2\varphi_0$	a mm	$2\Delta\varphi$	φ_t	t	$\Delta\varphi_t$	φ_{18}
54	68° 8′ 8″.9	+ 0.0894	49″.7	34° 4′ 29″.7	20°.9	4″.1	34° 4′ 33″.4
55	10 22 2	− 0.1518	1′ 24 3	29 0	20 7	3 8	32 8
57	7 25 6	+ 0.1660	1 32 1	28 9	21 4	4 7	33 6
58	9 31 8	− 0.0624	34 6	28 6	21 3	4 6	33 2
59	10 24 7	− 0.1527	1 24 8	30 0	20 8	3 9	33 9
60	7 34 9	+ 0.1545	1 25 8	30 3	20 4	3 4	33 7
61	10 7 2	− 0.1214	1 7 4	29 9	20 6	3 7	33 6
62	7 0 7	+ 0.2159	1 59 9	30 3	20 3	3 2	33 5
63	10 54 5	− 0.2025	1 52 5	31 0	20 0	2 8	33 8
64	10 29 0	− 0.1601	1 28 9	30 1	19 8	2 5	32 6
65	7 30 0	+ 0.1673	1 32 8	31 4	19 7	2 3	33 7
66	7 10 7	+ 0.1988	1 50 4	30 6	19 8	2 5	33 1
						Mean value:	34° 4′ 33″.4

Tube length = 371.52 ± 0.05 mm
Linear expansion coefficient $\alpha = 10.1 \cdot 10^{-6}$
$\Delta\varphi_t = 2.09\,(t - 18)\,\mathrm{tg}\,\varphi$
$d_1 = 1371.965$ X.U.
$d_\infty = 1372.002$ X.U.
$d_{\mathrm{calc}} = 1372.00$ X.U.

Table 3

Determination of the spacing of plane $30\bar{3}1$ with Mo Kα_1 in the first order

Plate No.	$2\varphi_0$	a mm	$2\Delta\varphi$	φ_t	t	$\Delta\varphi_t$	φ_{18}
51001	29° 55′ 47″.3	+ 0.4772	2′ 7″.7	14° 58′ 57″.5	18°.8	0″.6	14° 58′ 58″.1
51002	59 59 0	− 0.4639	2 4 1	57 5	18 6	0 5	58 0
51003	55 46 8	+ 0.4777	2 7 9	57 4	18 7	0 5	57 9
51004	59 53 7	− 0.4434	1 58 5	57 6	18 6	0 5	58 1
51005	57 8 2	+ 0.1690	45 3	56 8	19 0	0 7	57 5
51006	59 12 6	− 0.2870	1 16 8	58 0	18 7	0 5	58 5
51007	58 48 8	− 0.2050	54 6	57 1	18 5	0 4	57 5
51008	56 56 8	+ 0.2200	58 8	57 8	18 6	0 5	58 4
						Mean value:	14° 58′ 58″.0

Tube length = 771.01 ± 0.05 mm
Linear expansion coefficient α = $13.3 \cdot 10^{-6}$
$\Delta\varphi_t'' = 2.74\,(t-18)\,\mathrm{tg}\,\varphi$
d_1 = 1368.961 X.U.
d_∞ = 1368.998 X.U.
d_{calc} = 1368.99 X.U.

Table 4

Determination of the spacing of plane $22\bar{4}3$ with Mo Kα_1 in the first order

Plate No.	$2\varphi_0$	a mm	$2\Delta\varphi$	φ_t	t	$\Delta\varphi_t$	φ_{18}
51020	40° 53′ 9″.4	+ 0.3098	1′ 22″.9	20° 27′ 16″.1	18°.5	0″.5	20° 27′ 16″.6
21	56 11 0	− 0.3745	1 40 2	15 4	18 5	0 5	15 9
22	53 37 4	+ 0.2066	55 3	16 4	18 7	0 7	17 1
23	55 38 7	− 0.2532	1 7 7	15 5	18 6	0 6	16 1
24	56 38 3	− 0.4775	2 7 8	15 3	18 6	0 6	15 9
25	52 16 6	+ 0.5070	2 15 6	16 1	18 5	0 5	16 6
26	53 18 2	+ 0.2744	1 13 3	15 8	18 5	0 5	16 3
27	55 49 5	− 0.2949	1 18 9	15 3	18 5	0 5	15 8
						Mean value:	20° 27′ 16″.4

Tube length = 771.01 ± 0.05 mm
Linear expansion coefficient α = $11.7 \cdot 10^{-6}$
$\Delta\varphi_t'' = 2.42\,(t-18)\,\mathrm{tg}\,\varphi$
d_1 = 1012.737 X.U.
d_∞ = 1012.752 X.U.
d_{calc} = 1012.75 X.U.

The spacing of atomic plane $50\bar{5}2$ was determined by means of a combination of a tube spectrometer and a curved crystal. A quartz plate, cut for transmission so that plane $50\bar{5}2$ was perpendicular to the surface of the crystal plate, was bent in a crystal holder to a radius of 1162 mm.[1] The usual holder for a plane crystal plate

---

[1] The value of the radius was determined optically in the common way.

Table 5

Determination of the spacing of plane $50\bar{5}2$ with Mo $K\alpha_1$ in the first order

Plate No.	$2\varphi_0$	a mm	$2\Delta\varphi$	φ_t	t	$\Delta\varphi_t$	φ_{18}
51100	51° 44′ 59″.0	+ 1.2084	3′ 58″.5	25° 54′ 29″.1	19°.2	1″.6	25° 54′ 30″.7
01	45 6 3	+ 1.1672	3 50 4	28 2	19 3	1 7	29 9
02	54 54 0	− 1.8136	5 58 0	28 0	19 1	1 5	29 5
03	53 52 6	− 1.5023	4 56 5	28 1	19 2	1 6	29 7
04	53 56 7	− 1.5180	4 59 6	28 6	18 9	1 2	29 8
05	53 6 4	− 1.2484	4 6 4	28 6	19 1	1 5	30 1
06	44 53 0	+ 1.2322	4 3 3	28 2	19 0	1 3	29 5
07	44 49 4	+ 1.2458	4 5 9	27 7	19 3	1 7	29 4
				Mean value			25° 54′ 29″.8
				Correction for the refraction			+ 0 2
				$\varphi\infty$			25° 54′ 30 0

"Tube length" = 1045.0 mm
Linear expansion coefficient α = $13.1 \cdot 10^{-6}$
$\Delta\varphi_t = 2.70\,(t - 18)\,\mathrm{tg}\,\varphi$
$d\,\infty = 810.000$ X.U.
$d_{\mathrm{calc}} = 810.00$ X.U.

was removed from the tube spectrometer, and a crystal table with the curved crystal was fixed there. The crystal holder was adjusted so that the centre of the crystal was in the axis of rotation, and so that its surface was parallel to the axis of rotation. The slit system in the front end of the very tube was taken away. An accurate value of the radius of curvature was determined by means of leaning plates. The length of the tube was adapted so as to obtain as sharp lines as possible when exposing with Mo $K\alpha_1$-radiation. The measurements were made in the common way with double exposures of the $K\alpha_1$-line. The tube length is in this case the distance from the centre of the crystal to the plate. This distance cannot be determined with the same accuracy as in the case of the common tube spectrometer. In our case the distance was 1045 ± 0.5 mm. The accuracy is about $\pm 0.05\,\%$. This error will influence the angular correction, which is calculated from the distance between the two Mo $K\alpha_1$-lines and the tube length. As this correction is, as a rule, less than 5′, the error is less than 0.2″. Since the exposures are made so that the above correction is positive in half of the recordings and negative in the other half, its influence is eliminated in the mean value. As appears from Table 5, the measuring accuracy seems to be good.

The advantage with this arrangement is that such a great increase in the luminosity of the instrument is obtained that it is possible to make absolute wave-length determinations even in the hard X-ray region. It is also possible to use crystal lattices with a rather low reflection power. The increase in luminosity is shown by the fact that when we exposed our plates for two minutes, the lines had a more intense blackening than what was obtained after eight hours' exposure in the common tube spectrometer under the same working conditions of the X-ray tube.

The accuracy of the present investigations is determined by the error in the glancing angle which was estimated to less than 1″, corresponding to a maximum error in the spacings of about 0.02 X.U.

Table 6

The wave-length of Zn Kα_1

Plate No.	$2\varphi_0$	a mm	$2\Delta\varphi$	φt	t^0	$\Delta\varphi_t$	φ_{18}	λ X.U.
21	46° 27′ 52″1	+0.2558	2′ 22″0	23° 15′ 7″1	20.3	2″2	23° 15′ 9″3	1432.206
22	28 13 2	+0.2195	2 1 9	7 6	20.4	2 3	9 9	215
24	32 5 6	−0.2029	1 52 6	6 5	21.0	2 9	9 4	206
25	29 2 0	+0.1336	1 14 2	8 1	20.0	1 9	10 0	216
26	31 53 3	−0.1800	1 40 0	6 7	20.8	2 7	9 4	207
27	31 18 3	−0.1134	1 2 9	7 7	20.1	2 0	9 7	211
							Mean value:	1432.210

As quartz is a hexagonal crystal the spacing d of atomic plane $(h\,k\,i\,l)$ can be calculated from the relation

$$d = \frac{1}{\sqrt{\frac{4}{3}\,\frac{h^2+k^2+hk}{a^2}+\frac{l^2}{c^2}}},$$

where a and c are the lengths of the axes.

As is to be seen in the tables the agreement between calculations and experiments is very good. The differences are in all cases less than the experimental limit of error. Since we used quartz plates from different sources, it seems to be proved that if quartz crystals of good quality are compared, the eventual variation of the axes lengths is so small that it cannot be detected within the experimental limit of error.

We also want to point out the necessity of a careful investigation of all crystal plates to be used as crystal gratings in X-ray spectrometers and spectrographs. During our work we sometimes found a variation in the value of the glancing angle that was larger than the limit of error. We suspected that, in those cases, we had two (or more) "crystallites" in the surface. A careful control of the crystals with a two-crystal spectrometer proved that this was the correct explanation. We obtained double peaks in the rocking curve, and the angular difference between the two peaks was in good agreement with the variations observed with the tube spectrometer.

Earlier Tu (7) made an investigation of the possibility of using quartz crystals in X-ray spectrometers, but found that they were not suitable for precise wave-length measurements. When using the same face on different crystals, or different faces with the same spacings on the same crystal (for instance $10\bar{1}0$ and $01\bar{1}0$) Tu obtained different results. The deviations were far beyond any experimental error. The probable reason is that there happened to be more than one crystallite in the surface.

We also used one of the crystal plates $(11\bar{2}2)$ for a redetermination of the wave-length of the Kα-lines of zinc. The Kα_1-line was determined by double exposures in the common way. The Kα_2-line was measured relatively to the Kα_1-line. As appears from Tables 6, 7, and 8, our values agree within the limit of error (0.020 X.U.) with those obtained by Bearden and Shaw (5).

Table 7

The wave-length of Zn Kα_2

Plate No.	distance Zn Kα_1—α_2		Glancing angle of Zn Kα_2	Wawe-length X. U.
	in mm	in angle		
31	0.4276	3′ 57″4	23° 19′ 7″0	1436.043
32	0.4269	57 0	6 6	.037
33	0.4274	57 3	6 9	.042
34	0.4272	57 2	6 8	.040
35	0.4277	57 5	7 1	.045
36	0.4279	57 6	7 2	.047
			Mean value:	1436.042

Table 8

Earlier determinations of the wave-lengths of Zn Kα_1 and Kα_2

Kα_1	Kα_2	
1432.00	1435.90	Lang 1924
1432.06	1435.87	Leide 1925
1432.07	1435.87	Schör 1926
1432.174	1436.032	Edlén 1928
1432.218	1436.047	Bearden and Shaw 1935
1432.210	1436.042	Brogren, Haeggblom 1952

The work has been supported financially by a grant from Statens Naturvetenskapliga Forskningsråd (The Swedish Council of Natural Sciences) to whom we are very greatful. We also want to express our gratitude to the head of the department, Prof. A. E. Lindh for his great interest in our work.

The Physical Institute, University of Uppsala, May 1952.

REFERENCES

1. G. Brogren, Nova Acta Reg. Soc. Sci. Ups. Ser IV, Vol. *14*, N:o 4, 1949.
2. A. Larsson, Phil. Mag. (7), *3*, 1136, 1927.
3. J. R. Benoit, Travaux et Memoires d. Bur. Int. des Poids et Mes. *6*, 1, 1888.
4. A. H. Jay, Proc. Roy. Soc. *A 142*, 237, 1933.
5. J. A. Bearden and S. H. Shaw, Phsy. Rev. *48*, 18, 1935.
6. A. Larsson, Uppsala Universitets Årsskrift 1928.
7. Y. Tu, Phys. Rev. *40*, 662, 1932.

Tryckt den 17 januari 1953

Uppsala 1953. Almqvist & Wiksells Boktryckeri AB

ARKIV FÖR FYSIK Band 6 nr 19

Communicated 4 June 1952 by Oskar Klein and Ivar Waller

Photodisintegration of the deuteron at high energies

By B. Bruno and S. Depken

With 1 figure in the text

Summary. The photodisintegration of the deuteron is treated in the energy range 80 to 250 MeV. Processes involving the exchange of virtual mesons are taken into account and shown to give important contributions. Total cross sections and angular distributions are discussed, and comparison is made with recent experimental results.

Introduction

Recently investigations have been reported from Berkely [7, 10] and Cornell [1, 11] on the disintegration of the deuteron by γ-quanta in the energy range of 80 to 270 MeV. The experimental results, which do not include production of free mesons, agree on the following behaviour of the total cross section as a function of the photon energy. The cross section drops off rather rapidly at 80 MeV, attains a minimum value of roughly 30 μ-barns somewhere around 150 MeV and then rises slowly at higher energies.

This disagrees with the steep decrease at the energies considered of the cross sections provided by or extrapolated from earlier calculations by Schiff [15] and Marshall and Guth [12]. The calculations are, however, admittedly not applicable for energies above 150 MeV or so, where free meson effects become important. For energies less than 150 MeV uncertainties are introduced by the neglect of magnetic dipole transitions, which owing to the contributions from meson currents cannot be taken into account without reference to a specific meson theory of nuclear forces.[1]

At all energies the exchange of mesons is, of course, essential for the photoeffect as giving rise to the interaction potential between the nucleons. Beside this it is, however, conceivable that at sufficiently high energies processes involving mesons may give important contributions to the cross sections. In this way it may be possible to account for the large experimental values.

An investigation of the meson effects upon the deuteron photoeffect at high energies has, therefore, been carried through. Ordinary perturbation theory has been used and pseudoscalar meson theory applied, since all evidence seems to be in favour of pseudoscalar π-mesons (cf. [5]). A preliminary report on the results, which are in reasonable agreement with experiments, has already been given [3].[1] In the report only processes, in which the photon was absorbed by a meson, were considered. It turns out, however, that contributions of the same order of magnitude will be obtained from processes consisting of the absorption of the photon by the proton *after* the exchange of a meson. The phase relations for the two processes are favourable thereby providing an increase of the cross sections. In view of this the argument for the pseudovector coupling form, as put forward in the report, is somewhat weakened.

---

[1] At lower energies the influence of the meson currents upon the magnetic dipole cross sections has been estimated by Pais [14] and Hansson and Hulthén [8]. The effect turns out to be small.

On account of the importance of meson effects the usual procedure of expanding the interaction energy in successive multipole moments of the system (cf. MØLLER and ROSENFELD [13]) is not suitable for our calculations. This is so, since the transformed interaction energy will in addition to the multipole terms contain a part consisting of the time derivative of an operator. This part has previously been neglected, as it will not contribute to matrix elements corresponding to transitions between states of the system with the same energy. This does, however, only apply to a first order perturbation calculus. In our case, where a possible exchange of mesons is explicitly taken into account, the considered part of the interaction energy will give important contributions.

General considerations

In the calculations the pseudoscalar coupling form of the pseudoscalar theory will be used. It is easily shown that with the approximations used the pseudovector coupling will afford identical results, if — in agreement with the equivalence considerations by DYSON [6] and CASE [4] — the pseudovector coupling constant multiplied by $\frac{2M}{m_\pi}$ (M = nucleon mass and $m_\pi = \pi$-meson mass) is substituted for the pseudoscalar coupling constant.

The interaction HAMILTONIAN for nucleons, charged mesons and photons can then be written as

$$H_{MN} + H_{AM} + H_{AN} \tag{1}$$

where

$$H_{MN} = \sqrt{4\pi}\, c\, g \sum_k \beta^{(k)} \gamma_5^{(k)} T_N^{(k)} U(\boldsymbol{r}^{(k)}) + \text{conj. compl.}$$

$$H_{AM} = \sqrt{4\pi} \int \left\{ \frac{iec}{\hbar} [U^* (\boldsymbol{A} \cdot \nabla U) - (\nabla U^* \cdot \boldsymbol{A})\, U] + \frac{e^2}{\hbar^2} A^2 U^* U \right\} d\tau$$

$$d\tau = dx_1\, dx_2\, dx_3$$

$$H_{AN} = -\sqrt{4\pi}\, e \sum_k \boldsymbol{\alpha}^{(k)} \cdot \boldsymbol{A}(\boldsymbol{r}^{(k)}) \cdot \frac{1 - \tau_3^{(k)}}{2} \cdot$$

---

[1] Calculations along similar lines have been briefly reported by HUDDLESTONE and LEPORE [9]. Their results seem to be in general agreement with ours. Using statistical arguments WILSON [16] has estimated the contributions from free meson effects and thus obtained cross sections of the right order of magnitude above the meson threshold.

Here U describes the charged meson field and $\boldsymbol{A}$ the electromagnetic field. β, $\boldsymbol{\alpha}$ and γ are DIRAC matrices and τ_3 an isotopic spin matrix of conventional type. T_N converts a neutron into a proton and indices k refer to the nucleons. For processes involving neutral mesons a term describing the interaction between the nucleons and the neutral mesons has to be added.

As the weak coupling approximation will be used, we will confine ourselves to processes, in which one meson at the most is emitted and reabsorped. The following possibilities are then to be considered:

A. The proton absorbs the photon. No virtual meson is exchanged.
B. The proton absorbs the photon and a meson is then exchanged.
C. The proton absorbs the photon after the exchange of a meson.
D. A meson is emitted, whereupon the proton absorbs the photon before the absorption of the meson.
E. The exchanged meson absorbs the photon.

Transitions involving the emission and reabsorption of the meson by the same nucleon will be neglected. Along with the usual selfenergy effects they contain the counterpart to the transitions caused by the interaction of low energetic photons with the anomalous magnetic moments of the nucleons. The "magnetic" transitions are, however, expected to give rapidly decreasing contributions at high energies (see furthermore below).

The cross section arising from process A will show a steep decrease at high energies, since it contains a factor giving the probability of finding the proton in the deuteron with momentum $\boldsymbol{p}-\boldsymbol{k}$, where $\boldsymbol{p}$ is the final momentum of the proton and $\boldsymbol{k}$ the momentum of the photon.

On the other hand, in the processes, where mesons take part, the necessarily high momentum of one of the nucleons in the first intermediate state can be counterbalanced by the emission in the first step of a meson with roughly the opposite momentum, thus causing an increase in the absolute value of the corresponding matrix element. Because of this the cross section will not at high energies show the same rapid decrease as that belonging to the direct process A.

The considerations do not, however, apply to process B, where the photon is absorbed and no meson, therefore, emitted in the first step. If the proton roughly overtakes the photon momentum, the corresponding matrix element being proportional to the projection of the proton momentum in the direction of polarization of the photon will become small. The contribution from this process will, therefore, be neglected.

Of the processes D and E the latter will be much more important, since the absorption of the photon by the meson instead of by the proton is favoured by the smaller meson mass. Process D may thus also be neglected. The remaining process C cannot, however, be neglected in comparison to process E on similar grounds, since the decrease in the absolute value of the matrix element because of the absorption of the photon by the proton is compensated by an increase owing to the fact that no meson is present in the second intermediate state and the corresponding energy denominator, consequently, much smaller.

Summing up, we will expect the processes involving virtual mesons to be important at high energies. Amongst these the main contributions will come from C and E, while the remaining ones may be neglected.

Evaluation of cross sections

In the calculations the nucleons are treated unrelativistically.[1] Plane waves are used in the intermediate and final states. The following notations are used. $\boldsymbol{k}$, $\boldsymbol{q}$, $\boldsymbol{p}$ and $\boldsymbol{p}'$ are the momenta of the photon and the emitted meson and the final momenta of the proton and the neutron, respectively. $\boldsymbol{e}$ is the unit vector in the direction of polarization of the photon. θ and θ' denote the angles between the direction of the outgoing proton and neutron, respectively, and the incident photon.

The ground state of the deuteron is described by the wave function

$$C\frac{e^{-\gamma r}-e^{-\beta r}}{r}\chi_S^m\eta_A^0;\quad C=\sqrt{\frac{\beta\gamma(\beta+\gamma)}{2\pi(\beta-\gamma)^2}} \tag{2}$$

where χ_S^m denotes the symmetrical spine wave function with magnetic number m and

$$\eta_A^0=\frac{1}{\sqrt{2}}(\eta_p^{(1)}\eta_n^{(2)}-\eta_n^{(1)}\eta_p^{(2)})$$

$\eta_p^{(k)}$ and $\eta_n^{(k)}$ describing the charge states of a proton and a neutron, respectively. Following SCHIFF [15] we put

$$\gamma=\frac{\sqrt{M\varepsilon}}{\hbar};\quad \beta=1.4\cdot10^{13}\ \text{cm}^{-1} \tag{3}$$

where $\varepsilon=2.2$ MeV is the binding energy of the deuteron.

The perturbation formula for the differential cross section runs

$$\sigma_d(\theta)=\frac{4\pi}{\hbar c}\varrho_{E_F}\sum|\mathfrak{M}|^2 \tag{4}$$

where $\mathfrak{M}$ is the matrix element of the transition and ϱ_{E_F} the density of states pro unit energy, the two possibilities of charge distribution in the final state being explicitly taken care of by a factor 2. The summation symbol indicates summation over all spin directions in the final state and averaging over the two directions of polarization of the photon and the three possible spin directions of the deuteron. Since the energy of the system in the laboratory frame is given by

---

[1] At the energies considered this is, of course, no good approximation. The errors thereby introduced are, however, thought to be of minor importance in view of other approximations.

$$E_F = \frac{p^2}{2\,M} + \frac{(\boldsymbol{p} - \boldsymbol{k})^2}{2\,M}$$

we get

$$\varrho_{E_F} = \frac{p^2\,M}{\hbar^3\,(2\,p - k\,\cos\,\theta)}. \tag{5}$$

For the direct transition A it is with our approximations readily found that in the case of unpolarized γ-rays

$$\sum |\mathfrak{M}_A|^2 = \frac{4\,\pi^2\,e^2\,\hbar^2\,\beta\,\gamma\,(\beta+\gamma)^3}{M^2\,k\,c} \cdot \frac{p^2\,\sin^2\,\theta}{\left[\gamma^2 + \frac{(\boldsymbol{p}-\boldsymbol{k})^2}{\hbar^2}\right]^2 \left[\beta^2 + \frac{(\boldsymbol{p}-\boldsymbol{k})^2}{\hbar^2}\right]^2}. \tag{6}$$

Calculations for process E. The third order transition consisting of the absorption of the photon by an emitted and reabsorbed, positive π-meson gives after some calculations — using (1) and (2) and identifying in the final state the nucleons with indices 1 and 2 as a proton and a neutron, respectively — the matrix element

$$\begin{aligned} K \int \chi_F^* \{F\,(\boldsymbol{q},\,\boldsymbol{p}')\,[\sigma^{(1)}\cdot(\boldsymbol{q}+\boldsymbol{k})]\,(\sigma^{(2)}\cdot\boldsymbol{q}) - \\ - G\,(\boldsymbol{q},\,\boldsymbol{p}')\,[\sigma^{(1)}\cdot(\boldsymbol{q}+\boldsymbol{k})]\,(\sigma^{(1)}\cdot\boldsymbol{q})\}\,\chi_S^m\,d\,q \end{aligned} \tag{7}$$

with

$$\begin{aligned} F\,(\boldsymbol{q},\,\boldsymbol{p}') = \\ = (\boldsymbol{e}\cdot\boldsymbol{q}) \left\{ \sqrt{k\,c}\,E_q\,E_{q+k} \left(E_q + \frac{p'^2}{2\,M} + \frac{(\boldsymbol{p}'+\boldsymbol{q})^2}{2\,M}\right) \left(E_{q+k} + \frac{p'^2}{2\,M} + \frac{(\boldsymbol{p}'+\boldsymbol{q})^2}{2\,M}\right) \right\}^{-1} \cdot \\ \cdot \left\{ \left[\beta^2 + \frac{(\boldsymbol{p}'+\boldsymbol{q})^2}{\hbar^2}\right] \left[\gamma^2 + \frac{(\boldsymbol{p}'+\boldsymbol{q})^2}{\hbar^2}\right] \right\}^{-1} \end{aligned} \tag{7 a}$$

$$G\,(\boldsymbol{q},\,\boldsymbol{p}') = F\,(\boldsymbol{q},\,\boldsymbol{p}')\,\frac{\left[\beta^2 + \frac{(\boldsymbol{p}'+\boldsymbol{q})^2}{\hbar^2}\right]\left[\gamma^2 + \frac{(\boldsymbol{p}'+\boldsymbol{q})^2}{\hbar^2}\right]}{\left[\beta^2 + \frac{p'^2}{\hbar^2}\right]\left[\gamma^2 + \frac{p'^2}{\hbar^2}\right]} \tag{7 b}$$

and

$$K = \frac{\sqrt{2\,\pi}}{16\,\pi^2} \cdot \frac{c^2\,g^2\,e}{M^2} \sqrt{\beta\,\gamma\,(\beta+\gamma)^3}. \tag{7 c}$$

χ_F is the spin wave function of the final state and

$$E_q = c\,\sqrt{m_\pi^2\,c^2 + q^2} \tag{7 d}$$

the energy of a meson with momentum $\boldsymbol{q}$.

Only the first part of the integral (7) containing F corresponds to process E. The second part is caused by transitions due to the "magnetic" interaction implying the emission and absorption of the meson by the same nucleon. After the subtraction of the divergent parts the remainder must be expected to give contributions of decreasing importance with increasing energies. This is so, since the possibility of diminishing the denominators of F containing β and γ by choosing $\boldsymbol{q} \approx -\boldsymbol{p}'$ does not apply to G as shown by the relation (7 b).

The matrix element corresponding to the exchange of a negative π-meson is obtained from (7) by interchanging indices 1 and 2, substituting $\boldsymbol{p}$ for $\boldsymbol{p}'$ and reversing sign. As $\boldsymbol{p}+\boldsymbol{p}'=\boldsymbol{k}$, it is readily seen that the substitution $\boldsymbol{q}=-\bar{\boldsymbol{q}}-\boldsymbol{k}$ will bring it back to the form (7) except for a small change in two of the energy denominators. The change is insignificant in our unrelativistic treatment of the nucleons. The full matrix element, $\mathfrak{M}_E$, arising from transitions E are thus obtained by multiplying (7) by 2 and neglecting the G-dependent part.

When calculating the cross section we shall sum $|\mathfrak{M}_E|^2$ over all spin directions in the final state and average over the three possible spin directions in the initial state. Thus we have to evaluate the expression

$$(8)\qquad \tfrac{1}{3}\sum_{m,F}\{\chi_F^{*}[\boldsymbol{\sigma}^{(1)}\cdot(\boldsymbol{q}+\boldsymbol{k})](\boldsymbol{\sigma}^{(2)}\cdot\boldsymbol{q})\,\chi_S^{m}\}\cdot\{\chi_S^{M*}\,[\boldsymbol{\sigma}^{(1)}\cdot(\boldsymbol{q}'+\boldsymbol{k})](\boldsymbol{\sigma}^{(2)}\cdot\boldsymbol{q}')\,\chi_F\}.$$

This is readily done by replacing χ_S^m by the equivalent function

$$\frac{\boldsymbol{S}^2}{2}\,\chi_S^m=\tfrac{1}{8}\,(\boldsymbol{\sigma}^{(1)}+\boldsymbol{\sigma}^{(2)})^2\,\chi_S^m.$$

Since $\boldsymbol{S}$ vanishes when operating on the singlet spin wave function, the summation can then be extended to all spin directions in the initial state. The expression (8) is thus equal to (Tr denoting the trace)

$$(9)\quad \tfrac{1}{6}\,\mathrm{Tr}\,\{[\boldsymbol{\sigma}^{(1)}\cdot(\boldsymbol{q}+\boldsymbol{k})](\boldsymbol{\sigma}^{(2)}\cdot\boldsymbol{q})\,\boldsymbol{S}^2\,[\boldsymbol{\sigma}^{(1)}\cdot(\boldsymbol{q}'+\boldsymbol{k})](\boldsymbol{\sigma}^{(2)}\cdot\boldsymbol{q}')\}=\tfrac{1}{3}\,\{4\,(\boldsymbol{q}\cdot\boldsymbol{q}')^2-q^2\,q'^{\,2}+$$
$$+4\,(\boldsymbol{q}\cdot\boldsymbol{k})\,(\boldsymbol{q}\cdot\boldsymbol{q}')+4\,(\boldsymbol{q}'\cdot\boldsymbol{k})\,(\boldsymbol{q}\cdot\boldsymbol{q}')-(\boldsymbol{q}'\cdot\boldsymbol{k})\,q^2-(\boldsymbol{q}\cdot\boldsymbol{k})\,q'^{\,2}+3\,(\boldsymbol{q}\cdot\boldsymbol{q}')\,k^2\}.$$

The important values of q and q' will be of the order of magnitude p. As $\frac{k}{p}\approx\frac{v}{c}$, where v is the velocity of the outgoing proton, the last term in (9) is of the same order of magnitude as the relativistic corrections $\left(\frac{v^2}{c^2}\right)$ and is consistently to be omitted. It can be shown that the contribution to the cross section from the part of (9) depending linearly upon $\boldsymbol{k}$ is a function of θ of the form $\cos\theta f(\sin\theta)$. It will not, therefore, affect the total cross section in our approximation but only the angular distribution. This effect can, however, be estimated — as will be shown below — more directly.

Thus, in calculating the total cross section we have only to consider the first two terms on the right side of (9). Moreover, in $\boldsymbol{F}(\boldsymbol{q},\boldsymbol{p}')$ $\boldsymbol{p}'$ can be replaced by $-\boldsymbol{p}$

and $\boldsymbol{k}$ omitted by similar reasons. In order to simplify the calculations the terms $\frac{p'^2}{2M}$ and $\frac{(\boldsymbol{p}'+\boldsymbol{q})^2}{2M}$ in the energy denominators are omitted, the relative error thereby introduced being of the order of magnitude $\frac{v}{c}$. We thus replace $F(\boldsymbol{q}, \boldsymbol{p}')$ by

$$\overline{F}(\boldsymbol{q}, \boldsymbol{p}) = -\frac{\boldsymbol{e}\cdot\boldsymbol{q}}{\hbar^4 \sqrt{h\,c}\,E_q^{\frac{1}{2}}\,[\beta^2 k^2 + (\boldsymbol{p}+\boldsymbol{q})^2]\,[\gamma^2 \hbar^2 + (\boldsymbol{p}+\boldsymbol{q})^2]}. \tag{10}$$

The total cross section will now be given by

$$\sigma_{\text{tot}} = \frac{4\pi}{\hbar c} \int_0^{\pi} \varrho_{E_F} \overline{I}\, 2\pi \sin\theta\, d\theta. \tag{11}$$

The bar indicates an averaging over the directions of polarization of the photon and

$$I = \frac{4K^2}{3} \int \overline{F}(\boldsymbol{q}, \boldsymbol{p})\, \overline{F}(\boldsymbol{q}', \boldsymbol{p})\, [4(\boldsymbol{q}\cdot\boldsymbol{q}')^2 - q^2 q'^2]\, d\boldsymbol{q}\, d\boldsymbol{q}'. \tag{12}$$

It is convenient to choose one of the directions $\boldsymbol{e}$ in the plane containing $\boldsymbol{p}$ and $\boldsymbol{k}$ and the other direction perpendicular to the same plane. Introducing polar coordinates for $\boldsymbol{q}$ and $\boldsymbol{q}'$ with Φ and Φ' denoting the angles between $\boldsymbol{q}$ and $\boldsymbol{p}$ and between $\boldsymbol{q}'$ and $\boldsymbol{p}$, respectively, we find after some calculations

$$\overline{I} = 2\pi^2 \{(4 I_1^2 - I_2^2) \sin^2\theta + 4 (I_2 - I_1)^2\} \tag{13}$$

where

$$I_1 = \frac{\hbar^4}{c^4 \sqrt{k\,c}} \int_0^{\infty}\int_0^{\pi} \frac{q^5 \cos^3\Phi \sin\Phi\, dq\, d\Phi}{N(q, \cos\Phi)} \tag{13 a}$$

$$I_2 = \frac{\hbar^4}{c^4 \sqrt{k\,c}} \int_0^{\infty}\int_0^{\pi} \frac{q^5 \cos\Phi \sin\Phi\, dq\, d\Phi}{N(q, \cos\Phi)} \tag{13 b}$$

with

$$N(q, \cos\Phi) = \tag{13 c}$$
$$= (m_\pi^2 c^2 + q^2)^2 (\beta^2 \hbar^2 + p^2 + 2pq\cos\Phi + q^2)(\gamma^2 \hbar^2 + p^2 + 2pq\cos\Phi + q^2).$$

It is easily seen that the integration over q can be extended to $-\infty$, if the integration over Φ is performed between 0 and $\frac{\pi}{2}$. The integration over

q can then be carried out by complex integration. The remaining integrations over Φ are elementary but tedious. In the indicated way we thus obtain

$$I_1 = -\frac{\pi \hbar^2 m_\pi}{4c^3(\beta^2-\gamma^2)\,p\sqrt{kc}}\,D_3 \tag{14 a}$$

$$I_2 = -\frac{\pi \hbar^2 m_\pi}{4c^3(\beta^2-\gamma^2)\,p\sqrt{kc}}\,D_1\,. \tag{14 b}$$

Here

$$D_3 = -\left[\tfrac{5}{2}+\frac{3}{2y}(\alpha_\beta-1)\right](1-\sqrt{\alpha_\beta})+\frac{y+\alpha_\beta-1}{y+\alpha_\beta+1+2\sqrt{\alpha_\beta}}+ \\ +\frac{3(y+\alpha_\beta-1)^2}{4y^{\frac{3}{2}}}\zeta_{\alpha_\beta}-(\text{the same expression with } \alpha_\beta\to\alpha_\gamma) \tag{15 a}$$

$$D_1 = \frac{y+\alpha_\beta+1}{y+\alpha_\beta+1+2\sqrt{\alpha_\beta}}+2\sqrt{\alpha_\beta}-\frac{y+\alpha_\beta-2}{\sqrt{y}}\zeta_{\alpha_\beta}- \\ -(\text{the same expression with } \alpha_\beta\to\alpha_\gamma) \tag{15 b}$$

with the abbreviating notations

$$\left\{\begin{aligned} &\alpha_\beta=\frac{\beta^2\hbar^2}{m_\pi^2c^2};\quad \alpha_\gamma=\frac{\gamma^2\hbar^2}{m_\pi^2c^2};\quad y=\frac{p^2}{m_\pi^2c^2} \\ &\zeta_{\alpha_\beta}=\operatorname{arctg}\frac{\sqrt{y}}{\sqrt{\alpha_\beta}}+\operatorname{arctg}\frac{(y+\alpha_\beta-1)\sqrt{y}}{y(2+\sqrt{\alpha_\beta})+\sqrt{\alpha_\beta}(1+\sqrt{\alpha_\beta})^2}\,. \end{aligned}\right. \tag{16}$$

Calculations for process C. In the process C a meson is exchanged and after that the proton absorbs the photon. The meson can be charged or neutral and the result depends upon the kind of coupling between neutral mesons and nucleons. If the symmetrical theory is applied, the matrix elements of charged and neutral mesons are in phase. The following total matrix element $\mathfrak{M}_C$ is then obtained:

$$\mathfrak{M}_C = 3K\int\{\chi_F^*(\boldsymbol{\sigma}^{(1)}\cdot\mathbf{q})(\boldsymbol{\sigma}^{(2)}\cdot\mathbf{q})\chi_S^m\}\,F_C(\mathbf{q},\mathbf{p}')\,d\mathbf{q} \tag{17}$$

with

$$F_C(\mathbf{q},\mathbf{p}') = -(\mathbf{e}\cdot\mathbf{p}')\left\{\sqrt{kc}\,E_q\left[E_q+\frac{p'^2}{2M}+\frac{(\mathbf{p}'+\mathbf{q})^2}{2M}\right]p'^2c^2\right\}^{-1}\cdot \\ \cdot\left\{\left[\beta^2+\frac{(\mathbf{p}'+\mathbf{q})^2}{\hbar^2}\right]\left[\gamma^2+\frac{(\mathbf{p}'+\mathbf{q})^2}{\hbar^2}\right]\right\}^{-1} \tag{17 a}$$

K and χ_F having the same meaning as before. By comparing (17) with the corresponding part of (7) we see, since $\mathbf{e}\cdot\mathbf{q}\approx-(\mathbf{e}\cdot\mathbf{p}')$, that the interference is essentially constructive.

The calculations of the total cross section can be carried out in a way similar to that applied to process E. Instead of the integrals I given by (13) we are met with the integrals

$$J_1 = \frac{\hbar^4}{c^4 p \sqrt{k c}} \int_0^\infty \int_0^\pi \frac{q^4 \cos^2 \Phi \sin \Phi \, d q \, d \Phi}{N_C(q, \cos \Phi)} \tag{18 a}$$

$$J_2 = \frac{\hbar^4}{c^4 p \sqrt{k c}} \int_0^\infty \int_0^\pi \frac{q^4 \sin \Phi \, d q \, d \Phi}{N_C(q, \cos \Phi)} \tag{18 b}$$

with

$$N_C(q, \cos \Phi) = \tag{18 c}$$

$$= (m_\pi^2 c^2 + q^2)(\beta^2 \hbar^2 + p^2 + 2 p q \cos \Phi + q^2)(\gamma^2 \hbar^2 + p^2 + 2 p q \cos \Phi + q^2).$$

We find

$$J_1 = \frac{\pi \hbar^2 m_\pi}{4 c^3 (\beta^2 - \gamma^2) p \sqrt{k c}} D_2 \tag{19 a}$$

$$J_2 = \frac{\pi \hbar^2 m_\pi}{4 c^3 (\beta^2 - \gamma^2) p \sqrt{k c}} D_0 \tag{19 b}$$

were using the notations (16)

$$D_2 = 2 \sqrt{\alpha_\beta} - \frac{y + \alpha_\beta - 1}{y} (1 - \sqrt{\alpha_\beta}) - \frac{(y + \alpha - 1)^2}{2 y \sqrt{y}} \zeta_{\alpha_\beta} - \tag{20 a}$$

$$- (\text{the same expression with } a_\beta \to \alpha_\gamma)$$

$$D_0 = 4 \sqrt{\alpha_\beta} - \frac{2}{\sqrt{y}} \zeta_{\alpha_\beta} - (\text{the same expression with } \alpha_\beta \to \alpha_\gamma). \tag{20 b}$$

Results

Total cross sections. Without going into further details of the calculations we will give the final expression for the total cross section arising from processes C and E. Using symmetrical meson theory we get

$$\sigma_{C+E} = \frac{1}{3 \cdot 2^{11} \pi} \cdot \left(\frac{g^2}{\hbar c}\right)^2 \cdot \frac{e^2}{\hbar c} \cdot \left(\frac{m_\pi}{M}\right)^2 \cdot \left(\frac{\hbar}{M c}\right)^2 \cdot \sqrt{\frac{\varepsilon}{M c^2}} \cdot \left(\frac{M c^2}{k c}\right)^{\frac{3}{2}} \cdot \tag{21}$$

$$\cdot \frac{\beta (\beta + \gamma)}{(\beta - \gamma)^2} \cdot (S_C + S_E + 2 S_{CE}).$$

Here S_C and S_E arise from the processes C and E, respectively, while $2\,S_{CE}$ is the interference term. We have

$$(22)\qquad \begin{cases} S_C \;\;= 3\,(D_0^2 + 6\,D_2^2 - 4\,D_0\,D_2) \\ S_E \;\;= 8\,(D_1 - D_3)^2 + \frac{4}{3}\,(4\,D_3^2 - D_1^2) \\ S_{CE} = 12\,D_3\,D_2 - 4\,D_3\,D_0 - 4\,D_1\,D_2 + 2\,D_0\,D_1 \end{cases}$$

the functions D_0, D_2, D_1 and D_3 being given by (20) and (15), where we have to put p^2 equal to its approximate mean value $M\,k\,c$.

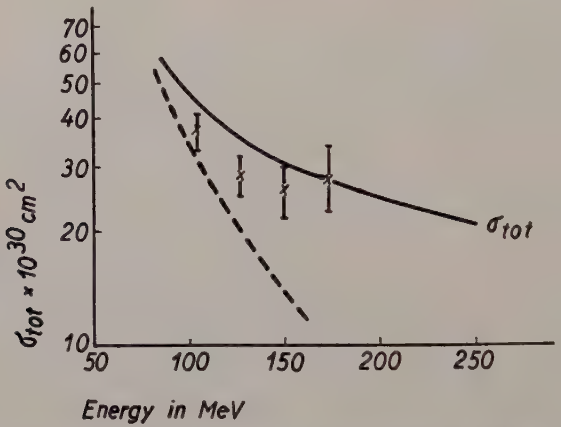

Fig. 1. Total photoelectric cross sections in the laboratory system. Experimental values are taken from BENEDICT and WOODWARD [1]. Dashed curve is the cross section calculated by MARSHALL and GUTH [12] for the direct transition.

In order to get the total cross section of the photoeffect (excluding meson production) we have to incorporate the contributions from the direct process A. The interference between the transition A and the transitions C and E is rather strong, and the phase relations are unfavourable. The total cross section is given in graphical form in fig. 1. The pseudoscalar coupling constant g was determined so as to give the experimental value of 30 μ-barns at 150 MeV. We find $g^2/\hbar\,c \approx 19$, which seems to be too large (cf. BETHE [2]). Better agreement is afforded by the pseudovector coupling form of the pseudoscalar theory. If f is the coupling constant, we have to put

$$f^2/\hbar\,c = (m_\pi/2\,M)^2 \cdot g^2/\hbar\,c \approx 0.10.$$

In view of the crude approximations reasonable agreement with experiments is obtained. The slow decrease at the high energy end in comparison with the mildly rising tendence according to the experiments [7, 10] may be understood as an effect of the relativistic corrections and of the exclusion of processes involving two or more mesons. Effects of heavier mesons may also contribute at these energies.

Angular distributions. The estimate of the angular distributions of the photoparticles at different energies is rather cumbersome because of the varied behaviour of the different processes. Without lengthy calculations it is, however, possible to get a rough idea of the state of things.

Using the conservation laws of energy and momentum and neglecting the binding energy of the deuteron we get

$$\left\{\begin{aligned} p &= \sqrt{M k c}\left(1+\tfrac{1}{2}\frac{v}{c}\cos\theta + 0\left(\frac{v^2}{c^2}\right)\right) \\ p' &= \sqrt{M k c}\left(1-\tfrac{1}{2}\frac{v}{c}\cos\theta + 0'\left(\frac{v^2}{c^2}\right)\right) \end{aligned}\right. \tag{23}$$

where v is the velocity of the ejected proton and the terms $0\,(v^2/c^2)$ and $0'\,(v^2/c^2)$ are of the order of magnitude v^2/c^2.

Neglecting terms in v^2/c^2, which are of the same order of magnitude as the relativistic corrections, we find from (4), (5) and (6) that the differential cross section of the direct transition depends upon θ by the factor

$$\sin^2\theta\,\frac{\left(1+\tfrac{1}{2}\frac{v}{c}\cos\theta\right)^4}{\left(1-\tfrac{1}{2}\frac{v}{c}\cos\theta\right)^4\left(1-\frac{v}{c}\,\frac{M k c}{M k c+\beta^2\hbar^2}\right)^2}. \tag{24}$$

The preference to the forward direction is, however, too strong to be consistent with experiments [1, 10]. In the centre of mass system the protons still favour the forward direction, while the neutrons, consequently, prefer the backward direction. This is due to the fact that the photon is absorbed by the proton.

On the other hand, in process E, in which the meson absorbs the photon, there will be no difference in the angular distributions of the protons and the neutrons. $\Sigma|\mathfrak{M}_E|^2$ as defined by (4) ($\mathfrak{M}_E$ being the matrix element of the transition E) is, therefore, the same function of θ as of θ'. The leading term is given by (13) (with $p^2 = M k c$), and the term in v/c is, as stated before, of the form $\cos\theta\, f(\sin\theta)$, where f can be shown to be at the most quadratic in $\sin\theta$. Omitting terms in v^2/c^2, $\Sigma|\mathfrak{M}_E|^2$ is consequently of the form

$$a\sin^2\theta + d + \frac{v}{c}(a_1\sin^2\theta + b_1\sin\theta + d_1)\cos\theta. \tag{25}$$

With the help of the relation

$$p'\sin\theta' = p\sin\theta$$

(25) can be expressed in θ'. We thus get

$$a \sin^2 \theta' \left(1 + 2\frac{v}{c} \cos \theta'\right) + d - \frac{v}{c}(a_1 \sin^2 \theta' + b_1 \sin \theta' + d_1) \cos \theta' =$$
$$= a \sin^2 \theta' + d + \frac{v}{c}(a_1 \sin^2 \theta' + b_1 \sin \theta' + d_1) \cos \theta'$$

giving $a_1 = a$ and $b_1 = d_1 = 0$. Using (13) and (14) and taking the statistical factor ϱ_E into account we thus find that the differential cross section depends on θ by the factor

$$\left(1 + \tfrac{1}{2}\frac{v}{c} \cos \theta\right)^2 \left[(4\,D_3^2 - D_1^2)\left(1 + \frac{v}{c} \cos \theta\right) \sin^2 \theta + 4\,(D_1 - D_3)^2\right] \tag{26}$$

where $4\,(D_1 - D_3)^2$ is rather small as compared with $4\,D_3^2 - D_1^2$. The preference for the forward direction is here much less accentuated than in the case of the direct transition and is too weak to fit the experimental results. In the centre of mass system the distribution is, of course, symmetric about 90°.

In the remaining process C the proton absorbs the photon (after the exchange of a meson). Because of the meson effects the forward direction is not favoured as much as in the case A but still considerably more than in the case E. $\Sigma\,|\mathfrak{M}_C|^2$, where $\mathfrak{M}_C$ is given by (17), is proportional to $S_C \cdot (\boldsymbol{e} \cdot \boldsymbol{p})^2 / p'^4$. In S_C (given by (22)) we have to substitute $p' = \sqrt{M\,k\,c}\left(1 - \tfrac{1}{2}\frac{v}{c} \cos \theta\right)$ for p. The differential cross section depends, therefore, upon θ by the factor

$$\frac{\left(1 + \tfrac{1}{2}\frac{v}{c} \cos \theta\right)^4}{\left(1 - \tfrac{1}{2}\frac{v}{c} \cos \theta\right)^4} \{S_C\}_{p \to p'} \tag{27}$$

where S_C that does not vary strongly with θ will favour the backward direction.

The preceding discussion shows that the superposition of the different processes may well produce angular distributions in reasonable agreement with experiments. BENEDICT and WOODWARD [1] have measured the differential cross sections $\sigma_d(\theta)$ at 60°, 90° and 120° in the energy range of 100 to 180 MeV. We have calculated $\sigma_d(60°)/\sigma_d(120°)$ at 150 MeV and obtained the value 3.6 as compared with the experimental value ≈ 3.2. In the energy range of 100 to 150 MeV the ratio considered is only increasing by some few tenths according to our estimates, while the experimental results seem to favour a larger increase. The discrepancy could possibly be explained as an effect of our neglect of the interaction between the nucleons in the final state, since this will probably imply an overestimation of the contributions from the direct transition.

Institute of Mathematical Physics, University of Stockholm, June 1952.

REFERENCES. [1] **Benedict** and **Woodward**, Phys. Rev. *85*, 924, 1952. — [2] **Bethe**, Phys. Rev. *76*, 191, 1949. — [3] **Bruno** and **Depken**, Phys, Rev. *86*, 1054, 1952. — [4] **Case**, Phys. Rev. *76*, 14, 1949. — [5] **Clark, Roberts** and **Wilson**, Phys. Rev. *83*, 649, 1952. — [6] **Dyson**, Phys. Rev. *73*, 992, 1948. — [7] **Gilbert** and **Rose**, Bull. Am. Phys. Soc. *26*, No. 8, 18, 1951. — [8] **Hansson** and **Hulthén**, Phys. Rev. *76*, 1163, 1949. — [9] **Huddlestone** and **Lepore**, Bull. Am. Phys. Soc. *27*, No. 3, 31, 1952. — [10] **Kikuchi**, Phys. Rev. *85*, 1062, 1952. — [11] **Littauer** and **Keck**, Bull. Am. Phys. Soc. *27*, No. 3, 19, 1952. — [12] **Marshall** and **Guth**, Phys. Rev. *78*, 738, 1950. — [13] **Møller** and **Rosenfeld**, Kgl. Danske Vid. Sels. Mat.-Fys. Medd. *20*, No. 12, 1943. — [14] **Pais**, Kgl. Danske Vid. Sels. Mat.-Fys. Medd. *20*, No. 17, 1943. — [15] **Schiff**, Phys. Rev. *78*, 733, 1950. — [16] **Wilson**, Phys. Rev. *86*, 125, 1952.

Tryckt den 17 januari 1953

Uppsala 1953. Almqvist & Wiksells Boktryckeri AB

ARKIV FÖR FYSIK Band 6 nr 20

Read 9 April 1952

On the solid-liquid transformation in metals

By G. Borelius

With 8 figures in the text

1. Summary

Thermodynamic calculations based on the assumption of continuity between the solid and liquid states and simple assumptions about the separation of the internal energy of metals into parts of vibrational and structural origin, lead to new possibilities of interpretation of the sub-coolability of liquid metals and of the thermal expansion phenomena.

2. Introduction and basic postulates

To-day there is a rather wide-spread conviction among physicists that there exist in the crystal lattices of solid metals, besides such disturbances which are due to impurities or coldworking, also lattice defects which are natural consequences of the thermal movements of the lattice and which increase in number or size with increasing temperature. It is also an attractive and fairly obvious idea, that the reversible lattice defects in the solid state should be a preparation on a small scale to what happens on a larger scale at the melting point, interpreting the fusion process as some kind of order-disorder transformation. Such lattice defects which increase with the temperature must be expected to give a contribution to the specific heat of the pure, undisturbed metal. It is a problem of fundamental interest how to separate this structural part of the specific heat from the part due to vibrations of the lattice. The purpose of the present paper is to show that it seems possible to make this separation without an elaborate atomic theory of fusion, just on the basis of two simple general postulates.

The first postulate is that there exists a continuous series of gemoetrically imaginable, though partly thermodynamically instable, structural states between the ordered structure of the crystal at low temperatures and the disordered liquid structures above the melting point, these states being defined by mutually connected values of structural energy and entropy.

The second postulate predicts that the vibrational part of the molar heat at constant low pressure is described in the liquid as well as in the solid state by a Debye function or some of the more complicated empirical functions proposed in the literature which at low temperatures represent the total molar heat and with rising temperature tends to exactly the classical value of three times the gas constant ($3\ R$).

These postulates are made on trial and their justification is dependent on the results which can be obtained from them by a purely thermodynamic investigation. Before we go into the thermodynamic applications in section 4, it might be of interest to look at some questions related to these postulates from a more general and historical point of view.

3. General discussion of the postulates

Our first postulate involves taking up a position with regard to a question often discussed. Ever since the continuity between the liquid and gaseous states was demonstrated by the theory of VAN DER WAALS, it has probably occurred to many physicists that there might be a similar continuity between the solid and liquid states, and the discussion has been stimulated by the development of the order-disorder transformations in alloys, first discussed by the author and this collaborators, and of other phenomena which have later been interpreted as disordering transitions. A rather superficial glance at the literature shows that among others POYNTING (1), PLANCK (2), KAMERLINGH ONNES (3) and FRENKEL (4) have looked upon continuity between the solid and liquid states as possible, whereas it has been judged as impossible or at least improbable by ROOZEBOOM (5), TAMMANN (6) and BRIDGMAN (7). BRIDGMAN's discussion is worth a special consideration as he bases his opinion on extensive experimental results obtained by his own measurements at high pressures. The question he discusses is whether or not there exists a critical point for the transition from liquid to solid state, above which this transition is continuous. In no case was such a critical point found below the maximum pressure of 12000 atmospheres used for these experiments. The discussion is thus about the right way of extrapolation. BRIDGMAN's chief argument for denying a critical point seems to be that the decrease in the change of volume on fusion with increasing pressure is somewhat retarded. However, in the opinion of the present author, BRIDGMAN's arguments are not convincing. In fact even in the case of the transition from gas to liquid the decrease in the change of volume with increasing pressure is retarded at pressures far below the critical pressure and becomes accelerated fairly near the critical point.

There seem so far to be no serious objections to the use of an assumption of continuity as a working hypothesis. It is obvious, however, that such continuity is limited to simple metals and cannot be generally valid, as shown immediately by the existence of polymorphism in the solid state. The liquid is not necessarily structurally connected even to that solid state, which at low pressure is the stable one nearest below the melting point. Thus, for instance, liquid bismuth is most probably not structurally connected to the ordinary rhombohedral solid phase, which has a lower density than the liquid itself.

The second postulate involves a repudiation of the usual way of looking at the specific heat of solids. Since in 1907 LEWIS (8) found his well known formula for computing the molar heat of a solid at constant volume C_v from the observed molar heat at constant pressure C_p, all who have worked on the theory of the heat capacity of solids seem to have compared their results with the empirical values of C_v. One would believe that the meaning of a procedure so generally accepted should have been discussed thoroughly from a theoretical point of view. This seems, however, not to be the case. One cannot but suspect that many physicists have drawn an ill-considered parallel from the theory of gases, where the difference between C_p and

C_v means the energy used for external work, and of solids where C_p, if measured in the usual way at practically zero pressure, involves no appreciable contribution from external work and thus is already a measure of increase of internal energy only. Even if the internal energy were of vibrational origin only, there is no well-founded reason why the lattice vibrations should depend in a simpler way on temperature, if the volume is kept constant by applying heavy pressures, than if the lattice is allowed to expand in the way it does at zero pressure. And if, as we now assume, the heat capacity and thermal expansion are partly due to structural changes, the correction from C_p to C_v involves a rather confusing complication. In fact, there are no such results obtained by considering C_v instead of C_p that they should prevent us from trying other ways of attacking the problem.

Our postulate that the vibrational part of C_p should be given by a function similar to the Debye function involves the simplification that the vibrational energy is a function of the temperature only and so completely independent of the structure that it is unchanged in the solid and liquid states at the melting point. Though in the following we are dependent on this assumption only at high temperatures where the vibrational part of the molar heat is rather near to the classical value of $3\,R$, it is of interest to note that a wider validity of this simplification can be inferred from measurements of the specific heats of substances which can be investigated both in the crystalline and in the vitreous state. Of such substances selenium, which has been discussed earlier by the present writer (9) is the one nearest comparable with the metals. Here ANDERSON (10) found, within the limits of experimental errors, the same specific heat for the crystalline and the vitreous states from room temperature down to —100° C. In this range of temperature the vibrational part of the specific heat dominates both in the crystalline selenium and in the vitreous selenium, which has the structure of supercooled liquid selenium frozen at the "glass point" at about 30° C. Thus it seems likely that we can use the same function for the vibrational specific heat for the solid and liquid (amorphous) states with a probable exception of the lowest temperatures where there occur mainly long wave vibrations, which may be supposed to be more sensitive to structural variations. The very low temperatures, however, are of less importance from our present point of view.

Besides the contributions to the molar heat from the structural and vibrational energy metals have also a small contribution from the free electrons. In accordance with the elctron gas theory, measurements at very low temperature have shown this contribution to be proportional to the absolute temperature.

4. Thermodynamic functions

According to our postulates and what was said in the preceding section, there exists a structural part C_s of the molar heat which is given by the formula

$$C_s = C_p - C_D - \gamma T \tag{1}$$

where C_p is the observed molar heat at constant, practically zero, pressure, C_D in the simplest cases a Debye function with a value of the characteristic temperature Θ determined from the temperature dependence of the specific heat at low temperatures, and γT the small contribution from the heat of the free electrons which is proportional to the absolute temperature T, the constant γ being known for a few metals from measurements at very low temperatures. As the vibrational energy is supposed to be a function of the temperature only, the heat of fusion L at the melting point T_m is entirely of structural origin, and the structural energy per mol of the solid at a temperature T is given by

$$U_s = \int_0^T C_s \, dT \tag{2}$$

and that of the liquid by

$$U_s = \int_0^{T_m} C_s \, dT + L + \int_{T_m}^{T} C_s \, dT. \tag{3}$$

In a similar way we obtain the structural part of the molar entropy of the solid

$$S_s = \int_0^T \frac{C_s}{T} \, dT \tag{4}$$

and that of the liquid

$$S_s = \int_0^{T_m} \frac{C_s}{T} \, dT + \frac{L}{T_m} + \int_{T_m}^{T} \frac{C_s}{T} \, dT. \tag{5}$$

The structural state of equilibrium is determined by the condition that the termodynamic potential which, when the pressure is practically zero, may be replaced by the free energy, has to be a minimum. The molar free energy may be written

$$F = F(T) + U_s - T S_s \tag{6}$$

where $F(T)$ contains the vibrational and electronic parts which are functions of the temperature only, and U_s and S_s are the structural parts of energy and entropy which, mutually connected, describe various geometrically possible structural states. The state of equilibrium at any temperature is given by the condition that F has to be a minimum. The derivative of F with respect to any variable describing the structure thus has to be zero, and we obtain from eq. (6) as a first condition for equilibrium

$$\frac{dU_s}{dS_s} = T. \tag{7}$$

A necessary condition for a minimum is that the second derivative is positive. Taking S_s as the independent variable we get

$$\left(\frac{\partial^2 F}{\partial S_s^2}\right)_T = \frac{d}{dS_s}\left(\frac{dU_s}{dS_s}\right) = \frac{dT}{dS_s} > 0 \tag{8}$$

where dT and dS_s are variations of T and S_s connected on the condition of equilibrium. The equilibrium values of U_s and S_s are obtained empirically by eqs. (1) to (5).

5. Continuation of the solid-liquid transition

A first test on our postulates is obtained by an examination whether the structural energy U_s and the structural entropy S_s determined from experiments by means of the formulae of the preceding section are mutually connected in such a way in the stable states, below and above the melting point, that a simple continuation through the range of instable states is possible. Instead of using for this purpose an U_s–S_s-diagram (such a diagram will be shown later in fig. 6) we have found it more convenient to use a diagram with S_s as a function of the derivative $d\,U_s/d\,S_s$, which according to equation (7) in the stable ranges is equal to the temperature T.

Unfortunately there are only three metals, mercury, lead and tin, for which the molar heat C_p has been measured both below and above the melting point with the accuracy necessary for our purposes.

In the case of Hg a recent work of PICKARD and SIMON (11) contains all the needed data from the lowest temperatures up to 300 °K, the melting point being 234.4 °K. For the range of temperature from the melting point up to 450 °K we have also taken into account results of RANDALL and LANGFORD (12). The vibrational part of the molar heat has been calculated by means of an empiric, two-term expression found by PICKARD and SIMON to describe the molar heat at low temperatures and consisting of the sum of a Debye function (characteristic temperature of $\Theta = 120°$) and an Einstein function ($\Theta = 25°$) or

$$C = \tfrac{3}{4}\ \text{Debye}\ (120) + \tfrac{1}{4}\ \text{Einstein}\ (25).$$

The electronic part of the molar heat is not known for Hg. Probably it is small, and it has not been taken into account in our calculations.

For Pb at low temperatures we have used the values given by EUCKEN in the tables of LANDOLT-BÖRNSTEIN (13), and in the range from 300 to 800 °K, on both sides of the melting point at 600 °K, the results of measurements by KLINKHARDT (14). According to EUCKEN the vibrational part of the molar heat is calculated by means of a Debye function with $\Theta = 88$. From the measurements of KEESOM and VAN DEN ENDE (15) at very low temperatures we have concluded that the electronic part, which is not exactly determined, is small and it has not been taken into account.

For Sn in the low temperature range we have again used the values of EUCKEN from the tables of LANDOLT-BÖRNSTEIN (13), and for a range from 250 to 850 °K on both sides of the melting point at 505 °K the measurements of KLINKHARDT (14). KLINKHARDT's results for Sn are only given by a diagram from which we have reproduced the original values by means of a measuring microscope. According to KEESOM and VAN LAER (16) the electronic contribution to the molar heat is 0.00040 T cal/degree and the contribution from the atomic vibrations is given by a Debye function with $\Theta = 185$. The entropy curve for low temperatures is probably somewhat unreliable and the entropy values at higher temperatures may be affected with a small constant error which, however, is of no importance for our main problem.

In the diagrams of fig. 1, 2 and 3 the entropy values obtained from the experimental data below and above the melting point are given by the crosses and the fully drawn lines AB and FG. These lines are such that they are easily connected by a continuous curve BCDEF, which has been calculated in the following way. We have taken as origin the point B, where the temperature is that of the melting

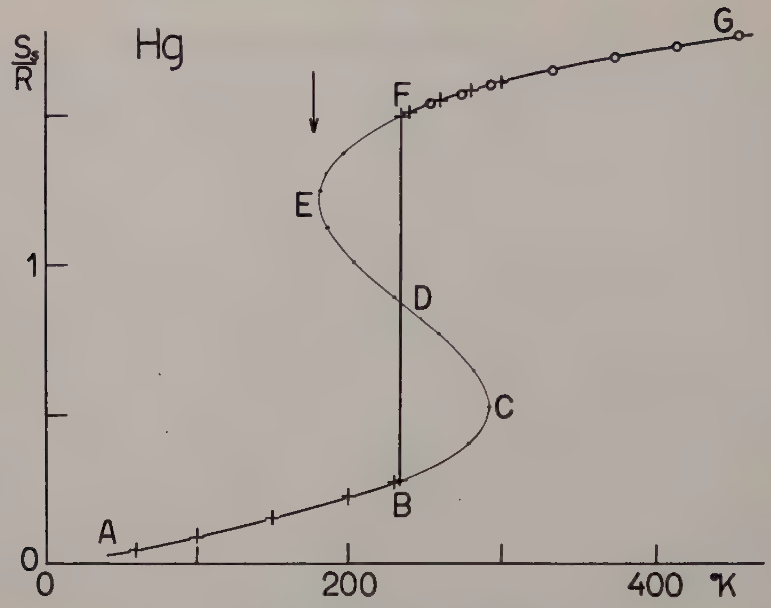

Fig. 1. Structural entropy versus temperature for Hg.

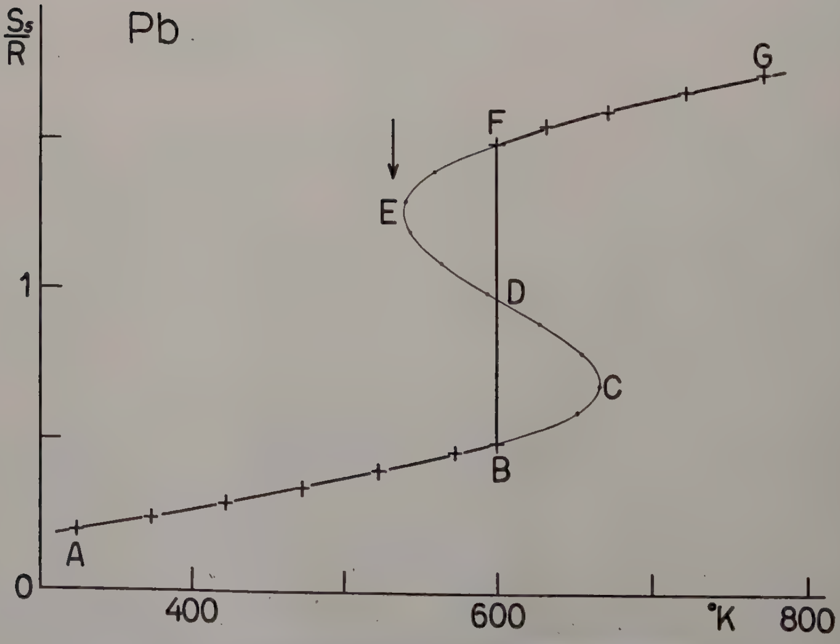

Fig. 2. Structural entropy versus temperature for Pb.

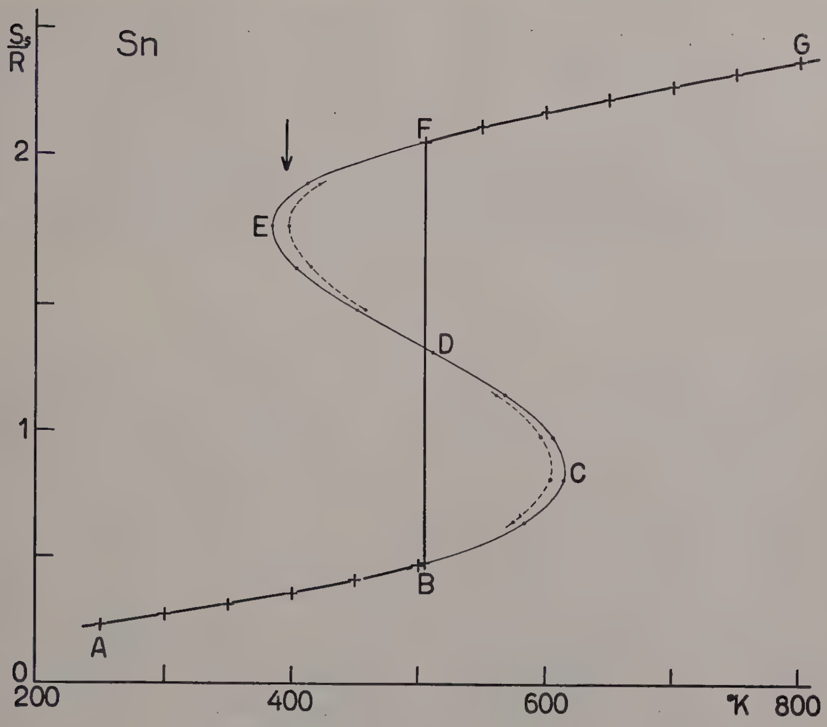

Fig. 3. Structural entropy versus temperature for Sn.

point T_m and the structural entropy that of the solid at the melting point S_m. Our variables thus are the differences $\tau = T - T_m$ and $\sigma = S_s - S_m$. These variables have to obey the following conditions. At $\sigma = 0$ we have $\tau = 0$ and $d\tau/d\sigma$ has to equal the empirical value $\alpha = dT/dS_s$ of the solid. At $\sigma = \Delta$, where Δ is the increase in entropy at fusion, we have $\tau = 0$ and $d\tau/d\sigma$ has to equal the empirical value $\beta = dT/dS_s$ of the liquid metal. A further condition is that the variation of internal energy along the line BCDEF has to be the same as directly along BDF. As the energy in a T–S-diagram is given by the areas, this condition means that the area BCDB has to equal the area DEFD or

$$\int_0^\Delta \tau \, d\sigma = 0.$$

These five conditions are satisfied, as found by simple calculations, by the formula

$$\frac{\tau}{\Delta} = \alpha \frac{\sigma}{\Delta} - \frac{9\alpha - 3\beta}{2}\left(\frac{\sigma}{\Delta}\right)^2 + (6\alpha - 4\beta)\left(\frac{\sigma}{\Delta}\right)^3 - \frac{5\alpha - 5\beta}{2}\left(\frac{\sigma}{\Delta}\right)^4. \tag{9}$$

The values obtained by this formula with values of σ/Δ from 0.1 to 0.9 are marked by dots on the extrapolated curves in the figures. Because of the special conditions for the formula the curves are probably quite reliable in spite of the fact that we could not expect an elaborate statistic theory to describe the transformation phenomenon by an algebraic function.

In the case of Sn we have also made a calculation including the electronic energy in the structural, as we were forced to do in the cases of Hg and Pb. Parts of the curves obtained in this way are shown by dotted lines in fig. 3. From the differences between this curve and the others we conclude that if a similar electronic part had been taken into account in the case of Hg and Pb, the temperature minimum at E would have been displaced a few degrees towards lower temperatures.

6. The sub-coolability of liquid metals

Of the curves in the figures 1, 2 and 3 the parts BC and FE, which have positive values of the derivative dT/dS_s and thus satisfy the condition of formula (8), correspond to thermodynamically metastable states. The part BC should correspond to a superheated solid state, which as is well known, is not realizable, probably because the crystal surfaces act as nuclei for the liquid state. The part FE corresponds to the sub-cooled liquid state. As the part EDC with negative values of d^2U_s/dS_s^2 corresponds to thermodynamically instable states, the temperature at the point E means a lower limit of ordinary metastable sub-cooling.

According to views held by the present author in discussions on sub-coolability in connection with disorder-order transformations and precipitation phenomena, the velocity of nucleation should increase rapidly when the temperature is lowered below the lower limit of thermodynamic metastability. In fact there is also in the present case, of liquid-solid transformation, a striking coincidence between the lower limit of metastability as calculated on the basis of our postulates, and the temperatures below which nucleation in the sub-cooled liquid metals is known from experiments to proceed with high velocity. On this subject valuable experimental information is to be had from recent studies by VONNEGUT (17), TURNBULL (18) and TURNBULL and CESH (19) on the ability to sub-cool of a number of pure metals in the form of small droplets. The dividing of the metals into droplets means isolating in a small number of the droplets the foreign particles, which already at slight sub-cooling act as crystallization nuclei. The rest of the droplets can be sub-cooled without crystallizing down to a fairly well defined temperature which, properly determined, seems to be a characteristic property of the metal itself. The distance of this lower limit of sub-cooling from the melting point was found to vary from 13 to 25 per cent of the absolute temperature of the melting point. The limits obtained for mercury, lead and tin are marked as arrows in our figures 1, 2 and 3. The differences between the empiric lower limits of sub-cooling and our calculated lower limits are within the limits of the uncertainty of the experimental data on which our calculations are based.

FISCHER, HOLLOMON and TURNBULL (20) have already tried another interpretation of these phenomena on the basis of a hypothesis, which was used in other fields of phase transitions by GIBBS and VOLMER and first applied to transformations in metals by BECKER (21), namely the hypothesis that the limiting phenomenon of nucleation is a surface energy of the nucleus. On this assumption they have calculated from the results of sub-cooling, the surface energy of the contact boundaries between solid and liquid metal phases. For a further test, however, this interpretation would need an independent determination of such surface energies. At least so far, the conception of surface energy has not been able to connect the sub-cooling phenomena with experimental results from other fields in such a simple way as the interpretation given in the present paper.

7. Specific heat of liquid metals in the sub-cooled state

If the diagrams of the figures 1–3 are right in principle, the derivative dT/dS_s has to approach zero when the temperature of the sub-cooled liquid is lowered towards the lower limit of metastability at E. Since in the ranges of temperature where the liquid is stable or metastable dS_s, according to the definition of entropy, is equal to $C_s dT/T$, we must expect T/C_s to approach zero at the limit E.

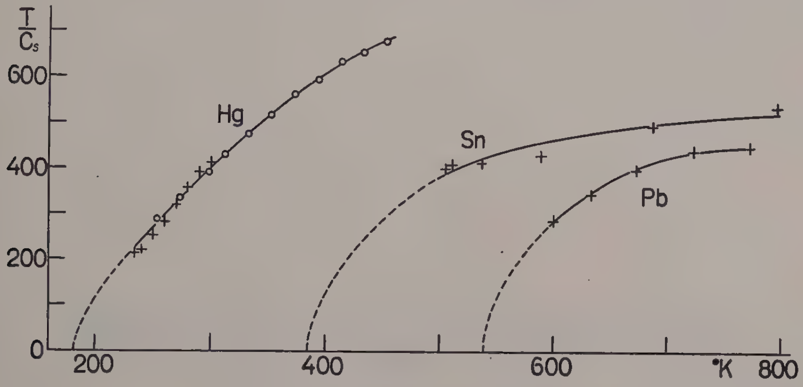

Fig. 4. dT/dS_s versus temperature.

Fig. 4 shows for Hg, Pb and Sn, the empirical values of T/C_s in the ranges above the melting points as a function of temperature and also the dotted continuations of the curves, extrapolated below the melting points according to the curves in the figures 1, 2 and 3. In the case of Hg the slope of the experimental curve indicates a lower limit of metastability somewhere in the neighbourhood of the empirical lower limit of sub-cooling. In this case the coincidence is thus independent of the assumption of continuity between the liquid and solid states and is made probable by the properties of the liquid only. On the other hand, in the case of Pb and especially Sn such a coincidence could scarcely be predicted without the aid of the assumption of continuity.

For the sub-cooled liquid we should expect, if the extrapolations of fig. 4 are correct, an accelerated increase of the specific heat. A determination of the specific heat of sub-cooled liquid metals, which may be difficult but probably not impossible, should thus give a conclusive test of the existence of a lower limit of thermodynamic metastability.

8. The structural energy

In section 5 we used an entropy-temperature diagram as the best one for calculating a curve describing the continuity of the transformation. The laws regulating the structural transition are, however, as well or more simply demonstrated by means

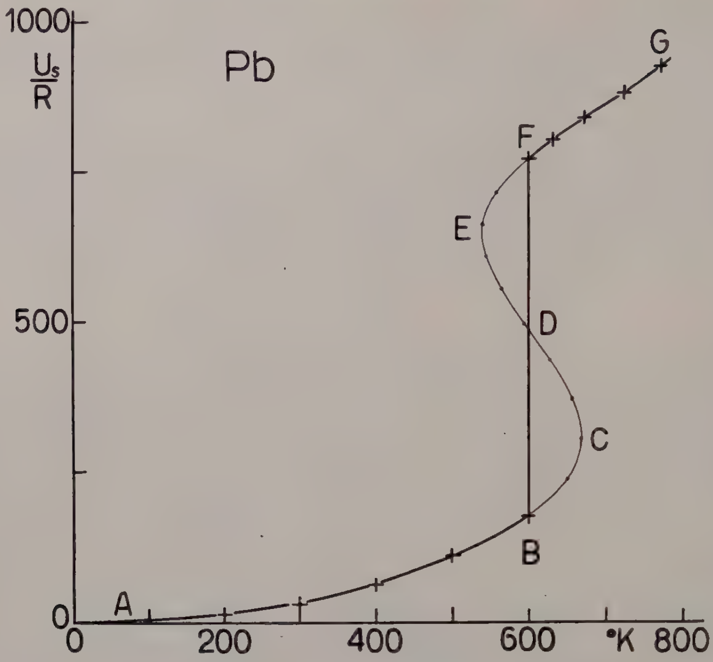

Fig. 5. Structural energy versus temperature for Pb.

of an energy-temperature diagram. Fig. 5 shows the values of U_s as calculated from empirical data for Pb plotted against T. Of this curve the parts AB and FG are obtained from empirical data according to eqs. (2) and (3), and the part BCDEF is calculated in accordance with the calculated continuation in fig. 1. Corresponding diagrams for Hg and Sn show the same principal features. Such diagrams may be a useful guidance for attempts towards a statistical theory of the fusion phenomena. It is of special interest to notice the difference between the curve of fig. 5 and a corresponding diagram in the case of an order-disorder transformation in an alloy. In that case the structural energy above the critical point approaches a constant limiting value, representing the full disorder, whereas in the case of liquid metals the structural energy increases approximately proportionally to the absolute temperature.

The aim of a statistic theory of the phenomena of fusion will probably be to find the energy U_s and the entropy S_s as functions of a suitable structural parameter. The mutually connected values of U_s and S_s will then, if our phenomenological description is correct, have to give a diagram like that shown in fig. 6 for Pb. The positive derivates dU_s/dS_s represent the temperature. The slope of the common tangent is the absolute temperature of the melting point.

9. Dependence of the thermal expansion on the internal energy

As shown long ago by GRÜNEISEN (22), there is a close relationship between the thermal expansion of a metal and its internal energy. At low temperatures the increase in volume above the volume at the absolute zero point is simply pro-

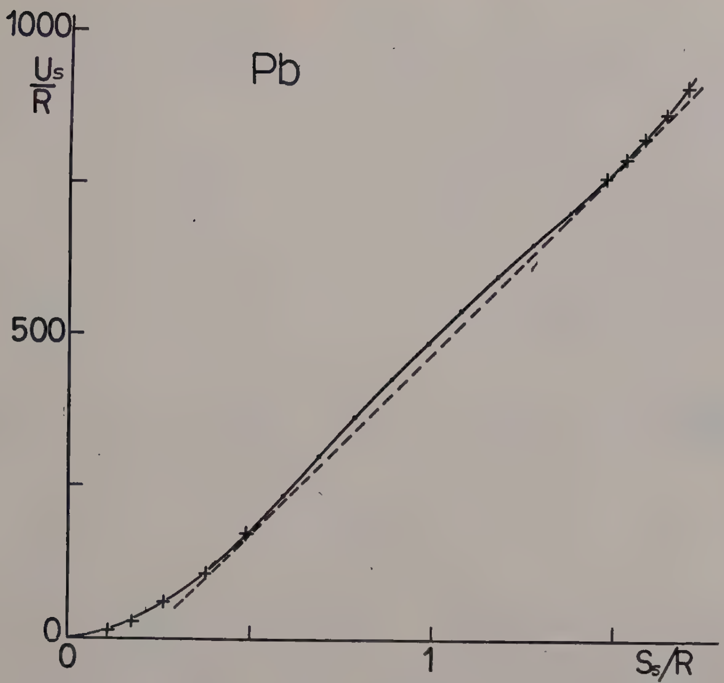

Fig. 6. Structural energy versus structural entropy for Pb.

portional to the increase of internal energy which at these low temperatures is predominately of vibrational origin. At higher temperature the increase in volume is greater than should be expected from this proportionality, and GRÜNEISEN has described this increase by well-known semi-empirical formulae. GRÜNEISEN confined himself, however, to the solid state, and his discussion does not include the change of volume at fusion and in the liquid state. From our present point of view it is tempting to ascribe this excess increase of volume including that of fusion to the structural part of energy, separated from the vibrational part by our basic assumption. The simplest possible working hypothesis would be that the total increase of volume is a sum of two parts, one proportional to the vibrational energy, and the other proportional to the structural energy. According to this hypothesis, we should have for the variations of the volume V the formula

$$\frac{V-V_0}{V_0}=a\frac{U_D}{R}+b\frac{U_s}{R} \tag{9}$$

where V_0 is the volume at absolute zero temperature, and a and b are empirical constants with the dimension of the reciprocal of temperature.

As shown by figure 7, formula (9) is well satisfied in the case of Pb. The lower diagram for the internal energy is obtained from the sources already mentioned in section 5. The sources for calculating the values of the volumes marked by crosses in the upper diagram have been, for temperatures below zero and up to 100° C, expansion measurements by EBERT (23) and GRÜNEISEN (22), for temperatures

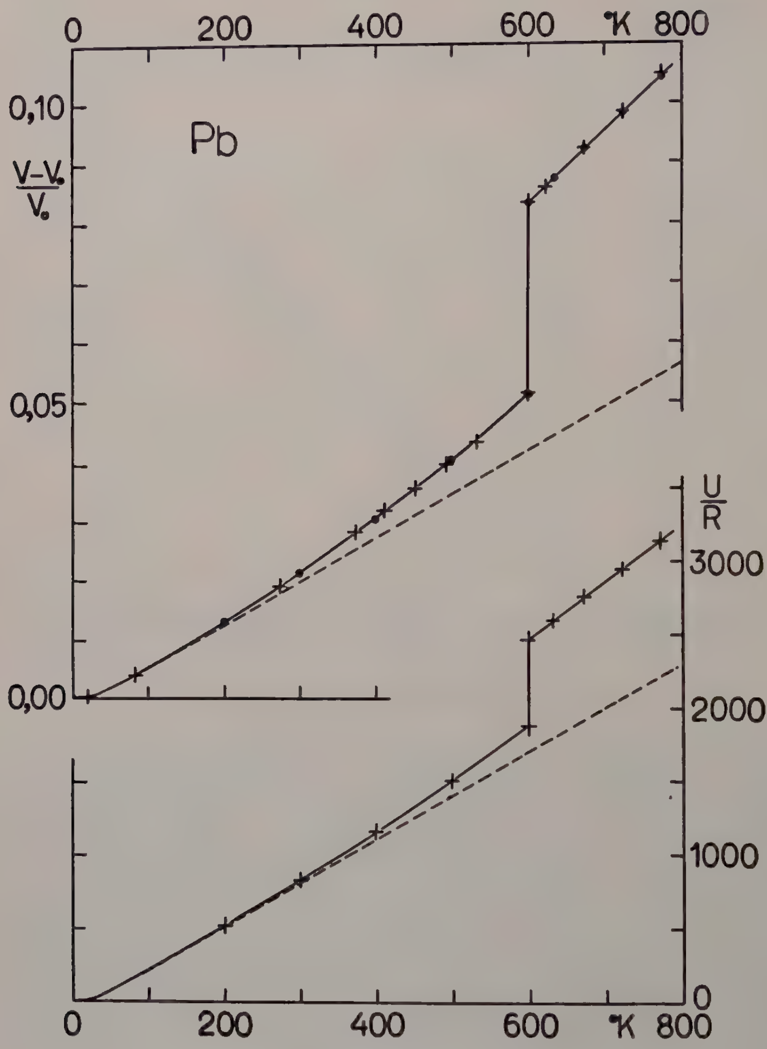

Fig. 7. Volume expansion compared with internal energy for Pb.

from 100 to 300° C measurements by UFFELMANN (24), above the melting point, density measurements by DAY, SOSMAN and HOSTETTER (25), and just below the melting point a density measurement by VICENTINI and OMODEI (26). The values calculated from eq. (9) with $a = 24.7 \times 10^{-6}$ and $b = 53.7 \times 10^{-6}$ are marked by dots. The scales of the diagrams are chosen in such a way that the calculated vibrational parts of the internal energy and volume marked by the dotted lines have the same size in both diagrams.

For the present, Pb seems to be the only metal for which we have sufficiently good experimental data for a full test of eq. (9). In the case of Hg and Sn there are measurements of the same kind as for Pb. As, however, these metals have non-cubic lattices with different coefficients of expansion parallel to and at right angles to the hexagonal or tetragonal axis, measurements of expansion coefficients on poly-crystalline specimens do not give reliable results about the real volume changes of the lattice. This fact has been clearly demonstrated by the present author in the case of selenium (9). Especially at low temperatures expansion measurements on single crystals or by X-ray methods are very much needed. In the cases of Al, Ag and Au, which have also been examined, measurements of the internal energy in the liquid state, which are rather difficult to perform, have so far only been made as an orientation for technical purposes. Concerning the liquid state the only conclusion to be made for the present is, that in all these cases an agreement with our formula is possible within the limits of the probable uncertainty of the experimental results.

In the case of solid copper we can, however, use extensive and concordant results of different authors on the thermal expansion and specific heat for a sensitive test within the range of temperature from 0 to 900° C. For this purpose we derive eq. (9) with respect to temperature, which gives $\alpha = a' C_D + b' C_s$ or

$$\frac{\alpha}{C_D} = a' + b' \frac{C_s}{C_D}. \tag{10}$$

Here α is the coefficient of volume expansion, as usual referred to the volume at 0° C. a' and b' are constants, differing from a and b in eq. (9) by a constant factor depending on the unities used. C_D is the specific heat calculated from the Debye formula with the characteristic temperature of copper taken as $\Theta = 325$, and C_s is the structural part of the specific heat calculated by means of eq. (1). Expansion coefficients at 400, 585, 721, and 821° C are taken from the lattice-constant determinations of HUME-ROTHERY and ANDREWS (27), which are also in good agreement with usual expansion measurements by ESSER and EUSTERBROCK (28). Expansion coefficients at 73, 241, and 437° C are taken from expansion measurements by NIX and MACNAIR (29). Values of the atomic heat C_p at these temperatures are interpolated from the tables of LANDOLT-BÖRNSTEIN, where the values, in the range of temperature concerned, are mainly based on the measurements of KLINKHARDT (14). A later determination by SEEKAMP (30) has given slightly lower values. For the sake of simplicity we have taken the values from the literature directly in calories per degree. The electron part of the atomic heat is taken as $0.000178\ T$ in accordance with the results at very low temperatures by KOK and KEESOM (31).

In figure 8 the circles give the values of α/C_D plotted against C_s/C_D. According to eq. (10) they lie within the limits of error on a straight line. The limiting value of α/C_D, $a' = 8.3 \times 10^{-6}$, at $C_s = 0$, that is at low temperatures, is in good agreement with the values obtained for α/C_p from measurements at low temperatures by GRÜNEISEN (22), BORELIUS and JOHANSSON (32), and NIX and MCNAIR (29), or 8.1, 8.1, and 8.3×10^{-6} respectively. The empirical value of the slope is $b' = 18 \times 10^{-6}$. This constant b' should also, according to our postulates, be obtainable in an independent way from the change of volume ΔV and internal energy L at the melting point. We get from eq. (9)

$$b' = \frac{\Delta V}{V_r L} \tag{11}$$

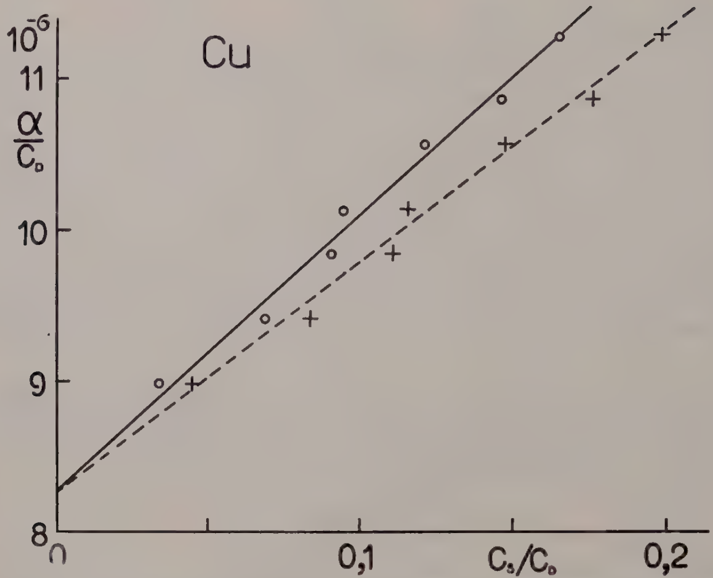

Fig. 8. Increase of expansion coefficient with increase of structural atomic heat for Cu.

where V_r is the volume at the reference temperature 0° C. An extrapolation of the lattice-constant values of HUME-ROTHERY and ANDREWS (27) up to the melting point at 1 084° C and down to 0° C give the ratio of volume between these temperature 1.068. An extrapolation of the density values of WIDAWSKI and SAUERWALD (33) for liquid copper down to the melting point gives $\varrho = 7.94$ g/cm^3, which compared with the X-ray value for 0° C, $\varrho = 8.939$, gives a volume ratio for the liquid of 1.126. The value of $\Delta V/V_r$ thus is 0.058. The latent heat of fusion was determined by WÜST, MEUTHEN and DURRER (34) to $L = 3\,240$ and by UMINO (35) to $L = 3\,180$. Using the mean value 3 200 we then obtain

$$b' = \frac{0.058}{3\,200} = 18 \times 10^{-6}$$

in full agreement with the value obtaind from the slope in fig. 8.

The crosses and the dotted line in fig. 8 is for a comparison calculated by neglecting the electron part in eq. (1), that is by including the electron energy in the structural energy. The slope of this line is 14.5×10^{-6} and is not in accordance with the observed discontinuities at the melting point. We must, however, emphasize that especially the determinations of the heat of fusion may be rather uncertain.

10. Concluding remarks

For the present an accurate test of our general assumptions has only been possible for a few metals, and the study of the literature has shown the need of further accurate calorimetric measurements at high temperatures and, concerning the changes in volume of the non-cubic metals, expansion measurements at low temperatures on single crystals or with X-ray methods. It is, however, already possible to calculate what we have called the structural parts of internal energy, entropy and volume expansion for many metals to a first rough approximation over a wide range of temperature. This will give a widened basis for the test of atomic and statistic theories of the liquid state, which have so far mainly been confronted with the changes of energy, entropy and volume at the melting point.

We have confined ourselves to a phenomenological and thermodynamic treatment and shall not enter upon the various attempts that have been made towards a statistical theory of the liquids, but just mention a few further observations from the phenomenological point of view.

It is a remarkable fact, pointed out by HUME-ROTHERY (27) and others, that the determination of lattice constants and measurements of outer dimensions of samples of single cubic solid metals give almost the same thermal expansion coefficients. The percentually considerable part of the expansion of the solid which we have called the structural part, thus cannot be ascribed to the opening of atom vacancies or other local thinnings of the lattice, without a compensation by interstitial atoms or other local concentrations. If we now have to assume that the liquid state is a continuation of the solid with the same type of disturbances, only on a larger scale, the theory of liquids will have to face the same limitations.

Another interesting experience is that the purely thermal lattice disturbances must have very short, if any, time of relaxation after a rapid variation of temperature. In fact, we have tried in our laboratory by the methods of isothermal calorimetry, which have made it possible to follow the evolution of heat during recovery after coldworking, to find relaxation phenomena after rapid variations of the temtperature of not coldworked metals, but so far without any result.

I am indebted to Mr LARS-ERIK LARSSON for good assistance in searching the literature and making numerical calculations.

Stockholm, Royal Institute of Technology, Physics Department.

LITERATURE

1. J. H. POYNTING. Phil. Mag. *12* (1881) 32.
2. M. PLANCK. Ann. d. Physik *15* (1882) 446.
3. H. KAMERLINGH ONNES and H. HAPPEL. Comm. Leiden *86* (1903).
4. J. FRENKEL. Trans. Faraday Soc. *33* (1937) 58. Kinetic Theory of Liquids, Oxford 1946.
5. H. W. BACKHUIS ROOZEBOM. Die heterogenen Gleichgew. Bd I (1903) 80.
6. G. TAMMANN. Kristallisieren und Schmelzen (1903) 8. Ann. d. Physik *36* (1911) 1027.
7. P. W. BRIDGMAN. The Physics of high pressure, 2nd ed. (1949) 201.
8. G. N. LEWIS. J. Amer. Chem. Soc. *29* (1907) 1165.
9. G. BORELIUS and K. Å. PAULSSON. Arkiv f. Mat., Astr. Fysik 33 A nr. 7 (1946).
10. C. T. ANDERSON. J. Amer. Chem. Soc. *59* (1937) 1036.
11. G. L. PICKARD and F. E. SIMON. Proc. Phys. Soc. *61* (1948) 1.
12. M. RANDALL and C. T. LANGFORD. Priv. Comm. to Int. crit. Tables VII (1930) 258.
13. LANDOLT-BÖRNSTEIN. Tab. 2. Erg. Bd. 1162.
14. H. KLINKHARDT. Ann. d. Physik *84* (1927) 167.
15. W. H. KEESOM and J. H. VAN DEN ENDE. Comm. Leiden 203 d (1930).
16. W. H. KEESOM and P. H. VAN LAES. Comm. Leiden 252 b (1938).
17. B. VONNEGUT. J. Colloid. Sci. *3* (1948) 563.
18. D. TURNBULL. J. Chem. Phys. *18* (1950) 768.
19. D. TURNBULL and R. E. CESH. J. Appl. Phys. *21* (1950) 804.
20. J. C. FISHER, J. H. HOLLOMON and D. TURNBULL. J. Appl. Physics *19* (1948) 775.
21. R. BECKER. Z. f. Metallkunde *29* (1937) 245.

22. E. GRÜNEISEN. Ann. d. Physik *26* (1908) 211. *39* (1912) 286.
23. H. EBERT. Z. f. Physik *47* (1928) 712.
24. F. L. UFFELMANN. Phil. Mag. *10* (1930) 663.
25. A. L. DAY, R. B. SOSMAN and J. C. HOSTETTER. N. Jahrb. Min. *40* (1915) 119.
26. G. VICENTINI and D. OMODEI. (1888) Tables of Landolt-Börnstein (1923) 291.
27. W. HUME-ROTHERY and K. W. ANDREWS, J. Inst. Metals *68* (1942) 19.
28. H. ESSER and H. EUSTERBROCK. Archiv Eisenhüttenwesen *14* (1941) 341.
29. F. C. NIX and D. MACNAIR. Phys. Rev. *60* (1941) 597.
30. H. SEEKAMP. Z. anorg. Chem. *195* (1931) 345, 363.
31. J. A. KOK and W. H. KEESOM. Comm. Leiden 245 a (1936).
32. G. BORELIUS and C. H. JOHANSSON. Ann. d. Physik *75* (1924) 23.
33. E. WIDAWSKI and F. SAUERWALD. Z. anorg. Chem. *192* (1930) 153.
34. F. W. WÜST, A. MEUTHEN and R. DURRER. Landolt-Börnstein Tabl. III. Erg. Bd. 2685.
35. S. UMINO, Techn. Rep. Tôhoku Univ. *8* (1926) 597.

Tryckt den 6 februari 1953

Uppsala 1953. Almqvist & Wiksells Boktryckeri AB

ARKIV FÖR FYSIK Band 6 nr 21

Read 10 September 1952

On fusion as order-disorder transition

By G. Borelius

With 3 figures in the text

The establishment of the existence of order-disorder transformations by the study of alloys led to an extension of the thermodynamics and statistics of transformations by introducing a new variable, the degree of disorder (or order). It was not long before this new possibility was tried on the theory of fusion, and there is now a variety of theories which treat the structure of the liquid state as a highly disordered crystalline structure. The early theories of this kind (1, 2) consider fusion as a transition from a rather highly ordered solid state to a liquid state with nearly complete disorder, thus approximately identifying the increase of energy and entropy at the melting point with a maximum energy or entropy of disorder. These theories have placed fusion very much on a level with a highly discontinuous order-disorder transformation in an alloy of stocheometric concentration. The calculation of the change of entropy under these conditions has met, however, with great difficulties.

A recent analysis by the present author (3) of the specific heat of metals led to a rather different view. According to this analysis, the structural part of the entropy, which is a kind of measure of the degree of disorder, should have reached values being an appreciable part of the melting entropy even at temperatures below the melting point, and should continue to increase above the melting point without showing any tendency to approach a limiting value.

On the basis of this interpretation we shall in the following give a description of the solid-liquid transition as an order-disorder phenomenon, which on the one hand has a formal similarity to the author's theoretical description of order-disorder phenomena in alloys, but on the other hand also takes into account and demonstrates the characteristic differences between the two phenomena. As a comparison between the two types of phenomena is of a certain interest, we shall start with a short reminder of the theory of the transitions in alloys before going on to our main subject, the solid-liquid transition of a pure metal.

The order-disorder transition in an alloy of the simple type AB was first described mathematically, in a way approximately fitting experimental facts, by the present author in 1934 (4). In full order the alloy contains two partial lattices, one with A-atoms only, and one with B-atoms only. The degree of disorder is defined as the fraction q of A-atoms and B-atoms, which have gone over to the wrong partial lattice. On the simplifying assumption that the distribution of the two types of atoms within each partial lattice is at random, the structural entropy is found to be

$$S_S = R\left[-q \ln q - (1-q) \ln (1-q)\right], \qquad (1)$$

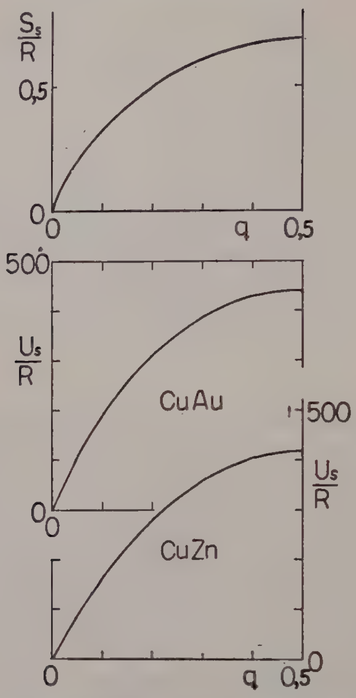

Fig. 1. Structural entropy and energy as functions of the degree of disorder in alloys.

R being the gas constant. The highest value of S_s is 0.693 R for $q = 0.5$, corresponding to full disorder. Values of q higher than 0.5 give nothing new because of the symmetry between q and $1-q$.

The structural energy U_s was calculated on the same simplifying assumption as the entropy and by ascribing different energy values to all the various groups of neighbouring atoms which differ from each other with respect to their numbers of A- and B-atoms and their geometric configurations. The equivalence of q and $1-q$ give a symmetrical expression of the type

$$U_S = R\,[\alpha\, q\,(1-q) + \beta\, q^2\,(1-q)^2 + \cdots] \tag{2}$$

where α, β... are constants to be determined by experiment. If groups of atoms containing more than five atoms are neglected, the expression is complete with the two terms.

The two expressions (1) and (2) with two empirical constants together with the thermodynamic condition for equilibrium, which may be written

$$T = \frac{d\,U_S}{d\,q} : \frac{d\,S_S}{d\,q} \tag{3}$$

determine the whole transition phenomenon from the point of view of long range order including the critical temperature and the structural energy and entropy as

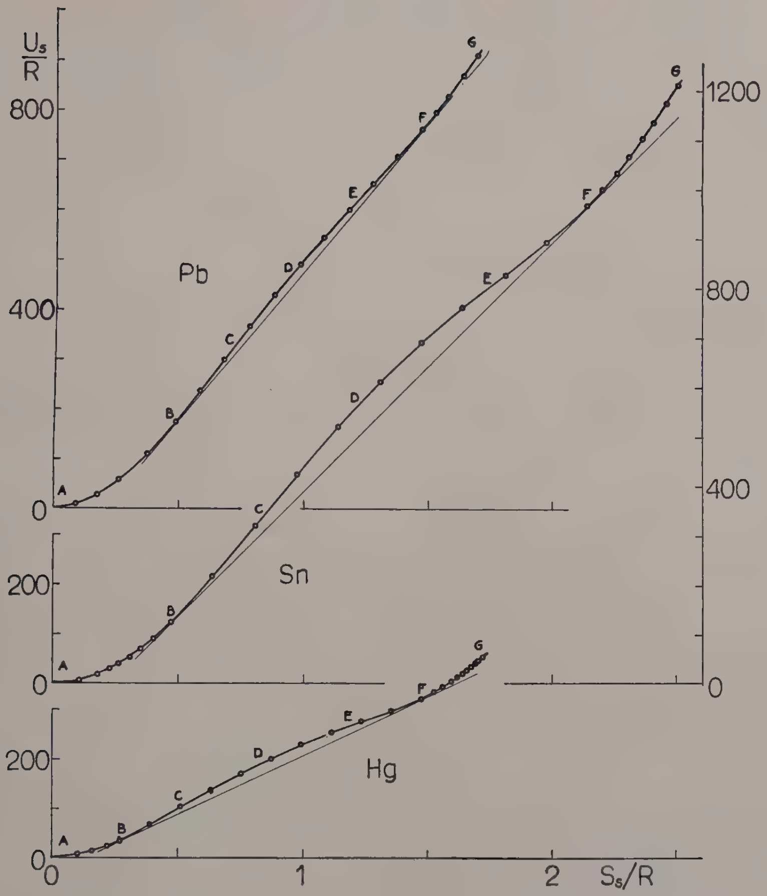

Fig. 2. Structural energy as a function of the structural entropy.

functions of the absolute temperature T. The constant β is always found to be negative.

The transition in CuAu, which has a discontinuity of the first order, is found to agree well with the values $\alpha = 2325$ and $\beta = -2250$ (5, 6). The transition in CuZn, which has no discontinuity of the first order, agrees with $\alpha = 1850$ and $\beta = -684$ (6). In figure 1 the upper diagram shows S_s/R as a function of q according to equation (1). The lower diagrams show U_s/R as a function of q for CuAu and CuZn calculated according to equation (2) with the constants mentioned. A seemingly small variation in the bending of the curves makes the discontinuity of the first order appear or disappear.

Concerning *the solid-liquid transition* we start from the structural energy U_s and structural entropy S_s of some pure metals, as calculated in the preceding paper. These calculations were carried out on the assumption that the observed molar heat C_p is the sum of three parts, the structural part C_s, the vibrational part C_D, which at high temperatures approaches the classical value $3\,R$, and a small contribution C_e

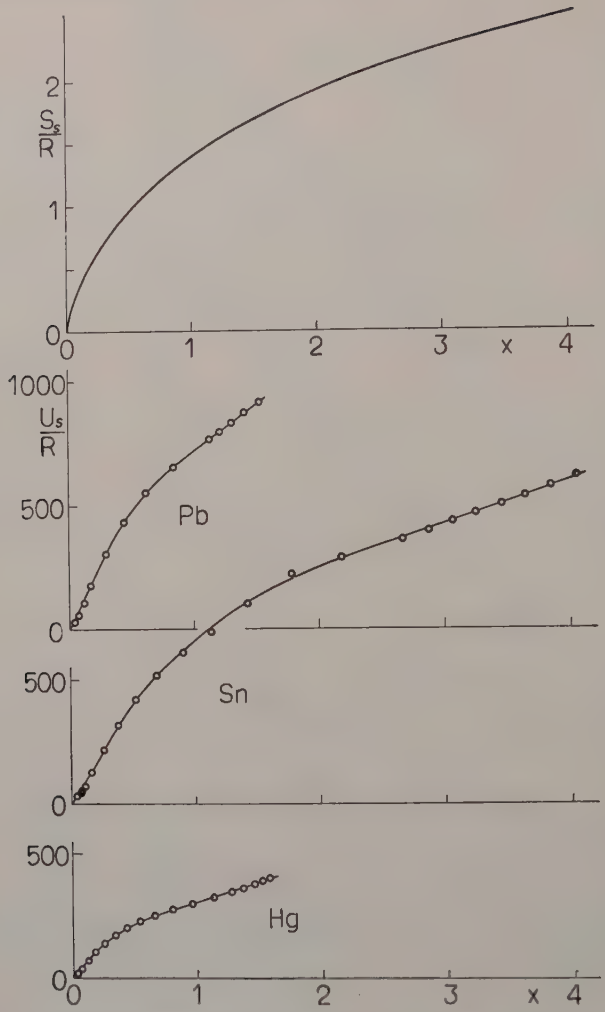

Fig. 3. Structural entropy and energy as functions of the degree of disorder in pure metals.

from the free electrons. The heat of fusion was assumed to be entirely of structural origin. Plotting corresponding values of U_s and S_s for the same temperature for Pb, Sn and Hg gives the diagrams shown in figure 2. In this figure the parts AB and FG correspond to stable states below and above the melting point. These parts are obtained from empirical data. The part BCDEF which corresponds to metastable or, from C to E, unstable states, is obtained by a mathematical expansion based on the assumption of continuity. For details we refer to the quoted papers (3).

The next step towards a description of the phenomenon of fusion analogous to that of order-disorder phenomena in alloys should be to bring the rather complicated dependence of U_s and S_s on T, or of U_s on S_s into the form of simple expressions for these quantities as functions of a suitable disorder parameter. After searching in different directions we have found the following approach to comply with these requirements and experimental conditions.

At the absolute zero point the N atoms of a gram atom have N possible sites. At a finite temperature T the thermal motion of the atoms has produced a certain thermal expansion thereby opening up $x\,N$ new sites. The total number of sites thus is $(1+x)N$, of which N are occupied by atoms and xN are not. The number of ways in which such states can be realized is

$$W=\frac{(1+x)\,N!}{x\,N!\,N!}. \qquad (4)$$

The structural entropy, defined by

$$S_S=k\ln W \qquad (5)$$

where k is the Boltzmann constant, becomes using the Stirling formula:

$$S_S=R\,[-x\ln x+(1+x)\ln(1+x)] \qquad (6)$$

$R=kN$ denoting the gas constant. S_s as a function of x is shown in the upper diagram of figure 3. The corresponding values of the structural energy U_s are obtained from the U_s–S_s-diagrams (fig. 2). U_s/R as a function of x for Pb, Sn and Hg are given in the lower diagrams of figure 3. We see that the parameter x as a measure of disorder fulfills the requirement that S_s and U_s should vary in a simple way with this parameter.

A comparison of the diagrams in figure 1 for order-disorder transitions in alloys and those of figure 3 for the solid-liquid transitions shows, that at low values of the disorder parameters q and x respectively the diagrams are rather similar, whereas there is a fundamental difference at higher values. q stops at 0.5 while x goes on at least to values of about 4 without sign of an upper limit.

The expression for the entropy in equation (6) is formally the same as was obtained earlier (1) on the assumption that the new sites appearing with increasing temperature should be holes where atoms are missing from the lattice. This hole model, however, is not consistent with the great number of new sites calculated on the basis of our phenomological analysis. Thus in lead, for instance the number of new sites just below the melting point is found to be 17 per cent of the number of atoms, and just above the melting point 110 per cent. If the holes were of the size of the atoms, one should expect a similar relative increase in volume above the volume at absolute zero temperature, whereas the increase in volume which was ascribed in the earlier paper (3) to structural variations was only about 1 and 4 per cent, respectively. The hole theory is also inconsistent with the fact that the expansion coefficients are found to be the same if determined from the outer dimensions of a sample or from the X-ray measurements of lattice constants.

The picture behind our development of formula (6) is not that of holes where atoms are missing but of new sites, opened up in a fluctuating way between the atoms. As a simple illustration we may consider three atoms A, B, and C, in a row. At the ordinary distance between A and C, the atom B has only one centre of force, that is one minimum of potential energy halfway between A and C. At a certain increase in the distance A C this minimum will divide into two minima with a potential barrier between them. The atom B has thus a choice between two centres around which to oscillate, instead of the only one as in the undisturbed lattice. Such a picture, however, can obviously not be finally accepted without a thorough theoretical test of its probability from a lattice-geometrical point of view.

Within the limits of experimental error the structural energy U_s at low values of x is found to be proportional to x. This is what must be expected from a suitable theory in the range where the new sites are few enough to be in general separate from each other. In the range from say $x=0.3$ to $x=1$, the U_s–x-curves bend and then continue with a smaller but rather constant slope. The bend appears, from our interpretation, to be the cause of and a necessary condition for the discontinuity in the solid liquid transition and should thus be looked upon as a very general and fundamental phenomenon. It is near at hand to search for the origin of this bend in a clustering of the new sites as chains or surfaces or bigger holes. A special possibility to consider is also that of a fluctuating network of surfaces dividing the specimen into cells with a rather undisturbed lattice, which is an idea, found in certain theories of the liquid state. However, also for such questions a further development of the theory on a geometrical and statistical basis is required.

Stockholm, Royal Institute of Technology, Department of Physics.

LITERATURE. 1. **J. Frenkel** (1932) and **S. Bresler** (1939). Reference **J. Frenkel** Kinetic theory of liquids. Oxford 1946, p. 106—107. — 2. **F. C. Frank,** Proc. Roy. Soc. A *170* (1939) 182. — 3. **G. Borelius,** Rapport de la Conférence sur les changements de Phase, Paris 1952 (to appear). Arkiv för Fysik 1952 (to appear). — 4. **G. Borelius,** Annalen d. Physik *20* (1934), 57. — 5. **O. Källbäck, J. Nyström,** and **G. Borelius,** Ing. Vetensk. Akad. Handl. nr *157* (1941). — 6. **G. Borelius,** Journ. Inst. of Metals *74* (1947) 17.

Tryckt den 6 februari 1953

Uppsala 1953. Almqvist & Wiksells Boktryckeri AB

ARKIV FÖR FYSIK Band 6 nr 22

Communicated 12 March 1952 by AXEL E. LINDH and IVAR WALLER

Evidence of a band structure in the Compton radiation from solids

By KESSAR ALEXOPOULOS and GÖSTA BROGREN

With 9 figures in the text

When X-rays strike matter they are scattered in various directions, partly without change of wave length (unmodified radiation or Rayleigh line) and partly with such a change (modified radiation or Compton line). The *Rayleigh* radiation can be divided into two parts: The first component may be understood in a classical way; because of its coherent nature, it gives interference effects and is not scattered in all directions from a poly-crystalline solid, but concentrates in certain directions giving the Debye-Scherrer lines. The second term is also unmodified — it has practically the same wave length as the incident radiation — and is due to thermal agitation in the crystal. Contrary to the first term, this second term is incoherent as there is no definite phase relation between the waves scattered on the different atoms. The *Compton* radiation is also incoherent and cannot show interference effects. Both terms are scattered in all directions, and consititute the diffusely scattered radiation. Their intensity, as a function of scattering angle φ, have been measured for Be (1, 2) and B (3) and have been found to agree satisfactorily with calculated values. The general trend of the intensity is to start from zero for $\varphi = 0$, and to increase with this angle.

The wave length of the Compton radiation depends on the state of the electrons that produce the scattering: When the electrons are at rest (case of free electrons) the spectrum of the modified radiation consists of a single line. When the electrons are bound, this line broadens symmetrically into a band. SOMMERFELD (4) has shown that, if the energy imparted to the electron is small, the band will have a sharp limit towards the short wave lengths, and a few "electronic Raman lines" will appear between the primary line and the limit. It is clear that this is valid only for electrons belonging to free atoms as only these have discrete energy levels. This picture should be modified for solids as the energy levels are replaced by energy bands. The spectrum of the scattered radiation will depend on the density distribution of states in the highest occupied zone, and in the free zone above it. The Compton band with a sharp limit and the electronic Raman lines will be replaced by broad bands, possibly with a structure. If the highest occupied zone is filled, and there is a forbidden zone above it — as is the case of isolators — the Compton band should show a limit towards short wave lengths. The energy shift between this limit and the primary line will be equal to the breadth of the forbidden band.

Although most experiments on Compton scattering have been done on solids,

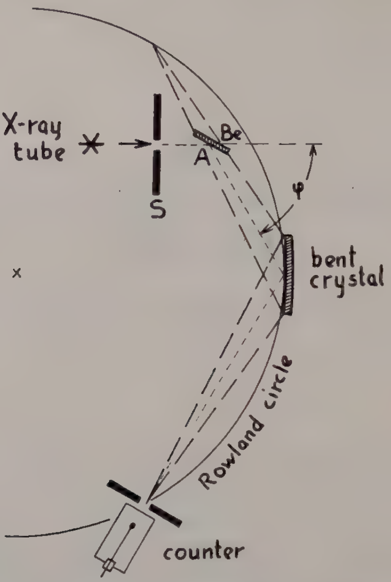

Fig. 1. Principle of the experimental arrangement.

such a structure has not yet been observed, because of the short wave lengths used. As far as we know no careful spectroscopic investigation in the large wave length region has been attempted. Here follows an account of experiments carried out under conditions suitably chosen so as to make an eventual structure observable. The choice of wave length, scattering angle, and scatterer has been discussed by FRANZ (5) in the case of free atoms, but the same considerations will be valid for solids. The present experiments were carried out with copper K α-radiation scattered on beryllium and carbon under angles between 17° and 45°.

Experimental arrangement

The arrangement consists in principle of an X-ray tube irradiating a solid and of a spectrometer analysing the spectrum of the scattered rays (Fig. 1). The spectrometer is of the bent crystal type; it collects rays scattered under angle φ and collimates them, according to their wave length, as points on the Rowland circle. The intensity of the radiation is measured with a Geiger Müller counter, covered with a slit-bearing screen. By measuring the intensity passing through this slit, when it is moved on the Rowland circle, we obtain the desired spectrum.

The X-ray source was of the standard type used in the Uppsala laboratory (6), but so constructed as to carry an adjustable slit (S) at a distance of 31 mm from the centre of its focal spot (Fig. 2). The target was of Cu and the focal spot had the dimensions 2 × 15 mm capable of withstanding a load of 50 kV and 40 mA. The angle between the surface of the anticathode and the line between the mid-point of the crystal and the centre of the focal spot was 8°. This arrangement limited the effective height of the focal spot to 2.1 mm.

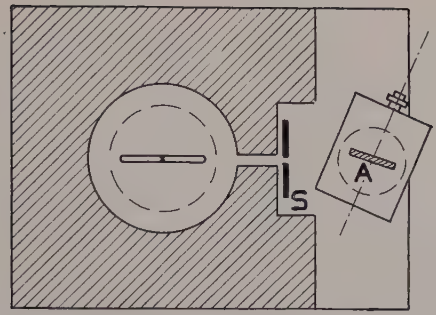

Fig. 2. The X-ray tube and the slide, carrying the scatterer.

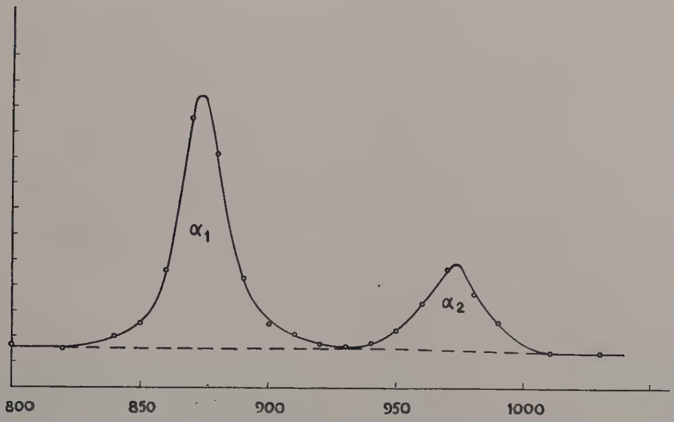

Fig. 3. The spectrum of the primary radiation.

The entire tube unit was placed on a flat iron table, and could be turned round a vertical axis A. The scattering solid was fixed on a slide permitting its horizontal displacement, so that its scattering surface could contain axis A. The slide was fixed on a cone permitting it to be turned round this axis.

The holder, bending the crystal, is a novel construction (7) consisting of four vertical steel rods held in a brass housing. The other parts of the spectrometer, i.e. turning table, its displacement slide etc., were the same as had been used in a previous work (6). The GEIGER MÜLLER counter was the Philips standard type 62019 with a thin mica window. Before going through the window the rays had to pass a slit, 100 μ wide and 14 mm long. The motion of the counter along the Rowland circle was caused in the usual way (6).

We choose as crystal grating a quartz plate cut along the $13\bar{4}0$ lattice plane. This plane has a spacing of 1177.3 X.U. and reflects the copper Kα lines at the convenient angle of about 40°. The structure factors of the higher orders are very small. This, together with the fact that the sensitivity of the G-M-counter rapidly decreases with decreasing wave-length, results in the fact that higher order reflections are negligible (8). The focussing qualities of the crystal were controlled optically during its bending, and a good result was obtained with a Rowland circle of radius

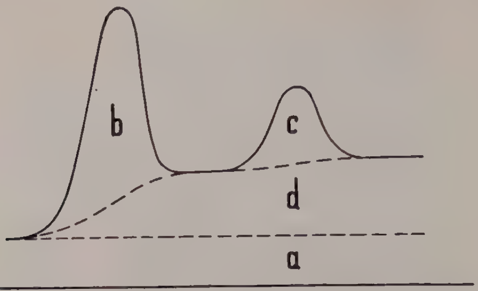

Fig. 4. Typical form of the spectrum of the scattered radiation.

$R = 254$ mm. Under these conditions the dispersion along the Rowland circle was 3.51 X.U./mm. The quality of the bent crystal was then further investigated with X-rays. In this preliminary experiment the X-ray tube was turned into such a position that the direct beam hit the bent crystal under the proper glancing angle. The spectrum of the primary radiation was recorded in this way (Fig. 3). The widths of the α_1 and α_2 lines constitute a measure of the quality of the spectrometer. The total observed width 220 μ (all measurements are given in μ along the Rowland circle) should be the sum of the natural width 165 μ ($= 0.58$ X.U.) the widening 30 μ due to the aperture of the curved crystal plus a small term due to the breadth of the slit. Thus, the preliminary experiment showed that there is no widening caused by imperfect bending.

The most important adjustment is to move the crystal table along its slide (M in reference 6) until the converging cone — shown in broken lines in Fig. 1 — contains the vertical axis A. In this position the rays emitted from the scatterer towards the curved crystal strike it under the proper glancing angle. This adjustment is done during the preliminary experiment by fixing a slit at the position of the vertical axis A, and sliding the crystal table until we obtain a maximum intensity of the reflected radiation. After the preliminary experiment the slit is replaced by the scatterer and the X-ray tube is turned round to such a position that the desired angle φ is reached.

A few words can be spared here on the obtained intensities, as this will give an idea of the ordinates in Figs. 4, 5, and 6. During the scattering experiments on Be, under the angle $\varphi = 35°$, and by using 49 kV and 26 mA, about 105 counts per minute were measured at the α_1 peak, and about 18 min^{-1} at the continuous background (position 800). From these, 12 min^{-1} were due to cosmic radiation, the counter being shielded on most sides with about 2 cm of lead.

Scattering experiments on beryllium

The scattering material consisted of two beryllium plates in contact, each of 12.5 mm diameter and 0.5 mm thickness. Such plates are ordinarily used as windows on sealed X-ray tubes. The nominal analysis of this beryllium, as given from the factory (Brush Beryllium Co.), is as follows: Fe .1 %, Al .1 %, Si .08 %, Be_2C .1 %, Be_2O .2 %, Ni .02 %, Mn .02 %, Cu .02 %. Total Be assay 99.5 %. The linear absorp-

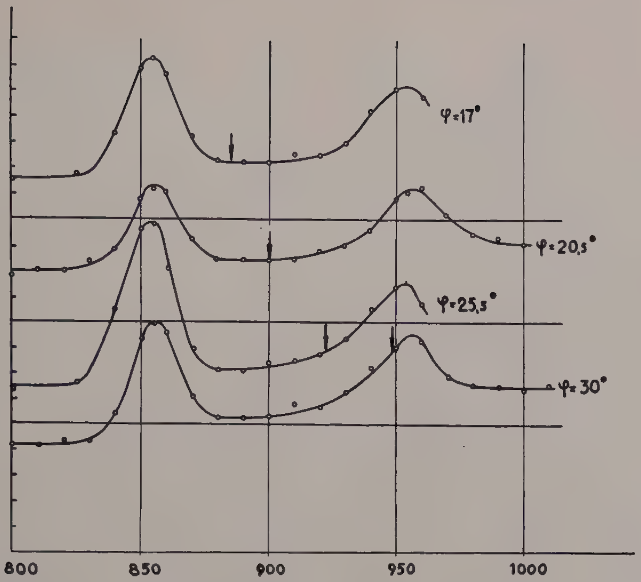

Fig. 5. Spectra of the radiation, scattered on beryllium. (On this and the following diagrams each division on the ordinate corresponds 10 counts/min.)

tion coefficient for $\lambda = 1540$ X.U. was found to be 3.8 cm^{-1} against 2.88 cm^{-1} for pure Be, which is in good agreement with the composition stated.

We will first describe a typical spectrum such as we have measured it (Fig. 4). The surface under the curve may be divided into the folllowing areas: a) background, b) line α_1, c) line α_2, d) Compton band.

In Figs. 5 and 6 we give the results for the various angles.. As to $\varphi = 17°$, each point was measured with an accuracy of approximately $\pm 3\,\%$. As we were mainly interested in the search for the existence of a structure (i. e. any sudden change of the intensity) in the Compton band, measurements at positions 900 and 910 were subsequently continued. We found that the difference in the two counting rates is very small. Thus, the large value at 910 should be attributed to an exceptionally great statistical fluctuation. The counting rates $I\alpha_1$ and $I\alpha_2$ at the maximum of the lines α_1 and α_2, the background I_{800} measured at the short wave-length side (i.e. position 800), the counting rate I_{900}^{C} *of the Compton band* midway between the lines α_1 and α_2 (position 900) and I_{1000}^{C} at position 1000 are given in Table I.

Table I

Scattering angle φ	I_{α_1}	I_{α_2}	I_{800} (background)	I_{900}^{C}	I_{1000}^{C}
17	44	—	16	6.5	—
20.5	31.5	25	20	4	10.5
25.5	61	—	15	7	—
30	43	23	42	11	23
35	78	38	20	13	17.5
40	97	36	20	15.5	18

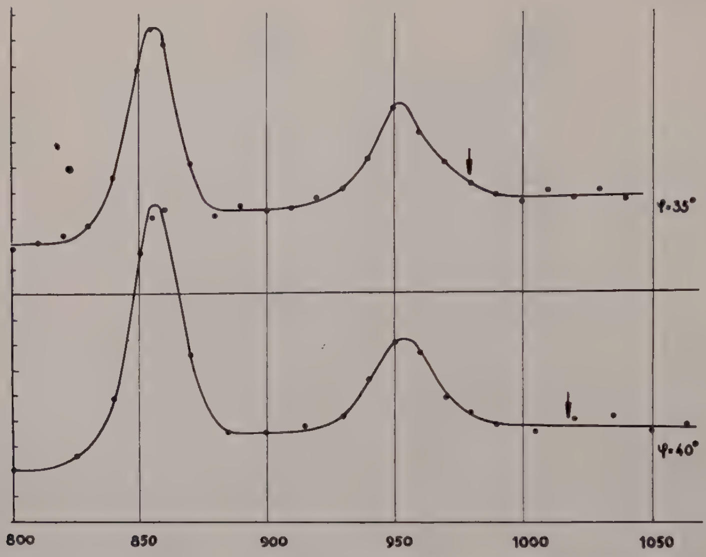

Fig. 6. Spectra of the radiation, scattered on beryllium.

The same experiment was carried out at angles 20.5°, 25.5°, 30°, 35°, 40°, and 45°. The counting rates for the various angles are not quite comparable with each other, as they would have been if the scattering material was of small dimensions and completely imbedded in the beam of primary rays. As a measure of the continuity of the obtained values, values of $I\alpha_1$ and $I\alpha_2$ are plotted as a function of φ (Fig. 7). We notice that $I\alpha_1$ and $I\alpha_2$ rise gradually until $\varphi = 45°$ where there is a sudden increase. This is due to the Debye-Scherrer line of plane (001) that occurs at 45°. In this case the coherent radiation becomes very intense and covers all other radiations, so that measurements at 45° are valueless. The background I_{800} is due to cosmic radiation (about 12 min^{-1}) and to the continuous spectrum of the primary radiation, scattered on the Be scatterer a) with change and b) without change of its wavelength. Both components are practically constant along the measured range of wave-lengths. The same is valid for any radiation caused by the α_1 radiation, diffusely scattered on the quartz crystal. For all these reasons the background should reveal no important change with φ. This is exactly what we find in column 4 of Table I. The exceptionally great value at $\varphi = 30°$, is occasioned by stray radiation in the laboratory entering the G-M-tube from behind. This was not noticed until the first two measurements ($\varphi = 20.5°$ and 30°) had been made; this was eliminated in subsequent measurements through suitable shielding.

According to the experimental curves, the Compton scattering starts immediately after the Rayleigh line, but does not show any noticeable maximum. The form of the distribution curve and the position of its maximum cannot be predicted at present. The width of the Compton band for *free* Be atoms can be extrapolated from Du Mond's (9) results at larger angles and shorter wave-lengths if we assume that it is proportional to λ and to $\sin \varphi/2$. The calculated widths are between 7.3 and 18.6 X.U. for the range of angles measured. On the scale of Fig. 5 this corre-

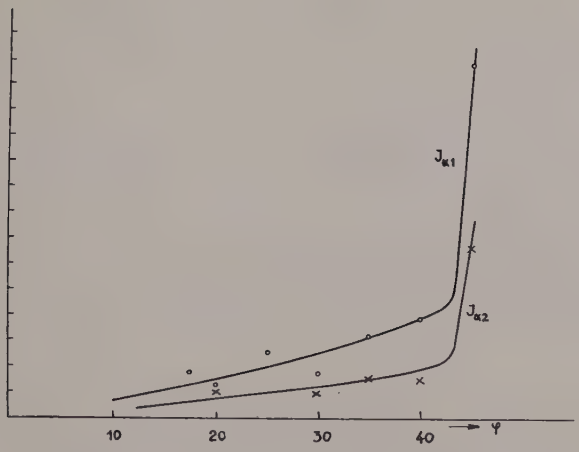

Fig. 7. Counting rate at the maximum of the α_1 and α_2-lines.

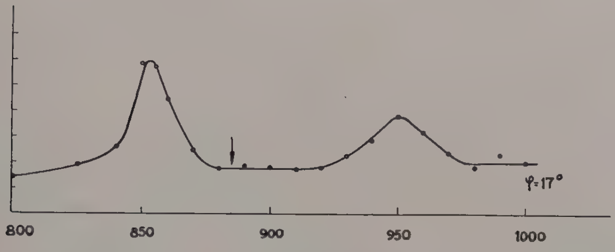

Fig. 8. Spectrum of the radiation, scattered on graphite.

sponds to lengths of 200 and 500 μ, respectively. Such a broad Compton band cannot give an appreciable maximum. Its position depends of course on the scattering angle and has been indicated on each curve with an arrow. *The experiment shows that towards long wave-lengths an extra intensity is observed which may be consistently attributed to the Compton scattering.* The intensity of the Compton band (i.e. the area *d* in Fig. 4) cannot be given as the curves have not been sufficiently extended towards longer wave-lengths, but if we consider the counting rates I_{900}^{C} and I_{1000}^{C} as indications of its intensity, we will notice a rise with increasing scattering angle, in conformity with measurements of the total diffuse scattering (1, 2).

Scattering experiments on carbon

Carbon was used in graphite and diamond modifications. As the results show differences, they will be treated separately. The load on the X-ray tube was 46 kV and 38 mA.

The *graphite* scatterer consisted of a block, at least 99.9 % pure. It was exposed to X-rays in the same way as the Be plates in the above experiments. Measurements were only carried out at angle $\varphi = 17°$ (Fig. 8) because the Debye-Scherrer-line for (002), which occurs for an ideal graphite crystal at about 26°, was found to be

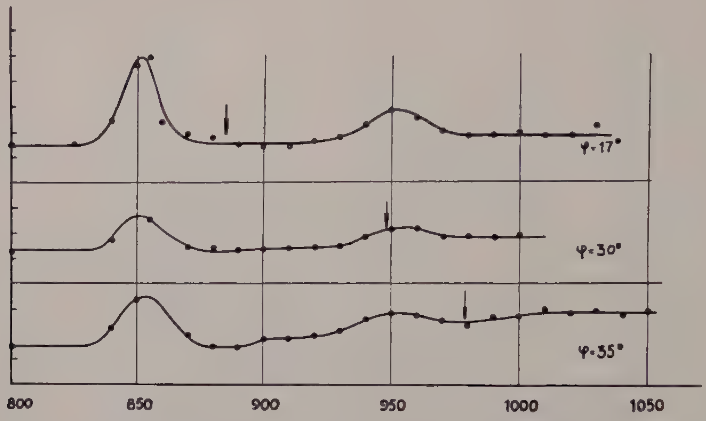

Fig. 9. Spectra of the radiation, scattered on diamond.

very broad in the case of the sample used, thus making measurements in the range of larger angles impossible. We notice in Fig. 6 that the Compton band has the same qualities as in Be. The points beyond the α_2 line were measured with less precision and show therefore greater fluctuations.

In the case of *diamond*, 8 flat diamonds, kindly lent to us by the firm Svenska Diamantborrningsbolaget, were cemented on a beryllium plate to form an approximately flat mosaic surface of about 0.4 cm². Because of their irregular shapes the area occupied was about 1 cm². Scattering experiments were carried out at angles 17°, 30°, and 35°.

The results are given in Fig. 9. The curve for $\varphi = 17°$ shows no intensity for the Compton band in the region between the lines α_1 and α_2. Considering possible errors, we may ascertain that $I^{C}_{900}/I\alpha_1$ is smaller than 1/20, as against 1/7 for the same position in the case of Be. For larger shifts (position 1010) the Compton band shows a relative intensity 1/11. The curves for $\varphi = 30°$ and $\varphi = 35°$ reveal the same qualities. Their results are given in Table II. In the case of $\varphi = 35°$, which was measured with great accuracy, the Compton band seems to start at a point between 890 and 900. The counting rates at these two points differ by 2.8 min⁻¹ whereas the statistical errors are ±0.84 and ±0.77 respectively, giving an error of ±1.1 for the difference. If we plausibly assume that the counting rate in positions 880 and 890 is constant

Table II

φ		I^{C}_{900}	I^{C}_{1010}	$I^{C}_{900}/I\alpha_1$	$I^{C}_{1010}/I\alpha_1$
17		<1	3	<1/33	1/11
	890 :				
30	900 :	<2	6	<1/16	1/5.5
	890 :	<0.5		<1/38	
35	900 :	1.5	12	1/10	1/1.6

and that the same is the case in positions 900–910, this error is reduced to ± 0.8 min^{-1}. In this case the observed step in the curve is 3.5 times larger than the statistical error. The above results can be summed up as follows: *The Compton band has no appreciable intensity near the primary line.* It can be detected easily at shifts of about 20 eV. In the curve for $\varphi = 35°$, there is a sudden change in the counting rate between 890 and 900. *As this change is nearly four times as large as the statistical fluctuations, it must be considered as real and occasioned by a sharp limit of the Compton band.* A similar change can be observed between 990 and 1010, which is probably due to the same sharp limit of the Compton band of the $K\alpha_2$-line. The fact that this change (between 890 and 900) was not observed in the curves for 17° and 30° can be explained by the much smaller intensity of the Compton band (see column 5 of Table II) and by the fact that the points there were measured with less accuracy.

Discussion of the results

This work was started with the ultimate objective of observing the structure of the Compton band. On the basis of the current theory of solids, a structure should occur, whenever differences in the density distribution of states produce it. The experiments indicate that no abrupt changes exist in the spectrum of beryllium and graphite, since the Compton band begins near the primary line. For diamond there is a limit towards short wave-lengths.

Because of the electric conductivity of Be, it has long been assumed that the zones overlap there, leaving no possibility for the existence of a forbidden zone. Recently (10) it has been shown that the absorption edge coincides with the high energy limit of the emission line. This fact directly proves that the above opinion is correct. Our present results agree with this point of view.

Graphite is a pure semiconductor if we limit ourselves to the hexagonal plane of a single crystal. The calculated (11) state distribution for $T = 0$ will give a Compton band with a zero intensity at zero energy shift and with growing intensity as the shift increases. The present experiment does not show this behaviour, a) because the experiment is not carried out at zero temperature (12), b) because the theory is only valid in the case of electrons moving in the hexagonal plane, whereas the graphite used was polycrystalline. This view is further corroborated by the observation (13) that the limit of the emission line towards short wave-lengths coincides with the (rather insecure) absorption edge.

Diamond has a fully occupied band that is separated (14) from the next free band by a forbidden region of about 7 eV. This has been found from absorption experiments in the ultraviolet. The present experiments also suggests the existence of such a forbidden region. If the width of the forbidden region is calculated from the distance between the centre of the α_1-line and the step near position 900, we get the value 7.5 eV.

The Physical Institute, University of Uppsala, February 1952.

REFERENCES

1. W. Scharwächter, Ph. Zs. *38* (1937), 165.
2. K. Alexopoulos & S. Peristerakis, Ph. Zs. *39* (1938), 688.
3. K. Alexopoulos & E. Scouluoudi, Phil. Mag. *40* (1949), 115.

4. A. Sommerfeld, Ann. d. Ph. *29* (1937), 715.
5. W. Franz, Ann. d. Ph. *29* (1937), 721.
6. G. Brogren, Nov. Act. Reg. Soc. Sc. Uppsala, Ser. IV, Vol. 14, N:o 4, 1949.
7. G. Brogren, Arkiv för Fysik, *3* (1951), 515.
8. G. Brogren, Ark. f Mat., Astr. o. Fys. Bd 36 B, No. 6, 1949.
9. J. Du Mond, Rev. Mod. Ph. *5* (1933), 1.
10. D. Tomboulian & R. Johnston, Phys. Rev. *83* (1951), 220.
11. C. A. Coulson, Nature *159* (1947), 265.
12. P. R. Wallace. Phys. Rev. *71* (1947), 622.
13. T. Magnusson, Nov. Act. Reg. Soc. Sc. Uppsala, Ser. IV. Vol. 11, No. 3, 1938.
14. G. Kimball, J, Chem. Phys. *3* (1935), 560.

Tryckt den 6 februari 1953

Uppsala 1953. Almqvist & Wiksells Boktryckeri AB

ARKIV FÖR FYSIK Band 6 nr 23

Communicated 24 May 1950 by Erik Hulthén and Oskar Klein

The vibrations and bending of pre-stressed circular plates

By Einar Lindholm

Introduction

The practical problem

When sawing wood with a circular saw the teeth are heated by the friction, while at the same time the central part of the saw is thoroughly cooled by the air. Owing to the uneven temperature thus obtained stresses appear. When they are great enough the saw looses its stiffness and cuts unevenly.

Methods of compensating for this disadvantage have been known for a long time. The first of these methods consists of a special device for heating of the central part of the saw as well during cutting. This method will be discussed in a later paper by the author.

The second method is that the central parts of the saw are worked with a hammer. This "tensioning" gives to the central parts an expansion causing initial stresses, which may compensate for the stresses from the heating of the periphery. The pre-stressing must of course be of a sufficient intensity to compensate for those stresses. On the other hand the intensity of the pre-stressing must not be so great that the saw becomes dish-shaped. Therefore one must be able to measure the intensity of the pre-stressing. As there are no direct methods the following indirect method must be used:

The saw is supported at two points of the periphery, diametrically opposite to each other, and then a straight-edge is placed across the saw at right angles to this diameter. For a circular plate without initial stresses the straight-edge will rest on the center of the plate, as the deflection is larger for the peripheral parts of the plate than for the center of the plate. (Nadai 1, 2, Timoshenko 3.) For a plate with initial compressive stresses in the central parts the deflection will be larger in the center than in the peripheral parts. Therefore the straight-edge will rest on the rim of the plate and daylight will be seen between the saw and the straight-edge. The intensity of the pre-stressing may be judged from the size of the clearance. The connection between the sag and the pre-stressing will be quantitatively discussed in the last part of this paper.

Outline of the theoretical investigation

In an earlier paper the author 4 has treated the stability of a circular plate at rest with a symmetrical temperature distribution. The differential equation for the buckling of a thin plate was solved by exact methods, and therefore only two simple cases could be investigated.

In the first case the rim of the plate is heated. It appeared that for a high enough rim temperature lateral buckling occurs. The buckling is characterized by two nodal diameters ($m=2$), and therefore two crests and two troughs are obtained at the rim.

In the second case the center of the plate is heated. Such a heating is equivalent to a pre-stressing of the center of the plate, and the pre-stressing is therefore conveniently characterized with the aid of the equivalent temperature. It appeared that when the pre-stressing temperature is high enough the plate buckles and becomes dish shaped ($m=0$). Of course it is of importance that the initial stresses do not exceed this critical buckling temperature for in that case it will be impossible to control the flatness of the plate.

This treatment of the statical cases forms of course only an introduction to the study of the stability of the saw when cutting the wood. When trying to investigate this general problem a difficulty at once arises: If the saw buckles at the periphery and at the same time rotates, the observer will find the saw vibrating with a frequency corresponding to double the angular velocity (as $m=2$). But such vibrations are not possible during cutting, for the cut in the wood prevents transverse vibrations at the point of cutting.

The solution of the problem is that the vibrations of the saw must be investigated dynamically. In the saw both standing waves and travelling waves are possible. And it may happen that a travelling wave may move backward in the saw at the same speed that the saw moves forward. These waves, although moving in the saw, are stationary in space. Therefore the cut in the wood has no damping influence on these waves and the amplitude of these waves may at resonance be large.

If the resonance is not exact, i.e. if the backward speed of the wave does not coincide exactly with the forward angular velocity of the rotating saw, the vibration will slowly rotate in space and the shape of the cut in the wood wil be like a sinus-curve. This agrees with experience in practice.

Earlier investigations as to the vibrations of plates

The transverse vibrations of a thin circular plate with free boundary have been investigated by KIRCHHOFF 5, 6, 7. SOUTHWELL 8 has extended KIRCHHOFF's solution to the case when a circular ring plate is clamped along the inner boundary.

The influence of the rotation on the vibration frequency has been investigated by STODOLA 9, 10 and by LAMB and SOUTHWELL 11, 8. The influence of the temperature distribution on the frequency has briefly been discussed by STODOLA 9 and FREUDENREICH 12.

Travelling transverse waves in rotating circular plates have been thoroughly investigated owing to their great importance for the stability of turbine discs by CAMPBELL 13 and FREUDENREICH 12. They have given the condition for the appearance of a backward-moving travelling wave that is stationary in space and have found the following relation: $p=m\omega$, where $p/2\pi$ is the vibration frequency of the turbine disc, ω is the angular velocity of the rotation of the turbine and m is the number of nodal diameters characterizing the travelling wave. — Their experiments show that this type of vibration may be caused by a small air or steam jet directed against one point of the rotating disc or by a small D.C. magnet placed near the disc. They found that as a result of this small force the turbine wheel developed a violent lateral vibration and broke. They have suggested that when such a wave develops under the action of steam in a turbine the cause for the trouble must be small irregularities in the nozzles (cf HORT 14). — In analogy to this the cause for such waves in the saw when cutting wood must be sought in the small force which the wood exerts on one side of the saw.

The aim of this investigation

In this paper we intend to investigate how the vibration frequencies of a circular plate with a free boundary are influenced by rotation, by pre-stressing of the central parts, by heating of the periphery and by clamping at the center. The vibrations are characterized by a varying number of nodal diameters. Vibrations with nodal circles will not be considered.

The theoretical results are then applied to a computation of the critical speed of a circular saw. Our intention is only to show that the results of our theoretical methods agree with experience in practice. No conclusions of value for the improvement of sawing may be inferred from this investigation. For this purpose it will be necessary first to investigate the case when the pre-stressing is performed within a circular ring-shaped domain.

For comparison with the findings of experimental experiences in practice we will apply our theoretical computations to a special circular saw with the following dimensions: radius $R = 50$ cm, collar radius $R_0 = 10$ cm, thickness $h = 0.325$ cm, modulus of elasticity $E = 2.1 \cdot 10^{12}$ dynes/cm^2, Poisson's ratio $\nu = 0.3$, density $\mu = 7.8$ g/cm^3, coefficient of linear thermal expansion $\alpha = 10^{-5}$ and the angular velocity of the rotation $\omega / 2\pi = 15$ s^{-1}. The pre-stressing and the temperature at the periphery will be stated below.

General theory

The variation problem

In our previous treatment of a circular plate at rest the buckling was computed by solving the differential equation for the buckling. In this paper we will take into consideration several circumstances which influence the problem at the same time. As the problem is now more complicated we must use a variational method. Such methods have previously been used in the treatment of transverse vibrations of circular plates by several authors (STODOLA 9, 10, LAMB and SOUTHWELL 11, SOUTHWELL 8, cf TIMOSHENKO 15).

In using this method the deflection of the plate is assumed to be $= w \cdot \cos pt$, where t is the time and $p/2\pi$ the vibration frequency. We obtain p from the following equation, where we choose w so as to make p a minimum:

$$p^2 \cdot \frac{\mu h}{2} \int_{R_0}^{R} \int_{0}^{2\pi} w^2 \, r \, d r \, d \theta = \frac{D}{2} \int_{R_0}^{R} \int_{0}^{2\pi} \left[\left\{ \frac{\partial^2 w}{\partial r^2} + \frac{1}{r} \frac{\partial w}{\partial r} + \frac{1}{r^2} \frac{\partial^2 w}{\partial \theta^2} \right\}^2 - \right.$$

$$\left. - 2 (1 - \nu) \left\{ \frac{\partial^2 w}{\partial r^2} \left(\frac{1}{r} \frac{\partial w}{\partial r} + \frac{1}{r^2} \frac{\partial^2 w}{\partial \theta^2} \right) - \left(\frac{1}{r} \frac{\partial^2 w}{\partial r \, \partial \theta} - \frac{1}{r^2} \frac{\partial w}{\partial \theta} \right)^2 \right\} \right] r \, d r \, d \theta + \tag{1}$$

$$+ \tfrac{1}{2} \int_{R_0}^{R} \int_{0}^{2\pi} \left[N_r \left(\frac{\partial w}{\partial r} \right)^2 + N_\theta \frac{1}{r^2} \left(\frac{\partial w}{\partial \theta} \right)^2 \right] r \, d r \, d \theta .$$

Here $D = \dfrac{E h^3}{12 (1 - \nu^2)}$ denotes the flexural rigidity of the plate and N_r and N_θ are the forces per unit length acting in the middle plane of the plate. The three integrals above mean the kinetic energy of the vibration, the strain energy of bending of the plate and the potential energy of the forces acting in the middle plane.

The boundary conditions that the function w must satisfy are the following: For $r = R_0$ the plate is clamped between the collars, and the conditions are

$$w = 0 \text{ and } \frac{\partial w}{\partial r} = 0. \tag{2}$$

For $r = R$ the edge is free and the bending moment and the equivalent shearing force vanish:

$$- D \left[\frac{\partial^2 w}{\partial r^2} + \nu \left(\frac{1}{r} \frac{\partial w}{\partial r} + \frac{1}{r^2} \frac{\partial^2 w}{\partial \theta^2} \right) \right] = 0 \tag{3}$$

$$- D \left[\frac{\partial^3 w}{\partial r^3} + \frac{1}{r} \frac{\partial^2 w}{\partial r^2} - \frac{1}{r^2} \frac{\partial w}{\partial r} - \frac{3 - \nu}{r^3} \frac{\partial^2 w}{\partial \theta^2} + \frac{2 - \nu}{r^2} \frac{\partial^3 w}{\partial r \, \partial \theta^2} \right] = 0. \tag{4}$$

For our following computations we assume that the vibration is characterized by m nodal diameters. We substitute

$$w = W \cdot \cos m \theta \tag{5}$$

in (1) and get

$$p^2 \cdot \frac{\mu h}{2} \int_{R_0}^{R} W^2 \, r \, d r = \frac{D}{2} \int_{R_0}^{R} \left[\left\{ \frac{\partial^2 W}{\partial r^2} + \frac{1}{r} \frac{\partial W}{\partial r} - \frac{m^2}{r^2} W \right\}^2 - \right.$$

$$\left. - 2 (1 - \nu) \left\{ \frac{\partial^2 W}{\partial r^2} \cdot \left(\frac{1}{r} \frac{\partial W}{\partial r} - \frac{m^2}{r^2} W \right) - \left(\frac{m}{r} \frac{\partial W}{\partial r} - \frac{m}{r^2} W \right)^2 \right\} \right] r \, d r + \tag{6}$$

$$+ \tfrac{1}{2} \int_{R_0}^{R} \left[N_r \left(\frac{\partial W}{\partial r} \right)^2 + N_\theta \frac{m^2}{r^2} W^2 \right] r \, d r .$$

The centrifugal forces

The forces N_r and N_θ in the middle plane of the plate are composed of the forces from the rotation of the plate, from the pre-stressing and from the heating of the periphery. When computing all these forces we shall assume that the clamping at the center of the disk does not prevent small radial displacements there. Further we assume that there is no hole in the center of the disk. These assumptions are of importance for the values of N_r and N_θ only in the central parts of the plate, where the plate is clamped and $\frac{\partial W}{\partial r}$ and W are small. Since in formula (6) N_r and N_θ are multiplied by these small quantities, our following computations are little influenced by these assumptions.

The expressions for the centrifugal forces are then

$$N_r = \frac{3+\nu}{8} h \mu \omega^2 [R^2 - r^2] \tag{7}$$

$$N_\theta = \frac{3+\nu}{8} h \mu \omega^2 \left[R^2 - \frac{1+3\nu}{3+\nu} \cdot r^2\right]. \tag{8}$$

The forces from the pre-stressing

We describe the pre-stressing with the aid of the equivalent temperature T, and assume that the pre-stressing is homogeneous from the center to the radius ϱ, and get:

$$\begin{aligned} T &= \vartheta \text{ for } r < \varrho \\ T &= 0 \text{ for } \varrho < r < R. \end{aligned} \tag{9}$$

Here ϑ means the constant pre-stressing temperature. For the forces in the middle plane we obtain (see TIMOSHENKO 16, p. 364)

For $$r < \varrho: \; N_r = -\frac{\alpha E h \vartheta}{2} \left[1 - \frac{\varrho^2}{R^2}\right] \tag{10}$$

$$N_\theta = -\frac{\alpha E h \vartheta}{2} \left[1 - \frac{\varrho^2}{R^2}\right] \tag{11}$$

For $$\varrho < r < R: \; N_r = -\frac{\alpha E h \vartheta}{2} \left[\frac{\varrho^2}{r^2} - \frac{\varrho^2}{R^2}\right] \tag{12}$$

$$N_\theta = +\frac{\alpha E h \vartheta}{2} \left[\frac{\varrho^2}{r^2} + \frac{\varrho^2}{R^2}\right] \tag{13}$$

The forces from the heating of the periphery

In the author's earlier computation of the buckling of a non-rotating circular plate the results were applied to a circular saw with radius 20 cm for which measurements of the periphery temperature were carried out by SKOGLUND 17. It appeared that, with sufficient accuracy, the temperatures measured by SKOGLUND might be approximated by a simple power function

$$T = t\,t'\,r^{12} \tag{14}$$

where T is the temperature at the distance r from the center, t is the periphery temperature and $t' = R^{-12}$.

The computations in this paper must be carried out for a larger circular saw. As no measurements of the temperatures are available it will be necessary to estimate the temperature distribution for this saw with the aid of the theory given by BECK 18.

According to BECK the temperature T in a circular disc that is heated along the periphery and air cooled along the sides of the body of the saw may be described with the aid of a modified Bessel function

$$T = \text{const} \cdot I_0\left(r \cdot \sqrt{\frac{2\alpha}{\lambda h}}\right) \tag{15}$$

where λ is the thermal conductivity and α here denotes the surface conductivity.

In one of SKOGLUND's measurements (see LINDHOLM 4, Table 1) he obtained for $r = 20$ cm $T = 66°$ and for $r = 19$ cm $T = 33°$. With these values and $h = 0.2$ cm and $\lambda = 0.07$ cal/cm · sec°C (cf HATTORI 22) we obtain $\alpha = 0.0037$ cal/cm²sec°C = 133 kcal/m²h°C.

JÜRGES 19 has experimentally investigated the dependence of the surface conductivity on the air velocity, and for large air velocities he has obtained the following connection

$$\alpha = 6.12 \cdot v^{0.78} \tag{16}$$

where v is the air velocity in m/sec. If for the air velocity we use the velocity of the periphery of the saw: $v = 47$ m/sec, we get $\alpha = 123$ kcal/m²h°C. If we take into consideration that a small error in SKOGLUND's temperature determination has a large influence on α and that the value of the thermal conductivity is rather uncertain, we must be satisfied with the agreement between the two determinations of α and may consider it as a support for our computations.

For the larger saw the velocity of the periphery has about the same value as for SKOGLUND's saw. Therefore, we may assume the surface conductivities to be equal and for the larger saw we can compute the ratio between the temperatures for $r = 50$ cm and $r = 48$ cm. This ratio is 3.1.

Then we assume that the temperature may be described by help of the function

$$T = t\,t' \cdot r^{s} \tag{17}$$

where $t' = R^{-s}$. By comparison with the ratio 3.1 we find that $s \approx 27$.

With this temperature function we compute the forces in the middle plane and obtain (α is here the coefficient of linear thermal expansion)

$$N_r = \frac{\alpha E h t t'}{s+2} [R^s - r^s] \tag{18}$$

$$N_\theta = \frac{\alpha E h t t'}{s+2} [R^s - (s+1) r^s]. \tag{19}$$

The deflection W

In the application of RAYLEIGH's method we substitute in (6) an assumed form for W and adjust this function so as to make the vibration frequency $p/2\pi$ a minimum. During this adjustment the function W should satisfy the four boundary conditions (2), (3) and (4).

STODOLA 10 used the function $W = r^n - R_0^n$. This function satisfies the boundary condition $W = 0$ for $r = R_0$ but not the condition $\frac{\partial W}{\partial r} = 0$. In that connection this is of small importance as the turbine disks in STODOLA's investigation have hyperbolic profile and are thus thick at the hub. From this follows that the deflection there is small, the power n is high and the second boundary condition is approximately satisfied. — In our investigation of the vibrations of plates of uniform thickness both boundary conditions for $r = R_0$ are, however, of essential importance.

In his investigation of the importance of the clamping STODOLA made use of the function $W = a(r - R_0)^2 + b(r - R_0)^3$, which may be brought to satisfy both boundary conditions for $r = R_0$. But the computations are very complicated with this function and therefore STODOLA made use of it only for a non-rotating turbine disc.

SOUTHWELL 8 carried out his computations only in a special case: $m = 0$ and $R_0 = 0$. He used the function

$$W = r^n - \tfrac{1}{4} n^2 (n-2) R^{n-2} r^2 \ln \frac{r}{R} \tag{20}$$

which satisfies both boundary conditions for $r = 0$ and one of the conditions for $r = R$. The function is complicated.

In using the RAYLEIGH-RITZ's method it may be proved, however, that it is not necessary to prescribe the boundary conditions for a free edge, but, on the other hand, it is necessary to prescribe them along a clamped edge. It was pointed out already by RITZ 20 that the boundary conditions for the free edge are satisfied with better accuracy when the vibration frequency $p/2\pi$ is approaching its limit. The simplest argument for this statement is perhaps that the boundary conditions for a plate may be derived from the strain energy integral (KIRCHHOFF 5, 6, LORD RAYLEIGH 7). According to a more general proof given by SOKOLNIKOFF 21 the function that shall minimize the potential energy must satisfy the boundary conditions on that portion of the surface where the displacements are prescribed. The portion of the surface on which the external forces are specified need not be taken into account in determining the set of admissible functions. This means that along a clamped edge the conditions $W=0$ and $\frac{\partial W}{\partial n}=0$ must be satisfied. The problem of finding a convenient function for the deflection has been highly simplified as a result of these observations.

We have to choose a function satisfying the boundary conditions (2) and have chosen:

$$W=r^n\left(\ln\frac{r}{R_0}\right)^2 \tag{21}$$

where n is the parameter to be determined. Below it will be shown by comparison with some exact solutions to our problems that the accuracy obtained with the aid of this function is sufficient. Probably, equally good results may be obtained with the function

$$W=r^n(r-R_0)^2 \tag{22}$$

but the computations are a little lengthier with this function.

Further, we are going to perform some computations for a plate without collars and choose then the function used by Stodola

$$W=r^n \tag{23}$$

which satisfies the boundary conditions (2) for $r=0$.

Computation of the energy integrals for a plate clamped between collars

For computation of the integrals we substitute (21) into (6). For the first integral that represents the kinetic energy we obtain

$$K=p^2\cdot\frac{\mu h}{2}\cdot R_0^{2n+2}\cdot\{K\} \tag{24}$$

with

$$\{K\}=\int_1^{R_1}(\ln x)^4 x^{2n+1}dx \tag{25}$$

and with

$$R_1=\frac{R}{R_0}\cdot \tag{26}$$

The second integral means the strain energy of bending of the plate. For its computation we use $\nu=0.3$ and get

$$V_D=\frac{D}{2}\cdot R_0^{2n-2}\cdot\{V_D\} \tag{27}$$

where

$$\{V_D\} = [n^4 - 1.4\,n^3 + 0.8\,m^2 n^2 + 1.4\,n^2 - 4.2\,m^2 n + 1.4\,m^2 + m^4] \cdot \int_1^{R_1} (\ln x)^4 x^{2n-3}\,dx +$$
$$+ [8\,n^3 - 8.4\,n^2 + 3.2\,m^2 n + 5.6\,n - 8.4\,m^2] \cdot \int_1^{R_1} (\ln x)^3 x^{2n-3}\,dx +$$
$$+ [20\,n^2 - 14\,n + 4.4\,m^2 + 5.6] \cdot \int_1^{R_1} (\ln x)^2 x^{2n-3}\,dx +$$
$$+ [16\,n - 5.6] \cdot \int_1^{R_1} \ln x \cdot x^{2n-3}\,dx + 4 \int_1^{R_1} x^{2n-3}\,dx. \tag{28}$$

The third integral is composed of contributions from the centrifugal forces, the pre-stressing and the heating of the periphery. The potential energy of the centrifugal forces is

$$V_\omega = \frac{3+\nu}{16} h\,\mu\,\omega^2 R_0^{2n+2} \cdot \{V_\omega\} \tag{29}$$

where

$$\{V_\omega\} = R_1^2 \Bigg[(n^2+m^2) \int_1^{R_1} (\ln x)^4 x^{2n-1}\,dx + 4\,n \int_1^{R_1} (\ln x)^3 x^{2n-1}\,dx +$$
$$+ 4 \int_1^{R_1} (\ln x)^2 x^{2n-1}\,dx \Bigg] - \left(n^2 + \frac{1+3\nu}{3+\nu} m^2\right) \int_1^{R_1} (\ln x)^4 x^{2n+1}\,dx -$$
$$- 4\,n \int_1^{R_1} (\ln x)^3 x^{2n+1}\,dx - 4 \int_1^{R_1} (\ln x)^2 x^{2n+1}\,dx. \tag{30}$$

The potential energy of the forces from the pre-stressing is

$$V_\vartheta = \frac{\alpha E h \vartheta}{4} \cdot R_0^{2n} \cdot \{V_\vartheta\} \tag{31}$$

with

$$\{V_\vartheta\} = \frac{\varrho^2}{R^2} \Bigg[(n^2+m^2) \int_1^{R_1} (\ln x)^4 x^{2n-1}\,dx + 4\,n \int_1^{R_1} (\ln x)^3 x^{2n-1}\,dx +$$
$$+ 4 \int_1^{R_1} (\ln x)^2 x^{2n-1}\,dx \Bigg] - \Bigg[(n^2+m^2) \int_1^{\varrho_1} (\ln x)^4 x^{2n-1}\,dx + 4\,n \int_1^{\varrho_1} (\ln x)^3 x^{2n-1}\,dx +$$
$$+ 4 \int_1^{\varrho_1} (\ln x)^2 x^{2n-1}\,dx \Bigg] - \varrho_1^2 \Bigg[(n^2-m^2) \int_{\varrho_1}^{R_1} (\ln x)^4 x^{2n-3}\,dx +$$
$$+ 4\,n \int_{\varrho_1}^{R_1} (\ln x)^3 x^{2n-3}\,dx + 4 \int_{\varrho_1}^{R_1} (\ln x)^2 x^{2n-3}\,dx \Bigg] \tag{32}$$

and with

$$\varrho_1 = \frac{\varrho}{R_0} \tag{33}$$

The potential energy of the forces from the heating of the periphery is

$$V_t = \frac{\alpha E h t}{2(s+2)} \cdot R_0^{2n} \cdot \{V_t\} \tag{34}$$

with

$$\begin{aligned}\{V_t\} = {} & (n^2+m^2)\int_1^{R_1} (\ln x)^4\, x^{2n-1}\,dx + 4n\int_1^{R_1} (\ln x)^3\, x^{2n-1}\,dx + 4\int_1^{R_1} (\ln x)^2\, x^{2n-1}\,dx - \\ & -\left(\frac{R_0}{R}\right)^s \Bigg[(n^2+m^2 s+m^2)\int_1^{R_1} (\ln x)^4\, x^{2n+s-1}\,dx + 4n\int_1^{R_1} (\ln x)^3\, x^{2n+s-1}\,dx + \\ & + 4\int_1^{R_1} (\ln x)^2\, x^{2n+s-1}\,dx\Bigg].\end{aligned} \tag{35}$$

Computation of the energy integrals for a plate without collars

For a solid plate without collars we substitute (23) into (6) and obtain

$$K = p^2 \cdot \frac{\mu h}{2} \cdot \frac{R^{2n+2}}{2n+2} \tag{36}$$

$$V_D = \frac{D}{2} \cdot \frac{R^{2n-2}}{2n-2} \cdot \left[(n^2-m^2)^2 - 2(1-\nu)(n-1)(n^2+m^2-2nm^2)\right] \tag{37}$$

$$V_\omega = \frac{3+\nu}{32}\, h\,\mu\,\omega^2 \cdot R^{2n+2} \cdot \left[\frac{n^2+m^2 n+m^2}{n(n+1)} - \frac{1+3\nu}{3+\nu}\,\frac{m^2}{n+1}\right] \tag{38}$$

$$V_\vartheta = \frac{\alpha E h \vartheta \varrho^2}{8} \cdot \left[R^{2n-2} - \varrho^{2n-2}\right]\left[\frac{m^2+n^2}{n} + \frac{m^2-n^2}{n-1}\right] \tag{39}$$

$$V_t = \frac{\alpha E h t}{2} \cdot \frac{R^{2n}}{s+2} \cdot \left[\frac{n^2+m^2}{2n} - \frac{n^2+m^2+s m^2}{2n+s}\right]. \tag{40}$$

The first two expressions (36) and (37) have already been computed by STODOLA 10.

Computation of the vibration frequency for two nodal diameters

The vibrations of a non-rating plate without initial stresses, clamped at its center between two collars

This case has been investigated by SOUTHWELL 8. He solved the differential equation for the vibration exactly with the aid of Bessel functions for several clamping diameters. By interpolation from Table I in his paper we may obtain the following value for the frequency for $R/R_0=5$

$$p^2=\frac{E\,h^2}{\mu\,R^4}\cdot 3.73. \tag{41}$$

Treating the problem with the variational method we put $K=V_D$. We take $m=2$ and compute p^2 for some values of the parameter n ($n=0$, 0.5, 1, 1.5, 2). The minimum of p^2 is obtained for $n=0.7$ and we get

$$p^2=\frac{E\,h^2}{\mu\,R^4}\cdot 3.80. \tag{42}$$

The agreement between our approximate and SOUTHWELL's exact computation must be considered satisfactory. This proves that the function (21) is a good approximation to the exact solution for W.

A considerable simplification of our computations would have been obtained if we instead had studied a plate without collars using the simpler function (23) for W. The result of such a computation is (in agreement with STODOLA and KIRCHHOFF)

$$p^2=\frac{E\,h^2}{\mu\,R^4}\cdot 2.66. \tag{43}$$

It appears from this that the collars have a great influence on the vibration frequency (cf SOUTHWELL 8). In a quantitative investigation of the stability of a circular saw one is therefore not allowed to neglect the influence of the collars.

The vibrations of a rotating membrane clamped at its center

In this case SOUTHWELL has solved the differential equation for the vibration with the aid of hypergeometric series and has been able to show that the vibration frequency is independent of the radius of the clamping circle and is computed with the following formula

$$p^2=\omega^2\cdot 2.35. \tag{44}$$

In our treatment of the problem with the variational method we put $K=V_\omega$. The minimum is obtained for $n=0.7$ and we find for $R/R_0=5$:

$$p^2=\omega^2\cdot 2.36. \tag{45}$$

The agreement is good. It has, however, with this method not been possible to prove that the vibration frequency is independent of the radius of the collars.

The vibrations of a rotating pre-stressed plate that is clamped at its center and heated along its periphery

We obtain the frequency from the equation $K = V_D + V_\omega + V_\vartheta + V_t$ and find

$$p^2 = \frac{E\,h^2}{12\,(1-\nu^2)\,\mu\,R_0^4} \cdot \frac{\{V_D\}}{\{K\}} + \omega^2 \cdot \frac{3+\nu}{8} \cdot \frac{\{V_\omega\}}{\{K\}} + \frac{\alpha\,E\,\vartheta}{2\,\mu\,R_0^2}\,\frac{\{V_\vartheta\}}{\{K\}} + \\ + \frac{\alpha\,E\,t}{(s+2)\,\mu\,R_0^2} \cdot \frac{\{V_t\}}{\{K\}}. \tag{46}$$

We begin by computing the values of the last two terms for some values of n. It appears that for the n-values of interest they are almost linear functions of n and that the change in their value in going from $n = 0.5$ to $n = 1$ is comparatively small. For that reason n will in the main be determined by the first two terms and for the saw under consideration it has appeared that p^2 is obtained with sufficient accuracy if n is determined entirely by the first two terms. As the first two terms both have minima for $n = 0.7$ when $R/R_0 = 5$, we should use this n-value in (46). After computation of the integrals there we obtain

$$p^2 = \frac{E\,h^2}{\mu\,R^4} \cdot 3.80 + \omega^2 \cdot 2.36 + \frac{\alpha\,E\,\vartheta}{\mu\,R^2} \cdot 0.94 - \frac{\alpha\,E\,t}{\mu\,R^2} \cdot 0.37. \tag{47}$$

This expression is valid only for $R/R_0 = 5$, $\varrho/R_0 = 4.5$ and $s = 27$ provided that the plate has such dimensions that the n-value is determined by the first two terms.

Determination of the critical periphery temperature for a saw without initial stresses

We shall use the formula above to investigate the stability of a saw without initial stresses. First we assume that its periphery is not heated. We take $\vartheta = t = 0$ and substitute further $E = 2.1 \cdot 10^{12}$, $h = 0.325$, $\mu = 7.8$, $R = 50$ and $\omega = 94.2$. We obtain $p^2 = 17\,300 + 21\,000 = 38\,300$. We observe that the frequency is determined by the stiffness and the centrifugal forces to about the same extent. The frequency is 31.2.

If now the periphery of this saw is heated during cutting the vibration frequency will diminish. When it has decreased to 30, i.e. to twice the angular velocity of the rotation, a backward moving travelling wave will develope. This is stationary or almost stationary in space and therefore the saw cut will be shaped like a sinus-curve. The critical periphery temperature is obtained from the following equation

$$4\pi^2 \cdot 900 = 17\,300 + 21\,000 - \frac{\alpha E t}{\mu R^2} \cdot 0.37 \tag{48}$$

and amounts in this case to 7° above the room temperature. Owing to this small value it is impossible to use this saw without pre-stressing. This result agrees with experience in practice with saws of this dimension.

Determination of the critical periphery temperature for a pre-stressed saw

We assume that the equivalent pre-stressing temperature amounts to half the critical buckling temperature. The reason for this assumption is given in the last part of this paper. The critical buckling temperature is obtained from our previous exact computation (Tab. 2, Lindholm 4) and we obtain ϑ from

$$\frac{\alpha \vartheta (1-\nu^2) R^2}{h^2} = \frac{4.01}{2}. \tag{49}$$

When the periphery is not heated, we get the vibration frequency from the equation $p^2 = 17\,300 + 21\,000 + 9\,400 = 47\,700$. We observe that the influence of the pre-stressing on the frequency is comparatively small. The frequency is 34.8.

When the periphery of this saw is heated during cutting the periphery temperature may rise to about 31° above the room temperature before the travelling wave developes.

No reliable measurements of the periphery temperature of a saw have been carried out with which this value may be compared. Skoglund 17 has made some measurements with a small saw and very low feed speed, i.e. a low periphery temperature. If these measurements are extrapolated, they show that our computed critical periphery temperature is of correct size.

The dependence of the critical periphery temperature on the angular velocity

If the angular velocity of a saw is raised, the critical periphery temperature will be lower and the intensity of the pre-stressing must be made higher. If in the case under consideration we increase the angular velocity of the saw to say 17, we obtain, when the periphery is not heated, $p^2 = 17\,300 + 26\,900 + 9\,400 = 53\,600$ from which the vibration frequency is computed to 36.9. The difference between this value and the critical value 34 is small and therefore the critical periphery temperature will be only 20° above the room temperature. It follows that the intensity of the pre-stressing must be higher for this saw as has been found in practice.

The accuracy of our computations

It appears from our results that the accuracy with which our computations have been carried out is necessary. If we had neglected the influence of the collars the computations would have been considerably simplified. But as the stability of the saw is determined by the difference between the vibration frequency and the angular velocity of the rotation the reliability of our results would then have been too small.

Determination of the vibration frequencies for other modes

After ascertaining that the instability of a circular saw with high periphery temperature and high speed may be explained by vibrations with two nodal diameters, it is of course necessary to investigate the possibilities of resonance phenomena in modes having another number of nodal diameters.

Vibrations with one nodal diameter: $m=1$

When computing the frequency for $m=1$ it appears that the first term, which corresponds to the vibration of a non-rotating plate, has a deep minimum for $n=0.25$. The second term which gives the frequency for a rotating membrane has a shallow minimum for $n=-0.4$. The n-value will therefore be determined entirely by the first term and we get

$$p^2=\frac{E\,h^2}{\mu\,R^4}\cdot 2.00+\omega^2\cdot 1.25-\frac{\alpha\,E\,\vartheta}{\mu\,R^2}\cdot 0.08+\frac{\alpha\,E\,t}{\mu\,R^2}\cdot 0.04. \tag{50}$$

The first term agrees with the expression that may be obtained by interpolation from SOUTHWELL's results. For the second term SOUTHWELL has obtained $\omega^2\cdot 1.00$. The cause of the difference must be that the shape of the plate is determined by the flexural rigidity in our computations and this shape does not agree with the shape of a rotating vibrating membrane.

Comparing (47) and (50) we observe immediately that the last two terms are very small. The frequency in the mode with one nodal diameter is therefore practically independent of pre-stressing and heating of the periphery for the saw under consideration.

If the pre-stressing has the same value as above and if $t=31^\circ$, we obtain for the saw under consideration $p^2=9\,100+11\,100-800+1\,340$ and for the frequency 22.9. The difference between this value and the critical value 15 is very great and therefore there is no risk of resonance phenomena occurring in this mode.

The symmetrical mode: $m=0$

For the symmetrical mode, too, n is determined by the first term and we obtain with $n=0.25$

$$p^2=\frac{E\,h^2}{\mu\,R^4}\cdot 2.50+\omega^2\cdot 0.85-\frac{\alpha\,E\,\vartheta}{\mu\,R^2}\cdot 0.42+\frac{\alpha\,E\,t}{\mu\,R^2}\cdot 0.14. \tag{51}$$

The first term agrees with SOUTHWELL's results, but it is impossible to compare the second term with SOUTHWELL's results, for he has only estimated the vibration frequency for a rotating plate without collars.

If in (51) we let ϑ vary between 0° and the whole critical buckling temperature and if t is assumed to vary between 0° and 31°, we obtain for the saw in question vibration frequencies varying between 16.3 and 24.5. As the critical value for this mode is 0, there is no risk of resonance.

Vibrations with three nodal diameters: $m=3$

In this mode the influence of the collars vill be negligible, because the deflection in the central parts of the plate must be small for this high m-value. This is evident from SOUTHWELL's tables, too. Therefore we compute the vibration frequency for a plate without collars and obtain with $n=2.2$

$$p^2=\frac{E\,h^2}{\mu R^4}\cdot 14.3+\omega^2\cdot 4.14+\frac{\alpha\,E\,\vartheta}{\mu\,R^2}\cdot 2.90-\frac{\alpha\,E\,t}{\mu\,R^2}\cdot 1.14. \tag{52}$$

If ϑ amounts to half the critical buckling temperature and the periphery is not heated, the frequency is 57.6, and for the periphery temperature 31° the frequency is 48.5. This is higher than the critical value 45 and therefore no resonance is obtained in the mode $m=3$ before it has already appeared in the mode $m=2$.

For higher m-values the frequencies are very high owing to the stiffness of the plate and there is no risk of resonance.

The bending of a circular plate, pre-stressed in the center and supported at two points of the periphery

There was in the introduction a description of how, when pre-stressing a circular saw, one is able to measure the intensity of the pre-stressing by supporting the saw at two diametrically opposite points of the periphery. We are now going to discuss how the equivalent pre-stressing temperature ϑ may be obtained from the deflection of the plate.

This method of measuring the internal stresses in the plate is the necessary condition for obtaining agreement between the theoretical and experimental results. CAMPBELL 13 has experimentally determined the vibration frequencies of some non-rotating circular plates. The agreement between his experimental results and KIRCHHOFF's theory was bad owing to internal stresses in the plates, which it was impossible for him to determine.

Nadai's results for a plate without internal stresses

For a uniformly loaded circular plate supported at two diametrically opposite points of the periphery NADAI 1, 2 has given the differential equation and solved it by means of a series. As the boundary is free except at the points of support where concentrated forces are acting, the boundary conditions are:
At the points of support for $r=R$ and $\theta=0$ or $=\pi$ we have $w=0$.
Along the periphery for $r=R$ we have $M_r=0$ and

$$V=-\frac{q\,R}{2}\left[1+2\cdot\sum_{m=2,\,4,\,6\ldots}^{\infty}\cos m\,\theta\right] \tag{53}$$

where q is the intensity of the uniform load and V the equivalent shearing force. NADAI's solution is $w = w_0 + w_1$ where

$$w_0 = \frac{q\,R^2}{64\,D}\left[\frac{(5+\nu)\,R^2 - 2\,(3+\nu)\,r^2}{1+\nu} + \frac{r^4}{R^2}\right] \tag{54}$$

and

$$w_1 = -\frac{q\,R^4}{2\,(3+\nu)\,D}\sum_{m=2,4,6\ldots}^{\infty}\left[\frac{1}{m\,(m-1)} + \frac{2\,(1+\nu)}{(1-\nu)\,(m-1)\,m^2} - \frac{r^2}{R^2\,m\,(m+1)}\right]\frac{r^m}{R^m}\cos m\,\theta + \text{const.} \tag{55}$$

w_0 means the deflection of a plate simply supported along the periphery.

The pre-stressed plate

In our approximate computation of the deflection of the pre-stressed plate w must be chosen so as to make the potential energy a minimum. The expression for the potential energy is (see for instance TIMOSHENKO 3 p. 95 and 312)

$$\frac{D}{2}\int_{R_0}^{R}\int_{0}^{2\pi}\left[\left\{\frac{\partial^2 w}{\partial r^2} + \frac{1}{r}\frac{\partial w}{\partial r} + \frac{1}{r^2}\frac{\partial^2 w}{\partial \theta^2}\right\}^2 - 2\,(1-\nu)\left\{\frac{\partial^2 w}{\partial r^2}\left(\frac{1}{r}\frac{\partial w}{\partial r} + \frac{1}{r^2}\frac{\partial^2 w}{\partial \theta^2}\right) - \left(\frac{1}{r}\frac{\partial^2 w}{\partial r\,\partial \theta} - \frac{1}{r^2}\frac{\partial w}{\partial \theta}\right)^2\right\}\right] r\,d\,r\,d\,\theta -$$

$$-\int_{R_0}^{R}\int_{0}^{2\pi} q\,w\,r\,d\,r\,d\,\theta + \int_{0}^{2\pi}\frac{q\,R}{2}\left[1 + 2\sum_{m=2,4,6\ldots}^{\infty}\cos m\,\theta\right] w\,d\,s +$$

$$+\int_{R_0}^{R}\int_{0}^{2\pi}\frac{1}{2}\left[N_r\left(\frac{\partial w}{\partial r}\right)^2 + N_\theta\,\frac{1}{r^2}\left(\frac{\partial w}{\partial \theta}\right)^2\right] r\,d\,r\,d\,\theta. \tag{56}$$

N_r and N_θ are the forces in the middle plane caused by the pre-stressing and q the uniform load (the weight of the plate).

The function w must satisfy only the following boundary condition: In the points of support we must have $w = 0$. The other two boundary conditions need not be taken into consideration when choosing the function w (cf SOKOLNIKOFF l. c.)

We take now

$$w = \sum_{0}^{\infty} W_m \cos m\,\theta \tag{57}$$

and compute the minimum of the potential energy for each m-value separately. It appears that for odd m-values $W_m = 0$.

Symmetrical deflection

For $m=0$ we choose the function

$$W_0 = c \cdot e^{-\frac{b}{2}\left(\frac{r}{R}\right)^2} \tag{58}$$

where b and c are the parameters to be determined, and obtain for the potential energy

$$\frac{D\,b\,c^2}{R^2}\left[1-e^{-b}\left\{\frac{b^2}{2}-b\,\nu+1\right\}\right]+\frac{2\,R^2\,q\,c}{b}\left[e^{-\frac{b}{2}}-1\right]+R^2\,q\,c\,e^{-\frac{b}{2}}+ \\ +\frac{\alpha\,E\,h\,\vartheta\,c^2}{4}\left[\frac{\varrho^2}{R^2}-1+e^{-\frac{b\,\varrho^2}{R^2}}-\frac{\varrho^2}{R^2}\,e^{-b}\right]. \tag{59}$$

Equating to zero the derivative of this expression with respect to c, we obtain an equation giving c as a function of b

$$c=\frac{2\,R^2\,q}{b}\left[1-e^{-\frac{b}{2}}\left(1+\frac{b}{2}\right)\right]\Big/\left\{\frac{2\,D\,b}{R^2}\left[1-e^{-b}\left\{\frac{b^2}{2}-b\,\nu+1\right\}\right]- \right. \\ \left. -\frac{\alpha\,E\,h\,\vartheta}{2}\left[1-\frac{\varrho^2}{R^2}+\frac{\varrho^2}{R^2}\,e^{-b}-e^{-\frac{b\,\varrho^2}{R^2}}\right]\right\}. \tag{60}$$

If this expression for c is substituted in (59), we may compute the potential energy for some b-values and obtain its minimum.

First we investigate a plate without initial stresses for comparison with NADAI's exact results. The minimum is obtained for $b=1.1$ giving $c=\frac{q\,R^4}{D}\cdot 0.152$ and the deflection $=\frac{q\,R^4}{D}\cdot 0.0641$. The agreement with NADAI's value 0.0636 is good and shows that the chosen funtion (58) is a good approximation to the exact deflection. A small change of b to for instance 1.2 has no appreciable influence on the good result.

Then we investigate a pre-stressed plate with no lateral load to obtain a comparison with the author's earlier computation of the buckling of a circular plate (LINDHOLM 4). We take $q=0$ and obtain the buckling condition by equating to zero the potential energy (59) and by computing the b-value that makes ϑ a minimum. We obtain $b=1.3$ and $\frac{\alpha\,\vartheta\,(1-\nu^2)\,R^2}{h^2}=4.23$. Our previous exact computation of the buckling temperature (LINDHOLM 4) gives for the constant the value 4.01. The agreement is rather good and forms a support for our choice of the function (58). — The advantages of this normal probability function are much more pronounced for smaller values of ϱ/R. When in these cases the plate buckles, the deflection takes place in the main near the center, and the normal probability function is then a better approximation to the true deflection than any other simple function.

In the general case we take $\varrho/R=0.9$ and $b=1.2$ and obtain

$$c=\frac{q\,R^4}{D}\cdot 0.122\bigg/\left\{0.850-\frac{\alpha\,\vartheta\,(1-\nu^2)\,R^2}{h^2}\cdot 0.200\right\}. \tag{61}$$

If we here take $\vartheta=$ the critical buckling temperature, c will be infinite. If we take $\vartheta=$ half the critical buckling temperature, we obtain $c=\frac{q\,R^4}{D}\cdot 0.287$.

The deflection for $m=2$ and $m=4$

For these and higher m-values we choose

$$W_m=c\cdot r^n \tag{62}$$

where c and n are the parameters. With the notations (37) and (39) the potential energy then becomes

$$c^2\,[V_D+V_\vartheta]+c\,q\,R^{2n+2}. \tag{63}$$

An approximate value of n may be obtained using the deep minimum of V_D. With this n-value we obtain c by taking the derivative of the potential energy with respect to c

$$c=-\frac{q\,R^4}{D}\cdot\frac{1}{R^n}\cdot 2\,(n-1)\bigg/\left\{(n^2-m^2)^2-2\,(1-\nu)\,(n-1)\,(n^2+m^2-2\,n\,m^2)+\right.$$
$$\left.+\frac{\alpha\,\vartheta\,(1-\nu^2)\,R^2}{h^2}\cdot 6\left(\frac{\varrho}{R}\right)^2\cdot\left[1-\left(\frac{\varrho}{R}\right)^{2n-2}\right]\left[2\,m^2-\frac{m^2+n^2}{n}\right]\right\}. \tag{64}$$

If we here take $\vartheta=0$ we obtain the result for a plate without initial stresses and may compare this with NADAI's values for the deflection. For $m=2$ and $m=4$ the difference is only 2 %, which shows that the chosen function (62) is satisfactory.

For a plate pre-stressed to half the critical buckling temperature we take $m=2$, $\varrho/R=0.9$, $n=1.8$ and $\frac{\alpha\,\vartheta\,(1-\nu^2)\,R^2}{h^2}=\frac{0.850}{2\cdot 0.200}$. The expression for ϑ is obtained from (61). With these values we obtain $c=-\frac{q\,R^4}{D}\cdot\frac{1}{R^n}\cdot 0.105$.

For $m=4$ we obtain similarly $n=3.3$ and $c=-\frac{q\,R^4}{D}\cdot\frac{1}{R^n}\cdot 0.012$.

The resulting deflection of the pre-stressed plate

By adding a constant to the sum of the expressions for the deflection, our solution will satisfy the boundary condition $w=0$ at the points of support, and we obtain

$$w = \frac{q\,R^4}{D}\left[0.287 \cdot e^{-0.6\frac{r^2}{R^2}} - 0.105\left(\frac{r}{R}\right)^{1.8}\cos 2\,\theta - 0.012\left(\frac{r}{R}\right)^{3.3}\cos 4\,\theta - 0.041\right]. \tag{65}$$

For $r=0$ we obtain $w=\frac{q\,R^4}{D}\cdot 0.246.$

For $r/R=1$ and $\theta=\pi/2$ we obtain $w=\frac{q\,R^4}{D}\cdot 0.210.$

If we place a straight-edge across the plate along the diameter $\theta=\pi/2$, the clearance between the straight-edge and the center of the plate will be $\frac{q\,R^4}{D}\cdot 0.036$. As the uniform load is the weight of the plate, we take $q=981\,h\,\mu$ and obtain for the saw under consideration the value 0.085 cm for ϑ = half the critical buckling temperature.

Similarly, we obtain the deflection of a plate pre-stressed to 3/4 of the buckling temperature.

For $r=0$ we obtain $w=\frac{q\,R^4}{D}\cdot 0.357.$

For $r/R=1$ and $\theta=\pi/2$ we obtain $w=\frac{q\,R^4}{D}\cdot 0.174.$

The clearance at the center will be $\frac{q\,R^4}{D}\,0.183=0.43$ cm.

In practice, the pre-stressing of circular saws of this size is carried out in such a way that the clearance at the center is a little more than 0.1 cm. That means that these saws are pre-stressed to a little more than half the buckling temperature.

SUMMARY

1. The transverse vibrations of a circular plate are investigated with variational methods. The plate is rotating, has a free boundary, is clamped at the center along a circular boundary and has a symmetrical temperature distribution. This temperature distribution consists of a heating of the periphery and a homogeneous heating of the central parts of the plate corresponding to initial compression stresses there. Vibrations with different numbers of nodal diameters are investigated.

2. The boundary conditions that must be satisfied when treating a plate with a free boundary by the variational method are discussed. This discussion facilitates the choice of functions for solving the problem.

3. Further, the investigation includes the resonance phenomena that appear when the travelling transverse wave has the same velocity as the rotation of the plate. The dependence of the resonance frequencies on the number of nodal diameters, the angular velocity and the temperature distribution are computed.

4. Finally, the bending of a homogeneously loaded circular plate is investigated. The plate is supported in two diametrically opposite points of the periphery and its central parts are homogeneously heated. This computation makes possible a quantitative measurement of the initial stresses in the plate.

5. The results are applied to the stability of a circular saw cutting wood.

May 1950, Physics Department, The University, Stockholm.

REFERENCES

1. Nádai, A., Phys. Zeits. *23,* 366, 1922.
2. ——, Elastische Platten, Berlin 1925.
3. Timoshenko, S., Theory of Plates and Shells, New York 1940.
4. Lindholm, E., Teknisk Tidskrift *80,* 243, 1950.
5. Kirchhoff, G., Journ. f. Math. *40,* 51, 1850.
6. ——, Pogg. Ann. *81,* 258, 1850.
7. Lord Rayleigh, Theory of Sound, Vol. I, London 1894.
8. Southwell, R. V., Proc. Roy. Soc. A *101,* 133, 1922.
9. Stodola, A., Dampf- und Gasturbinen, Berlin 1924.
10. ——, Schweiz. Bauz. *63,* 251, 1914.
11. Lamb, H. and Southwell, R. V., Proc. Roy. Soc. A *99,* 272, 1921.
12. von Freudenreich, J., Engineering *119,* 2, 1925.
13. Campbell, W., Trans. Am. Soc. Mech. Eng. *46,* 31, 1924.
14. Hort, W., Z. V. D. I. *70,* 1375, 1926.
15. Timoshenko, S., Vibration Problems in Engineering, New York 1937.
16. ——, Theory of Elasticity, New York 1934.
17. Skoglund, C., Föreningen Svenska Sågverksmän, Sjunde Årsmötet, Stockholm 1949.
18. Beck, E., Forschg. Geb. Ing.-Wes. *10,* 165, 1939.
19. Jürges, W., Beih. z. Ges.-Ing. Reihe 1, Nr 19, 1924.
20. Ritz, W., Ges. Werke, Paris 1911, p. 278.
21. Sokolnikoff, I. S., Mathematical Theory of Elasticity, New York 1946.
22. Hattori, D., Journ. Iron Steel Inst. *129,* 289, 1934.

Tryckt den 17 februari 1953

Uppsala 1953. Almqvist & Wiksells Boktryckeri AB

ARKIV FÖR FYSIK Band 6 nr 24

Communicated 4 June 1952 by OSKAR KLEIN and IVAR WALLER

On the slowing down of neutrons in heavy water

By GUNNAR HOLTE

With 1 figure in the text

In this paper a calculation is made of the stationary space energy distribution of slow neutrons in an infinite medium of heavy water, containing a point source of fast neutrons.

In two previous papers[1] a general method of dealing with such problems has been given and detailed calculations have been performed for mediums of carbon, deuterium and water. The method developed there is based on the transport equation, and for the single scattering process we have made the following additional assumptions, ordinarily used in these problems. Inelastic scattering is neglected; the elastic scattering is assumed to be isotropic in the centre-of-mass system of the neutron and the atom; the atoms of the medium are supposed to be at rest before a collision with a neutron occurs and their binding to other atoms is neglected. Further absorption is neglected, although it can be taken into account in simple cases, if necessary. The medium is supposed to be homogeneous and infinite. Problems where the medium is assumed to be inhomogeneous or finite will be treated in a forthcoming paper. With exception for the approximation which these assumptions may involve, no further approximations are made for the calculation of the slow neutron density. This is in contrast to the simplified treatment of the problem given by the ordinarily used age-theory. This theory, supposed to be valid for small distances r from the source and for slowly variable mean free path $\lambda(E)$ of the neutrons in the medium (E = neutron energy), can therefore be checked in detail. This is of importance for calculations concerning reactors, for example. Further we obtain complete information of the neutron density at intermediate distances outside the range of age-theory which is of interest for questions of shielding and related problems.

For the application of our general method of calculation to heavy water it must be noticed that the assumption of isotropy in the centre-of-mass system for the neutron-deuteron scattering is not strictly justified. It is well-known that marked deviations from pure S-scattering occur for neutron energies of the order 1 Mev, already. This is born out by experimental as well as theoretical work on this subject in a large number of papers.[2] It appears that the differential cross-section takes on its largest values for forward and backscattering while there is a minimum roughly for a scattering angle of 90° in the centre-of-mass system. For problems of slowing down it is important to know at what energy this anisotropy first sets in. An answer to this question has been given recently by WALT *et al.*[1] These authors report measurements at neutron energies from 0.22 to 2.5 Mev and find the scattering essentially isotropic at the lower limit. Now the slowing down from an initial energy of say 1 Mev to 1 ev requires at about 25–30 collisions in heavy water but according to this measurement the first three or four collisions only occur in the anisotropic range. Therefore it is reasonable to expect that the values we obtain for the collision density $F_0(r, E)$ by our general method, assuming isotropy for all collisions, will be fairly near the true value. It is not easy to take the anisotropy strictly into account from the start in a general treatment of the problem (because the anisotropy is energy dependent; otherwise it is simple). However, it is possible to calculate approximately the corrections on account of the anisotropy to the values of $F_0(r, E)$ obtained in neglecting this effect. In this way we expect to get values very close to the true value of $F_0(r, E)$ except for large r, where $F_0(r, E)$ is very small. But then, of course, we must not allow too large values of the energy E_0 of the neutron source for the correction to be significant. We have restricted us to consider values of E_0 roughly up to 1.5 Mev. This covers the most important part of the energy distribution curve of prompt neutrons resulting from the thermal neutron fission of U^{235}.[2]

---

[1] HOLTE, Ark. Fys. *2*, 523, 1950, and Ark. Fys. *3*, 209, 1951. These papers are referred to as I and II, respectively.

[2] Cf. e.g. BUCKINGHAM, HUBBARD and MASSEY, Proc. Roy. Soc. *211 A*, 183, 1952. Further references may be found there.

Measurements of the cross sections[3] of deuterium, oxygen, as well as of heavy water directly show that the total mean free path $\lambda(E)$ varies only very little with E in the energy interval 0–1.5 Mev. In fact, up to 1 Mev $\lambda(E) = \text{constant}$ is a very good approximation with exception for the resonance in the oxygen cross section at 0.44 Mev. Using for $\lambda(E)$ the mean value $\bar{\lambda}$ given by age-theory (cf. I (49)) this approximation can be taken even for energies up to 1.5 Mev where the value of $\lambda(E)$ is only at about 1/3 larger than for zero energy. Thus we adopt here the treatment of the problem given in I, assuming constant mean free path λ. For E_0 near 1.5 Mev this assumption will restrict the validity of our calculation to values of r not too large. However, this restriction is put anyhow by the occurrence of anisotropic scattering. Therefore it does not seem to be worth while making the refined treatment of the problem which is developed in II, taking the slight energy dependence into account exactly at the expense of more numerical work.

Following I we now proceed to the numerical calculations, thus disregarding at first the anisotropy of the first few collisions. We use the same notations as in I and knowledge of this paper will be assumed. All constants occurring in I which have to be calculated derive from certain functions $c_n(\eta)$ and their derivatives for $\eta = 1$. These functions are given by I (5) for a medium containing atoms of one kind only. For a mixture we have to take for $c_n(\eta)$ a sum of expressions of the form I (5) for the different values of M occurring, multiplying each term in the sum with a weight factor.[4] This factor is λ/λ_k, assumed to be constant, where λ is the total mean free path and λ_k is the mean free path for scattering by atoms of the kind k. From the measurements mentioned above we may take for heavy water $\lambda/\lambda_D = 0.65$, which is a good approximation even up to 1.5 Mev. Thus we take for $c_n(\eta)$ the formula

$$c_n(\eta) = 0.65\, c_{nD}(\eta) + 0.35\, c_{nO}(\eta).$$

The constants deriving from $c_{nD}(\eta)$ were calculated already in preparing Tables 1 and 2 in I which refer to pure deuterium. The functions $c_{no}(\eta)$ for oxygen are very easily handled as they give a rather small contribution to the sum above, in particular for $n > 0$ or when we calculate the derivatives. The constants h_n^i, I (12), deriving from the function $h_n(\eta) = 1 - c_n(\eta)$ and its derivatives at $\eta = 1$ are computed. The method given in I, sect. 3, for determination of the fundamental functions $B(\theta)$ and $A(\theta)$ for heavy water is then applied. These functions are given by developments around the points $\theta = 0$, I (11) and (14), $\theta = \theta_1 = 1$, I (26), (27) and (28), and $\theta = \infty$, I (29) and (30). The complete knowledge of these functions for all real positive values of θ makes it possible to evaluate the fundamental integral I (17) for the neutron density for all values of r, if either $x = \log(E_0/E)$ or r is large. It may be stressed that for calculation of the slow neutron density ($x \approx 10$–15) in the practical range (say $r \leq 80$ cm) only the values of C and β_n, I (11) and α_n, I (14) roughly up to β_6 and α_6 are needed. These coefficients are rapidly obtained. All the other coefficients given below in Table 1, which have required the main part of the numerical work, will have less practical use. They will be needed if one wishes to calculate the density of other neutrons than "slow" (say $x < 10$ but not too small) at intermediate distances in the practical range, or for obtaining the neutron density at increasing distances up to and including the range of the asymptotic formula. More figures in the constants in Table 1 have been given than would be strictly allowed, for we have treated the constant $\lambda/\lambda_D = 0.65$ as an exact number. This is necessary for mathematical reasons. The following values are obtained: $h_1 = 0.76835$, $h_0' = 0.51404$, $C = 1.0885$ and

---

[1] WALT, OKAZAKI and ADAIR, Bull. Amer. Phys. Soc. *27*, no. 3, 62, 1952.

[2] "Nuclear data for low-power reactors", Nucleonics *8*, no. 1, 78, 1951.

[3] ADAIR, Rev. Mod. Phys. *22*, 249, 1950.

[4] WALLER, Ark. mat. astr. fys. *34 A*, no. 5, 1946.

Table 1

n	β_n	h_n	k_n	α_n	l_n	m_n
0	(-1)	0.7497	(-1)	(1)	0.511	(0)
1	0.51218	-0.1699	0.367	-0.9063	0.254	1.08
2	-0.32105	0.0540	-0.16	0.7078	-0.126	-1.2
3	0.18102	-0.0179	0.1	-0.4497	0.060	
4	-0.08513	0.0059		0.2224	-0.029	
5	0.03085	-0.0020		-0.0789	0.015	
6	-0.00699			0.0156		
7	-0.000051			0.00015		
8	0.000554			0.00107		
9	0.000152			-0.00306		
10	-0.000402			0.00221		
11	0.000229			-0.00033		
12	-0.000010					
13	-0.000078					
14	0.000056					
15	-0.000009					
16	-0.000016					

In this table the last figure of the values of k_n, m_n and also of the four highest h_n and l_n has to be regarded as uncertain since it has been obtained by estimation of the rest term of the series used in performing the analytic continuation. From the values of the coefficients it appears that the three series developments of $B(\theta)$ and $A(\theta)$, respectively, around $\theta = 0$, $\theta = 1$ and $\theta = \infty$ very well cover all θ-values from 0 to ∞.

The integral I (17) is evaluated by the saddle-point method, deforming the path of integration to pass through the saddle-point θ_s which is always real and ≥ 0.

θ_s depends on the variables r and x only in the combination R/x, where $R = r/\lambda$. For the determination of θ_s it is not necessary to use the exact function $B(\theta)$. It is quite sufficient to take a good approximation $B_s(\theta)$ of $B(\theta)$ of simple form. In this way we can obtain analytic expressions for the function $\theta_s = \theta_s(R/x)$. For small R/x and θ_s this is provided by I (37), taking $B_s(\theta)$ as the first two terms in I (11). For larger θ I (32) was found to be very useful for $B_s(\theta)$, from which follows for larger R/x I (38) for θ_s. The constants a, b, and c in I (32), as well as the constants c, d and e in the analogous approximate expression $A_s(\theta)$ for $A(\theta)$ are given in Table 2. The first two columns of the table quote the intervals in θ (θ_s) and the corresponding intervals in R/x within which the different values of the constants are valid.

Table 2

θ_s	R/x	a	b	c	d	e	f
0.3	1.6	0.9925	0.3496	0.4394	−0.016	1.085	1.060
1.0	5.9	1	0.3690	0.474	0	1.045	1.05
7	150	1	0.367	0.44	0	1.08	1.1
∞	∞						

The approximations thus obtained give a maximum error at any point of about 10^{-4} for $B(\theta)$ and 10^{-3} for $A(\theta)$.

For the calculation of the neutron density I (40) is the main formula. An idea of the accuracy of the values it gives can be obtained by studying the successive zeroth, second and fourth approximations contained in the formula. For slow neutrons it was found that the simple second and the more involved fourth approximation lie very close to each other and the error of the second approximation can be estimated to less than 0.5 %, in general (the fourth approximation is of course even more exact). For very small r (0–5 cm) the conditions are not quite as good as that, but then a check of the fourth approximation with numerical integration of I (17) gives an excellent agreement. WALLER l.c., after his derivation of the basic formulas I (1) and (2) was also the first to evaluate I (1) to an explicit formula for $F_0(r, E)$ which is valid essentially beyond the range of age-theory. A comparison with our values shows a remarkably good accuracy of this rather simple formula (WALLER, l.c. formula (39), putting his constants $A = \beta_1 = 0.512$, $B = -\alpha_1 = 0.906$). It gives roughly 2 % too low values for $r = 0$, but for increasing values of r roughly up to 50 cm it is in error only with about 0.5 %. However, the main interest and purpose with this paper lies in the comparison of age-theory with our exact calculation. This theory is found to give appreciable errors even for small r. This will appear in detail from tables at the end of this paper.

Before reproducing any values of $F_0(r, E)$ obtained according to I we proceed to the problem of taking the anisotropic scattering into account. To start with we write down two well-known equations. If ϕ is the scattering angle of the neutron in the laboratory system, when incident with energy E' and scattered with energy E after the collision with a nucleus, we have

$$\cos\phi = \frac{1}{1-\alpha}\left(\sqrt{\frac{E}{E'}} - \alpha\sqrt{\frac{E'}{E}}\right), \tag{1}$$

with $\alpha = (M-1)/(M+1)$ (M = nucleus mass in units of the neutron mass). The corresponding relation for the scattering angle φ in the centre-of-mass system of the neutron and the nucleus is

$$\cos\varphi = \frac{2\frac{E}{E'} - 1 - \alpha^2}{1-\alpha^2}. \tag{2}$$

(1) and (2), which are valid for elastic collisions, are simple consequences of the laws of conservation of momentum and energy.

Now we introduce the function $\nu(E', E)$ which is defined by expressing that $\nu(E', E)\,dE$ is the probability for a neutron of initial energy E' to get in a collision a final energy between E and $E + dE$ ($dE > 0$) (cf. WALLER l.c.). This function which according to (2) is zero except for $E' > E > \alpha^2 E'$ may be determined in the following way. We denote by

$$\frac{1}{4\pi}\mu(E', \varphi)\,d\Omega_e \tag{3}$$

the probability that a neutron with initial energy E' will after the collision move in a solid angle $d\Omega_e$ in a direction specified by the unit vector $\boldsymbol{e}$ in the centre-of-mass system, forming the angle φ with the direction of the incident neutron. Thus the probability for this neutron to be scattered in the collision through angles between φ and $\varphi + d\varphi$ is

$$\tfrac{1}{2}\mu(E', \varphi)\,|d(\cos\varphi)|. \tag{4}$$

From (3) and (4) we must have on integrating over all directions $\boldsymbol{e}$

$$\frac{1}{4\pi}\int \mu(E', \varphi)\,d\Omega_e = \frac{1}{2}\int_{-1}^{+1} \mu(E', \varphi)\,d(\cos\varphi) = 1 \tag{5}$$

for all values of E'. But from (1) we get for a fixed value of E'

$$d(\cos\varphi) = \frac{2\,dE}{E'(1-\alpha^2)}, \tag{6}$$

which gives the final expression for $\nu(E', E)$

$$\nu(E', E) = \frac{\mu(E', \varphi)}{E'(1-\alpha^2)}. \tag{7}$$

For φ we have to substitute (2) in this expression. Multiplication of (7) with dE and integration from $E'\alpha^2$ to E' gives the result 1. WALLER l.c. has given a quite similar expression for $\nu(E', E)$, using instead the scattering probability in the laboratory system. It should be mentioned that our equation (7) could be obtained directly from WALLER's equations (9) and (1) if they are used for the angle φ instead of ϕ. For the practical applications it seems best to have the expression (7) because the scattering probabilities are ordinarily given in the centre-of-mass system.

So far, an exact solution of the transport equation has been possible only by means of a Laplace transformation in $x = \log (E_0/E)$. The reason for its usefulness is that when isotropy is assumed, i.e. $\mu(E', \varphi) = \text{constant} = 1$ the equation is of convolution type. Unfortunately this does not hold for a general form of $\mu(E', \varphi)$ and then the problem seems to be very difficult to solve exactly. However, it ought to be pointed out that the same exact treatment is possible also if μ is of the form

$$\mu(E', \varphi) = \mu(\varphi),$$

e.g. if we have anisotropy, but of exactly the same form for all energies. For according to (1) the kernels of the integrals in the equations resulting from developing the transport equation in spherical harmonics (cf. e.g. WALLER l.c. eq. (19), (21) and 24)) are then still functions of E/E' only and thus the Laplace transformation is as useful as for $\mu(\varphi) = 1$. This simple case of anisotropy is obtained in our general treatment in I merely by changing the form of the functions $c_n(\eta)$. The integral defining $c_n(\eta)$ now will contain a factor $\mu(\varphi)$ in the integrand, written as a function of $\cos \phi$, for example, if the form I (5) is used for $c_n(\eta)$. However, this case seems to be of little practical interest, although the procedure may be applied for estimating roughly the effect of the anisotropy in actual cases.

Thus we have to resort to an approximate treatment of the problem, and for heavy water we chose another obvious possibility of getting the anisotropy corrections but which involves no approximation of the function $\mu(E', \varphi)$ as in the case discussed above. Instead we study the age-approximation of the neutron density. At first we write down the usual age-theory value for $F_0(r, E)$, assuming isotropy throughout. Then we calculate the corresponding age-theory value for $F_0(r, E)$ with the anisotropy taken into account. A comparison of these two values provides us with a value of the anisotropy correction. This value will undoubtedly be near the true value of the correction except for large r, i.e. as long as age-theory gives the right order of magnitude for the neutron density. The correction is then applied to the value of $F_0(r, E)$ calculated by I (40), and in this way we may expect to get very near the real value of the neutron density in the range of practical interest.

In the age-approximation, F_0 is governed by the well-known age-diffusion equation. This contains as characteristic quantities the mean free path $\lambda = \lambda\ (x)$, the mean logarithmic energy loss in one collision $\xi(x)$ and the mean value of $\cos \phi$ in one collision $\beta(x) = \overline{\cos \phi}\,(x)$. These functions can all be put together in one quantity $\tau = \tau(x)$, the age of the neutrons

$$\tau(x) = \int_0^x \frac{\lambda^2(x')\,dx'}{3\,\xi(x')\,[1 - \beta(x')]}. \tag{8}$$

The functions $\xi(x')$ and $\beta(x')$ are mean values for all collisions with initial energy $E' = E_0 e^{x'}$ and are obtained by using (7) and integrating over the final energy $E = E_0 e^{-x}$ from $E'\alpha^2$ to E'. Taking x and x' as variables and then substituting $u = x - x'$ instead of x in the integrals and also in (1) and (2) we obtain

$$\begin{cases} \xi(x') = \int\limits_0^a \mu(E', \varphi)\, e^{-u}\, u\, du \\ \beta(x') = \int\limits_0^a \mu(E', \varphi) \cos \phi\, e^{-u}\, du \end{cases} \tag{9}$$

with $a = -\log \alpha^2$. For $\mu(E', \varphi) = \mu(\varphi)$, $\xi(x')$ and $\beta(x')$ are both constant. This holds in particular in the isotropic case $\mu(\varphi) = 1$, where $\xi(x') = h_0' = 1 - a\,\alpha^2/(1-\alpha^2)$ and $\beta(x') = 2/3\mathrm{M}$ ($h_1 = 1 - \beta(x')$ in our earlier notation in I). Eq. (8) is also valid for a medium containing several kinds of atoms if we take for $\xi(x')$ and $\beta(x')$ a sum of integrals of the form (9), one for each kind of atom and multiplied with the usual weight factor λ/λ_k.

Taking the age $\tau = \tau(x)$ (8) as the energy variable, we have for a point source in an infinite medium the following well-known solution of the age-diffusion equation

$$F_0(r, E) = \frac{K}{E\,(4\pi\tau)^{3/2}}\, e^{-\frac{r^2}{4\tau}}. \tag{10}$$

This function satisfies the diffusion equation all outside the source, and assuming that the source emits Q neutrons of energy E_0 per unit time we can also determine the constant K. Then in the isotropic case we know that K has the value $Q/h_0' = Q/\xi$. Now in integrating (10) over all space we obtain the age-theory value of the energy distribution function $F_0(E) = K/E$. But in the isotropic case it is well-known that an exact calculation gives $F_0(E) = Q/E\,h_0'$ for slow neutrons. Thus in this case age-theory gives the correct value of $F_0(E)$ for slow neutrons, which is a fact of basic importance for the usefulness of age-theory. Then in the anisotropic case we must determine the constant K so that we obtain again the correct value of $F_0(E)$ for slow neutrons from (10), or else we cannot claim to get the anisotropy correction consistently. Now a calculation of $F_0(E)$ shows that the exact value of this function for slow neutrons is still $F_0(E) = Q/E\,h_0'$, even when we have anisotropy in the first few collisions. This is true for an arbitrary form of anisotropy at the higher energies if only the range of isotropy at the lower energies is sufficiently large. The proof of this general theorem on the rôle of anisotropic scattering is given in the appendix.

Thus in (10) we have $K = Q/h_0'$ in both cases, and we need only the value of τ, calculated with the anisotropy taken into account; in the isotropic case we have immediately $\tau = \frac{1}{C^2}\int_0^x \lambda^2(x')\,dx'$. Then we have to compute the integrals (9) for deuterium, putting $M = 2$, $\alpha = 1/3$. This calculation can only be preliminary because of the incomplete knowledge of the function $\mu(E',\varphi)$. We assume the simplest possible form for μ in accordance with the main features of the various experimental and theoretical results on the neutron-deuteron differential scattering cross section (cf. Walt *et al.* l.c., also Buckingham *et al.* l.c., and further references there). We assume an angular dependence symmetrical around $\varphi = 90°$, taking the same maximum forward- and backscattering and minimum scattering for $\varphi = 90°$.

$$\mu(E', \varphi) = \frac{1 + \psi(E')\cos^2\varphi}{1 + \psi(E')/3} \tag{11}$$

which is normalized according to (5). $\psi(E')$ is supposed to be zero for $E' \leq 0.22$ Mev and equal to 1.5 for $E' = 2.5$ Mev (Walt *et al.* l.c.). Between these points $\psi(E')$ is simply supposed to vary linearly with E', thus

$$\psi(E') = 1.5\,\frac{(E' - 0.22)}{2.28} \tag{12}$$

for $E' \geq 0.22$, but $\psi(E') = 0$ for $E' \leq 0.22$. Then for deuterium (9) takes the simple form

$$\left\{\begin{aligned} \xi_D(x') &= \frac{1}{1+\psi/3}(0.725+\psi\cdot 0.283) \\ \beta_D(x') &= \frac{1}{3+\psi}(1+8\psi/35). \end{aligned}\right. \tag{13}$$

with $\psi = \psi(E')$, $E' = E_0 e^{-x'}$. Assuming oxygen to scatter isotropically, we then calculate $\xi(x')$ and $\beta(x')$ for heavy water by multiplying (13) with 0.65 and adding $0.35 \cdot 0.120$ and $0.35/24$, respectively. The function $\tau(x)$ is then calculated by numerical integration. It turns out that for slow neutrons (say $x > 10$) the anisotropy value of $\tau(x)$ is less than 0.5 % smaller than the usual isotropy value even for $E_0 = 1.5$ Mev. This result is very satisfactory, for it means that the corrections on account of anisotropy are very small except for very large r and the final values obtained for $F_0(r, E)$ can be expected to be very good. In fact, the anisotropy correction is somewhat smaller than the correction for the variation of $\lambda(E)$ which has been done before already by using a mean value $\bar{\lambda}$ instead of the constant low energy value λ in I (40).

We now reproduce some final results of our calculations. We have chosen three different values for E_0, 0.5, 1.0 and 1.5 Mev. For each of these source energies we have computed the collision density $F_0(r, E)$ for $E = 1$ ev at various distances r from the source. The values given in the tables are the final values, corrected for the anisotropy. The correction is made by multiplying the value obtained from I (40) with the factor, close to unity, which represents the ratio between the age-theory values of $F_0(r, E)$, eq. (10), calculated with anisotropy and without anisotropy taken into account, respectively. The table also contains the ordinary age-theory values of $F_0(r, E)$ (for pure isotropy), denoted by $F_{0_{\text{age}}}$. For the mean free path λ we have taken as the constant low energy value $\lambda = 2.87$ cm, corresponding to a density of heavy water of 1.10 g/cm³. For $E_0 = 0.5$ Mev this value was used directly in I (40) in calculating $F_0(r, E)$. But for $E_0 = 1.0$ Mev we have taken a value 0.5 % larger, and for $E_0 = 1.5$ Mev the value $\lambda = 2.90$ cm is used in I (40) in order to correct for the variation with energy of λ. These slightly higher values are mean values obtained from age-theory.

The number of figures of the values of $F_0(r, E)$ given in the table below is chosen in accordance with the accuracy which is provided mathematically by the method of calculation, with the last figure uncertain, in general. Then the basic value $\lambda = 2.87$ cm is considered as an exact number although, so far, the experimental determinations of the cross sections give an accuracy of some percents only. Besides, the value of λ also depends on the value of the density. Thus there may be considerable errors in $F_0(r, E)$ because of a possible error in λ, but the discussion of this lies beyond the scope of this paper. We only point out that the table is easily used also if an other basic value of λ has to be chosen. Then we have to remember only that $F_0(r, E)$ contains $1/\lambda^3$ as a factor and that it depends on r only in the combination $R = r/\lambda$, and for a change of the λ-value the table is useful for those new values of r which leave the R-values unchanged.

It is convenient to use the following abbreviations in the table; $G(r) = \frac{10^4}{Q} \cdot F_0(r, 1)$, $G_a(r) = \frac{10^4}{Q} F_{0_{\text{age}}}(r, 1)$. $G(r)$ is the number of collisions of neutrons

Table 3

r (cm)	0	5	10	18	30	50	80
$E_0=0.5$ Mev:							
$G(r)$	5.85	5.27	3.99	1.88	0.379	0.0119	$2.3\ 10^{-5}$
$Ga(r)$	4.84	4.52	3.68	2.00	0.411	0.0051	$1.2\ 10^{-7}$
$E_0=1.0$ Mev:							
$G(r)$	5.29	4.81	3.69	1.82	0.396	0.0142	
$Ga(r)$	4.42	4.14	3.41	1.92	0.434	0.0070	
$E_0=1.5$ Mev:							
$G(r)$	4.95		3.51	1.79	0.405		
$Ga(r)$	4.16		3.25	1.87	0.448		

of energy $E=1$ ev for a source strength $Q=10^4$. $G(r)$ is corrected for the anisotropy, but the correction is only of the order of magnitude 0.1 % except for r large. For $r=50$ cm the correction is -0.7 % for $E_0=0.5$ Mev, -3 % for $E_0=1.0$ Mev; for $r=30$ cm -1 % for $E_0=1.0$ Mev and -2 % for $E_0=1.5$ Mev; for $r=0$ $+0.2$ % for $E_0=1.0$ Mev and $+0.4$ % for $E_0=1.5$ Mev. The comparison of

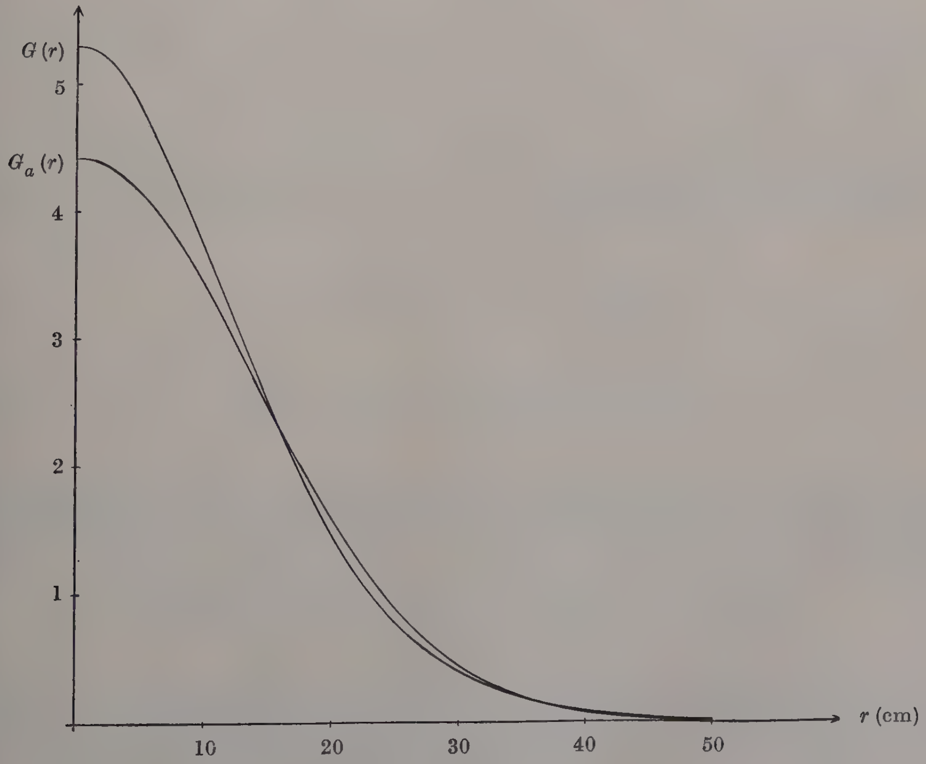

Fig. 1. $E_0=1.0$ Mev

$G(r)$ with $G_a(r)$ shows that the ordinarily used age-theory is not very useful for heavy water. It gives too low values for small r roughly up to 15 cm, with a maximum error of nearly 20 % for $r = 0$. In an intermediate range up to 35–40 cm it gives too large values with a maximum error of more than 10 % at about 25 cm. For large r it is well-known that age-theory gives too small values of quite the wrong order of magnitude.

This discussion also holds for slow neutrons in general. In fact, apart from the very small anisotropy correction and the factor $1/E$, $F_0(r, E)$ is a function of E only in the combination $x = \log E_0/E$, and the table contains results for three different values of x. As it is to be expected, the error of age-theory decreases slightly for increasing x. Further the distances from $r = 0$ to the two intersections of $G(r)$ with $G_a(r)$ increase slowly with x.

Figure 1 shows $G(r)$ and $G_a(r)$ for $E_0 = 1.0$ Mev as a further illustration of the inadequacy of age-theory.

It should be pointed out, however, that for practical applications the functions $rG(r)$ or $r^2G(r)$ rather than $G(r)$ usually are those of significance. This makes the maximum error of age-theory at $r = 0$ less serious but increases the importance of intermediate distances r.

Appendix

We are going to prove a general theorem on the asymptotic behaviour of the collision density $F_0(E)$ for small E. Let us in the future use $x = \log E_0/E$ as variable instead of E. Then we study the function

$$F_0(x) = E\,F_0(E)$$

which gives the number of collisions per unit of x. If the same transformation is made with the probability function (7)

$$\nu(x', x) = E\,\nu(E', E),$$

$F_0(x)$ is governed by the following integral equation

$$F_0(x) = \int_0^x F_0(x')\,\nu(x', x)\,dx' + Q\,\delta(x), \tag{14}$$

where $\delta(x)$ is Dirac's δ-function. Then absorption has been neglected as before, and elastic collisions have been assumed. For the kernel $\nu(x', x)$ we have the expression from (7)

$$\nu(x', x) = e^{x'-x}\,\frac{\mu(E', \varphi)}{1-\alpha^2}, \text{ for } 0 \leq x - x' \leq a, \text{ otherwise zero,} \tag{15}$$

for a medium containing a single element; for several kinds of atoms present $\nu(x', x)$ is a sum of expressions of this form, each multiplied with the weight factor λ/λ_k. Here in $\mu(E', \varphi)$ x and x' have to be substitued. According to the definition of $\nu(x', x)$, the integral in x of $\nu(x', x)$ is normalized to unity. That means that if we put

$$\mu(E', \varphi) = 1 + \chi(E', \varphi) \tag{16}$$

the integral in x over all x-values of the part of $\nu(x', x)$ which contains the factor $\chi(E', \varphi)$ is zero.

Now for isotropy in the centre-of-mass system we have $\chi(E', \varphi) \equiv 0$. Then (14) can be solved either by repeated integration[1] or, simpler, by means of a Laplace transformation[2]. In the general case $\chi(E', \varphi) \neq 0$ neither of these methods is applicable, but of course (14) can be solved numerically by iteration, starting at $x = 0$ and then passing step by step towards larger values of x. This is a rather cumbersome procedure, in particular if we are interested in large values of x. However, in all cases of physical interest we have isotropy for sufficiently low energies, but usually anisotropy for high energies. Thus we assume that $\chi(E', \varphi) \neq 0$ only for $0 \leq x' \leq x_a$, but identically zero for $x' > x_a$ (x_a is a constant ≥ 0). Naturally for small x $F_0(x)$ will have another form in this case than if χ were zero all down to $x' = 0$. But an important property of $F_0(x)$ is that for $x - x_a$ sufficiently large we still have the same constant value

$$F_0(x) = Q/h_0'$$

as in the case of isotropy for all collisions. This will now be proved.

Without loss of generality we may assume that in the interval of anisotropy $0 \leq x' \leq x_a$ χ has the form

$$\chi(E', \varphi) = \sum_i a_i(x')\, b_i(\varphi). \tag{17}$$

For a medium containing a mixture of atoms we have one function μ and χ for each kind of atom, to be denoted by an index k. In the proof to be given below, however, we shall assume a single element (or at least only one element scattering anisotropically). This is merely to avoid double indices in (17) and a double summation in (14); it is really not necessary to bother about this case in detail as the generalization is obvious. We now take the Laplace transform of (14). Except for the term $D(\theta)$ deriving from $\chi(E', \varphi)$ the result is well-known, thus

$$f(\theta) = f(\theta)\, C_0(\theta) + D(\theta) + Q, \tag{17}$$

with the notations

$$f(\theta) = \int_0^\infty e^{-\theta x} F_0(x)\, dx, \quad C_0(\theta) = \frac{1}{1-\alpha^2} \int_0^a e^{-u(\theta+1)}\, du, \tag{18}$$

resulting from the convolution theorem of the Laplace transformation. $C_0(\theta)$ is the function $c_0(\eta)$ encountered before, I (5) with the change of variables $\eta = 1 + \theta$. For the new function $D(\theta)$ we obtain, using again the convolution theorem and remembering that $\chi \equiv 0$ beyond x_a

$$D(\theta) = \sum_i \int_0^{x_a} F_0(x)\, e^{-\theta x} a_i(x)\, dx \cdot \frac{1}{1-\alpha^2} \int_0^a e^{-u(\theta+1)}\, b_i[\varphi(u)]\, du. \tag{19}$$

---

[1] Eriksson, Ark. mat. astr. fys. Bd *33 B*, no. 5, 1946.

[2] Adler, Phys. Rev. *60*, 279, 1941.

Here $b_i[\varphi(u)]$ means that in expressing $\cos\varphi$ in $x - x'$ from (2) the substitution $u = x - x'$ has to be made.

Now let us for a moment assume that $F_0(x)$ is already determined in the interval $0 \le x \le x_a$, by a numerical method, for example. Then $D(\theta)$ in (17) is a known function, and for other values of x $F_0(x)$ can be obtained by solving (17) for $f(\theta)$ and using the inversion of the transformation.

$$F_0(x) = \frac{1}{2\pi i}\int_{\theta_1 - i\infty}^{\theta_1 + i\infty} e^{x\theta}\frac{Q + D(\theta)}{h_0(\theta)}\,d\theta, \qquad \text{for } x > x_a \tag{20}$$

where $h_0(\theta) = 1 - C_0(\theta)$, cf. I (4). The path of integration is chosen to the right of all singularities of the integrand. As usual, the value of (20) is easily computed by summing the residues of the integrand at the poles, which are the zeroes of $h_0(\theta)$. The main contribution comes from the pole at $\theta = 0$, as all other poles lie further to the left in the θ-plane. Thus we have to calculate $D(0)$. But if we write down the integral in x from x' to $x' + a$ of the anisotropic part of $\nu(x', x)$, an integral of value zero, and then substitute $u = x - x'$ instead of x the resulting expression can be found in (19) for $\theta = 0$. The only difference in (19) for $\theta = 0$ is the multiplication with $F_0(x)$ and the integration from 0 to $+x_a$ (denoting the variable of integration x' instead of x for completeness). Thus we have $D(0) = 0$, and the main pole contribution to $F_0(x)$ has the usual value Q/h_0'. For the other poles we see from (20) and (19) that if $x - x_a$ is sufficiently large the contribution from $D(\theta)$ is negligible, which proves the theorem.

Finally it might be mentioned that the same result also can be obtained much simpler by an elementary but less rigorous reasoning. For as (14) for sufficiently large x is satisfied by a function $F_0(x) = \text{constant}$, it is rather obvious that the asymptotic solution always must be of this form, independent of the conditions for small x. In order to determine the value of this constant it is simplest to consider the slowing-down density $q(x)$ which is always constant $= Q$ under stationary conditions with no absorption. But $q(x)$ can also be computed from $F_0(x)$, and assuming this function to be constant ($x - x_a$ sufficiently large) one obtains the exact value $q(x) = h_0' F_0(x)$ ($h_0' = \xi$), thus $F_0(x) = Q/h_0'$.

I wish to express my gratitude to Professor IVAR WALLER for valuable discussions on the subject of this paper.

My thanks are also due to the *Swedish Atomic Committee* for a grant for performing the numerical calculations, and to Mr KLAUS APPEL, Mr STIG HOLMQUIST and Mr CLAES TENGDAHL for assisting me in carrying out this numerical work.

Uppsala, Institute for Mechanics and Mathematical Physics.

Tryckt den 17 februari 1953

Uppsala 1953. Almqvist & Wiksells Boktryckeri AB

ARKIV FÖR FYSIK Band 6 nr 25

Read 14 May 1952

Ions formed in a room by positive wire corona

By Harald Norinder and Reinhards Siksna

With 9 figures in the text

In the scope of the investigation of ions produced by corona discharge recently carried out at this Institute [1], [2], ions formed by *positive wire corona* have been included, and results of measurements of these ions will be given here.

The used experimental arrangement was the same as that for the investigation of ions formed by negative wire corona, which arrangement is in detail described in [1]. Only the high-tension equipment was switched for positive tension. The used measuring method was also the same, viz. that of *periodical alternation of chosen adjusted limit mobilities* of an Israël ion-counter, when measuring large-ions [1], [2]. The small-ions were measured with two Ebert ion-counters.

1. Phenomena observed

1.1. Corona wire switched on suddenly to a comparatively high positive voltage. The highest voltage used was c. 15 kV. If such a positive potential was *switched on* suddenly to the corona wire the following phenomena were observed (Figs. 1 and 3):

(1) A sudden increase of the number of positive ions measured with the Ebert counter up to comparatively high values, but these values were somewhat smaller than those of negative ions under the same conditions. Some variations also occur. The variations on a smaller scale may be caused by the variation of the total air-flow through the suction box, when the air-flow through the Israël counter was changed. The decrease on a larger scale shown in Fig. 1 at the end of the curve with the tension switched on, must be caused by another event, because of the simultaneous appearance of an increase of the number of larger ions caught with the Israël counter.

(2) The number of ions measured with the large-ion counter increases but not so much as in the case of negative corona [1]. Therefore the vertical scale of the number of ions measured with the Israël counter is the same as that of small-ions measured with the Ebert counter only in Fig. 1. The vertical scale of the number of larger ions is enlarged in all the following figures (Fig. 3, 4, 6, 8). Some variations of the number of ions measured with the large-ion counter may also be stated, as a special kind of these variations the indicated increase in Fig. 1 must be mentioned. We have no explanation of this increase.

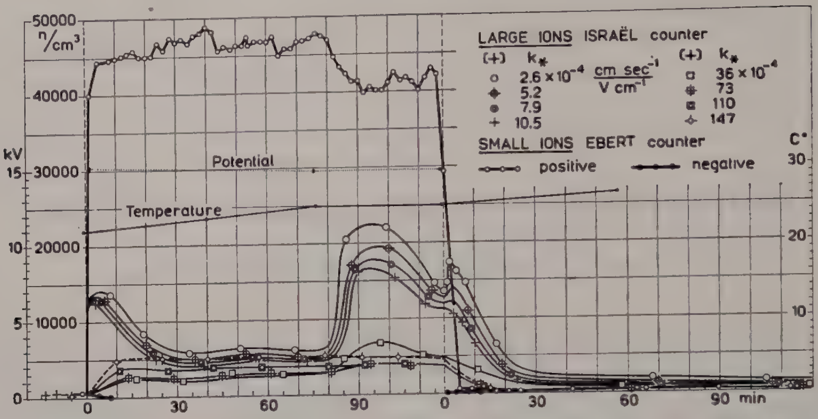

Fig. 1. Number of ions measured with the EBERT ion-counters and the ISRAËL large-ion counter adjusted at different limit mobilities k_*. The present ions were formed by corona discharge in a room, when a sufficiently high positive potential was suddenly switched on to a thin wire.

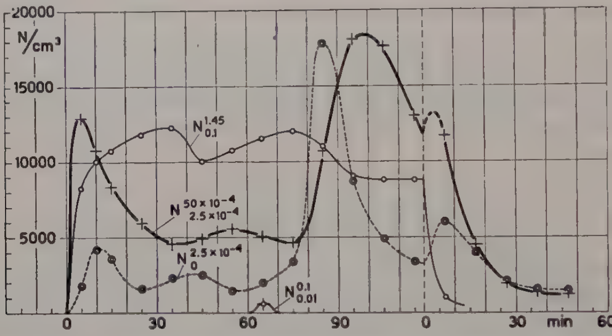

Fig. 2. Tendency of the groups of positive ions in different intervals of mobility during positive corona discharge. Calculated from the measurements shown in Fig. 1.

(3) Only one increase of positive ions was established with the EBERT counter and with the large-ion counter.

After *switching off* the potential and discharging the condenser of the rectifier:

(1) The number of positive small-ions measured with the EBERT counter decreases almost suddenly.

(2) The number of positive larger ions, on the contrary, increases somewhat from the beginning in order to decrease gradually later on.

(3) The number of negative small-ions increases gradually after switching off the potential and reaches after some time the level of the decreased number of positive ions.

1.2. Corona wire at gradually increased high voltage. In order to clarify the dependence of the concentration of ions on the potential applied to the corona wire, the voltage was increased gradually. Two series of measurements at increased potentials with different steepness are shown in Fig. 4 and 6. The curves (including

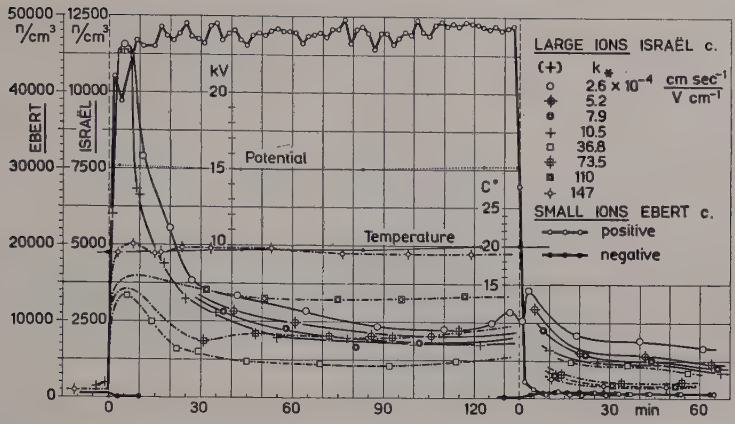

Fig. 3. Number of ions measured with the EBERT ion-counters and the ISRAËL large-ion counter adjusted at different limit mobilities k_*. Corona wire switched on suddenly to a comparatively high positive voltage.

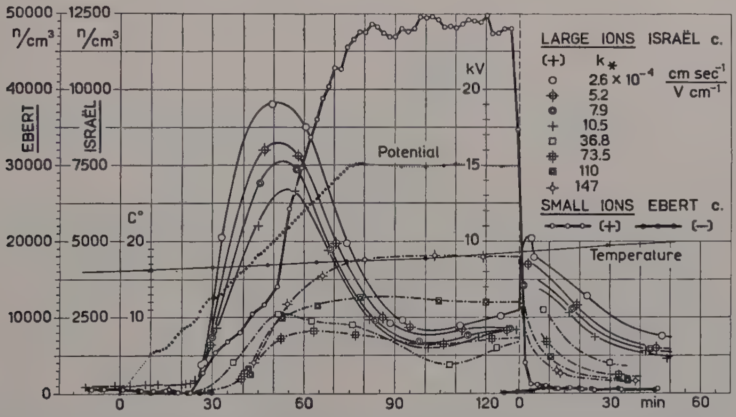

Fig. 4. Number of ions measured at a gradual increase of the applied positive potential.

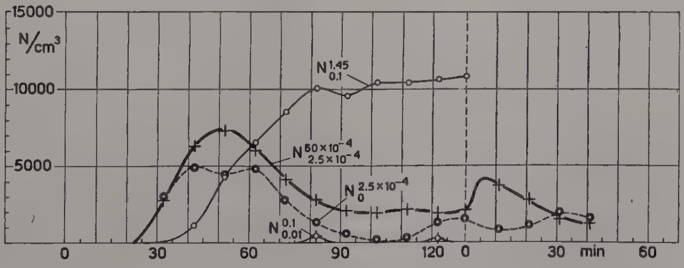

Fig. 5. Tendency of the groups of positive ions in different intervals of mobility during positive corona discharge. Calculated from the measurements shown in Fig. 4.

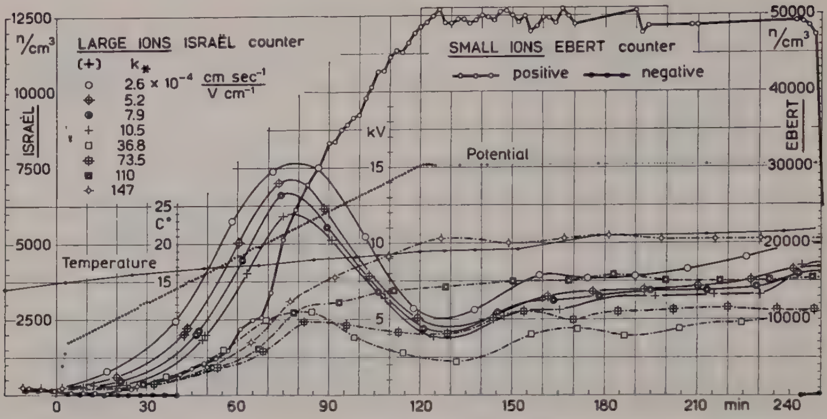

Fig. 6. Number of ions measured at a slower gradual increase of the applied positive potential.

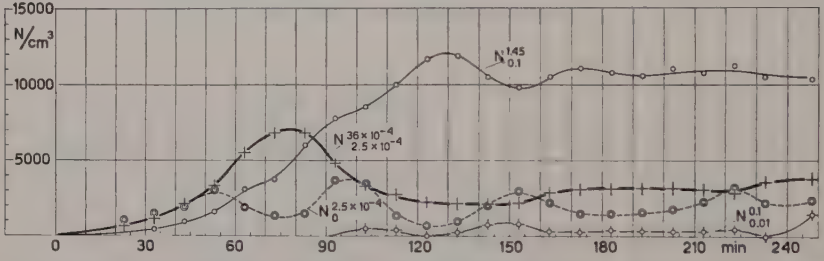

Fig. 7. Tendency of the groups of positive ions in different intervals of mobility during positive corona discharge. Calculated from the measurements shown in Fig. 6.

also the curves in Fig. 1 and 3) of the number of ions are generally of the same feature, only with different rapidity of the variations.

The following conclusions may be drawn from these curves.

At the applied potential:

(1) At the beginning the number of small-ions of both polarities decreases starting from the point of time at which the potential is applied. This decrease may be explained by a transport of the small-ions, normally present in the test-room, by the electric field to the electrodes of the corona device.

(2) The number of positive small-ions increases slowly at the beginning at a potential of c. 5 kV, but at c. 10 kV it increases more rapidly. During this increase the number of negative small-ions is not measurable.

(3) The number of positive larger ions measured with the ISRAËL counter at the adjusted limit mobilities of $k_* = 2.6$, 5.2, 7.9 and 10.5×10^{-4} (adjusted by variation of the air-flow through the first (I) condenser of the counter with a constant potential of 130 V) begins to increase at a potential below that necessary for small-ions, reaches a maximum at the potential at which the rapid increase of the small-ions starts (c. 10 kV, Fig. 4) or at a somewhat higher potential (c. 11 kV, Fig. 6) in order to decrease with some fluctuations to a lower level.

(4) The curves of the number of ions caught at the higher adjusted limit mobilities

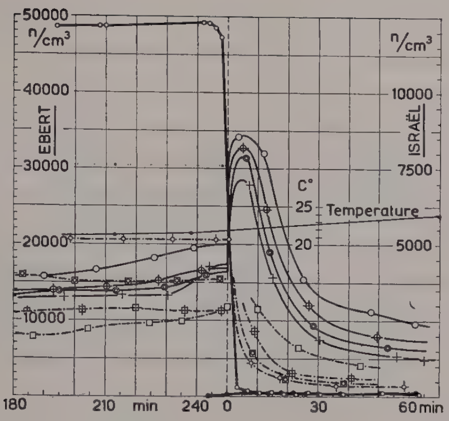

Fig. 8. Number of ions after switching off corona potential. Continuation of the curves shown in Fig. 6.

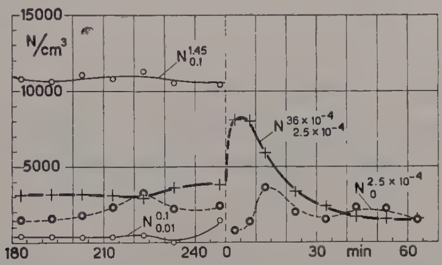

Fig. 9. Tendency of the groups of ions present in two intervals of mobility after switching off corona potential. Calculated from the measurements shown in Fig. 8.

of $k_* = 36.8$, 73.5, 110 and 147×10^{-4} (adjusted at a lower potential of 9.25 V applied to the second (II) condenser of the counter) are of another feature. The first curve (with $k_* = 36.8 \times 10^{-4}$) has a shape similar to that of the previously mentioned curves with lower k_*. The next three curves (with $k_* = 73.5$, 110 and 147×10^{-4}) show also similarity, but of another kind. Their increase is slower than that of the curves of lower k_*, but when these last curves have reached their maximum and begin to decrease again, the curves with higher k_* continue to increase and reach their higher values simultaneously with the curves obtained with the Ebert counter, and they remain on these levels all the time that the potential is applied. The curves of both the higher $k_* = 110$ and 147×10^{-4} exceed those of all the lower mobilities k_*. The shapes of the mentioned curves with the highest used $k_* = 73.5$, 110 and 147×10^{-4} are similar to those obtained with the Ebert counter, which fact indicates that these curves are defined by the presence of small-ions. A similar effect was discussed in the case of ions formed by negative corona [2], but for ions produced by positive corona the effect is pronounced more markedly. The effect is manifested very distinctly on the $n = F(1/k_*)$ characteristics elevating the curves at $1/k_* \to 0$.

(5) As shown by the considered trends of the number of ions produced by the positive corona, the variations are of another feature than those observed by negative corona [1]. The values of the measured number of ions under the same experimental

conditions are also different in both cases. This fact must be regarded as an indication of the difference in the mechanism of the production of positive and negative ions by corona discharge.

After *switching off* the potential and discharging the condenser of the rectifier, the general trends of the curves are the same as those considered in 1.1. Only the following facts must be added:

(1) The increase of the curves of the number of ions caught with the lower adjusted $k_* = 2.6$, 5.2, 7.9 and 10.5×10^{-4} after switching off the potential was higher, when the duration of the corona discharge in the test-room was longer (c. 4 hours in Fig. 6).

(2) In Fig. 4 and 8 it is shown more pronouncedly that instantly after the switching off, the curves of the number of ions caught at different adjusted limit mobilities arrange themselves below one another in the sequence of the adjusted limit mobilities k_* with the lowest k_* at the highest level and the highest k_* at the lowest level. This effect is the same as that observed in the case of ions produced by negative corona, and the mentioned order of the curves indicates that a transformation of the ions present at the moment of the switching off of the potential occurs during this stage of the processes in the air of the test-room in a way by which ions with higher mobilities will be transformed into ions with lower mobilities.

2. Distribution of the present ions in mobility groups

The distribution of the present ions in several groups of mobility is calculated from the curves of the number of ions measured at the adjusted limit mobilities in the way described in [2]. The tendency of groups of ions in different intervals of mobility is shown in Fig. 2, 5, 7 and 9.

During the corona discharge the predominant ions are the small-ions. It is evident that using the highest adjusted limit mobility $k_* = 147 \times 10^{-4}$, which is not at all included in the region of small-ions, it may not be expected that the calculated concentration of small-ions will be exact, but in spite of that the curves of the fraction of small-ions are surprisingly of the same shape as the curves of the number of ions measured with the EBERT counter (see especially Fig. 5 and 7). This fact may be regarded as an indication that our interpretation of the scanning of ions with the upper limit mobility of the condenser of the large-ion counter [2] is sufficiently correct and may be used for statements of the presence of ions with higher mobilities besides the larger ions scanned by the lower limit mobility adjusted to the condenser. Only the correct values of the concentration and of the mobility of the present ions with higher mobilities is a question, which may not be answered correctly with the present material at our disposal. It may be seen that the calculated concentration of ions in the fraction of small-ions is smaller than that obtained with the EBERT counter, but one must remember that the values calculated from the curves of the number of larger ions are results of extrapolation, and by using higher adjusted limit mobilities of the ISRAËL counter it may be expected to obtain more correct values of the concentration of the fraction of small-ions. In the present case this was not the principal thing, because by using the ISRAËL counter the intention was to determine the fractions of larger ions, and the information on the fraction of small-ions is obtained only as a by-result, but the obtained results indicate that by scanning the present ions with the upper limit mobility of the counter, results of importance may be obtained. The correct value of the mobility of ions scanned with the upper limit mobility of the counter is determined by the correctness of the perturbation coefficient a of the counter [2]. We have used the value given by ISRAËL himself.

Besides the considered small-ions ions of lower mobilities are also present during the positive corona, as shown in the figures, but their concentration is lower than during negative corona. From the beginning ultra-large ($N_0^{2.5\times10^{4}}$), Langevin-large and large-intermediate ($N_{2.5\times10^{-4}}^{60\times10^{-4}}$) ions were present in quanitities, which exceeded the amount of present small-ions ($N_{0.1}^{1.45}$). The Langevin-large and large-intermediate ions reached a maximum at the potential of c. 10 kV at which the rapid increase of the small-ions started. The presence in smaller quantities of smaller intermediate ions with mobilities of 0.01–0.1 is indicated in all the three figures. It seems that the fluctuations of the larger ions shown in the figures are real. We have no explanation of these fluctuations, nor of the elevation of the fraction of larger ions in Fig. 2.

After switching off the corona the presence of small-ions was not detectable with the used method. Only ultra-large, Langevin-large and larger intermediate ions remained.

Acknowledgements

The Swedish Natural Science Research Council deserves to receive thanks for placing means at the disposal of the Institute to perform this investigation. Mr. A. METNIEKS who assisted in the measurements and calculations deserves appreciation.

SUMMARY

Ions formed in a room by positive wire corona were measured with EBERT ion-counters and with an ISRAËL large-ion counter by periodical alternation of chosen adjusted limit mobilities. Only positive ions were established in a prevailing quantity during the corona discharge. The predominant ions present were the small-ions. But ions of lower mobilities were also established, though their concentration was lower than that during negative corona. The trends of the obtained curves show that the processes of production of ions by corona discharge must be different for positive and negative ions. After switching off the corona the present ions were transformed into larger intermediate, Langevin-large and ultra-large ions.

Institutet för högspänningsforskning vid Uppsala Universitet, May 1952.

REFERENCES

[1] H. NORINDER, and R. SIKSNA, Ions formed in a room by negative wire corona, *Ark. Fys.* in the press.
[2] R. SIKSNA, Mobility spectra of ions formed in a room by negative corona discharge, *Ark. Fys. 5*, Nr 26, 545–564, 1952.

Tryckt den 16 februari 1953

Uppsala 1953. Almqvist & Wiksells Boktryckeri AB

ARKIV FÖR FYSIK Band 6 nr 26

Communicated 10 September 1952 by MANNE SIEGBAHN

The decay energies of Pb^{209} and Si^{31}

By A. H. WAPSTRA[1]

With 3 figures in the text

Summary. An intermediate image β-spectrometer was calibrated with electron lines of known energy. The β-decay energies of Pb^{209} and Si^{31} were determined and found to be 635 ± 10 keV and 1486 ± 12 keV respectively.

0. Introduction. The sum of the generally accepted decay energies of Pb^{209}, Bi^{210} and Po^{210} is in disagreement with the sum of the binding energies of the last neutrons in Pb^{207}, Pb^{208}, Pb^{209} and Bi^{210} as determined from (n, γ) (1) and (d, p) reactions (2). In an earlier paper (3) it was assumed that the β-decay of Pb^{209} did not yield the ground state of Bi^{209}. No γ-rays were found in the decay of this isotope (4) (6). This may be explained in two ways: either a long-lived isomeric state in Bi^{209} is formed, or the missing 0.5 MeV is emitted in the form of some successive, highly converted low energy γ-rays, as supposed by HARVEY (5). The first possibility is improbable as experiments showed that the halflife of $Bi^{209\,m}$ should be at least 500 y (6). Here we will investigate the existence of low energy γ-transitions by measuring the β-spectrum. Older values of its maximum energy were 0.75 MeV (7), 0.70 MeV (8) and 0.64 ± 0.03 MeV (6) found by absorption, and 0.68 ± 0.03 MeV (9) and 0.71 MeV (10) determined by β-spectroscopy.

An analogous situation exists for Si^{31}. The difference in mass of P^{31} and Si^{28} computed from EWALD'S (11) mass spectrographical measurements is in disagreement with the reaction energies of some nuclear reactions. This difference can also be computed from the (d, p) reactions on the Si-isotopes (12) and the decay energy of Si^{31}. Earlier values for this β-energy, determined by cloud chamber and absorption measurements, are 1.85 MeV (13), 1.50 ± 0.01 MeV (14), 1.37 MeV (15), 1.48 MeV (16) and 1.53 ± 0.04 MeV (17). After our work had been completed Motz published a β-spectrometer value 1.471 ± 0.009 MeV (18).

1. Demagnetization procedure and calibration of the β-spectrometer. The β-spectrometer used in this investigation is the intermediate image spectrometer built by SLÄTIS and SIEGBAHN (19). It is necessary to demagnetize this instrument rather carefully in order to avoid complications due to remanent magnetism of the iron shell. The influence of remanent magnetism is most serious for low energy lines. The KLL Auger line in Xe^{131} was used for in-

---

[1] On leave from the "Instituut voor Kernphysisch Onderzoek", Amsterdam.

Table I

Position of the 24.44 keV KLL Auger line in Xe^{131} after different demagnetization procedures (all values are amperes)

Initial current	Steps	Last reversed current	Position of line
3.0	0.2	−0.4	0.921
4.0	0.5	−0.4	0.921
12.8	0.4	−0.4	0.924
13.2	0.4	−0.8	0.923
12.8	0.8	−0.8	0.922
14.0	0.8	−0.4	0.922

vestigating this influence. The Xe-sample was prepared by mass-separating some Xe extracted from I^{131} on a 0.15 mg/cm² Al backing. Table I shows the β-spectrometer current at the centre of gravity of the line after different demagnetization procedures.

The following method was used. The current was increased to the value shown in the first column in table I. Then the current was decreased to 0.3 Amp. (being the smallest current possible), reversed and raised again to a value, lower than the preceding one by the amount mentioned in the second column. This procedure was repeated until the current mentioned in the third column was reached. After this procedure the Xe Auger line was measured. Table I shows that the line position deviates not more than 0.2 % from the mean value. Therefore in all measurements the last, most convenient procedure mentioned in table I was used.

In an iron containing β-spectrometer the relation between the current and the momentum of the electrons is not quite linear. Therefore the instrument was calibrated by measuring some electron lines of wellknown energies. The results are collected in table II.

Table II

Electron lines used in calibrating the β-spectrometer

Nuclide	Line used	η	I	η/I	Reference
$Xe^{131\,m}$	KLL	0.3129 ± 0.0001	0.922	0.3392	(21)
$Kr^{85\,m}$	K_1	0.7733 ± 0.0004	2.290	0.3378	(21)
ThB	F	0.8147 ± 0.0001	2.407	0.3383	(22)
$Xe^{133\,m}$	K_2	0.9624 ± 0.0009	2.840	0.3389	(21)
$Kr^{85\,m}$	K_2	1.2090 ± 0.0007	3.550	0.3406	(21)
CS^{137}	K_1	1.9839 ± 0.0003	5.815	0.3413	(23)
Co^{60}	K_2	3.452 ± 0.001	10.075	0.3426	(24)

The third column shows the momentum of the electrons in relativistic units; it is connected to the Bρ-value by the relation $B\rho = 1704.43 \cdot \eta$ Gauss cm. The line width was 5 %. The last column shows the calibration "constant" η/I, which is plotted in fig 1.

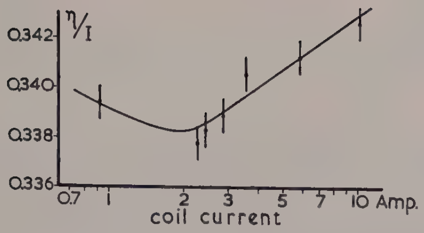

Fig. 1. Calibration curve of the β-spectrometer.

The errors in the values of η/I are due to three sources:

1. the error in η (see column 3).
2. the uncertainty in determining the current reading for the centre of the line; after judging the results of table I this error is assumed to be 0.2 % (1/25 of the line width which was 5 %).
3. possible errors in the current meter; these errors probably explain the shape of fig. 1.

Figure 1 shows that the deviations from the mean value 0.340 of the calibration constant are indeed less than 1 %, in agreement with SLÄTIS and SIEGBAHN (19).

2. The β-spectrum of Pb^{209}. Pb^{209} was prepared by bombarding metallic lead with 6 MeV deuterons in the small cyclotron of this Institute. The surface of the lead was scraped off, dissolved in nitric acid and repeatedly purified by precipitating with sulphuric acid, washing the precipitate and dissolving it in concentrated ammonium acetate solution. After this purification the decay was exponential for more than ten halflives; the halflife was found to be 3.30 hours. β-spectrometer samples were prepared by spreading the lead sulphate with insuline on a 0.15 mg/cm^2 Al backing. The average thicknesss of the thinnest sample was 0.9 mg/cm^2. The Fermi plot obtained with this sample is

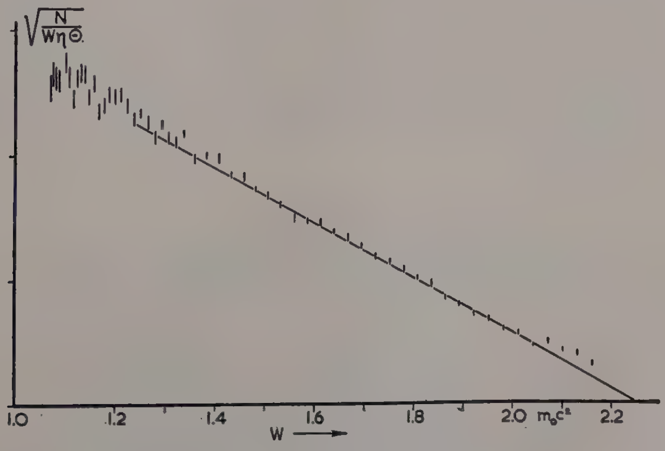

Fig. 2. Fermi plot of Pb^{209}.

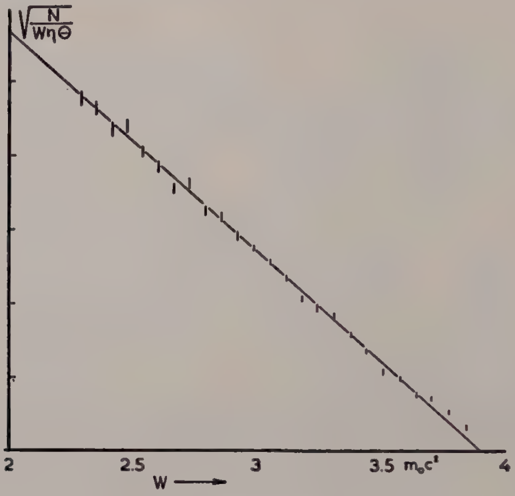

Fig. 3. Fermi-plot of Si^{31}.

linear above 200 keV (as shown in figure 2). The average endpoint of several runs is 635 ± 10 keV. This maximum β-energy is somewhat less than most earlier values but it agrees with our absorption value (6).

Due to the rather thick sample low energy electron lines should have been broadened. However, any electron line with an intensity of 5 % and an energy larger than 30 keV would probably have been detected. In order to look for low energy γ-radiations we studied a strong sample in a NaI (Tl) scintillation spectrometer (20). No γ lines between 10 keV and 150 keV were detected, nor the K-radiations reported by C. Shure (5). Hence this β-transition appears to be a ground state transition.

3. The decay energy of Si^{31}. The Si^{31} samples were prepared by bombarding P_3S_4 with fast neutrons from the small cyclotron and purified using the procedure of WENNERBLOM et al. (16). The β-samples were prepared in the same way as mentioned for Pb^{209}. The best sample had an average thickness of 0.5 mg/cm². Since this sample was rather weak only electrons with energy higher than 700 keV were measured. The Fermi-plot (fig. 3) is linear in the whole region investigated.

Table III

Nuclear reaction energies

No.	Reaction	Reaction energy
1	Si^{28} (d, p) Si^{29}	6.246 ± 0.008
2	Si^{29} (d, p) Si^{30}	8.388 ± 0.013
3	Si^{30} (d, p) Si^{31}	4.364 ± 0.007
4	P^{31} (p, α) Si^{28}	1.909 ± 0.010
5	P^{31} (d, α) Si^{29}	8.158 ± 0.011

The average maximum energy of two measurements with different samples was 1.486 ± 0.012 MeV, in good agreement with the value 1.471 ± 0.009 MeV published by MOTZ (18).

4. The difference in binding energies of P^{31} and Si^{28}. From Ewald's mass spectrographical measurements (11) we find P^{31}–Si^{28} = 26.314 ± 0.036 MeV. Reaction 4 in table III gives a value 26.374 ± 0.011 MeV for this difference in binding energies, reaction 5 and 1 26.373 ± 0.015 MeV. This is to be compared with a value 26.380 ± 0.020 derived from reactions 1, 2, 3 and the β-energy found above. Therefore our measurement confirms the reaction data and indicates that EWALD's value may be slightly low.

REFERENCES. (1) **B. B. Kinsey, G. A. Bartholomew** and **W. H. Walker,** Phys. Rev. *82,* 380 (1951). — (2) **J. A. Harvey,** Phys. Rev. *81,* 353 (1951). — (3) **A. H. Wapstra,** Physica *17,* 628 (1951). — (4) **J. S. Levinger** and **E. P. Meiners,** see "Nuclear Data", Bureau of Standards, Circular 499. — (5) **J. A. Harvey,** private communication. — (6) **A H. Wapstra,** Thesis, Amsterdam 1952. — (7) **W. Maurer** and **W. Ramm,** Z. Physik *119,* 602 (1942). — (8) **K. Fayans** and **A. F. Voigt,** Phys. Rev. *60,* 619 (1941). — (9) **W. Rall** and **R. G. Wilkinson,** Phys. Rev. *71,* 321 (1947). — (10) **J. S. Levinger** and **M. B. Sampson,** see "Nuclear Data", Bureau of Standards, Circular 499. — (11) **H. Ewald,** Z. Naturf. *6 a,* 293 (1951). — (12) **D. M. van Patter, A. Sperduto, P. M. Endt, W. W. Buechner** and **H. A. Enge,** Phys. Rev. *85,* 142 (1952). — (13) **F. N. D. Kurie, J. R. Richardson** and **H. C. Paxton,** Phys. Rev. *49,* 203 A (1936). — (14) **H. W. Newson,** Phys. Rev. *51,* 624 (1937). — (15) **E. E. Widdowson** and **F. C. Champion,** Proc. phys. Soc. *50,* 185 (1938). — (16) **A. Wennerblom, K. E. Zimen** and **E. Ehn,** Svensk Kemisk Tidskrift, *63,* 207 (1951). — (17) **A. H. Wapstra** and **B. Verkerk,** unpublished work. — (18) **H. T. Motz,** Phys. Rev. *85,* 501 (1952). — (19) **H. Slätis** and **K. Siegbahn,** Ark. Fysik *1,* 339 (1950). — (20) **B. Åström,** Ark. Fysik (in press). — (21) **I. Bergström,** Ark. Fys. *5,* 307 (1952) (KLL-energy, see formula 29). — (22) **G. Lindström,** Ark. Fys. *4,* 1 (1951). — (23) **G. Lindström, K. Siegbahn** and **A. H. Wapstra,** to be published in the Proc. phys. Soc. — (24) **D. A. Lind** and **A. Hedgran,** Ark. Fys. *5,* 29 (1952).

Nobel Institute of the Royal Swedish Academy of Sciences, Department for Physics, Stockholm, Sweden.

Tryckt den 28 februari 1953

Uppsala 1953. Almqvist & Wiksells Boktryckeri AB

ARKIV FÖR FYSIK Band 6 nr 27

Communicated 12 March 1952 by IVAR WALLER

On the coherent scattering of light by an electrostatic field according to the Dirac hole theory

By PER SVENONIUS

§ 1. Introduction

The aim of this paper is to discuss the interaction between photons and an electrostatic field V_0[1] according to the Dirac hole theory. We will limit our investigation to the case of coherent scattering. The whole system of particles is assumed to be enclosed in a cube of periodicity L^3. Letting $d\Phi$ denote the differential cross-section of the coherent scattering of a photon $\boldsymbol{k}, \boldsymbol{e}$ ($\boldsymbol{k}$ = momentum, $\boldsymbol{e}$ = unit vector of polarization) into a photon $\boldsymbol{k}', \boldsymbol{e}'$ in the element of solid angle $d\Omega$, we obtain upon considering second order perturbation[2]:

$$d\Phi = d\Omega\, \varepsilon^4 |S|^2 \mathcal{L}^2 \text{ where} \tag{1}$$

$$S = \sum_{\sigma=o} \sum_{\tau=e} \left(\frac{J_{\tau\sigma} J'^{+}_{\sigma\tau}}{E_\tau - E_\sigma - k} + \frac{J_{\sigma\tau} J'^{+}_{\tau\sigma}}{E_\tau - E_\sigma + k} \right) = S_1 + S_2; \tag{2}$$

ε = the electron charge;

$$J_{\sigma\tau} = \langle \sigma | J | \tau \rangle = \int \varphi_\sigma^* J \varphi_\tau \, d\boldsymbol{x}, \text{ etc.}; \tag{3}$$

$$J = \boldsymbol{\alpha} \cdot \boldsymbol{e}\, e^{i\boldsymbol{k}\cdot\boldsymbol{x}}, \quad J'^{+} = \boldsymbol{\alpha} \cdot \boldsymbol{e}'\, e^{-i\boldsymbol{k}'\cdot\boldsymbol{x}};$$

$\boldsymbol{\alpha}, \beta$ = the Dirac spin matrices;

(4) E_σ, φ_σ = eigenvalues and corresponding orthonormalized eigenfunctions of the Hamiltonian $H = \boldsymbol{\alpha} \cdot \boldsymbol{p} + \beta + V$ ($V = \varepsilon V_0$) of an electron moving in the electrostatic field V_0;

o, e = occupied and empty eigenstates of H.

---

[1] We use relativistic units ($\hbar = m = c = 1$). $\mathcal{L}$ denotes the relativistic unit of length: $1\,\mathcal{L} = \frac{h}{mc}$ cm.

[2] *Cf.* N. KEMMER: Helv. Phys. Acta 10 (1937) p. 113.

§ 2. Expansion of S in "powers" of V

Let H^L and φ_σ^L denote the charge-conjugated quantities of H and φ_σ, *i.e.*[1],

$$(5)\qquad \begin{cases} H=\boldsymbol{\alpha}\cdot\boldsymbol{p}+\beta+V, \\ H\varphi_\sigma=E_\sigma\varphi_\sigma, \end{cases}\qquad \begin{cases} H^L=\boldsymbol{\alpha}\cdot\boldsymbol{p}+\beta-V, \\ H^L\varphi_\sigma^L=E_\sigma^L\varphi_\sigma^L. \end{cases}$$

The charge-conjugated quantities then may be written

$$(6)\qquad \begin{cases} \varphi_\sigma^L=\overset{*}{\varphi}_\sigma, \\ E_\sigma^L=-E_\sigma, \end{cases}$$

if $\boldsymbol{\alpha}$ is taken to be real and β purely imaginary.[2] Another formulation of the connection between eigenfunctions of H and H^L in our case is as follows.

$$(7)\qquad \begin{cases} \varphi_\sigma^L=\beta\,\alpha_1\,\alpha_2\,\alpha_3\,\varphi_\sigma, \\ E_\sigma^L=-E_\sigma. \end{cases}$$

If we now perform in succession two conjugations of

$$(8)\qquad S_1=\sum_{\sigma=0}\sum_{\tau=e}\frac{J_{\tau\sigma}\,J_{\sigma\tau}'^{+}}{E_\tau-E_\sigma-k},$$

one according to (6) and the other according to (7), we get

$$(9)\qquad S_1=\sum_{\sigma=0}\sum_{\tau=e}\frac{J_{\sigma\tau}\,J_{\tau\sigma}'^{+}}{E_\tau-E_\sigma-k}.$$

Thus the operators J and J'^{+} may exchange places without affecting S_1 or S_2. From this, we conclude that S_1 and S_2 are unaffected by an exchange $\boldsymbol{e}\rightleftarrows\boldsymbol{e}'$, $\boldsymbol{k}\rightleftarrows-\boldsymbol{k}'$ and that S is an even function of k.

We shall now compute S_1. The calculation is limited to the case in which all negative-energy eigenstates are occupied and all the others empty ("vacuum"). V_0 is taken to be a weak potential, *i.e.*, V will be regarded as a perturbation parameter. As was recently remarked[3], the vacuum term[4] $S=\sum_{\overset{-}{\sigma}\overset{+}{\tau}}(+)$ always represents the difference between the coherent scattering amplitudes in a consequent hole theory and in a theory that regards only positive-energy particles as present.[5]

---

[1] See H. A. KRAMERS: Proc. Akad. Wet., sect. of sci., 40: 2 (Amsterdam 1937).

[2] For simplicity we make this special choice of the matrices $\boldsymbol{\alpha}$, β.

[3] K. J. le COUTEUR and S. ZIENAU: Proc. Phys. Soc. A 63 (nov. 1950) p. 1223.

[4] $\overset{-}{\sigma}$ represents all states satisfying $E_\sigma<0$ and $\overset{+}{\tau}$ all states $E_\tau>0$.

[5] From the mere fact that we can write eq. (2) in the form

$$\sum_{\sigma=0}\sum_{\tau=e}(\cdots)=\sum_{\sigma=0}\sum_{\tau=0+e}(\cdots)$$

we see that the contributions from the separate particles to the coherent scattering amplitude actually superpose.

The study of this vacuum scattering thus is of great interest for an appraisal of the hole theory and its consequences.

To evaluate

(10) $$S_1 = \sum_{\overset{-}{\sigma}\overset{+}{\tau}} \frac{J_{\tau\sigma} J'^{+}_{\sigma\tau}}{E_\tau - E_\sigma - k},$$

we start with a formal operational summation.[1] We may write

(11) $$S_1 = \sum_{\overset{+}{\tau}} \langle \tau | J \Omega J'^{+} | \tau \rangle$$

where

$$\Omega = \frac{1}{2} \frac{1 - \frac{H}{|H|}}{T + |H|},$$

(12) $$T = E_\tau - k \quad (T = \text{capital } \tau),$$

and

$$|H| \varphi_\sigma = |E_\sigma| \varphi_\sigma .$$

Letting $|n\rangle$[2] (and $|m\rangle$) denote the complete orthonormalized set of eigenkets of the operator $H_0 = \boldsymbol{\alpha} \cdot \boldsymbol{p} + \beta$, we can write

(13) $$S_1 = \sum_{\overset{+}{\tau}} \sum_{n\,m} \langle \tau | J | n \rangle \langle n | \Omega | m \rangle \langle m | J'^{+} | \tau \rangle .$$

The operator $|A+B|$ can always be expanded in powers of a "small" B in a representation where A is diagonal, even if A and B fail to commute. Assuming an expansion

(14) $$|A+B| = a + b + c + \cdots \quad (b \sim B,\ c \sim B^2 \text{ etc.})$$

we obtain upon squaring and identifying

$$a = |A|,$$

(15) $$b_{n\,m} = \frac{A_n + A_m}{a_n + a_m} B_{n\,m},$$

$$c_{n\,m} = \frac{(B^2 - b^2)_{n\,m}}{a_n + a_m} = \sum_s \frac{B_{n\,s} B_{s\,m} - b_{n\,s} b_{s\,m}}{a_n + a_m}$$

(16) where, *e.g.*, $b_{n\,m} = \langle n | b | m \rangle$, $|n\rangle$ being an eigenket of A.

---

[1] *Cf.* N. M. KROLL and W. E. LAMB, Jr.: Phys. Rev. 75 (1949) p. 392.

[2] Latin letters will throughout be used for free-particle states and Greek letters for bound states. Thus E_n is an eigenvalue of H_0 and E_σ an eigenvalue of H.

In this way, we expand the symmetric operator[1]

$$(17)\qquad \Omega=\tfrac{1}{4}[(1-\tfrac{1}{2}[H,|H|^{-1}]_{+}),\ (T+H)^{-1}]_{+}$$

to the second power of V. Having then eliminated the $\bar{\sigma}$-states in (10), we eliminate the $\overset{+}{\tau}$-states in the same way, putting $T=|H|-k$ and again expanding to the second power of V. The computation is straightforward but rather lengthy. From the final expression, containing only multiple sums over free-particle states, we can draw the following conclusions,

The zero order terms give no contribution if $\boldsymbol{k}\neq\boldsymbol{k}'$ and can be omitted.[2] Charge-conjugation reveals that the first order terms vanish identically. Thus the second order terms will give the main contribution to S_1. If we charge-conjugate these terms according to (6), we may write[3]

$$(18)\qquad S_1=-2\,(s_{1\mathrm{A}}+s_{1\mathrm{B}}),\ \text{where}$$

$$(19\,\mathrm{a})\quad s_{1\mathrm{A}}=\Bigg\{\sum_{\overset{+}{r}\overset{-}{n}\overset{+}{s}\overset{+}{m}} N_r n_s n_m+\sum_{\overset{+}{r}\overset{+}{n}\overset{-}{s}\overset{+}{m}} S_r s_n s_m+\sum_{\overset{+}{r}\overset{+}{n}\overset{+}{s}\overset{-}{m}} M_r m_n m_s+\sum_{\overset{+}{r}\overset{+}{n}\overset{-}{s}\overset{-}{m}} R_m n_s(n_m+R_s)+$$

$$+\sum_{\overset{+}{r}\overset{-}{n}\overset{+}{s}\overset{-}{m}} R_n m_s(n_s+R_m)+\sum_{\overset{+}{r}\overset{-}{n}\overset{-}{s}\overset{+}{m}} R_n m_s(n_m+R_s)+\sum_{\overset{+}{r}\overset{-}{n}\overset{-}{s}\overset{-}{m}} R_n R_s R_m\Bigg\}\cdot$$

$$\cdot\,\frac{E_r E_n E_s E_m}{a_r a_n a_s a_m} J_{rn} V_{ns} V_{sm} J'^{+}_{mr};$$

$$(19\,\mathrm{b})\quad s_{1\mathrm{B}}=\Bigg\{\sum_{\overset{+}{r}\overset{+}{n}\overset{-}{s}\overset{-}{q}} R_s s_n r_q+\sum_{\overset{+}{r}\overset{-}{n}\overset{+}{s}\overset{-}{q}} \tfrac{1}{2}(S_q+R_n)s_n r_q+\sum_{\overset{-}{r}\overset{+}{n}\overset{+}{s}\overset{+}{q}} R_n R_s r_q+$$

$$+\sum_{\overset{+}{r}\overset{+}{n}\overset{-}{s}\overset{+}{q}} S_r S_q s_n+\sum_{\overset{+}{r}\overset{-}{n}\overset{-}{s}\overset{+}{q}} R_n R_s S_q\Bigg\}\cdot\frac{E_r E_n E_s E_q}{a_r a_n a_s a_q} J_{rn} V_{ns} J'^{+}_{sq} V_{qr}.$$

The following notations are used here.

$a_i=|E_i|=(1+\boldsymbol{p}_i^2)^{\frac{1}{2}}\qquad (i=r,\,n,\,s,\,q);$

$\overset{+}{i},\ \overset{-}{i}=$ the positive and negative energy spectrum resp. of H_0;

$R_n=N_r=(a_r+a_n-k)^{-1}$, etc.;

$r_n=n_r=(a_r+a_n)^{-1}$, etc.

Performing a conjugation (7) of an arbitrary sum in (19), we see that interchanging $+$'s and $-$'s in the four summation indices does not affect the sum. A conjugation (6) and an index change $n\rightleftarrows m$ gives

$$(20)\qquad \sum_{\overset{\rho}{r}\overset{\nu}{n}\overset{\sigma}{s}\overset{\mu}{m}} f(a_r,\,a_n,\,a_s,\,a_m)\,J_{rn} V_{ns} V_{sm} J'^{+}_{mr}=\sum_{\overset{\rho}{r}\overset{\mu}{n}\overset{\sigma}{s}\overset{\nu}{m}} f(a_r,\,a_m,\,a_s,\,a_n)\,J'^{+}_{rn} V_{ns} V_{sm} J_{mr},$$

---

[1] $[\alpha,\beta]_{+}=\alpha\beta+\beta\alpha$.

[2] *Cf.* KEMMER: *loc. cit.*; COUTEUR and ZIENAU: *loc. cit.*

[3] *Cf.* KEMMER: *loc. cit.* eq. (14) p. 117.

where f is a function of four variables and ϱ, ν, σ, μ temporarily denote the signs of r, n, s, m respectively.

Using (20), we find that some sums in $s_{1\mathrm{A}}$ change into others under the transformation $\boldsymbol{e} \rightleftarrows \boldsymbol{e}'$, $\boldsymbol{k} \rightleftarrows -\boldsymbol{k}'$. The same is easily shown for $s_{1\mathrm{B}}$ upon making the substitutions $r \rightleftarrows s$, $n \rightleftarrows q$. We may now write

$$\begin{cases} S_1 = S_1' + S_1'', \\ S_1 = -(s_{1\mathrm{A}}' + s_{1\mathrm{B}}'), \end{cases} \tag{21}$$

where $S_1' \to S_1''$ when $\boldsymbol{e} \rightleftarrows \boldsymbol{e}'$, $\boldsymbol{k} \rightleftarrows -\boldsymbol{k}'$, and where

$$\begin{aligned} s_{1\mathrm{A}}' = \Bigg\{ & \sum_{\substack{+-++\\ r\,n\,s\,m}} 2 N_r n_s n_m + \sum_{\substack{++-+\\ r\,n\,s\,m}} S_r s_n s_m + \sum_{\substack{++--\\ r\,n\,s\,m}} 2 R_m n_s (n_m + R_s) + \\ & + \sum_{\substack{+-+-\\ r\,n\,s\,m}} R_n m_s (n_s + R_m) + \sum_{\substack{+---\\ r\,n\,s\,m}} R_n R_s R_m \Bigg\} \frac{E_r E_n E_s E_m}{a_r a_n a_s a_m} J_{rn} V_{ns} V_{sm} J_{mr}'^{+}; \end{aligned} \tag{22 a}$$

$$\begin{aligned} s_{1\mathrm{B}}' = \Bigg\{ & \sum_{\substack{++--\\ r\,n\,s\,q}} R_s s_n r_q + \sum_{\substack{+-+-\\ r\,n\,s\,q}} R_n s_n r_q + \sum_{\substack{-+++\\ r\,n\,s\,q}} 2 R_n R_s r_q + \sum_{\substack{+--+\\ r\,n\,s\,q}} R_n R_s S_q \Bigg\} \cdot \\ & \cdot \frac{E_r E_n E_s E_q}{a_r a_n a_s a_q} J_{rn} V_{ns} J_{sq}'^{+} V_{qr}. \end{aligned} \tag{22 b}$$

§ 3. Evaluation of the spurs

The following notations are now introduced.

$$|\iota\rangle = \text{the spinor ket of } |i\rangle, \textit{ i.e.},$$

$$|i\rangle = |L^{-3/2} e^{i \boldsymbol{p}_i \cdot \boldsymbol{x}}\rangle |\iota\rangle \quad \begin{cases} i = r,\ n,\ s,\ m. \\ \iota = \varrho,\ \nu,\ \sigma,\ \mu \ \text{resp.}; \end{cases} \tag{23}$$

$$\boldsymbol{p}_{ij} = \boldsymbol{p}_i - \boldsymbol{p}_j; \quad E_{\iota j} = E_\iota - E_j; \quad E^{\iota j} = E_\iota + E_j; \tag{24}$$

$$W(\boldsymbol{g}) = \int e^{i \boldsymbol{g} \cdot \boldsymbol{x}} V(\boldsymbol{x})\, d x^3; \tag{25}$$

$$\delta(\boldsymbol{p}) = \delta(p_1)\, \delta(p_2)\, \delta(p_3); \quad \delta(x) = \text{the Dirac delta function.} \tag{26}$$

We now treat the sums in (22 a). They are all of the type

$$\Sigma_A = \sum_{r\,n\,s\,m} f(a_r, a_n, a_s, a_m) \frac{E_r E_n E_s E_m}{a_r a_n a_s a_m} J_{rn} V_{ns} V_{sm} J_{mr}'^{+}; \tag{27}$$

where f is a function of four variables and where each index r, n, s, m runs over all positive- or all negative-energy eigenfunctions of H_0, this being not explicitly indicated in (27). It is now clear that

$$\sum_A = L^{-12}(2\pi)^6 \dot{\sum_{p_r p_n p_s p_m}} \frac{f(a_r, a_n, a_s, a_m)}{4\, a_r\, a_n\, a_s\, a_m}\, \delta(\boldsymbol{p}_{nr} + \boldsymbol{k})\, W(\boldsymbol{p}_{sn}) \\ W(\boldsymbol{p}_{ms})\, \delta(\boldsymbol{p}_{rm} - \boldsymbol{k}')\, \sigma_{rnsm}, \tag{28}$$

where

$$\sigma_{rnsm} = 4\, E_r\, E_n\, E_s\, E_m \sum_{\text{spin}} \langle \varrho | \boldsymbol{\alpha}\cdot\boldsymbol{e} | \nu \rangle \langle \nu | \sigma \rangle \langle \sigma | \mu \rangle \langle \mu | \boldsymbol{\alpha}\cdot\boldsymbol{e}' | \varrho \rangle. \tag{29}$$

In (28), each index $\boldsymbol{p}_r, \boldsymbol{p}_n, \boldsymbol{p}_s, \boldsymbol{p}_m$ runs over every eigenvalue of $\boldsymbol{p}$. The spin degeneration is accounted for in (29), where $\sum_{\text{spin}}$ indicates that every spin index runs over two spinor functions belonging to the same momentum and energy eigenvalues.

We change (28) into an integral and obtain

$$\sum_A = (2\pi)^{-6} \int d\boldsymbol{p}_r\, d\boldsymbol{p}_n\, d\boldsymbol{p}_s\, d\boldsymbol{p}_m \frac{f(a_r, a_n, a_s, a_m)}{4\, a_r\, a_n\, a_s\, a_m} \cdot \\ \cdot \delta(\boldsymbol{p}_{nr} + \boldsymbol{k})\, W(\boldsymbol{p}_{sn})\, W(\boldsymbol{p}_{ms})\, \delta(\boldsymbol{p}_{rm} - \boldsymbol{k}')\, \sigma_{rnsm}. \tag{30}$$

Dropping the index r for $\boldsymbol{p}_r$ and making the change of variable $\boldsymbol{p}_{sr} + \boldsymbol{k} \to \boldsymbol{g}$, we find

$$\sum_A = (2\pi)^{-6} \int d\boldsymbol{p}\, d\boldsymbol{g} \frac{f(a_r, a_n, a_s, a_m)}{4\, a_r\, a_n\, a_s\, a_m}\, W(\boldsymbol{g})\, W(\boldsymbol{K} - \boldsymbol{g})\, \sigma_{rnsm}; \tag{31}$$

where

$$\begin{cases} \boldsymbol{K} = \boldsymbol{k} - \boldsymbol{k}'; \\ a_i = +(1 + \boldsymbol{p}_i^2)^{\frac{1}{2}} = |E_i| \qquad (i = r, n, s, m); \\ \boldsymbol{p}_r = \boldsymbol{p}; \\ \boldsymbol{p}_n = \boldsymbol{p} - \boldsymbol{k}; \\ \boldsymbol{p}_s = \boldsymbol{p} + \boldsymbol{g} - \boldsymbol{k}; \\ \boldsymbol{p}_m = \boldsymbol{p} - \boldsymbol{k}'. \end{cases} \tag{32}$$

σ_{rnsm} (29) will be evaluated by successive operational elimination of the spinors.

$$\sigma_{rnsm} = 4\, E_r\, E_n\, E_s\, E_m \sum_{\text{spin}} \langle \varrho | \boldsymbol{\alpha}\cdot\boldsymbol{e} | \nu \rangle \langle \nu | \tfrac{1}{2} \left(1 + \frac{\boldsymbol{\alpha}\cdot\boldsymbol{p}_s + \beta}{E_s}\right) | \mu \rangle \langle \mu | \boldsymbol{\alpha}\cdot\boldsymbol{e}' | \varrho \rangle = \\ = \tfrac{1}{2} E_r\, E_n\, E_m \sum_{\text{spin}} \langle \varrho | \{ (E_{nr} + \boldsymbol{\alpha}\cdot\boldsymbol{k})\, \boldsymbol{\alpha}\cdot\boldsymbol{e} + 2\,\boldsymbol{e}\cdot\boldsymbol{p} \}\, (E^{sn} + \boldsymbol{\alpha}\cdot\boldsymbol{g}) \cdot \\ \cdot \{ 2\,\boldsymbol{e}'\cdot\boldsymbol{p} + \boldsymbol{\alpha}\cdot\boldsymbol{e}'\, (E_{mr} + \boldsymbol{\alpha}\cdot\boldsymbol{k}') \} | \varrho \rangle = \\ = \tfrac{1}{4} Sp\, [(E_r + \boldsymbol{\alpha}\cdot\boldsymbol{p} + \beta)\, (2\,\boldsymbol{e}\cdot\boldsymbol{p} + E_{nr}\, \boldsymbol{\alpha}\cdot\boldsymbol{e} + \boldsymbol{\alpha}\cdot\boldsymbol{k}\, \boldsymbol{\alpha}\cdot\boldsymbol{e}) \cdot \\ \cdot (E^{sn} + \boldsymbol{\alpha}\cdot\boldsymbol{g})\, (2\,\boldsymbol{e}'\cdot\boldsymbol{p} + E_{mr}\, \boldsymbol{\alpha}\cdot\boldsymbol{e}' + \boldsymbol{\alpha}\cdot\boldsymbol{e}'\ \boldsymbol{\alpha}\cdot\boldsymbol{k}')]. \tag{33}$$

We now introduce the following notation.

$$\tag{34 a} \tfrac{1}{4} Sp\, \boldsymbol{\alpha}\cdot\boldsymbol{A}\ \ \boldsymbol{\alpha}\cdot\boldsymbol{B} = \boldsymbol{A}\cdot\boldsymbol{B};$$

$$\tag{34 b} \begin{aligned}(\boldsymbol{A}, \boldsymbol{B}, \boldsymbol{C}, \boldsymbol{D}) &= \tfrac{1}{4} Sp\, \boldsymbol{\alpha}\cdot\boldsymbol{A}\ \ \boldsymbol{\alpha}\cdot\boldsymbol{B}\ \ \boldsymbol{\alpha}\cdot\boldsymbol{C}\ \ \boldsymbol{\alpha}\cdot\boldsymbol{D} = \\ &= \boldsymbol{A}\cdot\boldsymbol{B}\ \ \boldsymbol{C}\cdot\boldsymbol{D} - \boldsymbol{A}\cdot\boldsymbol{C}\ \ \boldsymbol{B}\cdot\boldsymbol{D} + \boldsymbol{A}\cdot\boldsymbol{D}\ \ \boldsymbol{B}\cdot\boldsymbol{C};\end{aligned}$$

$$\tag{34 c} \begin{aligned}(\boldsymbol{A}, \boldsymbol{B}, \boldsymbol{C}, \boldsymbol{D}, \boldsymbol{E}, \boldsymbol{F}) &= \tfrac{1}{4} Sp\, \boldsymbol{\alpha}\cdot\boldsymbol{A}\ \ \boldsymbol{\alpha}\cdot\boldsymbol{B}\ \ \boldsymbol{\alpha}\cdot\boldsymbol{C}\ \ \boldsymbol{\alpha}\cdot\boldsymbol{D}\ \ \boldsymbol{\alpha}\cdot\boldsymbol{E}\ \ \boldsymbol{\alpha}\cdot\boldsymbol{F} = \\ &= \boldsymbol{A}\cdot\boldsymbol{B}\,(\boldsymbol{C}, \boldsymbol{D}, \boldsymbol{E}, \boldsymbol{F}) - \boldsymbol{A}\cdot\boldsymbol{C}\,(\boldsymbol{B}, \boldsymbol{D}, \boldsymbol{E}, \boldsymbol{F}) + \\ &\quad + \boldsymbol{A}\cdot\boldsymbol{D}\,(\boldsymbol{B}, \boldsymbol{C}, \boldsymbol{E}, \boldsymbol{F}) - \boldsymbol{A}\cdot\boldsymbol{E}\,(\boldsymbol{B}, \boldsymbol{C}, \boldsymbol{D}, \boldsymbol{F}) + \boldsymbol{A}\cdot\boldsymbol{F}\,(\boldsymbol{B}, \boldsymbol{C}, \boldsymbol{D}, \boldsymbol{E}).\end{aligned}$$

The last equality in (34 c) is easily established. Using the notation $A = \boldsymbol{\alpha}\cdot\boldsymbol{A}$, etc., we have

$$\begin{aligned}2\,\boldsymbol{A}\cdot\boldsymbol{D}\ BCEF = BC\,(AD + DA)\,EF = (ABC + 2\,\boldsymbol{A}\cdot\boldsymbol{C}\ B - 2\,\boldsymbol{A}\cdot\boldsymbol{B}\ C)\,DEF + \\ + BCD\,(EFA + 2\,\boldsymbol{A}\cdot\boldsymbol{E}\ F - 2\,\boldsymbol{A}\cdot\boldsymbol{F}\ E).\end{aligned}$$

The spur of this identity gives (34 c). As is easily seen, the formulae (34) may be extended to any power of $\boldsymbol{\alpha}$.

We now have

$$\tag{35} \begin{aligned}\sigma_{rnsm} = {} & 2\,E^{sn} E^{nm}\, \boldsymbol{e}\cdot\boldsymbol{p}\ \ \boldsymbol{e}'\cdot\boldsymbol{p} + E_r E_{nr} E^{sn} E_{mr}\, \boldsymbol{e}\cdot\boldsymbol{e}' + 4\,\boldsymbol{e}\cdot\boldsymbol{p}\ \ \boldsymbol{e}'\cdot\boldsymbol{p}\ \ \boldsymbol{p}\cdot\boldsymbol{g} + \\ & + E_{nr} E^{mr}\, \boldsymbol{e}'\cdot\boldsymbol{p}\ \ \boldsymbol{e}\cdot\boldsymbol{g} + E_{mr} E^{nr}\, \boldsymbol{e}\cdot\boldsymbol{p}\ \ \boldsymbol{e}'\cdot\boldsymbol{g} - E_{nr} E_{mr}\, \boldsymbol{e}\cdot\boldsymbol{e}'\ \ \boldsymbol{p}\cdot\boldsymbol{g} + \\ & + 2\,\boldsymbol{e}'\cdot\boldsymbol{p}\,(\boldsymbol{p}, \boldsymbol{k}, \boldsymbol{e}, \boldsymbol{g}) + E^{sn} E_{mr}\,(\boldsymbol{p}, \boldsymbol{k}, \boldsymbol{e}, \boldsymbol{e}') + E_r E_{mr}\,(\boldsymbol{k}, \boldsymbol{e}, \boldsymbol{g}, \boldsymbol{e}') + \\ & + 2\,\boldsymbol{e}\cdot\boldsymbol{p}\,(\boldsymbol{p}, \boldsymbol{g}, \boldsymbol{e}', \boldsymbol{k}') + E^{sn} E_{nr}\,(\boldsymbol{p}, \boldsymbol{e}, \boldsymbol{e}', \boldsymbol{k}') + E_r E_{nr}\,(\boldsymbol{e}, \boldsymbol{g}, \boldsymbol{e}', \boldsymbol{k}') + \\ & + E_r E^{sn}\,(\boldsymbol{k}, \boldsymbol{e}, \boldsymbol{e}', \boldsymbol{k}') + (\boldsymbol{p}, \boldsymbol{k}, \boldsymbol{e}, \boldsymbol{g}, \boldsymbol{e}', \boldsymbol{k}').\end{aligned}$$

In the same way, we find

$$\tag{36} \begin{aligned}\sum\nolimits_B = \sum_{rnsq} f\,(a_r, a_n, a_s, a_q)\,\frac{E_r E_n E_s E_q}{a_r\, a_n\, a_s\, a_q}\, J_{rn} V_{ns} J_{sq}'^{+} V_{qr} = \\ = (2\,\pi)^{-6} \int d\boldsymbol{p}\, d\boldsymbol{g}\, \frac{f\,(a_r, a_n, a_s, a_q}{4\,a_r\, a_n\, a_s\, a_q}\, W(\boldsymbol{g})\, W(\boldsymbol{K} - \boldsymbol{g})\, \tau_{rnsq};\end{aligned}$$

$$\tag{37} \begin{aligned}\tau_{rnsq} = \tfrac{1}{4} Sp\,[(E_r + \boldsymbol{\alpha}\cdot\boldsymbol{p})\,(2\,\boldsymbol{e}\cdot\boldsymbol{p} + E_{nr}\,\boldsymbol{\alpha}\cdot\boldsymbol{e} + \boldsymbol{\alpha}\cdot\boldsymbol{k}\ \ \boldsymbol{\alpha}\cdot\boldsymbol{e})\,(E^{sn} + \boldsymbol{\alpha}\cdot\boldsymbol{g}) \\ (2\,\boldsymbol{e}'\cdot\boldsymbol{p}_s + E_{qs}\,\boldsymbol{\alpha}\cdot\boldsymbol{e}' + \boldsymbol{\alpha}\cdot\boldsymbol{e}'\ \ \boldsymbol{\alpha}\cdot\boldsymbol{k}')] = \\ = 2\,E^{sn} E_{qs}\, \boldsymbol{e}\cdot\boldsymbol{p}\ \ \boldsymbol{e}'\cdot\boldsymbol{p} + 2\,E^{rn} E^{sn}\, \boldsymbol{e}\cdot\boldsymbol{p}\ \ \boldsymbol{e}'\cdot\boldsymbol{p}_s + E_r E_{nr} E^{sn} E_{qs}\, \boldsymbol{e}\cdot\boldsymbol{e}' + \\ + 4\,\boldsymbol{e}\cdot\boldsymbol{p}\ \ \boldsymbol{e}'\cdot\boldsymbol{p}_s\ \ \boldsymbol{p}\cdot\boldsymbol{g} + 2\,E_r E_{nr}\, \boldsymbol{e}'\cdot\boldsymbol{p}_s\ \ \boldsymbol{e}\cdot\boldsymbol{g} + 2\,E_r E_{qs}\, \boldsymbol{e}\cdot\boldsymbol{p}\ \ \boldsymbol{e}'\cdot\boldsymbol{g} +\end{aligned}$$

$$+E_{nr}E_{qs}(\boldsymbol{p},\boldsymbol{e},\boldsymbol{g},\boldsymbol{e}')+2\,\boldsymbol{e}'\cdot\boldsymbol{p}_s(\boldsymbol{p},\boldsymbol{k},\boldsymbol{e},\boldsymbol{g})+E^{sn}E_{qs}(\boldsymbol{p},\boldsymbol{k},\boldsymbol{e},\boldsymbol{e}')+$$
$$+E_r E_{qs}(\boldsymbol{k},\boldsymbol{e},\boldsymbol{g},\boldsymbol{e}')+2\,\boldsymbol{e}\cdot\boldsymbol{p}(\boldsymbol{p},\boldsymbol{g},\boldsymbol{e}',\boldsymbol{k}')+E_{nr}E^{sn}(\boldsymbol{p},\boldsymbol{e},\boldsymbol{e}',\boldsymbol{k}')+$$
$$+E_r E_{nr}(\boldsymbol{e},\boldsymbol{g},\boldsymbol{e}',\boldsymbol{k}')+E_r E^{sn}(\boldsymbol{k},\boldsymbol{e},\boldsymbol{e}',\boldsymbol{k}')+(\boldsymbol{p},\boldsymbol{k},\boldsymbol{e},\boldsymbol{g},\boldsymbol{e}',\boldsymbol{k}').$$

The notations (32) are used and

$$\boldsymbol{p}_q=\boldsymbol{p}+\boldsymbol{g}-\boldsymbol{K}. \tag{38}$$

The evaluation of S_1 (21) now consists in computing (22) according to (31), (35), (36), and (37).

§ 4. The non-relativistic approximation

An expression like (31) or (36) seems difficult to treat exactly by any method. We therefore turn to the case of $k \ll 1$, the non-relativistic approximation. Introducing $k=0$ in (22) and then integrating according to (31) and (36) over $\boldsymbol{p}$-space (beginning with an integration over all directions of $\boldsymbol{p}$), we may verify that S_1 vanishes in this case. The computation is tedious but quite elementary. We can thus verify Kemmer's assumption that the terms of order 0 and 1 vanish when we expand S in powers of $k\,(=|\boldsymbol{k}|=|\boldsymbol{k}'|)$ in the non-relativistic case, as the linear terms in k, $\boldsymbol{k}$, and $\boldsymbol{k}'$ obviously give zero contribution.

We must now expand (21) to the second power of k. Before performing this expansion, we make the change of variable $\boldsymbol{g}\rightarrow\boldsymbol{x}-\boldsymbol{p}+\boldsymbol{k}$. We then have (cf. (31) and (36)):

$$\textstyle\sum_A=(2\pi)^{-6}\displaystyle\int d\boldsymbol{p}\,d\boldsymbol{x}\frac{f(a_r,a_n,a_s,a_m)}{4a_r a_n a_s a_m}W(\boldsymbol{x}-\boldsymbol{p}+\boldsymbol{k})\,W(\boldsymbol{p}-\boldsymbol{x}-\boldsymbol{k}')\;\sigma'_{rnsm}; \tag{39}$$

$$\textstyle\sum_B=(2\pi)^{-6}\displaystyle\int d\boldsymbol{p}\,d\boldsymbol{x}\frac{f(a_r,a_n,a_s,a_q)}{4a_r a_n a_s a_q}W(\boldsymbol{x}-\boldsymbol{p}+\boldsymbol{k})\,W(\boldsymbol{p}-\boldsymbol{x}-\boldsymbol{k}')\;\tau'_{rnsq}; \tag{40}$$

where as before $a_i=+(1+\boldsymbol{p}_i^2)^{\frac{1}{2}}$, but now

$$\left\{\begin{aligned}\boldsymbol{p}_r&=\boldsymbol{p};\\ \boldsymbol{p}_n&=\boldsymbol{p}-\boldsymbol{k};\\ \boldsymbol{p}_s&=\boldsymbol{x};\\ \boldsymbol{p}_m&=\boldsymbol{p}-\boldsymbol{k}';\\ \boldsymbol{p}_q&=\boldsymbol{x}+\boldsymbol{k}'.\end{aligned}\right. \tag{41}$$

The transformed spurs σ'_{rnsm} and τ'_{rnsq} may be written as follows.

$$\sigma'_{rnsm}=2\,\boldsymbol{e}\cdot\boldsymbol{p}\;\boldsymbol{e}'\cdot\boldsymbol{p}\,(E_s E^{nm}+2-\boldsymbol{x}\cdot\boldsymbol{k}-\boldsymbol{x}\cdot\boldsymbol{k}')+4\,\boldsymbol{e}\cdot\boldsymbol{p}\;\boldsymbol{e}'\cdot\boldsymbol{p}\;\boldsymbol{p}\cdot\boldsymbol{x}+ \tag{42 a}$$
$$+2\boldsymbol{e}\cdot\boldsymbol{p}\;\boldsymbol{e}'\cdot\boldsymbol{x}\,(E_r E_{mr}+\boldsymbol{p}\cdot\boldsymbol{k}')+2\boldsymbol{e}'\cdot\boldsymbol{p}\;\boldsymbol{e}\cdot\boldsymbol{x}\,(E_r E_{nr}+\boldsymbol{p}\cdot\boldsymbol{k})+$$

$$+E_{nr}E_{mr}(\boldsymbol{e},\boldsymbol{p},\boldsymbol{e},\boldsymbol{x})+\boldsymbol{e}\cdot\boldsymbol{e}'\,E_{mr}E_{nr}(E_rE_s-1)+E_sE_{mr}(\boldsymbol{e},\boldsymbol{e}',\boldsymbol{p},\boldsymbol{k})+$$
$$+E_sE_{nr}(\boldsymbol{e}',\boldsymbol{e},\boldsymbol{p},\boldsymbol{k}')-E_rE_{mr}(\boldsymbol{e},\boldsymbol{e}',\boldsymbol{x},\boldsymbol{k})-E_rE_{nr}(\boldsymbol{e}',\boldsymbol{e},\boldsymbol{x},\boldsymbol{k}')+$$
$$+(1+E_rE_s)(\boldsymbol{k},\boldsymbol{e},\boldsymbol{e}',\boldsymbol{k}')+(\boldsymbol{p},\boldsymbol{k},\boldsymbol{e},\boldsymbol{x},\boldsymbol{e}',\boldsymbol{k}');$$

$$\tau'_{rnsq}=2\,\boldsymbol{e}\cdot\boldsymbol{p}\;\;\boldsymbol{e}'\cdot\boldsymbol{p}\,(E_sE_{qs}-\boldsymbol{x}\cdot\boldsymbol{k}')+2\,\boldsymbol{e}\cdot\boldsymbol{x}\;\;\boldsymbol{e}'\cdot\boldsymbol{x}\,(E_rE_{nr}+\boldsymbol{p}\cdot\boldsymbol{k})+ \tag{42 b}$$
$$+2\,\boldsymbol{e}\cdot\boldsymbol{p}\;\;\boldsymbol{e}'\cdot\boldsymbol{x}\,(E_nE_s+E_rE_q+2+2\,\boldsymbol{p}\cdot\boldsymbol{x}-\boldsymbol{x}\cdot\boldsymbol{k}+\boldsymbol{p}\cdot\boldsymbol{k}')+$$
$$+E_{nr}E_{qs}(\boldsymbol{e},\boldsymbol{p},\boldsymbol{e}',\boldsymbol{x})+\boldsymbol{e}\cdot\boldsymbol{e}'\,E_{nr}E_{qs}(E_rE_s-1)+E_sE_{qs}(\boldsymbol{e},\boldsymbol{e}',\boldsymbol{p},\boldsymbol{k})-$$
$$-E_rE_{qs}(\boldsymbol{e},\boldsymbol{e}',\boldsymbol{x},\boldsymbol{k})+E_sE_{nr}(\boldsymbol{e}',\boldsymbol{e},\boldsymbol{p},\boldsymbol{k}')-E_rE_{nr}(\boldsymbol{e}',\boldsymbol{e},\boldsymbol{x},\boldsymbol{k}')+$$
$$+(1+E_rE_s)(\boldsymbol{k},\boldsymbol{e},\boldsymbol{e}',\boldsymbol{k}')+(\boldsymbol{p},\boldsymbol{k},\boldsymbol{e},\boldsymbol{x},\boldsymbol{e}',\boldsymbol{k}').$$

Supposing V_0 to be a Coulomb potential $-Z\,\varepsilon/r$, we have

$$V=-Z\,\varepsilon^2/r \text{ and} \tag{43}$$

$$W(\boldsymbol{g})=-4\pi Z\,\varepsilon^2/\boldsymbol{g}^2. \tag{44}$$

We now expand (22) to the second order of k, using (39), (40), (43) and (44). The evaluation of these terms is laborious but mathematically uncomplicated. In this way, we may get a correct first term in the non-relativistic expansion of the scattering amplitude. We hope to set forth results of the computation itself in a later communication. Kemmers[1] estimation of the amplitude is probably of the correct order of magnitude.

The author is very grateful to Professor Ivar Waller for suggesting the present problem and for many valuable discussions regarding it.

---

[1] *Loc. cit.* p. 182.

Tryckt den 28 februari 1953

Uppsala 1953. Almqvist & Wiksells Boktryckeri AB

ARKIV FÖR FYSIK Band 6 nr 28

Communicated 14 May 1952 by AXEL E. LINDH and HARALD NORINDER

Mobility spectra of ions formed by positive corona discharge

By REINHARDS SIKSNA

With 8 figures in the text

1. Introduction

Results of the measurements of ions formed in a room by positive wire corona, using the periodical alternation of chosen adjusted limit mobilities k_* of an ISRAËL large-ion counter [1], were employed to determine the *characteristics* (curves of the number of caught ions n with respect to $1/k_*$). The mode of the determination of the characteristics was the same as that used earlier to investigate the ions formed by negative wire corona in a similar experimental arrangement [2]. The number of positive ions formed by positive corona and caught at the same k_* was lower than that formed by negative corona, and the general shape was also of another feature. An increase of the characteristics was present at higher k_* (lower $1/k_*$) similarly as for negative ions but in a higher degree. This increase was caused by the scanning of the ions with the upper limiting mobility ak_* of the counter, as shown in [2]. Ions with corresponding mobilities (small-ions) must be present in a greater amount here. Further properties of the obtained characteristics may be found from the curves shown in [1]. Mobility spectra of ions formed by positive corona calculated from the obtained characteristics will be considered in this article. The mode of their calculation is the same as that used for determining the mobility spectra of negative corona ions [2]. Besides the mobility spectra obtained by scanning of the ions with the ISRAËL counter in the regions of larger ions, results of measurements with a small-ion counter will also be considered.

2. Mobility spectra of ions formed in a room by positive wire corona

Some examples of the obtained mobility spectra are shown in Fig. 1 and 2, for ions formed when a sufficiently high positive potential was suddenly switched on to the corona wire (from Fig. 1 shown in [1]), and in Fig. 3 and 4 at a gradual increase of the applied positive potential (from Fig. 4 in [1]). Generally the shapes are of a similar feature.

During the corona discharge:

(1) A wing of a band of large and large-intermediate ions is present. A band between mobilities of $(6–14) \times 10^{-4}$ is superposed on the wing of the larger band, partially at the beginning (Fig. 1 and 3).

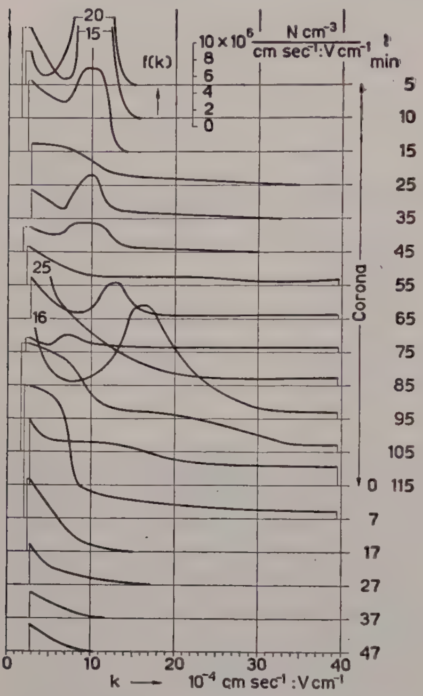

Fig. 1. Mobility spectra of ions formed in a room by positive wire corona when a sufficiently high positive potential (of c. 15 kV) was suddenly switched on to the corona wire. Region of large and large-intermediate ions.

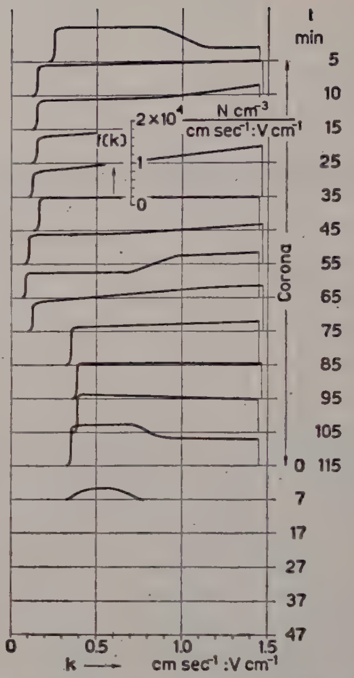

Fig. 2. Mobility spectra of ions formed in a room by positive wire corona when a sufficiently high positive potential (of c. 15 kV) was suddenly switched on to the corona wire. Region of small-intermediate and small-ions.

(2) A wing of an intensive band is present in the region of small-ions from $k = 0.2 \div 0.3$ cm sec^{-1}: V cm^{-1} (Fig. 2 and 4).

(3) The appearance of a smaller but well defined band may be stated in the region of smaller intermediate ions with $k = (0.04—0.1)$ during the development of the processes. These bands are not shown in all the figures.

After switching off the corona:

(1) The small-ions were not present here in amounts sufficient for measurements.

(2) The large-intermediate and large-ions were displaced to lower mobilities in the course of the transformation processes. Only a wing of these ions was established by the used adjusted mobilities.

3. The mobility band of the present small-ions

As it has been mentioned repeatedly [1], [2], it is evident that a more correct determination of the form of the distribution function of the small-ions with respect to the mobilities could not be expected by scanning the ions with the upper limit mobility of a large-ion counter. Therefore the intention was to determine the ions in the mentioned region of mobility of small-ions with a more appropriate apparatus. Some results of such measurements will be presented here.

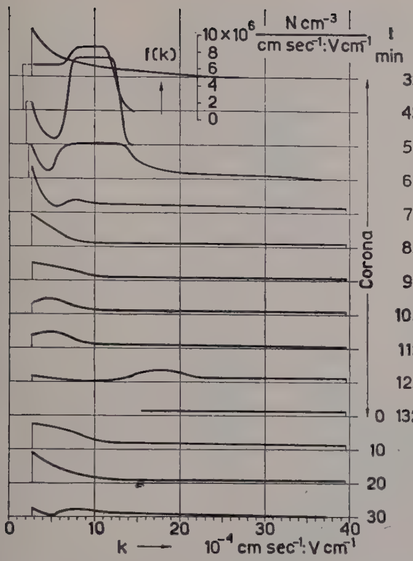

Fig. 3. Mobility spectra of ions formed in a room by positive wire corona at a gradual increase of the applied positive potential. Region of large and large-intermediate ions.

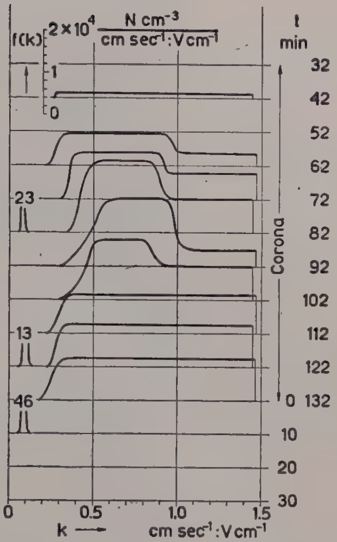

Fig. 4. Mobility spectra of ions formed in a room by positive wire corona at a gradual increase of the applied positive potential. Region of small-intermediate and small-ions.

3.1. The used small-ion counter for determination of the characteristics. For the mentioned purpose an ion-counter for small-ions was built at the Institute by using a Weger aspiration condenser [3]. The arrangement of this small-ion counter with its auxiliary devices is shown in Fig. 5. The small-ion counter was connected with the employed suction box instead of one of the Ebert counters, which had been used during the earlier measurements. Characteristics of the present small-ions were obtained with the small-ion counter by variation of the potential applied to the inner electrode of the Weger condenser at a constant air-flow through it. Because of the adsorption effect of the small-ions present in the counter and in the connection tubes, and because of some other transformations of the ions passing through the latter, it was not possible to use here the adjustment of the chosen limit mobilities of the condenser by varying the air-flow. The mentioned effects are of interest also from other points of view, and they will be considered at another place. One of the Ebert counters remained on the suction box, and it was used for carrying out comparisons with the new small-ion counter, and also for maintaining a sufficient air-flow through the suction box, because the aspiration through the new small-ion counter was too slow to replace the air of the suction box.

3.2. Obtained mobility bands of the small-ions formed in the test-room by the used corona wire. The height values of the obtained mobility bands were different dependent on the speed of the air-flow through the condenser and the Ebert aspirator (through the suction tubes and the suction box respectively), but the form of the bands remained comparatively characteristic. Some of the obtained mobility bands of small-ions are shown in Fig. 6. They start with a comparatively steep increase at c. 0.3–0.4 cm $\sec^{-1}$: V cm^{-1} (in good accordance with the starting mobility

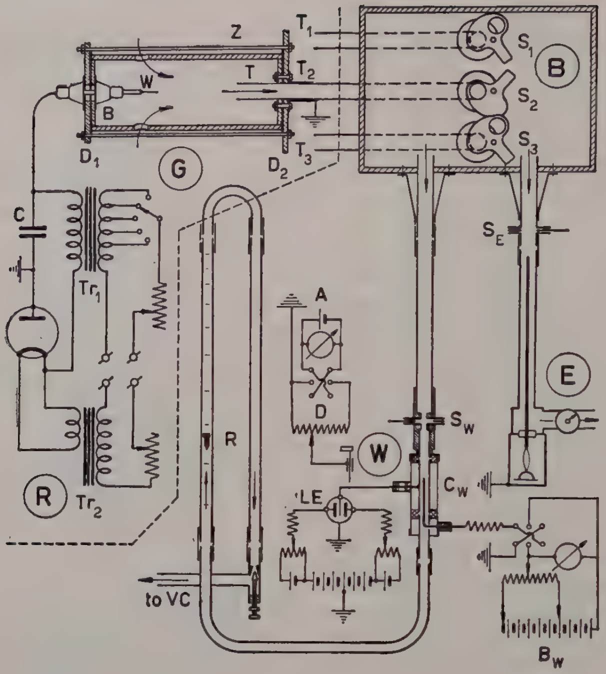

Fig. 5. Schematic diagram of the used arrangement of the small-ion counter and the small generator of corona ions. (*W*) small-ion counter with WEGER condenser C_W, S_W slide to the condenser, B_W battery of the condenser, *LE* LINDEMANN electrometer, *D* calibration device of the electrometer, *R* rotameter; (*E*) EBERT ion-counter, S_E slide to the EBERT counter; (*B*) suction box, S_1, S_2, S_3 slides of the suction tubes, T_1, T_2, T_3 suction tubes from the test-room; (*G*) generator of corona ions, *Z* bakelite cylinder, *B* bushing of the corona wire *W*; (*R*) rectifier, Tr_1 high-tension transformer, Tr_2 heating transformer.

established by scanning with the upper limit mobility of the large-ion counter). A maximum is reached at 0.4–0.5 cm $\sec^{-1}$: V cm^{-1}, and after that a slower decrease follows to the mobilities of 2–2.5 cm $\sec^{-1}$: V cm^{-1}.

3.3. A small generator of corona ions. As mentioned, some transformations in the test-room of the formed ions and during their passage through the suction device were indicated. Therefore it was attempted to diminish these transformations in order to catch fresher small-ions in the counter. For this purpose a special generator of corona ions was built by using the corona discharge of a short piece of wire. The construction of this ion generator is shown in Fig. 5. Against the ends of a bakelite tube of 15 cm diameter and of 38 cm length two bakelite disks were pressed with three bolts. Through the centre of one of the disks a small porcelain bushing was arranged. The corona wire, a 2–3 cm piece of a 0.05 mm thick kanthal wire, was fastened in this bushing. At the other disk a 33 mm brass connection tube was fixed. This tube was pulled outside the connection tube to the suction box. Two holes were made in the bakelite tube across the corona wire. Air was sucked through these openings into the generator. The device proved to be a useful generator of small-ions of one polarity. The concentration of the ions varied dependent on the air-flow through the generator. With an air-flow of 300 l/min through it the concentration of negative

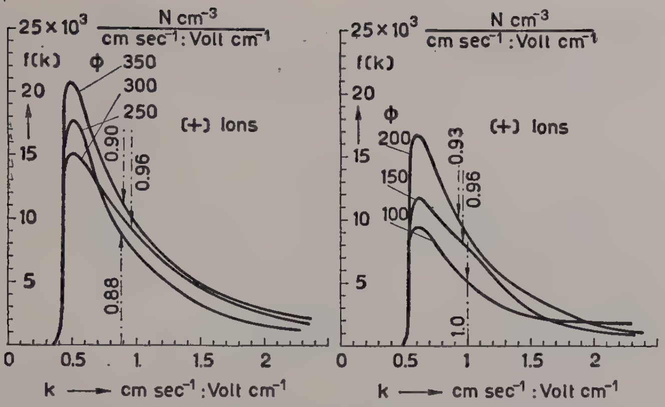

Fig. 6. Mobility bands of the positive small-ions formed in the test-room by the used corona wire. Φ air-flow through the counter in cm³ sec⁻¹.

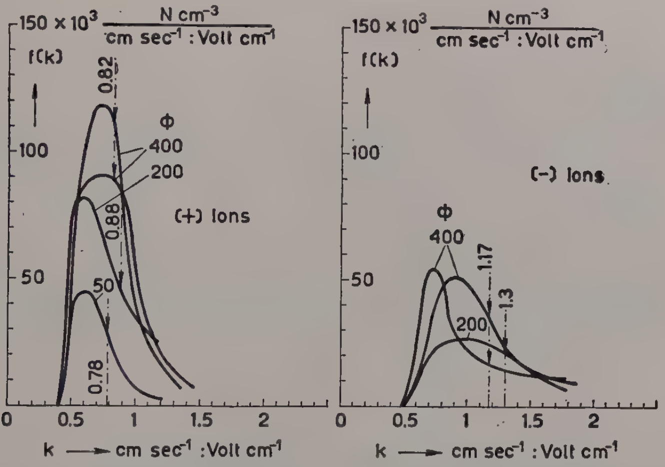

Fig. 7. Mobility bands of the small-ions formed by the corona generator. Φ air-flow through the counter in cm³ sec⁻¹.

ions was 80000 cm^{-3}, the concentration of positive ions was 120000 cm^{-3} at a corona potential of only 8 kV.

3.4. Mobility spectra of small-ions formed by the corona generator. The mobility spectra of small-ions formed in the corona generator and measured at different air-flow Φ through the condenser are shown in Fig. 7. In general, the shape of the bands is similar to that shown in Fig. 6, only, they do not tend to such great mobilities as there. Besides positive ions, negative ions measured under the same conditions are shown in Fig. 7. As may be seen, the total number of negative ions is lower than that of positive ions under the same conditions, and the shape of the bands is also somewhat changed. This difference of the bands of positive and negative ions is also shown in Fig. 8, where more careful measurements at a higher air-flow of 300 l/min through the suction box were used for the calculation.

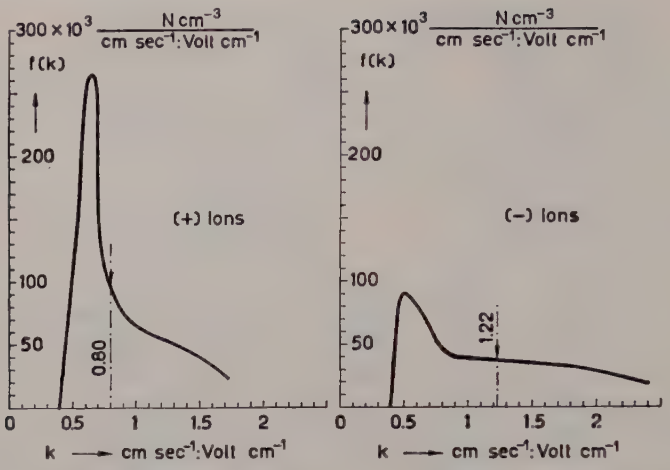

Fig. 8. Mobility bands of the small-ions formed by the corona generator. Air-flow $\Phi = 300$ l/min through the suction box.

3.5. Characteristic mobilities of the bands. Accepting a continual distribution of the ions over an interval of mobilities, we can introduce some mobilities by which the distribution band can be defined. Two mobilities k_1 and k_2 define the range of the interval over which the band is distributed. We will call these mobilities *range mobilities.* Unfortunately any determination of the range mobilities could not be carried out sufficiently correctly, partially because difficulties arose with the upper k_2 due to some properties of the characteristic at higher k_* (lower $1/k_*$).

By using the definitions of statistics we can distinguish two other mobilities characteristic of a distribution band: *the mode mobility* $k(mode)$ at which $f(k) = \max.$, and *the median mobility* $k(median)$ defined by the equations

$$k_1 < k\,(median) < k_2,$$

$$\int_{k_1}^{k\,(med)} f(k)\,dk = \int_{k\,(med)}^{k_2} f(k)\,dk = \frac{1}{2}\int_{k_1}^{k_2} f(k)\,dk = \frac{1}{2}N\Big]_{k_1}^{k_2}.$$

It seems that the median mobility may be very good to characterize the band. The median mobility can be determined very simply from $N = N(k_*)$ curves, and, as it will be shown, the values of $k(med)$ are in very good accordance with the values of the mobilities which are usually attributed to the small-ions in the atmospheric air. The mode mobility may be used as the second characteristic mobility of the band, and it seems that it characterizes some processes of the inner transformation of the mobilities in a band.

Additionally a third characteristic mobility could be named, the *arithmetic mean mobility* k_a defined by the equation

$$k_a = \frac{\int_{k_1}^{k_2} k\,f(k)\,dk}{\int_{k_1}^{k_2} f(k)\,dk}.$$

Preliminarily we shall not use this last mobility. The quoted characteristic mobilities of the band of small-ions formed by corona discharge and shown in Figs. 6, 7 and 8 are collected in Table 1. The accordance of the values of the median mobilities from Figs. 7 and 8 is surprising.

Table 1

Characteristic mobilities (in cm sec^{-1}:Volts cm^{-1}) of the bands of distribution of small-ions formed by corona discharge

	Range mobilities		k *median*	k *mode*	
	k_1	k_2			
(+) Ions formed by corona wire in the test-room	0.4	~3.0	0.90	0.5	Fig. 6
			0.88		
			0.96		
	0.5	~3.0	0.93	0.6	
			0.96		
			1.00		
(+) Ions formed by the generator of corona ions	0.4	~2.0	0.82	0.74	Fig. 7
			0.82	0.74	
			0.88	0.6	
			0.78	0.6	
	0.4	~2.0	0.80	0.65	Fig. 8
(−) Ions formed by the generator of corona ions	0.45	~3.0	1.17	0.9	Fig. 7
			1.17	0.74	
			1.30	0.92	
	0.4	~3.0	1.22	0.5	Fig. 8

The higher values of the same mobility from Fig. 6 may be explained by neglecting some corrections, which have been regarded, when the bands shown in Figs. 7 and 8 were calculated.

ACKNOWLEDGEMENTS

The author is grateful to the Director of the Institute of High Tension Research of the University of Uppsala, Professor H. NORINDER, for providing him with facilities to carry out this work and for his interest in its progress. The Swedish Natural Science Research Council deserves to receive thanks for placing means at the disposal of the Institute to perform this investigation. Mr A. METNIEKS, who assisted in the measurements and calculations, deserves appreciation.

SUMMARY

The mobility regions of the ions formed by positive corona discharge were fixed by the determination of the mobility spectra. The bands of small-ions, formed in the prevailing quantity by corona, were determined with characteristics obtained with a small-ion counter. Besides ions formed by positive corona wire in a larger test-room, bands of small-ions of both polarities formed with a generator of corona ions were investigated with the same method. The difference between the obtained mobility spectra and the difference between the number of positive and negative

ions formed by corona under the same conditions show that the mechanism of the production and transformation of corona ions and maybe the ions themselves must also be different for positive and negative polarity.

Institutet för högspänningsforskning vid Uppsala Universitet, May 1952.

REFERENCES

[1] NORINDER, H. and SIKSNA, R. Ions formed in a room by positive wire corona. *Ark. Fys.* 6, Nr 14, 127—140, 1952.
[2] SIKSNA, R. Mobility spectra of ions formed in a room by negative corona discharge. *Ark. Fys.* 5, Nr 26, 545—564, 1952.
[3] WEGER, N. Eine Verbesserung der Methodik der Kleinionen-Zählung. *Phys. Z.* *36*, 15–20, 1935.

Tryckt den 3 mars 1953

Uppsala 1953. Almqvist & Wiksells Boktryckeri AB

ARKIV FÖR FYSIK Band 6 nr 29

Communicated 4 June 1952 by Bertil Lindblad and Erik Hulthén

A phase contrast refractometer with high accuracy for gases and liquids

By Erik Ingelstam

With 19 figures in the text

1. Introduction and summary

As part of a programme of our laboratory for the study of phase contrast methods and their application to quantitative measurements, a refractometer for liquids and gases has been developed. This refractometer is useful for the determination of refractive index relatively, and, by inserting end gauges in the cell in order to get a well-defined and precise cell thickness, also absolutely. Preliminary papers dealing with this and similar methods have been published previously [1, 2, 3]. When working with the highest precision possible with the instrument, the accuracy obtained with a photoelectric device is about 1/1000 of a wavelength, which, for the 10 mm thick cells so far used, corresponds to an accuracy of refractive index of $0.04 \cdot 10^{-6}$. The measuring region extends from $0.05 \cdot 10^{-6}$ to $1500 \cdot 10^{-6}$. This relatively large range is achieved by combining the instrument with a Young double slit arrangement, which provides a coarse scale for the whole wavelengths included in the optical path difference measured. The theory has been worked out, and examples of measurements on oxygen are given. In many applications in which the utmost precision is not required very simple apparatus can be used. If only visual measurements are made, the accuracy is about 1/5 of that given above. A useful application is the study of streaming liquids and gases, whose changes in refractive index may be recorded automatically. An advantage is that only very small amounts of the liquid or gas under examination are necessary.

2. General principle of the method. Notation

In order to make phase contrast arrangements quantitative, it seems to the writer essential to stick to the one-dimensional phase variation case, which in this application means working with rectangular apertures and slits. This is not merely for the sake of the much simpler mathematical treatment of the diffraction geometry — as is well known, the analysis of the circular cases leads to such great mathematical difficulties that even approximate solutions are too complicated for practical use — but the one-dimensional case also makes it possible to work with photoelectric and other analyzing devices which are simpler and more accurate than in any other case.

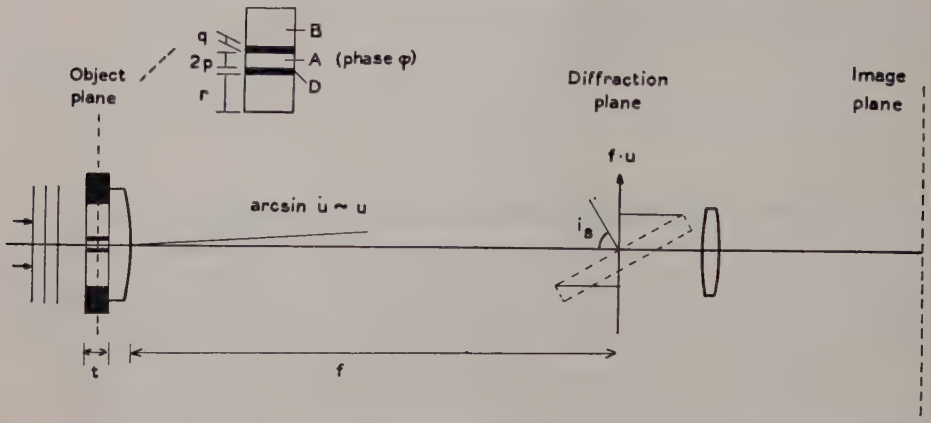

Fig. 1. The optical parts of the present method necessary for the development of the theory.

The fluid the refractive index of which is to be determined (n_1) fills a central part, A, of an aperture field as shown in Fig. 1, and the fluid acting as reference (refractive index n_2) fills the rest of the field, marked B, the regions A and B being separated by two walls D which are opaque. The technical construction of the cell providing this aperture will be described later in connection with Fig. 8, but at this stage it is sufficient to state that a plane and monochromatic linearly polarized wave traverses the A and B apertures, the geometric path in the fluids being t. On account of the difference in refractive index, the wave through A will have an advance in phase with respect to B, of

$$\varphi = \frac{2\pi}{\lambda} \cdot t(n_2 - n_1). \tag{1}$$

The ratio $\varphi/2\pi$ may be a fraction of unity, i.e. of the period, or may represent many periods, being limited by the number of wavelengths over which the monochromatic light will interfere with the required precision.

The diffraction pattern corresponding to this plane wave lies in the image plane of the entrance slit, which, as a consequence of the assumption of a plane wave-front, will be taken as being infinitely narrow. The desired phase contrast is achieved by the usual method of inserting a phase plate in this plane, the plate consisting of a central area introducing a phase shift ψ (expressed in radians) of the light falling onto it. The type of phase plate always used here is the phase mirror [4] orientated at the Brewster's angle i_B, either of the *a* type, where the central zone is a glass surface and the peripheral zones are of metal coated on the glass, or of the *b* type, having the inverse pattern [5]. The dimensions of the zones will always be given as the projections onto the plane perpendicular to the ray, and are thus reduced from those on the mirror in the proportion $\cos i_B$.

Let us introduce the following notation:

$2p$ = the width of the A aperture of the cell in Fig. 1.
q = the width of either of the opaque walls D.
r = the width of either of the B apertures.

f = the focal length of the lens refracting the plane wave-front to its diffraction image (one of the two lenses forming the cell as shown in Figs. 7 and 8).

u = the sine of the diffracting angle from the aperture, the linear ordinates on the phase plate being for the sake of simplicity expressed in this measure by dividing them by f.

k = the ratio $2\pi/\lambda$.

$2c$ = the width of the central zone of the phase plate.

$2C$ = the width of the whole phase plate.

2γ = an angular measure corresponding to $2c$ related to the diffraction geometry of the object plane as $2\gamma = 2ku(p+q+r) = k(p+q+r)\cdot 2c/f$.

2Γ = the analogous measure corresponding to $2C$.

ψ = the phase advance introduced by the central zone of the phase plate, this being obviously

$$\begin{cases} \text{for the } a \text{ mirror:} \quad \psi = 2\pi\left(1 - \dfrac{2(e\cos i_B - \delta)}{\lambda}\right) \\[2ex] \text{for the } b \text{ mirror:} \quad \psi = \dfrac{4\pi(e\cos i_B - \delta)}{\lambda} \end{cases} \tag{2}$$

e = the thickness of the metal layer of the phase mirror.

δ = the difference, expressed as half path difference, between the phase change at reflection against glass ($\lambda/4$) and against the metal, for the polarization in question.

g = the relative amplitude reflection factor for the central zone of the phase mirror under the existing polarization state, i.e. the ratio between the emerging amplitudes (central zone : peripheral zone) when incoming amplitudes are equal. The g factors are less than unity for the a mirrors and larger than unity for the b mirrors.

G = the magnification of the lens M imaging the object plane onto the image plane, its linear aperture being larger than $2C$.

A = amplitudes.

The general principle of this method is that the φ values, and thus by Eq. (1) the differences in refractive index, are determined from intensity measurements in the phase contrast image, and especially by measurement of the ratio of the intensities in the image areas corresponding to A and B. These measurements can be made in many different ways, depending on the precision and information required.

3. Extended theory of phase contrast for the refractometer

3.1. The vector representation of phase contrast

The first approximation theory of phase contrast, first developed by ZERNIKE in his classical work [8] and often used to estimate the contrasts to be expected in microscopy, assumes that the field as a whole consists of a plane wave front, except for an infinitely narrow area, whose wave front is advanced by an amount φ. A geometric treatment (see Fig. 2) is preferred here to algebraic calculation. The amplitude of the phase advanced area is represented in the complex plane by OA, the total field being represented by OB. Because of the assumption that the area corresponding to OA is extremely narrow, the width $2c$ of the central zone of the phase plate approximates to zero compared with the diffraction image of this area, which means that it falls entirely in the peripheral zone. The central zone is even so assumed large enough to include the whole diffraction pattern of the entire field. Further,

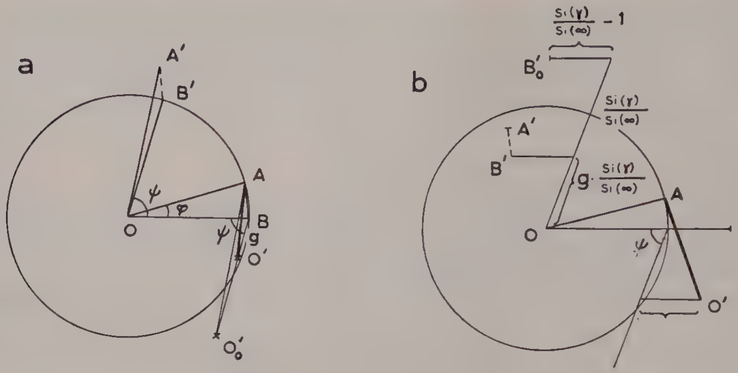

Fig. 2. Vector diagrams, a) of the first approximation theory, b) taking into account the finite area of central zone 2γ.

Γ approximates to infinity. The vector OB is obviously moved to the position OB′ by the central zone of the phase plate. The vector difference BA, which, previously, starting from B, ended at A, and indicated that OA and OB had the same length, should now be added to OB′, retaining its direction, and so the new vector corresponding to the area with phase advance ψ, is OA′. As it has a larger amplitude than OA, its corresponding image field stands out in "positive" phase contrast, according to ZERNIKE's notation. In this representation the origin of the vectors O has not been moved, but it is more convenient for the interpretation of the different parts of the images to make a transposition so as to retain the points A and B in their original positions on the circle, by moving the vector OB′ to the position O_0'B. The triangle OB′A′ is now shifted to O_0'BA, and the angle ψ enters as shown in the figure. The introduction of the factor g moves the new vector origin to O′, obviously in this case increasing the amplitude ratio O′A : O′B over the original O_0'A : O_0'B, a fact often made use of in microscopy.

3.2. Continuous variation of φ in the case of the refractometer field

The assumptions for Fig. 2a would be fulfilled for the field geometry of Fig. 1 only if $p \ll r$. In that case, the continuous increase of φ as would, according to Eq. (1), correspond to the decrease of n_1 when the gas pressure in the A part of the cell is continuously lowered, should mean that the O′A vector stretches and contracts during a period, while O′B, representing the amplitude of the reference gas field, is constant. The intensity from the walls D would correspond to a constant amplitude of an amount of O′O (not drawn in Fig. 2a). It should be added that O′ in our application is most often outside the circle, and the following figures are drawn accordingly.

A point of some importance in the construction of a phase contrast refractometer is the choice of the dimensions p, q and r, and the related γ and Γ. The first two must be considerably smaller than r, but for technical reasons, and for some methods of measurement, they must not be too narrow. On the other hand, r must be limited, in particular because of spherical aberration. Thus p is a certain fraction of r. The first approximation theory involving these geometrical facts is shown in Fig. 3a. Here OA and OB still represent the vectors corresponding to the zones A and B. The O′B vector is constructed as in Fig. 2 when $\varphi = 0$. However, when φ has another value

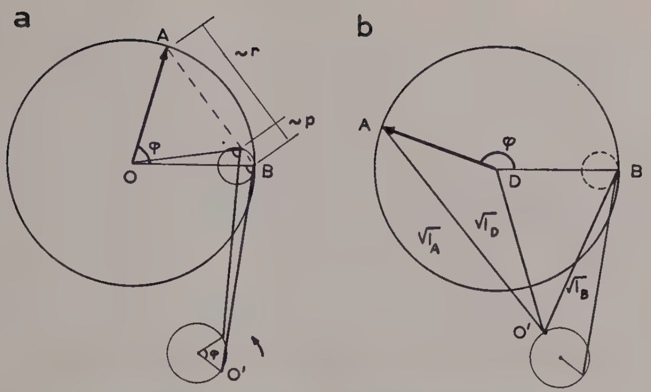

Fig. 3. a) Vector diagram showing the effect of the finite value of the ratio p/r, b) Construction of the amplitude vectors corresponding to areas A, B, and D for a given φ.

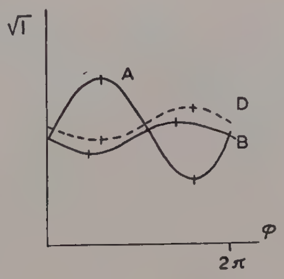

Fig. 4. Amplitude curves from the construction in Fig. 3b.

this vector must go out from the end of an average vector between A and B, weighted according to the widths of their respective zones, as constructed in the figure. During the period, the O′ point, instead of being fixed, moves in a circle uniformly with OA, this circle having the radius $\frac{p}{r}\sqrt{1+g^2-2g\cos\psi}$, and its corresponding points rotated with respect to the main circle an angle $\tan^{-1}[g\sin\psi/(g\cos\psi-1)]$. In the construction Fig. 3b, the amplitude of the A zone, denoting the square root of its intensity, varies in practically the same manner as in the case of Fig. 2, but the intensities of the zone B and the walls D also have a slight variation. Calculation gives amplitude variation curves as shown in Fig. 4. These curves are of special interest for their general forms and the approximate positions of the intersection points.

3.3. Diffraction calculation for the refractometer field

In order to take the theory further, the diffraction patterns corresponding to the object field must be calculated, and their interception by the phase plate investigated. Similar calculations have been necessary in other optical problems. Lord Rayleigh [6] treated the theory of Foucault's knife edge test, indicating the main points of the mathematics of this one-dimensional field, and Duffieux et al. [7] have made use of the same types of functions in order to corrolate their observations on diffractions from rectangular apertures. For phase contrast, ZERNIKE [8], FRANÇON [9], and BENNETT et al. [10], have made diffraction calculations, but they were specifically interested in microscopy, and made corresponding assumptions. WOLTER [11] and SCHUSTER [12] have, although with the same aim of microscopic interpretation, treated the one-dimensional case of one single phase-differing strip with special assumptions more in detail. In the present investigation it was necessary to make an exact calculation of the diffraction figure for the geometry of Fig. 1, and a semi-quantitative treatment of the mathematical procedure leading from the diffraction figure to the final phase contrast image.

The amplitudes in the diffraction figure from a rectangular opening filled with monochromatic light of the real or complex amplitude of $F(x)$ with variation only in the x direction, may be found by integration of the function

$$F(x)\,e^{i\left(-\omega t+2\pi\frac{x u}{\lambda}\right)}\,dx=F(x)\,e^{i(-\omega t+kux)}\,dx.$$

We consider that in this case $F(x)$ has a constant modulus for A and B, which is normalized to $\varrho/2$ for unit area (no amplitude contrast), and zero for the wall and surrounding parts; and further that the argument of $F(x)$ is zero for the B region and φ for the A region. Thus $F(x)$ is either $\varrho/2$ or $\varrho e^{i\varphi}/2$. Omitting the periodic part and incorporating φ, if present, in the angle function due to the diffraction path differences, the integrand can be written

$$(\varrho/2)\cos kux\,dx, \quad \text{or} \quad (\varrho/2)\cos(kux+\varphi)\,dx.$$

For one rectangular opening with the width $2a$, the integration leads to the well-known diffraction figure

$$g(u)=\frac{\varrho}{2}\int_{-a}^{+a}\cos kux\,dx=\varrho\Big/_{\!0}^{+a}\frac{\sin kux}{ku}=a\varrho\frac{\sin kua}{kua} \tag{3}$$

which is shown in Fig. 5. For the special geometry of Fig. 1 the solution is:

$$g(u)=\frac{\varrho}{2}\int_{-p}^{p}\cos(kux+\varphi)\,dx+2\frac{\varrho}{2}\int_{p+q}^{p+q+r}\cos kux\,dx=$$

$$=\varrho\frac{\sin kup\cdot\cos\varphi}{ku}+\varrho\frac{\sin ku(p+q+r)-\sin ku(p+q)}{ku}. \tag{4}$$

As p and q are smaller than r, it is of advantage to group together the terms which include them only; further, we prefer the complex form:

$$g(u)=\varrho\frac{p}{kup}[\sin kup\cdot e^{i\varphi}-\sin ku(p+q)]+\varrho\frac{p+r}{ku(p+r)}\sin ku(p+q+r). \tag{5}$$

Here the first term refers to the part of the diffraction pattern which is due to the narrow portions, and the second term represents the diffraction fringes due to the whole aperture.

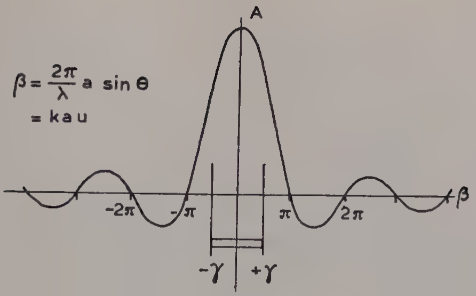

Fig. 5. Airy curve of amplitudes for a single slit, or for either term of Eq. (4).

After having given the values for the experimental case, we will come back to the interpretation of these diffraction amplitude equations.

Passing over from the linear units $f \cdot u$ to the angular units $\beta = ku(p+q+r)$, we now see that the diffraction figure is cut symmetrically by the phase plate in $(-\gamma, +\gamma)$. The periodic factor being the same for all terms in Eq. (4) and (5), the amplitudes for an entire zone of u can be found by direct integration, and the corresponding intensities by integration of the corresponding squares.

In order to find the corrections to the first approximation theory, the resulting amplitudes are calculated, assuming a distribution following the law $\sin\beta/\beta$, for the light falling within the central zone, which shifts the phase by ψ, and within the peripheral zone, which introduces no shift. The amplitudes are, accordingly,

in the central zone, and in the peripheral zone,

$$A_c = \int_0^{\gamma} \frac{\sin\beta}{\beta} d\beta = \mathrm{Si}(\gamma), \qquad A_p = \int_{\gamma}^{\Gamma(=\infty)} \frac{\sin\beta}{\beta} d\beta = \mathrm{Si}(\infty) - \mathrm{Si}(\gamma). \tag{6}$$

As will be shown in the following, Γ approximates to infinity for all the cases dealt with here, and for the sake of simplicity we will already assume this.

In practice, γ is dimensioned so as to correspond to a few turns of β, i.e. the angle in the last term of Eq. (5), so as to include the major part of its light. This angular γ value corresponding to the total B aperture can for easier remembrance be denoted $\gamma_B = k(p+q+r)u$. If all the light belonging to this aperture were incorporated, as assumed in the first approximation theory, A_c would be Si (∞), which corresponds to the unit radius of the circle of Fig. 2a. This should instead be Si (γ_B), and thus $\mathrm{Si}(\gamma_B)/\mathrm{Si}(\infty)$ should be substituted for the unit radius. The points B and B′ of Fig. 1 should therefore be displaced in the following way. Its radius is stretched in the said ratio, if $\mathrm{Si}(\gamma_B)$ is supposed $> \mathrm{Si}(\infty)$, as in Fig. 2b. The peripheral part A_p of the amplitude, normalized to $[1 - \mathrm{Si}(\gamma_B)/\mathrm{Si}(\infty)]$, and thus negative, is not shifted in phase, and this component should retain its horizontal direction on constructing the B_0' point. Considering that the phase-shifted part, $\mathrm{Si}(\gamma_B)/\mathrm{Si}(\infty)$, is also reduced in the ratio g, the final position of the point B′ is that indicated. By the same procedure as with Fig. 2a, we find that the final O′ point, (AO′ being vectorially equal to A′O) should lie displaced to a new position which has the rectangular coordinates

$$\left[(1-g\cos\psi)\frac{\mathrm{Si}\,(\gamma_B)}{\mathrm{Si}\,(\infty)};\quad -g\sin\psi\frac{\mathrm{Si}\,(\gamma_B)}{\mathrm{Si}\,(\infty)}\right].$$

We find that when γ_B is put $=\infty$, as assumed in the first-approximation theory, O′ is in the position shown in Fig. 2a, and when $\gamma_B=0$, there being then no central zone or phase contrast, its position is the centre O.

For the object zone differing in phase, which is represented by point A in Fig. 2a and corresponds to the first term of the diffraction amplitude in Eq. (5), the application of Eq. (6) means that, as its major part falls in the peripheral zone, $\gamma_A=p\gamma/(p+q+r)$ is only a small part of the period, the expression for the unit radius, $[\mathrm{Si}(\infty)-\mathrm{Si}(\gamma_A)]/\mathrm{Si}(\infty)=1-\mathrm{Si}(\gamma_A)/\mathrm{Si}(\infty)$, is close to unity. If different from unity, it means a change in circle radius which also affects the relative position of O′ with respect to the A points.

3.4. Diffraction effects in the phase contrast image

The preceding treatment is of use when dimensioning p, q, r, c and C in respect to each other, and the aim is to suppress the corrections as far as necessary for the measuring technique chosen. The displacements of the O′ point do not only change the resulting amplitudes. A more important point is that this geometrical effect influences the distribution of intensity inside the zones of the phase contrast image, giving rise to a pattern similar to diffraction fringes. As these could be serious for quantitative work of the sort considered here, their main characteristics will be examined.

The intensity distribution of the phase contrast image is calculated by integration from the diffraction pattern equation (5) multiplied with the wave propagation factor, taking the phase shift ψ and the factor g within the central zone into account. If, in (5), the variable u is changed to $\beta=k\,(p+q+r)\,u$, its both terms are written in concentration

$$g\,(\beta)=\varrho\,p\cdot G_A\left(\frac{p}{p+q+r}\beta;\varphi\right)+\varrho\,(p+r)\cdot G_B\left(\frac{p+r}{p+q+r}\beta\right) \qquad (5')$$

Denoting the image coordinate $x'=f'\cdot v$ where f' is the focal length of lens M and v the sine of the angle (corresponding to u), the image amplitude function is $[k'=f/(p+q+r)]$

$$F'\,(v)=g\,\varrho\,p\int_0^{\gamma}G_A\,(\beta,\varphi)\,e^{i\psi}\,e^{-ik'v\beta}\,d\,\beta+g\,\varrho\,(p+r)\int_0^{\gamma}G_B\,(\beta)\,e^{i\psi}\,e^{-ik'v\beta}\,d\,\beta+$$
$$+\varrho\,p\int_{\gamma}^{\Gamma=\infty}G_A\,(\beta,\varphi)\,e^{-ik'v\beta}\,d\,\beta+\varrho\,(p+r)\int_{\gamma}^{\Gamma=\infty}G_B\,(\beta)\,e^{-ik'v\beta}\,d\,\beta \qquad (7)$$

Here, the fourth and first terms are small if dimensions properly chosen, and correspond to the corrections dealt with in 3.3.

The calculations involved in (7) would be tedious, even when faciliated by the use of a mechanical Fourier analyzer. They are not either necessary as in this case a semi-quantitative procedure gives the necessary information. The two effects to be considered are the following.

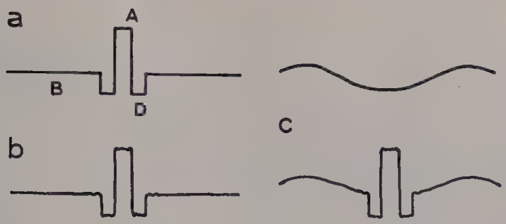

Fig. 6. Schematic intensity distribution curves for certain values of φ and $0'$, a) according to the first approximation theory, b) modification by diffraction (3.4 a), c) modification by diffraction (3.4 b), maxima mentioned in the text spaced approximately as for the present apparatus.

a) The approximate realization of condition $\Gamma = \infty$ gives rise to a type of diffraction ordinarily known in imagery. Let Fig. 6 a give the first-approximation distribution; then Fig. 6 b indicates the diffraction fringes causing the borders to be not quite sharp and the intensity in their vicinity to show a slight variation. The fringe system is the same as the Fresnel diffractions due to the total aperture $2\,C$, and the border effects rapidly decrease with increased C. There is no difficulty in dimensioning the phase mirror so as to make this effect negligible. Cf. still 6.2.

b) The finite width of the central zone of the phase mirror introduces a non-uniform illumination of the field. If γ is appropriately dimensioned with respect to the B aperture as indicated, it is the cut-off of the central part according to the first term of Eq. (7) which is the most important. This effect is well known in phase microscopy, was pointed out by ZERNIKE and recently treated by WOLTER [11]. In our geometry, where γ is small, the deviation from uniform illumination in the B field being approximately equivalent to the diffraction in the image plane which would be due to a single rectangular zone of linear width $2\,c$. The intensity distribution is modified as shown in Fig. 6 c. The maxima or minima, here always brought to fall far from the A and D regions, are spaced as given from $2\,c$ and the distances. Their relative intensity, obtained after amplitude additions, is a function of g and φ, or, more closely, of the O′A vector length for given p, q and r, but is approximately proportional to p for small values when varying this width, according to the function $\mathrm{Si}\,(p/p+q+r)\,\beta$. This simple treatment gives the same result as the calculation (cf. Ref. [11] Fig. 10 for small $b \cdot \gamma_i$ in the special case dealt with there), and has been checked experimentally by the writer.

The maxima shown in Fig. 6 c or their vicinity represent the best zone of photoelectric measurement on the B field, a fact made use of in the experimental realization.

3.5. Influence of lack of parallelism, spherical aberration, and optical imperfections

There is no advantage in extending the theories given under 3.3 and 3.4 in a more elaborate mathematical manner, as there are other effects of the same order of magnitude as the approximations involved in the present calculations. The assumed parallelism of the light wave traversing the cell is limited by the finite width of the slit, which cannot be too narrow if the intensity is to be adequate. A finite width modifies the diffraction figure of Eq. (4), which is for the narrow slit, since the rectangular integral should really be extended over the whole slit width. It is however of little importance if this is kept smaller than the $(p+q+r)$ fringe spacing. Further, the

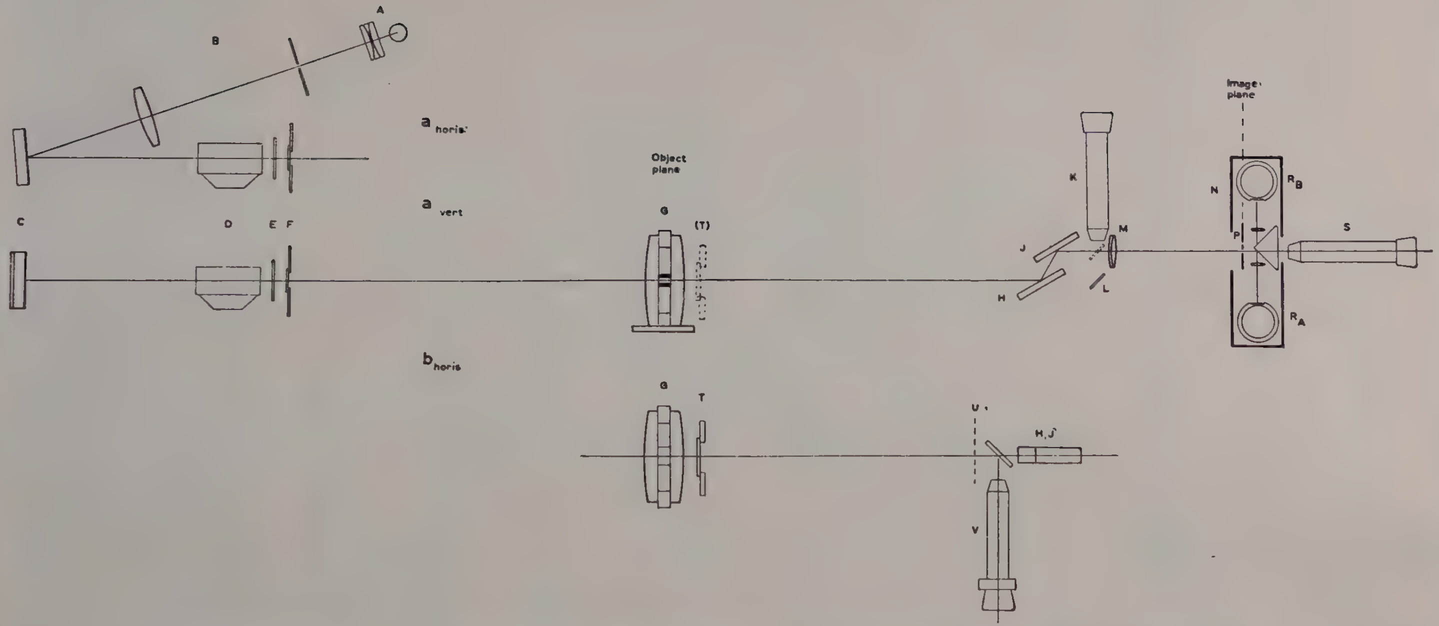

Fig. 7. a) Main parts of the phase contrast refractometer, straight type, for transmission. Not to scale. A Spectral lamp with condenser, B Collimation device, focused in the vicinity of F, C Plane grating acting as monochromator, D Beam turner unit consisting of three mirrors, set to turn the slit image through 90°, from vertical to horizontal, E Polaroid plate, F Entrance slit holder, G Cell for gases and liquids, the outer walls consisting of lenses imaging entrance slit on phase mirror H (diffraction plane), H Phase mirror, J Auxiliary mirror, K Microscope for adjusting slit image in the central zone of phase mirror H, L Mirror used in the upper position for the adjustment just mentioned, M Lens imaging cell ("object plane") on image plane at P, N Receiver unit, P Plate passing the light from two rectangular-shaped zones, R_A R_B Photomultiplier tubes, each receiving the light flux from a P zone imaged on a diffusing screen in front of it, S Microscope for visual observation or measurement of phase contrast image; b) Additional double-slit system for counting whole periods. T Double slit holder, U Plane in which the diffraction fringes are observed, V Microscope with ocular micrometer.

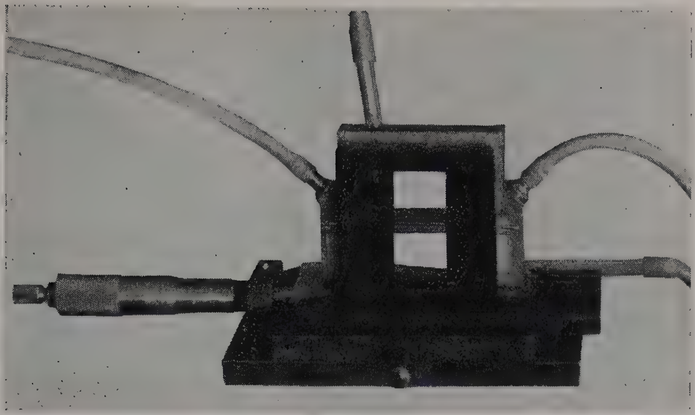

Fig. 8. Cell designed for gases, with external aperture screen.

lens system forming the cell introduces a spherical aberration. The relative aperture must be chosen so small as to keep it to below the 2γ width for the major part of the rays traversing the B field, but even so it often modifies the outer parts of the image of the B zone. Considering the accuracy corresponding to very small phase shifts of φ, which will interest us in this application, even zonal errors in the shapes of the lenses and imperfections in their polish will be of importance for the detailed intensity distribution of the phase contrast image. All these effects must be balanced so as to conform with the precision wanted for the measurements.

4. Practical construction of the apparatus

4.1. General outline

Fig. 7 is a schematic diagram of the apparatus showing the essential parts. Two somewhat different types have been built so far, differing in detail and in total length, the first having $f = 1\,700$ mm, the second having $f = 1\,000$ mm and being correspondingly shorter. The measurements reported here have been made with the first of these. The units have been set up on a rigid U-section girder, and are mounted either directly on base-plates (parts lettered G, H, J, K, L, and M), or on sliders which can be moved along V-section Zeiss bars screwed to the girder.

For routine measurements, it is convenient if all the parts behind G require as little adjustment as possible. In the latest type the entrance slit controls have been extended to a position near the microscope K. With these controls the slit can be displaced axially, for focusing, and also parallel to itself, for centering the image on the phase plate.

4.2. The cell

As emphasized in the first communication referring to apparatus of this type [1], it is essential in quantitative phase contrast work to introduce only the minimum of optical parts into the sensitive region of the system, i.e. near the object plane, as irregularities such as striae in the glass, zonal errors, and insufficiently smooth optical

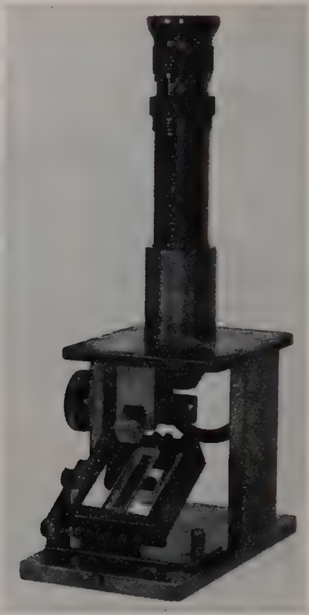

Fig. 9. Mirror unit containing parts H, J, K, L, and M of Fig. 7.

polish will cause unwanted phase shifts and thus intensity irregularities in the image, diminishing the accuracy of the method. The cell has, consequently, been constructed so that its walls are at the same time lenses. The material under test is contained in the plane-parallel space between two equal plano-convex lenses. Fig. 8 gives a photograph of the cell. The central part of the cell has been made of various materials, including brass, nickel-plated steel and hard-chromium-plated steel. The most critical part of the construction is to make the walls D between the A and B cells tight. Several successful methods have been used. If the cell is intended only for gases, it is easiest to use a cement, but if it is also to be used for liquids of different kinds, which dissolve the cement to a degree sufficient to spoil the great precision aimed at, it is better to rely on optical or capillary contact between the plane faces and the walls D, which are at least 1 mm thick.

Part A of the cell is about 20 mm long in the horizontal direction. Narrow channels of small volume lead to this part, the details of the construction depending on the material used. In the case where $t = 10$ mm, and $2\ p = 1.5$ mm, the volume of the cell is 0.3 ml not including the channels, and about 0.5 ml of liquid is required to fill the cell and channels.

The two symmetrical parts of part B of the cell are connected by channels passing round the ends of the A cell, the top and bottom portions being shaped so as to make it possible to empty out a liquid without removing the cell. For use with gases, the connections to cells A and B are made with rubber-gasketed nipples as shown in Fig. 8.

When in use, the part of the aperture inside the rectangular geometry shown in Fig. 1 is defined by a mask. It is often of advantage to define q (and at the same time p)

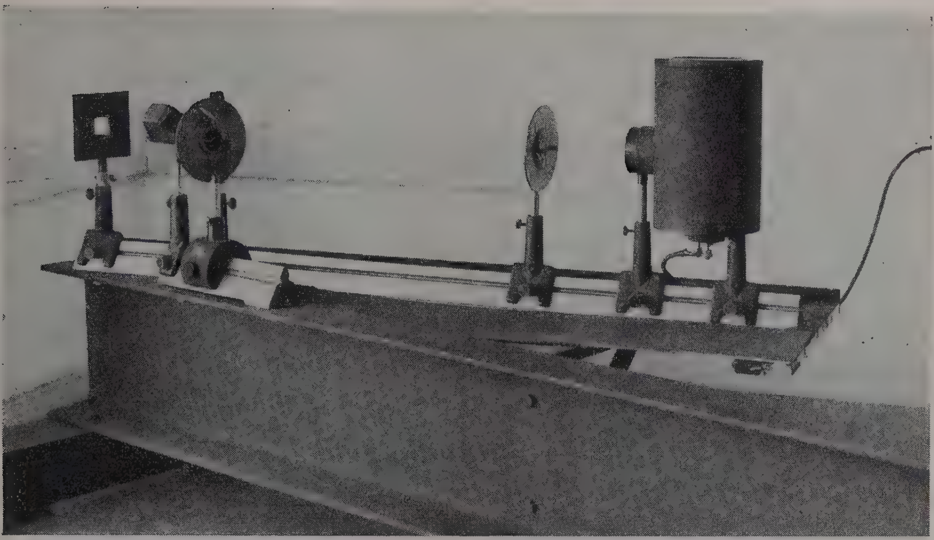

Fig. 10. Lamp and monochromator unit.

by masking carefully outside the cell with strips some tenths of a millimeter larger than the portions D defined by the cell itself, as such borders are smoother.

The lenses are manufactured by Svenska Aktiebolaget Gasaccumulator (AGA). They are cut from blocks of specially selected glass which is free from striae and irregularities, and are very carefully polished. Some difference between different lenses is however noticeable, due to zonal errors.

Appropriate adjustment devices are incorporated in the mounting of the cell system, as shown in Fig. 11.

4.3. Phase mirror system

Several different constructions have been used, the first of which, incorporating adjustment screws for turning and displacing, was of special value for the tests described below. The latest construction, shown in Fig. 9, is simpler, since all adjustment is transferred to the entrance slit. The mirrors H and J are rectangular in shape with a width considerably larger than necessary, i.e. the slit length, but the unit is provided with three interchangeable phase mirrors H_1, H_2, and H_3. Either of them can be placed in the central position by means of the slide, which is rigidly constructed in order not to disturb the calibration even if a mirror is changed (see 5.4). The microscope K, which is used to centre the slit image in H, is fixed, but the tilted mirror L may be moved downwards out of the optical path when it is not required. The lens M is part of this system.

4.4. Lamp, monochromator and entrance slit

A mercury lamp, BTH 250, has been used as source. For the applications hitherto studied it has been no disadvantage that this is a high-pressure lamp. The green line 5461 Å was ordinarily used, and it is isolated by the monochromator sketched in

Fig. 7, which consists of a plane grating 25 × 25 mm^2 with a good "blaze" in the first order of reflexion. The next unit D is a beam-turner, built in this laboratory, consisting of three mirrors, which serves to turn the image of the light column from vertical to horizontal, to suit the entrance slit direction. This mirror turner has the advantage that it has less light loss than a Dove or similar prism.

The entrance slit, which is mounted in a holder having micrometer adjustment in the vertical direction, consists of a uniform slit in an aluminium layer.

4.5. Receiving units, optical devices

The plane of the phase contrast image is indicated in Fig. 7. For general use, a screen P containing two parallel slits is placed in this plane. Their width and distance is chosen so that one covers most but not all of the A zone, while the other covers a selected region of the B zone. Alternatively, the second can be set in the D zone. Behind the screen the light from the two parts of the image is parted by an aluminized rectangular prism, throwing the pencils through lenses onto two photomultiplier tubes (RCA 931-A). They are well centered in housings whose openings are covered by diffusing screens. The power supply is described in another paper [13]. The receiving unit may be displaced sideways, making it possible to adjust the unit by studying the image with the microscope S. As will be described in more detail in 6.2., a direct visual measurement of intensities is often of advantage, and in this case screens, prisms, lenses etc. can be inserted in or before the image plane in order to obtain the desired field of view.

4.6. Ratio measuring unit

The aim of the method is to utilize the variation of intensity in the A zone according to the squares of the curves shown in Fig. 4, especially those portions where they are linear and steep, in order to determine the φ value. Of course it is of great advantage to use two phototubes, the second of which preferably measures the intensity in B, thereby measuring the ratio between the intensities, as this eliminates the influence of fluctuations of the lamp flux. In the beginning, several curves were taken for A and B separately in order to verify the vector diagram etc., but for the precision measurements the bridge circuit shown diagrammatically in Fig. 12 was always used. The currents from the A and B phototubes are brought through two potentiometers, whose sliders are regulated so as to make the current through the galvanometer zero. The one to the right, which has good linearity between its setting and its scale reading (0–300), is used for the measurement, after the left-hand one, of 25 kilohms, has been set to choose a proper range of the former. The two dry cells are inserted in the unit in order to compensate the dark current in the phototubes (switch in outer positions); these were always constant within the accuracy of the measurements. The galvanometer, which is thus always used as a null instrument, has a sensitivity of $2.6 \cdot 10^{-10}$ A per mm displacement; the currents were of the order of microamperes.

The combination of two phototubes compensates for incoming fluctuations when they are coupled to measure the ratio of the fluxes, but there remains as disadvantage that the change of sensitivity with time is always more or less different for the two tubes. This effect appears here as a change of ordinate height in the A/B curves with time, and necessitates special precautions. For this application and many other

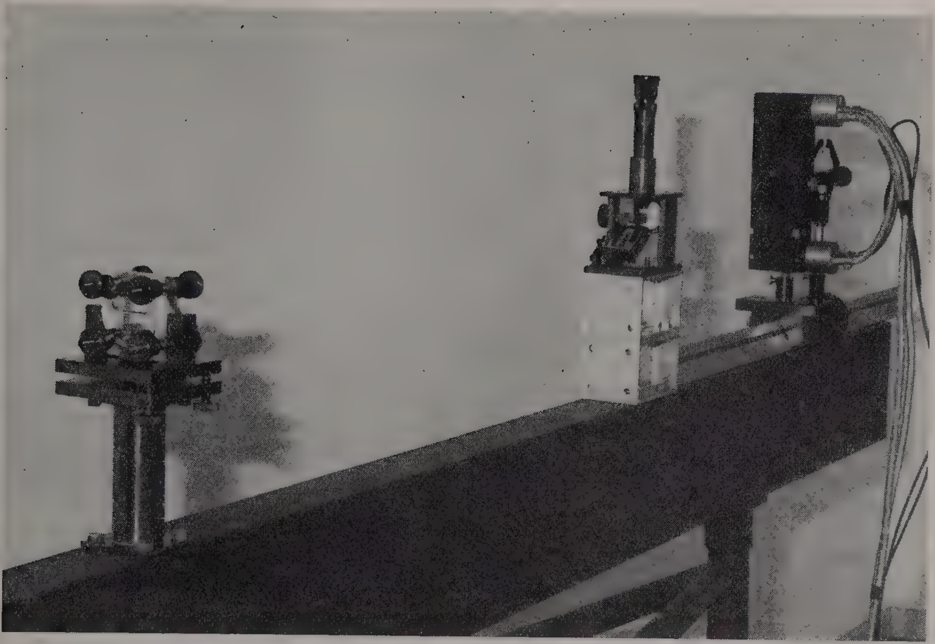

Fig. 11. Rear part of the refractometer, parts G–S of Fig. 7.

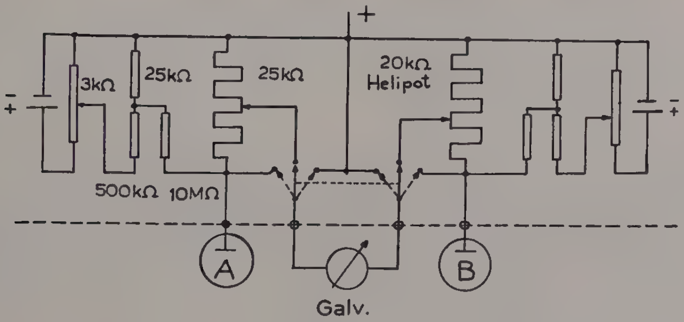

Fig. 12. Circuit of the ratio measuring unit.

similar measurements, such as on gradients of intensity, a ratio measuring device with only one tube switched between the different fluxes would be useful. Such a unit is under construction by Mr. Erik Djurle of this laboratory.

4.7. Double slit arrangement as a period scale

The determination of φ from intensity measurements using A/B curves of the sort shown in Fig. 4 requires the determination of the number of whole periods, 2π, entering into the phase difference. Often this number is known from an approximate knowledge of the refraction difference, as for solutions referred to the solvent or for a gas referred to a reference gas. In other cases, the number of whole periods in φ can be counted as the number of light fluctutations when the unknown gas is let into cell A instead the reference gas, which filled the cell before, and which the test gas displaces.

A general method of finding this number is, however, to place a double slit in front of the cell, so that one slit is in front of part A while the other is in front of part B. The fringes of this Young's experiment may easily be seen with a microscope. The light should be either white (zero order monochromator spectrum) or consist of the whole spectrum of mercury in order to identify the zero order fringe. This simple arrangement is attached to the apparatus as shown in Fig. 7 b. As is well known, the displacement of the fringe system is linear with φ, every period $\varphi/2\pi$ corresponding to a fringe distance. The ocular micrometer of the microscope V, focused on a certain plane U, reads the displacement of the zero order fringe from its position for $\varphi=0$, or, as was arranged in another device developed at this laboratory [14], an ocular scale is graduated directly in periods. Any of these two arrangements will give $\varphi/2\pi$ within one tenth of a unit, which is quite satisfactory. The double slit and the deviation mirror in front of the microscope are turned away during the phase contrast measurements.

5. Accuracy, tests and evaluations

5.1. Choice of constants

Some of the constants, such as those related to the phase plate, are critical, while others are not. The following list collects those data which have been used in the previous measurements and in those reported in this paper. When two or more are given, they relate to different devices.

Focal length of either of the cell lenses $f = 1700$ mm, 1000 mm.
Focal length of imaging lens M = 300 mm.
Cell apertures: $2\,p = 1.40$ mm, $q = 1.25$ mm, $r = 17$ mm, horizontal length = 17.5 mm.
Entrance slit, length 4.5 mm, width 25 microns, 18 microns.
Phase mirror dimensions, overall or masked portion; projection (Section 2)
  entire plate: $2\,C = 21.0$ mm, 18.0 mm
  central zone: $2\,c = 64$ microns, 50 microns
  horizontal length = 14 mm, 10 mm.
Magnification of lens M, $G = 0.20$
Widths of exit slits to the phototubes (see 4.5.) = 0.15 mm.

The desired position of the O′ vector origin is determined from the coordinates ψ and g. The angle ψ through which the phase is turned depends mainly on the thickness e of the mirror plate, according to Eq. (2), but also somewhat on the polarization direction (for δ). The amplitude reduction factor g may be found from the reflectivity ratio glass/metal and the polarization direction, by means of Fresnel's formulae.

The determination of these parameters so as to obtain a desired O′ position is not critical, as it is not used for evaluation. Going back to the schematic Fig. 4, we see that the best relation between φ and the intensity in A (or, the intensity ratio A/B, which has about the same general shape, since B varies only slightly) for measuring purposes are those portions where the curve descends or increases, espe-

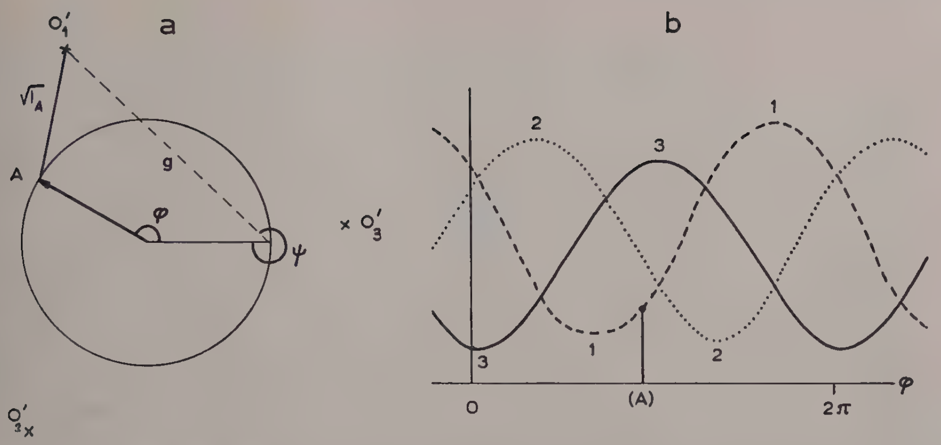

Fig. 13. a) Vector diagram of the three mirror system, the mirrors 1 and 2 being of *b* type, the mirror 3 of *a* type. b) General shapes of corresponding intensity curves.

cially where the intensity curves are approximately straight lines. Obviously there are portions to be avoided, namely those at the maxima and minima.

These arguments indicate where in the vector plane one should place the O′ points. A graphical treatment leads to the conclusion that these points should most conveniently lie outside the circle, but not much further than the radius of the unit circle. This often leads to the use of *b* mirrors which have sufficiently large *g* factors. In order to obtain equally precise measuring conditions over the whole period, it is of value to have two or preferably three interchangeable mirrors with different O′ in the apparatus; these are also incorporated in the construction (Section 4.3). Three equally spaced positions of O′ and the corresponding A/B curves to arbitrary scales are given in Fig. 13.

The preparation of a phase mirror for a desired ψ is made by controlled evaporation in vacuo. The precision obtained has been reported in a previous paper [13]. For the quantitative discussion of the contrasts it can be assumed to a close approximation that the edge of the central zone is infinitely sharp, and of uniform width and height (e). The polaroid used for varying g is of type HN 32, its oscillation direction being determined to within 0.5 degrees.

5.2. Photoelectric tests of the perfectness of optics etc.

The appearance of the diffraction figure when viewed by the microscope indicates that it is very perfect. The central image, which is the central lobe representing the second term of Eq. (5), stands out very brightly, and it must be dulled for the adjustment by inserting a second nearly crossed polaroid. It is, however, of great interest to scan it with a phototube device, and several photographs were also taken, with varied dimensions p and q (with lenses, without the central cell), as well as with varied φ in the apparatus. Fig. 14 reproduces a graph of this type, selected only to show the appearance. These curves correspond in detail to what is expected from Eq. (5) when the constants p, q and r are inserted. The finest visible fluctuations, of spacing 49 microns, are the period for the r (or B) apertures, these having twice the period

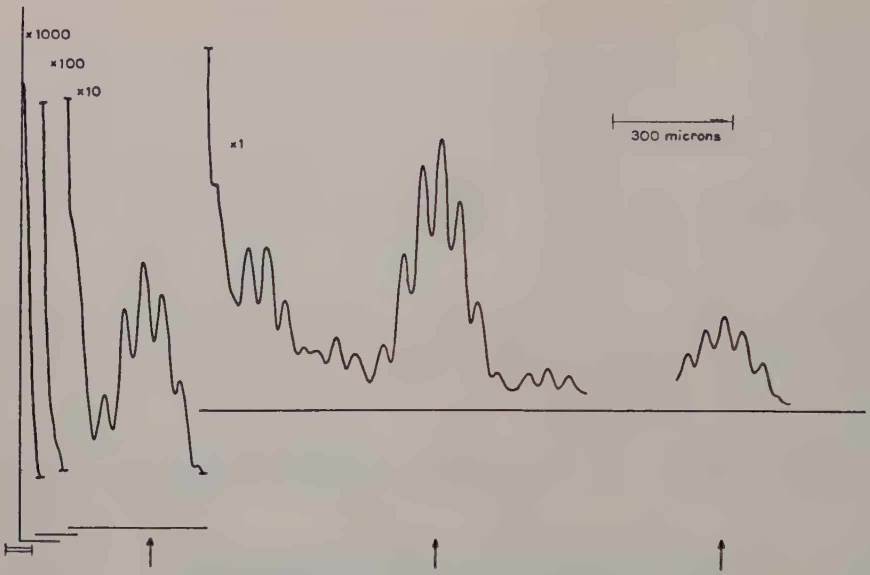

Fig. 14. Record of diffraction fringes corresponding to $\varphi = 0$.

for the total field $2\,(p+q+r)$ because of the symmetrical obstruction by the walls D. The first term in Eq. (5) gives rise to the slow variations of intensity, which may be interpreted as "beats" with a frequency of kuq. The distance measurable on Fig. 14 between the marked maxima, 740 microns, thus corresponds to the wall thickness q within the accuracy of a few per cent. In photographs of the patterns for the whole unobstructed aperture the fringes of spacing 25 microns are still visible, although of the same order as the slit width. By photographing with varied time of exposure, the whole diffraction field out to the borders of the phase contrast plate has been measured and checked with the theory given in 3.3. The range of intensities concerned is 10^6.

When φ is changed, by lowering or increasing the air pressure in cell A, the slow-variation fringes change their positions as may be calculated from Eq. (5) by considering the phase shift φ of one of the terms. The intensity image is symmetrical in φ.

This detailed study is of importance not for the analysis itself, but because of the information it gives about possible irregularities in the slits and optical elements. Some parts of the slit may be obstructed by dust, but this has no influence. Further, in some lenses, but not on those used, a "ghost line" may be seen near the central line, due to a zonal error. There is a reflection from the surface of the lenses, which appears at the interrupted part of Fig. 14 at one side; this is of no importance for the measurement as it does not enter into the phase contrast.

Another photoelectric test which is of still greater interest is the scanning of the phase contrast image. It gives, although with reduced fidelity compared to the main measurements on account of lamp variation, the field intensities. Fig. 15 represents a series of curves taken during a test, the variable being φ, here expressed in air overpressure in A. Besides verifying the general theory outlined above, these curves give information about disturbances due to diffraction and optical irregularities.

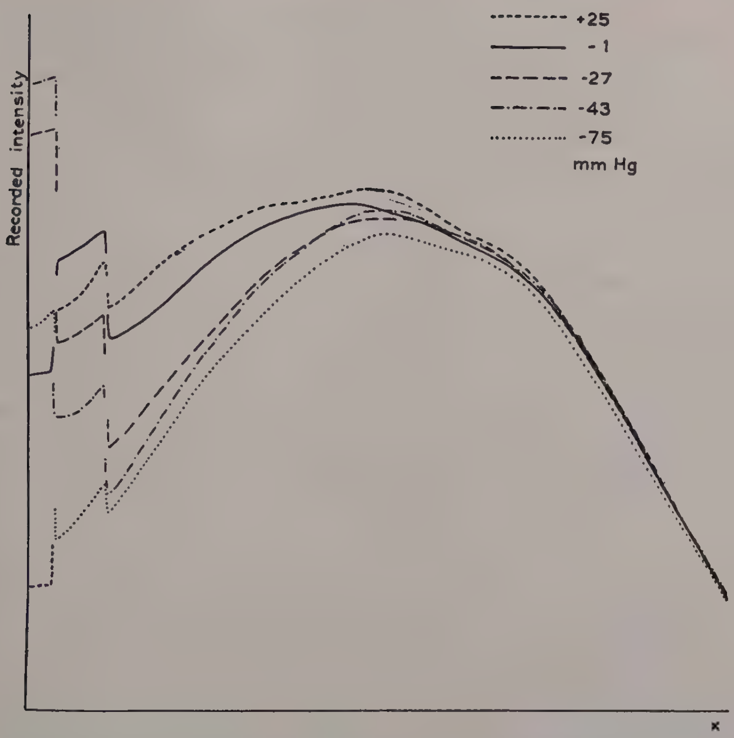

Fig. 15. Photoelectric image scannings with φ varied; the values ψ and g are different from those used for later measurements.

5.3. Influence of non-uniformity and of inexact adjustment

Any non-uniformity in the optics is revealed by scannings of the type described above. It integrates along all the slit, which is one of the advantages of the linear geometry. As a general rule it may be said that random irregularities in the intensity distribution are below 1 per cent of the average intensity. This does not at all mean that the measuring methods are subject to errors of this magnitude, as they are made with large zones, the same for all the measurements.

This applies also to the diffractions dealt with in 3.4. As they are due to the finite size of the phase plate, their maximum influence can be calculated. The "fine" diffractions at the image border e.g. between the A and D zones, are, at the place of the best focus, about or less than one per cent of the average intensity. The measured scanning curves confirm this; these fluctuations can hardly by distinguished from random variations. As seen from curves such as those in Fig. 15, the lack of uniformity in the B zone may be considerable, 20 per cent being calculated in this case. This effect combines with the spherical aberration. It is, as well known, several times larger in the arrangement of the two lenses with their plane sides facing one another, for forming the cell, than for the lenses turned, which is preferred for other measurements. The x ordinate corresponding to the rays just cutting the edge of the central zone is here, for the optimal focusing considering the entire ray pencil, about

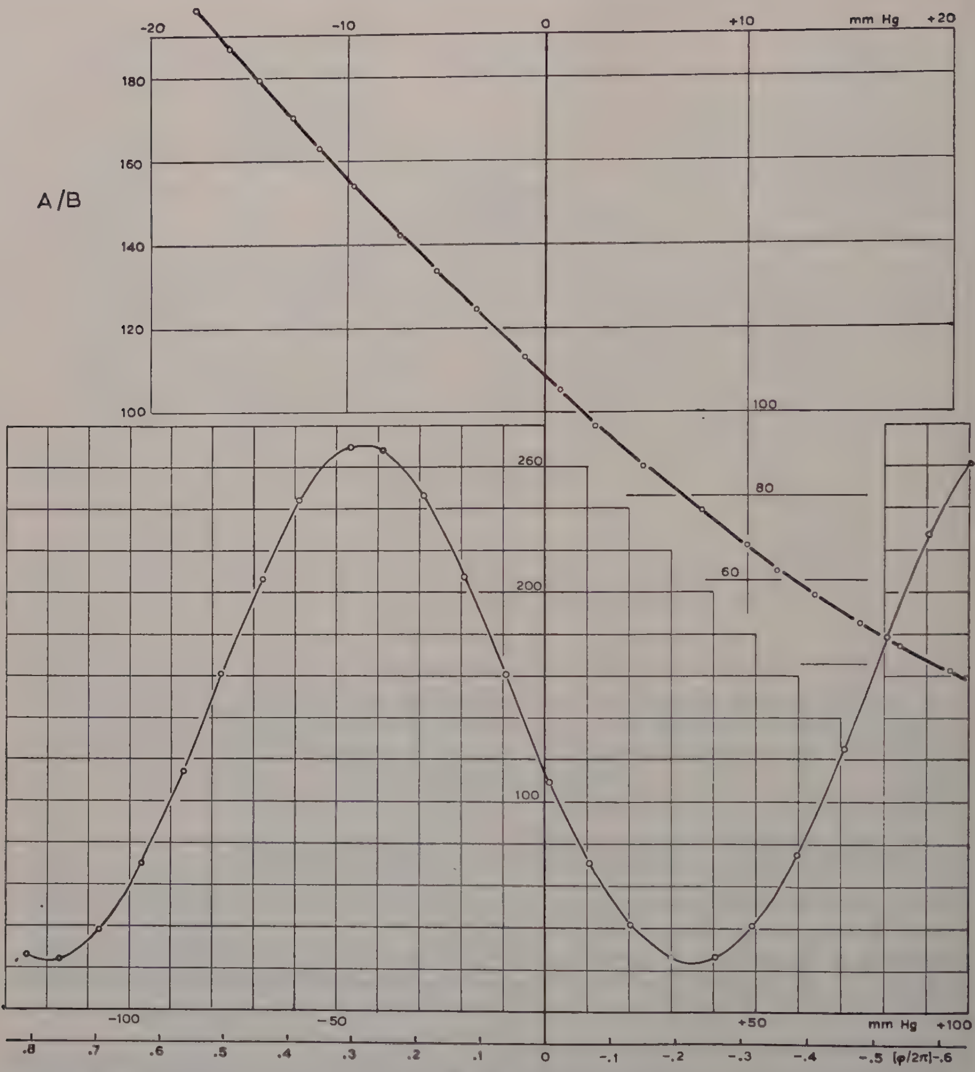

Fig. 16. Photoelectric evaluation curve of A/B, air, the lower curve for a whole period, the upper curve a section used for measurement, to a larger scale. The thickness of the upper curve corresponds to about 2/3 of the estimated maximum error of a carefully-made measurement (see 6.1.).

15 mm, this explaining the variation. For the measurements, the phenomenon is of no importance except that it suggests that the zone in the B region should be taken in a portion where the curve is fairly flat, as this will make it easier to achieve reproducibility after making readjustments.

A question of great importance is the following: What is the tolerance on the positioning of the centre of the diffraction fringe in the centre of the central zone? This applies to the rigidity of the apparatus, but also to the possibility of judging the symmetry of the positioning by eye when making adjustments. An error means that the diffraction pattern is cut unsymmetrically by the slit.

The changes in intensity in the two zones can be calculated from the diffraction integrals (7), introducing the ordinates of the cut $(+\gamma+\varkappa)$ and $(-\gamma+\varkappa)$ instead of symmetrical γ, $\varkappa$ being a small quantity compared to γ, a fifth at the most. However, the results cannot generally be given in comprehensive formulae, even when approximations are made, on account of the fluctuations of the functions Si and Ci entering into them. It is simpler to check these effects experimentally, which has been done for different φ values but only for one phase plate having a certain c of 32 microns. A displacement of $\varkappa$ corresponding to 6 microns gave on the average a displacement in the reading for A/B of about 2 per cent, which is about five times the average deviations of the readings. A displacement of only 3 microns gives reading deviations not exceeding the average deviations of one reading. Thus 3 microns or 1/10 of the zone width can be tolerated. A test series of the accuracy with which the symmetrical position could be reproduced when re-adjusting gave 1 micron, or 1/30 of the zone width, as the average deviation. Thus, the same calibration curve is still valid if interchangeable mirrors can be re-set with an accuracy of 3 microns, which is not difficult to achieve.

5.4. Evaluation curves and their accuracy

In Fig. 16 a typical evaluation curve for ordinary air is reproduced. The data of the phase mirror were, $\psi = 105°$ and $g = 2.0$. The pressure of the air in the A cell is varied, and measured with an accuracy of 0.1 mm Hg with respect to the normal air, cell B being open to the atmosphere. The technique and details of these measurements have been described by Mr. Lars Johansson and the present writer [15]. We find that the straight portions of the curve are very suitable for measurement, and in order to give an idea of the deviations of the observations one part of an approximately straight part of the curve is shown on a larger scale.

6. Determination of the refractive index of oxygen relative to air

6.1. Photoelectric determination

By means of a measuring technique described in detail in the paper quoted [15], check determinations of the refractive index of oxygen were made. As reference substance, filling the B cell, dry air free from carbon dioxide was used, the oxygen being obtained from a cylinder of the kind used for gas welding, and was thus of unknown purity: this was of no importance, as the purpose of the experiment was only to examine the accuracy with which the refractive index could be measured by two different procedures. On account of the time variation of the A/B sensitivity a full measurement had to be performed with at least three series of readings: calibration, measurement, calibration. Fig. 17 reproduces on small scale three curves taken up consecutively, given here as samples:

$$\left.\begin{array}{l}\text{oxygen, pressure varied (Oxygen 1)}\\ \text{air, pressure varied (Air)}\\ \text{oxygen, pressure varied (Oxygen 2)}\end{array}\right\}\ \text{reference cell: barometric air.}$$

Check tests showed that the decrease in the ordinates of the curves was continuous and linear with time, and that on changing the phototubes the readings increased, which proves that the effect is electrical and not due to other unforeseen influences.

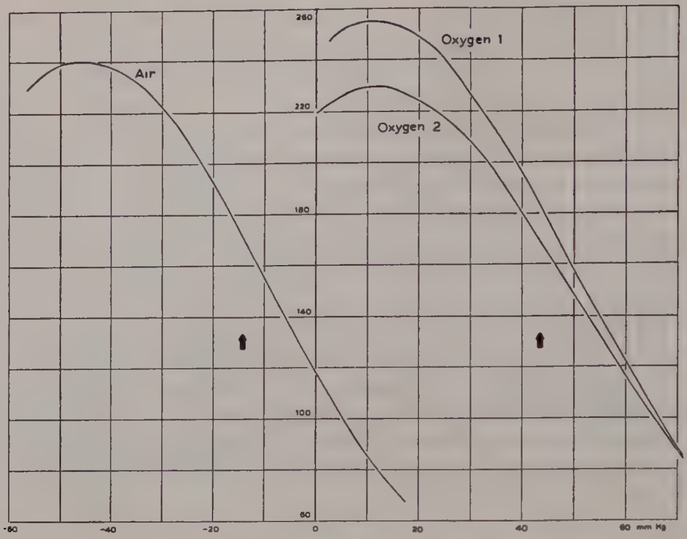

Fig. 17. Curves for measurements on oxygen (see 6.1.). The arrows give the positions of the visual measurements (6.2.).

In order to use these curves most efficiently, and at the same time to estimate the accuracy of the method, several points are taken on the portion sufficiently far from the maximum and minimum: Let n_N be the known refractive index of air at 20°C, 760 mm Hg, and call the refractivity $\mu_N = n_N - 1$. Denote the unknown index of oxygen analogously but with X instead of N. B is the barometric pressure, and p the over-pressure. Let the temperature excess over 20° be denoted by ϑ. On account of the proportionality of μ to the density, for a given gas, Eq. (1) may be written as

$$\varphi = \frac{2\pi}{\lambda_0} \cdot t \cdot \frac{293}{(293+\vartheta)\cdot 760} [B\mu_N - (B+p_X)\mu_X].$$

Assume that the same φ (i.e. the same A/B) corresponds to the over-pressure p_N for air (on the curve marked "air") and the over-pressure p_X for oxygen (average of curves 1 and 2). This gives

$$B\mu_N - (B+p_N)\mu_N = B\mu_N - (B+p_X)\mu_X, \tag{8}$$

and the excess $\mu_X - \mu_N$ is

$$\mu_X - \mu_N = \frac{\mu_N}{B}\left(p_N - \frac{\mu_X}{\mu_N} p_X\right) \tag{8'}$$

the expression in parentheses being the horizontal distance between the curves in Fig. 17, the part to the right of the zero axis being reduced to the "air period scale" by multiplication with the factor μ_X / μ_N, which is always known to a sufficiently close approximation. The calculations from the original curves are collected in Table 1. As the temperature was constant within 0.2 degrees during the run, no correction was

Table 1

Readings on original curves, as shown in Fig. 17
Barometric pressure *764.1* mm Hg, corrected to 0° C

A/B	Oxygen 1 22.5° C	(Air $(=p_N)$ 22.3° C	Oxygen 2 22.5° C	Average of Oxygen 1 and 2 $(=p_X)$	$\frac{\mu_X}{\mu_N} p_X$	$\left(p_N - \frac{\mu_X}{\mu_N} \cdot p_X\right)$	$\lvert \Delta (\ ) \rvert$
190	+41.6	−19.2	+36.8	+39.2	35.2	−55.4	0.2
180	+44.3	−16.8	+39.9	+42.1	38.8	−55.6	0
170	+46.7	−14.1	+43.1	+44.9	41.4	−55.5	0.1
160	+49.2	−11.5	+46.2	+47.7	44.0	−55.5	0.1
150	+52.1	− 8.8	+49.5	+50.8	46.9	−55.7	0.1
140	+55.0	− 6.1	+52.7	+53.8	49.6	−55.7	0.1
130	+57.9	− 3.4	+55.9	+56.9	52.5	−55.9	0.3
120	+60.8	− 0.3	+59.0	+59.9	55.3	−55.6	0
110	+63.6	+ 2.4	+62.0	+62.8	57.9	−55.5	0.1
100	+66.5	+ 5.4	+65.8	+66.2	61.1	−55.7	0.1
90	+69.3	+ 8.3	+69.1	+69.2	63.8	−55.5	0.1
						−55.60	
						corrected to 0° C −*55.40* mm Hg	
						corrected for better μ_X −*55.62* mm Hg	

made for this change. For μ_N, the value of BARRELL and SEARS [16] for 5461 Å was used, $273.10 \cdot 10^{-6}$. For oxygen the value $252 \cdot 10^{-6}$ was assumed.

The difference $\mu_X - \mu_N$ is calculated to be $-19.88 \cdot 10^{-6}$, and thus μ_X is found to be $253.22 \cdot 10^{-6}$.

The accuracy of the pressure difference readings was about 0.1 mm Hg. The resulting error in μ_X is below 4 units in 10^8 on account of the optical method. The absence of "drift" in the pressure readings indicates that there exists no residual error on account of the use of two cells, and further checks confirm this. The indidual pressure measurements are not quite certain to within 0.1 mm Hg, but regarded statistically the given limit of error is pessimistic, and is in fact the maximum error. As the period ($\varphi = 2\,\pi$) here corresponds to about 155 mm of mercury, the precision is better than 1/1000 of a period.

The temperature difference constancy between the gas examined and the reference gas must be good in order to maintain this great precision. In this respect the construction is very favourable, since the cell A is surrounded by the cell B bordering to it with relatively thin walls C, these arrangements rendering good heat contact. The thick glass lenses bordering to the cells in the other direction have a considerable heat capacity.

6.2. Visual determination

It is of interest to examine what precision can be reached by only visual comparisons of intensity. There are many ways in which such comparisons may be made, all of them of course requiring a judgement of the equality of illumination of two areas, arranged to be in contact with each other. Prism arrangements and maskings

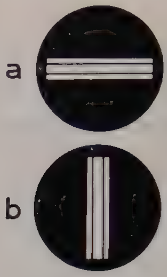

Fig. 18. Field of view in microscope S for visual measurements, a) as now used, b) preferable orientation.

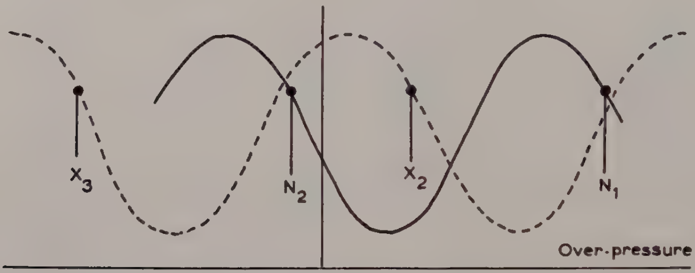

Fig. 19. Procedure for the visual measurements in 6.2.

may thus be used to place one part of zone A and one part of zone B together, and by means of polaroids or grey wedges etc. one of these intensities may be reduced in a measurable way.

The simplest way of making a comparison is in fact that indicated by the writer in a preliminary note [3], namely, to utilize those points where the A intensity equals the intensity of the two walls D. If this simple method is used it is only applicable to gases and entails the regulation of the pressure of the gas in cell A until this condition is fulfilled. From the diagram in Fig. 4 it is evident how these points will lie, and their real positions for the actual phase mirror are indicated by arrows in Fig. 17. Evidently they are favourable, being situated on a part of the curve having great slope, thus ensuring that the procedure has great sensitivity.

A test determination was made for the same gas as that measured photoelectrically. The reference part of the cell was kept filled with dry air free from carbon dioxide, and part A was alternately filled with the oxygen and the reference gas. Throughout these measurements the observer (E. I.) was able to regulate the pressure by means of a special arrangement while estimating the equal illumination of the A and D parts of the image in the microscope. The manometer was read by a second observer (L. J.). The appearance of the microscope field was as shown in fig. 18a, the proportions being as shown in the figure. The masking of the image outside the A and D portions in order to exclude all extraneous light helps the observer to concentrate on the measurement. When the A and D zones are of equal intensity they are separated only by a narrow diffraction fringe standing out some tenths of a per cent brighter than the rest of the field. Even though this quality of the borders is inferior to

Table 2

Visual determination. Averages of readings shown in Fig. 19. The figures in italics are the pressures reduced to 0° C.

	N_1 mm Hg	N_2 mm Hg	X_2 mm Hg	X_3 mm Hg	Temp.	B mm Hg
	+ 139.7	− 14.8			21.2° 21.3°	754.1
			+ 43.6	− 123.1	22.3° 21.6°	
	+ 140.0	− 14.1			21.6° 21.4°	753.7
			+ 43.2	− 123.9	21.3° 21.5°	
	+ 139.6	− 14.1			21.4° 21.3°	753.4
Average	+ 139.8 *+ 139.3*	− 14.3 *− 14.3*	+ 43.4 *+ 43.2*	− 123.5 *− 123.1*	21.5°	753.7 *751.1*

$N_1 - N_2 = 154.1$ *153.6* mm Hg (0°)
$X_2 - X_2 = 166.9$ *166.3* mm Hg (0°)

that in a Lummer-Brodhun photometer, the readings are astonishingly reproducible. A vertical orientation of the areas, as shown in Fig. 18b, would allow better use to be made of known physiological properties of the eye; the horizontal cell geometry has however been retained, because it is more convenient when working with liquids.

Two equally situated points on adjacent periods were read, denoted and situated as shown in Fig. 19. A setting was repeated 9 times (3 × 3), and only the averages of such series are collected in Table 2. The average of the absolute deviations from the mean values of the readings was 0.7 mm Hg [15].

The application of Eq. (8) to this determination gives the relations

$$\frac{\mu_X}{\mu_N} = \frac{B+N_2}{B+X_2} = \frac{B+N_1}{B+2X_2-X_3}\left(=\frac{N_1-N_2}{X_2-X_3}\right)$$

the last relation being of inferior precision. With the value quoted above for μ_N, the refractivity of the oxygen is $\mu_X = 253.4$, 253.1, (252.3), or in average $253.2 \cdot 10^{-6}$. From the average deviations of the values of Table 2, the maximum error of an average of pressure may be taken as 0.3 mm Hg, and of either of the numerators or denominators of the last equation, 0.5 mm Hg. This means a maximum error in μ_X of $\pm 0.2 \cdot 10^{-6}$.

The refractivity of the oxygen examined for 5461 Å light, and normalized to 20° C, 760 mm Hg, was thus found to be (maximum errors given)

$$\mu = n - 1 = (253.22 \pm 0.04) \cdot 10^{-6} \quad \text{photoelectrically,}$$
$$= (253.2 \ \pm 0.2 \ ) \cdot 10^{-6} \quad \text{visually.}$$

The conformity is thus better than expected. The oxygen sample was not pure (containing helium etc.), so no comparisons with previous measurements can be made. Compare the further material given in Ref. [15].

7. Procedures of measuring refractive indices of gases and liquids

7.1. Absolute determination for a gas or for a solution

Hitherto we have eliminated the cell thickness t as unnecessary for these relative measurements. However, several other measurements become possible if t be known with sufficient accuracy. Let us, provisionally, take the absolute error of the method to be that found in 6.1 and 6.2, where the maximum errors, counting in periods, were $d\left(\frac{\varphi}{2\pi}\right) = 0.6 \cdot 10^{-3}$, measuring photoelectrically, or five times this if the visual method was used.

From Eq. (1), and for the moment not considering errors in t, we find that the maximum absolute error of the refractive index difference is

$$d(n_1 - n_2) = d(\mu_1 - \mu_2) = \frac{\lambda}{t} d\left(\frac{\varphi}{2\pi}\right),$$

which gives, for a cell of $t = 10$ mm as used here, $d(n_1 - n_2) = 4 \cdot 10^{-8}$. It is possible to use a cell with larger t, and successful experiments have been performed with a geometric arrangement corresponding to $t = 100$ mm. There is no serious limitation to t from the optical point of view, as the light is parallel within the cell and so every section in the cell corresponds to the same image plane. The limitation probably lies in temperature constancy if the cell is lengthened as proposed. This cell of 100 mm would certainly give less than $1 \cdot 10^{-8}$ as the maximum error. It is also planned to build an apparatus using reflection, so that the light passes twice through the cell, being reflected from a plane mirror instead of passing through the second lens. This arrangement has advantages, but it presents some technical problems which are not yet solved.

If a cell is to be used for absolute measurements, its t must be known with a relative accuracy equal to or better than the index difference, i.e. dt/t must be less than $d(\mu_1 - \mu_2)/(\mu_1 - \mu_2)$. Large differences demand the greatest precision in t, and if this corresponds to 20 periods, the ratio will be $dt/t \leq 5 \cdot 10^{-5}$, or for a 10 mm cell, $dt \leq 0.5$ microns. This may be achieved without difficulty in the following way. Two symmetrically situated parts of the cells, namely, below and above the borders of the B portions, are spaced by means of two equal C. E. Johansson end gauges, the precision of which is about 10 times that required here. The cell assembly is then cemented together so that the end gauges are in optical contact with the plane glass surfaces of the lenses. The value of t is then known from the calibration of the gauges, corrected, if necessary, for lack of optical contact.

In determining the refractive index of a gas absolutely, both B and A are filled with the gas, and a series of measurements made at different pressures in A. The under-pressure can be reduced until vacuum is reached. It is of advantage to use the method of measuring on whole periods, the pressure being adjusted to points with equal A/B ratio in a series of consecutive periods. It should be pointed out that the precision in the pressure measurements must be equally high, which probably demands the capacity of a laboratory for standards, and that λ must in this case be known from standard measurements.

The same procedure can be used for the specific refractivity of solutions, the pure solvent being used as reference. In this case, however, some of the relative methods are more convenient.

In this connection it is necessary to consider how many whole periods may be included in the phase difference $\varphi/2\pi$ without reducing the precision, which depends on the equality of the intensity curves and the vector diagram for the consecutive periods. The limitation here lies in the limited monochromacy of the spectral line. Its fine structure broadens with higher period differences, which means that the "intensity centra" of the rotating vectors may be slightly differently situated with respect to the O′ point. For the Hg line 5461, however, this effect is negligible up to orders about 25 when working with a medium pressure spectral lamp. To make quite sure, a mono-isotopic source could be used. With a cell thickness of 10 mm, this means an upper limit of the measuring region of about $1500 \cdot 10^{-6}$. The total measuring region for $(n-1)$ without special precautions is thus

$$\text{from } 0.05 \cdot 10^{-6} \text{ till } 1500 \cdot 10^{-6}.$$

Cells with larger t divide these figures in the same proportion, and if the cells are chosen thinner (see Section 8), the limits are correspondingly raised.

A general comparison with interferometric refractometers such as the Jamin and Rayleigh types will be given in later communications dealing with measurements. One main advantage of the present method in the simplicity of the adjustments required. When a precise knowledge of the cell thickness t is not necessary, as for relative measurements, the two surfaces defining it, which have hitherto been assumed parallel, may in fact be inclined a considerable amount without loosing precision. A wedge-shaped geometry in the x-direction is no disadvantage, as the wavefront is allowed to be refracted as a whole, when only adjusting the phase plate as here to correspond to the central fringe; the equivalent t is that of the center of the cell A. The tolerance in the y-direction is also well fulfilled even with cemented parts.

7.2. Calibration curves and relative measurements

The measurement procedure is rather similar to those for interferometric refractometers, but some differences regarding technique and sensitivity should be mentioned.

An apparatus which is gas-tight is preferably calibrated with dry air free from carbon dioxide. The pressure in cell A is kept at an over-pressure of p mm Hg with respect of that in B, which can conveniently be the barometric pressure B. Denoting the standard value of refractivity at 20° C and 760 mm Hg by μ_N, we have, ϑ being the temperature excess over 20° C, for φ:

$$\varphi = \frac{2\pi}{\lambda_0} t \frac{293}{(293+\vartheta)\,760} [B-(B+p)]\,\mu_N. \tag{9}$$

The A/B or similar curves valid for the phase mirror in question when correctly adjusted (cf. 5.3), are thus related to this φ as the abscissa.

If the variation is exactly 1 period (as in 6.2) and the pressure difference between successive positions is P, we have

$$2\pi=\frac{2\pi}{\lambda_0}t\frac{293}{(293+\vartheta)\,760}\cdot P\cdot\mu_N \quad\text{and}\quad \frac{\varphi}{2\pi}=-\frac{p}{P}.$$

a) *Relative measurements for liquids*

Let A be filled with liquid 1, B with 2; φ is found from calibration curves in which the measured value of A/B enters; if t is known, Eq. (1) is preferred. Otherwise Eq. (9) may be combined with this to give

$$\varphi=\frac{2\pi}{P\cdot\mu_N}\cdot\frac{(293+\vartheta)\,760}{293}(n_2-n_1).$$

If the difference is totally unknown, the double slit method (4.7) should be used as a coarse scale, and the use of two or three mirrors (5.1) may give a gain in precision. The specific refractivity for a solvent is determined by measurements at different concentrations, which can be chosen to give appropriate positions on the curves.

b) *Relative measurements for gases*

The same precision as in an absolute determination (7.1) may be achieved by making a measurement relative to air, the value for which is well known. Cell B is filled with air, and cell A with the test gas. The calculation is straight-forward, either the pressure being varied to give a certain point on the A/B curve, or the same pressure being used in both cells, and the calibration curve used. More exact determinations can be arranged as described in 6.1.

c) *Relative or absolute method for gases, using visual observation*

This procedure is based on the discussion given above in 6.2. It would often be sufficient to use a precision barometer of aneroid type (such as the Paulin type) on which 0.1 mm Hg may easily be read, provided that the range of its scale is great enough to cover at least one period.

Instead of using the eye to judge equality of intensity, a photocell with two cathodes may be used, such as the RCA 5652. The two cathodes are coupled against each other through a galvanometer, which serves as a null instrument. Obviously one is not limited to equal intensities, as when comparing A and D by eye, and the method makes it possible to select an arbitrary point on the intensity curve (choosing a steep portion) and then to reduce the flux from either of the areas, so as to have always a zero reading on the galvanometer.

8. Applications and simplifications for streaming gases and liquids and for immersion of transparent materials

The need for only very small samples of the liquid to be examined is important when dealing with rare substances, such as isotope specimens, or some liquids of biological origin. It also makes it possible to examine streaming liquids continuously. The writer examined some streaming liquids as the first application of this method [1]. With the present state of the apparatus it is a simple application, the liquid under examination being fed through the cell A at the proper speed. On a change in refractivity of the stream the corresponding part of the curve in Fig. 16 is followed. If this intensity fluctuation is recorded with an electric recorder of time response faster than the corresponding rate of change of refraction in the stream — which may in fact be very rapid — complete information is obtained about the change of refractive index with time or volume. This is true for whole periods as well as for fractions thereof. When the liquid is so variable that it contains a great many periods per unit length in the cell thickness direction, the thickness t can be reduced to any desired value greater than about 1 millimeter. It would be difficult for technical reasons to reduce the thickness below this value. Retaining the other dimensions of the present apparatus, this means that a concentration determination may be made with every 0.03 milliliters of liquid.

Such fluctuations are very evident and are easily observed when a sample of a vapour, e.g. of some organic substance as ethyl-ether or toluene, is sucked through cell A, replacing the air. The method may possibly be of value in adsorptiometry.

It may be noted that the "dark-field" method is only a special case of the phase contrast arrangement in which $g=0$. In practice, this condition may be fulfilled by substituting for the phase plate an opaque black strip of the same angular width 2γ as that of the central zone of the phase plate. This method is inferior for making accurate measurements, but it may be used for rough determinations of periods and large fractions of periods.

The phase contrast method as applied here to liquids makes it possible to determine the refractive index and dispersion of minute glass splinters. They are suspended in the upper B cell, care being taken that the supporting thread is nowhere horizontal, as otherwise the diffraction image is disturbed. The refractive index of the immersion liquid, n_2, is then adjusted until it equals that of the glass, when the horizontal contours of specimen, which otherwise stand out in bright contrast, disappear. In this case, n_1 serves as standard for the measurement. This immersion method is more sensitive than for example the hollow spectroscopic prism method, and precautions should be taken to minimise troubles arising from the evaporation of the liquids.

The wavelength may easily be changed by changing the monochromator, though every new wavelength of course requires a new focal position and calibration curve.

9. Acknowledgements

My thanks are due in the first place to Mr. LARS JOHANSSON, who has devoted skill and energy to various parts of the new technique here elaborated, and to Mr. ERIK DJURLE for his construction of the electrical units. The work was possible thanks to grants to our laboratory from the State Council of Technical Research and the Swedish Natural Science Research Council.

Optics Laboratory, Royal Institute of Technology, Stockholm 70, May 1952.

REFERENCES

1. E. Ingelstam, Arkiv för fysik, *3*, Nr 20, 1951.
2. ——, Comm. Nr 2, Colloque international sur le contraste de phase et le contraste par interférence, en mai 1951. Editions de la Revue d'Optique. Paris 1952.
3. ——, Nature *168*, 960, 1951.
4. M. Françon and G. Nomarski, C. R. (Paris) *230*, 1392, 1950.
5. E. Ingelstam, Arkiv för fysik *3*, Nr 2, 1951.
6. Lord Rayleigh, Phil. Mag. (6) *33*, 161, 1917.
7 M. Duffieux, J. Tirouflet, N. Guenoche and G. Lansraux, Annales de Physique *19*, 355, 1944.
8. F. Zernike, Physica *9*, 686; 974, 1942.
9. M. Françon, Le contraste de phase en optique et en microscopie. Editions de la Revue d'Optique. Paris 1950.
10. A. H. Bennett, H. Osterberg, H. Jupnik and O. W. Richards, Phase Microscopy, Principles and Application. New York 1951.
11. H. Wolter, Annalen der Physik (6) *7*, 33, 1950.
12. K. Schuster, Jenaer Jahrbuch 1951, 22.
13. E. Ingelstam and E. Djurle, Arkiv för fysik *4*, Nr 27, 1952.
14. O. Hallén and E. Ingelstam, Experimental Cell Research, III, Nr 1, 1952.
15. E. Ingelstam and L. Johansson, Repts. Optics Lab. Roy. Inst. Technol., Stockholm, Nr 22, 1952.
16. A. A. Barrell and A. Sears, Philosophical Transactions A *238*, 1, 1939.

Tryckt den 26 februari 1953

Uppsala 1953. Almqvist & Wiksells Boktryckeri AB

ARKIV FÖR FYSIK Band 6 nr 30

Communicated 14 January 1953 by Bengt Edlén

A radioactive altimeter for stratosphere balloons

By Krister Kristiansson

With 2 figures in the text

In investigations of the cosmic radiation by means of stratospheric balloons it is of advantage to know the balloon's altitude. A simple device which gives information sufficiently accurate for most purposes is described in the following.

The altimeter

An aluminium tube 15 cm long and 2.5 cm in diameter is fitted at one end with a polonium α-source which is deposited on a silver foil. An Ilford C-2 type photographic plate is affixed at the other end (Fig. 1). Both α-source and plate are attached to the end-screws which close the aluminium tube. The interior of the tube is in communication with the outer air via a narrow brass tube wound in the form of a spiral around the aluminium tube. The long channel thus formed prevents the possible entry of moisture after the altimeter has descended. The total weight of the instrument is only ca. 75 gr.

When the balloon ascends the density of the air in the altimeter falls because of the diminution in pressure, and once a certain altitude is attained the α-particles are registered in the photographic emulsion. How far the α-particles penetrate the emulsion depends on the air density and hence on the pressure — whose altitude-dependence is known. By counting the number of tracks which reach different depths in the emulsion it is possible to estimate how long a time the balloon has spent at different heights, provided the strength of the α-source is known. It is thus possible from the length and number of α-particle tracks to study the vertical movements of the balloon.

Method of measurement

When the length of the vertically-directed α-particle tracks is being determined with a microscope it is of advantage to employ the newly-developed emulsion immediately after rinsing and before it has dried. The tracks are then longer because of swelling of the gelatine and the relative error in length-measurement is less. Further, if a plate containing vertical tracks is dried the grains in the tracks press upon one another and the tracks become somewhat to long.[1] To keep the water-content of the gelatine constant during measurements it suffices to cover the plate with an ordinary coverglass. Only relative

---

[1] J. Rotblat & C. T. Tai; Nature, *164*, 835 (1949).

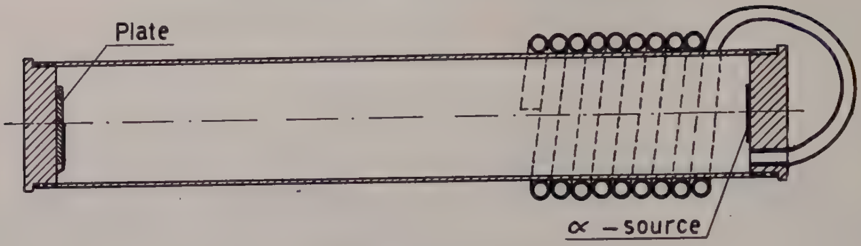

Fig. 1.

length-measurements are possible in the same plate because the water-content differs with development. Therefore one-half of the plate is shielded during the balloon flight and that portion is used for calibration. This is effected by irradiation in vacuo using the same polonium α-source. Test measurements carried out by irradiating at different pressures have shown that swelling of the gelatine is so uniform at different depths in the emulsion that no systematic error from this source can be observed.

The length of the α-particle tracks at a given pressure is not constant, because of straggling, and a mean range must therefore be determined and used in calculating the pressure. Check measurements at different pressures have been made and the difference between the pressures observed with a manometer and with α-particles has never exceeded 3 mm Hg.

In finding the maximum altitude it is not possible to obtain directly a mean range for the corresponding pressure since the pressure decreases continuously to a minimum. Instead a maximum extrapolated range for the α-particles is determined and then reduced to mean range. The difference between the extrapolated and the mean range can be found during calibration. It is appoximately constant and independent of the pressure, and can be used in reducing extrapolated to mean ranges without appreciably increasing the uncertainty of pressure estimation, even when the track-length distribution is that obtained by continuous reduction of the pressure to a minimum.

Registration of a balloon flight

The applicability of the altimeter has been tested in a balloon ascent to ca. 30 000 m. The number of tracks which came from the surface and penetrated to different depths was found by counting the number of tracks crossing different planes which were focussed in the microscope. This number is given in Fig. 2 as a function of the distance between the chosen plane and the surface. The strength of the α-source was known and this allowed an approximate determination of the time the balloon spent at different altitudes.The time is inserted on the righthand axis of the same figure and the corresponding height on the upper axis. The maximum altitude was found by measuring the length of about 50 tracks, each of which was more than 40 microscope scale divisions long (See Fig. 2). The extrapolated range was found and from it the maximum altitude was calculated to be 31 km. Because of the low pressure the uncertainty in the height measurements is relatively large. The accuracy can be improved. how-

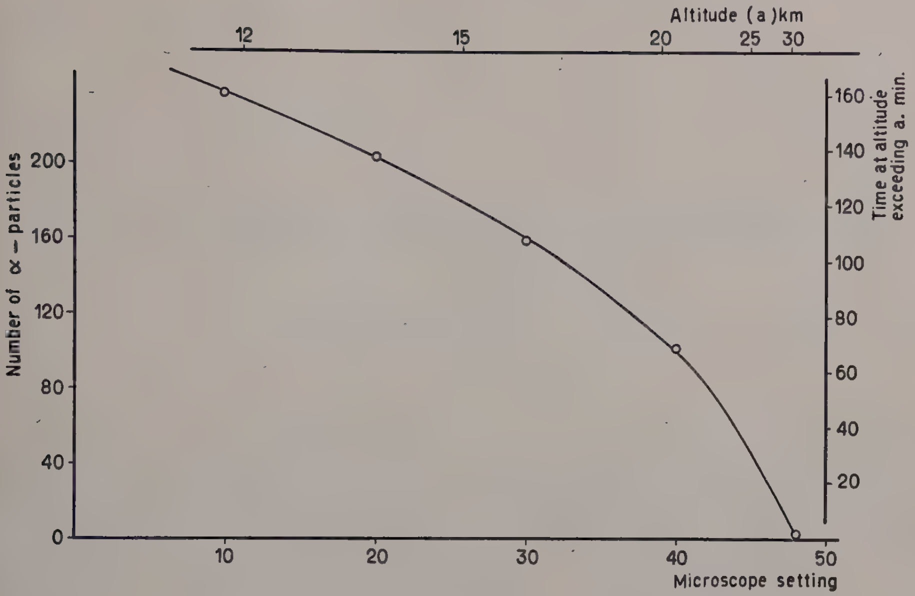

Fig. 2.

ever, by increasing the distance between α-source and plate. The temperature in the instrument during the flight was ca 0° C. An error of few degrees in the temperature data has but an insignificant effect on the accuracy of height determination.

Department of Physics, University of Lund, December 1952.

Tryckt den 28 februari 1953

Uppsala 1953. Almqvist & Wiksells Boktryckeri AB

ARKIV FÖR FYSIK Band 6 nr 31

Communicated 8 October 1952 by Axel E. Lindh and Erik Hulthén

The X-ray diffraction from quartz and the influence of surface treatment

By Gösta Brogren

With 8 figures in the text

During the last years we have carried out a series of investigations of different atomic planes in quartz which we expected to be suitable as crystal gratings in X-ray spectroscopy. The results hitherto published are those of the photographic investigations of a number of crystal lattices obtained by sawing crystal plates out of large single crystals with the surfaces parallel to suitable atomic planes. The crystal plates were then ground and polished very carefully.

Before it is possible to decide if quartz is a suitable material for X-ray lattices, it is necessary, firstly, to examine whether the surface layer of the crystals changes in such a way during the grinding and polishing as to influence the reflecting and the resolving powers; secondly, to calculate, for instance, the values of the reflecting power under the assumption that quartz is an ideal perfect crystal and to compare the calculations with the values experimentally determined.

We will first give a report about the experiments on the influence of the surface layer and how this layer was removed, and then investigate the agreement between the theoretical calculations and the experimental results.

I. The influence of surface treatment

The full width of a rocking curve at half maximum intensity is a measure of the resolving power of the two-crystal spectrometer. Hence, we used a pair of crystal plates and a two-crystal spectrometer to study the influence of the surface layer. The instrument is earlier described in detail [1]. With this we investigated the rocking curve, and in some cases also the percent reflection and the double crystal coefficient of reflection. The intensity was registered by an argon-filled Geiger–Müller counter, the sensitivity of which was about 50 % as to the radiation used (copper $K\alpha$-radiation). The voltage of the X-ray tube was always kept below the double threshold voltage so that no overlapping of the second order could take place. The filament was fed from a storage battery and the primary alternating current was stabilized by a stabilizing circuit, which kept the voltage constant within 0.5 %. No variations of the high voltage and the current through the X-ray tube could be observed during the recordings.

In order to remove the surface layer, the crystals were etched with 40 percent hydrofluoric acid at 18°–20° C. The rocking curves were measured after varying times of etching. Simultaneously the surfaces were photographed in a metal microscope with a magnification of 1 000 times.

All crystal plates, which were delivered cut and ground in the desired way, were first examined optically with polarized light in order to control that they were optically homogeneous. All the plates, but for those with the surface parallel to plane [10$\bar{1}$0], were polished so as to be optically plane and to give good optical reflections. In the metal microscope a few solitary irregularities could be observed, the diameter of which seemed to be about 1 μ or less. After some ten seconds of etching, there appeared scratch impressions, which must have been made during the grinding, as they constituted parallel lines in the surface. They had been filled with crystal powder and polishing material during the polishing so that smooth, optically good surfaces were formed. These defects appear more or less in different surfaces, probably because grinding powder of different sizes had been used and because the polishing had been carried out more or less carefully. The appearance of the defects is to be seen in Fig. 1. After two or three minutes of etching a number of small triangular etch-impressions appeared all over the surface, which grew more numerous and larger with an increase of the time of etching. In the case of some crystals, where the orientating measurements gave very asymmetric rocking curves or curves with double peaks, the surface was divided into two or more differently faceted areas after about five minutes of etching. [Fig. 2.] These crystal plates must be composed of two or more "crystallites", in which the atomic planes with the same indices were not parallel.

Atomic plane 10$\bar{1}$0. The crystal plates used were very badly polished and gave no good optical reflections. After the position of the atomic planes had been determined and the crystal holders adjusted so that atomic plane [10$\bar{1}$0] was parallel to the axis of rotation (see reference 1), the measurements and the etching were carried out. We tried to save the rear side of the crystal plates from the attack of the hydrofluoric acid by covering it with wax, sapon, and other organic substances. Because of its low viscosity, however, the acid did penetrate between the cover and the crystal surface. The best cover used was silicon grease, which prevented the attack in a few minutes. Hence, both surfaces were exposed to the acid when the time of etching was long.

As appears from Table 1 and Fig. 3, the width of the rocking curve was decreased from 54″ to 8″ in about four minutes. A continued etching had no influence. From other experiments it was determined that the thickness of quartz, etched away from each surface under these conditions, was 4000 Ångstrom/hour.

No determinations of the changes of the percent reflection and of the double crystal coefficient of reflection were made because of the very bad qualities of the original surfaces. The results show, however, that when a surface layer of a thickness of about 400 Ångstrom is etched away, a further etching does not alter the width and form of the rocking curve.

Etching experiments with atomic plane [11$\bar{2}$0]. These crystal plates were ground and polished very carefully and no defects could be observed in the optical examination. Scratch impressions appeared as soon as they were etched, but they disappeared after a few minutes. The width of the rocking curve at half maximum intensity, the percent reflection and the double crystal coefficient of reflection were determined as a function of the time of etching.

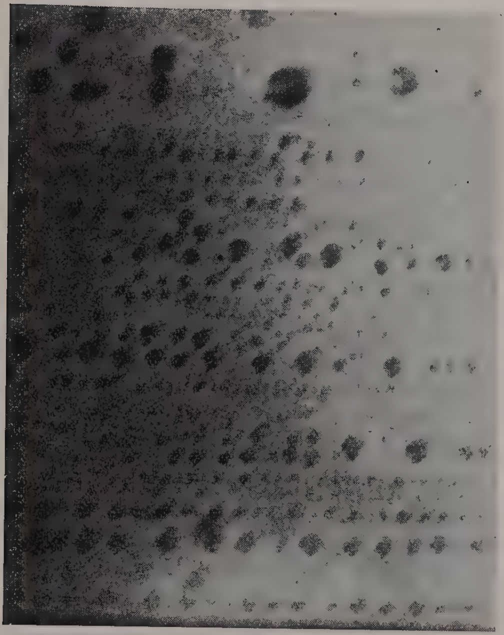

Fig. 1. Defects from grinding, microphotograph after 20 seconds time of etching.

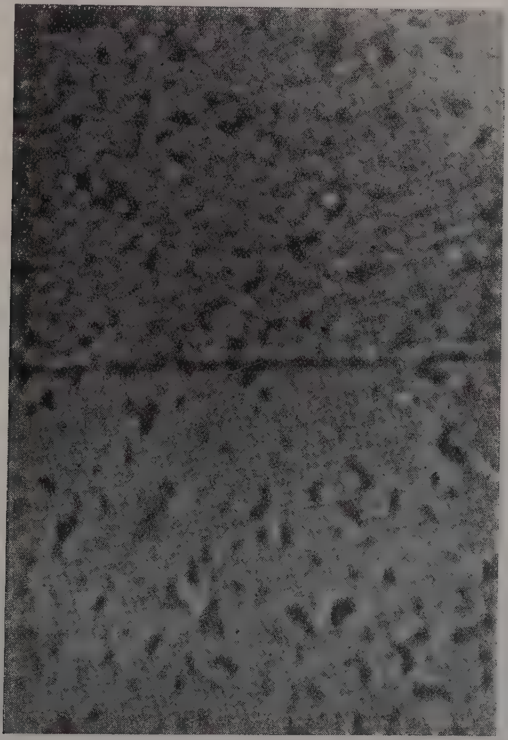

Fig. 2. Microphotograph of a surface, containing two crystallites. Time of etching 4 minutes.

Table 1

The etching of plane $10\bar{1}0$.

Time of etching in minutes	The full width of the rocking curve at half max. intensity
0	54″
1	36″
2	24″
4	8″
6	9″
10	10″
15	7″
30	8″
60	9″
120	8″
300	7″

As these crystal plates had very rough surfaces, it is probable that the two crystals did not keep the parallelism so very well. It is probable that the value of the width (8″) is somewhat too high.[1]

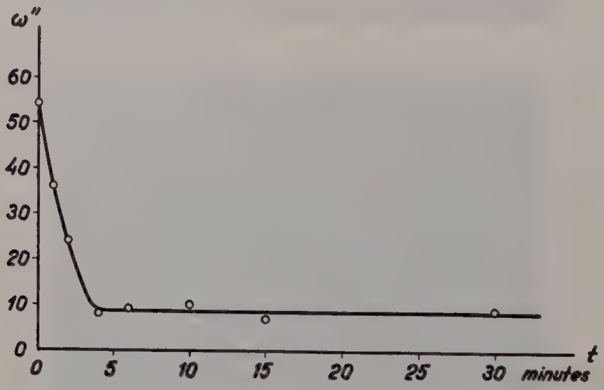

Fig. 3. The influence of etching on the width of the rocking curve at half maximum intensity, for atomic plane ($10\bar{1}0$).

As is to be seen in Table 2 and Fig. 4, the above quantities do not change after an etching of one minute. In one hour a layer 25000 Ångstrom thick was removed from each surface. Hence, only a few hundred Ångstrom had to be eliminated before constant conditions were valid.

---

[1] In connection with another investigation new measurements have been made with atomic plane $10\bar{1}0$. The crystal plates used, which were delivered by the firm of Steeg & Reuter, Bad Homburg, Germany, were very carefully polished. Before etching, rocking curves with a full width of 5.6″ at half maximum intensity were obtained. After etching, the width decreased to 5.0″. At the same time the percent reflection changed from 0.54 to 0.63 and the double crystal coefficient of reflection from $1.86 \cdot 10^{-5}$ radians to $1.81 \cdot 10^{-5}$ radians. Thus the coefficient of reflection remained nearly unchanged. As a comparison, it may be mentioned that the calculated values of these quantities are $w = 4.9''$, $R = 1.82 \cdot 10^{-5}$ radians, and $P = 0.64$.

Table 2

The etching of plane $11\bar{2}0$.

Time of etching in seconds	Width of the rocking curve	Percent reflection	Coefficient of reflection in radians
0	9.6″	0.37	$2.50 \cdot 10^{-5}$
20	5.7″	.44	$1.52 \cdot 10^{-5}$
40	3.9″	.51	$1.16 \cdot 10^{-5}$
60	3.2″	.55	$1.09 \cdot 10^{-5}$
120	3.4″	.54	$1.10 \cdot 10^{-5}$
300	3.5″	.53	$1.07 \cdot 10^{-5}$
600	3.4″	.53	$1.08 \cdot 10^{-5}$
1 200	3.4″	.53	$1.08 \cdot 10^{-5}$

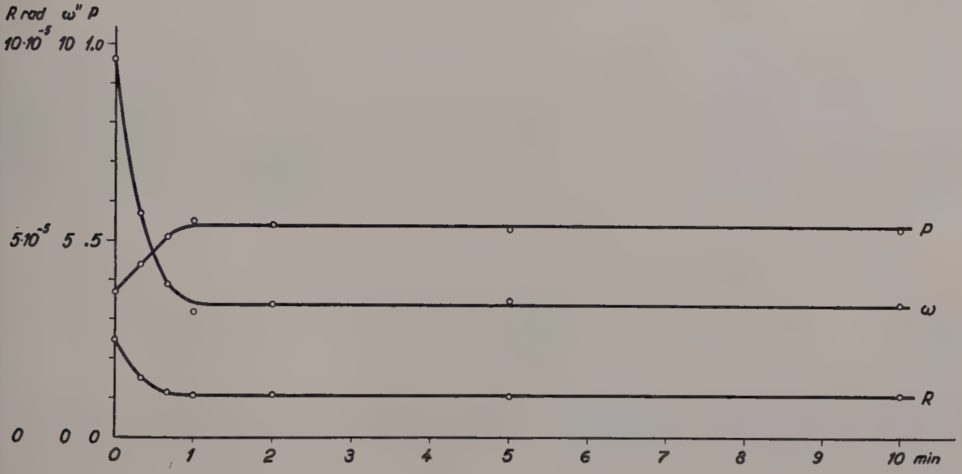

Fig. 4. The effect of etching on the width of the rocking curve at half maximum, on the coefficient of reflection, and on the percent reflection for the first order reflection of Cu Kα-radiation from a surface, parallel to atomic plane ($11\bar{2}0$).

Conclusions. From the above results it appears that, when a quartz crystal is ground and polished, a very thin deteriorated surface layer is formed. If the crystal is used as a crystal grating in an X-ray spectrometer, this surface layer diminishes the resolving power. The integrated reflection power is increased, on the other hand. The thickness of the destroyed surface layer is very slight. The main part of it seems to be defects in the very surface caused by the procedure of grinding, which are filled with a mixture of crystal powder and polishing material, so that a very smooth surface having good optical reflections is formed. The "deformed" surface layer can be removed by etching with hydrofluoric acid. Only a layer a few hundred Ångstrom thick need be etched away. The photographic control of the procedure shows that the powder filling out the irregularities in the surface is first attacked and removed.

II. Studies of the X-ray reflections at atomic plane [11$\bar{2}$0].

In order to investigate the qualities of the quartz crystal, we made a series of measurements of the full width of the rocking curve at half maximum intensity; of the percent reflection and of the double crystal coefficient of reflection at different wave-lengths. The results were compared with the data obtained by theoretical calculations.

The structure of quartz is well known and the parameters of the unit cell are determined with a high accuracy [2, 3], so that it is possible to calculate its structure factors. BRILL, HERMAN, and PETERS (3) discuss in their article the kind of bonds existing in the quartz crystal, and draw the conclusion that the bond is covalent with a partially ionic character. The structure factors are calculated in the following under the assumption that the bond is purely covalent. JAMES' and BRINDLEY'S [4] values of the atomic scattering factors of Si and O have been used. This assumption has hardly any influence on the following calculations, as for plane [11$\bar{2}$0] the scattering factors of the atoms are nearly identical with those of the ions. As they also found that quartz is a rather perfect crystal, the theory for the above quantities was carried out under the assumption that quartz is a perfect crystal.

The theory of the diffraction of X-rays from a lattice plane in a non-absorbing perfect crystal consisting of only one kind of atoms, has been developed by DARWIN [5] and EWALD [6–8]. If $F(l)$ is the ratio of the intensity reflected from the crystal to that incident upon it, and if we assume that the incident beam is parallel and unpolarised, we obtain

$$F(l) = \frac{1}{2}\left[\left|\frac{\frac{F}{Z}}{l \pm \sqrt{l^2 - \left(\frac{F}{Z}\right)^2}}\right|^2 + \left|\frac{\frac{F}{Z}\cos 2\vartheta_0}{l \pm \sqrt{l^2 - \left(\frac{F}{Z}\cos 2\vartheta_0\right)^2}}\right|^2\right]. \tag{1}$$

where F is the structure factor,
Z is the number of electrons in the unit cell,
ϑ_0 is the Bragg angle,

$$l = \frac{\sin 2\vartheta_0}{2\delta}(\vartheta - \vartheta_0) - 1. \tag{2}$$

δ is the deviation of the index of refraction from unity. The unit of l is thus $\frac{2\delta}{\sin 2\vartheta_0}$ radians. The sign to be used in the denominator of Eq. (1) is determined by the physical requirement that the ratio must be less than or equal to one. In a crystal composed of more than one kind of atoms $A = \frac{\Sigma F_i}{\Sigma Z_i}$ must be exchanged for $\frac{F}{Z}$, where the summation must be extended over all atoms in the unit cell.

In Equation (1), the first term of the expression refers to that part of the radiation whose electric vector is perpendicular to the plane of incidence (σ-polarized radiation) and the second to the radiation, whose electric vector lies in the plane of incidence (π-polarized radiation). Hence we can write

$$F(l) = \tfrac{1}{2} F_\sigma(l) + \tfrac{1}{2} F_\pi(l) \tag{3}$$

The radiation is totally reflected within an angular region $\varDelta_\sigma$ and $\varDelta_\pi$, given by

$$\varDelta_\sigma = \frac{4\,\delta}{\sin 2\,\vartheta_0} \cdot \frac{F}{Z} \tag{4}$$

$$\varDelta_\pi = \frac{4\,\delta}{\sin 2\,\vartheta_0} \frac{F}{Z} \cos 2\,\vartheta_0 \tag{5}$$

or

$$\varDelta_\pi = 4\,\delta \frac{F}{Z} \cot 2\,\vartheta_0 \,. \tag{5 a}$$

The integrated reflection power R_c calculated for unpolarized radiation is

$$R_c = \frac{8\,\delta}{3} \cdot \frac{F}{Z} \cdot \frac{1 + |\cos 2\,\vartheta_0|}{\sin 2\,\vartheta_0} \,. \tag{6}$$

The diffraction of X-rays in a perfect crystal with not negligible absorption is discussed by PRINS [9] and KOHLER [10]. PRINS develops DARWIN's theory and introduces the absorption by assuming that the coherent radiation scattered from an atom shows a phase displacement against the primary radiation, so that the intensity of the scattered radiation is decreased in such a way as the value of the absorption coefficient states. It follows from this that a complex quantity $\delta + j \cdot \beta$ must be exchanged for δ, where β is the absorption coefficient of the length $\frac{\lambda}{4\,\pi}$

$$\because \beta = \frac{\lambda}{4\,\pi} \cdot \mu_l \,, \tag{7}$$

where μ_l is the linear absorption coefficient.

Darwin's expression (1) now gets the following form:

$$F(l) = \frac{1}{2} \left| \frac{(A + j\,B)\,\frac{1}{\delta}}{l - j\frac{\beta}{\delta} \pm \sqrt{\left(l - j\frac{\beta}{\delta}\right)^2 - \left(\frac{A + j\,B}{\delta}\right)^2}} \right|^2 + $$

$$+ \frac{1}{2} \left| \frac{(A + j\,B)\,\frac{1}{\delta}\,|\cos 2\,\vartheta_0|}{l - j\frac{\beta}{\delta} \pm \sqrt{\left(l - j\frac{\beta}{\delta}\right)^2 - \left(\frac{A + j\,B}{\delta}\right)^2 \cos^2 2\,\vartheta_0}} \right|^2 . \tag{8}$$

The quantity $(A + j\,B)$ is related to the quantity $(\delta + j\,\beta)$ as the amplitude of the wave coherently scattered at angle $2\,\vartheta_0$ is to the amplitude of the wave scattered in the forward direction. If we further assume that the phase displacement of the coherently scattered radiation is not depending on ϑ_0 (that is if we assume that all electrons in the atom may be treated in the same way), we have

$$A + j\,B = \sum_i \frac{F_i}{Z_i}\,(\delta_i + j\,\beta_i), \tag{9}$$

δ_i and β_i being the contributions from atom i to the refractive index and the absorption coefficient respectively owing to the earlier definitions.

The quantities we want to calculate are the percent reflection P, the double crystal coefficient of reflection R, and the full width w of the rocking curve at half maximum intensity. The percent reflection is defined as the ratio of the maximum intensity of the beam, reflected from the second crystal to the intensity of the beam, incident upon the same crystal. We get

$$P = \frac{\int\limits_{-\infty}^{+\infty} F_\sigma^2(l)\,dl + \int\limits_{-\infty}^{+\infty} F_\pi^2(l)\,dl\ \text{[1]}}{\int\limits_{-\infty}^{+\infty} F_\sigma(l)\,dl + \int\limits_{-\infty}^{+\infty} F_\pi(l)\,dl}. \tag{10}$$

The double crystal coefficient of reflection is defined as the ratio of the integrated intensity of the beam reflected from the second crystal to the intensity of the beam reflected from the first crystal only. The integrated intensity refers to the area under the rocking curve when the angular unit is the radian. The general expression for R is

$$R = \frac{2\,\delta}{\sin 2\,\vartheta_0}\,\frac{\left[\int\limits_{-\infty}^{+\infty} F_\sigma(l)\,dl\right]^2 + \left[\int\limits_{-\infty}^{+\infty} F_\pi(l)\,dl\right]^2}{\int\limits_{-\infty}^{+\infty} F_\sigma(l)\,dl + \int\limits_{-\infty}^{+\infty} F_\pi(l)\,dl} \tag{11}$$

The full width w at half maximum of the rocking curve is obtained by plotting the function

$$\phi(k) = \frac{1}{2}\int\limits_{-\infty}^{+\infty} F_\sigma(l)\,F_\sigma(l-k)\,dl + \frac{1}{2}\int\limits_{-\infty}^{+\infty} F_\pi(l)\,F_\pi(l-k)\,dl \tag{12}$$

for different values of k. The angular unit k is converted into radians by multiplying with $\dfrac{2\,\delta}{\sin 2\,\vartheta_0}$.

Evaluation of the constants. All values are calculated starting from equation (8). The values of the refractive index δ are calculated from the relation [13]

$$\delta = 1.36 \cdot \varrho \cdot \lambda^2 \cdot 10^{-12}, \tag{13}$$

where λ is measured in X.U. The density of quartz ϱ was set to 2.6485 [14]. The values δ_{O} and δ_{Si} apply to the index of refraction of a substance, built up of only one kind of atoms (O and Si respectively). On calculating for instance δ_{O}, we inserted the value of the density that is obtained when all silicon atoms in the crystal are neglected.

---

[1] See reference (12) page 718 and following.

The β-values were obtained from Eq. (7). Table 3 contains the values of the mass absorption coefficients, taken from experimental data [15].

As quartz is a hexagonal crystal belonging to crystal class D_3^4 (or D_3^6), with well known crystallographic data, the structure factors are given by the relations

$$F = (H_{\mathrm{Si}} + j \cdot K_{\mathrm{Si}})\, f_{\mathrm{Si}} + (H_{\mathrm{O}} + j\, K_{\mathrm{O}})\, f_{\mathrm{O}}, \tag{14}$$

where

$$\begin{aligned} H = 2 \Big\{ & \cos \pi \left[(h-k)(x-y) + 2lz\right] \cos \pi i (x+y) + \\ & + \cos \pi \left[(k-i)(x-y) + 2lz\right] \cos \pi \left[h(x+y) - \frac{2l}{3}\right] + \\ & + \cos \pi \left[(i-h)(x-y) + 2lz\right] \cos \pi \left[k(x+y) + \frac{2l}{3}\right] \Big\}, \end{aligned} \tag{15}$$

$$\begin{aligned} K = -2 \Big\{ & \cos \pi \left[(h-k)(x-y) + 2lz\right] \sin \pi i (x+y) + \\ & + \cos \pi \left[(k-i)(x-y) + 2lz\right] \sin \pi \left[h(x+y) - \frac{2l}{3}\right] + \\ & + \cos \pi \left[(i-h)(x-y) + 2lz\right] \sin \pi \left[k(x+y) + \frac{2l}{3}\right] \Big\}. \end{aligned} \tag{16}$$

h, k, i, and l are the indices of the atomic plane, and x, y, z the coordinates of the atom. f is the atomic scattering factor.

Since $K = 0$ only if $l = 3n$ and $h = -k$ or $k = -i$ or $i = -h$, the structure factor of plane $[11\bar{2}0]$ is complex.

When calculating the above values, we used the coordinates determined by BRILL *et al.* [3].

$$x_{\mathrm{Si}} = 0.465 \qquad x_{\mathrm{O}} = 0.415 \qquad y_{\mathrm{O}} = 0.272 \qquad z_{\mathrm{O}} = 0.120.$$

A and B are now evaluated by inserting all values in Eq. (9).

Table 3 gives all the computed constants and the calculated values of P, R, and w for the wavelengths used. The structure factors are not corrected for the effect of the thermal vibrations of the atoms in the crystal, which decreases the structure factor values. A theory for the structure factor correction is worked out only in the case where the crystal has a simple cubic lattice, where we have, due to DEBYE and WALLER [17–21],

$$f_T = f_0 \cdot e^{-M}, \tag{17}$$

where

$$M = \frac{6h^2}{m \cdot k \cdot \theta} \left[\frac{\phi(x)}{x} + \frac{1}{4} \right] \frac{\sin^2 \vartheta}{\lambda^2}, \tag{18}$$

f_T and f_0 are the atomic scattering factors at absolute temperatures T and 0, h is Planck's constant, m the mass of the atom, k Boltzmann's constant, θ is the characteristic temperature of the crystal, $x = \frac{\theta}{T}$, where T is the temperature of the crystal, *T*

The constants, used

Wavelength X.U.	Glancing angle, ϑ	$\left(\frac{\mu}{\varrho}\right)_{\mathrm{Si}}$	$\left(\frac{\mu}{\varrho}\right)_{\mathrm{O}}$	δ_{Si} $\cdot 10^6$	β_{Si} $\cdot 10^6$	δ_{O} $\cdot 10^6$	β_{O} $\cdot 10^6$
2 498	30°38′	225	45.5	10.62	0.554	12.15	0.128
2 285	27°47′	180	36.4	8.77	0.405	10.03	0.094
1 932	23°15′	111	22	6.27	0.212	7.17	0.047
1 537	18°16′	60	11.2	3.99	0.093	4.60	0.011
1 205	14°14′	33	5.7	2.44	0.0392	2.79	0.0077
708	8°18′	6.4	1.2	0.84	0.0044	0.96	0.0010
558	6°32′	3.7	0.7	0.54	0.0020	0.61	0.0005

at which the measurements are made. The values of $\phi(x)$ are to be found in International Crystal Tables, p. 574, Vol. 2 [29]. θ may be roughly estimated from the relation between crystal hardness and characteristic temperature.

A similar correction should perhaps be applied to a hexagonal crystal, but as, in the case of quartz, the characteristic temperature is probably rather high, the correction ought to be rather small, at least in the case of plane [11$\bar{2}$0]. Some information may be obtained for instance by determining the double crystal coefficient of reflection R for the same wavelength, but with different atomic planes, where $\frac{\sin\vartheta}{\lambda}$ has different values.

Experimental. If full advantage of the double crystal spectrometer is to be obtained, its geometrical resolving power must be greater than its physical resolving power, the latter being referred to the diffraction patterns. The geometrical resolving power has the value

$$\frac{\lambda}{d\lambda} = \frac{4}{\psi^2} \tag{19}$$

where

$$\psi = \frac{h_1 + h_2}{2L} \tag{20}$$

h_1 and h_2 being the heights of the two horizontal slits and L the distance between them. h_1 and h_2 were 1 mm or less and the distance L was 300 mm, which gives a maximal horizontal divergence of 0.003 radians and a geometrical resolving power larger than 90 000. On the assumption that the spectral lines and the rocking curves are of the Gaussian error shape (in fact they deviate very little from this), the physical resolving power can be referred to the crystal diffraction patterns and defined in the same way as in optical spectroscopy [23]. Hence two spectral details are resolved if the distance between them is equal to the full width of the rocking curve at half maximum intensity. Calculating $\lambda/d\lambda$ from the Bragg equation, we obtain

$$\frac{\lambda}{d\lambda} = \frac{\operatorname{tg}\vartheta}{w}. \tag{21}$$

ulating P, R, and w.

δ 10^6	β $\cdot 10^6$	$\frac{\beta}{\delta}$	Angular unit l in seconds	$A \cdot 10^6$	$B \cdot 10^6$	w''	$P \cdot 10^2$	$R \cdot 10^5$ radians
2.77	0.682	0.0299	10.72	−4.277	0.373	5.4	47	1.60
3.80	0.499	0.0265	9.43	−3.401	0.325	4.7	51	1.41
3.44	0.259	0.0193	7.65	−2.419	0.252	3.6	59	1.24
3.60	0.104	0.0121	5.95	−1.528	0.165	3.0	66	1.08
5.23	0.0469	0.0090	4.53	−0.934	0.109	2.3	67	0.84
1.80	0.0054	0.0030	2.61	−0.319	0.039	1.3	68	0.52
1.15	0.0025	0.0022	2.10	−0.203	0.026	1.0	68	0.41

The theoretical values of the physical resolving power given in Table 4 are calculated from the theoretical values of w computed earlier. They are much less than the geometrical resolving power. This could be seen experimentally, since a decrease of the slit height had no influence on the width and form of the rocking curves.

The parallelism of the two faces of the crystal plates was controlled by studying the number and appearance of the interference fringes, when the plate was illuminated with parallel monochromatic light. The exact orientation of the actual atomic plane in the plate was determined with X-rays in the way earlier described [1]. Experiments proved that a crystal plate could be removed from the holder and inserted again without changing the position of the reflecting plane more than about 10″–15″.

The X-ray tube and the A crystal were adjusted so as to obtain maximum intensity of the actual X-ray line both in the (1, −1) and the (1, 1) positions, before P, R, and w were determined. The intensity was registered during 30 seconds in each point. Each rocking curve was described five to ten times. The intensity of the top was kept at 3 000–5 000 counts per 30 sec.

The percent reflection P was determined by registering the intensity of the incident radiation and the intensity of the peak of the rocking curve alternatingly. The percent reflection and the width of the rocking curve proved to be more sensitive to a deviation from the parallelism of the two crystals than the double crystal coefficient of reflection was.

Table 4

The theoretical physical resolving power.

λ	Resolving power
2 498	23 000
2 285	23 000
1 932	24 000
1 537	23 000
1 205	23 000
708	23 000
558	23 000

Table 5

Measurements on quartz $11\bar{2}0$. w = the full width at half maximum intensity (seconds of arc), P = percent reflection, R = coefficient of reflection (in radians), S = the physical resolving power.

Line	Wave-length X.U.	w		$P \cdot 10^2$		$R \cdot 10^5$		S	
		exp.	theory	exp.	theory	exp.	theory	exp.	theory
V $K\alpha_1$	2 498	6.3	5.4	39	47	1.59	1.60	17 000	23 000
Cr $K\alpha_1$	2 285	5.2	4.7	45	51	1.48	1.41	19 000	23 000
Fe $K\alpha_1$	1 932	4.0	3.6	53	59	1.26	1.24	20 000	24 000
Cu $K\alpha_1$	1 537	3.4	3.0	55	66	1.10	1.08	19 000	23 000
Tl $L\alpha_1$	1 205	2.7	2.3	54	67	0.88	0.84	19 000	23 000
Mo $K\alpha_1$	708	2.3	1.3	48	68	0.58	0.52	13 000	23 000
Ag $K\alpha_1$	558	2.3	1.0	39	68	0.55	0.41	10 000	23 000

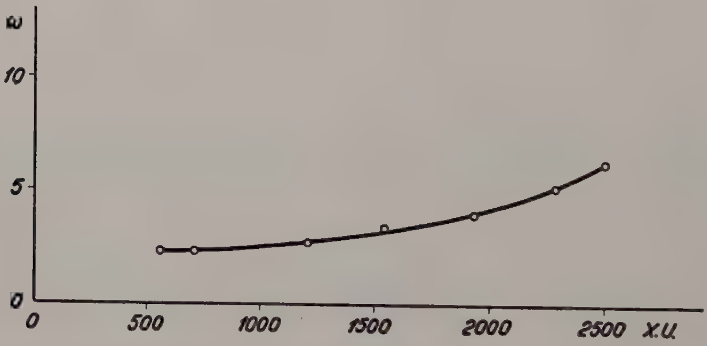

Fig. 5. The full widths of the rocking curves at half maximum intensity as a function of wave-length for plane $(11\bar{2}0)$.

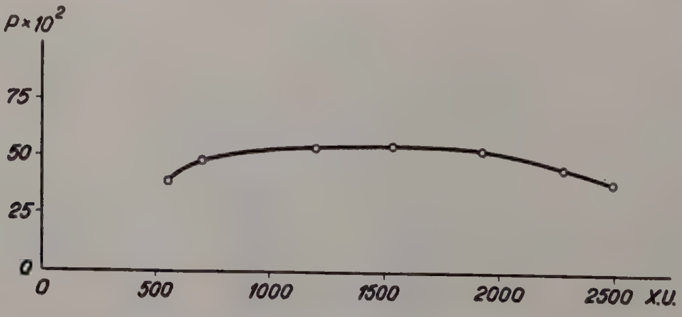

Fig. 6. The percent reflection as a function of wave-length for plane $(11\bar{2}0)$.

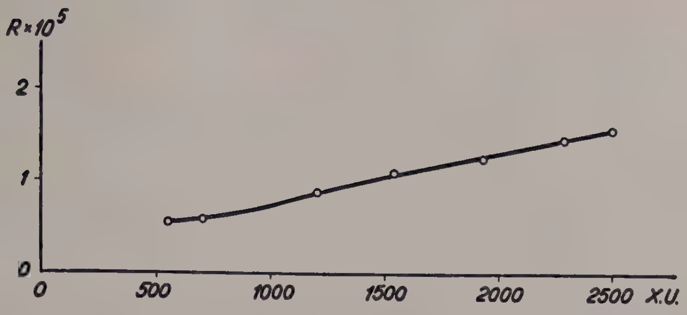

Fig. 7. The coefficient of reflection as a function of wave-length for plane $(11\bar{2}0)$.

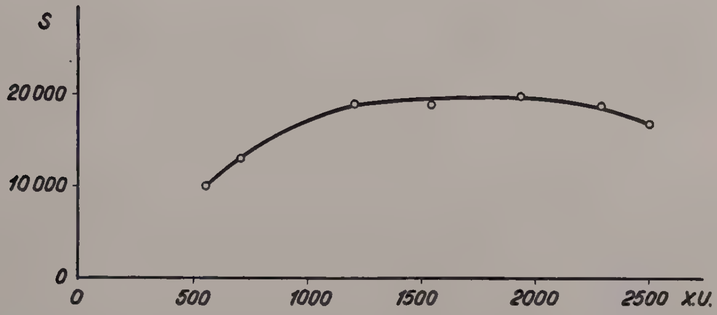

Fig. 8. The resolving power of the double-crystal spectrometer when using quartz $(11\bar{2}0)$.

Discussion of the results. The results of the experiments and of the calculations are given in Table 5 and Fig. 5–8. The experimental values of the widths of the rocking curves are larger than the calculated ones, but the opposite relation is valid as to the percent reflection. The agreement between experiments and calculations is very good as to the double crystal coefficient of reflection and the difference between them is always well within the experimental limit of error. The theoretical calculations were made under the assumption that quartz is a perfect crystal. The excellent agreement between theory and experiments states that this assumption must be correct.

This work was supported by a grant from the Swedish Natural Science Research Council (Statens Naturvetenskapliga Forskningsråd). I also wish to express my thanks to Mr L.-E. HAEGGBLOM for his assistance in the recordings with the double crystal spectrometer.

Department of Physics, University of Uppsala, Sept. 1952.

REFERENCES

1. G. Brogren, Arkiv för fysik, *3*, 507, 1951.
2. P. H. Wei, Zs. f. Krist. *92*, 355, 1935.
3. R. Brill, C. Hermann and C. Peters, Ann. d. Phys. *41*, 233, 1935.
4. R. W. James and G. W. Brindley, Phil. Mag. *12*, 81, 1931.
5. C. G. Darwin, Phil. Mag. *17*, 315 and 675, 1914.
6. P. P. Ewald, Ann. d. Phys. *54*, 419, 1918.
7. ——, Phys. Zs. *26*, 29, 1925.
8. ——, Phys. Zs. *27*, 182, 1926.
9. J. A. Prins, Zs. f. Phys. *63*, 477, 1930.
10. M. Kohler, Ann. d. Phys. *18*, 265, 1933.
11. M. von Laue, Erg. d. exakt. Naturw. *9*, 10, 1930.
12. A. H. Compton and S. K. Allison, X-Rays in Theory and Experiments, New York 1935.
13. A. Larsson, Uppsala universitets årsskrift. 1929.
14. Y. Tu, Phys. Rev. *40*, 622, 1932.
15. Landolt-Boernstein, Zahlenwerte und Funktionen etc. Sechste Auflage. Berlin 1950.
16. P. Debye, Ann. d. Phys. *43*, 49, 1914.
17. I. Waller, Zs. f. Phys. *17*, 398, 1923.
18. ——, Dissertation, Uppsala 1925.
19. ——, Ann. d. Phys. *79*, 261, 1926.
20. ——, Ann. d. Phys. *83*, 154, 1927.
21. ——, Zs. f. Phys. *51*, 213, 1928.
22. Internationale Tabellen zur Bestimmung von Kristallstrukturen, Bornträger, Berlin 1935.
23. S. K. Allison, Phys. Rev. *38*, 203, 1931.

Tryckt den 28 februari 1953

Uppsala 1953. Almqvist & Wiksells Boktryckeri AB

ARKIV FÖR FYSIK Band 6 nr 32

Communicated 27 February 1952 by ERIK HULTHÉN and G. BORELIUS

Determination of the diffusion length of thermal neutrons in graphite

By L. CARLBOM

With 8 figures in the text

Introduction

According to diffusion theory the diffusion length L is related to the transport mean free path λ_t and the absorption mean free path λ_a by the equation

$$L^2 = \frac{\lambda_a \cdot \lambda_t}{3}. \tag{1}$$

L is critically dependent on the presence of even small quantities of impurities, having a high neutron absorption cross section, as for example boron, which reduce λ_a, and L is thus a measure of the purity of the material, from the point of view of neutron physics.

Direct experimental measurements of L have been described in the open literature by HEREWARD, LAURENCE, PANETH and SARGENT (1), and by BOTHE and JENSEN (2). The author has also had access to an unpublished report on a determination of L which was carried out in the laboratories of the Commissariat à l'Énergie Atomique in Paris. HEREWARD and his collaborators found $L = 51 \pm 3$ cm, for a graphite of density 1.55 g/cm^3, while BOTHE and JENSEN found $L = 36 \pm 2$ cm for a graphite of density 1.68 g/cm^3.

The graphite used in the present investigation was manufactured by Skandinaviska Grafitindustri AB, Trollhättan, and had a density of 1.65 g/cm^3.

Method

Since no source of thermal neutrons is available it is necessary to start with fast neutrons and to slow them down in a moderator, which in this case was part of the graphite block in which the diffusion length was to be found. If the measurements are made at a sufficient distance from the source practically all the neutrons reaching the measurement region are thermal. In order to check whether the number of non-thermal neutrons reaching this region was enough to disturb the measurements, an additional experiment was made, in which a cadmium foil was interposed between the source and the measuring region. The differences between the two series of neutron density measurements were then used to calculate the diffusion length in the way described below. The difference in the values of L as calculated with and without this correction was small.

The graphite was built up into a parallelepiped having a square base and vertical sides. For a source-free region in such a geometry the diffusion equation for the neutron density ϱ:

$$\Delta\varrho - \frac{\varrho}{L^2} = 0 \tag{2}$$

can be solved, when the boundary conditions are given. This equation is however not valid at distances of the order of magnitude of one mean free path from the outer surfaces of the moderator. In this region the neutron density falls off approximately linearly, at a rate such that if it were to be extrapolated into the space outside the moderator it would reach zero at a distance 0.710 λ_t beyond the bounding planes provided that no neutrons are scattered back into the moderator.

If equation (2) is to be solved in cartesian coordinates it is thus convenient to take the coordinate planes 0.710 λ_t outside the geometric limits of the moderator. If $a = a_g + 2 \cdot 0.710\ \lambda_t$, where a_g is the length of the sides of the base, the solution, for the boundary conditions $\varrho = 0$ at

$$\begin{cases} x=0 \\ x=a \end{cases} \quad \begin{cases} y=0 \\ y=a \end{cases} \quad z=0 \qquad \text{can be written}$$

$$\varrho = \sum_{l,m} K_{l,m}(z) \sin\frac{l\pi x}{a} \sin\frac{m\pi y}{a} \tag{3}$$

where

$$K_{l,m}(z) = K'_{l,m} \operatorname{sh} \alpha_{l,m} \cdot z \tag{4}$$

and

$$\alpha^2_{l,m} = \frac{1}{L^2} + \frac{(l^2+m^2)\pi^2}{a^2}. \tag{5}$$

It follows from equation (4) that, if $K_{l,m}(z)$ can be determined for two different values of z

$$\frac{K_{l,m}(z_1)}{K_{l,m}(z_2)} = \frac{\operatorname{sh} \alpha_{l,m} \cdot z_1}{\operatorname{sh} \alpha_{l,m} \cdot z_2} \tag{6}$$

from which $\alpha_{l,m}$ can be found, and so, making use of equation (5), L can be calculated.

The measurements should thus be made in such a way that a Fourier coefficient $K_{l,m}(z)$ can be determined in at least two z-planes. From equation (5) it can be seen that for $l = m = 1$ the last term becomes as small as possible, and therefore the highest accuracy will result if K_{11} and α_{11} are determined. In the experimental measurement K_{11} was found for four different z-planes (see Fig. 1), giving six combinations for substitution in equation (6).

The neutron source was located on the vertical axis of the parallelepiped, and thus, because of the resulting symmetry, the terms in the Fourier expansion having even indices vanish.

$K_{11}(z_1)$ was determined from equation (3) by the measurement of several ϱ-values in the z_1-plane. In order to simplify the calculations the measuring points were chosen according to the formulae:

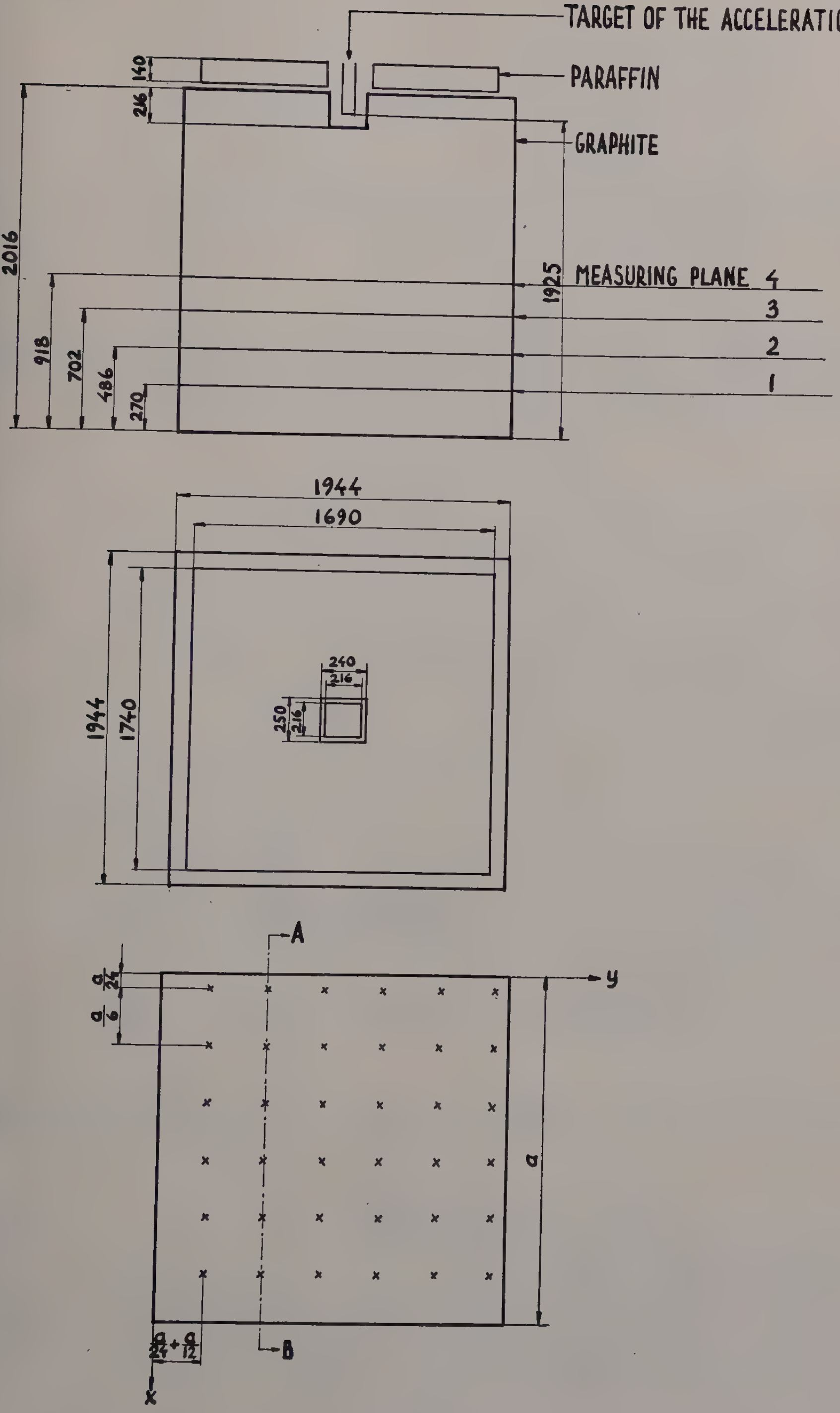
TARGET OF THE ACCELERATION TUBE
PARAFFIN
GRAPHITE
MEASURING PLANE 4
3
2
1
140
216
2016
918
702
486
270
1925
1944
1690
1944
1740
240
216
250
216
A
B
y
x
a
$\frac{a}{24}$
$\frac{a}{6}$
$\frac{a}{24}+\frac{a}{12}$

Fig. 1.

$$x_r = \frac{a}{2n} + r \cdot \frac{a}{n} \qquad r,\, s = 0,\, 1,\, \ldots\, (n-1).$$

$$y_s = \frac{a}{2n} + s \cdot \frac{a}{n} \qquad \text{and } n \text{ is an integer.}$$

If $\varrho_{r,\,s}$ are corresponding ϱ-values, then because of the symmetry:

$$\varrho_{r,\,s} = \varrho_{s,\,r} = \varrho_{n-r-1,\,s} = \varrho_{s,\,n-r-1} = \varrho_{r,\,n-s-1} = \varrho_{n-s-1,\,r} = \\ = \varrho_{n-r-1,\,n-s-1} = \varrho_{n-s-1,\,n-r-1}. \tag{7}$$

In order to obtain as much information as possible about the neutron distribution from a given number of measurements, and at the same time to test whether the system was fully symmetrical, the ϱ-values were measured at all even r-values and all odd s-values (Fig. 1). By substitution in equation (3) one obtains:

$$\varrho_{r,\,s} = \sum_{l,\,m} K_{l,\,m}(z) \sin\left(\frac{\pi l}{2n} + \frac{\pi l r}{n}\right) \sin\left(\frac{\pi m}{2n} + \frac{\pi m s}{n}\right) \qquad (l,\, m = 1,\, 3,\, \ldots).$$

From this equation $K_{l,\,m}(z)$ can be obtained:

$$K_{l,\,m}(z) = \frac{4}{n^2 \cos \dfrac{\pi l}{2n} \cos \dfrac{\pi m}{2n}} \cdot \sum_{r=0}^{n-1} \sum_{s=0}^{n-1} \varrho_{r,\,s} \sin \frac{\pi l r}{n} \sin \frac{\pi m s}{n}$$

and

$$K_{11}(z) = \frac{4}{n^2 \cos^2 \dfrac{\pi}{2n}} \sum_{r=0}^{n-1} \sum_{s=0}^{n-1} \varrho_{r,\,s} \sin \frac{\pi r}{n} \sin \frac{\pi s}{n}. \tag{8}$$

In the experiment 36 ϱ-values were measured in each z-plane, and $n = 12$

Since only ϱ-values at even r and odd s were measured (i e. ϱ-values at $r = 2\,p$ and $s = 2\,q + 1$, where $p,\, q = 0,\, 1 \ldots 5$), equation (8) can be written:

$$K_{11}(z) = \frac{1}{36 \cos^2 \dfrac{\pi}{24}} \sum_{p=0}^{5} \sum_{q=0}^{5} \left[\varrho_{2p,\,2q+1} \sin \frac{2\,p\,\pi}{12} \sin \frac{(2\,q+1)\,\pi}{12} + \right.$$

$$+ \varrho_{11-2p,\,2q+1} \sin \frac{(11-2\,p)\,\pi}{12} \sin \frac{(2\,q+1)\,\pi}{12} + \varrho_{2p,\,10-2q} \sin \frac{2\,p\,\pi}{12} \sin \frac{(10-2\,q)\,\pi}{12} +$$

$$\left. + \varrho_{11-2p,\,10-2q} \sin \frac{(11-2\,p)\,\pi}{12} \sin \frac{(10-2\,q)\,\pi}{12} \right].$$

Using equation (7) this expression reduces to:

$$K_{11}(z) = \text{const.} \cdot \sum_{p=0}^{5} \sum_{q=0}^{5} \varrho_{2p,\,2q+1} \cos \frac{(4\,q-9)\,\pi}{24} \cos \frac{(4\,p-11)\,\pi}{24}. \tag{9}$$

From equations (6) and (9) one obtains:

$$\frac{\operatorname{sh} \alpha_{11} z_1}{\operatorname{sh} \alpha_{11} z_2} = \frac{\sum\limits_{p=0}^{5} \sum\limits_{q=0}^{5} \varrho'_{2p,\,2q+1} \cos \frac{(4q-9)\pi}{24} \cos \frac{(4p-11)\pi}{24}}{\sum\limits_{p=0}^{5} \sum\limits_{q=0}^{5} \varrho''_{2p,\,2q+1} \cos \frac{(4q-9)\pi}{24} \cos \frac{(4p-11)\pi}{24}}. \tag{10}$$

ϱ' and ϱ'' are the ϱ-values in the z_1 and z_2 planes respectively. From equation (10) α_{11} can be calculated, and L then follows from equation (5):

$$L = \frac{1}{\sqrt{\alpha_{11}^2 - \frac{2\pi^2}{a^2}}}. \tag{11}$$

Experimental arrangement

The graphite pile

The graphite consisted of blocks of three different dimensions, 72 × 72 × 504, 72 × 72 × 576, and 108 × 108 × 648 mm. A few blocks of other sizes were used, for example round the hole for the introduction of the neutron source. The blocks were milled to tolerances of ± 0.05 mm for the two smaller dimensions, and ± 0.1 mm for the longer. The graphite was manufactured in two lots of approximately the same size, the blocks having the smaller dimensions being made from the first lot, and the larger ones from the second. The density of the first lot was 1.656 ± 0.006 g/cm^3, this being the average of the density of 15 blocks, while the average density of 48 bars made from the second lot was 1.640 ± 0.003 g/cm^3. The total weight of graphite used in the experiment was 12.5 metric tons.

Chemical and spectroscopic analyses have been made in order to determine the boron content of the graphite, since boron is the most dangerous impurity to be

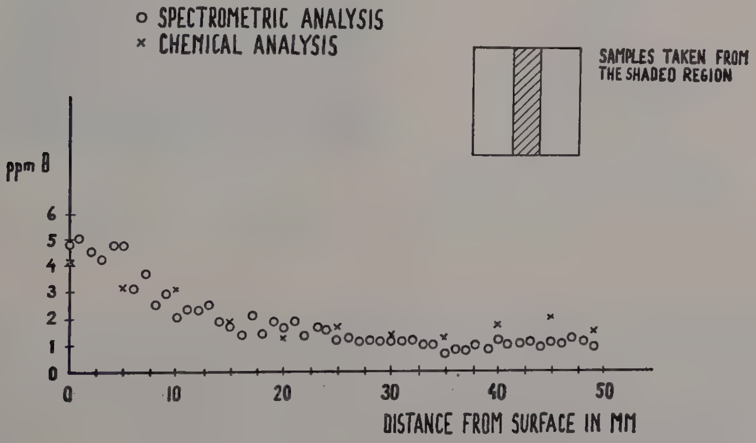

Fig. 2.

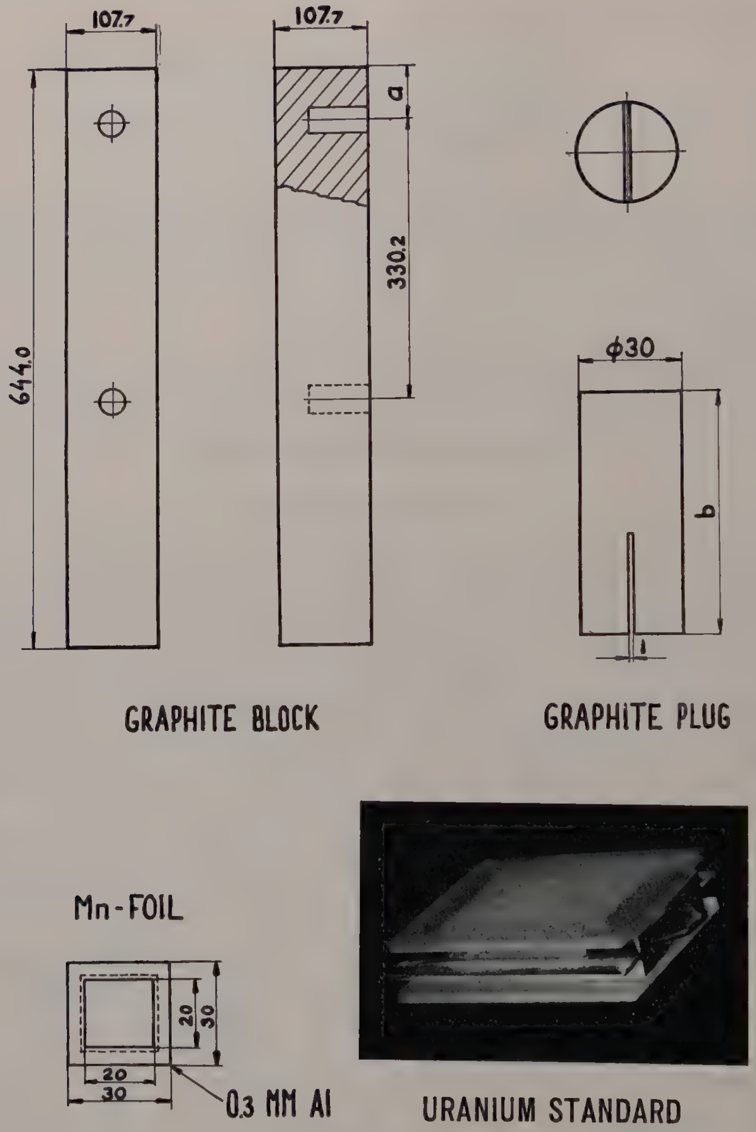

Fig. 3.

expected.[1] There was good agreement between analyses made by the two methods. Fig. 2 shows the boron content of samples taken at various depths from the surface of the central part of a machined graphite block from the second lot. There is a marked increase in boron content near the surface. In the outer part, which was milled

---

[1] The chemical analyses have been made at the chemical department of AB Atomenergi by miss T. Berggren. The spectrometric analyses have been made by dr. S. Landergren, Sveriges Geologiska Undersökning.

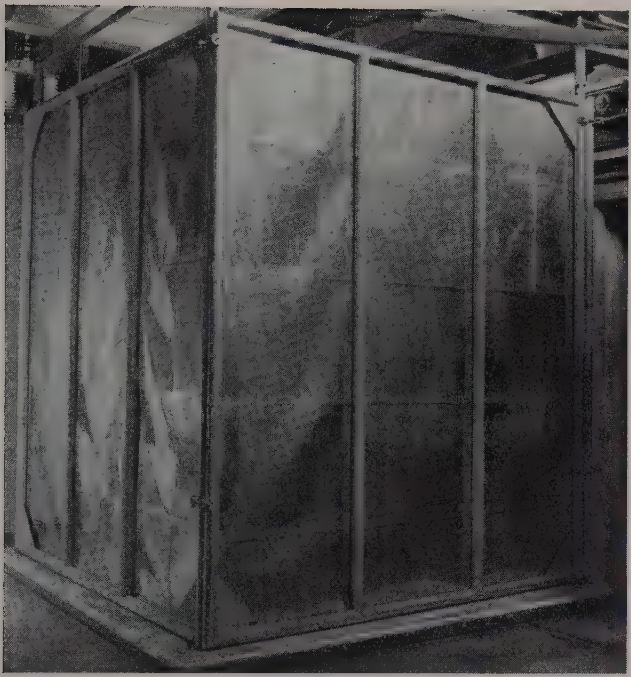

Fig. 4.

away during the machining process, the boron content varied greatly from block to block. In the second lot, in which the original block dimensions were 120 × 120 mm, it was between 1 and 42 ppm. It is clear that the boron impurities gather in the outer parts of the blocks during the manufacturing process, and for this reason it is very necessary to machine the surfaces of the blocks.

The dimensions of the parallelepiped in which the blocks were stacked are given in Fig. 1. The top of the pile was covered with a layer of paraffin wax, which acted as a neutron reflector and absorber. The Mn-Ni foils which were used as detectors were mounted in blocks dimensioned 107.7 × 107.7 × 648 mm, so that they could easily be slid in and out of the pile (Fig. 3). 72 blocks of this size were distributed amongst the four measuring planes. The graphite pile was surrounded on all vertical sides by 0.3 mm cadmium sheet, to reduce the number of thermal neutrons scattered back into the graphite (Fig. 4). Beneath the graphite was a 0.5 mm cadmium sheet, which lay on a flat concrete surface. The cadmium shields on two opposite faces of the pile were easily removable, so that the detector blocks could be withdrawn.

Neutron source

The neutron source was a 200 kV accelerator, in which a heavy ice target was bombarded with deuterons. This equipment has been described by Mr. N. G. SJÖSTRAND (3), who was responsible for its operation throughout the present experiment.

The mean neutron intensity varied between the limits 7–12 g Ra-Be equivalent.

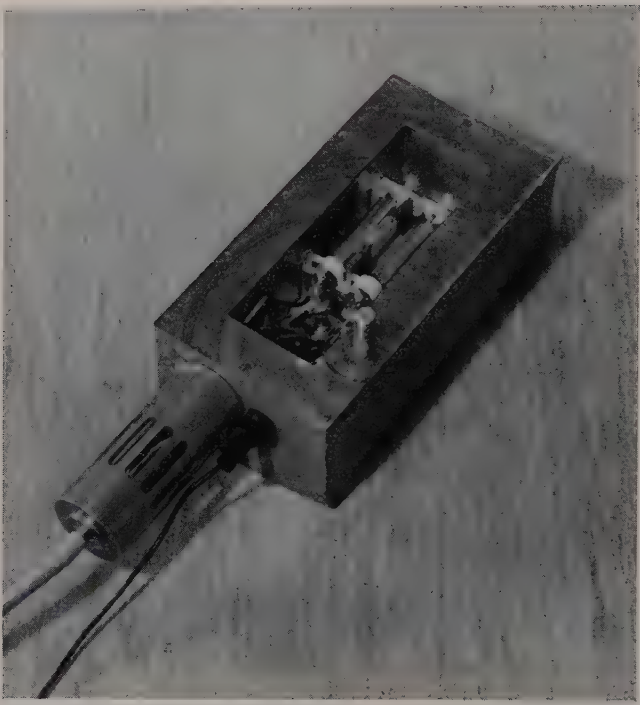

Fig. 5.

Neutron detectors

The neutron detectors consisted of 24 Mn-Ni foils, 20 × 20 × 0.2 mm, mounted in aluminium frames (Fig. 3). The alloy used, which consists of 90 % Mn and 10 % Ni, can conveniently be rolled into foils, while pure Mn cannot.[1] The half-life of the Mn^{56} formed by the capture of a slow neutron was found by measurement to be 154.9 ± 0.4 minutes. Ni^{65} is also formed, but the activation cross section for Ni^{64} is 2 barns, and nickel contains only 1.16 % of this isotope, while the cross section for manganese is 13 barns, so that the nickel activity is negligible. Moreover the half-life is 2.6 hours, which is very close to the half-life of manganese. The advantage of Mn as a detector lies in that its absorption cross section follows the 1/v law for energies up to several eV, and thus its efficiency as a detector is independent of energy for neutrons in the thermal region. Another advantage is that Mn^{56} emits hard β-rays, which can easily be counted by a GM tube with reasonably thin walls.

Geiger counter equipment

The activity of the Mn-Ni foils, which is a measure of the neutron density at the point where the foil was irradiated, was measured with pairs of β-sensitive GM tubes coupled in parallel. These tubes were mounted in lead screens, as shown in Fig. 5. The GM tubes were of the type described in an earlier publication (4). 8

---

[1] This alloy is due to Dr. L. KOWARSKI.

counting equipments were used, each consisting of a pair of GM tubes, a high tension set, and a scale of 64. The GM tubes were coupled to the scalers through cathode followers. Uranium glass standards were used in order to check the constancy of the GM tubes (Fig. 3). A measurement with a manganese foil in a double GM counter having solid angle 4π showed that the solid angle for the foils in the parallel counter arrangements was 34 %. The use of two GM tubes coupled in parallel has three advantages compared to a single tube: the effect of small displacements of the foil in the plane of the GM tubes is reduced, the resolving time of the two tubes is half that of the single tube, and the statistical error is 30 % less, when the same activity is counted for the same time.

Calibration of the foils and uranium standards

The resolving time τ of a GM counting equipment having two tubes coupled in parallel can be calculated from a knowledge of the resolving times τ_1 and τ_2 for the two tubes in the same equipment, when each tube in turn is alone connected. Because of the symmetry of the arrangement half the counting rate can be assumed to be due to each tube. If n' is the true pulse rate, and n is the counting rate registered, we find that:

$$n' = \frac{n}{2}\left(1+\frac{n}{2}\tau_1\right)+\frac{n}{2}\left(1+\frac{n}{2}\tau_2\right)=n\left[1+\frac{n}{4}(\tau_1+\tau_2)\right].$$

By comparison with the formula for a single GM tube, it follows that:

$$\tau=\frac{\tau_1+\tau_2}{4}.$$

When the impulses counted are due to an activated foil the correction formula becomes somewhat more complicated. If N_0 is the background counting rate, I' the true intensity of the radiation from the foil in the geometry in question, I_0' the initial intensity, N the number of impulses counted in time t, and n' the true number of β-particles passing through the GM tube, then:

$$N=\int_0^t (I'+N_0)\,[1-(I'+N_0)\,\tau]\,dt.$$

From this can be found, by making suitable approximations:

$$n'=(N-N_0 t)\left[1+\frac{N\lambda\tau(1+e^{-\lambda t})}{2(1-e^{-\lambda t})}\right].$$

τ_1 and τ_2 were determined by a method described by D. Willard and C. G. Montgomery (5). The GM tube was triggered by pairs of impulses from a 15 kV X-ray tube pulsed by a radar modulator, at a repetition frequency of about 175 pulses per second. One pulse of each pair could be shifted with respect to the other. When the interval between these pulses is large, the counting rate is twice the repetition frequency, but when the spacing is less than the resolving time of the apparatus only the first pulse of each pair is counted. Fig. 6 is a curve taken for one of the GM tubes.[1]

---

[1] The electronic equipment used for the determination of the resolving time was designed by Mr. R. Vestergaard.

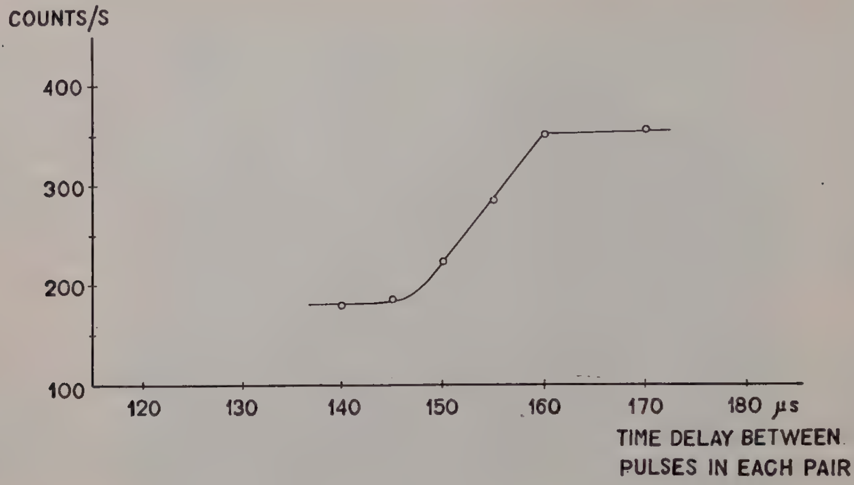

Fig. 6.

The intensity of the neutron generator was not constant during each irradiation period, so the calibrations were made using a 750 mg Ra-Be source. The neutron source was placed in the graphite pile, and a detector block selected such that a foil placed in it would receive a convenient activation. The 24 Mn-Ni foils were placed in turn in this block, each being irradiated for the same length of time, in the same geometry. The activities of the foils were measured by counting with them for a period of 64 minutes, beginning 8 minutes after the end of the irradiation. Each foil was assigned to the one of the counting equipments, in which it was always measured, and each equipment had its own uranium glass standard. The background and standard counting rates were measured before and after each foil measurement. Denoting the activities of the standard and of the foil by s and n respectively, a coefficient $k = s/n$ was defined for each foil, which is a measure of the efficiency of the foil as a detector. This method of calibration has the advantage that the depression in the neutron density caused by the introduction of the foil, which is proportional to the neutron density, is included in the detector coefficient. Since the foils are all of approximately the same size, and since the ratio between the measured neutron densities in two measuring planes is used in the calculation of L, the disturbance of the neutron distribution due to the introduction of the foils is in this case of no importance.

Measurements

The relative neutron intensities ϱ at the measuring points in the graphite pile were determined as follows. One foil was always placed at the same place in the graphite pile, and was used as a monitor, giving a measure of the integrated neutron intensity during the irradiation period. Seven other foils were distributed amongst the other measuring points, being arranged as far as possible so that no two foils were close together, and the neutron generator was then run for a period of 1–5 hours. The activity of each foil was subsequently measured for 64 minutes, and the counting equipments checked for background and standard counting rate. The

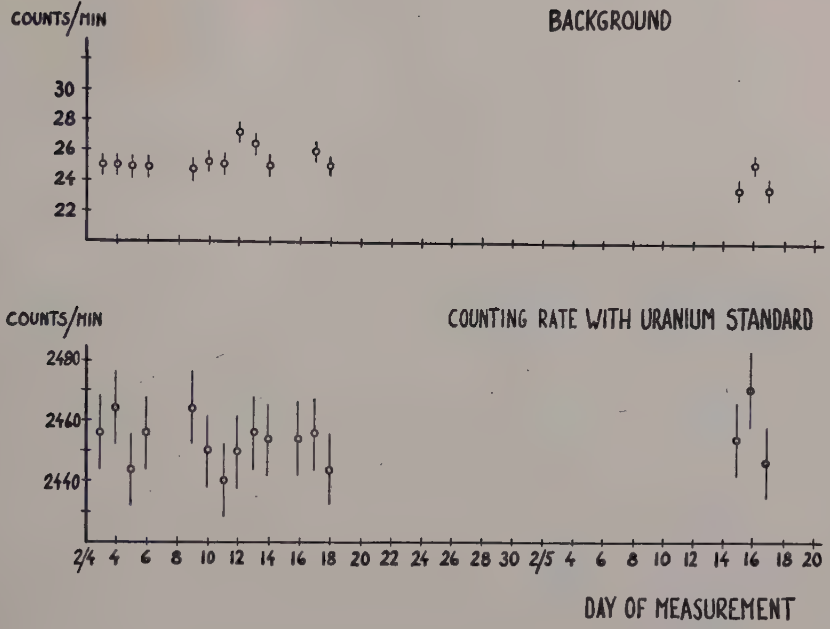

Fig. 7.

number of impulses counted, for a foil in the measuring position nearest the vertical axis of the pile, was about 20000 for the first measuring plane, 50000 for the second, 100000 for the third, and 200000 for the fourth. The normalized activity for the position i is defined as:

$$a_i = \frac{n_i}{s_i} \cdot k_i \cdot$$

If the normalized activity of the monitor foil is a_m, the relative neutron density is given by:

$$\varrho_i = \frac{a_i}{a_m} \cdot$$

Fig. 7 gives the background and standard activity as measured with one GM counting equipment, over many days, showing that the constancy was good.

The foils were placed horizontally in the detector blocks, but a special investigation showed that their activity was independent of orientation during irradiation. An investigation was also made to determine how much of the activity was due to neutrons having energies above the cadmium cut-off. A foil enveloped in 0.7 mm Cd sheet was placed in the top measuring plane. The activity was only 0.8 ‰ of that without the cadmium envelope, and the contribution of neutrons above the cadmium cut-off to the activation was thus very small.

Results

In order to calculate a, and thus L, it is necessary to know λ_t. Using experimental values given by Auger, Munn and Pontecorvo (6), λ_t for graphite of the density of

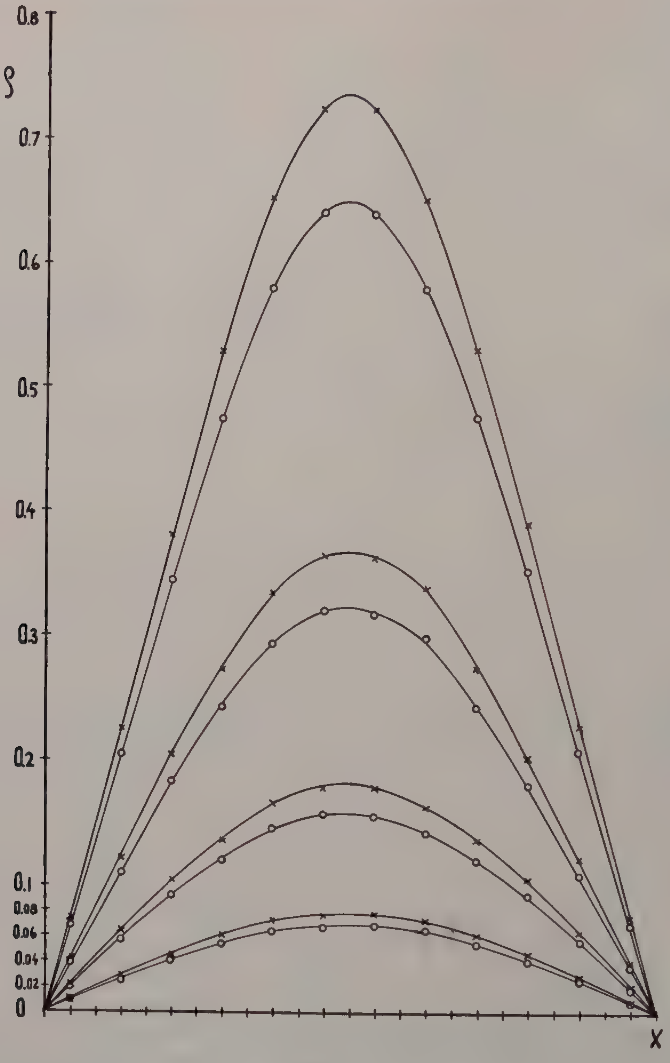

Fig. 8.

that used in the present measurements can be calculated to be 2.5 cm. A calculation of λ_t from σ_s for carbon gives $\lambda_t = 2.7$ cm. The average value 2.6 cm has been taken here.

In order to give an idea of the distribution of neutron density in the four measuring planes, the ϱ-values corresponding to $\begin{cases} p=0, \ldots 5 \\ q=1 \end{cases}$ and $\begin{cases} p=4 \\ q=0, \ldots 5 \end{cases}$ are plotted in Fig. 8 (marked as crosses). The resulting curves show the neutron distribution in the measuring planes, along a line parallel to the X-axis (the line AB in Fig. 1). If L_{ij} is the L-value calculated from the ϱ-values measured in the i and j planes, we find the following values for L:

$$L_{21} = 46.2 \pm 1.0 \text{ cm}$$
$$L_{31} = 45.2 \pm 0.4 \text{ cm}$$
$$L_{32} = 45.7 \pm 0.6 \text{ cm}$$
$$L_{41} = 46.4 \pm 0.2 \text{ cm}$$
$$L_{42} = 46.5 \pm 0.3 \text{ cm}$$
$$L_{43} = 47.2 \pm 0.5 \text{ cm}$$

The mean value is: $L = 46.3 \pm 0.2$ cm. The errors given are standard deviations.

A series of ϱ-determinations was made with a 0.1 mm cadmium sheet inserted in the graphite pile at a height of 1296 mm above its base. It was necessary to use a new monitor position above the cadmium sheet, and this was taken at a point 1620 mm from the base of the pile, 936 and 231 mm from the vertical sides. This monitor position was normalized with respect to that in the upper measuring plane which was used previously, by simultaneously irradiating two foils, one in each monitor position, before the cadmium sheet was put in. It was found that the insertion of the cadmium plate resulted in a disturbance in the neutron density at the upper monitor position of about 25 %, which had to be corrected for. This correction was determined by placing a Ra-Be source (850 mg Ra) close to the target, and measuring the activation at the upper monitor position with and without the cadmium sheet.

The number of pulses counted with foils which had been irradiated at the measuring points nearest the vertical axis were, for plane 1 about 1900, plane 2 about 5400, plane 3 about 12000 and for plane 4 about 30000. In Fig. 8 the differences between the ϱ-values found without and with the cadmium sheet are marked as circles. The following values for L are calculated from these differences.

$$L_{21} = 45.7 \pm 1.1 \text{ cm}$$
$$L_{31} = 45.3 \pm 0.4 \text{ cm}$$
$$L_{32} = 44.9 \pm 0.7 \text{ cm}$$
$$L_{41} = 45.5 \pm 0.3 \text{ cm}$$
$$L_{42} = 45.4 \pm 0.3 \text{ cm}$$
$$L_{43} = 45.9 \pm 0.6 \text{ cm}$$

The mean value is $L = 45.4 \pm 0.2$ cm

Discussion of the results and sources of error

The expression "thermal neutrons" is not always welldefined, and this is especially so in graphite, in which "cold" neutrons arise. In this case the thermal neutron energy spectrum must depend on the geometry used. Since L depends on the energy of the neutrons, a determination of L made in the way described above will give a mean value corresponding to the energy spectrum in the region in which the measurements are made.

L is also dependent on the presence of neutron-absorbing impurities in the graphite. One can easily calculate that a content of 1 ppm of boron, which is the most dangerous impurity in this respect, would reduce the diffusion length by about 8 %.

The difference method for making measurements with thermal neutrons, as described above, has often been used, but the results show that in many cases a well-defined thermal neutron spectrum was not produced. The factors which influence the energy spectrum, in such difference experiments, are the following: the energy spectrum of the neutrons in the region where the cadmium sheet is placed, the energy dependence of the cadmium absorption cross section, the thickness of the cadmium sheet, and the geometry of the experimental arrangement.[1] However, even if the method does not give a well-defined neutron spectrum, it gives, in the present case, a reduction in the number of epithermal neutrons at the measuring planes.

All the values for L as found by the two methods agree well, with the exception of the L_{4j} values found by the direct method. This seems to indicate that the number of epithermal neutrons in plane 4 is not negligible, but that their effect is eliminated by the cadmium difference method. The discrepancies are small, however, and the possiblity remains that they may be due to errors in the measurements.

The best value for the diffusion length for thermal neutrons in graphite, as found by this experiment, is thus 45.4 ± 0.2 cm, where the error given is the standard deviation.

The disagreement between the values for L found by combinations of measurements from the various measuring planes is not large, using the cadmium difference method, which indicates that the effect of the geometry is small. Impurities in the graphite, on the other hand, have a considerable effect on the value of L, and the accuracy of the present method is such that an impurity content greater than the equivalent of 0.5 ppm of boron causing a decrease in the diffusion length of 4 % can be estimated with certainty.

ACKNOWLEDGEMENTS

This experiment was performed at AB Atomenergi, Department of Physics. I want to thank the director of this department, Dr. S. Eklund, for his encouraging interest in this investigation. I also want to thank the crew of the acceleration tube and especially Mr. Å. Franzon for a valuable technical assistance.

REFERENCES

1. H. G. Hereward, G. C. Laurence, H. R. Paneth, B. W. Sargent: Can. J. of Res. A *25*, 15 (1947).
2. W. Bothe, P. Jensen: Zeitschrift für Physik *122*, 749 (1944).
3. N. G. Sjöstrand: Appl. Scient. Research B *2*, 227 (1951).
4. L. Carlbom, C. Taylor: J. Sci. Instr. *29*, 296 (1952).
5. D. Willard, C. G. Montgomery: Rev. Sci. Instr. *21*, 520 (1950).
6. P. Auger, A. M. Munn, B. Pontecorvo: Can. J. of Res. A *25*, 143 (1947).

---

[1] An investigation on these problems by Mr. N. G. Sjöstrand is going on in this laboratory.

Tryckt den 2 mars 1953

Uppsala 1953. Almqvist & Wiksells Boktryckeri AB

ARKIV FÖR FYSIK Band 6 nr 33

Communicated 12 November 1952 by Oskar Klein and Hilding Faxén

Space reflection, time reversal and charge conjugation of spinor fields

By H. A. S. Eriksson

§ 1. Introductory remarks as to the basis and purpose of the present investigation

If invariance of the Lagrange density (L) with respect to time reversal as well as the existence of a corresponding linear transformation of the components of ψ (— and a similar transformation of the components of ψ^*, *i.e.* the transformation shall be reducible in the composed $\{\psi, \psi^*\}$-space) is postulated, then ψ must be composed of 8 components. (Cf. a previous paper by the author, (1), where the arguments for a theory with 8 components are formulated in another manner). However, in the present paper we will (— according to the customary view) consider wave functions with 4 components, thus omitting one of the above-mentioned two requirements. It will be shown that if the former requirement is omitted, *i.e.* if we permit that $L \to -L$ under those two kinds of discontinous Lorentz transformations, which can continously (– *i.e.* by means of a rotation of the four-dimensional space) be transferred either to the inversion $\boldsymbol{x} \to \boldsymbol{x}$, $t \to -t$ or to the inversion $\boldsymbol{x} \to -\boldsymbol{x}$, $t \to -t$ (— but not to the inversion $\boldsymbol{x} \to -\boldsymbol{x}$, $t \to t$), then the theory will describe only particles with vanishing rest-mass. Thus we are led to require the invariance of L with respect to all Lorentz transformations, including the three kinds of discontinuous transformations (inversions).

Recently the question, whether four or two representations of space reflection exist, has become urgent. As to the representation of time reversal, there exists much obscurity in the literature. We hope that the present investigation (— and the results obtained by Caianiello) will help to clarify these two questions.

§ 2. Spinor representation

As pointed out in (1) the behaviour under space reflection may be suitably studied by means of the spinor representation of rotations of the five-dimensional space, but, if moreover the behaviour under time reversal is to be studied, a spinor representation of rotations of the six-dimensional space (— where the sixth coordinate is of the same nature as the time coordinate) should be built up. The spinor representation of rotations of the five-dimensional space is given in a previous paper by the author, (2). Contrary to the current view, but in accordance with the result recently obtained by Caianiello, (3), only two representations (— if the ambiguity of sign is taken into account) of space reflection were obtained in (2). The reason for that will be clear from the considerations at the end of this section, where it will be shown that it was due to a certain requirement (— not explicitly pronounced, it is true), which seems to be unnecessary. After omitting this requirement a new possibility will appear. (However, in § 4 it will turn out that this can be used only if time reversal is not included in the Lorentz transformations).

In order to investigate whether a generalization of the representation of space reflection *a priori* is possible, we try to introduce a constant factor j into the 'space reflection part' of the spinor transformation in (2), p. 6:

$$\begin{cases} u_1' = -\varphi^* u_1 - \lambda^* u_2 + j\alpha u_3 + j\beta u_4 \\ u_2' = -\varepsilon^* u_1 - \psi^* u_2 + j\gamma u_3 + j\delta u_4 \\ u_3' = -j\delta^* u_1 - j\gamma^* u_2 - \psi u_3 - \varepsilon u_4 \\ u_4' = -j\beta^* u_1 - j\alpha^* u_2 - \lambda u_3 - \varphi u_4. \end{cases}$$

A further generalization is necessary for the investigation of time reversal. The spinor representation of rotations of the six-dimensional space has been built up (— but not yet published). The calculations are very extensive and, therefore, we will not give them here in the general case, but since the special result, which appeared after specialization from six-dimensional to five-dimensional space, is very easily understood we can use it here without puzzling the reader.

At first we notice that the 'Lorentz transformation ' in six-dimensional space

$$A'^{\mu} = a^{\mu}{}_{\nu} A^{\nu} \qquad (\mu, \nu = 1, \ldots.. 6)$$

after the above-mentioned specialization is broken up into the following two parts:

1) a five-dimensional 'Lorentz transformation'

$$A'^{\mu} = a^{\mu}{}_{\nu} A^{\nu} \qquad (\mu, \nu = 1, \ldots.. 5)$$

2) the transformation

$$A'^{6} = a^{6}{}_{6} A^{6}.$$

When building up a spinor formalism by means of the Cayley parameters the determinant must necessarily be = + 1. Thus

$$\Delta_6 = \Delta_5 \, a^6{}_6 = +1,$$

where Δ_k ($k = 5{,}6$) is the determinant of the 'Lorentz transformation' in k-dimensional space.

The investigation of time reversal in five-dimensional space and thus also in four-dimensional space (— note that it is discontinuous in five-dimensional as well as in four-dimensional space, whereas space reflection is discontinuous in four-dimensional space but continuous in five-dimensional space) is now rendered possible, since Δ_5 can assume also the value $-1 (a^6{}_6 = -1)$.

Is turned out that Δ_5 appeared as a factor as follows:

If A^μ $(\mu = 1, \ldots.. 5)$ is a contravariant five-vector and

$$\left\{\begin{array}{l} B_1 = A^1 + i\,A^2 \\ B_2 = A^1 - i\,A^2 \\ B_3 = -A^3 + A^4 \; (A^4 = -A_4) \\ B_4 = A^3 + A^4 \\ B_5 = A^5 \end{array}\right.$$

then the matrix $((b_{ik}))$ of the transformation of the B-quantities became (— Cf. (2), p. 5):

$$((b_{ik})) = \left\{\begin{array}{l} \psi^*\varphi + \alpha^*\delta,\ \varepsilon^*\lambda + \beta^*\gamma,\ \Delta_5(\psi^*\lambda + \alpha^*\gamma),\ \Delta_5(\varepsilon^*\varphi + \beta^*\delta),\ 2\Delta_5(\delta\lambda - \gamma\varphi) \\ \lambda^*\varepsilon + \gamma^*\beta,\ \varphi^*\psi + \delta^*\alpha,\ \Delta_5(\lambda^*\psi + \gamma^*\alpha),\ \Delta_5(\varphi^*\varepsilon + \delta^*\beta),\ 2\Delta_5(\delta^*\lambda^* - \gamma^*\varphi^*) \\ \psi^*\varepsilon + \gamma^*\delta,\ \varepsilon^*\psi + \delta^*\gamma,\ \Delta_5(\psi^*\psi + \gamma^*\gamma),\ \Delta_5(\varepsilon^*\varepsilon + \delta^*\delta),\ 2\Delta_5(\delta\psi - \gamma\varepsilon) \\ \lambda^*\varphi + \alpha^*\beta,\ \varphi^*\lambda + \beta^*\alpha,\ \Delta_5(\lambda^*\lambda + \alpha^*\alpha),\ \Delta_5(\varphi^*\varphi + \beta^*\beta),\ 2\Delta_5(\beta\lambda - \alpha\varphi) \\ \gamma^*\varphi - \alpha^*\varepsilon,\ \varphi^*\gamma - \varepsilon^*\alpha,\ \Delta_5(\gamma^*\lambda - \alpha^*\psi),\ \Delta_5(\delta^*\varphi - \beta^*\varepsilon),\ \Delta_5[1 - 2(\alpha\delta - \beta\gamma)]. \end{array}\right\}$$

After a subsequent specialization from five-dimensional to four-dimensional space it turned out that for Lorentz transformations, which by means of a rotation of the four-dimensional space can be transferred

a) to the identical transformation, we have

$$\alpha = \beta = \gamma = \delta = 0;\ \Delta_5 = \Delta_4 = 1$$

b) to space reflection, we have

$$\psi = \varphi = \lambda = \varepsilon = 0;\ \Delta_5 = 1,\ \Delta_4 = -1 \text{ (Cf. (2), p. 8)}$$

c) to time reversal, we have

$$\psi = \varphi = \lambda = \varepsilon = 0;\ \Delta_5 = \Delta_4 = -1$$

d) to space reflection and time reversal, we have

$$\alpha = \beta = \gamma = \delta = 0;\ \Delta_5 = -1,\ \Delta_4 = 1.$$

The following special cases are of interest (– for the sake of brevity the ambiguity of sign is disregarded):

a′) identical transformation

$$\psi = \varphi = -1,\ \lambda = \varepsilon = 0$$

b′) space reflection

$$\alpha = i,\ \delta = -i,\ \beta = \gamma = 0$$

c′) time reversal

$$\alpha = \delta = 1,\ \beta = \gamma = 0$$

d′) space reflection and time reversal

$$\varphi = i,\ \psi = -i,\ \lambda = \varepsilon = 0.$$

The appearance of the factor Δ_5 in the matrix $((b_{ik}))$ is now easily understood. For, owing to this factor, $A^\mu (\mu = 1, \ldots\ldots 4)$ behaves like a four-vector not only under the transformations (a) and (b) but also under (c) and (d).

The aforementioned considerations have nothing to do with spinors ($\psi, \varphi, \alpha, \beta, \ldots\ldots$ etc. are connected with the Cayley parameters, which in their turn are connected with the transformation coefficients $a^\mu_{\ \nu}$).

Thereafter the spinor representation of rotations of the six-dimensional space was built up. After specialization from six-dimensional to five-dimensional space the following generalized spinor representation of rotations of the five-dimensional space together with representation of the two types of discontinuous time reversal appeared:

$$\begin{cases} u'_1 = -\varphi^* u_1 - \Delta_5 \lambda^* u_2 + j\alpha u_3 + \Delta_5 j\beta u_4 \\ u'_2 = -\varepsilon^* u_1 - \Delta_5 \psi^* u_2 + j\gamma u_3 + \Delta_5 j\delta u_4 \\ u'_3 = -j\delta^* u_1 - \Delta_5 j\gamma^* u_2 - \psi u_3 - \Delta_5 \varepsilon u_4 \\ u'_4 = -j\beta^* u_1 - \Delta_5 j\alpha^* u_2 - \lambda u_3 - \Delta_5 \varphi u_4 . \end{cases}$$

On using the relations between the coefficients of this transformation (— see (2), p. 4; it turned out that these relations still hold after the generalization) one finds the following expression for its determinant:

$$d = [\psi\varphi - \lambda\varepsilon + j^2(\alpha\delta - \beta\gamma)]^2.$$

Now, one of the relations just mentioned reads as follows:

$$\psi\varphi - \lambda\varepsilon + \alpha\delta - \beta\gamma = 1.$$

Thus, if we require that $d = 1$ (— *i.e.* the usual requirement of modularity of a spinor representation) for a general rotation of the five-dimensional space, it is necessary that $j^2 = 1$.

However, if the world is four-dimensional and we, therefore, consider only those spinor transformations, which correspond to four-dimensional Lorentz transformations (— *i.e.* the transformations a, b, c, d in the preceding), one of the following two cases must occur:

a, d) $\alpha = \beta = \gamma = \delta = 0$, whence $\psi\varphi - \lambda\varepsilon = 1$

b, c) $\psi = \varphi = \lambda = \varepsilon = 0$, whence $\alpha\delta - \beta\gamma = 1$.

It is seen that the unimodularity is secured, even if the less restrictive condition $j^4 = 1$ is satisfied.

If $j^2 = 1$, those spinor transformations, which correspond to the two types (a) and (b) of four-dimensional Lorentz transformations, can be continuously transferred into each other by means of rotations of the five-dimensional space, but if $j^2 = -1$, they cannot.

The result obtained by the author in (2), that only two representations of space reflection (— corresponding to $j^2 = 1$) are possible, is obviously due to the method of employing the five-dimensional space as a continuous conjunction between the identical transformation and space reflection.

In the following we do not require a corresponding continuous conjunction also in the spinor representation, and therefore we start with the condition

$$j^4 = 1.$$

(However, we cannot suppress the feeling that the condition $j^2 = 1$ is more attractive from a mathematical point of view).

§ 3. Construction of vectors and scalars

Let u and v be two four-spinors.

On using the formula for the matrix $((b_{ik}))$, where, on account of the limitation to the four-dimensional space, either $\alpha = \beta = \gamma = \delta = 0$ or $\psi = \varphi = \lambda = \varepsilon = 0$, it can be seen that the following bilinear forms

$$\begin{cases} A^1 = u_1 v_3 + u_2 v_4 - j^2 u_3 v_1 - j^2 u_4 v_2 \\ A^2 = i(u_1 v_3 - u_2 v_4 - j^2 u_3 v_1 + j^2 u_4 v_2) \\ A^3 = u_1 v_4 - u_2 v_3 + j^2 u_3 v_2 - j^2 u_4 v_1 \\ A^4 = u_1 v_4 + u_2 v_3 - j^2 u_3 v_2 - j^2 u_4 v_1 \end{cases}$$

behave like the components of a contravariant four-vector.

Now we notice that if the spinor transformation is written in concentrated form

$$u' = Tu$$

and we introduce the notation

$$w = \begin{pmatrix} \bar{u}_4 \\ \bar{u}_3 \\ -j^2 \bar{u}_2 \\ -j^2 \bar{u}_1 \end{pmatrix},$$

then w is transformed according to

$$w' = \Delta_5 T w.$$

Thus, if in the four-vector A, u is replaced by w, all the coefficients $a^{\mu}_{\ \nu}$ of the transformation are multiplied by the factor Δ_5. For the quantity C so obtained we introduce the name *quasi-vector*. (Compare the name pseudo-vector, if the factor Δ_4 appears).

$$\begin{cases} C^1 = \bar{u}_1 v_2 + \bar{u}_2 v_1 + \bar{u}_3 v_4 + \bar{u}_4 v_3 \\ C^2 = -i(\bar{u}_1 v_2 - \bar{u}_2 v_1 + \bar{u}_3 v_4 - \bar{u}_4 v_3) \\ C^3 = \bar{u}_1 v_1 - \bar{u}_2 v_2 - \bar{u}_3 v_3 + \bar{u}_4 v_4 \\ C^4 = \bar{u}_1 v_1 + \bar{u}_2 v_2 + \bar{u}_3 v_3 + \bar{u}_4 v_4 . \end{cases}$$

(If time reversal is disregarded, C behaves like an ordinary four-vector).

Further it is found that the quantity

$$n = u_1 v_2 - u_2 v_1 + j^2 u_3 v_4 - j^2 u_4 v_3$$

is transformed according to

$$n' = \Delta_5 \, n.$$

Thus, n is a *quasi-scalar.*

Then, on replacing u by w, it is seen that

$$m = \bar{u}_1 v_3 - \bar{u}_2 v_4 - \bar{u}_3 v_1 + \bar{u}_4 v_2$$

is a scalar.

§ 4. Lagrangian, wave equations and transformation properties of the wave function

At first we notice that the quasi-scalar n vanishes for $v = u$. A theory with quasi-invariant Lagrangian can therefore describe only particles with vanishing rest-mass. Since the Lagrangian cannot be invariant for some particles and quasi-invariant for other particles, we conclude that it must be invariant. Thus A (– and not C) is to be used, when constructing that part of the Lagrangian, which contains the derivatives. The differentiation symbol $\partial_\mu (= \partial / \partial x^\mu)$ is therefore to be put between the two factors in each term of A^μ, and then v is to be equated to u. On summing with respect to μ it is seen that the case $j^2 = -1$ gives a four-divergence. Thus only the case $j^2 = 1$ can be used. From that we infer that A vanishes for $v = u$. Thus C must be used, when constructing that part of the Lagrangian, which contains the electromagnetic interaction. From that we conclude that the electromagnetic potential U must behave like a quasi-vector. (Cf. CAIANIELLO, (7), p. 752). Finally we notice that there are two possible forms for the Lagrangian, since that part which contains the derivatives is complex. The two cases can be treated simultaneously by introducing a quantity k, which can assume the values ± 1 and $\pm i$.

The Lagrange density to start with is then

$$L = ik^3\{u_1[(\partial_1 + i\partial_2)u_3 + (\partial_3 + \partial_4)u_4] + u_2[(\partial_1 - i\partial_2)u_4 - (\partial_3 - \partial_4)u_3] + u_3[-(\partial_1 + i\partial_2)u_1 + (\partial_3 - \partial_4)u_2] + u_4[-(\partial_1 - i\partial_2)u_2 - (\partial_3 + \partial_4)u_1]\} + \text{compl. conj.} + 2i\varkappa(\bar{u}_1 u_3 - \bar{u}_2 u_4 - \bar{u}_3 u_1 + \bar{u}_4 u_2) + 2U_1(\bar{u}_1 u_2 + \bar{u}_2 u_1 + \bar{u}_3 u_4 + \bar{u}_4 u_3) - 2U_2 i(\bar{u}_1 u_2 - \bar{u}_2 u_1 + \bar{u}_3 u_4 - \bar{u}_4 u_3) + 2U_3(\bar{u}_1 u_1 - \bar{u}_2 u_2 - \bar{u}_3 u_3 + \bar{u}_4 u_4) + 2U_4(\bar{u}_1 u_1 + \bar{u}_2 u_2 + \bar{u}_3 u_3 + \bar{u}_4 u_4).$$

(The coupling factor is included in U_μ).

The following wave equations are derived from L:

$$\begin{cases} (\partial_1 + i\partial_2)u_1 - (\partial_3 - \partial_4)u_2 + ik(U_1 + iU_2)\bar{u}_4 - ik(U_3 - U_4)\bar{u}_3 - k\varkappa\bar{u}_1 = 0 \\ (\partial_1 - i\partial_2)u_2 + (\partial_3 + \partial_4)u_1 + ik(U_1 - iU_2)\bar{u}_3 + ik(U_3 + U_4)\bar{u}_4 + k\varkappa\bar{u}_2 = 0 \\ (\partial_1 + i\partial_2)u_3 + (\partial_3 + \partial_4)u_4 - ik(U_1 + iU_2)\bar{u}_2 - ik(U_3 + U_4)\bar{u}_1 - k\varkappa\bar{u}_3 = 0 \\ (\partial_1 - i\partial_2)u_4 - (\partial_3 - \partial_4)u_3 - ik(U_1 - iU_2)\bar{u}_1 + ik(U_3 - U_4)\bar{u}_2 + k\varkappa\bar{u}_4 = 0. \end{cases}$$

In order to obtain a gauge invariant form of the theory (— or to write the equations as Dirac equations) the following substitution is suitable:

$$\begin{cases} \varphi_1 = u_1 - k\,\bar{u}_4 \\ \varphi_2 = u_2 - k\,\bar{u}_3 \\ \varphi_3 = u_3 + k\,\bar{u}_2 \\ \varphi_4 = u_4 + k\,\bar{u}_1 \end{cases}$$

i.e.:

$$\varphi = u - kw.$$

Hence

$$\begin{cases} (D_1 + i\,D_2)\varphi_1 - (D_3 - D_4)\varphi_2 - \varkappa\varphi_4 = 0 \\ (D_1 - i D_2)\varphi_2 + (D_3 + D_4)\varphi_1 + \varkappa\varphi_3 = 0 \\ (D_1 + i D_2)\varphi_3 + (D_3 + D_4)\varphi_4 + \varkappa\varphi_2 = 0 \\ (D_1 - i\,D_2)\varphi_4 - (D_3 - D_4)\varphi_3 - \varkappa\varphi_1 = 0, \end{cases}$$

where D_μ stands for $\partial_\mu - i\,U_\mu$.

A more familiar form is obtained by means of the subsequent substitution:

$$\begin{cases} \psi_1 = \varphi_1 - i\,\varphi_3 \\ \psi_2 = \varphi_2 + i\,\varphi_4 \\ \psi_3 = \varphi_1 + i\,\varphi_3 \\ \psi_4 = \varphi_2 - i\,\varphi_4 \end{cases}$$

Hence

$$(D_4 + \boldsymbol{\alpha}\cdot\boldsymbol{D} + i\varkappa\beta)\psi = 0,$$

where α_1, α_2, α_3, β are the usual specialized Dirac matrices:

$$\alpha_k = \begin{pmatrix} 0 & \sigma_k \\ \sigma_k & 0 \end{pmatrix}, \qquad \beta = \begin{pmatrix} 1_2 & 0 \\ 0 & -1_2 \end{pmatrix}$$

$$\sigma_1 = \begin{pmatrix} 0 & 1 \\ 1 & 0 \end{pmatrix}, \qquad \sigma_2 = \begin{pmatrix} 0 & -i \\ i & 0 \end{pmatrix}, \qquad \sigma_3 = \begin{pmatrix} 1 & 0 \\ 0 & -1 \end{pmatrix}.$$

On inserting in the gereralized spinor representation the values of Δ_5, α, β, γ, δ, ψ, φ, λ, ε given in § 2 for the special transformations a', b', c', d' we infer that these transformations induce the following transformations of ψ:

$$a'\ (\boldsymbol{x} \to \boldsymbol{x},\ t \to t):\ \psi \to \psi$$

$$b'\ (\boldsymbol{x} \to -\ \boldsymbol{x},\ t \to t):\ \psi \to -\,j\beta\psi$$

$$c'\ (\boldsymbol{x} \to \boldsymbol{x},\ t \to -\ t):\ \psi \to -\,jk\alpha_3\alpha_1\overline{\psi} = -\,jk\alpha_3\alpha_1 K\psi$$

(K denotes the operation of complex-conjugation).

$$d'\ (\boldsymbol{x} \to -\ \boldsymbol{x},\ t \to -\ t):\ \psi \to -\ k\beta\alpha_3\alpha_1 K\psi$$

(We remember that $j^2 = 1$, $k^4 = 1$).

In order to investigate the charge conjugation we consider the wave equations in the u-variables. It is readily shown that these equations remain invariant, except that U changes its sign, if $u_1 \to \pm ik\bar{u}_4$, $u_2 \to \pm ik\bar{u}_3$, $u_3 \to \pm ik\bar{u}_2$, $u_4 \to \pm ik\bar{u}_1$. Thus, charge conjugation corresponds to the following transformation:

$$ch:\quad \psi \to \psi^{ch} = \pm ik\beta\alpha_2 K\psi$$

For later use we calculate the transformation composed of time reversal and charge conjugation:

$$c' + ch: \quad \psi \rightarrow \pm j i \alpha_1 \alpha_2 \alpha_3 \beta \psi$$

§ 5. Comparison with the results of other authors

Ever since 1936–37, when the papers by PAULI, (4), and RACAH, (5), appeared, it has been customary to believe that the following four representations of space reflection are possible with consideration to the theory of relativity:

$$\psi \rightarrow \varrho_s \beta \psi,$$

where $\varrho_s = \pm 1$ or $= \pm i$.

Recently it has been pointed out by YOUNG and TIOMNO, (6), and by CAIANIELLO, (7), (8), (9), that the number of possible values of ϱ_s is of importance when investigating the possibility of a universal Fermi-type interaction. YOUNG and TIOMNO have based their investigation on the possibility of assigning the four values ± 1, $\pm i$ to ϱ_s, whereas CAIANIELLO has excluded the values $\pm i$. This latter view is in agreement with the result of our present investigation, where the case $j^2 = -1$ actually has become excluded. However, it must be kept in mind that this result will not hold, if it appears in the future that considerations connected with time reversal have no physical basis. For then the difference between vectors and scalars, on the one hand, and quasi-vectors and quasi-scalars, on the other hand, will disappear, and we can construct a Lagrangian, starting from C and m in § 3. But since neither C nor m contains the phase-factor j we cannot exclude the values $j = \pm i$. From our point of view it is important for the question, whether time reversal shall be included in the Lorentz transformations, that different assumptions as to the number of representations of space reflection are made when investigating the possibility of a universal Fermi-type interaction. (In this connection it may be mentioned that if it appears in the future that the neutrino is described by the Majorana abbreviation of the theory, then time reversal cannot be included in the Lorentz transformations. For it is clearly seen that if Δ_5 could assume the value -1 no identification of the wave function with the charge-conjugated wave function could be made).

CAIANIELLO'S arguments for excluding the values $\varrho_s = \pm i$ will now be mentioned. In (3) he has employed the five-dimensional space as a continuous conjunction between the identical transformation and space reflection. As explained at the end of § 2 in the present paper we do not believe that the values $\pm i$ can be ruled out by such considerations. In (9), p. 341 he has given another argument, based on requirements as to commutativity between operators. We have not analysed this argument, but we have noticed that considerations connected with time reversal also enter there. We have found it very interesting that our method of employing the spinor calculus gave rise to the same result.

Concerning the representation of time reversal the following two views are found in the literature:

The components of ψ are transformed into the components of 1) ψ, 2) ψ^*.

1) The former view:

The following four representations of time reversal are possible with consideration to the theory of relativity:

$$\psi \rightarrow \varrho_t \, \alpha_1 \alpha_2 \alpha_3 \beta \psi,$$

where the phase-factor ϱ_t can assume the values ± 1 and $\pm i$.

As to this view we refer again to the papers by PAULI and RACAH. (See also PAULI, (10), p. 221). A consequence of the above-mentioned transformation is that $\psi^* \beta \psi$, and thus also the Lagrange density, changes its sign under time reversal. (The difficulty which then arises when the contributions of integral spin fields are also considered, has recently been discussed by SCHWINGER, (11).)

It is readily seen that $\psi^* \beta \psi$ is identical with the scalar m in § 3 of the present paper, and that the above-mentioned transformation is, in the main (— *i.e.*, if the phase-factor is disregarded), the same as that found at the end of § 4 (time reversal + charge conjugation). We cannot therefore accept the PAULI–RACAH view.

2) The latter view:

On considering the degeneracy of stationary states in quantum-mechanical problems with an odd number of electrons, WIGNER, (12), has been led to represent time reversal by an operator composed of a linear transformation and a transition to the complex conjugated wave function. So far as we know, this point of view is not very often met with in the current field theories.

This latter view is obviously in agreement with the result of our present investigation.

It should be noted that CAIANIELLO in (9) considers the type $\psi \to \varrho_t \alpha_3 \alpha_1 K \psi$ (— called WIGNER type) as well as the PAULI–RACAH type of time reversal. He also points out that the one type can be obtained from the other on multiplying by the charge-conjugation operator. However, this lack of clarity as to the terminology is not found in his preceding paper, (8), where time reversal is represented solely by the WIGNER type.

SUMMARY

Method:

The Lagrange formalism in connection with a consistent use of spinor notation. (The spinor formalism is built up by means of the Cayley parameters).

Results:

1) Number of possible representations of space reflection ($\boldsymbol{x} \to - \boldsymbol{x}$, $t \to t$):

	If time reversal ($\boldsymbol{x} \to \boldsymbol{x}$, $t \to -t$)	
	is	is not
	included in the Lorentz transf.	
Customary view	4	4
Caianiello's result	2	2
Our result.............	2	4

It is seen that CAIANIELLO's statement in the first column, based on considerations quite different from ours, is verified.

2) It is found that to each representation of space reflection there correspond four possible representations of time reversal. The components of ψ are transformed into the components of ψ^*. (WIGNER type).

Department of Mechanics II, Royal Institute of Technology, Stockholm, November 1952.

REFERENCES

1. H.A.S. ERIKSSON, Ark. f. mat., astr., fys. 33B, n:o 6 (1946).
2. ——, Ark. f. mat., astr., fys. 29A, N:o 14 (1943).
3. E. R. CAIANIELLO, Phys. Rev. 86 (1952), 564.
4. W. PAULI, Ann. Inst. Poincaré 6 (1936), 109.
5. G. RACAH, N. Cim. 14 (1937), 322.
6. C. YOUNG and J. TIOMNO, Phys. Rev. 79 (1950), 495.
7. E. R. CAIANIELLO, N. Cim. 8 (1951), 534.
8. ——, N. Cim. 8 (1951), 749.
9. ——, N. Cim. 9 (1952), 336.
10. W. PAULI, Rev. Mod. Phys. 13 (1941), 203.
11. J. SCHWINGER, Phys. Rev. 82 (1951), 914.
12. E. WIGNER, Nach. Ges. Wiss., Göttingen (1932), 546.

Tryckt den 3 mars 1953

Uppsala 1953. Almqvist & Wiksells Boktryckeri AB

ARKIV FÖR FYSIK Band 6 nr 34

Communicated 8 October 1952 by Erik Hulthén

A $^2\Delta$–$^2\Pi$-system in germanium hydride (GeH)

By Bengt Kleman and Erik Werhagen

With 2 figures in the text

A rotational analysis has been made of a violet bandsystem 3 700–4 200 Å which is emitted from a King's furnace containing germanium and hydrogen. This system proves to be a $^2\Delta - {}^2\Pi$ ground-state transition of GeH. The $^2\Delta$-term is regular with small multiplet-splitting and the $^2\Pi$-term regular and near case a. The $^2\Delta$-term is predissociated at about $K = 22$ in $v = 0$ and $K = 12$ in $v = 1$. The calculated constants are in good agreement with what can be expected from the corresponding transitions in the hydrides of the carbon group. In addition to this violet system there is an extended red system 5 400–7 000 Å.

Introduction

No band-systems belonging to GeH have, as far as is known to us, hitherto been reported in the literature. From the knowledge of the spectra of the other hydrides in the carbongroup it can be predicted that the strongest system in GeH will prove to be a $^2\Delta - {}^2\Pi$-transition around 24 000 cm^{-1}. It is also highly probable that GeH has a weaker $^2\Sigma - {}^2\Pi$ system in the red analogous to SnH (1).

From a King's furnace containing germanium and hydrogen we obtained in emission two band-systems, one violet system and one red system. The violet system is in this paper identified as the $^2\Delta - {}^2\Pi$ ground-state transition of GeH. The red system, of which the analysis is not yet completed, will be treated in a later paper.

Experimental

As light-source a King's furnace (2) was used. The dimensions of the heating graphite tube were: length 80 mm, diameter 21 mm and wall-thickness 0.9–1.0 mm. In the middle of the heating tube a small graphite ship containing germanium was inserted. The furnace was then filled with hydrogen to a pressure of about half an atmosphere. The temperature was kept at 2 300–2 350° C, corresponding to a current of about 800 amp. through the heating tube. The lifetime of the heating tube at this temperature was between a quarter of an hour and half an hour. In the final exposures four tubes were used, and the ship was refilled with about one gram of germanium each time.

A 21-foot concave grating was used in the first order (dispersion ~1.25 Å/mm). All exposures of the violet system were made on Ilford Zenith plates.

Appearance of the bands

The most marked heads of the bands in the violet system which are degraded to the red are:

λ Å		Estimated intensities:
3 718.6	${}^SR_{21}$ (1 – 0)	1
3 727.8	R_1 (1 – 0)	2
3 728.8	${}^RQ_{21}$ (1 – 0)	2
3 845.5	R_2 (1 – 0)	1
3 854.4	${}^QR_{12}$ (1 – 0)	2
3 874.4	${}^SR_{21}$ (0 – 0)	5
3 897.6	R_1 (0 – 0)	10
4 015.3	R_2 (0 – 0)	6
4 037.2	${}^QR_{12}$ (0 – 0)	10
4 135.7	R_2 (1 – 1)	1
4 147.7	${}^QR_{12}$ (1 – 1)	2

The appearance of the 0 – 0 band is shown in Figure 1. The careful measurement of the lines in the comparator is made difficult by their being somewhat broad and diffuse. There are several reasons for this. The broadness of the lines is due to the lightsource. There are several germanium isotopes, the components of which are not resolved. Owing to the smallness of the Λ-splitting in $\Pi_{3/2}$, the splitting is not clearly resolved until $K'' = 16$. There is also a heavy overlapping in the heads of the bands, especially in the R- and ${}^RQ$ heads of (0–0) ${}^2\Delta - {}^2\Pi_{\frac{1}{2}}$.

The lines in the (1 – 0) and (1 – 1) bands are rather weak and of diffuse appearance, the latter probably due to isotope-splitting.

The intensities of the branches are in the order $I_Q > I_R > I_P$. The satellite branches are of about equal intensity with the main branches. The ${}^OP_{12}$-branch is the weakest branch in the bands.

The wave-numbers of the lines are given in Table 1.

${}^2\Pi$-state

The Λ-splitting in the ${}^2\Pi$-state is the typical one for case *a*. This makes possible the statement that the ${}^2\Pi$-term is regular. The constants for the Λ-splitting in $v = 0$ are determined from the case-*a* relations by MULLIKEN and CHRISTY (3)

$${}^2\Pi_{\frac{1}{2}} : \Delta\, \nu_{dc} = + p_0\, (J + \tfrac{1}{2})$$

$${}^2\Pi_{3/2} : \Delta\, \nu_{dc} = - \left(\frac{p_0}{Y^2} + \frac{2\, q_0}{Y} \right) (J - \tfrac{1}{2})\, (J + \tfrac{1}{2})\, (J + \tfrac{3}{2}).$$

The rotational constants for this state are calculated by using Hill–van Vleck's expressions for the rotational energy of a doublet state:

Table 1. Wave-numbers of the band-lines

$(0-0)\ {}^2\Delta - {}^2\Pi_{\frac{1}{2}}$.

K''	R_{1cd}	R_{1dc}	Q_{1d}	Q_{1c}	P_{1cd}	P_{1dc}	${}^SR_{21d}$	${}^SR_{21c}$	${}^RQ_{21cd}$	${}^RQ_{21dc}$	${}^QP_{21d}$	${}^QP_{21c}$
0												
1							25 662.11	25 661.07				
2			25 602.41	25 600.87			680.17	678.75				
3	25 642.36*	25 640.45*	592.88	590.91			696.87	694.85	25 634.58	25 632.48		
4	645.29*	642.36*	583.33	580.87			712.56	710.15	638.41*	635.71	25 575.58	25 573.29
5	647.66	644.64	573.29	570.40			727.19	724.27	640.45*	637.83	566.15	563.24
6	649.18*	645.81*	562.72	559.18	25 488.39	25 484.97	740.72	737.47	642.36*	639.15*	555.64	552.33
7	649.74*	645.81*	551.11	547.27	464.82	460.88	753.29	749.41	642.81	639.15*	544.49	540.58
8	649.74*	645.29*	538.89	534.37	440.56	436.18	764.66	760.28	642.36*	638.41*	531.94	527.80
9	648.29	643.51	525.81	521.08	415.45	410.59	774.84	769.97	640.96	636.49*	518.88	513.95
10	645.81*	640.45*	511.83	506.60	389.50	384.21	783.57	778.37	638.41*	633.30	504.55	499.17
11	642.36*	636.49*	496.80	491.05	362.67	356.97	790.87	785.42	634.58	628.77	489.19	483.61
12	637.19*	631.11*	480.50	474.50	334.82	328.53	796.62*	790.87	629.18	623.09	472.74	466.80
13	631.11*	624.42	463.06	456.59	305.99	299.73	801.10	794.53	622.48	616.03	454.99	448.65
14	623.09*	616.03*	444.30	437.45	276.12	269.43	803.46*	796.62*	614.44	607.60	436.18	429.25
15	613.16	606.05	423.99	416.85	245.04	238.12	803.46*	796.62*	604.30	597.11	415.45	408.28
16	601.60	594.16	402.02	394.45	212.58	205.06	801.88	794.53	592.42	584.80	393.19	385.60
17	588.12	580.18	378.33	370.59	178.77	170.75	797.55	789.76	578.65	570.70	369.28	361.31
18	572.10	563.97	352.73	344.74	143.16	135.02	790.87	782.38	562.72	554.32	343.22	334.82
19	553.47	545.24	325.15	316.61	105.88	097.33	780.71	772.30	543.54	535.30	315.24	306.94
20	531.94	523.61	294.88	286.15	067.58	—	767.44	758.64	521.99	513.30	284.96	276.12
21	507.65	499.17	262.14	253.24	024.50	015.72		744.11	496.80	489.19	251.73	243.11
22			227.22	218.25								

* Overlapped lines.

Tab. 1 (cont.).

$(0-0)\ ^2\Delta - {}^2\Pi_{3/2}$.

K''	R_{2dc}	R_{2cd}	Q_{2c}	Q_{2d}	P_{2dc}	P_{2cd}	$^QR_{12c}$	$^QR_{12d}$	$^PQ_{12dc}$	$^PQ_{12cd}$	$^OP_{12c}$	$^OP_{12d}$
0												
1												
2	24 781.88						24 754.93					
3	799.37		24 748.70*				757.84					
4	815.06		752.59*				760.37		24 709.95			
5	829.51		754.93*		24 692.42		761.94*		700.18*		24 650.68	
6	842.76		756.14*		681.63		762.98*		688.82*		626.62*	
7	854.71		756.14*		669.59		762.98*		676.50		601.82	
8	865.31		754.93*		656.40		761.94*		663.23		576.74	
9	874.58		752.59*		642.05		759.52		648.96		550.24	
10	882.42		748.70*		626.62		756.14*		633.59		523.13	
11	889.05		743.77		609.89		751.26		617.18		494.87	
12	893.83		737.65*		591.97		745.01		599.44		465.44	
13	897.02		729.33		572.68		737.65*		580.51		434.86	
14	898.09*		719.67*		552.09		728.20		560.10		403.58	
15	898.30	24 897.02	708.55		529.99		717.30		538.30		370.54	
16	894.92	894.44	695.60	24 695.16	506.61	24 506.16	704.66	24 704.11	515.15*	24 514.72	336.11	
17	889.83	889.05*	680.62	680.02	481.15	480.66	689.79	688.82	490.14	489.55	300.58	
18	882.42*	881.62	663.23*	662.48	454.05	453.32	672.80	672.07	463.12	462.37	263.08	
19	871.68	871.09	643.55	642.86	424.60	423.77	653.28	652.52	434.00	433.25	224.10	
20	858.35	857.43	621.23	620.28	392.98	392.12	631.14	630.11	402.71	401.77		
21	841.38	840.38	595.81	594.86	358.87	357.63	606.08	605.22	369.01	367.97		
22	820.55	818.79	567.17	566.06	321.96	320.73	577.83	576.74	332.24	330.95		
23			534.99	533.91	282.08	280.82	545.84	544.74	293.42*	291.36		
24			498.89	497.59	238.59	237.28						

* Overlapped lines.

Tab. 1 (cont.).

(1 – 0) $^2\Delta - ^2\Pi_{\frac{1}{2}}$.

K''	$R_{1\,cd}$	$R_{1\,dc}$	$Q_{1\,d}$	$Q_{1\,c}$	$P_{1\,cd}$	$P_{1\,dc}$	$^SR_{21\,d}$	$^SR_{21\,c}$	$^RQ_{21\,cd}$	$^RQ_{21\,dc}$	$^QP_{21\,d}$	$^QP_{21\,c}$
0												
1												
2	26 817.70	26 816.59*					26 856.16	26 855.09				
3	816.59*	814.45	26 772.01	26 770.13			866.73	864.57*	26 810.91	26 808.68		
4	813.41	810.91	757.78	755.23			874.57	872.50*	807.81	805.29		
5	807.81	805.29	740.96	738.50			880.13*	877.45*	802.67	799.84		
6	800.61	797.46	722.86	719.61			883.46	880.13*	795.26	792.00	26 717.88	26 714.84
7	790.85	787.19	702.84	698.84	26 625.32	26 621.78	883.80	880.13*	785.34	781.61	697.35	—
8	778.59	774.57	680.22	675.88	592.03	587.85	882.08	877.45*	773.31	768.91	674.73	670.41
9	764.26	759.49	655.30	650.34	556.55	551.64	877.45*	872.50*	758.33	753.76	649.54	644.91
10	746.74	741.50	627.94	622.49	518.86	513.69			740.96	735.72	621.78	616.90
11		720.30	597.78	592.03	478.35	472.93					592.03	586.28
12			564.92	558.90	435.89	430.10					558.90	552.65
13			529.12	522.67							522.67	516.15
14			483.79									477.42

(1 – 0) $^2\Delta - ^2\Pi_{3/2}$.

K''	R_2	Q_2	P_2	$^QR_{12}$	$^PQ_{12}$
0					
1					
2	25 963.53				
3	975.46			25 937.25	25 904.69
4	984.93	25 928.82		934.58	890.43
5	991.67	924.79		930.47	874.75
6	995.82	918.22		923.79	857.05
7	997.34	908.99	25 831.53	914.75	837.16
8	995.82	897.60	—	903.15	814.75
9	991.94	883.32	25 784.62	889.01	789.76*
10		866.84	757.49	871.94	763.23
11		846.55		852.51	733.24
12		823.42			700.72
13					

(1 – 1) $^2\Delta - ^2\Pi_{3/2}$.

K''	R_2	Q_2	P_2	$^QR_{12}$	$^PQ_{12}$
0					
1					
2	24 128.25				
3	141.31			24 102.63	24 069.82
4	151.89	24 095.70		101.79	057.22
5	160.50	093.54		099.17	043.49
6	166.71	089.18	24 021.98	094.55	027.92
7	170.89	082.84	005.17	088.10	010.55
8	172.63*	073.96	23 986.02	079.52	23 991.35
9	172.63*	063.13	964.48	069.02	969.94
10		050.20	941.69	055.82	946.64
11			915.18	040.40	920.98
12			887.14	021.98	893.11
13				000.87	862.61

* Overlapped lines.

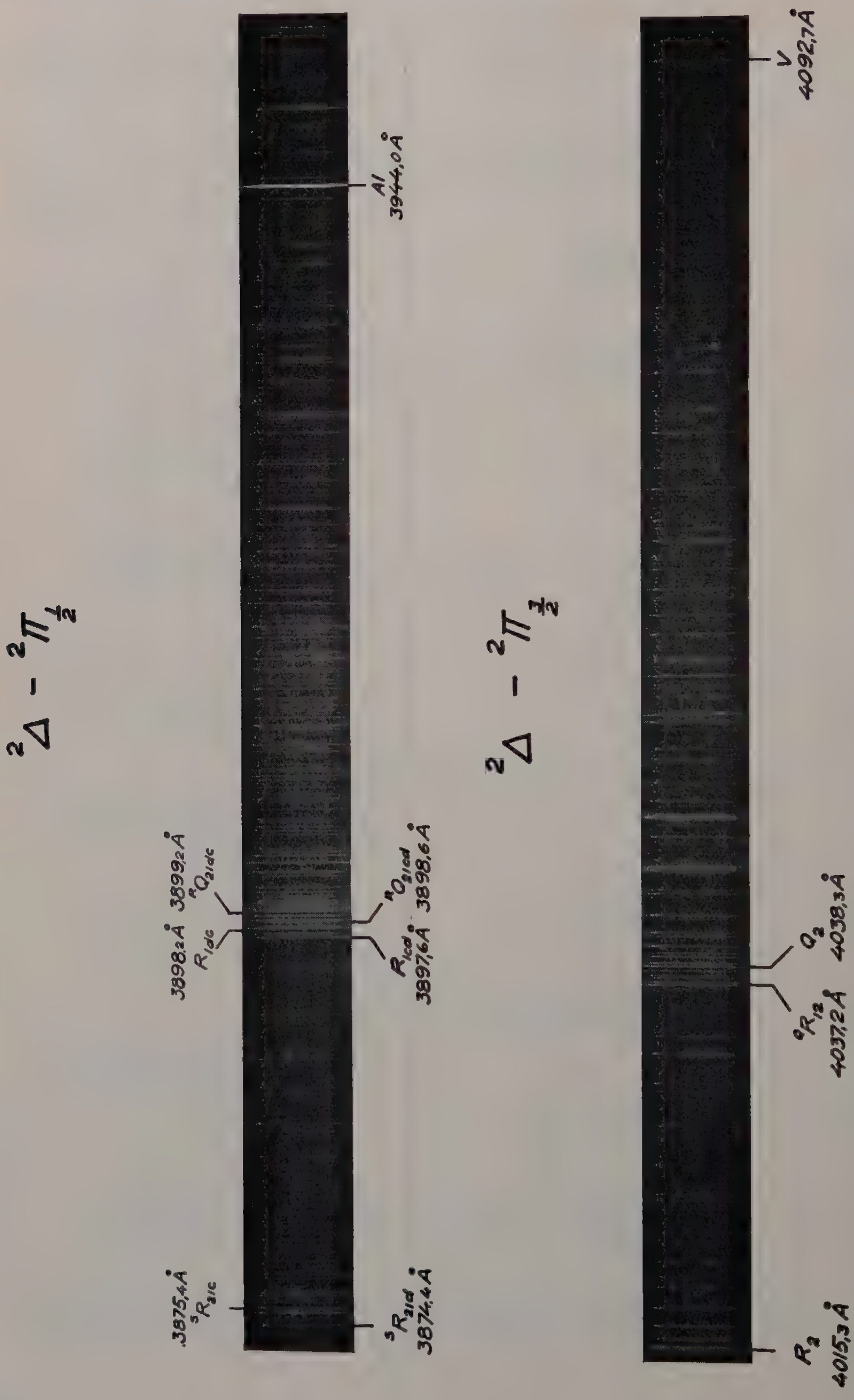

Fig. 1. The (0–0) band of $^2\Delta$–$^2\Pi$.

$$J=K+\tfrac{1}{2}\quad F_1(J)=B_v\left[(J+\tfrac{1}{2})^2-\Lambda^2-\tfrac{1}{2}\sqrt{4(J+\tfrac{1}{2})^2+Y(Y-4)\Lambda^2}\right]-D_v J^4$$

$$J=K-\tfrac{1}{2}\quad F_2(J)=B_v\left[(J+\tfrac{1}{2})^2-\Lambda^2+\tfrac{1}{2}\sqrt{4(J+\tfrac{1}{2})^2+Y(Y-4)\Lambda^2}\right]-D_v(J+1)^4,$$

$$\text{where } Y=\frac{A}{B_v}.$$

The coupling constant A is determined by solving Y in the equated expressions for the separation in the J-doublets $F_2(J)-F_1(J)=B_v\sqrt{4(J+\tfrac{1}{2})^2+Y(Y-4)\Lambda^2}$. B_v and D_v are calculated graphically from the second differences

$$[\Delta_2 F(J)]_{\text{mean}}=\frac{\Delta_2(F_{1c}+F_{1d}+F_{2c}+F_{2d})}{4}=4B_v(J+\tfrac{1}{2})+8D_v(J+\tfrac{1}{2})^3.$$

In the level $v=1$ the first differences of F_1 are used to calculate an effective B-value of the $\Pi_{3/2}$ component. This is slightly higher than B_1 according to the relation (4)

$$B_1=B_{1(3/2)}-\frac{B_1^2}{A}.$$

ω_e is calculated from the origins of the bands (see later paragraph) using the relation $\omega_e x_e \approx 3B_e$.

$^2\Delta$-state

The $^2\Delta$-state is predissociated. Due to the thermic nature of the light-source the break in intensity is not abrupt. The intensity vanishes at about $K'=22$ in $v=0$ and $K'=12$ in $v=1$. On account of the strength of the 0—0 band, it is probable that the predissociation-limit in $v=0$ to be comparable with that in $v=1$ should be put somewhat lower.

When $\dfrac{[\Delta_2 F(J)]_{\text{mean}}}{(J+\frac{1}{2})}$ or $\dfrac{[\Delta_1 F(J)]_{\text{mean}}}{(J+1)}$ is plotted graphically against $(J+\tfrac{1}{2})^2$ and $(J+1)^2$ respectively it shows that the curve is straight only up to about $J=15$. This departure from the straight line is interpreted as an incipient depression of the levels at the predissociation limit. The constants B_0 and D_0 are calculated from the straight part of the curve.

The coupling conditions are studied from the separation in the K-doublets $\Delta F(K)=F_1(K)-F_2(K)$. We attempt to express this separation by

$$\Delta F(K)=B f_z(K)+f_\gamma(K),$$

where $B f_z(K)$ is the part resulting from the (L,S) coupling. This is obtained by expanding the Hill–van Vleck's expressions, letting $z=\dfrac{Y(4-Y)\Lambda^2}{4}$

$$f_z(K)=\frac{z}{2}\left(\frac{1}{K+1}+\frac{1}{K}\right)+\frac{z^2}{8}\left(\frac{1}{(K+1)^3}+\frac{1}{K^3}\right)+\frac{z^3}{16}\left(\frac{1}{(K+1)^5}+\frac{1}{K^5}\right)+$$
$$+\frac{5}{128}z^4\left(\frac{1}{(K+1)^7}+\frac{1}{K^7}\right)+\cdots$$

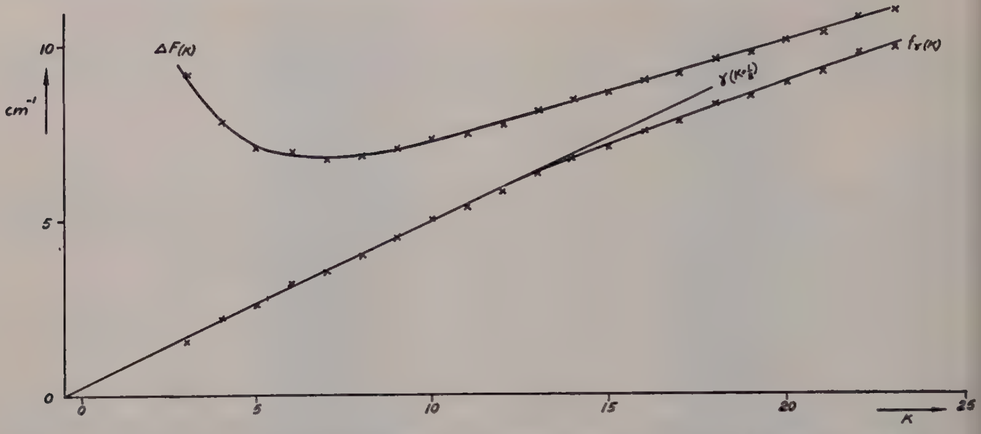

Fig. 2. The separation in the K-doublets $\Delta F(K) = F_1(K) - F_2(K)$ and $f_\gamma(K) = \gamma(K+\frac{1}{2}) + \cdots$

The dominating term in $f_\gamma(K)$ should be $\gamma(K+\frac{1}{2})$, resulting from the (K, S) coupling. The two parts are separated in the following way. An approximative value $\bar{\gamma}$ for γ is obtained from $\Delta F(K)$ in the region $K = 8-16$. We subtract $\bar{\gamma}(K+\frac{1}{2})$ from $\Delta F(K)$ and solve $\bar{z}$ from the equations $\Delta F(K) - \bar{\gamma}(K+\frac{1}{2}) = B f_{\bar{z}}(K)$; $(K = 3-10)$. $\bar{z}$ is then extrapolated to $K+\frac{1}{2} = 0$, giving $z = Y(4-Y) = 3.80$. γ is obtained as the slope of the straight part of the curve

$$f_\gamma(K) = \Delta F(K) - B f_z(K) = \gamma(K+\tfrac{1}{2}) + \cdots$$

For Y two roots are obtained $Y_1 = 1.55$ and $Y_2 = 2.45$, giving $A = 10\ \mathrm{cm}^{-1}$ and $15\ \mathrm{cm}^{-1}$ respectively. Of these we prefer the first one, $A = 10\ \mathrm{cm}^{-1}$, since it seems from the first lines in the bands as if the lowest level $J = 3/2$ belongs to F_2.

The Λ-doubling in the $^2\Delta$-state is not detectable in the differences.

Origins of the bands

The origin of a band is calculated in the following way.

$$[F(J)]_{\text{mean}} = T_0 + B_v(J+\tfrac{1}{2})^2 - \cdots,$$

where $[F(J)]_{\text{mean}}$ is the mean of F_{1c}, F_{1d}, F_{2c} and F_{2d}

$$\bar{\nu}_{00} = \overline{T_0' - T_0''} = [Q(J)]_{\text{mean}} - (B_v' - B_v'')(J+\tfrac{1}{2})^2 = [{}^{P,R}Q(J)]_{\text{mean}} - (B_v' - B_v'')(J+\tfrac{1}{2})^2.$$

$\bar{\nu}_{00}$ is extrapolated to $J+\frac{1}{2} = 0$, giving ν_{00}.

For the $(1-1)$ band this method can not be used, since the $^2\Delta - {}^2\Pi_{\frac{1}{2}}$ subband has not been measured. The origin is instead calculated from the following relation

$$\bar{\nu}_{11}=[Q_2(J),\,{}^PQ_{12}(J)]_{\mathrm{mean}}+\frac{B_v''}{2}\sqrt{4\,(J+\tfrac{1}{2})^2+Y''\,(Y''-4)}-(B_v'-B_v'')\,(J+\tfrac{1}{2})^2,$$

where $\bar{\nu}_{11}$ must be extrapolated to $(J+\frac{1}{2})=0$ to give ν_{11}. The coupling constant in ${}^2\Pi$ $A''=B_1''Y''$ is here taken from the level $v=0$.

Constants of the ${}^2\Delta-{}^2\Pi$ system

Origins in wave-numbers

v'/v''	0	1
0	25 179	
1	26 366	24 530

${}^2\Pi$

$B_0''=6.633$ cm^{-1} $B_1''=6.458$ » $B_e''=6.720$ »	$\alpha_e''=0.174$ cm^{-1} $D_0''=3.28\cdot10^{-4}$ cm^{-1} $D_1''=4.12\cdot10^{-4}$ »	$r_e''=1.591$ Å $\omega_e''=1\,876$ cm^{-1}	$v=0\begin{cases}A''=892\ \mathrm{cm}^{-1}\\ p_0=0.483\ \mathrm{cm}^{-1}\\ q_0=0.0060\ \text{»}\end{cases}$

${}^2\Delta$

$B_0'=6.242$ cm^{-1} $B_1'=5.622$ » $B_e'=6.551$ »	$\alpha_e'=0.620$ cm^{-1} $D_0'=6.49\cdot10^{-4}$ cm^{-1} $D_1'=8.72\cdot10^{-4}$ »	$r_e'=1.611$ Å $\omega_e'=1\,227$ cm^{-1}	$v=0\begin{cases}A'=10\ \mathrm{cm}^{-1}\\ \gamma=0.472\ \mathrm{cm}^{-1}\end{cases}$

Physical Institute, University of Stockholm, September 1952.

REFERENCES

1. Howell, G., Proc. Phys. Soc. *57*, 37, 1945.
2. Grundström, B., Spectroskopische Untersuchungen über die Erdalkalihydride, Dissertation, Stockholm, 1936.
3. Mulliken, R. S., Christy, A. Phys. Rev. *38*, 87, 1931.
4. Mulliken, R. S., Rev. Mod. Phys. *3*, 89, 1931.

Tryckt den 2 mars 1953

Uppsala 1953. Almqvist & Wiksells Boktryckeri AB

ARKIV FÖR FYSIK Band 6 nr 35

Communicated April 1952 by S. Nauckhoff and G. Borelius

Influence of air pressure on the velocity of ejected explosion gases

By C. H. Johansson[1] and Sten Ljungberg[1]

With 7 figures in the text

Summary

The ejection velocity of the explosion gases from the end area of charges in glass tubes has been determined at different air pressures from 0.5 mm Hg to 25 atm. The causes for the great velocities obtained at low pressures have not yet been clarified in detail, but they are certainly connected with the finite length of the reaction zone. When the detonation front reaches the end surface of the explosive, the intact parts in the reaction zone are accelerated to a high particle velocity, and when detonating, cause an increased front velocity.

In an earlier investigation has been established, that the velocity with which the explosion gases escape from detonating charges, is to a high degree dependent on the pressure of the surrounding air (1). The present investigation gives a quantitative relation between air pressure and velocity.

Experimental arrangements

The investigation was carried out with cast charges of 40 percent TNT and 60 percent PETN with a diameter of 15 mm and a length of 80 to 100 mm. The speed of detonation and the front velocity of the explosion gases were determined with a camera with rotating mirror. Fig. 1 shows the arrangement of the charge and the camera. The slit in front of the charge had a width of 0.3 mm. Fig. 2 shows the glass

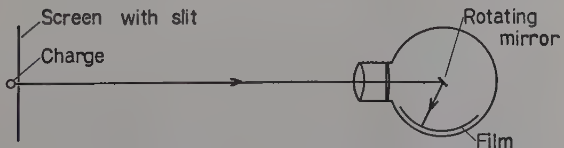

Fig. 1. Arrangement of charge and camera.

---

[1] Nitroglycerin AB., Physical Research Department.

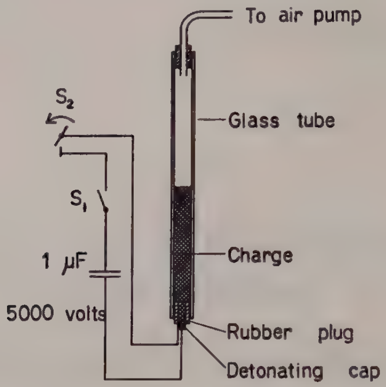

Fig. 2. The charge and circuit diagram for initiating and synchronizing.

tube with charge and detonating cap, the connection to the air-pump and the circuit diagram for initiating and synchronizing. The cap was ignited by the discharge of a high-voltage condenser. The switch S_1 is connected to the shutter of the objective so that it closes when the shutter obtains its greatest aperture, and S_2 consists of a rotating contact on the mirror axis which synchronizes the initiation with the position of the mirror. Each charge was cast in the same glass tube which was used in determining the velocity and thus filled up the glass tubes well. Fig. 3 gives an example of a film taken at a pressure of 12 mm Hg.

Results

By graphic derivation of the traces of the light-emitting front on the films, the front velocity has been determined as a function of the distance from the end surface of the charge. The diagram in fig. 4 represents the velocity of the light-emitting front as a function of the distance at different pressures. The velocity decreases with

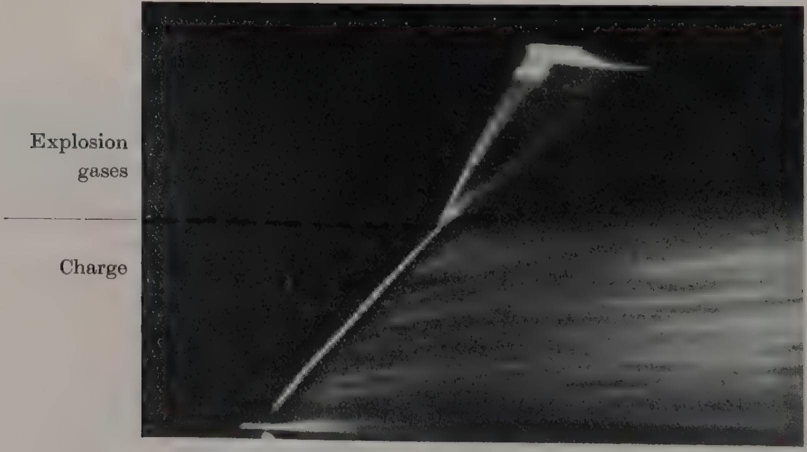

Fig. 3. Film obtained at 12 mm Hg.

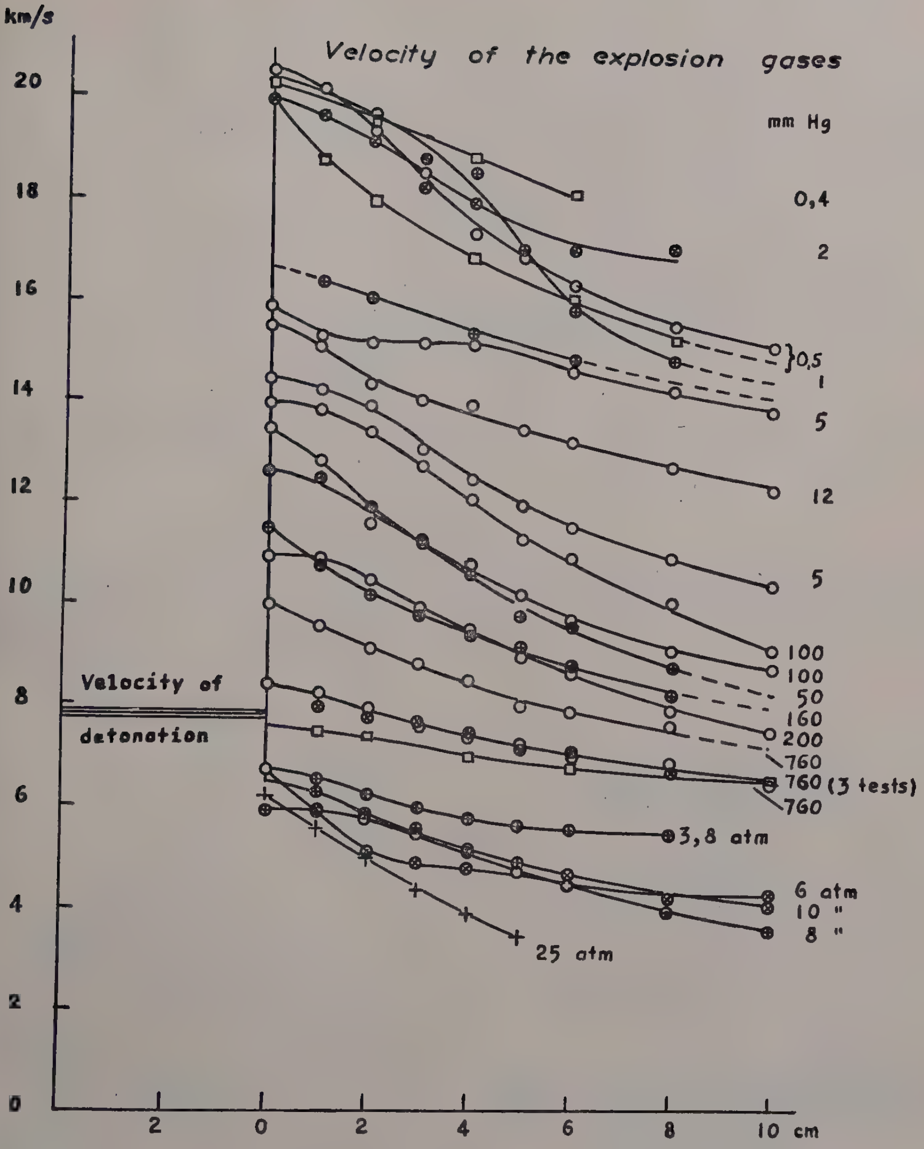

Fig. 4. Velocity of the explosion gases as a function of the distance from the end surface.

the distance, and most of the curves are concave toward the abscissa at small distances and convex at greater distances. Certain curves have, however, a different course. The cause for this has not yet been made clear. Possibly the velocity and its decrease with the distance are sensitive to the shape and character of the end surface. Fig. 5 shows the initial velocity as a function of the air pressure on a logarithmic scale. In the diagram a curve is also drawn for pressed TNT[1], calculated without

---

[1] According to a calculation by S. Petersson.

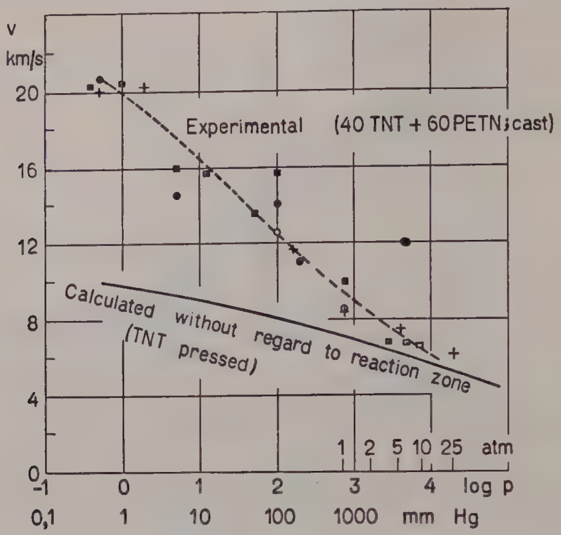

Fig. 5. Velocity of the explosion gases at the end surface as a function of the air pressure.

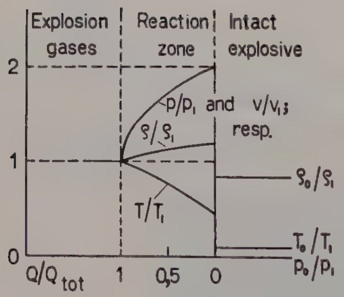

Fig. 6. Conditions in the reaction zone as a function of the rate of freed heat to total explosion heat according to Eyring, Powell, Duffey and Parlin.

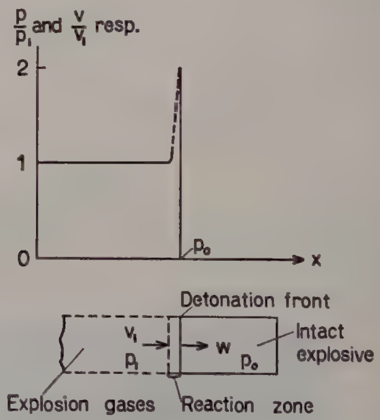

Fig. 7. Course of pressure in a detonating bar of explosive.

regard to the reaction zone. A corresponding calculation for a composition of TNT and PETN would probably have given somewhat higher values, but the non-agreement, especially at low pressures, probably depends only to a small degree on the difference in explosives.

The cause of the great increase of the front velocity with decreasing pressure is not clear in detail, but it is certainly connected with the finite length of and the extreme conditions in the reaction zone. Fig. 6 shows according to EYRING, POWELL, DUFFEY and PARLIN (2) pressure, density, temperature and particle velocity in the reaction zone as a function of the fractional part of the total quantity of explosive which has detonated, or, in other words, as a function of the quantity of heat made free in relation to the total explosion heat. Fig. 7 shows the pressure curve for a detonating bar of explosive.[1] The fall of pressure behind the front has been marked with dashes, as the functional relation between Q/Q_{tot} in fig. 6 and the x-coordinate in fig. 7 are unknown. The condition calculated according to Rankine-Hugoniot occurs at the back of the reaction zone, where the whole of the explosion heat has been freed. It is especially noteworthy that pressure and particle velocity are twice as large in the proper front. When the detonation front reaches the end surface of the explosive the parts of the explosive in the reaction zone which are intact are accelerated to a high particle velocity and, when detonating, cause an increased front velocity. Dr. H. SELBERG, who drew attention to this possibility, has estimated a front velocity exceeding 20 km/sec at low pressures.[2]

The present investigation has been supported by a grant from the Swedish Council for Technical Research.

Stockholm, April 1952.

LITERATURE. 1. **C. H. Johansson.** The state of detonating explosive and the velocity of the ejected gases. Kungl. Svenska Vetenskapsakad. Arkiv f. fysik *1* (1950) 563–567. — 2. **H. Eyring, R. E. Powell, G. H. Duffey** and **R. B. Parlin.** The stability of detonation. Chem. Rev. *45* (1949) 69–181.

---

[1] Compare C. H. JOHANSSON (1) Fig. 4.

[2] Verbal communication.

Tryckt den 2 mars 1953

Uppsala 1953. Almqvist & Wiksells Boktryckeri AB

ARKIV FÖR FYSIK Band 6 nr 36

Mitgeteilt am 3. Dez. 1952 durch I. WALLER und H. NORINDER

Negativer Durchschlag von Luft in der Funkenstrecke Kugel–Platte bei Stosspannungen

Von W. PUCHER

Mit 4 Figuren im Text

ÜBERSICHT

Es wird eine Formel abgeleitet für die negative Durchschlagspannung von Luft der Funkenstrecke Kugel–Platte bei Atmosphärendruck, die mathematisch sehr einfach anwendbar ist und eine überschlagsmässige Berechnung der Durchschlag- und Koronaspannung auch für grosse Funkenstreckenlängen erlaubt.

Im Folgenden werde der Versuch unternommen, die Durchschlagsbedingungen, die bisher immer noch nur für verhältnismässig kleine Funkenstrecken gelten, zu erweitern und ihre Anwendbarkeit auch für grössere Elektrodenabstände zu ermöglichen. Dazu benützen wir eine Vorstellung, die schon einige Verwendung gefunden hat in der elektrischen Festigkeitslehre [1] und in der Theorie der Korona [2]: Das Vorwachsen der Entladung von der Kathode sei als vollkommen gleichwertig angesehen mit einem Durchschlag über den Teilbereich der Entladungstrecke, der bereits von der Entladung überbrückt wurde. Dieser wird dadurch vollkommen leitend und es resultiert ein Feld, das gleich dem ist, welches auftritt, wenn die Kathode um diesen Teilbereich näher an die Anode herangerückt wäre. Diese Vorstellung auf den Fall Kugel–Platte übertragen, den wir im Folgenden nur behandeln wollen, entspricht einem Anwachsen der Kugel d. h. einer Vergrösserung des Kugelradius bei gleichbleibender Spannung. Mit dieser Ausdehnung der kathodischen Kugel geht eine Veränderung des Feldes an der Kugeloberfläche Hand in Hand. Das Feld nimmt dabei anfangs ab, durchläuft ein Minimum und wächst mit weiterer Annäherung der Kathode an die Anode über alle Grenzen an. Durch die Forderung einer bestimmten Mindestfeldstärke im Minimum ist es möglich, zunächst einmal auf rein geometrischer Grundlage eine Bedingung für das Eintreten des Durchschlages aufzustellen. Erst die Bestimmung der Minimumfeldstärke selbst wird uns — wie wir später sehen werden — dazu zwingen, mehr über die Art des Mechanismus, von dem wir glauben, dass er die Entladung beherrscht, auszusagen. Dass die hier entwickelte Vorstellungsweise nur auf den Fall negativer Kugel anwendbar ist, wird klar wenn man bedenkt, dass praktisch nur den Elektronen eine Beweglichkeit zukommt.

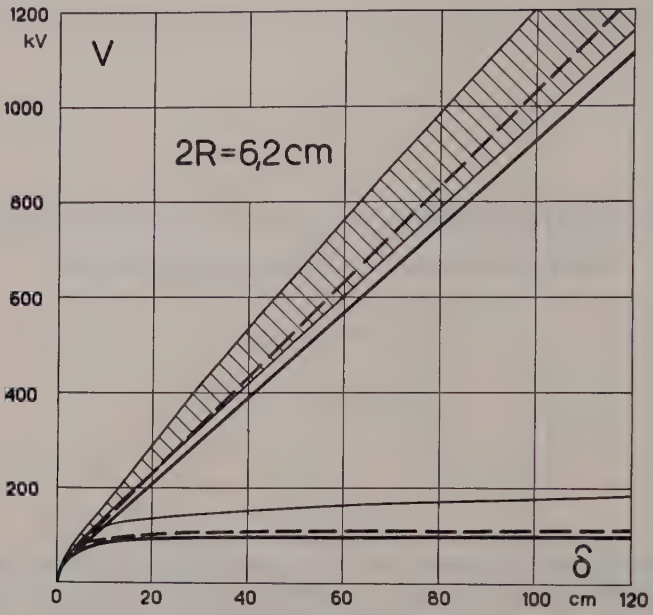

Fig. 1.

Gemeinsamer Text zu den 4 Abbildungen

Durchschlag- und Koronaspannung für die Kugeldurchmesser $2R = 6.2$; 15; 25; 50 cm: Die 4 oberen Kurven geben jeweils die Durchschlagspannung, die 3 unteren die Koronaspannung wieder. Die schwach ausgezogenen Kurven wurden experimentell gefunden, wobei die schraffierte Fläche den mittleren Streubereich zwischen 3 prozentigem und 97 prozentigem Durchschlag anzeigt. Die stark ausgezogenen Kurven sind nach den Gln. (5) und (8), die strichlierten Kurven nach den Gln. (12) und (13) errechnet.

Zur rechnerischen Durchführung unseres Programmes beginnen wir mit der Feldstärke E längs der Achse der Funkenstrecke Kugel–Platte [3]:

$$E = \frac{V\,2\delta\,[\delta^2(f+1) + y^2(f-1)]}{[\delta^2(f+1) - y^2(f-1)]^2}$$

mit V = Spannung
δ = Länge der Funkenstrecke
$f = \frac{1}{4}\left[(2p-1) + \sqrt{(2p-1)^2+8}\right]; \quad p = 1 + \frac{\delta}{R}$
R = Kugelradius
y = Koordinate längs der Achse, beginnend von der Platte.

An der Stelle der wachsenden Kugeloberfläche ($y = \delta$) ist dann das Feld

$$E = \frac{V}{\delta} f \tag{1}$$

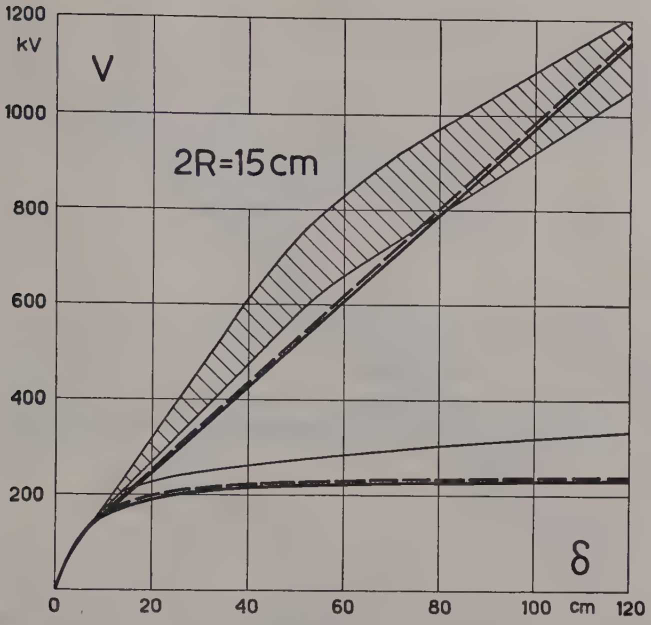

Fig. 2.

oder, wenn wir $\delta = l - R$ setzen und unter l den Abstand Kugelmittelpunkt–Platte verstehen,

$$E = \frac{V}{4} \frac{1}{(l-R)R}\left[2l - R + \sqrt{(2l-R)^2 + 8R^2}\right] \tag{2}$$

Dieses Feld als Funktion von R hat ersichtlich ein Minimum für ein R_0 zwischen $0 \leqq R_0 \leqq l$. Die Stelle, an der dieses eintritt, wird bestimmt durch die Gleichung $\frac{dE}{dR} = 0$ zu $R_0 = 0.49\,l$ und die Minimumfeldstärke selbst zu

$$E_{\min} = 3.56 \frac{V}{l} \tag{3}$$

Damit nun ein Durchschlag wirklich eintreten kann muss $E_{\min}$ eine bestimmte Grösse erreichen, die eine weitere Ionisation in der Funkenstrecke möglich macht.

Nachdem in der Umgebung des Minimums eine Kugelvergrösserung nur eine sehr kleine Feldstärkenveränderung zur Folge hat, praktisch die Feldstärke an der Kugeloberfläche also konstant bleibt, werden die Verhältnisse dort sehr ähnlich denen einer Funkenstrecke Platte–Platte sein. Für eine solche von einer Längeneinheit nimmt man aber eine Durchbruchfeldstärke von $E = 32.2$ kV/cm [4] an. Wir wählen also vorläufig auch hier

$$E_{\min} = 32.2 \text{ kV/cm} \tag{4}$$

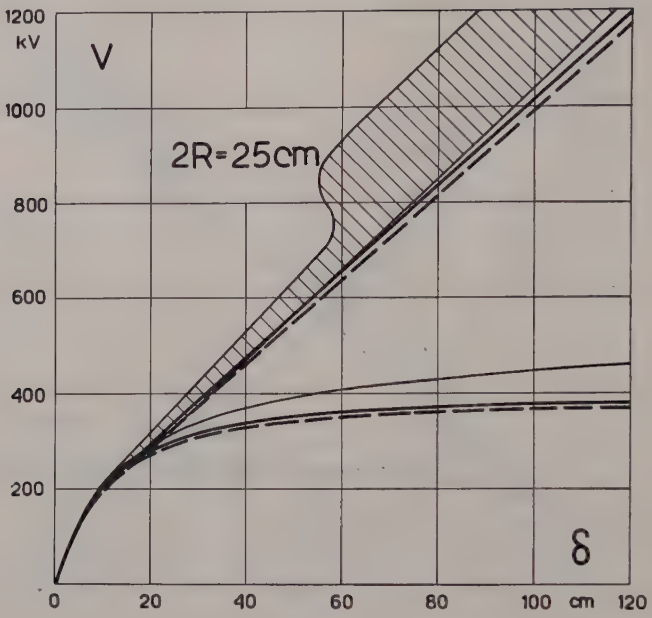

Fig. 3.

und erhalten daraus zusammen mit (3) die Durchschlagsformel

$$V_s = 0.281\, E_{\min}\, l = 9.04\, l = 9.04\,(R + \delta)\ \text{kV}. \tag{5}$$

Jetzt ist noch der Gültigkeitsbereich für Gl. (5) zu bestimmen, der ihr auf Grund der Herleitung zukommt. Voraussetzung für unsere Rechnung war, dass sich die Minimalstelle zwischen Kugeloberfläche und Platte befindet. Der Gl. (5) kommt also nur eine sinnvolle Bedeutung zu für Werte von R, die kleiner oder gleich R_0 sind, d. h. wegen

$$R_0 = 0.49\, l = 0.49\,(\delta + R) \geqq R$$

für alle Kugelfunkenstrecken, die der Relation

$$\delta \geqq 1.04\, R \tag{6}$$

genügen.

Nehmen wir nun andererseits an, der Radius der Kugel sei so gross, dass die Minimalstelle nicht ausserhalb sondern in die Kugel zu liegen kommt

$$R_0 \leqq R \text{ bzw. } \delta \leqq 1.04\, R \tag{7}$$

so würde das bedeuten, dass jedes Vorwachsen von Entladungserscheinungen an der Kugel — was nach unseren Vorstellungen einer Vergrösserung der Kugel selbst gleichkommt — eine Erhöhung der Feldstärke zur Folge hat.

Der Vorgang also einmal eingeleitet, wird nie bei Koronaerscheinungen allein verbleiben können sondern wird unbedingt zum Durchschlag führen. In einer graphischen Zusammenstellung kommt das dahingehend zum Ausdruck, dass Durchschlagskurve und Koronakurve zusammenfallen. Zur Ableitung einer Durchschlagsformel für Funkenstrecken der Art (7) gehen wir aus von der Gl. (1) für die Feldstärke an der Kugeloberfläche, ohne hier aber $l = R + \delta$ zu setzen

$$E = \frac{V}{4}\frac{1}{\delta R}\left\{R + 2\delta + \sqrt{(R + 2\delta)^2 + 8R^2}\right\} \tag{1a}$$

Nach dem oben Gesagten befinden wir uns jetzt in dem Teil der Kurve $E = F(R)$, wo E mit wachsendem R monoton zunimmt. Den kleinsten Wert nimmt E an der Elektrode an. Wir können daher dort die Feldstärke in der obigen Darstellung als $E_{\min}$ identifizieren und damit ein Durchschlag möglich wird, ihr die früher verwendete Grösse 32.2 kV / cm zuschreiben. So erhalten wir aus (1 a) die Durchschlagspannung

$$V_s = \frac{4\,E_{\min} R\,\delta}{R + 2\delta + \sqrt{(R + 2\delta)^2 + 8R^2}} = \frac{128.8\,R\,\delta}{R + 2\delta + \sqrt{(R + 2\delta)^2 + 8R^2}}. \tag{8}$$

Zusammenfassend kann man sagen: Die Bedingung für das Eintreten eines elektrischen Durchschlages der Funkenstrecke negative Kugel–geerdete Platte lässt sich formulieren mittels zweier Funktionen (5) und (8) der Form

$$V_s = f(R, \delta),$$

in die R als Parameter eingeht und deren Gültigkeitsbereiche durch (6) und (7) bestimmt sind. Formel (8) kann darüberhinaus auch für alle $\delta > 1.04\,R$ als Darstellung der Koronaspannung angesehen werden, denn sie fordert, dass an der Kugeloberfläche eine bestimmte zur Stossionisation dort ausreichende Feldstärke herrsche. Der Verlauf der Funktionen (5) und (8) ist aus den beigefügten Abbildungen ersichtlich, die auch einen Vergleich mit den im Rahmen der Arbeit [5] am hiesigen Institut von J. R. M. Alger, E. B. Skolnikoff und L. Asztalos experimentell gefundenen Durchschlagspannungen ermöglichen.[1] Über die experimentelle Durchführung der Aufnahme dieser Kurven und deren physikalische Bedeutung wurde dort ausführlich berichtet. Die errechneten Kurven geben qualitativ den Verlauf der Durchschlagspannung sowie auch Koronaspannung richtig wieder und die Übereinstimmung ist quantitativ oft so gut, dass nur Abweichungen vom Experiment auftreten, die innerhalb der Fehlergrenzen liegen. Eine Abweichung ist jedoch recht deutlich für die Koronaspannung bei abnehmendem Kugelradius und ein Versagen der errechneten Durchschlagspannung für die grösste Kugel ($2R = 50$ cm). Die Ursachen dafür können von verschiedenster Art sein, wenn man bedenkt, von welch einfachen Vorstellungen wir ausgegangen sind und sie zum Mechanismus dieser verwickelten Vorgänge im Funken erhoben haben. Die Abweichungen, die auftreten bei Verwendung kleiner Kugeln kann möglicherweise auch herrühren von dem Einfluss der Zuleitungen auf das Feld in der Entladungstrecke, während andererseits für grosse Kugeln die Vorstellung eines Anwachsens des Radius bereits zu grob wird. Im

---

[1] Diese Resultate waren bisher unveröffentlicht und ich verdanke sie einer persönlichen Mitteilung.

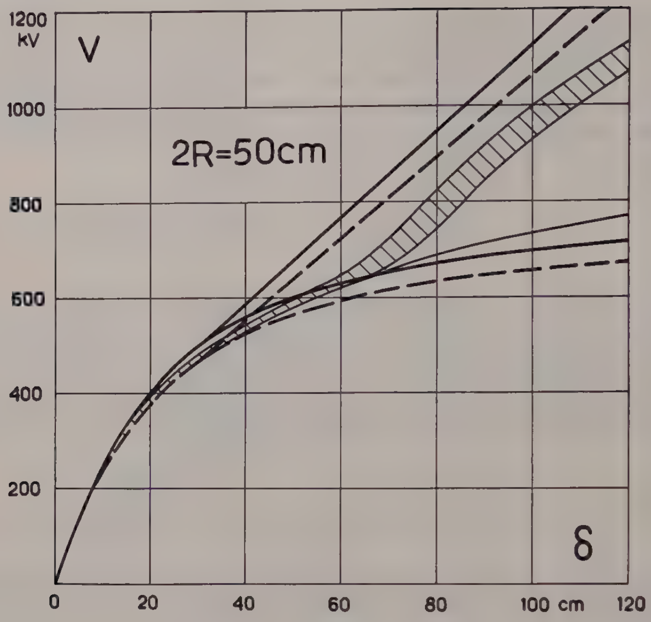

Fig. 4.

übrigen haben wir den Wert der Mindestfeldstärke ziemlich willkürlich gewählt und nur eine recht fadenscheinige Rechtfertigung für diese Wahl vorgebracht. Es wird also vor allem unsere Aufgabe sein im Folgenden darauf näher einzugehen und mit Hilfe von bestimmteren physikalischen Vorstellungen $E_{\min}$ zu präzisieren.

Bisher wurde immer stillschweigend angenommen, dass die Feldstärke der einzig wesentliche Faktor für das Vorwachsen der Entladung ist, und dann eine bestimmte solche Feldstärke (4) festgesetzt, die den Durchschlag ermöglichen soll. Diese Feldstärke war konstant für jede Art von Funkenstrecke, daher in unserem Fall unabhängig vom Radius der Kugel und der Länge der Funkenstrecke. Weiters wurde dem Ionisierungsprozess keine Beachtung geschenkt. Alles dies zeigt schon ziemlich deutlich, wie unvollkommen unsere Annahme war. Nun haben die Untersuchungen des Entladungsmechanismus bei relativ kleinen Elektrodenabständen gezeigt, dass die Feldstärke nur indirekt von Bedeutung ist. Man fand nämlich ein Gesetz der Form [6]

$$\int_0^\delta \alpha\, dx = K \qquad (9)$$

$K =$ constans
$\alpha =$ Koeffizient der Stossionisierung

für die Feldstärke, die zum Durchschlag notwendig ist. Dabei hängt α nach der Art

$$\alpha = A(E - B)^2 \qquad (10)$$

von der Feldstärke E ab. Gleichung (9) fordert eine bestimmte durch Elektronenstoss erzeugte Ladung, die den rapiden Spannungsausgleich ermöglichen soll. Die freie Ladung in der Funkenstrecke ist also in erster Linie von entscheidendem Einfluss auf die Entladung, während die Feldstärke selbst nur über den Zusammenhang (10) sich geltend macht. Aus (9) und (10) ersieht man auch dass unsere Forderung einer bestimmten Feldstärke in einem Punkt nicht ausreichend sein kann, da (9) einen Integralwert der Feldstärke über die Funkenstrecke verlangt. STEPHENSON [6] hat gezeigt, dass (9) zusammen mit (10) die näherungsweise Darstellung der Feldstärke an der Kugeloberfläche

$$E = 1.11\,E_0\,\varrho + M\sqrt{\frac{\varrho}{R}} \tag{11}$$

mit E_0 = Durchschlagsfestigkeit der Luft
M = Konstante
ϱ = Luftdichte
zulässt.

Mit Formel (11) haben wir wieder zurückgefunden zur Durchbruchsfeldstärke und können somit die früher gefundenen Gesetze mit den hier dargelegten Vorstellungen verbinden. Die Feldstärke (11) entspricht vollkommen dem $E_{\min}$ wie es in Gl. (8) auftritt und in Gl. (4) definiert wurde. Da nun ferner die zwei Durchschlagsbedingungen (5) und (8) an der Stelle $\delta = 1.04\,R$ stetig ineinander übergehen müssen, folgt notwendig, dass $E_{\min}$ in beiden Formeln gleich sein muss, d. h. auch in Gl. (5) ist $E_{\min}$ durch (11) zu ersetzen. Wir erhalten somit als neue und verbesserte Lösung

$$\begin{aligned} V_s &= \frac{4\left(1.11\,E_0\,\varrho + M\sqrt{\frac{\varrho}{R}}\right)R\,\delta}{R + 2\,\delta + \sqrt{(R+2\,\delta)^2 + 8\,R^2}}; \quad \delta \leqq 1.04\,R \\ V_s &= 0.281\left(1.11\,E_0\,\varrho + M\sqrt{\frac{\varrho}{R}}\right)(R+\delta); \quad \delta \geqq 1.04\,R \end{aligned} \tag{12}$$

Voraussetzung für die Gültigkeit der zweiten Formel (12) ist allerdings, dass die Entladung durch die Gesetze (9) und (10) bzw. (11) noch beherrscht wird bei den Elektrodenabständen $\delta = 1.04\,R$. Sonst ist der Übergang dort von der ersten Formel zur zweiten nicht in dieser Art möglich.

Bei der graphischen Wiedergabe der Lösung (12) benutzen wir nicht die von STEPHENSON angegebenen Werte

$$E_0 = 28.4\ \mathrm{kV/cm} \qquad M = 17.5$$

sondern ziehen PEEKS Formel [7]

$$E = 27.2\,\varrho\left(1 + \frac{0.54}{\sqrt{\varrho R}}\right) \tag{13}$$

vor, die uns besser den experimentell gefundenen Kurven angepasst erscheint.

Die zeichnerische Darstellung der Durchschlagspannung nach (12) zusammen mit den Werten (13) ist in den Abbildungen strichliert eingetragen. Sie zeigt teilweise bessere, teilweise schlechtere Übereinstimmung mit dem Experiment als unsere früher gefundene Kurve, dürfte aber doch im grossen und ganzen der Wirklichkeit mehr gerecht werden. Die berechneten Koronaspannungen fallen durchwegs zu klein aus, ein Umstand, der darauf schliessen lässt dass die Vorentladungen anderen Gesetzen unterworfen sind als der Durchschlag. Wahrscheinlich haben wir es nicht mit einem einheitlichen Mechanismus bei verschiedenen Grössen der beiden Parameter δ und R zu tun, sondern je nach Parametergrösse mit verschiedenen in einander übergehenden Entwicklungsprozessen. Eine solche Vermutung wird auch nahe gelegt durch die experimentellen Durchschlagskurven für die Kugel mit 25 cm Durchmesser. Bei $\delta = 58$ cm verbreitert sich plötzlich das Streuband bedeutend, obwohl unseren Rechnungen zufolge dafür überhaupt kein Grund vorhanden wäre. Die Ursachen hierfür aufzuklären muss einer eigenen Untersuchung vorbehalten bleiben. Trotz dieser hier aufgezeigten Schwächen unserer Formeln können die gefundenen Resultate sehr gut als Näherungsformeln in der Praxis für vorläufige Orientierungen benutzt werden, da andererseits auch die experimentellen Werte stark streuen.

Die vorliegende Untersuchung wurde von Prof. Dr. H. NORINDER angeregt, dem ich für seine vielseitige Unterstützung zu grossem Dank verpflichtet bin. Ebenso bin ich Herrn Dipl. Ing. O. SALKA für viele fördernde Diskussionen Dank schuldig.

Institutet för högspänningsforskning vid Uppsala Universitet, November 1952.

LITERATUR

1. SCHWAIGER, A., Elektrische Festigkeitslehre, Berlin 1925, S. 150.
2. PEEK, F. W., Dielectric Phenomena in High-Voltage Engineering, New York 1915, S. 27.
3. NORINDER, H., SALKA, O., Mechanism of positive spark discharges with long gaps in air at atmospheric pressures, Arkiv för Fysik, Vol. 3, Nr. 19, 1951.
4. LOEB, L. B. and MEEK, J. M., The Mechanism of the Electric Spark, Stanford University Press, California 1940, S. 46.
5. NORINDER, H., SALKA, O., Mechanism of long-gap negative spark discharges, Arkiv för Fysik, Vol. 5, Nr. 24, 1952.
6. STEPHENSON, Mr. J. D., Electrical Discharge in Gases at Normal Pressures and Temperatures, Phil. Mag., Vol. 15, 1933, S. 46.
7. Siehe [2] S. 93.

Tryckt den 3 mars 1953

Uppsala 1953. Almqvist & Wiksells Boktryckeri AB

ARKIV FÖR FYSIK Band 6 nr 37

Mitgeteilt am 3. Dez. 1952 durch I. WALLER und H. NORINDER

Form der Negativen Vorentladung in Luft bei Atmosphärendruck für Stosspannungen

Von W. PUCHER

Mit 5 Figuren im Text

Übersicht

Es werden Berechnungen durchgeführt, die das Deuten photographischer Bilder von Vorentladungen der Gasentladungsstrecke Kugel–Platte erleichtern sollen. Eingangs wird die Frage untersucht, welche die vorherrschenden Kräfte sind, die magnetischen oder die elektrischen, und dahingehend entschieden, dass die ersteren gegenüber den zweiten praktisch vernachlässigt werden können. Dann wird die Möglichkeit einer Fokusierung von „Elektrodenstielen" durch die von ihnen aufgebaute Raumladung bewiesen und schliesslich die Bahnform einer Elektronenwolke berechnet, die sich in Bereichen, wo keine Stossionisation mehr auftritt, im Felde bewegt. Dadurch ist es möglich aus der Bahnform auf die Anzahl der bewegten Elektronen zu schliessen.

1. Einleitung

In einer früheren Arbeit [1] wurde die Entwicklung der Vorentladung experimentell eingehend untersucht und dabei gefunden, dass diese in ihrem ersten Stadium einen Verlauf zeigt, der in recht charakteristischer Weise in Abb. 1 a zum Ausdruck kommt. In Abb. 1 b haben wir dasselbe Bild noch einmal schematisch wiedergegeben und erkennen daraus, dass der Vorgang von einem Punkt an der Elektrode startet, sich dann ausweitet bis zu einer maximalen Dicke (Abschnitt a) um daraufhin wieder zu konvergieren (Abschnitt b). Nach der Konvergenzstelle zeigt dann dieser sogenannte „Elektrodenstiel" — bezüglich der Bezeichnungen hier wie im Folgenden sei auf die eingangs zitierte Arbeit verwiesen — eine mehr oder weniger starke Divergenz (Abschnitt c).

Ziel der vorliegenden Arbeit ist nun, die Form der Entladung in den Abschnitten b und c mit theoretischen Mitteln zu studieren. Dabei werden wir uns der Anschauung bedienen, dass Abschnitt b durch das Vorhandensein von Raumladungen charakterisiert ist, während wir den Elektronen, die sich im Abschnitt c bewegen, nicht mehr die Fähigkeit zuschreiben, ionisieren zu können.

Fig. 1 a.

2. Elektrische und magnetische Kräfte zwischen zwei parallelen Konvektionsströmen

Um zu einer Vorstellung zu gelangen, von welcher Grössenordnung die bei Konvektionsströmen auftretenden elektrischen und magnetischen Kräfte sind und so entscheiden zu können, welche von ihnen die ausschlaggebenden sind, mögen sie für den Fall zweier paralleler gleichgerichteter Ströme

$$I_{1/2} = \varrho v$$

(ϱ = Ladung pro Längeneinheit; v = Geschwindigkeit des Ladungstransportes) im Abstand a voneinander berechnet werden. Der Abstand a sei dabei gross im Verhältnis zum Durchmesser des Querschnittes des stromführenden Volumens. Für einen Konvektionsstrom (Elektronenstrahl) allein wurde diese Berechnung bereits von E. E. Watson [2] sowie von B. v. Borries und J. Dosse [3] vorgenommen und zeigte, dass die elektrischen Kräfte die magnetischen bedeutend überwiegen und die letzteren praktisch vernachlässigt werden können. Dass dies auch für unseren Fall gilt, zeigt nachfolgende Rechnung:

a) Unter der Voraussetzung, dass die Ströme unendlich lang sind, gibt das Durchflutungsgesetz angewendet auf den Strom 1 (siehe Abb. 2)

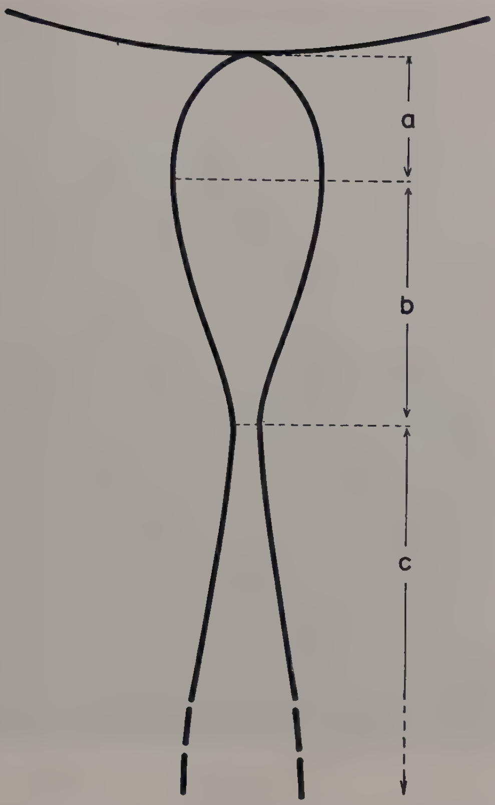

Fig. 1 b.

$$H_{\varphi} = \frac{2\,I}{c}\,\frac{1}{r}$$

und an der Stelle des Stromes 2

$$H_y = \frac{2\,I}{c}\,\frac{1}{a}$$

(H ist die magnetische Feldstärke; x, y, z sind rechtwinkelige kartesische Koordinaten und r, φ, z die entsprechenden Zylinderkoordinaten; c = Lichtgeschwindigkeit).

Die Kraft k_m pro cm mit der sich zwei Ströme derselben Stärke anziehen ist daher nach

$$k_m = \frac{1}{c}\,(\bar{J} \times \bar{H})$$

gegeben durch

$$k_m = -\frac{2\,I^2}{c^2}\,\frac{1}{a} = -\frac{2\,\varrho^2\,v^2}{a\,c^2}$$

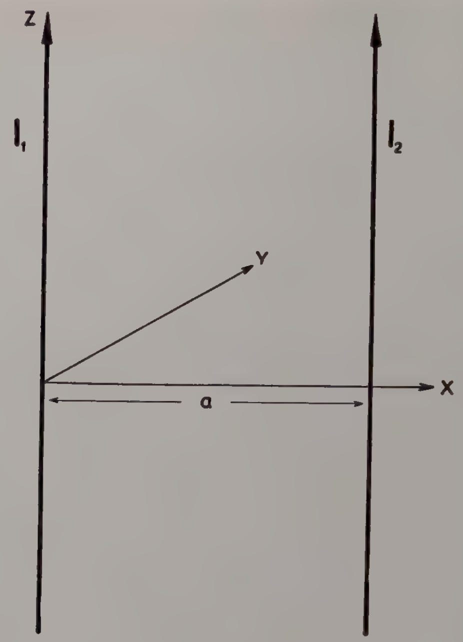

Fig. 2.

b) Das elektrische Feld eines Stromes erhält man aus dem Gesetz des Kraftflusses zu

$$E_r = \frac{2\varrho}{r}$$

und daraus die auf die Längeneinheit des zweiten Stromes wirkende elektrische Kraft

$$k_e = \frac{2\varrho^2}{a}$$

Die Gesamtkraft ist daher

$$k = k_e + k_m = \frac{2\varrho^2}{a}\left(1 - \frac{v^2}{c^2}\right)$$

und das Verhältnis der beiden Kräfte zueinander

$$\frac{k_m}{k_e} = -\frac{v^2}{c^2}$$

Wegen $v < c$ (v ist etwa 2.10^7 cm/sec [4]) ist

$$\frac{v^2}{c^2} \ll 1$$

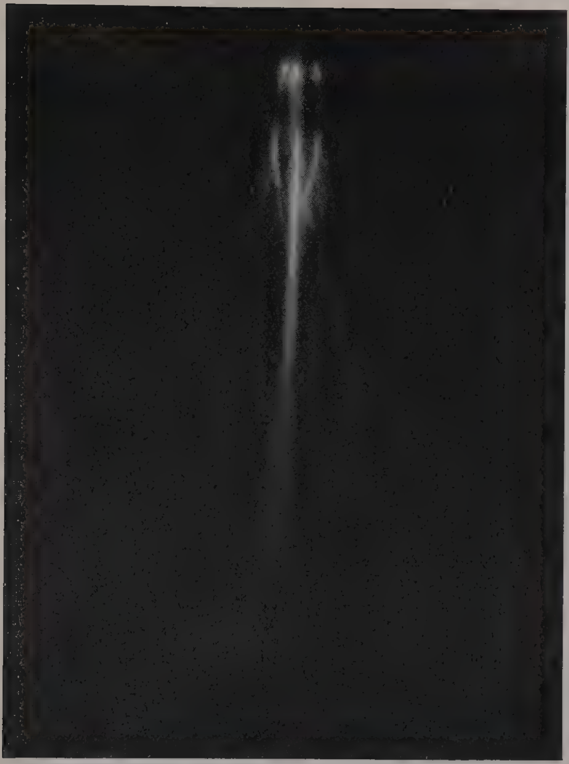

Fig. 3.

und somit der Beweis erbracht, dass die elektrischen Kräfte die allein vorherrschenden sind. Im Folgenden können wir also ruhig von den magnetischen Kräften absehen und uns nur auf die elektrischen beschränken.

Diese Erkenntnis ermöglicht aber eine Aussage, die eine Erscheinung bei Vorentladungen betrifft:

Zwei Elektrodenstiele, die an verschiedenen Stellen die Kathode verlassen, sich später aber vereinigen, tuen dies nicht auf Grund der wirkenden magnetischen Kräfte sondern allein durch elektrische, herstammend von Raumladungen (Abb. 3). Man wird so zu der Vorstellung geführt, dass beide Prozesse nicht gleichzeitig starten und somit die Elektronenwolke des zweiten Strahles von der zurückgebliebenen Raumladung des ersten angezogen wird. In Fällen, wo sich zwei Elektrodenstiele voneinander entfernen (Abb. 4) deutet dies darauf hin, dass beide Prozesse zur selben Zeit einsetzen und vor sich gehen, da dann die an der Spitze fliegenden Elektronen das Bestreben haben sich voneinander abzustossen.

3. Bewegung der Elektronen in dem Bereich, wo durch Stossionisation Raumladung erzeugt wird

Wir gehen von der Annahme aus: Ein Elektron startet von der Kathode der Gasentladungsstrecke Kugel (negativ)–Platte (geerdet) in der Symmetrieachse der Anordnung und erzeugt pro cm zurückgelegten Weges α neue Elektronen, die

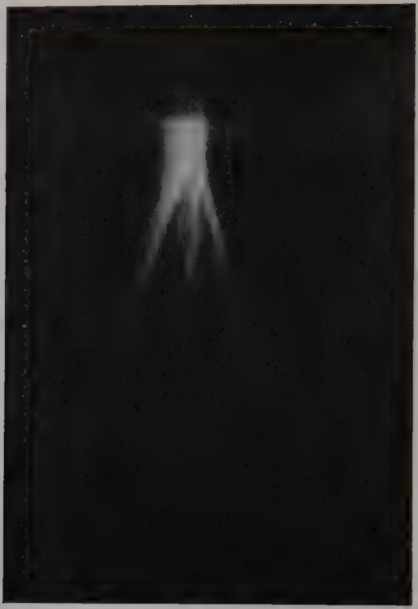

Fig. 4.

ihrerseits ebenfalls befähigt sind zu ionisieren. Auf diese Art entsteht eine Elektronenlawine, die sich in Richtung zur Platte (Anode) hin bewegt, dabei positive Raumladung auf ihrem Weg zurücklassend, da ja den positiven Ionen nur sehr kleine Beweglichkeiten zukommen. Wir fragen uns nach den Bahnen der Elektronen im Bereich b (Abb. 1) bzw. interessiert uns besonders die Bahnform der am Rande fliegenden Elektronen.

Für die Berechnung bedienen wir uns eines zylindrischen Koordinatensystems (r, φ, z) mit dem Ursprung in der Symmetrieachse der Anordnung und an der Oberfläche der Kathode und rechnen z positiv in Richtung zur Anode. Ferner machen wir noch die vereinfachende Annahme, dass die positive Raumladung nur auf die Symmetrieachse konzentriert und daselbst gleichmässig verteilt sei. Das Potential einer solchen belegten Strecke ist aber bekannt und nach ABRAHAM-BECKER [5]

$$\varphi = \frac{Q}{z_0} \ln \frac{z + \sqrt{z^2 + r^2}}{z - z_0 + \sqrt{(z - z_0)^2 + r^2}} \tag{1}$$

wenn z vom Beginn der belegten Strecke an gerechnet wird und z_0 deren Länge ist. Q stellt die gesamte Ladung dar, in unserem Fall also

$$Q = \varepsilon e^{\int_0^{z_0} \alpha \, dz}$$

(ε = Elementarladung) und Q/z_0 damit die Ladungsdichte auf der belegten Strecke. Durch die Annahme einer gleichmässigen Ladungsverteilung kann die zu beweisende Fokusierung nur abgeschwächt werden. Die Raumladung liegt nämlich nach dem Gesetz

$$\varrho = \varepsilon \alpha e^{\int_0^{z_0} \alpha d z}$$

verteilt, ist folglich an der Stelle der fliegenden Elektronen am grössten und hat auch wegen der Kürze des Abstandes die grösste Wirkung auf die Elektronen.

Aus (1) ergeben sich die zugehörigen Feldstärken

$$E_z = -\frac{Q}{z_0} \frac{1}{z+\sqrt{z^2+r^2}} \cdot$$
$$\cdot \frac{\left(z-z_0+\sqrt{(z-z_0)^2+r^2}\right)\left(1+\frac{z}{\sqrt{z^2+r^2}}\right)-\left(z+\sqrt{z^2+r^2}\right)\left(1+\frac{z-z_0}{\sqrt{(z-z_0)^2+r^2}}\right)}{z-z_0+\sqrt{(z-z_0)^2+r^2}}$$

$$E_r = -\frac{Q}{z_0} \frac{1}{z+\sqrt{z^2+r^2}} \frac{\left(z-z_0+\sqrt{(z-z_0)^2+r^2}\right)\frac{r}{\sqrt{z^2+r^2}}-\left(z+\sqrt{z^2+r^2}\right)\frac{r}{\sqrt{(z-z_0)^2+r^2}}}{z-z_0+\sqrt{(z-z_0)^2+r^2}}$$

Nachdem die fliegenden Elektronen sich immer an der Stelle $z=z_0$ d. h. am Ende der Raumladung befinden, interessieren uns im Folgenden nur die dort herrschenden Feldstärken

$$\text{(2)} \quad \begin{aligned} E_z &= -\frac{Q}{r z_0} \frac{1}{z_0+\sqrt{z_0^2+r^2}}\left[r\left(1+\frac{z_0}{\sqrt{z_0^2+r^2}}\right)-\left(z_0+\sqrt{z_0^2+r^2}\right)\right] \\ E_r &= -\frac{Q}{r z_0} \frac{1}{z_0+\sqrt{z_0^2+r^2}}\left[\frac{r^2}{\sqrt{z_0^2+r^2}}-\left(z_0+\sqrt{z_0^2+r^2}\right)\right] \end{aligned}$$

Hierin sind nun r und z_0 die laufenden Koordinaten der Bewegung. Im Weiteren wollen wir der Einfachheit halber wiederum z_0 durch z ersetzen und wissen was wir darunter verstehen.

Dazu kommt dann noch das ursprünglich gegebene Feld der Konfiguration Kugel–Platte [6]

$$\text{(3)} \quad E_{0z} = A \frac{B^2+(l-z)^2}{[B^2-(l-z)^2]^2}$$

$$A = \frac{2Vl}{f-1} \qquad f = \frac{1}{4}\left[(2p-1)+\sqrt{(2p-1)^2+8}\right]$$

$$B = l^2 \frac{f+1}{f-1} \qquad p = 1+\frac{l}{R}$$

(l = Abstand Kugel–Platte; R = Kugelradius; V = Spannung) und die radiale Feldstärke der Elektronenwolke, die diese auszudehnen sucht

$$E_{1r} = -\frac{Q}{r^2} \tag{4}$$

Die Verwendung von (4) bedingt eine Beschränkung auf den Randstrahl, da diese Formel nur für den Rand und das Gebiet ausserhalb der Wolke gilt.

Setzen wir die Geschwindigkeiten der fliegenden Teilchen proportional den Feldstärken — der Vorgang spielt sich in Luft bei Atomopshärendruck ab — so gelangen wir zur Bewegungsgleichung

$$\frac{dr}{dz} = \frac{E_r + E_{1r}}{E_z + E_{0z}} \tag{5}$$

oder zusammen mit (2), (3) und (4)

$$\frac{dr}{dz} = \frac{\dfrac{r^2}{\sqrt{z^2+r^2}} - \left(z+\sqrt{z^2+r^2}\right)\left(1-\dfrac{z}{r}\right)}{\left(z+\sqrt{z^2+r^2}\right)\left\{r\left[\dfrac{1}{\sqrt{z^2+r^2}} - A\,\dfrac{B^2+(l-z)^2}{[B^2-(l-z)^2]^2}\cdot\dfrac{z}{Q}\right]-1\right\}} \tag{6}$$

Beschränkt man sich auf die Betrachtung achsennaher Strahlen ($r^2 \sim 0$) so vereinfacht sich (6) zu

$$\frac{dr}{dz} = \frac{\dfrac{z}{r}-1}{r\left[\dfrac{1}{z} - A\,\dfrac{B^2+(l-z)^2}{[B^2-(l-z)^2]^2}\,\dfrac{z}{Q}\right]-1} \tag{6 a}$$

Eine Fokusierung des Strahles wird nun dann auftreten, wenn die erzeugte Raumladung genügend gross ist, d. h. wenn Q/z vergleichbar mit dem primären Feld E_{0z} wird oder wie wir für den Beweis das formulieren wollen, wenn gilt

$$\frac{1}{z} \gg -A\,\frac{B^2+(l-z)^2}{[B^2-(l-z)^2]^2}\cdot\frac{z}{Q} \tag{7}$$

Dann ist (6a) ungefähr äquivalent folgender integrablen Differentialgleichung

$$\frac{dr}{dz} = \frac{\dfrac{z}{r}-1}{\dfrac{r}{z}-1} \tag{8}$$

mit der Lösung

$$z^2 + r^2 = C^2 \tag{9}$$

Bestimmen wir die willkürliche Integrationskonstante C durch die Bedingung, dass an der Stelle $z = Z$ der Strahl den Radius $r = R$ haben möge, so wird aus Gl. (9)

$$z^2 + r^2 = Z^2 + R^2$$

Diese Gleichung sagt: Hat der Strahl an der Stelle $z = Z$, von der an die Näherung (7) gilt, den Radius $r = R$ so ist er an der Stelle $z = \sqrt{Z^2 + R^2}$ fokusiert. Damit ist auch der Beweis erbracht, dass eine Fokusierung überhaupt eintritt.

Zusammenfassend kann festgestellt werden: Die Raumladung, die von einer in Luft fliegenden Elektronenwolke durch Stossionisation erzeugt wird, vermag die Elektronen umgekehrt so zu leiten, dass deren Bahnen konvergieren, oder dass — die Gesamtheit der Bahnen als Strahl gesehen — dieser Strahl fokusiert wird. Dazu ist nicht ein kontinuierlicher Elektronenstrom notwendig, sondern, wie die Ableitung zeigt, widerfährt dies bereits der ersten Welle einer Elektronenlawine.

Über die Verhältnisse an und nahe bei der Kathode (Bereich a Abb. 1 b) vermag Gl. (6) keine Auskunft zu geben, da sie auf Grund der gemachten Annahmen dort die Verhältnisse nicht richtig wiedergeben kann. Auch ist es sehr fraglich, ob der Vorgang so abläuft, dass er in einem Punkt beginnt, dann rasch divergiert um schliesslich nach Aufbau einer bestimmten Raumladung wieder zu konvergieren. In der Umgebung der Kathode kann nämlich auch Photoionisation von kurzer Reichweite zu einem bedeutenden Ausmass mitspielen und so die Verhältnisse im Gebiet *a* verändern.

Um nun über den Wert $z = Z$ eine Vorstellung zu bekommen, sei ein numerisches Beispiel angeführt. Für den Fall: $2R = 50$ cm; $l = 96$ cm; $V = 728$ kVolt wird

$$E_{0z}\, z/Q = 87{,}5\ \text{cm}^{-1} \quad \text{bei}\ z = 1{,}5\ \text{cm bzw.}\ 1/z = 0{,}66\ \text{cm}^{-1}$$
$$E_{0z}\, z/Q = 3{,}64.10^{-3}\ \text{cm}^{-1} \quad \text{»}\ z = 2\ \text{cm bzw.}\ 1/z = 0{,}5\ \text{cm}^{-1}$$
$$E_{0z}\, z/Q = 5{,}57.10^{-6}\ \text{cm}^{-1} \quad \text{»}\ z = 2{,}5\ \text{cm bzw.}\ 1/z = 0{,}4\ \text{cm}^{-1}$$

also ist bei $z = 2{,}5$ cm die Relation (7) auf jeden Fall erfüllt und folglich $Z = 2{,}5$ cm, ein Wert der grössenordnungsmässig gut mit den Beobachtungen ([1] Fig. 22) übereinstimmt. Die Konvergenz tritt allerdings etwas zu rasch ein. Den Grund dafür sehen wir ein, wenn wir uns der Vorstellung RAETHERS [7] bedienen und annehmen, dass die Elektronen in einer etwa kugelförmigen Wolke fliegen, die ihr eigenes Potential aufbaut. Dann wirkt auf diejenigen Elektronen, die im vordersten Bereich fliegen eine bedeutend grössere Feldstärke in Bewegungsrichtung ein, die die rückwärts wirkende Kraft der Raumladung aufhebt und den Konvergenzpunkt weiter hinausschiebt.

4. Bewegung der Elektronen in dem Teil der Gasentladungsstrecke, wo keine neuen Ladungen mehr erzeugt werden

Abschliessend wollen wir nun noch untersuchen, in welchen Bahnen sich die Elektronen einer Elektronenwolke zwischen Kugel und Platte im Gebiet *c* (Abb. 1 b) bewegen, wenn ihre Energie nicht dazu ausreicht neue Ladungsträger zu erzeugen.

Die Elektronen seien in einer zylindrischen Scheibe konzentriert und dort gleichmässig verteilt. Das radiale Feld E_r, das dadurch erzeugt wird, beziehen wir angenähert vom unendlich langen Zylinder

$$E_r = \frac{2Q}{r} \tag{10}$$

Dabei ist Q die gesamte Ladung der zylindrischen Scheibe. Dieses Feld überlagert sich dem ursprünglichen (Gl. 3). Wieder unter der Annahme, dass die Geschwindig-

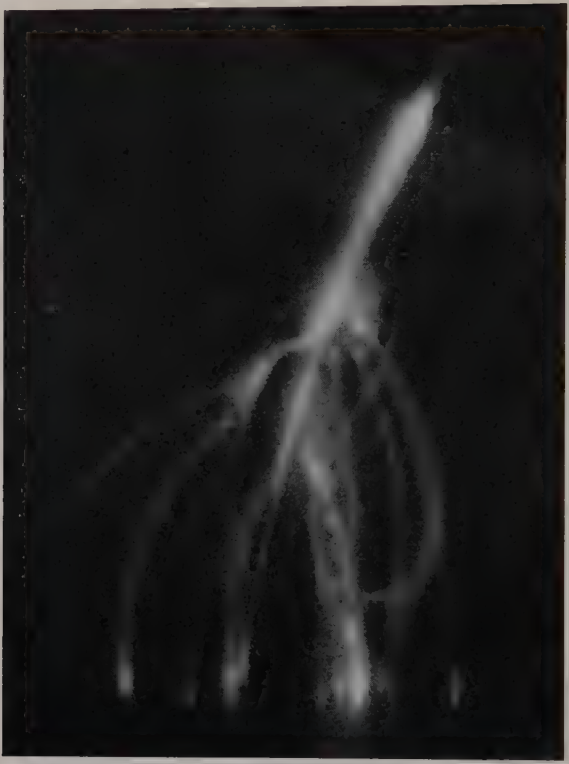

Fig. 5.

keiten der Elektronen proportional den herrschenden Feldstärken sind, erhalten wir mit den Gln. (10) und (3) die Gleichung für die Bahnform des Randstrahles

$$\frac{dr}{dz}=\frac{2Q}{r}\frac{1}{A}\frac{[B^2-(l-z)^2]^2}{B^2+(l-z)^2} \tag{11}$$

deren Lösung gegeben wird durch

$$r^2=r_0^2+\frac{4Q}{A}\left\{\frac{(l-z_0)^3}{3}+4B^3\left(\operatorname{arctg}\frac{l-z_0}{B}-\operatorname{arctg}\frac{l-z}{B}\right)-\frac{(l-z)^3}{3}-3B^2(z-z_0)\right\} \tag{12}$$

Hier sind z_0, r_0 die Koordinaten des Punktes von dem an wir den Randstrahl verfolgen, der die Elektronenscheibe längs ihrer Bahn einschliesst; r, z, sind die laufenden Koordinaten des Randstrahles. Gl. (12) gibt uns die Möglichkeit aus der Verbreiterung des Strahlenbüschels auf die transportierte Ladung zu schliessen. Abb. 5 zeigt in recht anschaulicher Weise eine solche Spreitzung des Strahles und gleichzeitige Aufspaltung in mehrere Kanäle. Mit den Daten des schon früher betrachteten Beispieles ergibt sich eine Verbreiterung von $r_0 = 0{,}05$ cm auf $r = 1{,}77$ cm längs eines Weges von $z_0 = 3$ cm bis $z = 12$ cm bei der Annahme, dass $n = 10^{10}$ Elektronen bewegt werden. Diese Elektronenzahl ist bei der hier verwendeten Spannung und

Länge der Entladungsstrecke ein kritischer Wert. Für Werte $n > 10^{10}$ tritt nämlich eine starke seitliche Spreitzung des Bündels auf. Ein solcher kritischer Wert muss natürlich für jeden einzelnen Fall eigens bestimmt werden, da er ja von Spannung, Kugelradius, Länge der Funkenstrecke und Lage des Bündels innerhalb der Funkenstrecke abhängt. Schliesslich sei erwähnt, dass eine Auseinanderspreitzung des Elektrodenstieles immer verbunden ist mit einer Aufspaltung in mehrere Äste.

Es ist mir eine angenehme Pflicht, Herrn Prof. Dr. H. Norinder für die Anregung und die stete Förderung dieser Arbeit zu danken. Ebenso schulde ich Herrn Dipl. Ing. O. Salka Dank für zahlreiche wertvolle Diskussionen.

Institutet för högspänningsforskning vid Uppsala Universitet, November 1952.

LITERATURVERZEICHNIS

1. H. Norinder, O. Salka, Mechanism of long-gap negative spark discharges in air at atmospheric pressure. Arkiv för Fysik, Band 5, Nr. 24, S. 493, Stockholm 1952.
2. E. E. Watson, Dispersion of an Electron Beam. Phil. Mag., Vol. 3 (1927), S. 849.
3. B. von Borries und J. Dosse, Arch. Elektrotechn. 32 (1938) S. 221.
4. L. B. Loeb and J. M. Meek, The Mechanism of the Electric Spark. Stanford University Press, California 1940.
5. Abraham-Becker, Theorie der Elektrizität I. B. G. Teubner in Leipzig und Berlin 1932, S. 62.
6. H. Norinder, O. Salka, Mechanism of positive spark discharges with long gaps in air at atmospheric pressure. Arkiv för Fysik, Band 3, Nr. 19 (1951), S. 369.
7. H. Raether, Zur Entwicklung von Kanalentladungen. Arch. Elektrotechn. 34 (1940), S. 49.

Tryckt den 12 mars 1953

Uppsala 1953. Almqvist & Wiksells Boktryckeri AB

ARKIV FÖR FYSIK Band 6 nr 38

Communicated 28 January 1953 by BENGT EDLÉN

A release mechanism for cosmic-ray-balloon experiments

By S. v. FRIESEN and G. LEIDE

With 2 figures in the text

Investigations of the cosmic radiation by means of open balloons usually require that the instruments get released after a predetermined lapse of time, to descend by parachute. The release mechanism must not fail even when the loads are heavy and the temperature low. The weight of the instruments amounts to 10 to 20 kilograms in most cases. The forces are often considerably greater a the launching. During a flight the apparatus meets varying temperatures somtimes as low as —80° C. It is desirable to keep its own weight low. We have designed and built a mechanical device, which fulfils the different requirements.

The load is suspended from a brass cap B, on the inner wall of which a groove has been turned. This cap fits over the lower part of a brass tube C (see Fig. 1). In C there are three holes opposite to the groove in B. The holes hold steel balls, which can be forced into the groove by means of a tapered steel rod which moves inside C. If the steel rod is kept pressed down the balls prevent the cap from falling off. When the rod is lifted, on the other hand, the pressure on the balls from the cap and its load, forces the balls back into the holes, so that the load gets released. The rod must press downwards with a certain force to counteract the forces exerted by the load. The force on the rod can be made quite small by a suitable choice of its taper. For our loads which have been of the order of 10 to 15 kilograms the top angle of the rod has been 75 degrees.

The time is set by means of an alarm clock. This clock is mounted on an aluminium disc close to the side of the tube in such a way that the cogs of the springwheel for the alarm engage grooves in the upper part of the steel rod (Fig. 2). When the alarm starts the rod is lifted and releases the load. It is convenient to use a 24 hour clock, since an ordinary alarm clock does not allow exposures of more than 11 $^1/_4$ hours duration.

The clock and the other parts of the mechanism are enclosed in a cylinder of some suitable light material e.g. pertinax. The aluminium disc forms the bottom of the cylinder and a similar disc acts as a lid. The discs are joined by three brass rods symmetrically arranged round their circumference. In the lid there is a ring for the strings from the balloon dirctly opposite the brass tube.

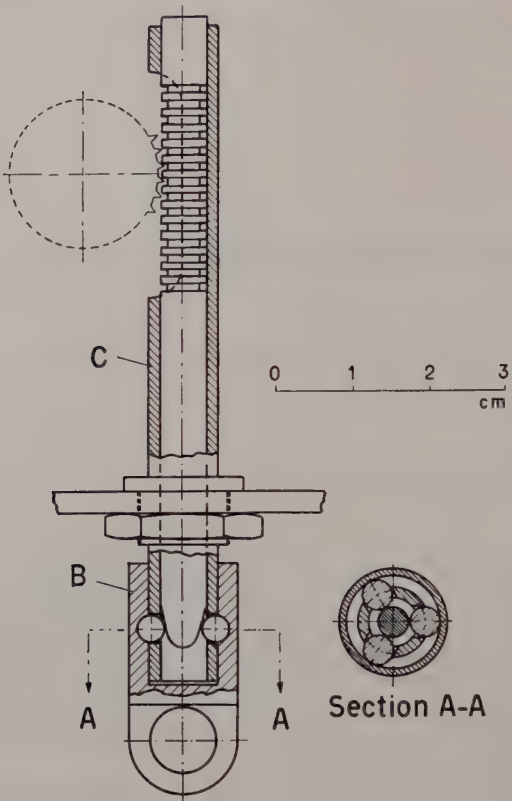

Fig. 1. Cross section of the release mechanism.

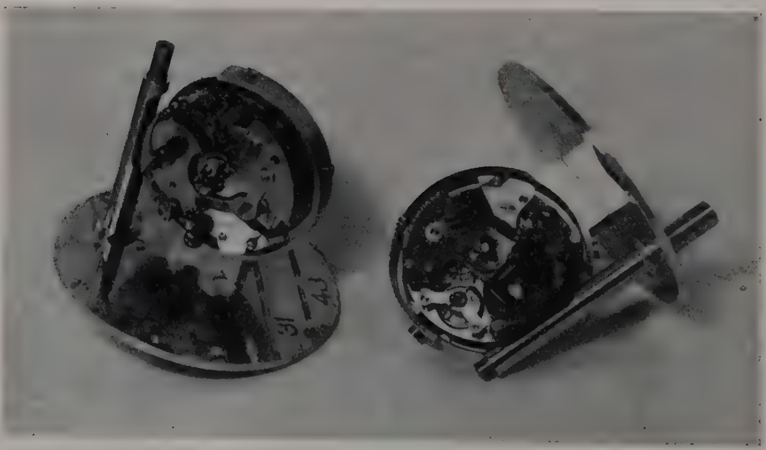

Fig. 2. Release mechanisms and alarm clocks mounted on the end plates of the protective covers.

Precautions must be taken to prevent the clock-work from being stopped by the low temperature. For flights which take place during day-time it is sufficient to paint the lid and cylinder black and to wrap the apparatus in some layers of poly-ethylene. The radiation from the sun will then keep the clock warm. For night-fligths all oil must be removed from the clock.

This mechanism has been tried in several flights by the physical laboratory of Lund university and it has always functioned in a very satisfactory manner.

The Physical laboratory, University of Lund. Lund. Dec. 31, 1952.

Tryckt den 12 mars 1953

Uppsala 1953. Almqvist & Wiksells Boktryckeri AB

ARKIV FÖR FYSIK Band 6 nr 39

Communicated 14 January 1953 by Erik Hulthén

A $^4\Sigma^-$—$^2\Pi$-system in germanium hydride (GeH)

By Bengt Kleman and Erik Werhagen

With 2 figures in the text

In the band-spectrum of GeH emitted from a King's furnace there is a red system in the region 6 000–6 650 Å. A rotational analysis has been made, from which we conclude that the system is due to a transition from a $^4\Sigma^-$-state to the $^2\Pi$-ground-state. The appearance of the system is in good agreement with the theoretical observations by Budó and Kovács regarding such a transition. The splitting in the $^4\Sigma^-$-term is rather considerable, and is only approximately described by a constant λ for the spin-spin interaction and a constant γ for the magnetic interaction between $\boldsymbol{K}$ and $\boldsymbol{S}$.

Appearance of the system

The existence of a red system in the band-spectrum of GeH has been briefly mentioned by us in previous reports of the $^2\Delta$–$^2\Pi$ system (1, 2). The red system was obtained with the same method as the violet system, with a King's furnace in emission (~ 2 300° C) (2). It was photographed in the first order of a 21-foot concave grating in Eagle mounting (dispersion ~ 1.15 Å/mm) and with Kodak 103 a F-plates. The effective exposure time was about 70^m and the hydrogen pressure was kept at about 400 mm Hg.

After sorting out bands due to impurities (among others CaH) it proved that the extension of the system had been exaggerated in the previous reports. There remained only two bands with their easily recognised origins at about 15 370 and 16 245 cm^{-1}. The bands are rather weak and have no obvious heads. A feature common to all branches is that they show very small second differences between successive lines. The band at 16 245 cm^{-1} has only two branches of acceptable strength. Of these, the red one is rather strong. In the band at 15 370 cm^{-1} there are three dominant branches of about equal strength, two to the violet and one to the red. The one to the red is accompanied by a weaker branch. In addition to these branches, there are in both bands several others which are only just measurable. The region of the bands is entirely free from impurities of the same strength as the stronger branches. The bands are overlapped by a continuum which makes the measurement of the weakest branches difficult. Despite this, repeated measurements and the analysis show that the accuracy of the measurements of the band-lines is better than it was for the $^2\Delta$–$^2\Pi$-system (2). No isotope-splitting of the band-lines is detectable. We refrain from publishing a photograph of the bands, since their weakness and the overlapping continuum do not permit of an acceptable reproduction.

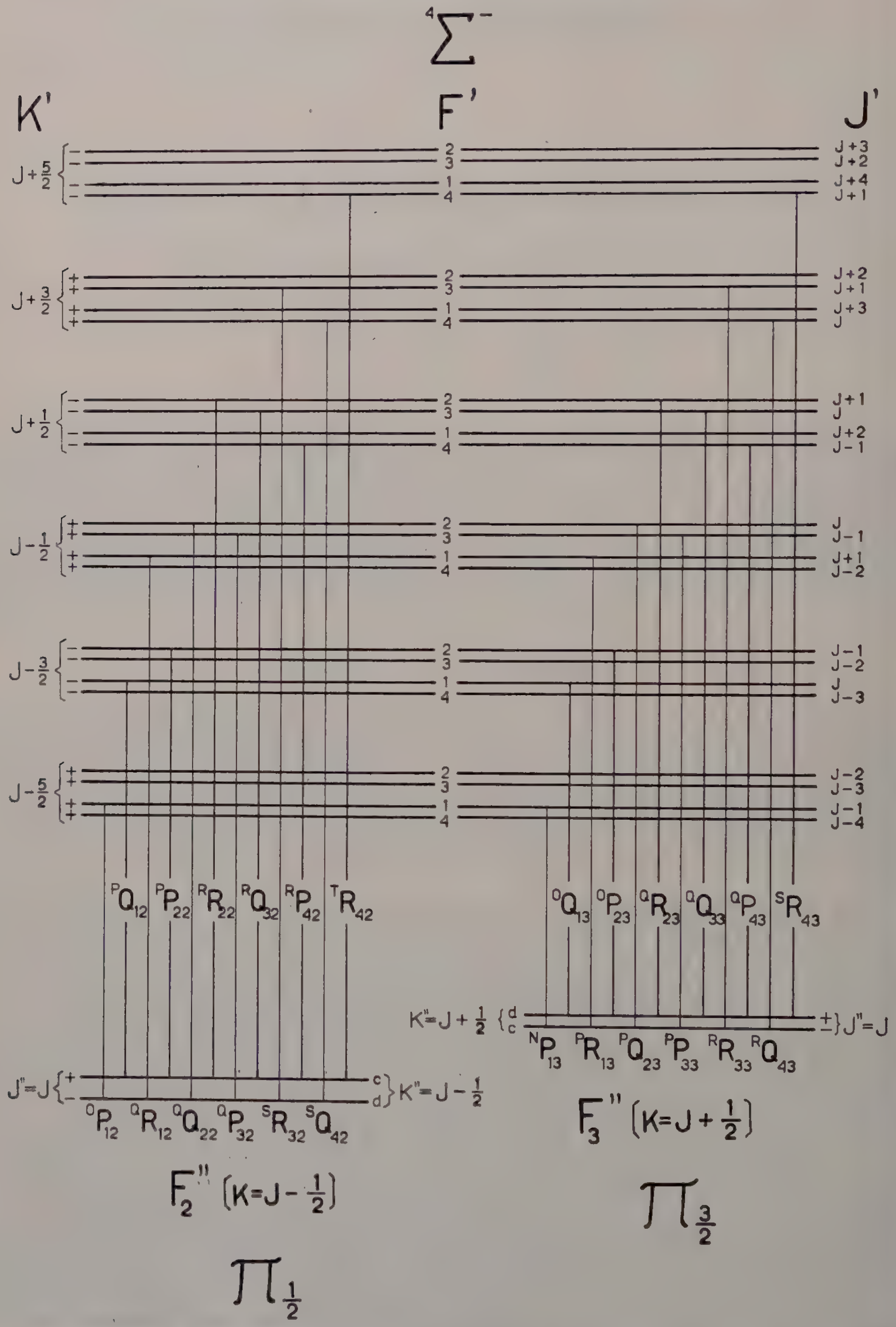
$^4\Sigma^-$
K'
F'
J'
J + 5/2
J + 3/2
J + 1/2
J − 1/2
J − 3/2
J − 5/2
J+3
J+2
J+4
J+1
J
J−1
J−2
J−3
J−4
$^PQ_{12}$ $^PP_{22}$ $^RR_{22}$ $^RQ_{32}$ $^RP_{42}$ $^TR_{42}$
$^OQ_{13}$ $^OP_{23}$ $^QR_{23}$ $^QQ_{33}$ $^QP_{43}$ $^SR_{43}$
K" = J + 1/2
J" = J
$^NP_{13}$ $^PR_{13}$ $^PQ_{23}$ $^PP_{33}$ $^RR_{33}$ $^RQ_{43}$
J" = J
K" = J − 1/2
$^OP_{12}$ $^QR_{12}$ $^QQ_{22}$ $^QP_{32}$ $^SR_{32}$ $^SQ_{42}$
F_2'' (K = J − 1/2)
F_3'' (K = J + 1/2)
$\Pi_{\frac{1}{2}}$
$\Pi_{\frac{3}{2}}$

Fig. 1. Energy level diagram of $^4\Sigma^- - ^2\Pi_{\text{reg}}$ after Budó and Kovács (4). The *c* and *d* notations of the Λ-split levels in $^2\Pi$ are those used for GeH in (2).

Analysis of the system

Some conclusions about the origin of the system may be drawn immediately from the appearance of the bands. The distance between the origins of the bands indicates that the lower state is the $^2\Pi$-ground-state of GeH and that the upper state has a slight splitting. This latter state must be a Σ-state, since a doubling of the branches would otherwise have been recognizable. The B-value of the upper state is about the same as for the $^2\Pi_{3/2}$ sub-state (6.69 cm^{-1}).

It is possible to number the lines in four branches after J″. The multiplet splitting ΔF_{dc} (J) calculated for $v = 0$ in the $^2\Pi$-term is found between the lines in the violet branch of 16 245 cm^{-1} and the lines of one of the two violet branches of 15 370 cm^{-1}. ΔF_{cd} (J) is found between the lines of the red branch of 16 245 cm^{-1} and the lines of the weaker of the two red branches of 15 370 cm^{-1} mentioned above. It is not possible to attach the two strong branches left over in 15 370 cm^{-1} to the two numbered branches in this band by means of the combination differences of $^2\Pi_{3/2}$.

There are only three low-lying Σ-states which may be expected to occur in GeH (cf. the treatment by Mulliken (3) of the term-scheme of CH, which has an analogous electronic configuration) viz. $^4\Sigma^-$, $^2\Sigma^-$ and $^2\Sigma^+$. The number and relative intensities of the branches and the absence of the $^2\Pi_{3/2}$ combination-differences between the four branches in 15 370 cm^{-1} are not in accordance with the assumption of a $^2\Sigma$–$^2\Pi$ transition.

$^4\Sigma$–$^2\Pi$ transitions have been theoretically discussed by Budó and Kovacs (4). Fig. 1 shows the transition $^4\Sigma$–$^2\Pi_{\text{reg}}$ and table 1 the relative intensities of the branches for high J-values, assuming $B' = B''$. For a study of the intensity of the lines at the beginning of the branches the complete intensity factors must be used.

The $^2\Pi$-term in GeH has a coupling-constant of 892 cm^{-1}, and we can assume that the relative intensities of the branches will be best described by the intensity factors for $^4\Sigma$–$^2\Pi$ (case a). From Table 1 we see that we shall have in the $^4\Sigma$–$^2\Pi_{\frac{1}{2}}$ sub-band (16 245 cm^{-1}) the two main branches $^QR_{12}$ and $^RP_{42}$ and in the $^4\Sigma$–$^2\Pi_{3/2}$ sub-band (15 370 cm^{-1}) the four main branches $^PR_{13}$, $^QR_{23}$, $^PP_{33}$ and $^QP_{43}$. It must

Table 1

$^4\Sigma$–$^2\Pi_{\frac{1}{2}(\text{reg})}$

	$^OP_{12}$	$^PQ_{12}$	$^QR_{12}$	$^PP_{22}$	$^QQ_{22}$	$^RR_{22}$	$^QP_{32}$	$^RQ_{32}$	$^SR_{32}$	$^RP_{42}$	$^SQ_{42}$	$^TR_{42}$
rel. int. $^2\Pi$ case a	0	1.5	3	1	0.5	0	0	0.5	1	3	1.5	0
rel. int. $^2\Pi$ case b	0	3	6	2	0	2	2	1	0	0	0	0

$^4\Sigma$–$^2\Pi_{3/2(\text{reg})}$

	$^NP_{13}$	$^OQ_{13}$	$^PR_{13}$	$^OP_{23}$	$^PQ_{23}$	$^QR_{23}$	$^PP_{33}$	$^QQ_{33}$	$^RR_{33}$	$^QP_{43}$	$^RQ_{43}$	$^SR_{43}$
rel. int. $^2\Pi$ case a	0	1.5	3	1	0.5	4	4	0.5	1	3	1.5	0
rel. int. $^2\Pi$ case b	0	0	0	0	1	2	2	0	2	6	3	0

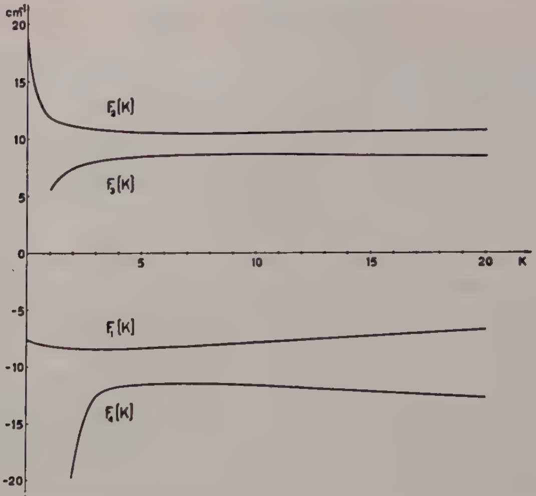

Fig. 2. The theoretical splitting of the F(K) levels with $\lambda = 0.950$ and $\gamma = 0.045$

be remarked that we can only compare the intensities of the branches in the same sub-band and that the intensities even for large coupling-constants show pronounced departures towards case *b* (cf. discussion by MULLIKEN (5)). Making allowance for departure towards case *b*, we can arrange the main branches in the following order of intensity

$$^4\Sigma\text{–}^2\Pi_{\frac{1}{2}}: {}^QR_{12} > {}^RP_{42}$$

$$^4\Sigma\text{–}^2\Pi_{3/2}: {}^QR_{23} \sim {}^PP_{33} \sim {}^QP_{43} > {}^PR_{13}.$$

Since the main branches in each sub-band emanate from different levels of $^4\Sigma$, they should show no $^2\Pi$-combination differences. Taking the branches $^QR_{12}$ and $^PR_{13}$ and $^RP_{42}$ and $^QP_{43}$ respectively from the different sub-bands they should, however, combine through the multiplet-splitting $\Delta F(J)$ of $^2\Pi$.

The appearance of the main branches in the two bands 16 245 cm⁻¹ and 15 370 cm⁻¹ is obviously in agreement with the assumption of a $^4\Sigma^-$–$^2\Pi$ transition.

The sub-band at 16 245 cm⁻¹ is stronger than the other one, and here the weaker branches $^PQ_{12}$ and $^PP_{22}$ have been measured. $^PP_{22}$ is only just measurable. Fragments of $^SR_{32}$ and $^SQ_{42}$ are found. In the sub-band at 15 370 cm⁻¹, $^OQ_{13}$, which according to the intensity factors should be strong at the beginning of the branch, can be followed up to $J = 14.5$. Fragments of $^PQ_{23}$, $^RQ_{43}$ and $^RR_{33}$ are found. In the very weak branches denoted above as fragments, the measured series of lines are not complete over a wider range. The possiblility of measuring these lines depends on the continouous background on the plates, which is somwehat uneven.

An investigation of the first lines of the branches has been made, and as far as they can be followed their intensity seems to be in agreement with the intensity factors.

We do not know the number of the vibrational level in the $^4\Sigma^-$-term from the analysis, but we will consider the band as a (0–0)-band. The equality in *B*-values

Table 2

Wave-numbers (cm^{-1}) of the band lines of the (0–0)-band

$^4\Sigma^- - ^2\Pi_{\frac{1}{2}}$				$^4\Sigma^- - ^2\Pi_{3/2}$				
$^PQ_{12}$	$^QR_{12}$	$^PP_{22}$	$^RP_{42}$	$^OQ_{13}$	$^PR_{13}$	$^QR_{23}$	$^PP_{33}$	$^QP_{43}$
	16 228.65			15 333.12		15 395.05		
	222.95		16 257.80	313.81*	15 341.95	401.80*	15 358.08	15 378.54
	217.64		266.41	294.48	335.35*	409.02	352.56	386.49
16 156.26	212.73		274.87	275.58	329.68*	416.14	346.76	394.14
137.93	208.24		283.38	256.28	323.73	423.59	341.07	401.80
119.92	204.22	16 139.13	292.06	237.20	318.04	431.10	335.35	409.49
102.39	200.45	121.45	300.98	218.07	312.55	438.68	329.68	416.93
085.30	197.07	104.10	310.19	199.68	307.10	446.37	324.51	424.39
068.48	193.95	087.42	319.55	—	301.79	453.94	318.99	431.97
052.24	191.12	—	329.00	162.89	296.72	461.52*	313.81*	439.49
036.40	188.48	054.98	338.46	144.63	291.53	469.04	308.55	446.89
020.78*	186.07	038.79	348.12	126.62	286.41	476.59	303.38	454.27
005.48	183.82	024.00	357.67*	108.21	281.28	483.98	298.15	461.52*
15 990.29	181.64	008.46	367.44	091.20	276.14	491.03	292.87	468.28
975.58	179.57	15 993.96	376.91		270.94	497.88*	287.64	475.00
960.91	177.58	979.31	386.24		265.57	504.47	282.21	481.37
946.45	175.48	964.79	395.50		260.00	510.67*	276.53	487.34
	173.25	950.03	404.40*		254.31	516.44	270.55	492.79
	170.84	936.22	412.74		248.45	521.62	264.53	497.88*
	168.19		420.67		241.91	525.89	258.05	502.35
	165.17		428.00		235.61	530.30	251.10	505.96
	161.82		434.71			533.49	243.76	508.89
	157.89		440.49					510.67*
	152.28		445.53					511.76*

* Overlapped lines.

between the upper and lower levels makes it practically impossible to assume that a transition with another v'-value should be stronger than the (0–0)-transition.

The branches can be followed to higher J''-values than was possible in the (0–0)-band of $^2\Delta - ^2\Pi$, where there is a break-off due to predissociation at about $K = 22$ in the $^2\Delta$-term. It is, however, as a rule not possible to utilize these lines in the analysis, since this presupposes a knowledge of the $^2\Pi$-differences.

The $^4\Sigma^-$-term

We use the general formulas developed by BUDÓ (6) and add the usual corrections for the influence of the centrifugal force and the magnetic interaction between the ***K***- and ***S***-vectors

$$F_1(J) = B\{J^2 + \tfrac{3}{4} - [4J^2 + 3\lambda(2J-3) + 9\lambda^2]^{\frac{1}{2}}\} - D(J-1)^4 + 3\gamma(J-3/2); \quad (J = K + \tfrac{3}{2})$$

$$F_2(J) = B\{J^2 + 2J + \tfrac{7}{4} - [4(J+1)^2 - 3\lambda(2J+5) + 9\lambda^2]^{\frac{1}{2}}\} - DJ^4 + \gamma(J - \tfrac{7}{2}); (J = K + \tfrac{1}{2})$$

$$F_3(J) = B\{J^2 + \tfrac{3}{4} + [4J^2 + 3\lambda(2J-3) + 9\lambda^2]^{\frac{1}{2}}\} - D(J+1)^4 - \gamma(J + \tfrac{9}{2}); \quad (J = K - \tfrac{1}{2})$$

$$F_4(J) = B\{J^2 + 2J + \tfrac{7}{4} + [4(J+1)^2 - 3\lambda(2J+5) + 9\lambda^2]^{\frac{1}{2}}\} - D(J+2)^4 - 3\gamma(J + \tfrac{5}{2}); \quad (J = K - \tfrac{3}{2}).$$

The B_0 and D_0-values are determined graphically by taking the mean of the four first differences $\Delta_1 F'(J) = F'(J+1) - F'(J)$.

$$[\Delta_1 F'(J)]_{\text{mean}} = 2[B - 8D](J+1) - 4D(J+1)^3.$$

The differences $\Delta_1 F'(J)$ are calculated from the main branches by means of the $^2\Pi$-differences.

To obtain the splitting in a K-quartet we substitute K for J in the formulas for $F(J)$ and omit the terms $BK(K+1)$ and $-D(K+\frac{1}{2})^4$.

$$F_1(K) = B\{2K+3-\sqrt{X_1}\} + 3\gamma K; \qquad [X_1 = (2K+3)^2 + 6\lambda K + 9\lambda^2]$$

$$F_2(K) = B\{2K+3-\sqrt{X_2}\} + \gamma(K-3); \qquad [X_2 = (2K+3)^2 - 6\lambda(K+3) + 9\lambda^2]$$

$$F_3(K) = B\{-2K+1+\sqrt{X_3}\} - \gamma(K+4); \quad [X_3 = (2K-1)^2 + 6\lambda(K-2) + 9\lambda^2]$$

$$F_4(K) = B\{-2K+1+\sqrt{X_4}\} - 3\gamma(K+1); \quad [X_4 = (2K-1)^2 - 6\lambda(K+1) + 9\lambda^2].$$

To calculate λ and γ we insert $\lambda = \bar{\lambda} + \Delta\lambda$ in these formulas and expand the square roots for small $\Delta\lambda$. The predetermined approximate value of λ used was $\bar{\lambda} = 0.960$. The separation between two of the levels is calculated, according to these formulas neglecting terms containing higher powers of $\Delta\lambda$, and put equal to the experimental value. From the resulting linear equations ($K = 4-20$) λ and γ are determined by the method of least squares. We get the following values of λ and γ from the different separations between the $F(K)$ levels:

	λ	γ
$\Delta F_{23}(K)$	—	0.039 ± 0.003
$\Delta F_{21}(K)$	0.945 ± 0.006	0.027 ± 0.004
$\Delta F_{24}(K)$	0.927 ± 0.005	0.056 ± 0.002
$\Delta F_{31}(K)$	0.968 ± 0.004	0.039 ± 0.002
$\Delta F_{34}(K)$	0.953 ± 0.004	0.056 ± 0.003
$\Delta F_{14}(K)$	—	0.042 ± 0.001

As is seen from the obtained values of λ and γ, the splitting in the $^4\Sigma$-term is not adequately described by single values of λ and γ. Especially the method of considering the magnetic interaction between $\boldsymbol{K}$ and $\boldsymbol{S}$ by adding the term $\gamma[J(J+1) - K(K+1) - S(S+1)]$ seems to be too primitive.

The only $^4\Sigma$-term which to our knowledge has been studied hitherto is a $^4\Sigma^-$-term of O_2^+. (7, 8). In this term the splitting constants were determined from $\Delta F_{21}(K)$ and $\Delta F_{34}(K)$. Though the splitting is much less ($\lambda \approx 0.1$) than in the $^4\Sigma^-$-term of GeH, no unique value of λ was obtained from the two relations. In the three vibrational levels $v = 0, 1, 2$ the λ-value determined from $\Delta F_{21}(K)$ is a few percent lower than that derived from $\Delta F_{34}(K)$, whereas γ, which is small, is rather indefinite.

Origin of the band

The origin of the band is calculated in the following way:

$$^4\Sigma^-; [F'(J)]_{\text{mean}} = \frac{F_1'(J) + F_2'(J) + F_3'(J) + F_4'(J)}{4} = T_0' + B_0'(J+\tfrac{1}{2})^2 - \ldots$$

$$^2\Pi;\ [F''(J)]_{\text{mean}} = \frac{F''_{2c}(J) + F''_{2d}(J) + F''_{3c}(J) + F''_{3d}(J)}{4} = T_0'' + B_0''(J+\tfrac{1}{2})^2 - \ldots$$

$$\overline{\nu_{00}} = \overline{(T_0' - T_0'')} = [Q(J)]_{\text{mean}} - (B_0' - B_0'')(J+\tfrac{1}{2})^2,$$

where $[Q(J)]_{\text{mean}}$ is the mean of four $Q(J)$-lines of which none has an upper level common to another of these lines. $\bar{\nu}_{00}$ is extrapolated to $(J+\tfrac{1}{2}) = 0$, which gives $\nu_{00} = T_0' - T_0''$.

The $Q(J)$ lines have been calculated from the main branches, using the $^2\Pi$-differences.

Red system of SnH

In the band-spectrum of SnH there is a red system situated in the same wavelength region as the $^4\Sigma^-$–$^2\Pi$-system of GeH. This system has been considered as a $^2\Sigma$–$^2\Pi$-ground-state transition (9), but the attempt at a rotational analysis on this basis by WATSON and SIMON (10, 11) was not successful. The similarity in the electronic configurations of SnH and GeH and the resemblance in the appearance of their red systems make it probable that they involve the same electronic transition. An analysis of this system of SnH will be attempted.

Constants of the $^4\Sigma^-$–$^2\Pi$ system in GeH

Origin of the (0–0) band.

$$\nu_{00} = 15\,816.2\ \text{cm}^{-1}$$

$^2\Pi$-*term*: the constants are given in (2).
$^4\Sigma^-$-*term*: $B_0 = 6.775\ \text{cm}^{-1}$; $D_0 = 4.72 \cdot 10^{-4}\ \text{cm}^{-1}$.
Coupling constants: (Spin-spin) interaction $\lambda = 0.95$, $\varepsilon = B\lambda \approx 6.4\ \text{cm}^{-1}$.
($\boldsymbol{K}$, $\boldsymbol{S}$) interaction $\gamma \approx 0.04\ \text{cm}^{-1}$.

Physical Institute, University of Stockholm January 1953.

REFERENCES

1. KLEMAN, B., WERHAGEN, E. Nature 1953 (in press).
2. ——. Arkiv f. Fysik, *6*, 359, 1953.
3. MULLIKEN, R. S. Rev. of Mod. Phys. *4*, 1, 1932.
4. BUDÓ, A., and KOVACS, I. Zeitsch. f. Physik *116*, 693, 1940.
5. MULLIKEN, R. S. Rev. of Mod. Physik, *3*, 90, 1931.
6. BUDÓ, A. Zeitsch. f. Physik *105*, 73, 1937.
7. NEVIN, F. E. Phil. Transact. *A 237*, 471, 1938.
8. ——, Proc. of Royal Soc. *A 174*, 371, 1940.
9. HOWELL, H. G. Proc. of Phys. Soc. *57*, 37, 1945.
10. WATSON, W. W., and SIMON, R. Phys. Rev. *55*, 358, 1939.
11. ——. Phys. Rev. *57*, 708, 1940.

Tryckt den 9 april 1953

Uppsala 1953. Almqvist & Wiksells Boktryckeri AB

ARKIV FÖR FYSIK Band 6 nr 40

Communicated 28 January 1953 by Erik Hulthén

The 2700 Å-system in the band-spectra of AlH and AlD

By Bengt Kleman

With 2 figures in the text

In the band-spectra of both AlH and AlD there is in the region (2700–2730) Å a band of complex and irregular nature. The appearance of the AlH-band indicates that it is both perturbed and predissociated. In AlD there appear, further, two weak bands degraded to the red with their heads at 2738.4 and 2648.6 Å. A rotational analysis of these bands has been made and they are shown to be the (1–1)- and (1–0)-bands respectively of a $(c)^3\Pi_r - (a)^3\Pi_r$-transition in AlD, where $(a)^3\Pi_r$ corresponds to the $(a)^3\Pi_r$-state in AlH known from the $(b)^3\Sigma - (a)^3\Pi_r$-transition in this molecule. The $(c)^3\Pi_r$-state, which has a small splitting, is perturbed. It is predissociated in $v=1$ at about $K=16$. The bands in the region (2700–2730) Å of AlH and AlD are considered to be the (0–0)-bands of the $(c)^3\Pi_r - (a)^3\Pi_r$ system.

Experimental

A strong system around 2700 Å (1) is known to exist in the band-spectra of AlH and AlD.

These systems have been photographed in the first order of a 21-foot concave grating in Eagle mounting (disp. ~ 1.3 Å/mm). A water-cooled hollow cathode was used as light-source. In the exposures of AlD small amounts of deuterium had to be let into the circulating system. In the case of AlH the hydrogen enclosed in the aluminium cathode was sufficient to produce the spectrum. The exposure times used were for AlH up to 11 hrs. and for AlD up to 5 hrs. The spectra were photographed on Kodak O III plates.

Appearance of the system

The systems of AlH and AlD around 2700 Å are shown in Fig. 1.

An attempt at a rotational analysis of the bands in the region (2700–2730) Å of AlH and AlD was not successful.

It seems impossible to pick out any regular branches in the AlH-band. The band is uncommonly short also in arc-exposures. These observations imply that there are probably both perturbations and predissociation in the electronic states involved.

The AlD-band is more rich in lines than the AlH-band and here, too, it is difficult to pick out any distinct branches. The extension of the band seems to be the normal one for a deutride-band with small splitting constants. The AlD-band thus seems to be perturbed but not predissociated.

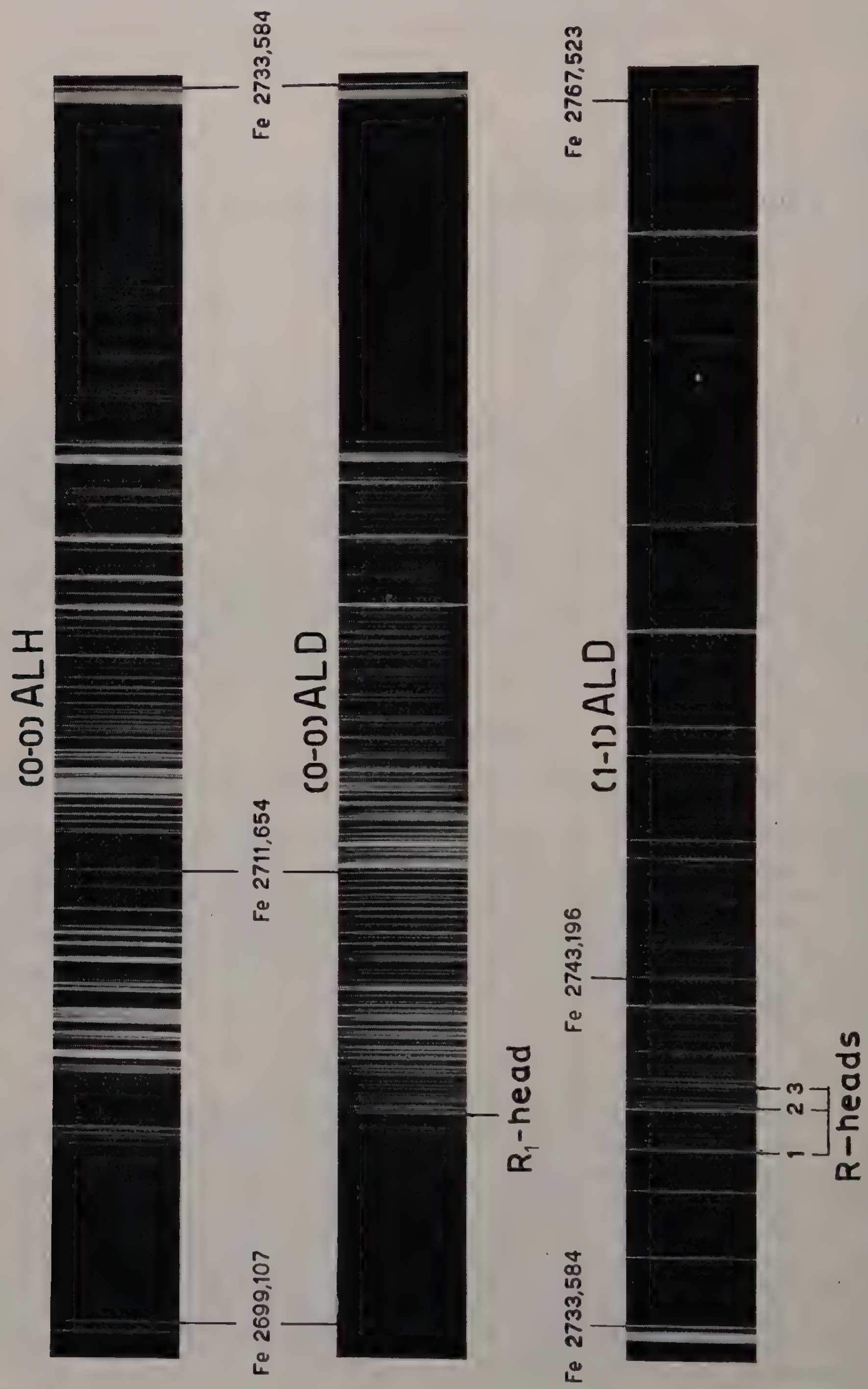

Fig. 1. The 2700 Å-systems of AlD and AlH.

From the positions of these two bands it can be concluded that they are the (0–0)-bands of the same electronic transition.

In AlD there are two weaker bands degraded to the red with their main heads at 2738.4 and 2648.6. Their positions indicate that they are the (1–1)- and (1–0)-bands respectively of the same electronic transition as the postulated (0–0)-band.

The (1–1)- and (1–0)-bands are very similar in appearance. The most characteristic feature of both bands is that the lines emerging form the above-mentioned heads split up into doublets of which one of the components suddenly vanishes. The P-branches have an open structure and are easy to follow, whereas there is considerable overlapping of the lines in the R-branches. There are very few lines due to impurities in the regions of the bands. In the (1–0)-band, however, the last R-lines and some P-lines are masked off by the strong Al-doublet at 2660.4 and 2652.5 Å and its ghosts.

Rotational analysis of the (1–1)- and (1–0)-bands of AlD

The analysis shows that the bands consist of three R-branches and three P-branches. Some lines are split up into two Λ-components. The widths of the K-triplets formed by the lines at the beginning of the branches are considerable (~ 25 cm^{-1} at $K=5$).

From the appearance of the bands it can be seen that the electronic transition involves no change in Λ-value and that $\Lambda \geqq 1$. It is not possible to assume $\Delta\Lambda = \pm 1$ and to explain the absence of Q-branches as due to partial predissociation.

The only acceptable assumption as to the electronic transition is a $^3\Pi - {}^3\Pi$ and it will be designated (c)$^3\Pi$ – (a)$^3\Pi$.

Rotational formulae for a $^3\Pi$-state have been given by Budó (2).

$$F_1(J) = B_v[J(J+1) - \sqrt{Z_1} - 2Z_2] - D_v\left(J - \frac{1}{2}\right)^4 \qquad J = K+1$$

$$F_2(J) = B_v[J(J+1) + 4Z_2] - D_v\left(J + \frac{1}{2}\right)^4 \qquad J = K$$

$$F_3(J) = B_v[J(J+1) + \sqrt{Z_1} - 2Z_2] - D_v\left(J + \frac{3}{2}\right)^4 \qquad J = K-1$$

$$Z_1 = Y(Y-4) + \frac{4}{3} + 4J(J+1)$$

$$Z_2 = \frac{1}{3Z_1}\left[Y(Y-1) - \frac{4}{9} - 2J(J+1)\right].$$

The B_v and D_v values are determined graphically by taking the mean of the three second differences $\Delta_2 F(J)$.

$$[\Delta_2 F(J)]_{\text{mean}} = 4[B_v - 6D_v]\left(J + \frac{1}{2}\right) - 8D_v\left(J + \frac{1}{2}\right)^3.$$

The origins of the bands are determined from

$$\bar{\nu}_0 = [Q(J)]_{\text{mean}} - (B_v' - B_v'')J(J+1),$$

where $\bar{\nu}_0$ is graphically extrapolated to $J(J+1) = 0$, to give ν_0. The Q-lines are calculated from the P- and R-lines.

It is apparent from the splitting constants discussed later in this paper, that the branches (R_1, P_1), (R_2, P_2) and (R_3, P_3) constitute the ($^3\Pi_0 - {}^3\Pi_0$)-, ($^3\Pi_1 - {}^3\Pi_1$)- and ($^3\Pi_2 - {}^3\Pi_2$)-sub-bands respectively.

The ordinary Λ-splitting in case *a* is for a $^3\Pi$-state greatest in $^3\Pi_0$ and negligibly small in $^3\Pi_2$. In case *b* there is the same splitting in all three sub-states. The state (c)$^3\Pi$ is near case *b* and (a)$^3\Pi$ of intermediate type ($Y \approx 12$). In the present transition we observe the sum of the Λ-splittings in the two states and it is difficult to predict the appearance. We can, however, expect the Λ-splitting to be greatest in the $^3\Pi_0 - {}^3\Pi_0$ sub-band. Experimentally, one finds a splitting of the lines in this sub-band, but the greater part of this is obviously due to a perturbition in (c)$^3\Pi$, since one of the components suddenly vanishes. In the sub-band $^3\Pi_2 - {}^3\Pi_2$ the last lines are diffuse, indicating an incipient splitting off of the lines. It is probable that this splitting is also to be interpreted as a perturbation.

A study of the intensity-factors (3) for the lines in a ($^3\Pi - {}^3\Pi$)-transition shows that no other lines than those belonging to the main R and P branches can be expected to be found in the rather weak (1–1)- and (1–0)-bands.

The wave-numbers of the band-lines are given in table 1.

(a)$^3\Pi$ AlD

The lowest expected stable triplet-state in AlD is a $^3\Pi_r$. It is natural to presume that the (a)$^3\Pi$-state is identical with this expected lowest state.

We calculate the B_0 and D_0 values for the corresponding AlH-state with the help of the following relations:

$$B_e^i = \varrho^2 B_e \quad \alpha_e^i = \varrho^3 \alpha_e \quad D_e^i = \varrho^4 \cdot D_e \quad B_v = B_e - \alpha_e \left(\mathrm{v} + \frac{1}{2}\right) \quad D_e \approx D_0.$$

For ϱ^2 the band-spectroscopic ($X^1\Sigma$)-value 0.5188 is used. The following constants are obtained

$$\left.\begin{aligned} B_0^{\mathrm{AlH}} &= 6.705 \ \mathrm{cm}^{-1} \\ D_0^{\mathrm{AlH}} &= 4.1 \cdot 10^{-4} \ \mathrm{cm}^{-1} \end{aligned}\right\} \text{(calculated from AlD).}$$

In AlH two triplet states (b)$^3\Sigma$ and (a)$^3\Pi_r$ are known, of which the latter is the lower one. The constants for (a)$^3\Pi_r$ in AlH given by CHALLACOMBE and ALMY (4) are

$$\left.\begin{aligned} B_0^{\mathrm{AlH}} &= 6.704 \ \mathrm{cm}^{-1} \\ D_0^{\mathrm{AlH}} &= 4.00 \cdot 10^{-4} \ \mathrm{cm}^{-1} \end{aligned}\right\} \text{(experimental).}$$

The agreement between the constants for AlH calculated from the deutride and the experimental values confirms the correspondence between the (a)$^3\Pi$-state in AlD and the earlier known (a)$^3\Pi_r$-state of AlH.

The $\Delta_2 F'(K)$-values show that the (c)$^3\Pi$-state in AlD is near case *b*. We attempt to calculate the splitting constant in (*a*)$^3\Pi$ from the assumption that the splitting in a *K*-triplet in (c)$^3\Pi$ is negligible.

From the rotation formulae for the $^3\Pi$-state we obtain

$$F_3''(J) - F_1''(J) = 2B''\sqrt{Z_1''} + \dots$$

and put this equal to the experimental value (Fig. 2) e.g.

$$\Delta F_{31}''(J) = R_1(J) - P_3(J) = 2B''\sqrt{\bar{Z}_1''}.$$

$\bar{Z}_1''$ is extrapolated to $J = 0$. The obtained values for the coupling-constant are

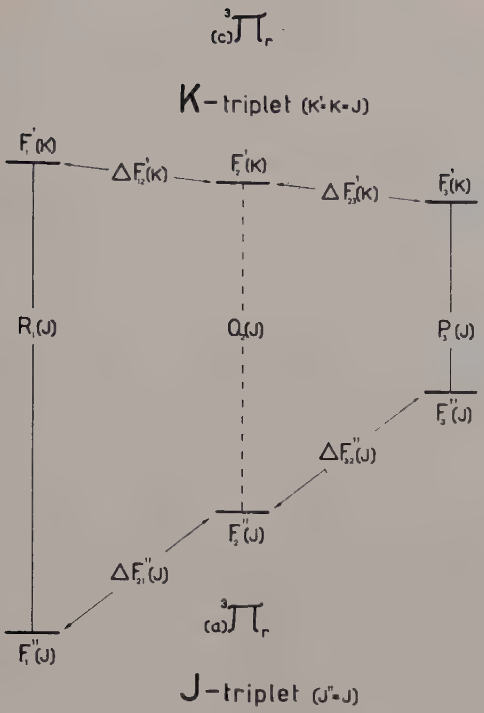

Fig. 2. Energy-level diagram for $(c)^3\Pi_r$-$(a)^3\Pi_r$ of AlD.

$$\begin{array}{l} (a)^3\Pi_r \\ \text{AlD} \end{array} \left\{ \begin{array}{l} v''=0;\ A_0''=(41.3\pm0.2)\ \text{cm}^{-1} \\ v''=1;\ A_1''=(41.3\pm0.2)\ \text{cm}^{-1} \end{array} \right.$$

CHALLACOMBE and ALMY (4) have made a careful determination of the coupling-constant for AlH

$$\begin{array}{l} (a)^3\Pi_r \\ \text{AlH} \end{array} \left\{ v''=0 \quad A_0''=40.4\ \text{cm}^{-1} \right.$$

The coupling-constant for a deutride state is generally, within very narrow limits, the same as for the corresponding hydride state. The discrepancy between the obtained value for $(a)^3\Pi_r$ in AlD and the known value in AlH must be interpreted to mean that $(c)^3\Pi$ of AlD has a detectable splitting (the $F_1'(K)$ levels lying above the $F_3'(K)$ levels; cf. Fig. 2).

(c)³Π AlD

To make a study of the coupling in $(c)^3\Pi$ in AlD we adopt the coupling-constant for $(a)^3\Pi$ from AlH. We calculate the $\Delta F''(J)$-values from the rotation formulae, using $A''=40.4$. The splitting of $(c)^3\Pi$ in a K-triplet is determined in the range $K=5-10$ from relations of the following type (Fig. 2).

$$\Delta F'_{12}(K) = R_1(J) - Q_2(J) - \Delta F''_{21}(J)$$
$$\Delta F'_{13}(K) = R_1(J) - P_3(J) - \Delta F''_{31}(J).$$

In this way it is found that the $F'(K)$-levels lie in the following order: $F'_1(K) > F'_2(K) > F'_3(K)$. The width of the $F(K)$-triplet is around 1 cm^{-1} at $K = 5$ and decreases with increasing K. This splitting must be interpreted as being due to (Λ, S)-coupling with a coupling constant $0 < Y' < 4$ $(0 < A' < 12\ \text{cm}^{-1})$ (cf. (4)). For the (c)$^3\Pi$-state one might expect a splitting due to (K, S)-coupling, but this would certainly be smaller and should increase with increasing K. We will thus consider the (c)$^3\Pi$-term to be regular.

As has already been mentioned, there is a perturbation in the $^3\Pi_o$-sub-state at $v' = 1$ in (c)$^3\Pi$. It seems as if only one of the sets of rotational levels (designated $^3\Pi_{oc}$) is perturbed in the observed region. This indicates that the perturbing state is a Σ-state.

The level $v = 1$ of (c)$^3\Pi$ is predissociated at about $K' = 16$.

Vibrational analysis

Since the potential curve of (c)$^3\Pi$ is very shallow there is no point in trying to relate the vibrational constants of this state to the rotational ones by means of empirical relations. (cf. the (A)$^1\Pi$-state of AlH and AlD.)

If we presume that the main head (Fig. 1) of the (0–0)-band of AlD is the R_1-head, the following table of heads is obtained

R_1-heads of AlD (c)$^3\Pi$—(a)$^3\Pi$

v' \ v''	0	1
0	36 959.2	
1	37 744.0	36 506.6

Using the relation $\omega''_e x''_e \approx 3 B''_e$, we get from the table $\omega''_e = 1260\ \text{cm}^{-1}$, which agrees with the value determined from the origins. ω'_e is around 800 cm^{-1}. This low value seems to be normal for a predissociated state. It must, however, be remarked that there is probably a considerable $\omega'_e x'_e$-value and that the R_1-branch due to a high α'_e-value turns at a higher rotation-number in the (0–0)-band than in the (1–0)- and (1–1)-bands. For these reasons the estimated value of ω'_e is probably too low.

That only the (0–0)-band appears in AlH is understandable from the low stability of the (c)$^3\Pi$-state. A calculation from the data of AlD shows that the depth of the potential curve (c)$^3\Pi$ is $\sim 2000\ \text{cm}^{-1}$. From this it follows that we can expect a predissociation in $v = 0$ of AlH around $K' = 15$.

An independent method of estimating the predissociation limit in (c)$^3\Pi$ gives the extension of the (0–0)-band of AlH, which is less than 400 cm^{-1}. Comparing this with the second differences of (a)$^3\Pi$, we see that the predissociation in $v' = 0$ of (c)$^3\Pi$ AlH occurs at $K' \leq 14$.

(1 − 1)

	(c) $^3\Pi_0$ − (a) $^3\Pi_0$				(c) $^3\Pi_1$ − (a) $^3\Pi_1$		(c) $^3\Pi_2$ − (a) $^3\Pi_2$	
K	R_{1c}	R_{1d}	P_{1c}	P_{1d}	R_2	P_2	R_3	P_3
4		36 506.55 Hd				36 434.36		36 423.33
5		505.68 d		36 441.33 d	36 489.09 *	424.76		414.97 *
6	504.83	504.44		428.39 d	490.05 H	413.87	36 482.02 *	405.51
7	503.15	502.50		414.97 *	490.05 *	401.99	482.61 H	394.48
8	500.81	500.17		400.73 d	489.09 *	389.19	482.02 *	382.25
9	497.82	497.03	386.12	385.64	486.99	375.51	480.47 *	369.22
10	493.74	492.98	370.65	370.12	484.06	360.95	478.28	355.05
11		488.75	354.72	353.75	480.47 *	345.58	474.90	339.99
12		483.03		336.67	475.72	329.30	470.25 *	324.10 d
13		476.89 dd		319.01	470.25 *	312.18	465.44 d	307.27
14		470.25 *		300.52	463.91	294.50	459.22 d	289.73 d
15		462.74	281.16 ?	281.61	456.81	275.69		271.31 d
16		454.54		261.77		256.41		252.21 d
17				241.49 d		236.33		232.22 d
18				219.98 d				
(1 − 0)								
3		(37 744.0 − 42.6) Hd						
4		741.78 d						
5		740.14 d		37 675.56 d	37 723.56 H	37 659.44	37 715.30 *	37 650.35
6	738.12	737.77		661.57 d	723.56 *	647.04 *	716.05 H	639.50
7	735.07	734.73		647.04 *	722.40	634.18	715.30 *	627.18
8	731.08	730.57		631.12 d	719.78 *	620.10	713.20 *	613.64 *
9		725.86		614.83 *	716.05 *	604.70	710.04	598.55
10		719.78 *	597.64	597.13	711.36	588.16	705.56 *	582.58
11		713.20 *		—	705.56 *	570.82	700.20	565.45
12		705.56 *		559.34	698.52	552.06		547.17
13				539.58 *		532.58		527.86
14				518.14		512.09		507.63 d
15			495.73 ?	496.25		490.54		486.73 *
16				473.44		468.32		464.74 d
17				449.90		444.96		$\begin{cases}441.30\\440.86\end{cases}$

* overlapped d diffuse dd very diffuse H head

Some of the lines in the (1 − 0)-band are masked by the strong Al-lines at 37 690 and 37 578 cm^{-1} and their ghosts.

Constants of AlD $(c)^3\Pi_r$–$(a)^3\Pi_r$

Origins in wave-numbers

$\nu_{11} = 36\,470.6$ cm^{-1}
$\nu_{10} = 37\,708.0$ cm^{-1}

$(a)^3\Pi_r$

$B_o'' = 3.497$ cm^{-1} $\alpha_e'' = 0.096$ cm^{-1} $r_e'' = 1.593$ Å
$B_1'' = 3.401$ » $D_o'' = 1.1 \cdot 10^{-4}$ cm^{-1} $\omega_e'' = 1260$ cm^{-1}
$B_e'' = 3.545$ » $D_1'' = 1.0 \cdot 10^{-4}$ »

$(c)^3\Pi_r$

$B_1' = 2.938$ cm^{-1} $D_1' = 3 \cdot 10^{-5}$ cm^{-1} $0 < A' < 12$ cm^{-1}
$\omega_e' \sim 800$ cm^{-1}

The photographic plates used for the measurements of the band-lines were taken in a survey of the band-spectra of AlH and AlD together with Fil. kand. ÅKE LAGERCRANTZ and Fil. lic. ULLA UHLER (5), to whom I am much indebted for this help in getting the experimental material for the above investigation.

Physical Institute,
University of Stockholm.
January 1953.

REFERENCES

1. HOLST, W. Z. f. Physik, *89*, 47, 1934.
2. BUDÓ, A. Z. f. Physik, *96*, 219, 1935.
3. ——, Z. f. Physik, *105*, 579, 1937.
4. CHALLACOMBE, C. N., ALMY, G. M. Phys. Rev. *51*, 930, 1937.
5. KLEMAN, B., LAGERCRANTZ, A., and UHLER, U., Arkiv f. Fysik, *34*, 359, 1950.

Tryckt den 9 april 1953

Uppsala 1953. Almqvist & Wiksells Boktryckeri AB

ARKIV FÖR FYSIK Band 6 nr 41

Communicated 14 January 1953 by MANNE SIEGBAHN and ERIK HULTHÉN

A semicircular permanent magnet beta-ray spectrograph for photographic recording of conversion lines

By HILDING SLÄTIS

With 15 figures in the text

Contents

Introduction 415
I. Earlier permanent magnet beta spectrographs and earlier measurements of magnetic fields by means of the electromagnetic balance method 416
II. The new permanent magnet beta spectrograph 418
  1. The magnet 418
  2. The magnetization coils 420
  3. The vacuum chamber 420
  4. The source- and film-holder 423
  5. The vacuum system 427
  6. The temperature regulator 427
  7. Equipment for measuring the strength of the magnetic field 427
  8. The strength of the magnetic field 430
  9. The beta spectrum of ThB + C + C″ 430
  10. The $H\rho$-values for the ThB *F*- and *I*-lines 431
  11. Influence of the balance current on the remanence 431
  12. The constancy of the remanence 432
  13. Influence of the temperature on the remanence 432
  14. Resolving power of the spectrograph and inherent half-width of the K-conversion lines in the beta spectrum of ThB + C + C″ 432
Summary 435

Introduction

At present a large number of different types of beta spectrographs exist. We have the old semicircular spectrograph and the double focusing spectrometer, which belong to the so-called flat spectroscopes — a spectroscope in which the central electron path lies in a plane. On the other hand, the solenoidal, long lens, short lens, and the ntermediate image beta spectrometers belong to the so-called helical spectroscopes, n which the electron paths are of helicoidal shape. An excellent review of all these various types of beta-ray spectrographs and spectrometers has recently been given by PERSICO and GEOFFRION (1).

The most important characteristics of a given spectrometer are the resolving power and the transmission. Generally an improvement of the resolving power will reduce the transmission. The choice of the spectrograph type therefore depends on the actual problem. If conversion lines are to be studied with a very high resolution, the flat spectroscopes seem to be preferable. In addition, if photographic recording is desirable, the old semicircular spectrograph type may again be the best one. Often the sample itself limits the resolution obtainable. If the specific activity is low, the absorption of energy of the beta particles in the sample itself decreases the resolution. In some cases, however, the active deposit in the source may be so thin that no absorption of energy is detectable. This is the case for ThB + C + C″, RaB + + C + C″ and AcB + C + C″. These activities are, as is well known, daughter substances from noble gases (Tn, Rn and An respectively) and may be made to deposit on a negatively charged thin wire while the activities are in an ionized state. In addition, sources of these materials are available in sufficient strength. It is therefore tempting to construct a spectrograph with the highest possible resolution, for cases where the properties of the source do not limit the resolution.

In order to get a high resolving power one has to produce a magnetie field of the highest constancy. Such fields are easily obtainable by means of the modern permanent magnet alloys, if these are kept at a constant temperature.

I. Earlier permanent magnet beta spectrographs and earlier measurements of magnetic fields by means of the electromagnetic balance method

In 1931 KAPITZA (2, 3) suggested that the cobalt steel available at that time made possible the construction of permanent magnets as powerful as electromagnets, without unduly increasing the weight of iron. COCKCROFT, ELLIS and KERSHAW (2) point out the advantages of permanent magnets in many different types of experiment, for instance mass spectrograph work, determination of magnetic susceptibility, and, of course, beta-ray spectroscopy. A permanent magnet with an air-gap of 5.5 cm and with pole-pieces 17 × 29 cm (500 cm²) was constructed.

If H_s be the field strength in the steel and H_g the field strength in the air-gap, we have

$$\int H_s\, d\, l_s + \int H_g\, d\, l_g = 0.$$

The length l_s of the steel necessary is then approximately

(1) $$l_s = \frac{H_g}{H_s}\, l_g,$$

where l_g is the width of the air-gap.

The condition of constancy of flux gives

(2) $$A_s\, B_s = A_g\, H_g\, q,$$

where B_s is the flux density in the permanent magnet steel and A_s and A_g the cross sections of the steel and air-gap, respectively. q is a leakage factor. Hence, the volume of magnet steel required is

(3) $$A_s\, l_s = H_g^2\, A_g\, l_g\, q / H_s\, B_s.$$

This equation shows that the higher the product $H_s\, B_s$, the smaller the volume of steel required. It is assumed that the loss of magnetic potential in the yoke is negligible. The yoke was of high permeability steel and had a weight of 680 kg, the weight of the permanent magnet steel being about 230 kg and that of the magnetization coils 180 kg. The yoke was of U-shape.

The permanent magnet of COCKCROFT, ELLIS and KERSHAW has been used in a number of beta spectroscopical investigations, the first of which were those of ELLIS (4, 5) on the gamma-rays of ThB + C.

A permanent magnet for 5300 gauss between poles of an area about 8 × 26 cm and 19 mm apart was built by BRIGGS (6). No device for changing the remanence was used. SCOTT (7) studied the energy of the most intense beta-ray line (1931.8 gauss cm) from RaB, using a permanent magnet beta spectrograph. The field strength was measured by the COTTON (8) balance method. The magnetic field was horizontal, and a rectangular coil was hung from a balance, perpendicular to the magnetic field, and so that only the lower, horizontal, part of the coil was situated in the field to be measured. The force on this part was measured by the balance when a known current was passed through the coil. The effective length of the horizontal part is equal to the distance between the two parallel vertical parts of the coil. This distance is easily measured, if the coil is supported by an optically worked glass plate of rectangular shape. According to COTTON this method makes it possible to measure the magnetic field with an accuracy greater than one part in 20000.

The dimensions of the rectangular glass plate in SCOTT's work were 30 × 3 × 0.45 cm. Thin silver strips were fastened to the sides of the plate, and a system of light aluminium and tin strips supplied current to the silver strips. The value of the force measured was 200 mg, which could be measured to less than one part in 10000. However, according to ROGERS (9), who used the apparatus of SCOTT, this figure for the accuracy is rather too optimistic and should be 1 part in 1000. Rogers investigated the three most intense RaB conversion lines.

A similar balanc was used by BRIGGS and HARPER (10) and by BRIGGS (11) for measuring magnetic fields of the order of 10000 gauss in determinations of the velocity of the alpha particles from RaC′. The current i_1, which brings the balance into equilibrium when the direction of this current is such that the force on the coil is downward, is first observed. An appropriate mass M is then added to the coil, and equilibrium again etablished by adjusting the current to a new value i_2. The field is given by the equation

$$(H - H')\, n L (i_1 + i_2) = 2\, M g, \tag{4}$$

where L is the effective mean width of the rectangular coil. H is the magnetic field strength at the base of the coil, and H' is the stray field at the top of the coil. The number of windings is n, and g is the gravitational acceleration.

The sensitivity of the balance method for measuring magnetic fields is of course greatest for strong fields. Fields of 10000 gauss were measured in international units to a few parts in 10^5.

A large permanent magnet for work in beta spectroscopy was also made by SURUGUE (12). The shape of the magnet was similar to that of COCKCROFT, ELLIS and KERSHAW. The permanent steel contained 36 per cent cobalt. This steel gives a remanence of 8800 gauss and a coercive force of 260 gauss. The size of the air-gap was 25 × 37 × 6 cm, and the corresponding fields strength 1430 gauss. Another pair of pole-pieces gave the figure 33 × 45 × 12 cm at 780 gauss. On each side of the pole-pieces packets of 10 (altogether 20) pieces of permanent steel were situated. The size of the pieces was 2.84 × 14 × 50 cm. The weight of the permanent steel was 340 kg, of the yoke 640 kg, and of the whole magnet with magnetization coils 1480 kg.

The conversion lines of ThB + C + C″, AcB + C + C″ and RdAc + AcX + · · · were recorded on Ilford X-ray plates, and the Hϱ-values for the lines determined by absolute measurements. The field strength was measured by a coil of known area, which was removed from the field. The current induced was compensated with a current induced by mutual induction from another, external, coil, when a known current in this coil was broken at the moment when the coils were removed. A fluxmeter served as zero-instrument.

HARPER and ROBERTS (13) made precise measurements of the $H\varrho$ values of beta-rays from RaB by means of photographic spectrographs of the type used by ELLIS, and also that of SCOTT. Field measurements were made by the method developed by BRIGGS and HARPER, and the $H\varrho$-values obtained were considered to be correct to 1 part in 10^4.

A permanent magnet beta-ray spectrograph is also described by PLESSET, HARNWELL, and SEIDL (14). The pole-pieces were vertical and in the middle of a rectangular yoke. The weight of the "Alnico" steel was 204 kg, the total weight of the permanent magnet being 1360 kg. The maximum field was 3000 oersteds in a gap 20.3 × 40.6 × × 4 cm³. The beta spectra were recorded on photographic films, and some tests were made on lines in the spectrum of RaB + C as well as on the continuous beta spectrum of RaE. The relationship between blackening and exposure was studied.

CORK (15) also uses the photographic method in magnetic spectrometers of the semi-circular focusing type. Two spectrographs described by him have permanent magnets. The magnet steel is "Alnico", situated on each side of the horizontal pole-pieces, which are in the middle of a rectangular yoke. The magnet steel, consisting of ground cylinders between the polepieces and the yoke, are surrounded by the magnetization coils. The magnetic field is measured by a rotor with commutator driven at constant speed by a synchronous motor, and the direct voltage output of the d.c. generator so formed is applied to a potentiometer.

The largest permanent magnet constructed so far was built by ROSENBLUM and TSAI (16) in Bellevue. The yoke consists of two concentric iron rings of 4 m diameter. The pole-pieces are in the centre of these rings and the gap can be regulated between 0 and 30 cm. The permanent steel consists of Ni-Al-steel pieces of 2.1 × 6.2 × 38 cm. Two layers of these pieces, or 5750 kg Ni-Al-steel, are situated on each side of the pole-pieces, which are 120 cm in diameter and 37 cm in height, and shaped so that the active air-gap has a rectangular form 44 × 78 cm. The Ni-Al-steel (altogether 11500 kg) is surrounded by the magnetization coils. The permanent field is 13000 gauss when the air-gap is 18 mm. ROSENBLUM and his co-workers have used this field for alpha-particle energy measurements for a great number of alpha-active elements.

It is remarkable that none of the earlier permanent magnet spectrographs have been equipped with arrangements to maintain a constant temperature. As will be shown below, a constant temperature is necessary to obtain high resolution.

II. The new permanent magnet beta spectrograph

1. *The magnet.* It was desired to obtain a permanent magnetic field of 2000 gauss in an air-gap of circular area, diameter 40 cm, the distance between the pole surfaces being 4 cm. Formula (3) gives

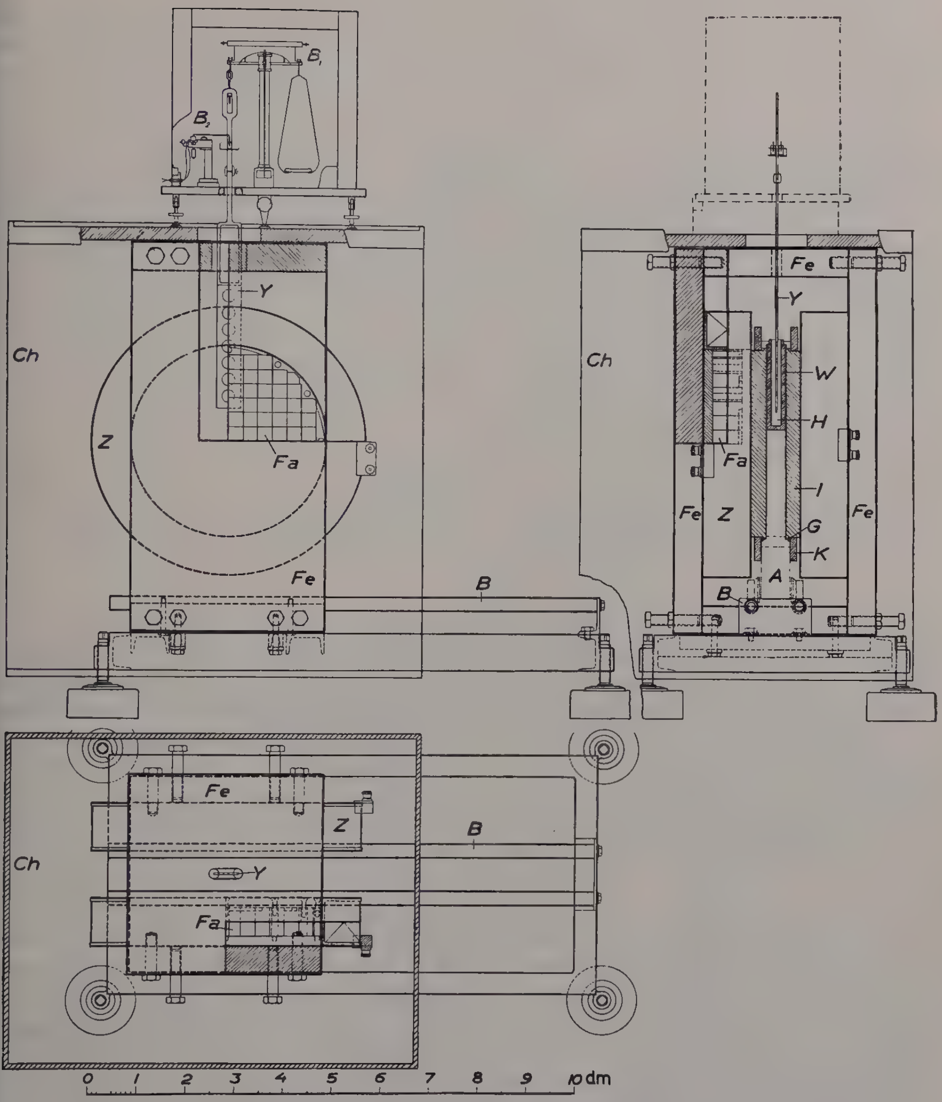

Fig. 1. Design of the semicircular permanent magnet beta spectrograph. For details see the text.

$$A_g\, l_s = 2000^2 \cdot \pi \cdot 20^2 \cdot 4 \cdot 1.6/1\,200\,000 = 27\,000 \text{ cm}^3,$$

if the leakage factor is 1.6, and we use the aluminium-nickel-cobalt steel "Fama 700" from the Swedish firm Fagersta in Dannemora. The figure 1 200 000 for $H_s B_s$ is given in the data issued by the factory. We thus get for l_s the value 8 cm. It is assumed that the magnetic resistance in the iron yoke can be neglected. For safety we have used a larger amount of magnetic steel, two layers, each of thickness 6 cm.

The area of the Alnico steel was assumed to be $\pi \cdot 20^2 = 1\,257$ cm². We have used the "Fama 700" in prismatic pieces of 3 × 3 × 6 cm^3. The number of these pieces was 120 in each layer, giving an area of 1080 cm^2 (instead of 1257 cm^2). The pieces were ground to 6 cm length with an error of $\pm$ 0.01 mm. The weight of the permanent steel was 91 kg.

The shape of the iron yoke may be seen from Fig. 1, which shows the spectrograph diagrammatically. The yoke *Fe* has a rectangular form with a height of 80 cm, width 40 × 42 cm, the thickness of the iron being 6 cm. The permanent magnet pieces *Fa* are fixed between two circular iron discs of 40 cm diameter, the discs being kept in position by brass screws as well as by the brass reels for the magnetization coils *Z*. The iron discs *I* are also of 40 cm diameter, but of 3 cm thickness, and constitute the walls of the circular, vertical vacuum chamber.

The distance 30 cm between the vertical, inner walls of the yoke, and hence the distance between the pole shoes, can be increased by means of the screws between these walls and the horizontal parts of the yoke in order to permit insertion of the vacuum chamber between the pole shoes.

In the upper part of the yoke there is an opening for the frame for the balance coil Y, which is used to measure the magnetic field.

The yoke is mounted on an iron frame, which rests on screws bearing on discs on the floor. By means of these screws the yoke can be adjusted so that it is vertical.

The weight of the iron yoke is 550 kg.

2. *The magnetization coils.* The position of the magnetization coils Z may be seen in Fig. 1, and a part of them in the photograph Fig. 5. The first coil (to the right in Fig. 5) consists of 870 turns of cotton-covered copper wire of 2.3 mm diameter, wound on a brass reel. The second coil, which is of the same size, has 748 + 124 turns. It is possible to use an alternating current in the last 124 turns in order to make experiments on ageing the field when exciting the permanent alloy. The weight of the copper wire is 100 kg, the length 2660 m, the resistance 11.4 ohms. The inner radius of the windings is 21 cm, the outer 28 cm, and the width of the windings in each coil 8.5 cm. Between the windings and the reel there is an insulation layer of mica.

3. *The vacuum chamber.* The vacuum chamber is illustrated in Fig. 2. It rests on wheels on the rails *B* and is thus easily pushed in and out of the yoke. A brass ring *L*, resting on the carriage A, serves as a frame, and together with the circular iron discs *I* of 3 cm thickness makes up the walls of the vacuum chamber. A pocket H permits the insertion of the measuring balance coil in the magnetic field between the pole shoes *I*. The actual pole distance for the magnet will be equal to the distance between the walls *I*. This distance is 39.83 mm. The pocket *H* and the frame *O* for the sample- and film-holder *C* have the same thickness, in order to diminish the indentation of the iron discs by the atmospheric pressure, when the chamber is evacuated. Without these supports the indentation would amount to 0.02 mm per disc, and hence cause an error of 0.1 % in the pole distance at the centre of the chamber. The brass supports make this error negligible. The iron discs were annealed, cooled slowly, and ground. The deviation of the pole faces from a plane is smaller than 0.01 mm.

Fig. 3 shows a photograph of the vacuum chamber when one of the pole-piece walls is removed. The yoke and the holders for the permanent magnets are seen to the left. In order to get conformity with Fig. 2, the vacuum chamber was turned

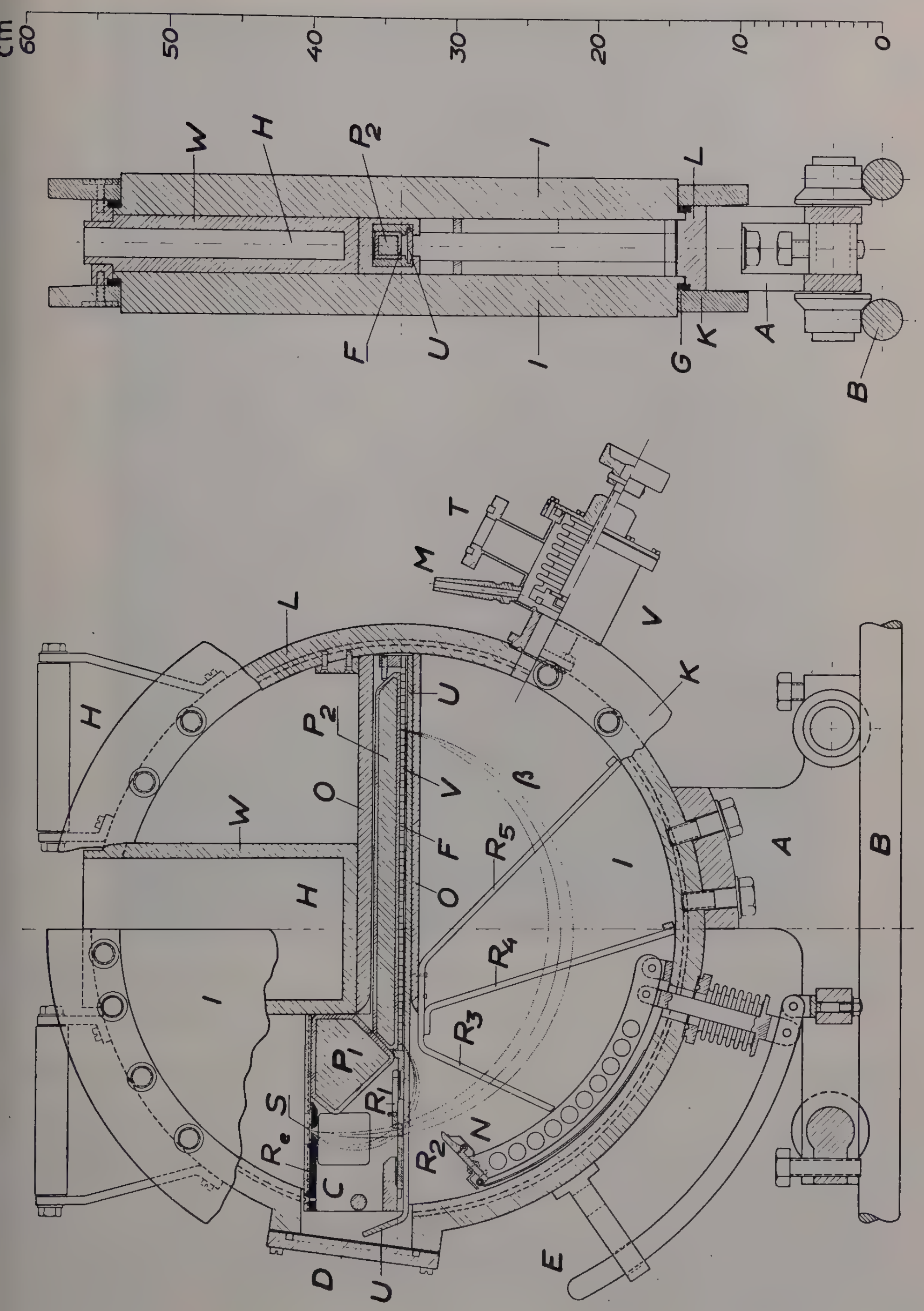

Fig. 2. Design of the vacuum chamber with source- and film-holder. For details see the text.

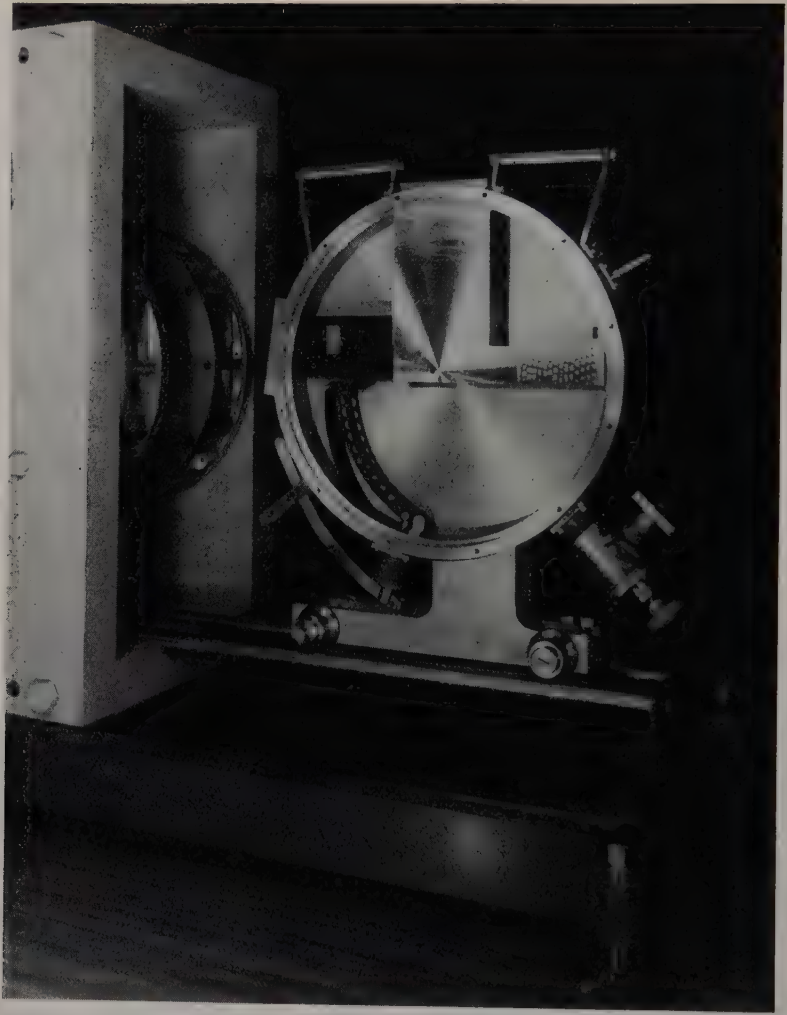

Fig. 3. Photograph of the vacuum chamber. The front wall pole piece is removed. The yoke and the permanent magnet holders without coil reels are seen to the left. The vacuum chamber should be rotated through 180° about a vertical axis through the centre of the chamber; the position in the figure is chosen in order to get conformity with Fig. 2.

through 180° about a vertical axis through the centre of the chamber; the position in Fig. 3 is consequently not correct.

R_3, R_4 and R_5 are aluminium baffles which prevent scattering of the electrons from the iron walls. These baffles are close to the pole faces and 10 mm in height over these planes, so that the width of the space for electron paths is 20 mm (the baffles are not present in Fig. 3).

N is a shutter, which can be operated by the handle *E* from outside the vacuum chamber. In this way exposures can be made only when the vacuum is good.

A valve *V* with a tube *T* to the pump and a tube *M* for the vacuum gauge are seen to the right. *H* are handles.

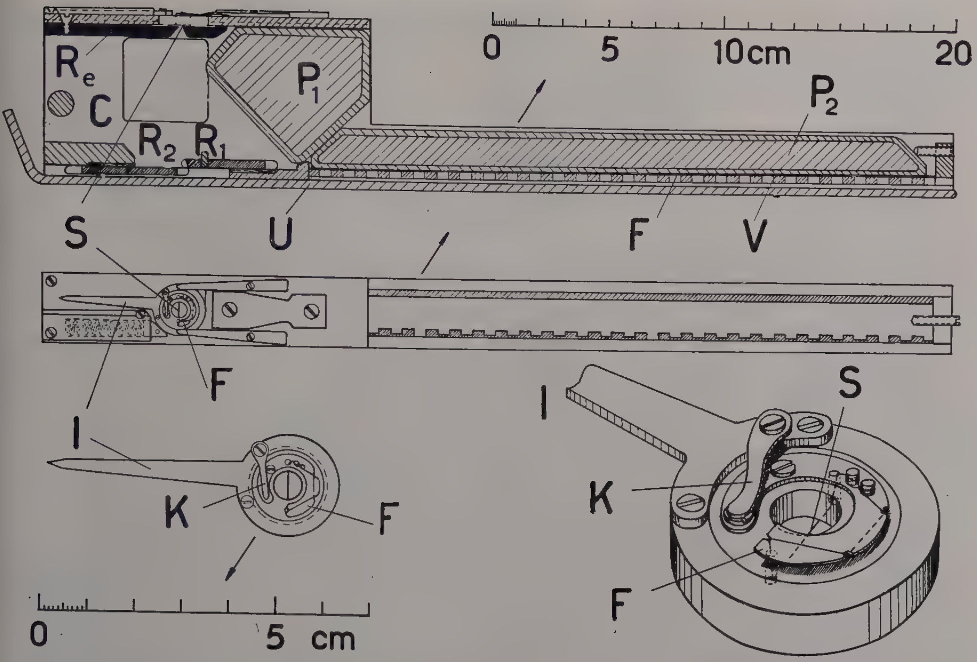

Fig. 4. 1) The source- and film-holder. R_e = ebonite baffle, R_1, R_2 = brass baffles. 2) The source-holder for ThB + C + C″ or RaB + C + C″. The activity is deposited on a thin platinum or tungsten wire S, 25 or 12 μ thick.

4. *The source- and film-holder*. Fig. 4 shows the design of the source- and film-holder. The position of the holder in the spectrograph is seen in Fig. 2 (C) and in Fig. 3. In Fig. 4, S is the source, and P_1 and P_2 are lead shieldings. R_e is an ebonite baffle, which screens off radiation from contaminated parts of the source holder (this baffle is used if the spectrum of ThB + C + C″ or RaB + C + C″ is taken, because the source holder is a part of the activation vessel when the wire is activated, and is thus to a certain degree contaminated). R_1 and R_2 are the edges of a baffle of brass, F is the film (19 × 270 mm), V is a row of calibration edges 10 mm apart, which will appear on each film as light edges in the darkening caused by the continuous spectrum or by light (see Fig. 11) and U an opaque sliding cover. The holder is kept in position by the frame O (see Fig. 2). The source- and film-holder, which is made of brass, can be inserted or taken out through the opening D (see also Fig. 5).

Fig. 4 shows the arrangement used when the beta spectra of ThB + C + C″ or RaB + C + C″ were investigated. R is a brass ring with an index I. Inside the brass ring there is a ring of lava. The diameter of the hole in the lava ring is 6 mm. A thin wire of platinum (25 μ diameter) or tungsten (12 μ) is connected to the brass spring F, which keeps the wire stretched. By means of the small switch K the wire may be insulated from the brass ring or connected to it. The former position is used when the wire is activated by for instance ThB. The wire-holder is then placed as a cover over a vessel in the bottom of which is a radiothorium source, and the wire is connected to a negative potential, in the well-known manner. During this procedure the hole in the lava disc is closed by a small cover. Later, when the wire-holder is brought

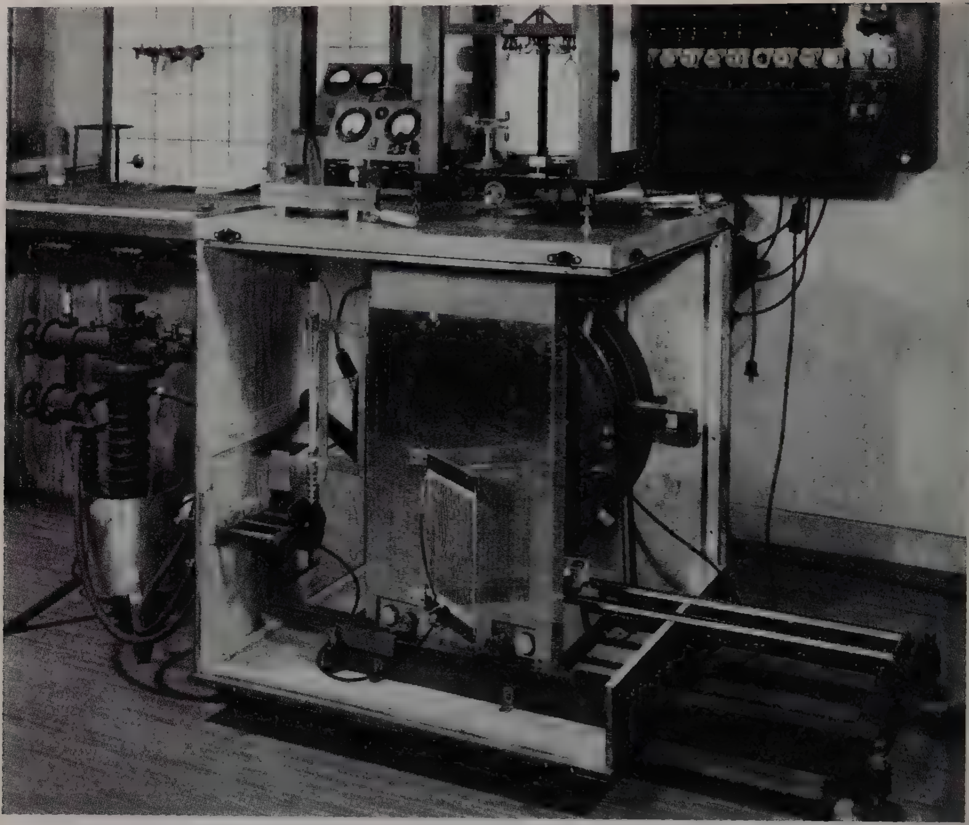

Fig. 5. Photograph of the permanent magnet beta spectrograph. The front wall and the right-hand wall of the cabinet are removed in order to show the thermostat, which consists of a contact thermometer, a heating grid, a relay (not visible, behind the left-hand wall), and a fan. An aluminium sheet between the heating grid and the yoke prevents the front side of the yoke from being heated by radiation from the grid. The sample- and film-holder is partly inserted into the vacuum chamber, between the magnetization coils. On the table: a balance, a vaccuum gauge, and a device to cut the films.

into position in the source- and film-holder, the switch K connects the wire to the brass ring and hence to the ground, which prevents the accumulation of charge on the wire when the active deposit decyas. A charge on the wire would of course influence the velocity of the beta particles.

When the leadshielding P_2 and the sliding cover U are removed, *the distance d between the wire and the calibration edges is measured directly by means of a comparator* (more correctly, the quantity measured is the projection of this distance in a plane perpendicular to the wire, i.e. in a plane parallel to the large side walls of the source and film-holder). Fig. 6 indicates the position of the source- and film-holder C and how the distances d are measured by means of a comparator K. In the case reproduced the distance d_{23} is obtained by focusing first the wire S in the microscope M_1 and then the edge V_{23}, the measuring microscope M_2 being read each time and the difference between the readings taken. A and B are support blocks.

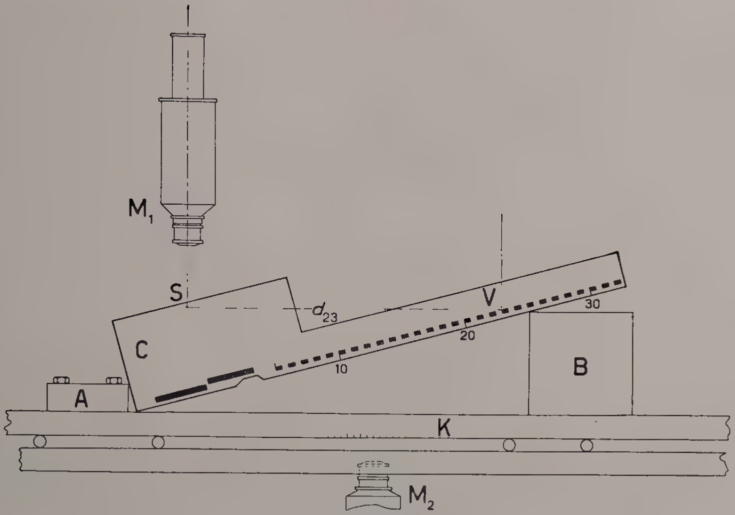

Fig. 6. Method of measuring the diameter 2ϱ of the electron paths.

The diameter 2ϱ of the electron paths corresponding to a conversion line L is computed from the distance x of the line from an adjacent calibration edge, using the distance d of this edge from the wire S, and the distance a of the edge from the baffle (see Fig. 7). Simple geometric considerations give

$$2\varrho=\sqrt{d^2+2ax+x^2}=d+a\cdot\frac{x}{d}+\frac{h^2}{2d}\cdot\frac{x^2}{d^2}+\cdots. \tag{5}$$

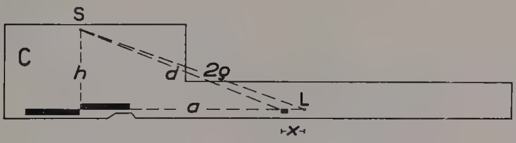

Fig. 7. Principle for measuring the diameter 2ϱ of the electron paths.

When this method is used only an approximate value for the distance a (or h) is necessary. a is not measured directly, because the location of the baffle is not well-defined, but it is computed from the measured spacings between the calibration

Table I

n = number of edge	$a_n - a_{13}$ mm	d_n mm	$c_n = d_n^2 - (a_n - a_{13})^2$
13	0	148.310	21 996
17	40.049	185.435	32 782
18	50.065	194.926	35 489
22	90.052	233.212	46 279
23	100.058	242.873	48 977
31	179.940	320.835	70 556

edges and from the distances d. Thus we do not measure the distances a_6, a_7, $a_8 \cdots$ but the differences $a_7 - a_6$, $a_8 - a_3$ and so on. This is easily done with a comparator. We give here the figures obtained in a measurement. In table I the first column gives the number n of the edge, the second column the difference $a_n - a_{13}$ and the third column the corresponding distance d_n. The equation

$$a_n^2 + h^2 - d_n^2 = 0 \tag{6}$$

can be written

$$(a_n - a_{13})\,\xi + \eta - c_n = 0, \tag{7}$$

if we introduce

$$\begin{cases} \xi = 2\,a_{13} \\ \eta = a_{13}^2 + h^2 \\ c_n = d_n^2 - (a_n - a_{13})^2 \end{cases} \tag{8}$$

The values in Table I give six equations of the form (7). By means of the method of least squares we get the solutions

$$\begin{aligned} \xi &= 269.895 \pm 0.056 \\ \eta &= 21981 \pm 5.4, \end{aligned}$$

or

$$\begin{aligned} a_{13} &= 134.948 \pm 0.028 \text{ mm} \\ h &= 61.400 \pm 0.076 \text{ mm}. \end{aligned} \tag{9}$$

The errors given in (9) are probable errors. The accuracy of the values (9) is quite sufficient for high precision measurement of the $2\,\varrho$-values by means of (5), As will be shown below, the smallest half-width obtained for the L-conversion lines of ThB + + C + C″ so far is about 1 part in 10000 of the $H\varrho$-value. The highest accuracy desired in measurement for $2\,\varrho$-values should therefore be 1 part in 100000. This means an error of 1–3 μ in the $2\,\varrho$-values, which vary from about 100 to 300 mm. If we measure the distances d and the differences x with this accuracy and want to get 2ϱ with about the same degree of precision, the differentiated equation (5)

$$\Delta\, 2\,\varrho = \left(1 - \frac{a\,x}{d^2}\right)\Delta\, d + \frac{a}{d}\,\Delta\, x + \frac{x}{d}\,\Delta\, a + \cdots \tag{10}$$

shows that Δa, the error in a, may be of the order 12–60 μ, because x is always ≤ 5 mm when we measure the distance between a line and the nearest calibration edge. Thus the error in a may be just that obtained in (9).

It is well known (see for instance PERSICO and GEOFFRION, loc. cit.) that two different arrangements can be used in the semicircular method. In the first arrangement the baffle lies in the plane of the film, while the source does not. The image formed has then a similar shape over a large $H\varrho$-interval, and the "paraxial rays" from a monoenergetic source always correspond to the edge of a line. This is a good feature of this arrangement, but it has been considered difficult to measure the distance 2ϱ. In the second arrangement (17) the source is in the plane of the film, while the baffle is not. This arrangement has the advantage that the distance $2\,\varrho$ can be measured directly by means of a comparator, and furthermore the rays penetrate the emulsion perpendicularly to its plane. On the other hand it may be a disadvantage that, when larger samples are used, lines which differ considerably in $H\varrho$-values will have different line shapes. This phenomenon will be eliminated if the lines investigated are put in approximately the same position by changing the strength of the magnetic field. This is, however, rather inconvinient with permanent magnets, because of the small creep which occurs in the remanence immediately after every remagnetization. The method used in the present spectrograph combines the advantages of the two arrangements: the edge of a conversion line always corresponds to paraxial rays, and the distance 2ϱ can be measured with high accuracy.

For precision measurement of 2ϱ one should of course use plates instead of films, because a deviation of the surface of the emulsion from the plane defined by the calibration edges will introduce errors in x and hence in 2ϱ.

5. *The vacuum system.* The vacuum chamber is evacuated by a Welch No. 1405 two-stage duoseal vacuum pump as backing pump (0.5 l/sec.) in conjunction with an oil diffusion pump with a cpacity of about 100 l/sec. Because of the small volume of the vaccum chamber (4 l) high vacuum is obtained in about one minute, when the oil diffusion pump is heated beforehand. By means of a system of three valves (see Fig. 5) the diffusion pump is connected in series between the Welch pump (not seen in the figure) and the vaccum chamber, when a sufficiently good fore-vacuum has been obtained.

6. *The temperature regulator.* A constant temperature is necessary in order to get a high resolving power. The spectrograph was therefore surrounded by a cabinet, *Ch* in Fig. 1. A photograph of the spectrograph with the cabinet, from which the front wall and the right-hand wall have been removed, is seen in Fig. 5. To the left is a contact thermometer and a fan, driven by an 8 watt electric motor on the outside of the wall. In front of the yoke is a heating grid, and between this and the yoke is an aluminium sheet, the function of which is to prevent heat radiation from the grid to the yoke. Air circulates in the cabinet and between the yoke and the aluminium sheet. The grid is regulated by the contact thermometer and a commercial "Electronic Relay, Sunvic Type EA3" (on the outside of the left-hand wall in Fig. 5 not visible). A small neon lamp indicates when the grid is heated. The front wall and the right-hand walls are furnished with lagre glass windows, by which it is possible to observe the temperature regulator. There is a removable cover in the right-hand wall for inserting the sample- and film-holder.

7. *Equipment for measuring the strength of the magnetic field.* The method used for measuring the strength of the magnetic field was that of COTTON (loc. cit.). A new arrangement for leading the current into the rectangular measuring coil was used. The principle of the method is seen in Fig. 8. B_1 is the balance for measuring the force induced on the coil C when a current passes through it. A second balance B_2 is introduced, the purpose of which is to connect the terminals M_2 and M_3 of the coil with the terminals M_1 and M_4 of the current source. This connection is made by the conductors K. M_1, M_2, M_3 and M_4 are small copper cups filled with mercury. By means of the counter-weights A and D the balance B_2 is first adjusted to an indefinite equilibrium or to a stable equilibrium with a very long time of oscillation, the mercury cups M_2 and M_3 being removed during this procedure. M_2 and M_3 are then put in position and the weight D moved to the right, as a result of which the conductors K enter the mercury and take up a constant displacement in relation

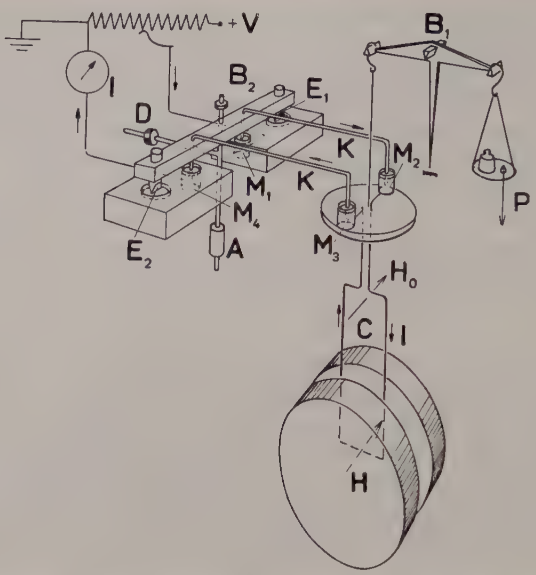

Fig. 8. Principle of the method for measuring the strength of the magnetic field.

to the mercury in the cups M_2 and M_3. This means that the balance B_2 will follow the oscillations of the balance B_1. The displacement in the mercury cups M_1 and M_4 will also be constant, because the surfaces of the mercury in these cups are at the same levels as the glass surfaces on which the stainless steel edges E_1 and E_2 of the balance are supported. The places where the conductors K penetrate the mercury surfaces and the edges E_1 and E_2 are in the same straight line. The time of oscillation of the balance B_1, 5 seconds, was almost unchanged by introducing the balance B_2.

The spectrograph is constructed in order to get a high resolving power and a high precision in relative measurements. No attempt has yet been made to use the spectrograph for accurate *absolute* measurements. The current was therefore measured simply by a Weston Laboratory Standard D.C. ammeter, Model 5. The readings of this are reliable to 1 part in 1000, which is also the limiting accuracy of the field strength measurement (compare § 10).

The form of the measuring coil frame is seen in Fig. 1, Y, and Fig. 9. The lower part consists of a rectangular glass plate, $4.9685 \times 25.5 \times 0.4$ cm^3, in which 7 holes of diameter 2.5 cm are bored in order to decrease the weight of the frame and to facilitate the assembly of the windings. The long sides of the glass frame were ground plane parallel with an accuracy of ± 0.01 mm. The upper part of the coil frame is made of plexiglass, the form of which is seen in Fig. 9. The windings consist of 14 turns of 0.54 mm enamelled copper wire, placed in two layers, 7 turns in each. The layers are separated by a celluloid film of 0.5 mm thickness. The mean length of the horizontal parts of the coils is thus 51.265 mm. The copper wire is pressed against the glass frame and the celluloid film by means of plexiglass rods of semicircular cross section, which are fixed to the glass frame by Scotch tape and silk thread.

The height of the rectangular coil is 41 cm. When the lower part is some cm above the bottom in the vacuum chamber pocket, the upper part is outside the yoke, between the yoke and the base-plate of the Sartorius balance.

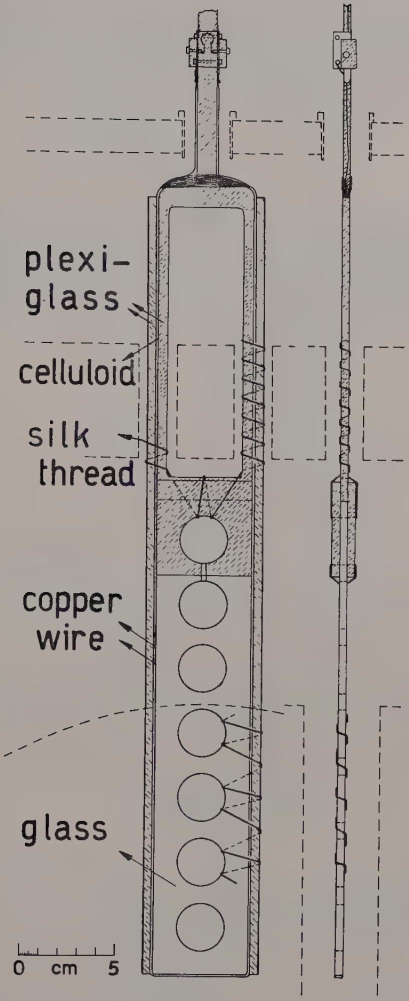

Fig. 9. Design of the rectangular measuring coil.

A design of the current supply balance B_2 for the field measurement coil is shown in Fig. 10.

A field strength of 147 gauss and a current of about 0.65 amp. corresponds to a counterweight of 700 mg. An accuracy of 1 part in 1000 for this counterweight is easily obtained in the weighing procedure. Currents higher than about 0.7 amp. should not be used in order not to influence the remanence of the spectrograph (compare § 11).

The horizontal component of the stray field above the yoke was measured by means of an oscillating magnet needle and found to be only 0.01 gauss. This field,

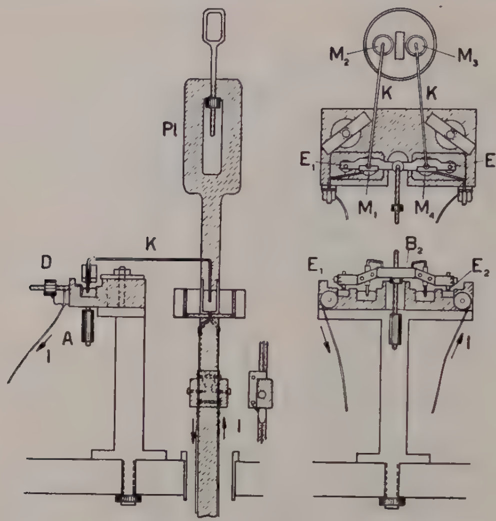

Fig. 10. Design of the current supply balance for the field measurement coil.

in which the upper part of the measuring coil was situated, was thus only about 1 part in 10000 compared with the field between the pole pieces, and could therefore as a rule be neglected.

8. *The strength of the magnetic field.* The formula (4) gives, when we neglect the stray field H', which according to the measurements mentioned in the paragraph above is only of the order of magnitude 1 part in 10000 of the field between the pole pieces,

$$H = \frac{2\,Mg}{n\,L\,(i_1 + i_2)} \tag{11}$$

Taking $n = 14$, $L = 51{,}265$ mm, $g = 982{,}58$ cm $\times$ sec^{-2},[1] and $M / 2(i_1 + i_2) = 1.0795 \pm 0.006$ (mean of 12 weighings), we find for H the value

$$H = 147.80 \text{ gauss.}$$

This values is valid 6 cm above the centre of the pole gap. When the balance was raised an increase in the field strength by 0.039 % per cm was observed.

9. *The beta spectrum of ThB + C + C''.* Fig. 11 shows the beta spectrum of ThB + C + C''. The two strips are parts of the same film, the size of which was 19 × 270 mm. The source was a platinum wire of 25 μ thickness, activated with a ThB + C + C'' deposit, the strength of which was about 330 μ C. Scopix G green sensitive film (Gevaert) was exposed for 23 hours (later Ilford Selochrome 120 was always used, because of its thinner emulsion, 15 μ instead of 20 μ). The width of the ebonite baffle (= length of radiating wire) was 3 mm, and the width of the slit R_1R_2 was 3 mm.

---

[1] The value for g is computed from the formula of HEISKANEN in Hb. d. Exp. Ph. XXV, 2. Teil, Geophysik, 1931, page 159.

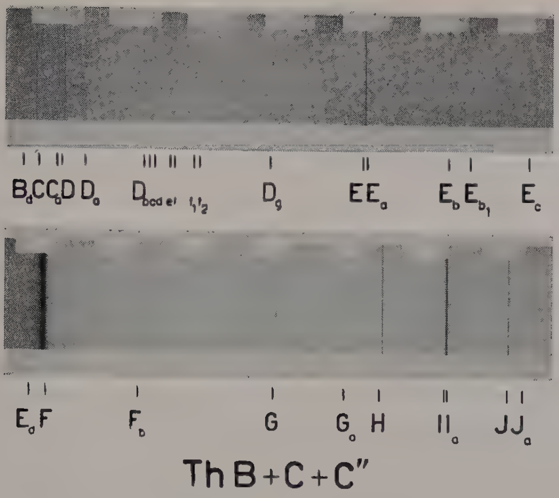

Fig. 11. Beta spectrum of ThB + C + C″.

10. *The $H\varrho$-values for the ThB F- and I-lines.* As already mentioned, the spectrograph was not designed for high precision *absolute* measurements, but for high resolving power. The amperemeter used permitted an accuracy of only some parts in 1000. However, it was interesting to compute the $H\varrho$-values within the accuracy given by the amperemeter. The 2 ϱ-values for the F- and I-lines were found to be 18.8953 and 23.8630 cm, respectively. By means of the HARTREE (18) correction the mean field strengths H_F and H_I along the F- and I-electron paths were calculated and the following values obtained:

$$H_F = 147.24 \text{ gauss}$$
$$H_I = 147.12 \text{ gauss.}$$

Thus we found the $H\varrho$-values

$$H\varrho(F) = 1391 \text{ gauss cm}$$
$$H\varrho(I) = 1755 \text{ gauss cm.}$$

The best values so far measured are probably those of LINDSTRÖM (19):

$$H\varrho(F) = 1388.56 \pm 0.15 \text{ gauss cm}$$
$$H\varrho(I) = 1754.01 \pm 0.20 \text{ gauss cm.}$$

The differences between these values and ours are 1.8 and 0.6 parts in 1000, respectively. This is the accuracy to be expected with the present current measuring equipment. A higher accuracy could easily be obtained if the current were measured by means of a standard resistance and a potentiometer with standard cell. However, this was not of importance for the purpose of investigating the inherent half-width of conversion lines, as discussed below.

11. *Influence of the balance current on the remanence.* The question arises as to what extent the current in the balance coil may change the remanence in the magnet. In order to investigate this effect the ThB I-line was exposed on the same film before and after different weighing experiments. The baffles were adjusted for high

resolution. Fig. 15 shows the result. The *I*-line in the first column was exposed in the absence of disturbing balance-current fields. When the weighing of the field strength was carried out using a current of ± 1.4 amp. there was a decrease in the field strength by 0.044 gauss, or a relative change $= \Delta H / H = -3 \times 10^{-4}$, which is demonstrated by the double *I*-line obtained, and shown in the second column in the figure. On the other hand, when the balance current was ± 0.65 amp., the last column shows that no disturbing effects on the remanence could be obesrved.

12. *The constancy of the remanence.* The same remanence has been used for more than for a year, and the constancy of the field has been tested by measuring the positions of the ThB *I*-line in relation to the calibration edges. It was found that the change over a period of one year was about 1 part in 10000.

13. *Influence of the temperature on the remanence.* The beta spectrum of ThB was taken at three different temperatures, 20°, 25° and 30° C. The change in the 2 ϱ-values was almost exactly proportional to the temperature, giving a decrease in the field strength of 2.2 parts in 10000 per degree centigrade. This is about 12–18 times larger than the change in field strength which depends on the thermal coefficient of expansion of the brass in the vacuum chamber or of the iron in the yoke, and shows the importance of keeping permanent magnets for precision work at a constant temperature.

14. *Resolving power of the spectrograph and inherent half-width of the K-conversion lines in the beta spectrum of* $ThB + C + C''$. In order to determine the highest possible resolution of the spectrograph, and the inherent half-widths of some conversion lines, the beta spectrum of $\mathrm{ThB} + \mathrm{C} + \mathrm{C}''$ was photographed using different combinations of baffles and exposing times. In the following the half-widths will be expressed in terms of the $H\varrho$-value of the line in question.

The reason for investigating the half-widths of the conversion lines in the beta-spectrum of $\mathrm{ThB} + \mathrm{C} + \mathrm{C}''$ was the observation of LINDSTRÖM (loc. cit.) that the *F*-line was broader than the *I*-line by 0.04 % (the half-width of the *F*-line was 0.14 % and that of the *I*-line 0.08 %. The resolving power of LINDSTRÖM's spectrograph was 0.1 %. In order to investigate if the broadening of the *F*-line was

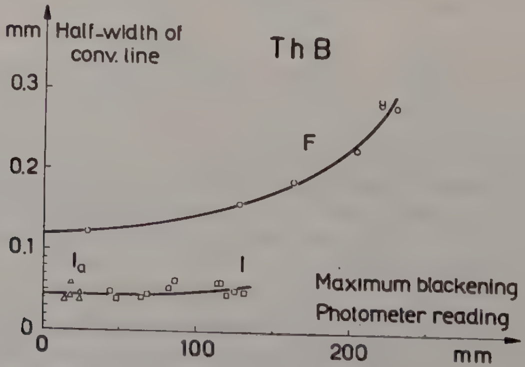

Fig. 12. Half-widths of the *F*-line (⊙), *I*-line (⊡) and I_a-line (△) as functions of the maximum blackening measured on photometer records.

caused by unresolved components or by an inherent half-width of the line, it was necessary to increase the resolution.

When the half-width of conversion lines recorded on photographic emulsions is studied by means of photometer diagrams representing the blackening in the emulsions, one has to consider the influence of the maximum blackening (corresponding to the top of the line) on the half-width measured. An overexposed line will have a large half-width. Only lines of the same maximum blackening should be compared. Because of the greater intensity of the F-line, several (at least two) films have to be exposed for different times (or with sources of different strengths). Fig. 12 shows the half-widths of the F-, I- and I_a-lines as functions of the maximum blackening measured on photometer records of 6 different films, obtained with different exposure times but under the same other conditions (ebonite baffle or active length of the platinum wire $= 3$ mm, thickness of the wire $= 25\ \mu$, baffle $R_1R_2 = 0.5$ mm, Ilford Selochrome 120 film, $H = 147{,}2$ gauss).

The figure shows that for small values of the blackening there is no increase in the half-width, but that for higher photometer readings the half-width measured increases rapidly. Furthermore, for small values of the blackening, the half-widths of the I- and I_a-lines are the same (in any case there is no observable difference), but for the F-line the half-width is larger by a considerable amount.

The half-widths are $x = 0.044$ mm for the I-lines and 0.119 mm for the F-line. The corresponding $2\ \varrho$-values are 238 mm and 187 mm, and the corresponding a-values 230 mm and 177 mm, respectively. The formula (5) gives for the differences in $2\ \varrho$ the values 0.0425 mm and 0.113 mm, or 1.8 and 6.0 parts in 10000 respectively for the half-widths in terms of the $H\varrho$-values. Hence the half-width of the F-line is about 4 parts in 10000 larger than that of the I-line. In addition, the F-line is found to be simple, because the resolution used (1.8 parts in 10000) would have shown the components proposed, the suggested distance between them being 8 parts in 10000 (see LINDSTRÖM, loc. cit.). The shapes of the F- and I-lines may be seen in Fig. 13.

Of course, before we accept the figures 6.0 and 1.8 parts in 10000 for the half-widths of the F- and I-lines, respectively, we should compute the width of the image formed in our spectrograph at the two places of interest. The width Q'' of the image formed is[1]

$$Q'' = F + Q + \varrho(\varphi_0^2 + \psi_0^2), \tag{10}$$

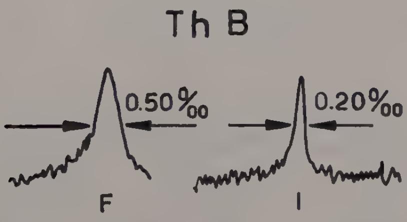

Fig. 13. Photometer records of the F- and I-lines in the beta spectrum of ThB. The lines are taken from two different films, exposed under the same conditions but with different exposure times in order to get the same maximum blackening at the top of the line. The half-width for the F-line is 3 parts in 10000 larger than that for the I-line.

---

[1] Compare PERSICO and GEOFFRION, loc. cit.

where Q is the width of the wire, F the width of the slit in the photometer, φ_0 the angle extended by the baffle $R_1 R_2$ at the wire, or more properly the maximum angle between the electron paths in a plane parallel to the pole pieces, and ψ_0 the maximum deviation of the electron paths from this plane. The formula (10) should in our case be completed with a term depending on the thickness e of the emulsion. We thus get

$$Q''' = F + Q + \varrho(\varphi_0^2 + \psi_0^2) + e \cdot \frac{h}{a}. \qquad (11)$$

This formula gives the values $Q''' = 42\ \mu$ and $40\ \mu$ for the F- and I-lines, respectively (the width of the photometer slit was only $0.7\ \mu$). It is interesting to see that the value $40\ \mu$ agrees closely with the experimental value $44\ \mu$ found for the half-width of the I-line. We also see, that the difference $2\ \mu$ in half-width, depending on the different positions of the lines on the film, is of no importance for our conclusions above concerning the inherent half-width of the F-line.

The ThB F-line orginates in the K-shell in the ThC atom (20). According to SURUGUE (21), a part of the F-line belongs to the L_I shell, corresponding to the transition responsible for the K-line known as Df. The intensity of this K-line is, however, only 1 part in 600 of the F-line intensity. Thus it is not likely that the L-line of this transition gives an observable contribution to the shape of the F-line.

In any case it was, however, of interest to investigate the half-width of some other K-lines, and, preferably, such lines in the vicinity of the I-line, in order to exclude some imaginable systematic error depending on the position of the line on the film.

The G-line and especially the H-line are not far away from the I- and I_a-lines (see Fig. 11). Both lines originate in the K-shell, the G-line belonging to the transition ThC$''\rightarrow$ThD and the H-line to ThB$\rightarrow$ThC. Fig. 14 shows the result. The half-widths of the G- and H-lines are equal, within the experimental errors, and again about 3 parts in 10000 larger than the half-width for the I-line. The I_a-line originates in the L_{II}-shell.

The half-width 0.012 per cent for the I_a-line also gives the best resolution so far obtained with the spectrograph: 1.2 parts in 10000.

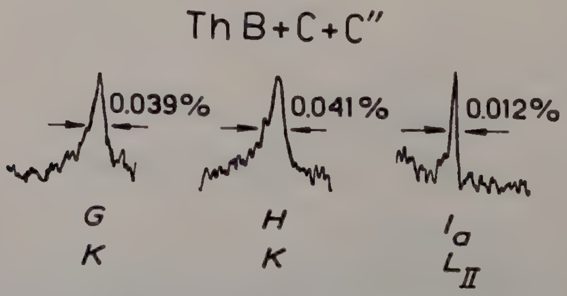

Fig. 14. Photometer records of the G-, H-, and I_a-lines in the beta spectrum of ThB + C + C$''$. The half-width for the G- and H-lines, which originate in the K-shell, is again about 3 parts in 10000 larger than the half-width for the I_a-line, which originates in the L_{II}-shell.

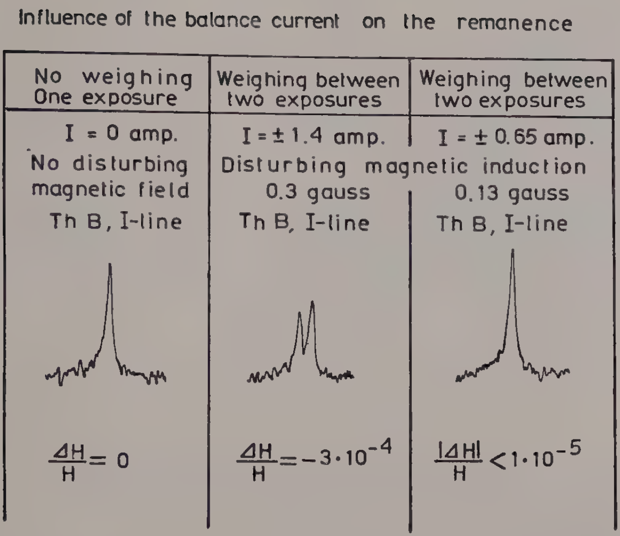

Fig. 15. Influence of the balance current on the remanence.

The broadening in momentum corresponds to about 80 eV in energy, and seems to be the same for all K-conversion lines in the beta spectrum of ThB + C + C″. Professor KAI SIEGBAHN[1] has suggested the following explanation of the observed inherent line width of the K-conversion lines: The fact that all the K conversion lines investigated so far in the ThB spectrum have the same width indicates that the line broadening is essentially independent of the particular nuclear configurations of the states between which the transition takes place. The refilling of the empty place in the K-shell, which occurs within a time which is very short compared to the lifetime of the nuclear state, is accompanied mainly by the emission of K gamma-radiation. The width of this radiation must therefore be expected to show up in the width of the emitted K electron line. An inspection of existing data (22) on K_α-line widths gives quantitative support to this view. For $Z = 20$ to 40 the K_α-line widths increase from 1.7 to 6.8 eV. At $Z = 74$ (W) the K_α-line width is already 42.5 eV and a reasonable extrapolation to $Z = 83$ yields a line width of 70 ± 5 eV, in remarkably good agreement with the widths of the K conversion lines reported above. The widths of the L conversion lines would be expected to be about 10 eV, which is just too small to be observed at present.

SUMMARY

1. A review of earlier permanent magnet beta-ray spectrographs is given.

2. A semicircular permanent magnet beta spectrograph for photographic recording of conversion lines is described.

3. A high resolution is obtained by the use of thin sources, narrow baffle apertures, and especially by maintaining a constant temperature.

---

[1] The author is indebted to prof. K. SIEGBAHN and prof. L. HULTHÉN for valuable discussions on the origin of the broadening effect of the K-lines.

4. A new method for precision measurement of the distance between the source and the conversion lines is described.

5. Absolute measurements by means of the Cotton balance method were made for the $H\varrho$-values of the ThB F- and I-lines.

6. A new arrangement for leading current to the balance measuring coil is described.

7. A resolving power of 1.2 parts in 10000 is obtained.

8. The observation of Lindström that the half-width of the F-line was larger than that for the I-line is confirmed. In addition it is shown that the F-, G-, and H-lines, which originate in K-shells, are broader by the same amount, or 3 parts in 10000, than the I- and I_a-lines, which belong to the L_I and L_{II} shells respectively.

Nobel Institute of Physics, Stockholm 50, Sweden.

REFERENCES

1. E. Persico and C. Geoffrion, Rev. Mod. Phys. *21*, 945, 1950.
2. J. D. Cockcroft, C. D. Ellis, and H. Kershaw, Proc. Roy. Soc. A *135*, 628, 1932.
3. P. Kapitza and W. L. Webster, Proc. Roy. Soc. A *132*, 442, 1931.
4. C. D. Ellis, Proc. Roy. Soc. A *138*, 318, 1932.
5. ——, Proc. Roy. Soc. A *143*, 350, 1932.
6. G. H. Briggs, Journ. Sci. Instr. *9*, 5, 1932.
7. F. A. Scott, Phys. Rev. *46*, 633, 1934.
8. A. Cotton and G. Dupouy, Congrès International d'Électricité, III, Sec. 2 E, 208, 1932.
9. F. T. Rogers, Jr., Ph. Rev. *50*, 515, 1936; *51*, 588, 1937.
10. G. H. Briggs and A. F. A. Harper, J. Sci. Instr. *13*, 119, 1936.
11. G. H. Briggs, Proc. Roy. Soc. A *157*, 183, 1936.
12. J. Surugue, J. de Phys., Série VII, VI, 2, p. 94, 1935. Ann. de Phys. *8*, 484, 1937.
13. A. F. A. Harper and N. F. Roberts, Proc. Roy. Soc. A *178*, 170, 1941.
14. E. H. Plesset, G. P. Harnwell, and F. G. P. Seidl, Rev. Sci. Instr. *13*, 351, 1942.
15. J. M. Cork, Phys. Rev. *72*, 581, 1947.
16. S. Rosenblum and B. Tsai, Compt. Rend. *224*, 1278, 1947.
17. K. Siegbahn, Arkiv f. Mat. Astr. Fys. Bd *30 A*, No 20, 1944.
18. D. R. Hartree, Proc. Camb. Phil. Soc. *21*, *746*, 1923.
19. G. Lindström, Arkiv. f. Fysik, *4*, No 1, 1951.
20. See for instance Landolt-Börnstein, 6. Auflage, Zahlenwerte und Funktionen, I. Band, 5. Teil, Atomkerne, 1952, pag. 264 and 265.
21. J. Surugue, Ann. Physique *8*, 483, 1937; J. Phys. Radium *9*, 439, 1938.
22. A. H. Compton and S. K. Allison, X-rays in Theory and Experiment, New York 1935.
23. N. F. Verster, Progress in Nuclear Physics, Vol. 2, p. 1, London 1952.

Tryckt den 20 april 1953

Uppsala 1953. Almqvist & Wiksells Boktryckeri AB

ARKIV FÖR FYSIK Band 6 nr 42

Communiqué le 14 mai 1952

Etude spectrophotométrique d'étincelles de grande longueur dans l'air

Par Mme Arlette Vassy, MM. Harald Norinder et Etienne Vassy

Avec 6 figures dans le texte

Résumé

On a effectué l'étude spectrophotométrique d'étincelles dans l'air sous haute tension. De nombreuses raies et bandes ont été identifiées, les bandes sont faibles; les raies sont dues principalement à O II et N II et quelques-unes à O I, N I, O III, O IV, N III et N IV.

Lorsque la tension augmente, le spectre s'enrichit en raies et en bandes principalement dans l'ultra-violet au-dessous de 3500 A. La formation d'ozone et de peroxyde d'azote par l'étincelle a été étudiée spectrographiquement. L'étude de la forme et de la variation des raies montre que la décharge électrique n'est pas un phénomène unique, mais un ensemble d'événements successifs correspondant à des conditions d'excitation différentes, qui s'interprètent aisément dans le cadre de la théorie de Loeb et Meek. On a également effectué une étude quantitative du spectre continu émis par l'étincelle; ce spectre présente une répartition énergétique en bon accord avec celle de la lumière émise par le corps noir à une température de 16000° K, ce qui suggère pour cette émission l'hypothèse d'une origine thermique.

I – Dispositif expérimental et méthode

Nous avons étudié à l'Institut des Hautes Tensions, les spectres produits par la décharge électrique dans l'air à la pression atmosphérique entre électrodes dont les distances variaient de 17 cm à 1,55 m, correspondant à un potentiel explosif du million de volts environ.

Le générateur à haute tension est installé dans la grande salle de 15 × 30 m de l'Institut. Ce générateur a été décrit en détails (1). Rappelons brièvement qu'il s'agit d'un générateur d'impulsions pouvant donner un voltage maximum de 2300 KV; il consiste en 15 condensateurs de 0,0375 μF chacun, avec une capacité totale lors de la décharge de 2500 $\mu\mu$F et une énergie totale de 6300 watt-secondes. L'étincelle était produite entre une sphère de cuivre et une pointe de cuivre de distances variables.

La lumière produite par la décharge était photographiée avec un spectrographe à prisme-objectif en quartz (montage stigmatique), placé à une distance de 15,85 m;

le tirage avait été mis au point pour cette distance. L'intensité était suffisante pour qu'une seule décharge donne un spectre de noircissement correct et photométrable, sur plaques Gevaert Superchrom et Kodak 103–O pour l'ultra-violet, sur plaques Ilford HP3 pour le visible; quelques spectres infrarouges ont été pris avec des plaques Kodak IL, mais la sensibilité moins grande de ces plaques n'a permis d'obtenir que les raies et bandes les plus intenses, jusqu'à 9600 A. En effet l'emploi du prisme-objectif ne permet pas de superposer deux étincelles successives, car chaque longueur d'onde du spectre reproduit la forme de l'étincelle source, forme toujours assez tourmentée. L'obturateur restant ouvert pendant tout le temps que l'on fait croître la tension jusqu'à la décharge, il est à noter que la plaque photographique enregistre non seulement la lumière de la décharge principale, mais aussi celle des pré-décharges, ou effets couronne s'ils existent. L'intensité de ces dernières étant considérablement plus faibles, nous n'avons pas été gênés dans les mesures.

L'étalonnage de la plaque en vue de la mesure des intensités était fait soit avec un tube luminescent pour le visible, soit avec un tube à hydrogène pour l'ultra-violet, placés à la même distance du spectrographe que l'étincelle; l'étude de la répartition spectrale énergétique de ces sources a été faite à Paris au laboratoire de Physique de l'Atmosphère. Le tube luminescent était utilisé sans système de projection; il était placé immédiatement derrière un écran opaque percé d'une ouverture rectangulaire de 58 mm de hauteur et 1 mm de largeur orientée dans le sens vertical; cette ouverture constituait la source; l'affaiblissement de la lumière était obtenu au moyen de plages gris neutre (plaques photographiques impressionnées et renforcées) de différentes densités placées devant l'ouverture et dont le facteur d'affaiblissement a été mesuré 1° dans les conditions d'emploi, 2° au densitomètre. Le temps de pose employé avec cette source était 10 secondes.

Le tube à hydrogène était placé à 60 cm derrière une lentille en quartz de 40 cm de distance focale formant l'image du capillaire dans le plan de la face d'entrée du prisme-objectif du spectrographe; dans ces conditions, c'est la lentille qui joue le rôle de source secondaire; sa surface était limitée par deux écrans laissant entre eux une fente de 1 mm de largeur; l'intensité était affaiblie au moyen de grilles situées immédiatement devant la lentille, grilles de densité optique mesurée au laboratoire. Le temps de pose était de 1/5e de seconde; il était commandé par un obturateur Compur placé entre le tube et la lentille.

Accessoirement, pour les réglages et l'établissement de la courbe de dispersion, on a utilisé un arc au mercure; mais les trois sources (étincelle, tube luminescent et tube à hydrogène) comportant par elles-mêmes des raies bien connues et faciles à identifier, le repérage des longueurs d'onde n'a exigé aucune opération spéciale.

La durée de l'étincelle étant de l'ordre de la micro-seconde, on voit que nous avons été contraints d'employer des temps de pose différents pour l'étincelle et les sources de comparaison, ce qui soulève le problème de la variation du facteur de contraste γ avec le temps de pose, c'est-à-dire le problème du coefficient p. Ce problème, qui se présente dans l'étude de toutes les sources très brèves, avait déjà été examiné par l'un de nous (2) à la fois des points de vue théorique et expérimental, et la conclusion était que si cette méthode ne permet pas d'obtenir en toute rigueur les intensités en valeurs absolues (lumens par exemple), elle est cependant correcte quand il ne s'agit d'obtenir qu'une répartition énergétique, c'est-à-dire les rapports des énergies pour les différentes longueurs d'onde. Cette conclusion a été également adoptée par J. ROMAND (3) pour une comparaison de sources de brillances très différentes.

Nous avons dit que le spectrographe était à prisme-objectif; il a été décrit précédemment (4); toutefois dans le cas présent, il n'était pas utilisé en montage astigmatique, mais stigmatique; sa dispersion est, avec les réglages que nous avons utilisés, 175 A par mm pour le rouge (6200 A) et 11 A par mm pour l'ultra-violet (2500 A). Nous avons également utilisé un spectrographe à fente à deux prismes de quartz, dont la dispersion était du même ordre de grandeur, mais qui grâce à sa fente donnait des raies plus fines, car la largeur des raies au prisme-objectif est déterminée dans la présente étude par la largeur du canal lumineux de l'étincelle, largeur variable avec les circonstances comme nous le verrons. Ce spectrographe, beaucoup moins lumineux que le premier, ne pouvait pas donner de spectre utilisable avec une seule étincelle; il était nécessaire d'en superposer plusieurs, environ une vingtaine, pour tenir compte du fait que l'image de l'étincelle projetée sur le plan de la fente pouvait se former en dehors de cette fente et ainsi ne pas concourir à la formation du spectre.

Nous avons utilisé principalement les distances explosives suivantes: 17 cm, 30 cm, 50 cm, 71 cm, 155 cm, entre une tige pointue située en haut et une sphère de 25 cm de rayon au-dessous, son centre passant par la verticale de la tige supérieure; on a également pris des spectres d'étincelles entre deux sphères de même diamètre. Les polarités étaient inversées de sorte que pour chaque distance explosive, nous avons des spectres pris avec la pointe positive et négative.

La mesure de la tension de décharge a été faite par comparaison avec la distance explosive de deux sphères de 1,50 m de diamètre.

Ces tensions sont approximativement

17 cm (sphère positive)	400 Kv
30 cm (sphère positive)	545 Kv
50 cm (sphère positive)	707 Kv
71 cm (sphère positive)	865 Kv
155 cm (sphère négative)	957 Kv

II – Etude qualitative

Le spectre obtenu se compose d'un nombre important de raies et bandes et d'un spectre continu dus à l'étincelle; en outre au voisinage immédiat de l'électrode et limitée à une région ne dépassant pas quelques millimètres à partir de cette électrode, on observe les raies du métal constituant l'électrode; ces raies sont intenses, et le spectre est assez riche. Mais en aucun cas, même pour des raies ultimes telles que 3273,962 A et 3247,540 A du cuivre, cette présence des raies du métal des électrodes ne dépasse une région correspondant aux 2 ou 3 millimètres indiqués plus haut. Rappelons en effet que le spectrographe à prisme-objectif permet d'obtenir le spectre de chaque point de l'étincelle individuellement.

Nous avons fait l'étude des raies et bandes d'abord sur des spectres correspondant aux plus grandes distances explosives qui donnent le plus de raies et aussi les canaux les plus fins, et par suite les raies et bandes les plus fines et qui se détachent le mieux les unes des autres et du fond continu; le spectre est en effet très riche et avec des étincelles larges, il se produit des recouvrements gênants; nos mesures de longueurs d'onde on pu ainsi être faites à plus ou moins 1 A pour les raies fines dans l'ultra-violet; les raies intenses sont malheureusement plus larges et il se produit des superpositions. Nous avons relevé les raies et bandes suivantes, dont les attributions ont été faites grâce aux Tables de longueurs d'onde du M.I.T. (5) et aux listes de PEARSE et Gaydon (6). En outre les raies d'ionisation élevée (O III, O IV, N III, N IV) ont été indentifiées grâce aux travaux de Mihul (7) et de Freeman (8). Nous nous sommes aidés pour les attributions des intensités indiquées par les Tables du M.I.T., bien que nos conditions d'excitation amènent des modifications des rapports d'intensités des raies.

Tableau I

λ	Attributions	Intensités MIT
9599	N_2 1^{er} *pos.*	*3,3*
9362	N_2 1^{er} *pos.*	*4,4*
8911	N_2 1^{er} *pos.*	*1,0*
8521	A I	2000
8222–27–30– –33	O I	5000
7772–74–75	O I	1400
6645	N I	500
6563	Hα	
6482–5	N I et N II	800 + 500
6453–54–56	O I	750
6300	O	
6156–58	O I	150, 300, 1000
6008	N I	800
5942	N II	200
5932–28	N II	150, 50
5710	N II	100
5679–76–66	N II	900
5560	N I	200
5554	O I	100
5496	N II	70
5435	O I	370
5356	N I	50
5329–30	O I	500, 150, 100
5339	N II	20
5190–79	O II + N II	30 + 85
5045	N II	200
5001–3–7–10	N II	350, 500, 150, 100
4941–42	O II	150
4935	N I	250
4861	Hβ	
4803	N II	30
4803–2–1	O I	95
4788	N II	25
4705–699	O II	300 + 130
4776–61	O II	250
4651–49–42	O II	520
4643	N II	100
4630	N II	300
4601	N II	100
4554	N_2^+ 3,5 ?	
4530	N	25
4516	N_2^+ *4,6*	
4447	N II	300
4433	N II	30
4417–15	O II	450
4368	O I	1000
4349	O II	300
4340	Hγ	
4319–17	O II	300
4278	N_2^+ *0,1*	
4242	N II	100
4237	N	30
4233	O	100
4185–90	O II	650
4153	O II	200
4151	N I	1000
4142	N_2 *3,7* 2^e *pos. ?*	
4121–20–19	O II	420
4110	N I	1000
4105–3	O II	225
4076–72	O II	800 + 300
4043–4041– –35	N II	45 floue
3995	N II	300
3998	N_2 *1,4* 2^e *pos.*	
3973	O II	125
3956	N II	35
3954	O I	100
3947	O I	350
3943	N_2 *2,5* 2^e *pos.*	
3919	N II	35
3914	N_2^+ *0,0*	
3912	O II	155
3895	N_2 *3,6* 2^e *pos.*	
3884	N_2^+ *1,1*	
3882	O II	52
3860	N_2^+ *2,2*	
3838–42	N II	25
3835	N_2^+ *3,3*	
3805	N_2 *0,2* 2^e *pos.*	
3794	O II	10
3777	O II	18
3755	N_2 *1,3* 2^e *pos.*	
3748	O II	125
3734	O_2^+ *1,7*	
3727	O II	50
3712	O II	25
3706	O_2^+ *1,7*	
3639	O	10
3612	N_2^+ *dégr. vers le rouge*	
3594	O_2^+ *2,7*	
3593	N II	10
3582	N_2^+ *1,0*	
3577	N_2 *0,1* 2^e *pos.*	
3564	N_2^+ *2,1*	
3549	N_2^+ *3,2*	

Tableau I (cont.).

λ	Attributions	Intensités MIT
3518	O_2^+ *1,6*	
3494	O_2^+ *1,6*	
3483–5	N IV	
3478	N IV	
3471–70	O II	125
3451–48	O III	
3437	N II	35
3410	O II	25
3408	N II	10
3390	O II	100
3371	N_2 *0,0 2e pos.*	
3367	AIR N III	
3354	AIR N III	
3339	N_2 *1,1 2e pos.*	
3331–30–29	N II	30
3324	N II	5
3290–87	O II	88
3277	O II	25
3273	O II	35
3271	O II	25
3265	O III	
3246		
3227	O_3 ?	
3175	O_3 ?	
3159	N_2 *1,0 2e pos.*	
3136	N_2 *2,1 2e pos.*	
3138–35	O II	135
3123–24	O II	25
3117	N_2 *3,2 2e pos.*	
3089	*OH 0,0*	
3078	*OH 0,0*	
3067	*OH 0,0*	
3063	*OH 0,0*	
3047	O III	
3043	O_2^+ *2,4 ou NO*	
3035	*NO β*	
3024	N II	5
3018		
3007	N II	50
3008 à 5	O II	52
2984	O III	
2962	N_2 *3,1 2e pos.*	
2953	N_2 *4,2 2e pos.*	
2920	O_2^+ *4,4*	
2902	O_2^+ *4,4*	
2896	CO_2^+	
2883	CO_2^+	
2840	O_2^+ *3,3*	
2808–06	O IV	15
2799	N II	25
2747	O II	25
2733	O II	150
2719–15	O II	7 + 15
2710	N II	50
2696	O III	7
2688	O_2^+ *3,2*	
2681	O IV	7
2665	O III	
2647–46–45	N IV	
2594	O_2^+ *5,2*	
2591	N II	25
2575	O II	100
2558	O III	
2546	O_2^+ *6,2*	
2543	O III	
2527	O II	25
2523	O II	15
2522–21	N II	40

Les accolades réunissent les diverses attributions possibles ou simultanées pour une même raie.

On remarquera dans ce tableau la présence, qui n'a rien de surprenant, de quelques raies d'atomes deux et trois fois ionisés, ainsi que celles, plus nombreuses, d'atomes neutres. La majorité des raies est due aux atomes d'azote et d'oxygène une fois ionisés.

Les bandes sont toutes très faibles, exceptées les bandes 2883 et 2896 dues à CO_2 et attribuées à CO_2^+; on sait que ces bandes s'observent trés aisément toutes les fois que l'excitation est énergique et que le CO_2 est présent, même à l'état d'impureté; CO_2 étant un constituant normal de l'atmosphère, c'est certainement le cas dans la salle où nous opérions; elles sont bien visibles sur le spectre (voir enregistrement fig. 1).

Les bandes relevées sont dues à O_2^+ (dit 2e système négatif de l'oxygène), à N_2 (2e système positif de l'azote), à N_2 (1er système positif, dans l'infrarouge) et à N_2^+, ce dernier système bien développé. On a relevé aussi outre la bande due à CO_2, une bande due à OH, 3063, 3067, 3078, 3089, bande 0,0 du système $^2\Sigma \rightarrow {}^2\Pi$. Nous avons pensé pouvoir attribuer à NO (système β) une bande située à 3035 A, malgré

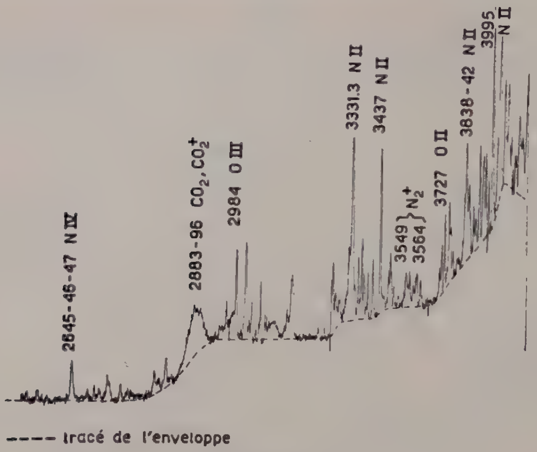

Fig. 1.

l'absence d'autres bandes du système; en particulier, la bande 3043 qui devrait apparaître également se superpose à une bande de O_2^+ dont la présence est très probable. Nous avons également attribué à l'ozone deux bandes d'émission à 3225 et à 3175 A, bien que les données expérimentales sur le spectre d'émission de l'ozone soient encore confuses.

Parmi les raies atomiques, outre celles de l'oxygène et de l'azote, nous avons trouvé Hα, Hβ et peut-être Hγ. Une raie faible à 8521 A a été attribuée à l'argon.

Les éléments non identifiés du spectre sont très faibles en intensité; ils s'observent aux longueurs d'onde suivantes:

3246 A, qui pourrait être dû à CO_2, CO_2^+ (système Fox, Duffendack et Barker) et 3018 A.

Ceci concerne les éléments du spectre se présentant en émission superposés au fond continu.

L'étude quantitative (voir plus loin) nous a montré l'existence de NO_2. On sait que le spectre de NO_2 n'a été observé qu'en absorption; cette absorption est particulièrement intense, tout le monde connait les vapeurs «rutilantes» du peroxyde d'azote. Les spectres de Zenneck et Strasser (9) montrent les bandes superposées à un fond continu entre 4800 et 4100. Si les longueurs d'onde auxquelles s'observent les bandes sont bien connues (entre 5095 et 4081 A avec maximum à 4480 A), les données quantitatives sur les coefficients sont rares. Nous avons retenu celles données par Dixon (10) bien qu'elles aient été déterminées avec une largeur de fente très supérieure (40 et 15 A) au pouvoir séparateur de notre instrument, qui donnait au spectre de NO_2 une apparence continue avec quelques ondulations correspondant aux bandes. Pour 4500 A, Dixon obtient une valeur de son coefficient k telle que $\log k = 3{,}9$; ceci donne un coefficient d'absorption de 6,08 pour 1 cm à la pression atmosphérique. Notre absorption (difficile à apprécier avec précision en raison du grand nombre de raies d'émission superposées) est d'environ 0,25; cela correspond à une épaisseur réduite de NO_2 de 0,4 mm, tout à fait raisonnable. Cette épaisseur de NO_2 augmente toujours pour une même série d'expériences au fur et à mesure des étincelles successives; elle est assez variable d'une série d'expériences à une autre.

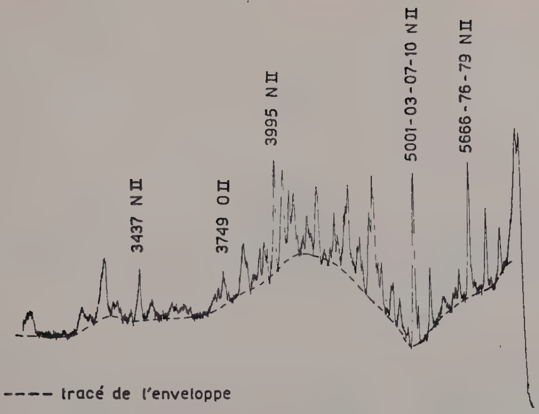

Fig. 2.

Nous avons recherché la présence d'ozone par son absorption ultra-violette; comme rien n'était visible sur les spectres d'étincelles pris dans les conditions ordinaires, 5 à 6 étincelles pour une même plaque, nous avons fait une expérience en ce but: 3 spectres d'étincelles sous 865 KV ont été photographiés; puis on a fait une série de 15 étincelles; ensuite une nouvelle étincelle a été spectrographiée. Ce dernier spectre a montré la présence d'une faible absorption ultraviolette à 2500 A, correspondant à une formation d'ozone avec une épaisseur réduite de 2μ. Donc la formation d'ozone est très faible, tandis que celle du peroxyde d'azote n'est pas négligeable. Ces résultats sont en accord avec ce que l'on sait de l'action de l'étincelle sur l'air à à la température ordinaire (voir PASCAL, 11). Pour la décharge silencieuse (faible intensité, forte différence de potentiel), il y a formation d'ozone et d'un peu d'oxyde d'azote; pour des intensités plus fortes, donnant des étincelles, il y a formation surtout de peroxyde d'azote, et d'un peu d'ozone; pour des courants intenses, formation de NO_2 seul et pas d'ozone.

La présence des bandes d'absorption du NO_2 nous fait considérer comme douteuse l'attribution des bandes en émission à 4554, 4516 et 4142 A; il pourrait s'agir d'un effet de contraste, dû à la présence en *absorption* des bandes 4480, 4545 et 4133 du NO_2 (ces dernières longueurs d'onde sont les maxima des bandes et non les têtes). Remarquons que s'il s'agissait de bandes d'émission de l'azote, elles seraient isolées, les autres bandes de la même séquence étant absentes.

Enfin, toujours en anticipant sur le chapitre suivant, nous avons également trouvé une bande d'absorption entre 5200 et 6000 A; puisque l'ozone est hors de cause, il semblerait raisonnable d'attribuer cette bande à NO_3. On sait d'après les travaux de WULF et JONES (12) que NO_3 présente une bande d'absorption dans l'intervalle 5300–6100 A avec quelques détails plus ou moins apparents, plus deux fortes bandes étroites à 6250 et 6650 A. Cette substance est extrêmement absorbante ainsi qu'il résulte des mesures de SPRENGER (13) qui a trouvé pour la forte bande à 6650 A un coefficient de 500 pour 1 cm à la pression atmosphérique; on sait que NO_3 se forme dans la décharge dans une atmosphère d'azote et d'oxygène froids (PASCAL). Cependant nous ne voyons pas bien nettement apparaître la bande à 6250 A. Dans

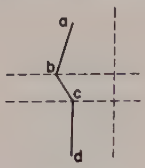

Fig. 3.

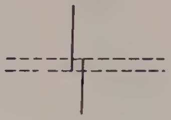

Fig. 4.

l'incertitude où nous sommes, non seulement des coefficients, mais encore de la structure de cette bande, nous ne pouvons donner cette interprétation que comme probable.

III – Variations du spectre

Ayant examiné ainsi les spectres les plus riches en raies et bandes, nous avons recherché s'il se présentait des modifications de ce spectre pour différentes conditions.

Nous considérerons d'abord l'allure générale du spectre. Son noircissement n'est pas uniforme dans toute sa hauteur, on voit des renforcements brusques qui apparaissent aussi bien sur les raies que sur le fond; certains de ces renforcements s'expliquent simplement par la forme de l'étincelle; elle est très rarement rectiligne, présentant des angles aux changements de direction; on observe quelquefois des dédoublements; il est normal que si l'étincelle affecte par exemple la forme du schéma 3, la partie du spectre continu correspondant à bc présente un noircissement plus grand dû à l'inclinaison de la partie bc sur la normale à l'axe du spectre; il s'agit d'un effet purement géométrique. Le cas est le même pour une étincelle brisée avec juxtaposition comme sur la figure 4. Mais souvent ces renforcements s'observent sans qu'il y ait changement de direction; circonstance intéressante, ces renforcements sont beaucoup plus marqués dans l'ultraviolet; dans la région visible le spectre est beaucoup plus uniforme en hauteur (mis à part les coudes dont nous avons parlé); sur les spectres pris sur plaques Ilford HP3 qui couvrent le domaine 6563–2850 A, on peut voir les renforcements se former progressivement vers 4000 A; un examen plus approfondi montre alors que les raies n'ont pas exactement la même forme dans le visible et l'ultraviolet, bien qu'il s'agisse de la même étincelle; dans l'ultraviolet, le renforcement ne correspond à aucun accident géométrique, mais dans le visible, à la hauteur correspondante, on observe un accident, angle, élargissement du canal, décalage des 2 parties de l'étincelle; en nous référant à la théorie de l'étincelle proposée par LOEB et MEEK (14), il nous semble que ces points singuliers peuvent correspondre à un certain tâtonnement dans l'établissement de la décharge, par exemple à l'extrémité d'une avalanche, ou à la rencontre d'un «streamer» venant en sens inverse des premiers streamers, etc.; il est curieux que ce phénomène s'atténue dans l'ultraviolet, comme si l'excitation plus énergique correspondant aux raies ultraviolettes était une étape différente et légèrement postérieure de la décharge. Bien entendu les raies visibles auxquelles nous nous référons sont des raies fortes appartenant certainement à l'étincelle et non à une pré-décharge. Ces renforcements affectent les raies aussi bien que le fond continu.

Si nous portons notre attention sur les éléments plus faibles du spectre, nous observons parfois que certaines raies ou bandes ne se présentent que sur une partie du trajet de l'étincelle, du côté de la pointe (et non du côté de la sphère); dans ces cas, la pointe était reliée au pôle négatif; nous verrons un peu plus loin une observation assez voisine. Nous avons observé ce phénomène en particulier sur les raies 3485 de

N IV, 3273 de O II, 3047 de O III, 3024 de N II, 2984 de O III et aussi la bande 2962 de N_2 (2^e système positif).

Voyons maintenant comment le spectre se modifie lorsque l'on fait varier la distance explosive de 17 cm à 1,55 m ou lorsque l'on inverse les polarités.

Nous constatons d'abord que la largeur des raies, c'est-à-dire la largeur du canal umineux de l'étincelle, est variable; elle diminue quand la distance explosive augmente, de sorte que les raies les plus fines s'observent pour 71 et 155 cm.

De plus, on voit immédiatement, et particulièrement dans l'ultraviolet, que les spectres des petites distances explosives sont beaucoup moins riches en raies, cette disparition de certaines raies tient évidemment en partie à l'élargissement signalé plus haut, les éléments peu intenses du spectre se fondant avec le spectre continu orsque la largeur plus grande de la source entraîne un étalement de la raie. Mais l y a incontestablement un phénomène tenant à l'excitation; certaines raies et bandes n'apparaissent que pour les grandes distances explosives. Nous avons groupé dans le tableau II les raies et bandes existant dans les étincelles de 155 cm et qui ont disparu dans les étincelles de 17 cm.

Tableau II

λ	Attributions	Intensités MIT
4676–61	O II	250
4433	N II ?	30
3912	O II	155
3805	N_2 *0,2* 2^e *pos.*	
3794	O II	10
3777	O II	18
3755	N_2 *1,3* 2^e *pos.*	
3734	O_2^+ *1,7*	
3706	O_2^+ *1,7*	
3639	O	10
3612	N_2^+	
3594	O_2^+ *2,7*	
3593	N II	10
3518	O_2^+ *1,6*	
3483–85	N IV	
3478	N IV	
3451–48	O III	
3371	N_2 *0,0* 2^e *pos.*	
3339	N_2 *1,1* 2^e *pos.*	
3324	N II	5
3277	O II	25
3265	O III	
3247		
3225	O_3 ?	
3175	O_3 ?	
3159	N_2 *1,0* 2^e *pos.*	
3123–24	O II	25
3117	N_2 *3,2* 2^e *pos.*	
3089–78–67–63	*OH 0,0*	
3035	*NO β*	
3018		
2984	O III	
2962	N_2 *3,1* 2^e *pos.*	
2953	N_2 *4,2* 2^e *pos.*	
2920	O_2^+ *4,4*	
2902	O_2^+ *4,4*	
2840	O_2^+ *3,3*	
2808–06	O IV	
2747	O II	25

et toutes les suivantes excepté 2527 de O II.

On voit que les éléments qui ont disparu sur les courtes étincelles sont soit des aies d'atomes plusieurs fois ionisés, soit des éléments relativement faibles du spectre; mais nous voulons insister sur le fait que leur disparition ne tient pas à la variation de largeur de la raie; la variation de largeur se traduit par un aspect plus flou, et euls les éléments très faibles ne peuvent être retrouvés dans ce cas. La plupart des bandes ultraviolettes ont disparu, exceptée celle due à CO_2 qui s'observe sur tous es spectres.

Nous sommes donc amenés à cette curieuse remarque que l'augmentation de la distance et de la tension disruptive provoque l'apparition à la fois de raies exigeant une forte excitation, O IV, N IV, et de bandes relativement faciles à exciter. Nous pensons que la présence de ces bandes est peut-être en rapport avec les pré-décharges qui se développent lorsque la distance est grande (Voir LOEB et MEEK). Peut-être s'agit-il aussi d'un spectre d'afterglow. Nous ne pouvons trancher pour le moment cette question puisque nous enregistrons non seulement l'étincelle, mais aussi tout phénomène lumineux qui la précède ou la suit immédiatement.

Nous avons essayé de voir comment variait l'intensité de quelques raies avec la position le long de l'étincelle. Ces déterminations sont approximatives car la photométrie de raies, même avec une plaque étalonnée est une opération délicate où interviennent la largeur de la raie et les conditions d'enregistrement microphotométrique. Pour la même distance disruptive, nous avons des spectres pris près de la pointe, près de la sphère et au milieu (toute l'étincelle ne tient pas dans le champ de l'instrument, sauf pour 17 cm).

Une première étude a porté sur la raie 3331 de N II. Un résultat est très net: du côté de la pointe, quelle que soit sa polarité, la raie est plus intense, de 20 % en moyenne; nous avons vu plus haut que certains éléments ne s'observaient quelquefois que du côté de la pointe. Mais il n'est apparu aucune corrélation avec la distance. La raie présente des variations qui peuvent être importantes même d'une étincelle à l'autre, mais ne paraissent pas liées à la tension.

Une autre étude a porté sur la raie 4630 de N II également; elle présente aussi des fluctuations importantes, mais une certaine relation semble se dégager; l'intensité croît d'abord avec la distance, de 17 cm à 50 cm, où elle passe par un maximum pour décroître ensuite aux distances plus grandes. Pour cette raie, l'intensité est toujours plus forte du côté du pôle négatif, que ce soit la pointe ou la sphère.

On voit donc qu'aucune règle générale ne peut être établie; le spectre ne se modifie pas dans son ensemble; les rapports d'intensité ne se maintiennent pas.

IV – Etude quantitative — Fond continu

Nous avons dit que le spectre de l'étincelle comportait une émission continue; elle est particulièrement accessible dans l'ultraviolet où les raies et les bandes sont plus espacées. Nous avons fait l'étude de ce spectre continu. Une première étude brute a consisté à tracer au plus serré l'enveloppe des raies (voir figures 1 et 2) et à déterminer la répartition énergétique correspondant à ce tracé. Si cette enveloppe suit parfaitement le fond continu dans les régions 3200–2500 A, ou encore vers 5000 A, il n'en est pas de même entre 3800 et 4200 A par exemple où le grand nombre et la proximité des bandes permettent difficilement d'atteindre le fond. La répartition spectrale énergétique est déterminée par comparaison avec les sources utilisées; elle est connue à un facteur constant près, qui n'est pas le même pour l'ultraviolet et le visible; mais la région commune s'étendant de 3800 à 4200 A a permis dans tous les cas de raccorder les deux parties sans ambiguité; les résultats obtenus sont portés sur la figure 5, où chaque courbe représente la moyenne des résultats obtenus pour une distance d'étincelle donnée.

On voit que les courbes, sans être exactement parallèles, ont même allure. Une région régulièrement descendante de 2500 à 3700 A; un renforcement de l'émission avec maximum à 4050 A; un profond minimum à 4600 A; une remontée à 4900–5000 A, un deuxième minimum et une deuxième remontée. En outre la courbe pour 50 cm présente à 2900 une émission correspondant aux bandes de CO_2 plus intenses sur le spectre.

Le renforcement autour de 4000 A s'explique immédiatement par le grand nombre

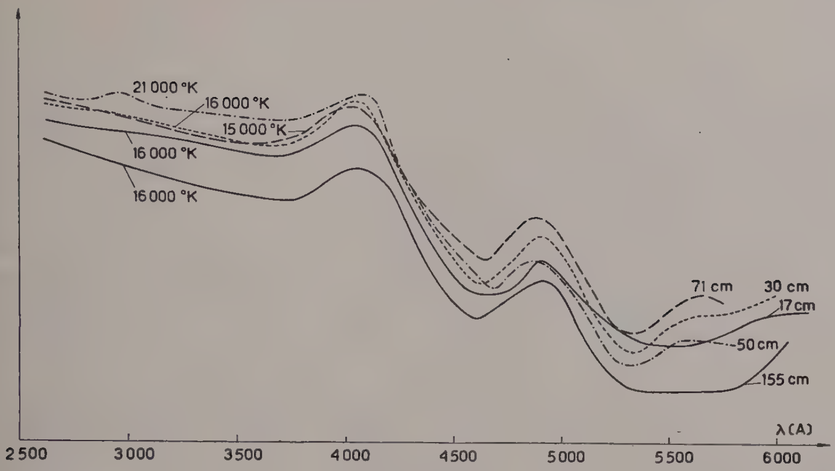

Fig. 5.

e raies et bandes; comme il était à prévoir, le tracé de l'enveloppe est incertain car n n'atteint pas le fond; les raies et bandes sont distantes de quelques angströms, eaucoup sont assez larges dans cette région et il est possible que certaines émissions ient lieu dans un domaine plus large que le canal de l'étincelle (afterglow), ce qui, u prisme-objectif, se traduit par une raie élargie.

Examinons maintenant le maximum secondaire à 4900–5000 A. On voit immédia- ement qu'il se place à peu près dans le prolongement de la partie de la courbe 600–3700 A.

Cette circonstance éclaire la nature des minima à 4600 et 5300 A; il s'agit de andes d'absorption plus ou moins continues.

La première est due au peroxyde d'azote formé par l'étincelle. Nous avons étudié variation de cette bande sur les différents spectres; son intensité croît très régulière- ient de la première à la dernière étincelle sur toutes les plaques; la quantité formée arie sensiblement avec chaque série d'expériences, du simple au quadruple, mais e manifeste pas de corrélation avec la tension; peut-être des circonstances extérieures, umidité et température de l'air ambiant, interviennent-elles pour masquer une telle orrélation. Nous avons dit plus haut comment, grâce aux coefficients déterminés ar Dixon, nous avons pu montrer que la quantité de NO_2 interposé entre l'étincelle le spectrographe est de l'ordre de 0,4 mm (épaisseur réduite) pour une série de où 5 étincelles. Nous avons également indiqué la possibilité que la 2^{me} bande, 200–6100 A, soit due à la présence de NO_3.

Une fois établie ainsi l'existence de l'absorption entre 4600 et 5100 A nous allons ouvoir étudier la répartition énergétique du fond continu, et voir en particulier il correspond à l'émission du corps noir à une température déterminée. On sait que areille émission a déjà été observée dans le cas de gaz soumis aux fortes compressions rovoquées par une onde de choc (2). Nous avons donc calculé grâce aux Tables de abry (15) la répartition énergétique du corps noir entre 2600 et 5800 A pour un rtain nombre de températures; quelques-unes des courbes obtenues sont portées ır la figure 6. On cherche ensuite laquelle coïncide avec la courbe expérimentale près les avoir fait concorder pour une longueur d'onde quelconque, ici 2600 A.

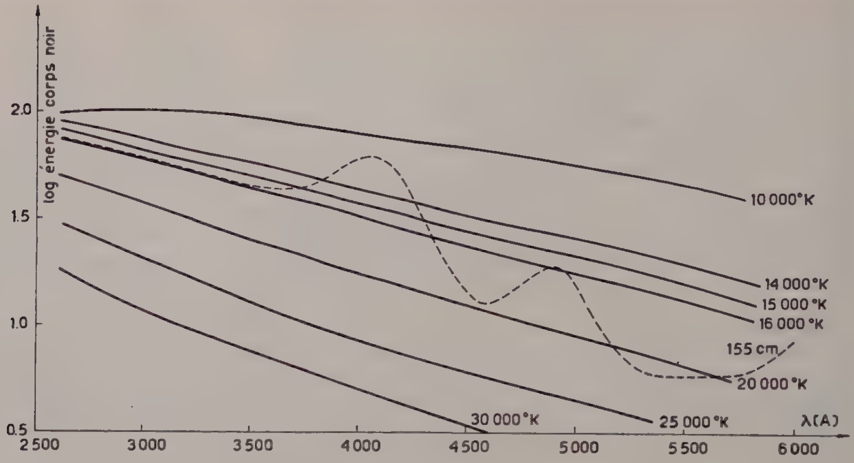

Fig. 6.

Pour ne pas surcharger la figure, on a porté une seule des courbes expérimentales, celle correspondant à une distance explosive de 1,55 m. On voit que la courbe 16000° K correspond bien à cette courbe; dans la région 2600–3700 A, elle suit exactement la pente de la répartition spectrale, et vient la rejoindre vers 4900 A entre les deux bandes d'absorption. C'est donc sur un intervalle spectral de 2300 A que porte l'accord entre les courbes théorique et expérimentale, ce qui rend raisonable l'attribution du fond continu à un spectre d'émission thermique. Nous avons retrouvé la même valeur 16000° K pour 155 cm, 17 cm et 30 cm. La courbe pour 71 cm donne 15000° K. Enfin la distance 50 cm correspond à 21000° K; l'agrément des deux courbes n'est pas aussi excellent que dans les autres cas, car des bandes sont encore visibles ainsi que nous l'avons déjà dit.

Autre résultat assez remarquable: l'énergie émise pour une longueur donnée d'étincelle varie assez peu; en d'autres termes, la brillance d'une région de l'étincelle varie peu avec la longueur; nous employons le mot brillance pour mieux représenter le phénomène, mais en fait nous mesurons l'énergie totale émise par une certaine partie de l'étincelle pendant toute sa durée; si la durée du phénomène varie avec la distance disruptive, ce ne sont plus des brillances que nous comparons, mais des quantités d'énergie. Nous conserverons pourtant cette expression pour plus de commodité.

Donc la brillance varie peu avec la distance disruptive; cependant elle est maximum pour 50 cm, qui donne aussi la température de couleur la plus élevée. Comme nous avons vu que les bandes sont plus intenses pour 50 cm, et que la raie 4630 est également maximum pour 50 cm, il semble que cette distance corresponde à des conditions d'excitation particulières.

CONCLUSION

Ce que nous voudrions principalement conclure de cette étude, c'est que l'étincelle électrique n'est pas un événement simple et unique, mais une série de phénomènes correspondant à des conditions d'excitation différentes. La succession de ces phénomènes et leurs rapports d'intensité sont très probablement variables avec la tension de décharge. Cette étude n'a pas permis de séparer ces divers événements dont la succession constitue l'étincelle; mais en s'aidant de la théorie de Loeb & Meek, on peut aisément se faire une idée provisoire et grossière de l'émission lumineuse. Aux stades préparatoires constitués par les avalanches et les «streamers» correspondent les émissions de faible excitation, la plupart des bandes et les raies d'atomes neutres en particulier; ces stades préparatoires sont sans doute plus nombreux et plus puissants pour les étincelles de grande distance car le chemin à frayer est plus long, ce qui explique l'intensité croissante des bandes pour des tensions croissantes; au phénomène brutal de la décharge principale correspondent ensuite les raies de forte excitation: atomes plusieurs fois ionisés. Il ne faut pas exclure non plus l'existence d'une lueur légèrement postérieure à la décharge. Le spectre continu nous paraît indiscutablement lié à la décharge principale, où plutôt à cette lueur postérieure. Il est sans doute en relation avec le phénomène sonore qui accompagne l'étincelle.

Une telle détermination de la température, sur de grandes étincelles, n'avait encore pas été faite; en effet les auteurs qui ont étudié le spectre de l'étincelle ont travaillé dans le visible où la détermination d'une température de couleur n'est pas possible en raison du trop grand nombre de raies d'émission et aussi des bandes d'absorption dont seule la région ultraviolette du spectre continu permet d'affirmer la présence et de mesurer l'importance.

Toutefois, nos conclusions sont intéressantes à rapprocher de celles de Craggs & Meek (16), bien que ces auteurs aient opéré sur des étincelles beaucoup plus courtes: 1 cm. Par une étude et des moyens complètement différents, évolution de l'intensité lumineuse au cours de l'étincelle, détermination de la concentration en ions par effet Stark, application de l'équation de Saha, ils ont pu déterminer la température de l'étincelle et trouvé 12000 à 15000° K; ils ont noté l'existence d'un afterglow intense, variable en durée avec le gaz dans lequel se produit l'étincelle, qui n'est pas dû au courant parcourant le canal. Ces conclusions sont donc essentiellement les mêmes que les nôtres. Mais nous nous séparons au sujet de l'interprétation du spectre. Craggs & Meek, ayant opéré dans le spectre visible n'ont pas aperçu l'importance du spectre continu dont le maximum en raison de la température se place vers 2000 A. La part de l'excitation d'origine thermique est sans doute plus grande qu'ils ne l'ont supposé.

En outre l'application de l'équation de Saha suppose que l'équilibre thermique est atteint. Or une récente théorie de Weizel & Rompe (17), qui ont eu l'idée intéressante de considérer les variations de température du canal au cours de l'étincelle, attire l'attention sur le fait que la température des électrons et celle du gaz ne peuvent se mettre en équilibre en raison de la brièveté du phénomène.

Ces légères différences ne sauraient faire oublier le bon accord entre des conclusions obtenues par des voies aussi différentes.

Ce travail a été effectué avec l'aide d'une subvention du Svenska Statens Naturvetenskapliga Forskningsråd et avec la collaboration technique de Messieurs O. Salka, ingénieur à l'Institut des Hautes Tensions d'Uppsala et B. Leroy, Technicien du Centre National de la Recherche Scientifique et nous sommes heureux d'adresser nos remerciements à ces personnes et ces organismes dont l'aide a permis d'accomplir cette étude.

Institutet för högspänningsforskning, Uppsala Universitet; Physique de l'Atmosphère, Université de Paris. Avril 1952.

BIBLIOGRAPHIE

1. H. Norinder, Institutet för högspänningsforskning vid Uppsala Universitet, Uppsala 1949.
2. A. Michel-Levy, H. Muraour et E. Vassy, Rev. Opt. 20, 1941, p. 149.
3. J. Romand, C. R., 224, 1947, p. 35.
4. D. Chalonge et E. Vassy, Rev. Opt., 13, 1934, p. 113.
5. Mass. Inst. of Techn. Wavelength tables, New York 1939.
6. R. W. B. Pearse & A. G. Gaydon, The Identification of Molecular spectra, Londres 1941.
7. M. C. Mihul, Ann. de Physique, 9, 1928, p. 261.
8. L. J. Freeman, Proc. Roy. Soc., 121, 1928, p. 318 et 127, 1930, p. 330.
9. J. Zenneck & B. Strasser, Phys. Zeits. 12, 1911, p. 1201.
10. J. K. Dixon, Jour. Chem. Phys., 8, 1940, p. 157.
11. P. Pascal, Traité de Chimie Minérale, tome 3, p. 138.
12. O. R. Wulf & E. J. Jones, J. Chem. Phys., 5, 1937, p. 873.
13. Sprenger & Schumacher, Zeits. physik. Chem., 136, 1928, p. 77.
14. Loeb & Meek, The mechanism of Electrical Sparks.
15. Fabry, Introduction générale à la Photométrie.
16. Craggs & Meek, Proc. Roy. Soc., 186, 1946, p. 241.
17. Weizel & Rompe, Ann. der Phys., 1, 1947, n. 285.

Tryckt den 5 maj 1953

Uppsala 1953. Almqvist & Wiksells Boktryckeri AB

ARKIV FÖR FYSIK Band 6 nr 43

Communicated 28 January 1953 by MANNE SIEGBAHN and ERIK HULTHÉN

A study of the (αp)-reaction in nitrogen by means of photographic emulsions

By ELIS HJALMAR and HILDING SLÄTIS

With 6 figures in the text

1. Introduction 451
2. Earlier investigations on nitrogen 451
3. Bombardment of nitrogen 455
4. Elastically scattered protons 457
5. Possible improvements in the method used 460
Summary 462

1. Introduction

In previous papers[1,2] we have given surveys of earlier investigations concerning (αp)-reactions, in particular reactions on aluminium, boron, fluorine and sodium. Methods of determining the Q-values for the (αp)-reactions were described. A new arrangement for measuring the Q-values by means of modern photographic nuclear research emulsions and a polonium α-particle source was developed.

We have now continued these investigations by bombarding nitrogen with α-particles from the same source. In addition we have investigated the effect of elastically scattered protons, originating in the thin mica window, which covered the polonium source in order to prevent the target, the emulsion and other surfaces in the vacuum chamber from being contaminated with polonium sample fragments.

Furthermore, we have compared the range distribution of the α-particles from the polonium sample with the range distribution of the α-particles from ThC + C′ in order to measure how much of the energy spread in the polonium α-particles is due to straggling and scattering in the sample itself and in the mica window.

2. Earlier investigations on nitrogen

As is well known, $N^{14}(\alpha p)O^{17}$ was the first artificial nuclear reaction ever observed. The discovery was made by RUTHERFORD[3,4], who in 1919 bombarded light elements with α-particles from RaC′. Even in these early experiments the effect of recoil protons from hydrogen in the target material or window was observed. BLAC-

---

[1] H. SLÄTIS, E. HJALMAR, and R. CARLSSON, Arkiv f. Fysik *3*, No 17, 1951; Phys. Rev. *81*, 641, 1951.

[2] E. HJALMAR and H. SLÄTIS, Arkiv f. Fysik *4*, No 14, 1952.

[3] E. RUTHERFORD, Phil. Mag. *37*, 537, 1919. Nature *103*, 415, 1919.

[4] E. RUTHERFORD, Proc. Roy. Soc. A. *97*, 374. 1920.

KETT's[5] important Wilson-chamber investigations later gave evidence for the fact that when a proton is expelled, the α-particle is captured by the nitrogen nucleus. CHADWICK, CONSTABLE, and POLLARD[6] bombarded nitrogen with α-particles from polonium and found evidence for one group of protons corresponding to Q = about -1.3 MeV. STEUDEL[7] also used polonium α-particles. He observed only one proton group, the range of which was 17.2 cm.

One proton group was also found by HAXEL[8], who used α-particles with ranges 4–8.6 cm. The Q-value of the group was -1.27 MeV. He observed that the proton yield decreased for α-particle ranges exceeding 6 cm, depending on the increasing neutron yield from the competing (αn)-reaction. STEGMANN[9] believed that he found three groups, with the Q-values -0.41, -0.95, and -1.60 MeV. This result seems to be in disagreement with other investigations. He used polonium α-particles.

FISCHER-COLBRIE[10] bombarded dicyandiamide in thick layers and thin gaseous nitrogen layers with RaC α-particles. FISCHER-COLBRIE and STETTER[11] deduced from these experiments two groups, the Q-values of which are -1.4 and -2.8 MeV. The difference 1.4 MeV seems to agree with the energy 1.3–1.5 MeV of the gamma rays observed by SAVEL[12]. Gamma-rays from nitrogen bombarded with polonium alphas have also been recorded by one of us[13].

The excited states of the residual nucleus O^{17} can also be studied in the $O^{16}(dp)O^{17}$-reaction. COCKCROFT and LEWIS[14] bombarded targets of quartz and HPO_3 with 575 keV deuterons and found three groups of protons. Two of these groups belonged to the oxygen reaction and gave the Q-values 1.91 and 1.03 MeV. This gives for the excited state in O^{17} the energy 0.88 MeV. LIVINGSTON and BETHE[15] have corrected these values for the thickness of the target, and give 0.83 MeV for the excited state in O^{17}.

BURCHAM and SMITH[16] bombarded metallic fluoride deposits (KF, NaF, AgF, BaF_2) with 0.85 MeV deuterons (from an accelerating tube) and found five alpha particle groups from the $F^{19}(d\alpha)O^{17}$ reaction. The energy of the lowest excited O^{17} level was 0.83 MeV.

ROTBLAT[17, 18, 19] studied the levels in O^{17} using the reactions $O^{16}(dp)O^{17}$ and $F^{19}(d\alpha)O^{17}$ for 7.8 MeV deuterons. The protons and alpha particles were recorded by means of photographic plates. He found 10 levels. The energy of the first excited O^{17}-level was 0.875 MeV.

GUGGENHEIMER, HEITLER, and POWELL[20] made scattering experiments with 6.5

---

[5] P. M. S. BLACKETT, Proc. Roy. Soc. *A 107*, 349, 1925.

[6] J. CHADWICK, J. E. R. CONSTABLE, and E. C. POLLARD, Proc. Roy. Soc. *A 130*, 463, 1931.

[7] E. STEUDEL, Z. f. Ph. *77*, 139, 1932.

[8] O. HAXEL, Z. f. Ph. *93*, 400, 1935.

[9] H. STEGMANN, Z. f. Ph. *95*, 72, 1935.

[10] E. FISCHER-COLBRIE, Ak. W. Wien, *145*, 283, 1936.

[11] G. STETTER, Z. f. Ph. *100*, 652, 1936.

[12] P. SAVEL, C. R. *198*, 1404, 1934.

[13] H. SLÄTIS, Nature *161*, 899, 1948: Arkiv f. Astr. Mat. Fys. *35 A*, No 31, 1948.

[14] J. D. COCKCROFT and W. B. LEWIS, Proc. Roy. Soc. *A 154*, 261, 1936.

[15] M. S. LIVINGSTON and H. A. BETHE Rev. Mod. Phys. *9*, 245, 1937.

[16] W. E. BURCHAM and C. L. SMITH, Proc. Roy. Soc. *A 168*, 176, 1938.

[17] J. ROTBLAT, Nature *160*, 462, 1947.

[18] W. F. HORNYAK, T. LAURITSEN, P. MORRISON, and W. A. FOWLER, Rev. Mod. Phys. *22*, 291, 1950.

[19] F. AJZENBERG and T. LAURITSEN. First draft copy of a contemplated revision of Energy Levels of Light Nuclei (ref. 18), July 16, 1952, Rev. Mod. Phys. *24*, 321, 1952.

[20] K. M. GUGGENHEIMER, H. HEITLER, and C. F. POWELL, Proc. Roy. Soc. *A 190*, 196, 1947.

IeV deuterons on a number of light elements, the protons being recorded by means f photographic emulsions. They obtained an energy of 0.85 MeV for the first excited tate in O^{17}. Pollard and Davison[21] used an absorption cell for determining the nergy of the protons and found 0.86 MeV for the same state. They also used the N^{14}(αp)O^{17}-reaction, obtaining the Q-values −1.31 and −2.12 MeV, giving for the xcited level the energy 0.81 MeV. Heydenburg and Inglis[22] used deuteron energies rom 0.65 to 3.05 MeV and thin oxide targets. The protons observed by means of n ionization chamber gave 0.87 MeV for the first O^{17}-level.

Heydenburg, Inglis, Whitehead, Jr., and Hafner[23] give the redetermination .91 MeV. Buechner, Strait, Sperduto, and Malm[24] analyzed the protons from the euteron bombardment of O^{16} targets with a high resolution magnetic spectrometer nd obtained 0.876 ± 0.009 MeV as the energy of the first excited state in O^{17}.

Alburger[25] studied the Compton electrons released in a radiator by the gamma ays emitted from the excited O^{17}-nucleus. The energy distribution of the electrons vas measured in a lens spectrometer. The energy for the first excited level was ound to be 900 ± 50 keV.

Champion and Roy[26] bombarded gaseous nitrogen with polonium alpha particles nd studied the angular distribution of the proton tracks in a Wilson chamber, inding an approximately isotropic distribution for protons ejected by alpha particles f energy less than 3 MeV, but a preponderance at about 90° for the protons ejected y alpha particles of range about 2 cm in air at N.T.P. (3.4 MeV). Roy[27] used the hotographic emulsion technique, and found the Q-values −1.16 and −2.0 MeV for he N^{14}(αp)O^{17}-reaction. The angular distribution of protons in the centre-of-mass ystem has a maximum at 90° for the ground state, and is isotropic for the excited tate. The experiments showed resonance out for two different alpha particle nergies, 3.6 and 4.2 MeV.

Burrows, Powell, and Rotblat[28] determined the energy of the excited states f the O^{17} nucleus by observations on the protons from the O^{16}(dp)O^{17} reaction nd the alpha particles from the reaction F^{19}($d\alpha$)O^{17}. The protons and the alpha articles were recorded by means of photographic emulsions. Thirteen excited states f O^{17} were observed. We give here only the mean energy value for the first excited tate: 0.87 ± 0.02 MeV. Watson (see ref. 22) determined the energy of the α-particles n the F^{19}($d\alpha$)O^{17}-reaction by means of a magnetic spectrometer and found for the irst state the energy 883 ± 11 keV. Van Patter (see ref. 18 and 19) has given the alue 880 ± 5 keV for this energy.

Thomas and Lauritsen[29] have used a beta spectrometer for determining the nergy of the gamma-ray from the first excited O^{17}-state and found 870.5 ± 2 keV.

The results previously obtained together with our values are summarized for onvenience in Table I. It is seen that only a few investigations were made on the

---

[21] E. Pollard and P. W. Davison, Phys. Rev. *72*, 736, 1947.

[22] N. P. Heydenburg and D. R. Inglis, Phys. Rev. *73*, 230, 1948.

[23] N. P. Heydenburg, D. R. Inglis, W. D. Whitehead, Jr., and E. M. Hafner, Phys. Rev. *75*, 1147, 1949.

[24] W. W. Buechner, E. N. Strait, A. Sperduto, and R. Malm, Phys. Rev. *76*, 1543, 1949.

[25] D. E. Alburger, Phys. Rev. *75*, 51, 1949.

[26] F. C. Champion and R. R. Roy, Proc. Roy. Soc. *A 191*, 269, 1947.

[27] R. R. Roy, Centre de Phys. Nucleaire, Univ. Libre de Bruxelles, No *21* Sept. 1950; Phys. Rev. *82*, 227, 1951.

[28] H. B. Burrows, C. F. Powell, and J. Rotblat, Proc. Roy. Soc. *A 209*, 461, 478, 1951.

[29] R. G. Thomas and T. Lauritsen, Phys. Rev. *88*, 969, 1952.

Table 1

Author	Year	Ref. No.	Photo plate = X	$N^{14}(\alpha p)O^{17}$			$O^{16}(dp)O^{17}$ E_1	$F^{19}(d\alpha)O^{17}$ E_1
				Q_0	Q_1	E_1		
				MeV	MeV	MeV	MeV	MeV
CHADWICK, CONSTABLE, and POLLARD	1931	6		−1.3				
HAXEL	1935	8		−1.27				
FISCHER-COLBRIE, STETTER	1936	10, 11		−1.4	−2.8	1.4		
SAVEL	1934	12				1.3–1.5		
COCKCROFT and LEWIS	1936	14					0.88	
LIVINGSTON and BETHE, above value corrected	1937	15					0.83	
BURCHAM and SMITH	1938	16						0.83
ROTBLAT	1947	17, 18, 19	X				0.875	0.875
GUGGENHEIMER, HEITLER and POWELL	1947	20	X				0.85	
POLLARD and DAVISON	1947	21		−1.31	−2.12	0.81	0.86	
HEYDENBURG and INGLIS	1948	22					0.87	
HEYDENBURG, INGLIS, WHITEHEAD, Jr., and HAFNER	1949	23					0.91	
BUECHNER, STRAIT, SPERDUTO and MALM	1949	24					0.876 ± 0.009	
ALBURGER	1949	25					0.900 ± 0.050	
ROY	1950	27	X	−1.16	−2.0	0.84		
BURROWS, POWELL, and ROTBLAT	1951	28	X				0.87 ± 0.02	0.87 ± 0.05
WATSON	1952	19						0.883 ± 0.011
VAN PATTER	1952	19					0.880 ± 0.005	
THOMAS and LAURITSEN	1952	29					0.8705 ± 0.002	
HJALMAR and SLÄTIS	1952	this paper	X	−1.16	−2.02	0.86		
Nominal value		18		−1.198				

$N^{14}(\alpha p)O^{17}$-reaction and that the Q-values measured by different authors are inconsistent. The nominal Q-value computed from mass-spectroscopical data is also quoted (ref. 18). The energy for the first excited state in the O^{17}-nucleus has been studied very thoroughly by means of the $O^{16}(dp)O^{17}$-reaction. It is seen that the results obtained by the different workers agree closely between themselves and with the results from the $F^{19}(d\alpha)O^{17}$-reaction. The mean of all these E_1-values is 0.8705 MeV, which is exactly the value given by THOMAS and LAURITSEN[29].

The photographic emulsion technique has been used earlier only four times in connection with the nucleus O^{17} and only once for the $N^{14}(\alpha p)O^{17}$ reaction. It was therefore interesting to check the earlier results and to make a new determination of the Q_0-value for this reaction. The emulsion studied in the present work had already been exposed in June 1950, before the interesting paper by ROY (see Table I) had appeared.

3. Bombardment of nitrogen

The experimental arrangement for investigating proton tracks from the nitrogen target bombarded with alpha particles from a polonium source was the same as that described in our previous papers[1,2]. As mentioned above, the bombardment of the nitrogen target was performed in 1950, using the same polonium sample as that used for the other bombardments described.

The nitrogen target consisted of a chromium-plated copper sheet, on which a thin layer of chromium nitride had been formed by heating the plate in an atmosphere of pure nitrogen.* The size of the target was the usual one, 5×10 cm. Exposure was made for 23 hours, the strength of the polonium source being about 12 mC. The Q-values obtained from 262 proton tracks are presented diagrammatically in Fig. 1. We have again used the integration method described in ref. 1. The Q-values belonging to individual tracks are seen below in the figure (indicated by short vertical lines, group a in the figure). We have also marked false Q-values, which originate in elastically-scattered protons from the window (the individual false Q-values are indicated in the line group b, Fig. 1). The phenomenon of the elastically scattered protons is treated in section 4. These protons were found by bombarding a target of iron with alpha particles. This was also done in ref. 1 (compare Fig. 12, which gives the false Q-values for boron), but was now studied in more detail. Thus 162 proton tracks were measured. The distribution of the false nitrogen Q-values is indicated by the dotted curve e in Fig. 1. The height of the distribution curve corresponds to the intensity valid for the nitrogen target and is computed from the exposing times for the N- and Fe-plates, the emulsion areas scanned, and the strength of the polonium source when the exposures were made. When the dotted curve e is subtracted from the curve c for the Q-values for protons from the nitrogen target we get the curve $f\,g$, which belongs to the $N^{14}(\alpha p)O^{17}$-reaction. The curve shows two marked maxima, indicating the Q-values for a transmission to the ground state and to the first excited level of O^{17}, respectively.

Fig. 1 shows that the Q-value for a transmission to the ground state of O^{17} is $Q_0 = -1.16$. The half-width of the corresponding distribution curve is 0.48 MeV or exactly the same as for the most prominent line ($Q = 0.14$) in the Q-values obtained for the $Al^{27}(\alpha p)Si^{30}$-reaction (Fig. 10 in ref. 1), when the Q-values are integrated

---

* We are indebted to Fil. lic. WILHELM FORSLING, Nobel Institute of Physics, Stockholm, who kindly carried out this nitration.

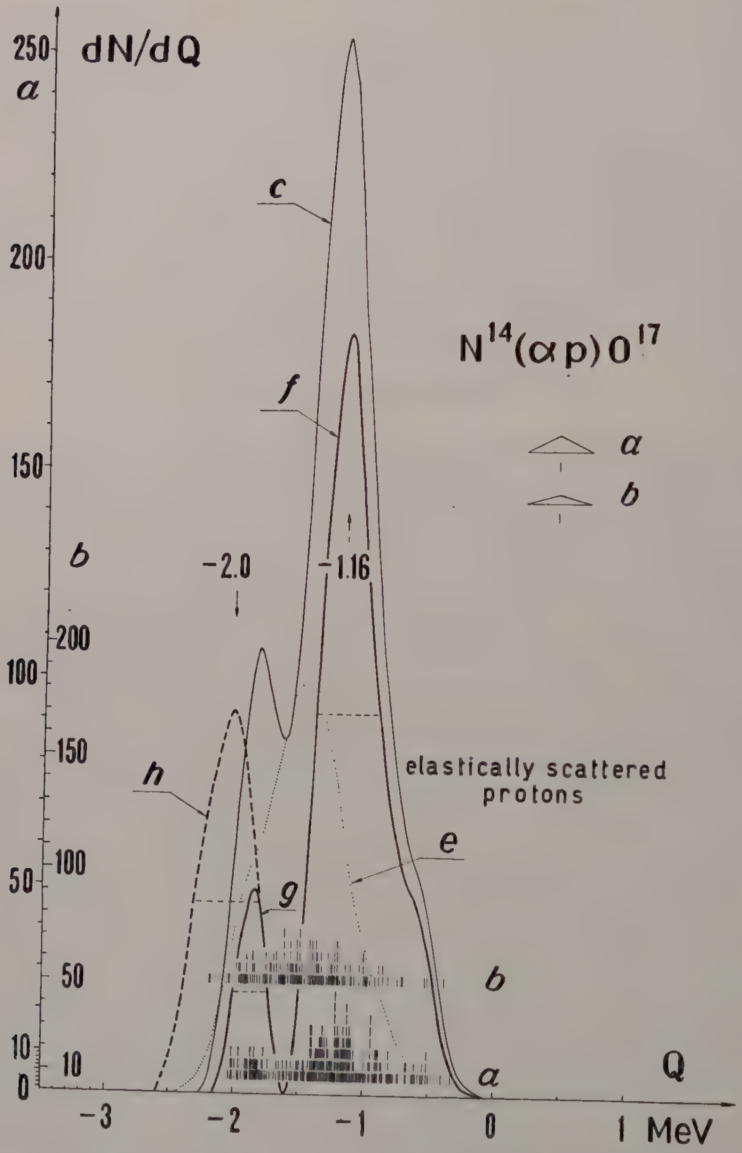

Fig. 1. The most probable Q-values for the $N^{14}(\alpha p)O^{17}$-reaction, computed from the Q-values obtained from 262 proton tracks. *a*) Individual Q-values for protons from a thin chromium nitride layer on a chromium-plated copper sheet. *b*) Individual Q-values for protons from an iron target, the protons considered as belonging to the $N(\alpha p)O$-reaction. *c*) Distribution curve obtained when the Q-values (*a*) are integrated. Each *a*-value is replaced by a triangle (*a*) seen to the right in the figure. *e*) Distribution curve for the Q-values (*b*). *f*, *g*) Difference between the distributions *c* and *e*. *h*) Corrected size and position of *g* (see the text).

using the same base (0.5 MeV) for the triangle belonging to each individual Q-value. This shows that the thickness of the chromium nitride was of the same order of magnitude, viz. 0.15 mg/cm^2, which was also confirmed by weighing. However, the half-width of the Q-value distribution belonging to the first excited state is only 0.28 MeV. This is because no proton tracks shorter than 25 μ were counted in order to ensure that no contaminating alpha particles were included (the range for 5.3 MeV alpha particles is 22.3 μ). The lack of a second maximum in the false Q-value distribution e (Fig. 1) shows that this rule was sufficient to prevent the counting of alpha particles (a small hump in the curve e shows, however, that in spite of this rule a few alpha particles were indeed counted). It is not likely that many tracks on the right-hand side of the peak g have been omitted (the range for the track giving $Q = -1.71$ MeV was for instance 34.5 μ). We have therefore considered the upper energy limit of the peak g as being correct, and broadened the peak, taking the point at $Q = -1.64$ MeV as fixed, until the half-width was 0.52 MeV. This value was considered as the most probable half-width of the line in question, for the following reasons. The half-width of a Q-value peak increases when the proton energy decreases. This will be a consequence of the difficulty in measuring h, the depth of the end of the proton track in the emulsion. The half-width of the -1.75 MeV Q-line in Fig. 11, ref. 1, is 0.65 MeV and that of the 0.65 MeV line is 0.53 MeV. If the broadening effect of 0.12 MeV is considered proportional to the difference of the corresponding proton energies, we interpolate for the nitrogen case a broadening effect of 0.04 MeV. The half-width of the f-line in Fig. 1 is 0.48 MeV. This gives the value 0.52 MeV for the half-width of the corrected f-line. In this way we obtain the distribution h, which we consider to be a probable Q-value distribution for the first excited state in O^{17}. Of course the procedure used involves a certain arbitrariness, and the value $Q_1 = -2.02$ MeV obtained has not at all the same accuracy as the Q_0-value. However, the difference $Q_0 - Q_1 = 0.86$ MeV is in perfect agreement with the well known energy 0.87 MeV for the first excited level in O^{17}, measured from the $O^{16}(dp)O^{17}$ and $F^{19}(d\alpha)O^{17}$ reactions (see Table I). Our values agree almost exactly with those found by ROY.

The agreement between the nominal value $Q_0 = -1.198$, computed from mass-spectroscopy data[18, 19], and our value -1.16 is also good.

4. Elastically scattered protons

By elastic collisions between alpha particles and protons a large number of recoil protons are released in the mica window in front of the polonium sample. These recoil protons are in turn elastically scattered by the heavy nuclei in the target and form in this way a background for the protons, which belong to the (αp)-process studied. We have already shown how this background can be experimentally determined and corrected for. However, it may be of interest to check the interpretation of the recoil protons by some theoretical deductions.

First we calculate the energy E_p of those protons, which emerge essentially perpendicular to the mica window (Fig. 2, see also Fig. 5 in ref. 1). *Po* is the polonium sample. An alpha particle α is emitted from the sample and hits the mica window at the point M_1. The angle between the α-particle path and the normal of the window is Θ. A proton may be emitted perpendicularly to the window at M_1, at M_2 or between M_1 and M_2. The loss ΔE_α in energy for the alpha particle between M_1 and M_2 will

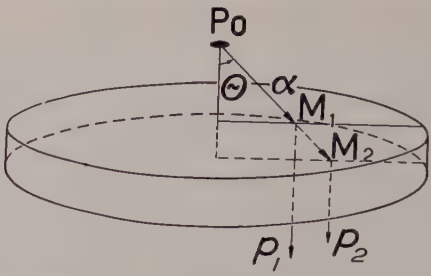

Fig. 2. Protons emerging from the mica window covering the polonium sample *Po*. The protons p_1 and p_2 are expelled by elastic impact at M_1 and M_2 of alpha particles from the polonium sample.

be approximately $\Delta E_0/\cos\Theta$ if ΔE_0 is the energy loss for $\Theta = 0^0$. The energy of the proton emitted is found from the well known formula (see ref. 1).

$$Q = E_p\left(1+\frac{M_p}{M_r}\right) - E_a\left(1-\frac{M_a}{M_r}\right) - \frac{2\sqrt{E_p E_a M_p M_a}}{M_r}\cos\Theta. \tag{1}$$

Q is the excess of the sum of the kinetic energy E_p of the proton and the energy E_r of the residual nucleus over the energy E_a of the incident alpha particle. M_a, M_p and M_r are the masses of the alpha particle, the proton, and the residual nucleus, respectively. We have $Q = 0$ for elastic collisions. In the case considered $M_p = 1$, $M_a = M_r = 4$, and hence

$$E_p = 0.64\, E_a \cos^2\Theta. \tag{2}$$

The highest value for the energy E_p is obtained if the impact happens at the point M_1. Then, because $E_a = 5.3$ MeV,

$$E_{p_1} = 0.64\cdot 5.3\cos^2\Theta - \Delta E_{p_1}. \tag{3}$$

ΔE_{p_1} is the loss of energy for the proton penetrating the window. ΔE_{p_1} is found for instance from the curves given by LIVINGSTON and BETHE, ref. 15. (the air equivalent of the window is known from the fact that the 5.3 MeV polonium alpha particles have the mean energy 4.6 MeV after penetrating the mica window. This gives an air equivalent of 0.73 cm). The smallest value for the energy E_p occurs if the impact takes place at M_2. Then

$$E_{p_2} = 0.64(5.3 - \Delta E_0/\cos\Theta)\cos^2\Theta \tag{4}$$

In order to find the mean energy $\bar{E}_p$ for the protons emerging normally to the window we have to find the intensity N of the protons as a function of Θ. The number of protons emitted in directions for which Θ is between Θ and $\Theta + d\Theta$ is proportional to the area of a ring, the radius of which is $\sin\Theta$ and the width $d\sin\Theta = \cos\Theta\, d\Theta$. Thus, if A is a constant,

$$dN/d\Theta = A\sin\Theta\cos\Theta.$$

We are interested in the number of protons emitted essentially normal to the window or inside a differential pyramid, the height of which is 1 and the base area $a = d\Theta\cdot d\Theta$. Fig. 3 shows that $dN = A\sin\Theta\cos\Theta\, d\Theta\cdot d\Theta/2\pi\sin\Theta = B\cos\Theta\, da$,

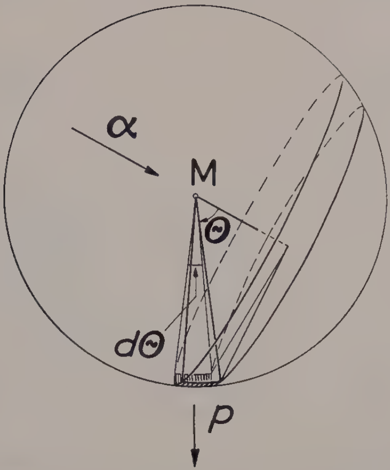

Fig. 3. Deduction of the intensity of the recoil protons emerging approximately perpendicularly to the mica window.

where B is a constant. The intensity of the protons emitted normally to the window is thus

$$dN/da = B \cos \Theta \tag{5}$$

Fig. 4 shows the number of protons dN/da as a function of the proton energies E_{p_1} and E_{p_2}, computed by the formulas (3), (4), and (5). Proton tracks shorter than 25 μ are not counted (see § 3), and hence protons of energy below 1.5 MeV are not included in the calculation. Now the protons recorded in the emulsion have been scattered from the target. If the protons were elastically scattered, the 1.5 MeV protons originate in about 1.6 MeV protons before the scattering (this is easily confirmed by formula (1), if we put $M_p = M_a = 1$, $Q = 0$, and $E_a =$ the energy of the proton before scattering). The equations (3) and (4) give the maximum and minimum energies for a given Θ. If we consider also the energies between these limits, we get a mean distribution of the recoil protons represented by the line P in Fig. 4 and a mean proton energy $\bar{E}_p = 2.47$ MeV.

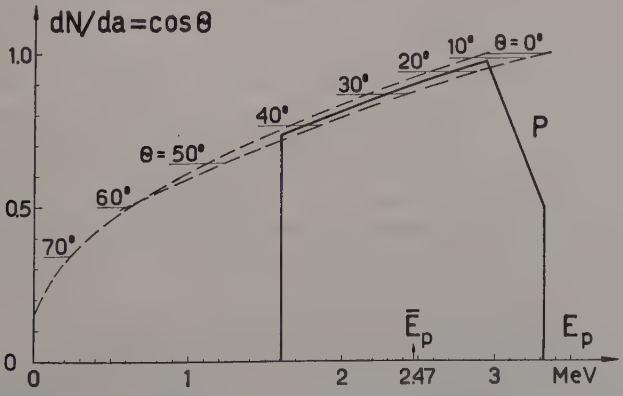

Fig. 4. Energy distribution P of the protons emerging approximately perpendicularly to the mica window.

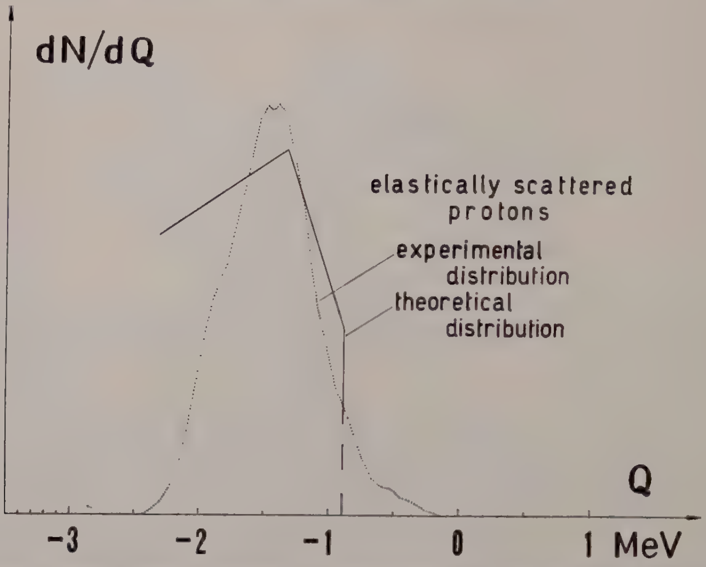

Fig. 5. Theoretical false Q-value distribution (originating in elastically-scattered recoil protons considered as belonging to the N(αp)O-reaction) compared with the experimental curve, used as background in computing the nitrogen Q-values in Fig. 1.

The distribution of false Q-values can now be computed by means of the distribution P and compared with the experimental distribution, curve e in Fig. 1. The elastically scattered protons were all recorded by tracks studied in a limited area of emulsion with $\xi = 7$–8 cm (see Fig. 7 in ref. 1), and hence we can use the same value $\vartheta = 65°$ for protons emerging normally to the window when we estimate the energy of the protons scattered from the iron target. The energies 1.6, 2.94, and 3.32 MeV of the protons before the elastic scattering will then correspond to the energies 1.55, 2.84, and 3.20 MeV after the scattering, respectively. By means of the formula (1) we get the false Q-values -2.40, -1.34, and -0.89, respectively, when we consider the protons as originating in the $N^{14}(\alpha p)O^{17}$-reaction. Fig. 5 shows the theoretical distribution obtained in the way described above compared with the experimental curve which we have used as background in computing the nitrogen Q-values in Fig. 1. It is seen that the agreement is remarkably good, when we consider that the decrease in the intensity of the experimental Q-values in the negative direction depends on the fact that tracks with a length smaller than 25 μ were not included in the count.

In order to increase the accuracy of our method for measuring of Q-values for (αp)-reactions it is obviously desirable to diminish the number of elastically scattered protons. This would be possible if thinner mica windows or other alpha particle sources were used, such as for instance ThC + C′.

5. Possible improvements in the method used

In ref. 1 we have discussed the accuracy of the method introduced for determining Q-values of (αp)-reactions. It was shown that the largest errors arise from the measurement of h, the depth of the end of the track in the emulsion. An error in h causes an

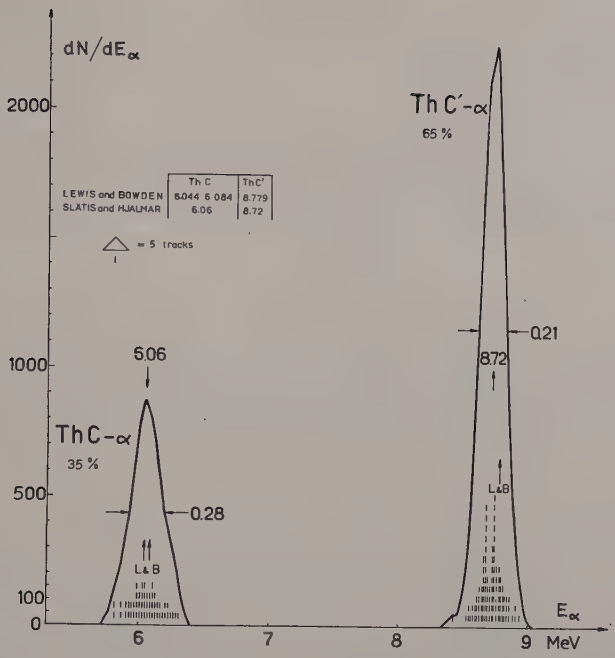

Fig. 6. Measurement of the energy of the ThC + C′ alpha particles by means of nuclear research emulsions. The peak values are compared with the spectrometer values obtained by Lewis and Bowden.

error in v (angle between the track and the surface of the emulsion) and hence in the track length and thus in the energy of the proton. This error can be reduced by the use of small angles v. The accuracy in the values of ϑ (angle between the direction of motion of the proton and that of the alpha particle) could be greatly increased by the use of target sizes and positions such that $v \approx \frac{1}{2}\vartheta$. But already in our equipment as used so far the half-widths ΔQ of the Q-value distribution peaks have been of the same order of magnitude (0.48 MeV) as the half-width ΔE_a of the energy distribution (0.4 MeV) for the alpha-particles (see Fig. 6 in ref. 1). If we consider the half-width ΔQ of the Q-value distribution peak to be composed only of the uncertainty ΔE_a and the uncertainty ΔE_e introduced by the emulsion technique, we find $\Delta E_e = \sqrt{\Delta Q^2 - \Delta E_a^2} = 0.26$ MeV. This half-width in the energy distribution is hence to be expected if we investigate the energy distribution of a monoenergetic source. We have tested this by a study of the alpha particle energy distribution for ThC and ThC′. Fig. 6 shows indeed that the half-width for the ThC′ peak is only 0.21 MeV and thus of the expected order of magnitude. In addition the alpha particle energies found by us are compared with the corresponding values of Lewis and Bowden[30], who measured the deflection of the alpha particles in an annular magnetic field, the particles being counted by means of an ionization chamber. The 6.06 MeV peak consists of two components, which are not resolved by the emulsion technique. The energies and the intensities are according to Lewis and Bowden 6.044_{45} MeV and 6.083_{69}

---

[30] W. B. Lewis and B. V. Bowden, Proc. Roy. Soc. *A 145*, 235, 1934.

MeV, 69.8 % and 27.2 % respectively. The difference between our value 6.06 MeV and the weighted mean 6.055 MeV is only ~0.08 per cent. The difference between the values for ThC′ is still smaller.

The half-width 0.21 MeV found for the alpha particle energy distribution for ThC′ and our discussion above indicate that half-widths of about 0.25 MeV in the Q-value peaks are to be expected if monoenergetic alpha particle sources and the improvements suggested above in our method for measuring Q-values for (αp)-reactions are introduced.

SUMMARY

1. A survey is given of earlier investigations concerning the $N^{14}(\alpha p)O^{17}$-reaction, and the energy of the first excited level in O^{17} as determined from other reactions.
2. By means of an arrangement developed earlier using nuclear research emulsions we have observed two proton groups from the (αp)-reaction in nitrogen, with $Q = -1.16$ and -2.0 MeV, respectively, in close agreement with the values obtained by Roy.
3. The energy distribution of the elastically scattered protons originating in (αp)-recoils in the mica window of the polonium source was estimated theoretically. The result was in close agreement with the experimentally measured energy distribution.
4. The energy distributions of the alpha particles from ThC and ThC′ were studied by means of nuclear research plates, and the energies found were compared with the spectrometer results obtained by Lewis and Bowden.
5. Improvements in our emulsion technique method are suggested.

Nobel Institute of Physics, Stockholm 50, Sweden.

Tryckt den 5 maj 1953

Uppsala 1953. Almqvist & Wiksells Boktryckeri AB

ARKIV FÖR FYSIK Band 6 nr 44

Communicated 26 November 1952 by E. HULTHÉN and G. BORELIUS

Phase contrast measurements of the ruling structure of optical gratings. II.

By ERIK INGELSTAM and ERIK DJURLE

With 12 figures in the text
Sections, figures and tables are numbered in succession from Part I

8. Further developments of the method

This second part of a paper whose first part was published last year (1) reports technical improvements, and includes a more extensive theoretical treatment. The methods described should be of use for studying gratings of intermediate and large size for scientific spectroscopy. Using these techniques it is possible to construct a true phase map of the wave-fronts from the grating, within the limits of error given in Part I, and which are calculated more closely in this paper. Such an investigation of a grating, where the wave-front phase function can be found to about 1° ($\approx \lambda/400$) within a sideways resolution of about 50 microns, reveals interesting features of the grating structure, some of which are of theoretical and practical value for the spectroscopic performance, and for the process of manufacture.

Another development lies in the standardization of this test method so that it may be carried out with especially simple accessories, requiring for example only a photographic record through a gray wedge, instead of photoelectric scanning. This method is only treated briefly as it has been published elsewhere (2).

9. Possible correction of the vector zero point of the phase diagram

The method of obtaining the position of the point O′ of the vector diagram Fig. 7 on page 432 of part I, from which the light amplitude vectors in the phase contrast field start, was given in Section 2, pages 425–427. This treatment presumes that the ideal conditions of this method as mentioned in Section 1 are quantitatively valid, namely, that all the light emanating from the main diffraction line (the main spectral line) is rotated in phase through the angle ψ, and that the diffraction spectrum due to the periodic structures (the ghost lines) remains equally quantitatively unchanged in phase.

This assumption is practically always valid, but the width of the central zone of the phase plate must be dimensioned so as to fulfil conditions imposed by the angular aperture of the grating, and the width of the spectral line used. As a guide to the correct application of this method it may be of some use to treat the diffraction

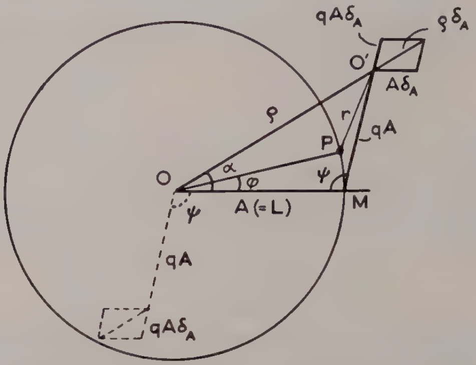

Fig. 18. Vector diagram with correction applied to the O′ position.

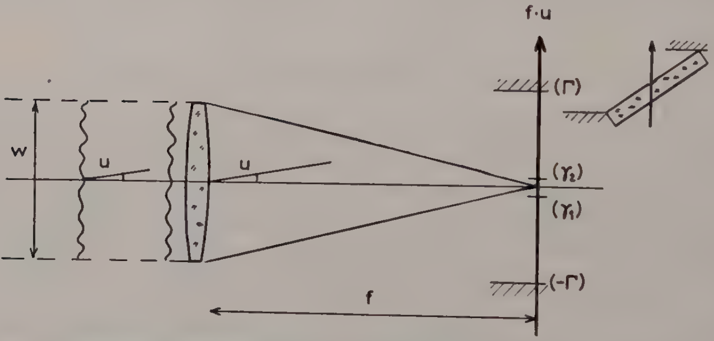

Fig. 19. Wave-front forming diffraction figure in the plane of the phase plate (really a phase mirror, as indicated in the upper right-hand corner).

problem in general showing the degree of approximation inherent in the above assumption.

The treatment follows that previously given for phase-uniform rectangular apertures by one of the writers (3). Fig. 18 is essentially the same vector diagram as that in Fig. 7a, OM representing the amplitude of the main line, which is focused on the central area of the phase mirror. However, the image of a slit which is, provisionally, assumed infinitely narrow and illuminated with strictly monochromatic light, is a diffraction figure having the well-known amplitude function $A \sin \beta / \beta$, where β is a quantity proportional to the linear extension perpendicular to the slit and zone borders. In this case, as is obvious from Figure 19,

$$\beta = \frac{2\pi}{\lambda} \cdot u \cdot w = \frac{2\pi\Omega}{\lambda} \cdot f \cdot u$$

where Ω is the angular opening of the grating, and $f \cdot u$ represents the length coordinate in the plane of the spectrum (i.e. at the phase mirror, in a direction perpendicular to the optical axis). The focal length f is alternatively that of a lens behind a plane grating, or the distance to a concave grating in its actual mounting. To simplify the

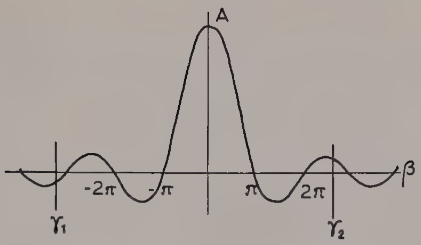

Fig. 20. Amplitude distribution curve of diffraction figure.

notation and to make comparison with the diffraction geometry easier, we convert all linear widths, even those of slits and wavelength dispersions, from the $f \cdot u$ length coordinates to β angular measure.

The amplitude length OM is the integral

$$\int_{-\infty}^{+\infty} A \frac{\sin \beta}{\beta} \, d\beta$$

normalized to unity for a zone of the wave-front of unit area, and the usual assumption when using the vector representation is that all of this light is rotated in phase. If, in general, the borders of the central zone cut the diffraction pattern at γ_1 and γ_2, Fig. 20, only the part

$$\int_{\gamma_1}^{\gamma_2} A \frac{\sin \beta}{\beta} \, d\beta$$

is rotated, and the parts in the regions of integration $(-\infty, \gamma_1)$ and $(\gamma_2, +\infty)$ are unchanged. The contributions from these regions should be used for correcting the O′ point, by adding two vectors in the zero and ψ angle directions (3).

Now regarding the width of the slit, which in angular measure is $2z$, the diffraction figure is built up by the superposition of non-coherent infinitely thin slits of the amplitude function just given. At every point, the intensity is given by the summation

$$\text{(I)} \qquad \int_{\beta-z}^{\beta+z} A^2 \frac{\sin^2 t}{t^2} \, dt = A^2 \Big/_{\beta-z}^{\beta+z} \left[\operatorname{Si}(2t) - \frac{\sin^2 t}{t} \right], \text{ where } \operatorname{Si}(x) = \int_0^x \frac{\sin t}{t} \, dt.$$

The spectral line acting as source of the wave-front is not strictly monochromatic; it has an amplitude function $L(\lambda)$ which is determined by the atomic structure of the emitting element and the excitation conditions in the lamp. This means that the wave-fronts indicated in Fig. 19 consist of a series, each member slightly tilted an angle corresponding to the dispersion. The intensity of the real spectral line can thus be written

$$\text{(II)} \qquad I(\beta) = \int_{\lambda_1}^{\lambda_2} \left[L^2(\lambda, \beta) \int_{\beta-z}^{\beta+z} \frac{\sin^2 t}{t^2} \, dt \right] d\lambda$$

where λ_1 and λ_2 are the limits between which the line has a noticeable intensity.

The influence in this respect of the three factors, the diffraction phenomenon itself, the slit width, and the lack of monochromacy, depends greatly on the spectral line used, the choice of which is often a question of intensity. As is well known, spectroscopists often choose the slit width so that the diffraction figure will be sufficiently narrow to let the fine structure appear. For a phase contrast examination the demands of monochromacy are often not severe, and on the other hand all intensity gain is welcome when the image is scanned photoelectrically. For this reason, a medium pressure spectral mercury lamp was often used, emitting the green 5461 A line, which could be as broad as 1 A. For the high-resolving grating reported later in this paper, the sodium line 5890 A was used, and if the test is to be taken to its limit of accuracy, the 198 mercury lamp or another single-isotope lamp could be used with advantage.

Considering now the vector diagram, Fig. 18, the correction of the O′ position should be performed. For ease of calculation, the line from O′ to the centre O is drawn and the polar coordinates ϱ and α are introduced instead of A $(=L)$, ψ and q. The correction of O′ to its real position for a phase diagram, corresponding to an infinitely thin slit, situated at a distance ζ in angular measure from the centre of the entrance slit, for a given intersection of the zone borders of the phase plate at γ_1 and γ_2 has the same argument α as OO′, and the modulus $\varrho\,\delta_A$. The value of δ_A is found to be

$$\text{(III)} \qquad \delta_A = \frac{1}{\pi}[\text{Si}\,(\gamma_1+\zeta)+\text{Si}\,(\gamma_2-\zeta)-\pi],$$

and the proof of the rule of direction is given by the geometrical conditions.

The phase contrast image is built up firstly by superposition of non-coherent phase contrast images for these infinitely thin slits. Secondly an other kind of superposition is due to the amplitude function $L(\lambda)$. The superposition of phase diagrams as Fig. 18 gives, if δ_A is the correction and L is the amplitude for the different diagrams in question, and terms of higher orders than δ_A are neglected,

$$\text{(IV)} \qquad \delta = \frac{\sum L^2\delta_A}{\sum L^2}.$$

The superposition is carried out in the two steps indicated, firstly for the function $L(\lambda)$ with λ constant over the entrance slit. As the entrance slit is uniformly illuminated, $L(\lambda)$ is constant at this procedure. We get, as an application of formula IV combined with III,

$$\delta_\lambda = \frac{1}{2\pi z}\int_{-z}^{+z}[\text{Si}\,(\gamma_1+\zeta)+\text{Si}\,(\gamma_2-\zeta)-\pi]\,d\zeta =$$

$$\frac{1}{2\pi z}\left[\int_{-z}^{+z}d\zeta\int_0^{\gamma_1+\zeta}\frac{\sin\beta}{\beta}d\beta+\int_{-z}^{+z}d\zeta\int_0^{\gamma_2-\zeta}\frac{\sin\beta}{\beta}d\beta-2\pi z\right].$$

Si (x) oscillates about $\pi/2$ for $x \geqslant 0$ with its maxima and minima values at $x = n\cdot\pi$, where n are integers. The oscillation of $\sin\beta/\beta$ can conveniently be approximated by a broken saw-tooth curve as shown in the first curve of Fig. 21. When integrated with respect to β, we obtain the variation of Si $(\gamma+\zeta)$ with ζ. The second curve of

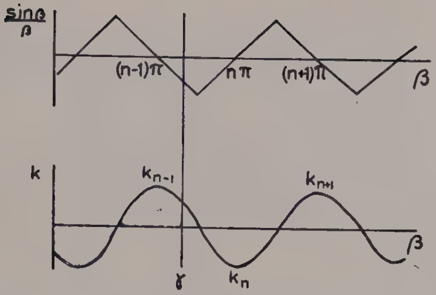

Fig. 21. Approximated sin x/x and Si (x) curves.

Fig. 21 represents this integral, diminished by the asymptotic value $\pi/2$, the values denoted k. The construction of the first curve was performed so that the k values for $\gamma = n \cdot \pi$ are correct. The integral over the slit width (between $-z$ and $+z$) is thus the average value of the surface below the second curve in the region $(\gamma - z, \gamma + z)$. Because the function is oscillating, these corrections vary, depending on where the γ values fall. The corrections are greatest for $\gamma = \pm n \cdot \pi$.

For carrying out the second superposition, that for the wavelength distribution within the spectral line, the different $L(\lambda)$ need to be calculated from the recorded intensity curve $I(\beta)$. Coherence exists between the light included in the $I(\beta)$ function insofar as it involves scattered light or line broadening on account of aberrations, while the parts which really belong to other wavelengths are non-coherent. If non-coherence is assumed, $L(\lambda)$ can be calculated from II following an approximate method. Instead of a continuous spectrum for $L(\lambda)$ a series of discrete spectral lines is supposed to lie at the centre, and at the zero values of the diffraction function, $+\pi$, $+2\pi$, $+3\pi$, etc. Each of these lines has an intensity distribution as given by formula I. The unknown L for the discrete values at the positions $\pm n \cdot \pi$ can be calculated, since $I(\beta) = \sum L^2(\lambda, \beta)$. A determinant is obtained for $L(\lambda)$, which can be limited to the nearest lines, as the intensity falls off rather quickly for every line, according to the $\sin\beta/\beta$ function.

The values δ_λ and $L(\lambda)$, obtained by these procedures, combine to the final correction δ according to formula IV.

Calculations have been made according to this scheme for the 5461 A mercury light used, and for two different phase mirror zones, corresponding to $\pm\gamma = 9\pi$ and $\pm\gamma = 4\pi$, both of which correspond to cases which have occurred in practice. The results are as follows.

A symmetrical cut at $\gamma_{1,2} = \pm 9\pi$ gives a correction of $\delta = -0.1\,\%$. If the cut is unsymmetrical, so that $\gamma_1 = -10\pi$ and $\gamma_2 = +8\pi$, the amount is the same, namely $-0.1\,\%$. In this case, which corresponds to dimensions which for several reasons may be recommended for examining mainly periodic errors (2), the correction is negligible in comparison with other errors involved in the procedure.

For the narrow central zone of the phase plate, corresponding to a symmetrical intersection at the phase plate of $\gamma = \pm 4\pi$, the values are considerably higher; thus $\delta = -1.0\,\%$. In cases where $\gamma < \pm 2\pi$, the phase contrast method can no longer be said to be quantitative; the image has a light distribution due to interferences which must be taken into account and which make the records less true in regard to the real phase function of the object.

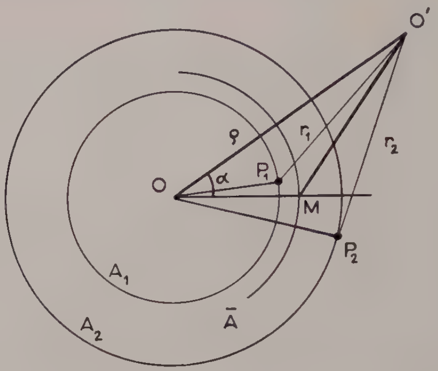

Fig. 22. Evaluation in the case of mixed amplitude-phase contrast.

10. Mixed amplitude-phase contrast

In two practical cases it may happen that different parts of the object field have different intensities. In this case the required investigation of the phases is complicated by the presence of amplitude variations. The first of these practical cases is when the shape of the grooves of a grating varies along the surface, which is not seldom the case when the grating is strongly "blazed", as the diamond can have changed its shape. The second case is when the grating is not uniformly illuminated.

As in these cases the light from all the object field is coherent, the phase contrast diagram is still valid, and vectorial additions of amplitudes are permissible, although there is now a new variable, the incoming amplitudes, as is shown in Fig. 22. Not more than two distinct amplitudes A_1 and A_2, are represented in the figure. The vector OM, which will be denoted by $\bar{A}$, is the average amplitude built up by A_1 and A_2, weighted according to the respective areas of the field. If A_1 and A_2 were known, the phase angle φ could be determined from the measured r_1^2 and r_2^2 by means of a curve such as Fig. 7 b.

In general, A being variable, within the limitations just stated, intensities in the phase contrast image are functions $r^2 = f(A, \varphi)$, which, as φ is required, may be written $\varphi = g(A, r^2)$. According to the geometry of the figure, the function is

$$\cos\left[\varphi(x) - \alpha\right] = \frac{\varrho^2 - r^2(x)}{2\,\varrho \cdot A(x)} + \frac{A(x)}{2\,\varrho}.$$

It is possible to find the unknown function of A by an ordinary imaging. This is done by adjusting the phase mirror so that the whole diffraction figure falls on its peripheral part, no auxiliary re-adjustments being made, and scanning the image. The average intensity is evaluated from the average height of the planimetered curve, and thus the factor ϱ is known, as well as the function A, which is the square root of the curve scanned. The function r^2 is, as usual, the scanned phase contrast intensity. According to the equation given, φ is then found from a double nomogram where the corresponding readings r^2 and A enter.

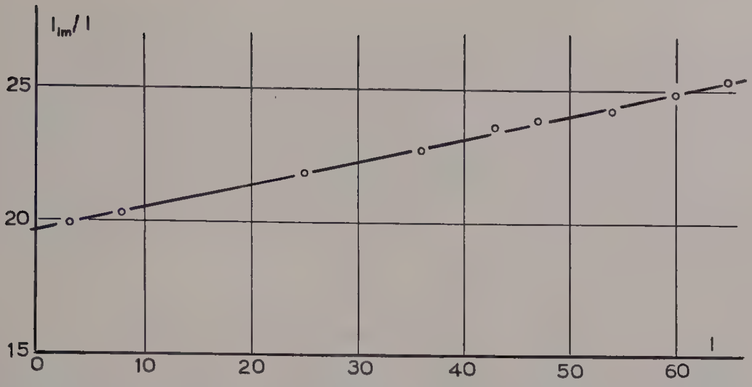

Fig. 23. Graph of measurements for back-ground intensity correction. A medium pressure mercury lamp, with a single-prism monochromator, was used.

11. Influence of background intensity

In Section 9 it was shown that, if the central zone of the phase plate is properly dimensioned, the non-coherent light falling inside this central zone does not effect the quantitative evaluation of the phase contrast intensity curve. However, non-coherent light often extends very far from the main line, even if the distribution falls off steeply at the feet of the lines. The non-coherent part of the light falling outside the central zone gives a superposed picture with generally constant intensity, diminishing the contrast and acting as a back-ground level to the record. For a given grating, this intensity is for well-known reasons greatly dependent on the lamp current density.

In some cases of gratings and lamps it is advisable, in order to get a precise knowledge of the amounts of phase variation, to correct for the back-ground thus present. This can be done by means of a separate simple photoelectric procedure, including readjustment to get an ordinary image as described in the preceding Section, although for another reason. The total light flux belonging to the phase contrast image is measured by the photocell itself, which is easily done by placing a diffusing screen before it; the result is denoted by I_{im}. In the same way, the total light flux belonging to the ordinary image is measured, and denoted by I. These measurements are made for different lamp intensities, to which I is proportional. When the ratios I_{im}/I are plotted against I in a graph, the points lie on an increasing curve, as in Fig. 23. This proves that the lamp gives an amount of non-coherent light proportional with the square of the total flux (higher pressure), and that this light vanishes at the extrapolated value for $I = 0$. By means of the values of the graph Fig. 23, the back-ground value is subtracted from the phase contrast image records before they are analyzed. In the worst cases here examined, this correction has amounted to 19.5 per cent.

12. Improved analysis of the phase curve by means of a mechanical harmonic analyzer

The aim of this method is to obtain a true φ diagram of the grating surface, as this is usually the most interesting information both for the manufacturers and for the users.

However, as a continuation of the harmonic analysis of the phase curves reported in Section 6 of Part I, which was performed with a simple calculation scheme giving six periods, the writers have now made use of a mechanical analyzer, manufactured by the Math.-mech. Institut A. Ott (4). This apparatus, whose accuracy corresponds well to that of the records and recalculated phase curves, makes it possible to calculate about 25 harmonics of a selected fundamental. As will be shown in the section dealing with experiment, this analysis is also of value in revealing non-uniformities along the grating, as well as checking the quantitative calculations given in the preceding sections.

13. Simplified test procedure

As described so far, the method is quantitative, in that on the one hand the theory of the various physical factors has been taken into account fairly completely, while on the other hand the limiting accuracy of the method has been reached.

Recommendations for routine use and for the construction of simple analyzing devices suitable for non-specialized laboratories have been given in another paper (2), which also took account of modern progress in grating ruling. A detail of this development which will be mentioned here is the replacement of the photoelectric device by a photograph taken through a gray wedge, which allows an intensity scale to be constructed by means of micro-densitometric measurements. This is a quantitative continuation of the original tests of the method (5). Some examples are given in Section 14.

14. Experiment

Modifications to the apparatus. The main optical and electrical arrangements described in Sections 2 and 3 have been maintained, being adjusted for larger focal lengths in some cases. The first polaroid was ordinarily placed in front of the entrance slit S (part I figure 1) and the second behind the imaging lens; they were always set so that the light undulation plane was parallel to the central zone, in order to give q its maximum value.

The receiver unit which scans the image plane was rebuilt in order to secure a more uniform drive, utilizing slides instead of rollers. Tests have shown that the carriage always moves linearly with time, within an accuracy of less than one micron.

It should also be pointed out that if a grating is to be masked off, precautions should be taken to make the mask so as to avoid as much as possible any scattered light, which may cause considerable trouble, not only in these measurements, but also in spectrophotometrical work. The edges of the mask require special care. We have found it convenient to mask with a screen having its front side and the edges of the opening covered by dull-black velvet.

Analysis of G 73, a concave grating of 1 metre radius. The main examinations were made with a phase mirror No. 3 (see part I page 427) having the following data: Central zone width projection (corresponding to $2\,\gamma) = 210$ microns; $\psi = 102.6°$, $q = 0.415$. This zone width gives a negligible correction according to Section 9. The total width $2\,\Gamma$ of the phase mirror, together with the finite widths of entrance and photomultiplier slits, limit the smallest domain of the grating which can be "resolved" with respect to phase variation, to about 50 microns. The

Table 2

Harmonic analysis of grating G 73, spacing 17 360 A

Periods No.	Amplitude values counted in cm, frequency corresponding to ghost number					
	1		2		3	
	sin	cos	sin	cos	sin	cos
1 − 6	−3.47	−0.39	−0.30	−0.68	+0.48	+0.33
7 − 12	−2.34	−1.07	−0.66	−0.78	+0.20	+0.66
13 − 18	−2.50	−0.72	+0.13	−0.51	−0.25	−0.24
19 − 24	−1.18	+0.20	−0.08	+0.16	0	−0.15
25 − 30	−1.80	−0.21	+0.20	−0.35	−0.32	−0.13
31 − 36	−1.85	−0.20	+0.24	−0.58	0	0
Scale in cm	2.37		0.47		0.05	
Phase angle	4.74°		0.94°		0.10°	
Error in position at grating surface	228 A		45 A		5 A	

grating was masked to 48 mm, from the total width of 82 mm, the former being the zone within which the monochromator gave fairly uniform illumination.

In studying this grating, use has been made of the procedure described in Section 10 to take amplitude variations into consideration; the maximum variation of A within the utilized area of the grating was ± 5 per cent. The phase curve given as Fig. 24 is thus true even in this respect.

The detailed analysis of the wave-front curve compared to its Fourier intensity spectrum as measured with the photoelectric cell, may also be of interest.[1] This intensity spectrum is recorded with the same device, but at the focal plane. The minute intensity distribution is rather sensitive to which plane is chosen, especially if, as in this case, the grating is not exactly uniform but has some extrafocal properties, and so the position of greatest intensity for the main line was chosen. The ghost are as a whole faint, only the first and traces of the second being visible. Some very minute but reproducible structure details are present but not analyzed.

In the phase curve of Fig. 24 the period length was determined by the method of repeated intervals. 36 periods, covering 45 mms of the grating surface, were analyzed according to Section 12, 6 periods at each time. The results are listed in Table 2.

The discontinuity of term No. 1 between the eighth and eighteenth periods is clearly seen, a large cos term nearly vanishing. Also the other terms show some small discontinuities.

For a further study of this spectrum, see Section 15.

The amplitude value of 230 A obtained by the Fourier's analysis for the periodicity No. 1 corresponds to a ghost intensity of 0.17 %, compared to the observed value of 0.22 %. In order to check the supposed cause of this discrepancy, various period

---

[1] In Part I, page 436 and Fig. 16, the ghost numbers of grating G 15 were numerated from the basic period used by the analysis, not conventionally, whence No. 2 is really the first Rowland ghost.

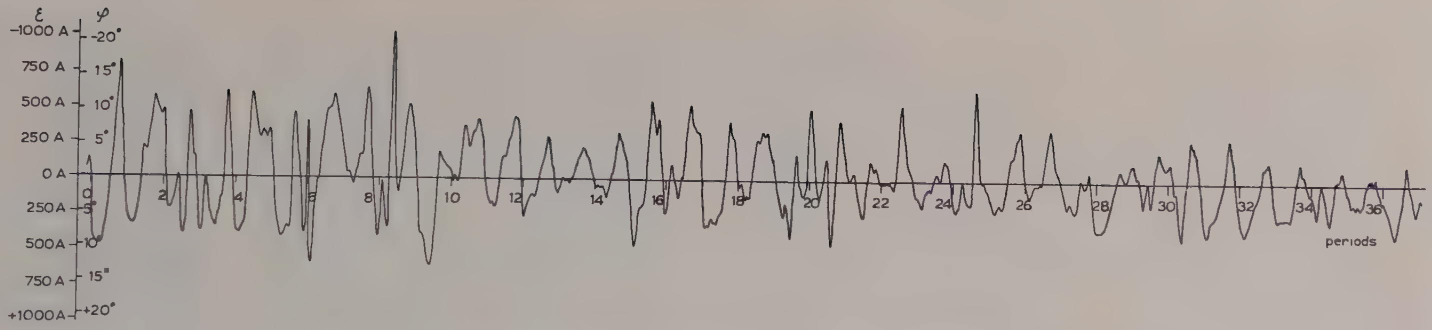

Fig. 24. Phase structure of wave-front in first order reflexion from grating G 73.

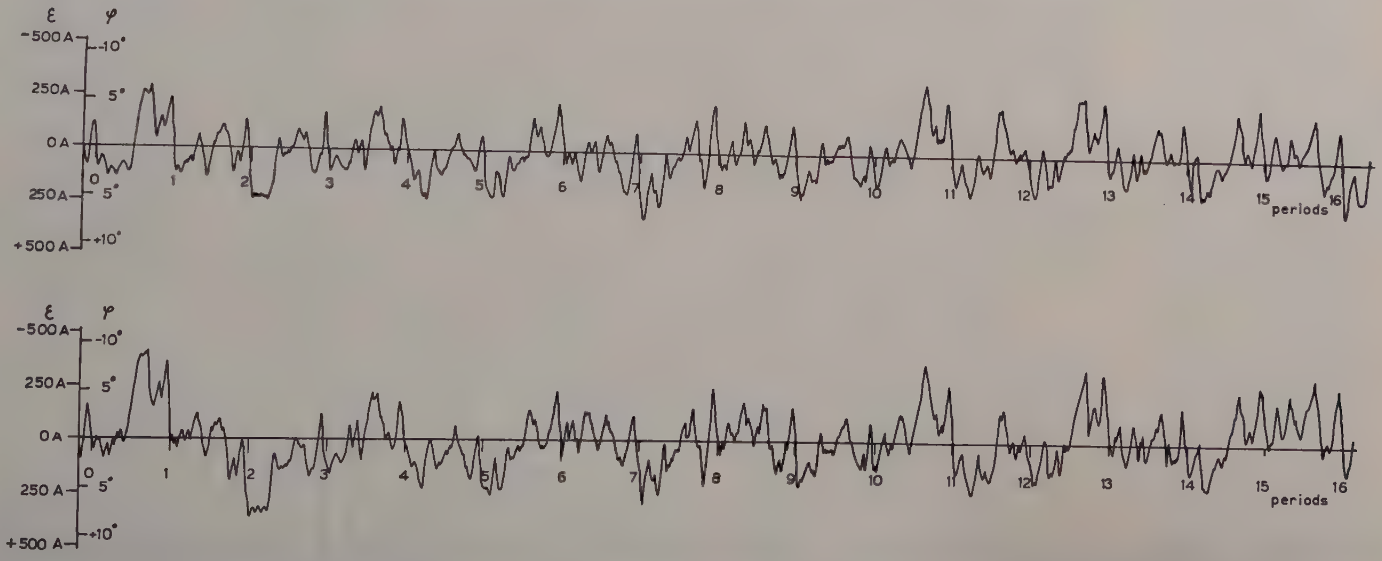

Fig. 27 and 28. Phase structure of wave-front from grating 90A1, analyzed by means of phase mirrors No. 3 and 5 respectively.

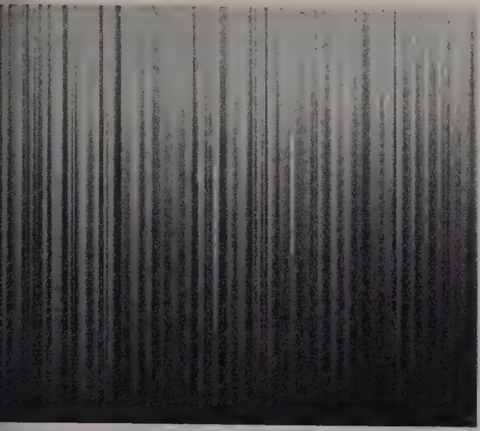

Fig. 25. Phase contrast photograph of grating G 73 through gray wedge for phase evaluation. Phase mirror No. 3.

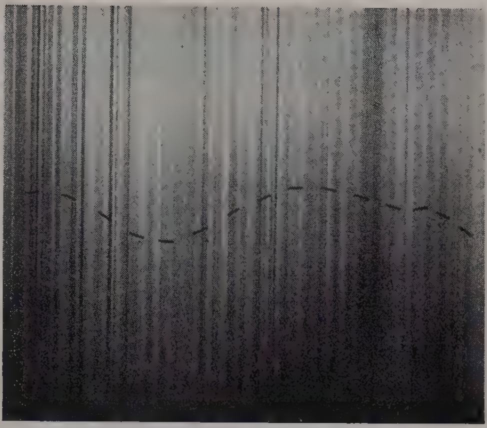

Fig. 26. The corresponding photograph with phase mirror No. 4 used. Observe the superstructure indicated by the dotted line for equal average intensity.

Table 3

Harmonic analysis of grating 90A1, spacing 16700 A. The table gives errors in position at grating surface (in A)

Phase mirror No.	Frequency corresponding to ghost number					
	1	2	3	4	5	6
3	90	15	57	41	40	20
5	91	11	56	43	41	18

lengths close to the value used before were used in analyzing five periods on this terms. The amplitude values thus obtained showed a rather extended maximum when plotted as a curve. The positions of the maxima correspond to period values of 26.78 mms, compared to the average value 26.53 for the whole grating. This proves that there is a real variation across the front. The ghosts, or the harmonic intensity spectrum lines, are due to super-positions. Thus, instead of the discrete frequencies, given by the Fourier sum, the continuous spectrum given by the Fourier integral should be used, which will give a larger intensity. As the calculation of the integral is tedious even by means of the apparatus, it was not performed, as it would serve only to evaluate a correction, the origin of which is already known. When comparing the recorded intensities with those calculated from the analyzed phase curve, the interaction between phase-differing parts should be taken into account (6). The amplitude addition for building up the ghost intensity is treated in a coming paper by one of the writers.

Two comparative photographs were also taken according to Section 13, with the phase mirror No. 3 and with a phase mirror No. 4, which has a 2 γ corresponding to 65 microns, the other data being $\psi = 82.0°$ and $q = 0.415$. The two photographs are reproduced as Figs. 25 and 26. On account of the narrower intersections in the last case, which are still however permitted without correction (Sect. 9), slower variations are revealed, giving rise to light near the main line, as expected.

Analysis of 90A1, a plane replica test grating. This sample of a grating made by a replica technics is of special interest, as the periodic errors are low. The ruling spacing is 16700 A, and the area is 50 × 50 mm; the surface was partially damaged, so only 32 mm of the width was analyzed. Visually, ghosts Nos. 1, 3, 4, and 5 are visible, the first being estimated at less than 0.1 per cent; the three last were extremely faint. The phase mirrors Nos. 3 and 5 (data: 2γ corr. to 110 microns, $\psi = 82{,}0°$, $q = 0.415$) were used, and the phase curves are shown in Figs. 27 and 28. The amplitudes of the successive periodicities as found by mechanical harmonic analysis are given in Table 3.

The agreement is obviously very good. The somewhat greater correction in the position of O′ according to Section 9 influences the ratios of the r vectors by amounts which are smaller than the uncertainty in r itself, and in that arising in the conversion from intensities to phases.

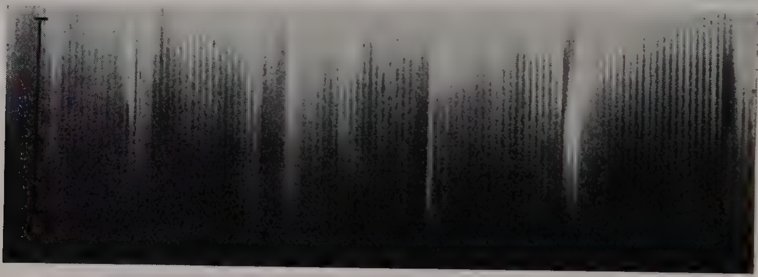

Fig. 29. Phase contrast photograph of the Rowland grating through gray wedge. The vertical mark indicates a phase difference of 25° (symmetrically about zero) for points with equal intensity. For more detailed such analysis, see Ref. (2).

A comparison of Figs. 27 and 28 shows a super-structure in the last scanning partly due to interferences and partly to real phase variations.

Analysis of a concave Rowland grating, radius 21′. Among other gratings examined, a Rowland grating ruled on speculum metal in the year 1889 in the possession of the Physics Institute of the University of Stockholm showed several interesting characteristics. This grating has been analyzed for its resolving power by Prof. E. Hulthén and Miss Uhler of that Institute (7).

In this case it was necessary to work with a line having fine structure not exceeding a small fraction of the periodicities and the structure of the Fourier spectrum due to phase variations, yet still having as high an intensity as possible; for practical reasons, we have chosen the sodium 5890 A line from a low-pressure spectral lamp and separated it from the adjacent 5896 A line and the rest of the spectrum by a monochromator consisting of a 1 metre concave grating, placed in front of the entrance slit. The grating itself was in the astigmatic Eagle-mounting for first order spectrum. A photoelectric record could not be taken, as the intensity with the rather small aperture was too low, but the necessary information was obtained by photographic exposures through gray wedges placed in front of the plane of the phase contrast image. Fig. 29 gives a reproduction of one of these photographs, with a mark for the phase function across the grating as found from the calibrated wedges and a knowledge of the O′ position.

The phase mirror No. 3 was used here, its central zone width being suitably dimensioned according to the dispersion. The outer limits $\pm \Gamma$ cut off the ghost spectrum from No. 4 upwards, which is however of no importance here.

The observations shown in Fig. 29 are very interesting, as they reveal important abrupt changes in phase. They are maximally 25° or about $0.1\,\lambda$, but the changes themselves are limited to narrow regions. These changes in phase are, according to the diffraction treatment, not serious for the resolving power, which for this grating reaches about 80 per cent of the theoretical value given by the Rayleigh limit (7), but they influence the building up of the total intensity by the amplitude addition of the different, phase-differing zones. We touch here the important problem of "phasing-in" two similar gratings by means of phase contrast observations, which will be dealt with elsewhere.

15. Screening the diffraction image thereby realising a frequency band-stop filter

In part I (page 436) the idea was put forward of modifying the diffraction image by blocking off one particular order, while still maintaining the phase shift between zero and all other orders. This has now been experimentally established.

The phase contrast method can be said to function as a band-pass filter for the frequencies in the wave-front structure which correspond to the extensions between $\pm \gamma$ and $\pm \Gamma$ of the phase plate; they are all converted to intensity variations and appear in the analysis of the scanned phase contrast image. By obstructing, symmetrically, a part of the band-pass region, the corresponding frequencies vanish, and the structure due to them disappears from the intensity image. In this way, by inserting suitably dimensioned apertures and stops at the phase plate (which is very easily done in the linear case in question), it is possible to make band-pass or sharp cut-off filters.

In examining the grating G 73 the ghost No. 1 was removed in this way. This was done by placing, as closely as possible to the phase mirror, two black sewing-threads covering the corresponding ghosts. The dull surface to a great extent prevented stray light, but it could not be helped that some obstruction also took

Table 4

Comparative analysis of grating G 73, with screening of the diffraction image. Cf. Table 2

Amplitude values	Frequency corresponding to ghost number		
	1	2	3
without blocking	230	45	5
with blocking	40	15	5

place for other regions, especially at the position of the 2nd order, as the threads are at a finite distance from the mirror. The opposite Table 4 shows the amplitudes as analyzed from scannings of the unobstructed and obstructed spectra. The screening has clearly been rather successful. A transparent phase plate instead of the phase mirror would of course be preferable for similar studies in other applications.

16. Acknowledgements

The writers' thanks are due to Prof. M. SIEGBAHN for kind interest in their work, for many discussions and for helping them in many other ways. We also owe thanks to Prof. E. HULTHÉN for the loan of a high-quality grating, and for a stimulating exchange of ideas on the subject of grating diffraction.

Optics Laboratory, Royal Institute of Technology, Stockholm 70, Nov. 1952.

REFERENCES

1. E. INGELSTAM and E. DJURLE, Arkiv för fysik *4*, Nr 27, 1952.
2. ——, J. O. S. A. (in the press).
3. E. INGELSTAM, Arkiv för fysik *6*, Nr 29, 1953.
4. Apparatus Model 214, Pamplet No. Ad. 341, Math.-mech. Institut A. Ott, Kempten-Allgäu, Germany.
5. A. M. CAMUS, M. FRANÇON, E. INGELSTAM and A. MARÉCHAL, Revue d'Optique *30*, 121,1950.
6. See e.g. N. A. FINKELSTEIN, C. H. BRUMLEY, and R. J. MELTZER, J. O. S. A. *42*, 121, 1952, with references.
7. E. HULTHÉN and ULLA UHLER, Arkiv för fysik *3*, Nr 21, 1951.

Tryckt den 20 april 1953

Uppsala 1953. Almqvist & Wiksells Boktryckeri AB

ARKIV FÖR FYSIK Band 6 nr 45

Communicated 11 March 1953 by ERIK HULTHÉN

Microwave spectrum of fluorobenzene

By GUNNAR ERLANDSSON

This spectrum has been investigated in the region 17.5–26.7 kMc/s. 20 lines have been identified as arising from the rotational transitions $J=3$–4, 4–5, 5–6 and 6–7. Within the limits of error in the frequency measurements (± 5Mc/s) these lines agree well with the formulas for the rigid asymmetric rotator. The rotational constants are

$$A=0.18967\ \mathrm{cm}^{-1},\quad B=0.08576\ \mathrm{cm}^{-1},\quad C=0.05896\ \mathrm{cm}^{-1}.$$

Calculated and observed frequency values are given in Table 1.

The rotational assignments of the observed lines have been confirmed by Stark-effect observations and observations on relative intensities in so far as

Table 1

Transition	Calculated frequency Mc/s	Observed frequency Mc/s	Transition	Calculated frequency Mc/s	Observed frequency Mc/s
$3_{3.1}$–$4_{3.2}$	17 588	—	$4_{2.2}$–$5_{2.3}$	23 388	23 388
$3_{3.0}$–$4_{3.1}$	17 676	—	—	—	23 642
—	—	17 724	—	—	23 941
—	—	18 370	—	—	23 973
$3_{2.1}$–$4_{2.2}$	18 425	18 420	—	—	24 185
$3_{1.2}$–$4_{1.3}$	18 636	18 633	—	—	24 895
—	—	18 806	—	—	25 312
$4_{1.4}$–$5_{1.5}$	19 217	19 217	—	—	25 403
—	—	19 429	$5_{2.4}$–$6_{2.5}$	25 425	25 425
$4_{0.4}$–$5_{0.5}$	19 679	19 674	—	—	25 589
$4_{2.3}$–$5_{2.4}$	21 388	21 388	—	—	25 758
—	—	21 551	—	—	26 174
—	—	21 608	—	—	26 280
—	—	21 889	$5_{5.1}$–$6_{5.2}$	26 377	26 374
$4_{4.1}$–$5_{4.2}$	21 995	21 991	$5_{5.0}$–$6_{5.1}$	26 378	
$4_{4.0}$–$5_{4.1}$	22 006	22 001	$5_{3.3}$–$6_{3.4}$	26 442	26 441
$4_{3.2}$–$5_{3.3}$	22 027	22 028	$6_{1.6}$–$7_{1.7}$	26 458	26 457
—	—	22 228	$5_{4.2}$–$6_{4.3}$	26 481	26 479
$4_{3.1}$–$5_{3.2}$	22 322	22 321	$5_{4.1}$–$6_{4.2}$	26 529	26 526
$5_{1.5}$–$6_{1.6}$	22 860	22 862	$6_{0.6}$–$7_{0.7}$	26 606	26 603
$4_{1.3}$–$5_{1.4}$	22 938	22 939	$5_{1.4}$–$6_{1.5}$	26 958	—
—	—	22 943	$5_{3.2}$–$6_{3.3}$	27 163	—
$5_{0.5}$–$6_{0.6}$	23 136	23 132	$5_{2.3}$–$6_{2.4}$	28 271	—

such observations have hitherto been possible (except that the line $6_{1.6}$–$7_{1.7}$ is unexpectedly weak).

Assuming the regular hexagonal structure of the benzene molecule to be undisturbed by the fluorine substitution and assuming the value 1.05 ± 0.02 Å for the C–H bond distance the C–C and C–F distances may be calculated from the above constants. The results are

$$C\text{–}C = 1.3916 \pm 0.0020 \text{ Å}; \quad C\text{–}F = 1.348 \pm 0.005 \text{ Å}.$$

Stockholm, March 11, 1953.

University of Stockholm, Department of Physics.

Tryckt den 20 april 1953

Uppsala 1953. Almqvist & Wiksells Boktryckeri AB

ARKIV FÖR FYSIK Band 6 nr 46

Communicated 28 January 1953 by Axel E. Lindh and Gunnar Hägg

Concerning the possibility of using ground calcite crystals as X-ray gratings

By Gösta Brogren

With 1 figure in the text

In an earlier communication Aminoff (1) pointed out the possibility of using alcite in order to obtain crystal gratings with small spacings and large dispersion. Surfaces having such qualities do not exist as natural ones in any crystals. For that eason, it is necessary to grind crystals so as to get faces parallel to suitable atomic lanes. Calcite offers especially good possibilities since the natural cleavage suraces can be used as reference surfaces in the grinding procedure. The cleavage suraces possess very good optical qualities so that it is possible to make a very accurate djustment of the plane of grinding. As large natural calcite crystals are available ood ground crystals can be made. Calcite belongs to the rhombohedral system and t may be considered a perfect crystal. Its structure is well determined (2–3).

If the influence from the absorption is neglected, Darwin's (4) theory of the relection of perfect crystals can be applied. The integrated reflection R_c is then given y (5)

$$R_c = \frac{8 F \delta (1 + \cos 2\Theta)}{3 Z \sin 2\Theta} \tag{1}$$

where Θ = the Bragg angle
F = the crystal structure factor
Z = the number of electrons in the unit cell
$\delta = 1 - \mu$
μ = the index of refraction.

In order to find the atomic planes that possess the highest reflection power, the rystal structure factor F must be calculated. Commonly, F can be written

$$F_{hkl} = \sum_j f_j e^{2\pi i (hx_j + ky_j + lz_j)} \tag{2}$$

here f_j is the atomic scattering factor, h, k, and l are the Miller indices of the plane nd x_j, y_j, and z_j the coordinates of the atom j in the unit cell. The summation must e extended over all atoms in the unit cell. In this case it is a rhombohedral one ontaining two molecules of $CaCO_3$ characterized by the constants $a = 6361$ X.U. nd $\alpha = 46° 7'$ (3). The coordinates of the atomic positions are (6)

2 Ca at	$\frac{1}{4}$	$\frac{1}{4}$	$\frac{1}{4}$;	$\frac{3}{4}$	$\frac{3}{4}$	$\frac{3}{4}$
2 C at	0	0	0;	$\frac{1}{2}$	$\frac{1}{2}$	$\frac{1}{2}$
6 O at	$\frac{1}{4}\,\frac{3}{4}\,0$;	$\frac{3}{4}\,0\,\frac{1}{4}$;	$0\,\frac{1}{4}\,\frac{3}{4}$;	$\frac{1}{4}\,\frac{3}{4}\,\frac{1}{2}$;	$\frac{3}{4}\,\frac{1}{2}\,\frac{1}{4}$;	$\frac{1}{2}\,\frac{1}{4}\,\frac{3}{4}$

F can now be calculated by inserting these coordinates in (2) and performing th summation. After simplifying we get three different cases.

1. $h+k+l=2n+1$.

Then there are no contributions from the calcium and the carbon atoms and w have

$$F=\pm 2f_O\left[\sin\frac{\pi}{2}(h-k)+\sin\frac{\pi}{2}(k-l)+\sin\frac{\pi}{2}(l-h)\right]. \tag*{(3}$$

2. $h+k+l=4n+2$.

$$F=2f_{Ca}-2f_C-2f_O\left\{\cos\frac{\pi}{2}(h-k)+\cos\frac{\pi}{2}(k-l)+\cos\frac{\pi}{2}(l-h)\right\}. \tag*{(4}$$

3. $h+k+l=4n$.

$$F=2f_{Ca}+2f_C+2f_O\left\{\cos\frac{\pi}{2}(h-k)+\cos\frac{\pi}{2}(k-l)+\cos\frac{\pi}{2}(l-h)\right\}. \tag*{(5}$$

If we have different atomic planes with about the same spacings the highest inte grated reflection is obtained when the structure factor F has its maximum value.

The last case, $h+k+l=4n$, will give the highest values of F. The very maximum value is obtained, when the three cosinus terms are equal to one, which occurs whe both h, k, and l are multiples of four when we obtain $F=2f_{Ca}+2f_C+6f_O$. Thi case is only realized in the fourth order of reflection. In the first order the highes values are attained, when the sum of the three cosinus terms is positive. This occurs when one of the three differences $(h-k)$; $(k-l)$; and $(l-h)$ is a multiple of four an the two others are odd. In that case we have

$$F=2(f_{Ca}+f_C+f_O). \tag*{(6}$$

Hence, if we have several atomic planes with the same spacings, the reflectio power of the first order will have a maximum when

$$\begin{cases} h+k+l=4n & n=0,1,2\ldots \\ k-l=4m & m=0,1,2\ldots \end{cases}$$

Then h is an even number and k and l both odd. If $k=l$, so that we have a plan $(h\,k\,k)$, another advantage will be attained. The cleavage surface of calcite is paralle to plane (211), which fullfils the above conditions. A plane $(h\,k\,k)$ will cut the surfac of the cleavage rhombohedron parallel to an edge line, which reduces the difficultie of orientating the crystal on the grinding apparatus.

Table 1 gives the calculated values of the spacings and the structure factors of a number of planes that seem to be useable in X-ray spectroscopy. They are choosen rather arbitrarily. The following notations are used. The rhombohedral indices are referred to the true unit cell, so that the cleavage face is (211). The correspondin hexagonal Bravais' indices are referred to the hexagonal cell, deduced from the

Table 1

The spacings and structure factors of some atomic planes in calcite.

Indices		Spacing X.U.	Structure factor of the order No.			
Rhombohedral	Hex. Bravais		1	2	3	4
1 0 0	1 0 $\bar{1}$ 1	4 190	0	30.3	0	34.6
2 1 1	1 0 $\bar{1}$ 4	3 029	51.2	18.0	25.0	26.4
1 0 $\bar{1}$	1 1 $\bar{2}$ 0	2 490	23.0	11.6	14.3	24.0
3 3 2	0 1 $\bar{1}$ 8	1 900	39.0	14.8	18.0	19.4
3 1 0	2 1 $\bar{3}$ 4	1 520	18.8	13.6	9.6	14.2
11 8 5	1 1 $\bar{2}$ 8	1 488	18.8	13.5	9.6	13.8
2 $\bar{1}$ $\bar{1}$	1 0 $\bar{1}$ 0	1 435	31.4	13.0	14.2	12.4
4 3 1	1 2 $\bar{3}$ 8	1 280	16.8	12.2	9.3	10.0
5 4 3	1 1 $\bar{2}$ 12	1 220	16.6	12.0	9.0	10.0
3 2 $\bar{1}$	1 3 $\bar{4}$ 4	1 150	26.2	11.4	10.8	
5 2 1	3 1 $\bar{4}$ 8	1 040	23.8	10.1	8.8	
6 5 5	1 0 $\bar{1}$ 16	1 032	23.8	10.1	8.7	
5 5 2	0 1 $\bar{1}$ 4	1 000	23.8	9.5	8.6	
4 1 $\bar{1}$	3 2 $\bar{5}$ 4	962	14.8	9.0		
2 1 $\bar{3}$	1 4 $\bar{5}$ 0	941	23.5	8.8		
3 3 $\bar{2}$	0 5 $\bar{5}$ 4	884	21.6	8.3		
7 7 6	0 1 $\bar{1}$ 20	821	21.4	8.1		
6 1 1	5 0 $\bar{5}$ 8	798	21.0	7.6		
7 6 3	1 3 $\bar{4}$ 16	790	21.0	7.5		
7 3 2	4 1 $\bar{5}$ 12	781	21.0	7.4		
5 0 $\bar{1}$	5 1 $\bar{6}$ 4	761	13.6			
7 4 1	1 1 $\bar{2}$ 4	716	12.6			
5 1 $\bar{2}$	4 3 $\bar{7}$ 4	699	19.2			
9 6 5	3 1 $\bar{4}$ 20	684	19.0			
7 7 2	0 5 $\bar{5}$ 16	666	18.6			
10 7 7	1 0 $\bar{1}$ 8	627	18.3			
6 $\bar{1}$ $\bar{1}$	7 0 $\bar{7}$ 4	607	18.0			
10 9 9	1 0 $\bar{1}$ 28	592	17.4			
5 5 $\bar{2}$	0 7 $\bar{7}$ 8	591	17.3			
11 7 6	4 1 $\bar{5}$ 24	560	16.6			
9 4 1	5 3 $\bar{8}$ 14	552	16.5			
6 1 $\bar{3}$	5 4 $\bar{9}$ 4	547	16.3			
10 3 3	7 0 $\bar{7}$ 16	533	15.9			
9 2 1	7 1 $\bar{8}$ 12	528	15.9			
11 11 10	0 1 $\bar{1}$ 32	520	15.6			
7 $\bar{1}$ $\bar{2}$	8 1 $\bar{9}$ 4	501	15.0			
9 9 2	0 7 $\bar{7}$ 20	496	14.9			
11 11 6	0 5 $\bar{5}$ 28	491	14.6			
10 5 1	5 4 $\bar{9}$ 16	487	14.5			
7 7 $\bar{2}$	0 3 $\bar{3}$ 4	453	13.5			
13 6 5	7 1 $\bar{8}$ 24	442	13.4			
9 1 $\bar{2}$	8 3 $\overline{11}$ 8	397	11.9			
15 14 11	1 3 $\bar{4}$ 40	396	11.9			
17 10 5	7 5 $\overline{12}$ 32	324	8.4			
23 15 10	8 5 $\overline{13}$ 48	256	5			
10 7 $\overline{17}$	1 8 $\bar{9}$ 0	168	3			

true rhombohedral cell. The clevage face is here $(1\,0\,\bar{1}\,4)$. In the cases where the structure factors are given they are calculated from (3–6). The values of the atomic scattering factors f_{Ca}, f_C, and f_O are taken from JAMES and BRINDLEY (8). As a rule, the planes given in Table 1 are not to be found as natural surfaces. If we want a crystal plate with the surface parallel to a certain atomic plane, it is necessary first to grind a surface parallel to the desired plane on a great crystal, after which a plate is sawn out. The sawn surface must then be ground and polished very carefully, so that a surface having good optical qualities is obtained. However, calcite is a very brittle crystal and it is possible that this procedure will influence the structure of the crystal. Hence, it is necessary to investigate the qualities of the plates which are prepared in the above way.

A series of crystal plates was prepared with the dimensions 15 × 25 × 0.4 mm and with the surface 15 × 25 parallel to the planes suggested by Aminoff. Five different atomic planes were used, *viz* (211) (= the cleavage surface which was ground and polished in this case), (310), (655), (741), and (1033). In order to obtain accurate values of the axes lengths, the spacings of planes (655) and (1033) were determined by double exposures by means of a "tube spectrometer" in the usual manner. The X-ray tube was furnished with a molybdenum target and the $K\alpha_1$-line was used. The instrument and the method are earlier described in detail (9). The results are given in Tables 2 and 3. The following designations are used:

t = the temperature in °C;
$2\varphi_0$ = the angle obtained from reading the angular scale;
a = the distance between the $K\alpha_1$-lines of the double exposure;
$2\Delta\varphi$ = the angle computed from a and the tube length;
$\varphi_t = \varphi_0 + \Delta\varphi$ = the glancing angle at t °C;
$\Delta\varphi_t$ = the temperature correction of the glancing angle;
$\varphi_{18} = \varphi_t + \Delta\varphi_t$ = the glancing angle at 18° C.

The temperature correction is calculated in the usual way (10)[1]. In doing so we used the following values of the linear expansion coefficient parallel to the axis $\alpha_{//}$ and of that perpendicular to the axis $\alpha_{\perp}$:

$$\alpha_{//} = (25.135 + 0.0236\,t)\cdot 10^{-6},$$
$$\alpha_{\perp} = (-5.578 + 0.00276\,t)\cdot 10^{-6}\ (11).$$

The spacings are calculated by using the value of the wavelength of Mo $K\alpha_1$ determined by LARSSON (9), $\lambda = 707.831$ X.U. The real interatomic distances were obtained from the modified Bragg equation

$$n\cdot\lambda = 2d\left(1 - \frac{4d^2}{n^2}\,\frac{\delta}{\lambda^2}\right)\sin\varphi_n \tag{7}$$

where

$$\frac{\delta}{\lambda^2} = 3.687\cdot 10^{-6}.\ (10)$$

The error in the mean values of the glancing angles is about 0.5″ which gives a maximum error in the spacing of 0.007 X.U. as to d_{655}, and 0.004 X.U. as to d_{1033}.

---

[1] See ref. 10 p. 45.

Table 2

Calcite 6 5 5.

Plate No.	$2\varphi_0$	a mm	$2\Delta\varphi$	φ_t	t °C	$\Delta\varphi_t$	φ_{18}
351	40° 0′ 3.7″	+0.8916	3′ 58.5″	20° 2′ 1.1″	19.7	3.0″	20° 2′ 4.1″
352	8′ 4.6″	−0.9101	4′ 3.5″	0.6″	19.9	3.4″	4.0″
353	7′ 52.6″	−0.8600	3′ 50.0″	1.3″	19.3	2.3″	3.6″
354	0′ 4.0″	+0.8898	3′ 58.0″	1.0″	20.0	3.6″	4.6″
355	8′ 31.3″	−1.0087	4′ 29.9″	0.7″	19.9	3.4″	4.1″
356	0′ 5.4″	+0.9052	4′ 2.4″	3.9″	18.3	0.5″	4.4″
357	7′ 52.7″	−0.8581	3′ 49.6″	1.6″	19.2	2.2″	3.8″
358	39° 59′ 55.9″	+0.9389	4′ 11.1″	3.5″	18.6	1.1″	4.6″
359	40° 7′ 57.0″	−0.8750	3′ 54.1″	1.5″	19.2	2.2″	3.7″
						Mean value	20° 2′ 4.1″

Tube length 771.01 mm
$d_1 = 1\,033.072$ X.U.
$d_\infty - d_1 = 0.016$ X.U.
$d_\infty = 1\,033.088$ X.U.

Table 3

Calcite 10 3 3.

Plate No.	$2\varphi_0$	a mm	$2\Delta\varphi$	φ_t	t °C	$\Delta\varphi_t$	φ_{18}
400	83° 5′ 43.4″	+1.1028	4′ 55.0″	41° 35′ 19.2″	22.7	2.0″	41° 35′ 21.2″
401	15′ 10.5″	−1.0254	4′ 34.4″	17.8″	21.8	1.6″	19.4″
402	7′ 14.1″	+0.7541	3′ 21.7″	17.9″	21.6	1.6″	19.5″
403	7′ 23.1″	+0.7243	3′ 13.7″	18.4″	21.9	1.7″	20.1″
404	12′ 51.4″	−0.5005	2′ 13.9″	18.8″	21.2	1.4″	20.2″
405	7′ 36.2″	+0.6850	3′ 3.2″	19.7″	22.1	1.8″	21.5″
406	13′ 6.4″	−0.5601	2′ 29.9″	18.3″	21.3	1.4″	19.7″
						Mean value	41° 35′ 20.2″

Tube length 771.01 mm
$d_1 = 533.181$ X.U.
$d_\infty - d_1 = 0.003$ X.U.
$d_\infty = 533.174$ X.U.

The lengths of the axes of the primitive hexagonal cell were obtained from the above spacings and the spacing of plane (211). We got

$$a = 4\,980.02 \pm 0.03 \text{ X.U.}$$
$$c = 17\,025.12 \pm 0.10 \text{ X.U.}$$

The investigations of the qualities of the crystal lattices were made by registering the rocking curves and by determining the percent reflection and the double crystal coefficient of reflection. The apparatus and procedure are described earlier (12, 13).

Calcite has been investigated by ALLISON (14) and PARRATT (15, 27). They showed that natural calcite surfaces may be obtained by cleavage, which give results in the double spectrometer, very close to perfect crystal calculations, if the incident wavelength is not too short. Later MANNING (16) succeeded in improving less good cleavage surfaces by a cautious polishing, followed by a slight etching with 0.7 normal hydrochlorid acid, so that he also obtained results in good agreement with ALLISON and PARRATT.

These results show that the above qualities should be calculated by assuming that calcite is a perfect crystal. If unpolarized radiation is incident upon a perfect single crystal, whose absorption is not negligible, the diffraction pattern is given by (5, 13).

$$F(l)=\tfrac{1}{2}\left|\frac{(A+iB)\frac{1}{\delta}}{l-i\frac{\beta}{\delta}\pm\sqrt{\left(l-i\frac{\beta}{\delta}\right)^{2}-\left(\frac{A+iB}{\delta}\right)^{2}}}\right|^{2}+$$

$$+\tfrac{1}{2}\left|\frac{(A+iB)\frac{1}{\delta}\cos 2\vartheta_0}{l-i\frac{\beta}{\delta}\pm\sqrt{\left(l-i\frac{\beta}{\delta}\right)^{2}-\left(\frac{A+iB}{\delta}\right)^{2}\cos^{2}2\vartheta_0}}\right|^{2} \qquad (8)$$

where

$$A+iB=\sum_j\frac{F_j}{Z_j}(\delta_j+i\beta_j), \qquad (9)$$

F_j = the structure factor of atom j in the unit cell,
Z_j = the number of electrons, belonging to atom j,
δ = the amount with which the index of refraction deviates from unity,
δ_j = the amount of δ that comes from atom j
$\beta=\frac{\lambda\cdot\mu_l}{4\pi}$, where μ_l = the linear absorption coefficient,
β_j = the amount of β originating from atom j,
ϑ_0 = the glancing angle,

$$l=\frac{\sin 2\vartheta_0}{2\delta}(\vartheta-\vartheta_0)-1. \qquad (10)$$

Eq. (8) can also be written

$$F(l)=\tfrac{1}{2}F_{\sigma}(l)+\tfrac{1}{2}F_{\pi}(l) \qquad (11)$$

since the first term gives the diffraction pattern of the component of the incident radiation, which is polarized so that its electric vector lies perpendicular to the plane of incidence (σ-polarized radiation), and the second that of the π-polarized radiation, where the electric vector lies in the plane of incidence.

The rocking curve, the percent reflection P and the double crystal coefficient of reflection R can now be calculated in the usual way.[1]

---

[1] The rocking curve is given by the function

$$\phi(k)=\tfrac{1}{2}\int_{-\infty}^{+\infty}F_{\sigma}(l)\cdot F_{\sigma}(l-k)\,dl+\tfrac{1}{2}\int_{-\infty}^{+\infty}F_{\pi}(l)\cdot F_{\pi}(l-k)\,dl. \qquad (12)$$

On calculating the different constants in eq. (8), we assumed that the chemical binding was pure covalent, so that the scattering factors of the atoms were used. This is not strictly true since the binding is partly of ionic type. The error introduced is, however, very slight and can here be neglected. The values of the scattering factors were taken from JAMES and BRINDLEY. These values are calculated for zero °K. The effect of the thermal vibrations is to decrease the values of the scattering factors. This influence has been studied theoretically in the case of a simple cubic lattice containing only one kind of atoms. Due to DEBYE and to WALLER (17–21), the scattering factor correction is

$$f_T = f_0 \cdot \bar{e}^{M}; \tag{15}$$

where

$$M = \frac{6\,h^2}{m\,k\,\Theta_M}\left\{\frac{\Phi(x)}{x} + \frac{1}{4}\right\}\frac{\sin^2\vartheta}{\lambda^2}, \tag{16}$$

h being PLANCK's constant, m the mass of the atom, k BOLTZMANN's constant, Θ_M the characteristic temperature, $x = \frac{\Theta_M}{T}$ and $\Phi(x)$ a function which was evaluated numerically be DEBYE (17).[1] In the isotropic crystals, M is a function of $(\sin\vartheta/\lambda)$ only. For crystals with lower symmetry, this will in general not be true, since in anisotropic crystals the elastic constants are different in different directions. Very little progress has been made towards the theoretical calculations of M for such crystals. ZENER (24) has attempted to calculate M numerically as to zinc and cadmium, which are both hexagonal, but the results he obtained do not agree with the measurements of BRINDLEY (25, 26) in the case of zinc. A relation, similar to (16), must be valid also in the case of calcite. In order to estimate the influence from the thermal vibration in our case we adapted the method suggested by PARRATT (27). We used eq. (16), inserting for m the mean mass of the atoms in $CaCO_3$ $3.30 \cdot 10^{-23}$ g and for Θ_M PARRATT's value 360 °K. Calculations were carried out both with corrected and uncorrected values of the atomic scattering factors in order to find the importance of the correction.

All constant that are necessary for the calculations are given in Table 4. A and

---

For P and R, we have

$$P = \frac{\int_{-\infty}^{+\infty} F_\sigma^2(l)\,d\,l + \int_{-\infty}^{+\infty} F_\pi^2(l)\,d\,l}{\int_{-\infty}^{+\infty} F_\sigma(l)\,d\,l + \int_{-\infty}^{+\infty} F_\pi(l)\,d\,l}; \tag{13}$$

$$R = \frac{2\,\delta}{\sin 2\vartheta_0}\,\frac{\left[\int_{-\infty}^{+\infty} F_\sigma(l)\,d\,l\right]^2 + \left[\int_{-\infty}^{+\infty} F_\pi(l)\,d\,l\right]^2}{\int_{-\infty}^{+\infty} F_\sigma(l)\,d\,l + \int_{-\infty}^{+\infty} F_\pi(l)\,d\,l}. \tag{14}$$

The form of eq. (8) is such that the calculations are very tedious and difficult. All integrations must be carried out graphically.

[1] A table will be found in International Crystal Tables, 22, Table IV, p. 574, Vol. 2.

Table 4

The constants used in evaluating equation (8).

Atomic plane	Glancing angle	$A \cdot 10^6$	$B \cdot 10^6$	$A_1 \cdot 10^6$	$B_1 \cdot 10^6$
2 1 1	6° 43′	0.935	0.00978	0.902	0.00942
4 2 2	13° 30′	0.344	0.00658	0.298	0.00570
6 3 3	20° 34′	0.442	0.00514	0.320	0.00372
8 4 4	28° 0′	0.500	0.00450	0.282	0.00254
3 1 0	13° 27′	0.344	0.00658	0.298	0.00571
6 2 0	27° 43′	0.250	0.00430	0.141	0.00242
6 5 5	20° 2′	0.450	0.00552	0.329	0.00382
10 3 3	41° 34′	0.294	0.00340	0.092	0.00106

As all measurements were made with the same radiation, the values of μ_l, and δ were the same for all planes. μ_l was taken from experimental data, δ and β were calculated in the way indicated earlier (13). The following values were used: $\mu_l = 23.4$, $\delta_{\mathrm{Ca}} = 3.68 \cdot 10^{-7}$, $\delta_{\mathrm{C}} = 1.11 \cdot 10^{-7}$, $\delta_{\mathrm{O}} = 1.47 \cdot 10^{-7}$, $\delta = 1.82 \cdot 10^{-6}$, $\beta_{\mathrm{Ca}} = 6.16 \cdot 10^{-9}$, $\beta_{\mathrm{C}} = 6.2 \cdot 10^{-11}$, $\beta_{\mathrm{O}} = 1.24 \cdot 10^{-10}$, $\beta = 1.32 \cdot 10^{-8}$.

Table 5

Calculated and observed values of the full width of the rocking curve, of the percent reflection and of the double crystal coefficient of reflection. w, R and P are calculated from A and B, w_1, R_1 and P_1 from A_1 and B_1.

Plane	Width of the rocking curve in sec. of arc			Coefficient of reflection in radians			Percent reflection		
	w	w_1	w_{exp}	$R \cdot 10^5$	$R_1 \cdot 10^5$	$R_{\mathrm{exp}} \cdot 10^5$	$P \cdot 10^2$	$P_1 \cdot 10^2$	$P_{\mathrm{exp}} \cdot 10^2$
2 1 1	4.6	4.5	5.2	2.03	1.96	2.31	77	75	68
4 2 2	0.8	0.7	1.2	0.35	0.29	0.39	73	70	47
6 3 3	0.7	0.5	1.1	0.30	0.21	0.33	71	69	45
8 4 4	0.6	0.3	0.7	0.25	0.14	0.16	70	64	32
3 1 0	0.9	0.7	1.5	0.36	0.30	0.47	73	69	45
6 2 0	0.3	0.2	0.9	0.12	0.07	0.19	65	55	45
6 5 5	0.7	0.6	1.0	0.30	0.22	0.33	71	67	26
10 3 3	0.3	0.1	0.8	0.13	0.03	0.07	65	47	10

B refer to the uncorrected values of the scattering factors; A_1 and B_1 to the corrected ones.

All investigations were carried out with molybdenum $K\alpha$-radiation. When possible, measurements were made in higher orders too, in which cases the overlapping from lower orders was depressed with suitable absorption foils. The voltage of the X-ray tube was always kept below the double threshold voltage so that no overlapping could occur when the first order reflections were investigated.

As is mentioned previously, all the crystal plates used were ground and polished. After the plates were adjusted parallel to the axes of revolution, the percent reflection P, the double coefficient of reflection R and the width w of the rocking curve were always determined in the first order. Then the crystal plates were etched with 0.7 normal hydrochloric acid until constant values of P, R, and w were obtained. It proved that in all cases an etching time of 5 seconds was sufficient.

Table 6

The influence from etching.

Plane	Values, obtained before etching			Values obtained after etching		
	w sec.	$P \cdot 10^2$	$R \cdot 10^5$ rad.	w sec.	$P \cdot 10^2$	$R \cdot 10^5$ rad.
2 1 1	16.2	31	3.4	5.2	68	2.31
3 1 0	5.6	25	1.2	1.5	45	0.47
6 5 5	2.5	26	0.37	1.0	47	0.32
1 0 3 3	4.0	6	0.15	0.8	10	0.07

Table 7

A comparison between Parratt's results, obtained with natural cleavage surfaces, and those obtained in the present investigation. (Index P is applied to Parratt's results, index B to the writer's.)

Plane	w_P sec.	w_B sec.	$P_P \cdot 10^2$	$P_B \cdot 10^2$	$R_P \cdot 10^5$ rad.	$R_B \cdot 10^5$ rad.
2 1 1	5.2	5.2	66	68	2.40	2.31
4 2 2	1.1	1.2	49	47	0.37	0.39
6 3 3	1.1	1.1	49	45	0.34	0.33
8 4 4	0.7	0.7	40	32	0.20	0.16

The results of the measurements are given in Table 5. The agreement between the calculated values of the double crystal coefficient of reflection R and those experimentally determined is very good. The values R_1 calculated by means of the atomic scattering factors corrected for the thermal vibrations, are always less than those experimentally obtained. In two cases, the fourth order of the clevage plane = plane (844), and plane (1033), the experimental determinations are less than the R-values calculated from the uncorrected atomic scattering factors. These two planes have the smallest spacings and thus the largest values of $(\sin \vartheta / \lambda)$, so that due to eq. (33) and (34), the temperature correction is greatest there. As the R- and R_1-values are calculated under the assumption that calcite is a perfect crystal, and as an eventual "feature" of mosaic structure must increase these values, the measurements on planes (844) and (1033) verify that some kind of correction for the thermal vibrations should be applied. It is, however, not possible to draw any conclusions about the size of the correction.

The experimental values of the full width of the rocking curve at half maximum intensity are always greater than those calculated, but the experimental values of the percent reflection are less. The calculated values of the width w go down to very small values (only a few tenths of a second of arc), and those determined are in some cases less than one second of arc. Studying the cases of the minimum values, planes (844), (620), and (1033), we find, that the experimental values of the percent reflection are usually small and that the differences between the calculated values and the experimental ones are greater than usual. The reason for this seems to be that the crystals are not perfect in the sense of being single complete specimens, but are

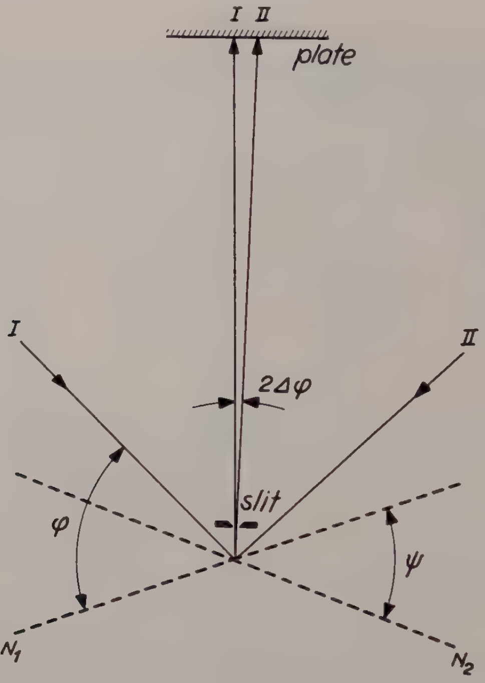

Fig. 1.

built up of small blocks which are roughly, but not exactly, oriented in the direction of the crystal axes. This would cause the reflection to spread itself over a greater angular width than that calculated for a perfect crystal. Hence, the width of the rocking curve would increase, and the percent reflection decrease. The coefficient of reflection would increase but it would not be influenced as much as the width of the rocking curve. As the influence from a disorientation partly compensates the influence from the thermal vibrations it is impossible to obtain information about the size of the correction term.

Table 6 shows the influence from the etching. In the grinding and polishing, the regular crystal structure is disrupted and a thin surface layer of powdered crystal fragments is produced. This layer will increase the coefficient of reflection and the width of the rocking curve. As appears from the table, the elimination of the surface layer causes a decrease of the coefficient of reflection and of the width, and an increase of the percent reflection and of the physical resolving power.

The quantities R, P, and w have previously been determined by PARRATT with natural calcite surfaces (27). He used the clevage plane (211) and made investigations with Mo Kα, in the first five orders. A comparison with his results shows (see Table 7) that the agreement is very good. This indicates that the sawing and polishing influence only a very thin surface layer. When this is removed (by etching with hydrochloric acid) a crystal grating is obtained, the qualities of which are in good agreement with what is predicted by the theory of perfect crystals.

The calcite plates were cut out parallel to the atomic planes, suggested by AMINOFF (1). As appears from Table 1, his choice was not the best. Plane (310) could have been exchanged for $(2\bar{1}\bar{1})$, and (741) for (651) or $(51\bar{2})$, in which cases the coefficient of reflection would have increased more than fifty per cent.

The investigation, however, confirms the earlier observations that calcite is nearly a perfect crystal. Its structure is such that there are a large number atomic planes with different spacings, but with a good reflection power, which can be used as X-ray gratings. The deformations produced when a crystal plate is cut out parallel to a certain atomic plane, are located in the very surface layer and can be eliminated by cautious etching with diluted hydrochloric acid.

The purpose of the investigation was to point out the possibility of obtaining crystal gratings with small spacings and great reflection power suitable for X-ray spectroscopy. This makes it possible to increase the accuracy of precision measurements of wave-lengths etc. as the resolving power increases when the spacing decreases. As to precision determination of wavelengths, calcite is of very great interest from another point of view. The symmetry of calcite results in the fact that we have always three planes with the same qualities (for instance (211), (121), and (112)). As appears from Fig. 1, it is sometimes possible to make a very accurate determination of the wave-length of an emission line without using a circular scale. N_1 and N_2 are two equivalent planes, which intersect each other under angle ψ. The spacing of the planes is such as to make the glancing angle φ of a certain wave-length nearly equal to $90° - \frac{\psi}{2}$. If a thin slit and a photographic plate are mounted as Fig. 1 shows, and if two exposures are made with the X-ray beams I and II respectively, two lines are obtained on the plate. From distance a between the lines on the plate and from distance b between slit and plate, angle $\Delta\varphi$ can be determined. ψ is obtained direct from the structure of the crystal and from the lattice parameters with very high accuracy. Hence

$$\Delta\varphi = \mathrm{tg}^{-1}\frac{a}{2b};$$

$$180 - 2\varphi = \psi - 2\Delta\varphi;$$

$$\lambda = 2d\sin\varphi.$$

The method was pointed out by Kossel (23), but it has not been used for precision measurements. As calcite has a lot of suitable atomic planes with high reflection power, but with various spacings, the above method seems to be very applicable there. By using intersections between not identical planes with different spacings the possibilities of wave-length determinations are increased. The elimination of the angular scale is such a great advantage as to well compensate the elaborate calculations of various ψ. Our intention is to utilize this method in order to make some redeterminations of wave-lengths. We also intend to use some atomic planes with small spacings in a tube spectrometer for determining some X-ray lines with short wave-lengths.

This investigation has received financial support from the Swedish Natural Science Research Council, which is gratefully acknowledged. My thanks are also due to Mr Öved Adell, F.M., for assisting me in the recordings with the double crystal spectrometer.

Physical Institute, University of Uppsala, Uppsala, Sweden. September 1952.

REFERENCES

1. G. AMINOFF, Nature *157*, 517, 1946.
2. W. L. BRAGG, Proc. Roy. Soc. A *89*, 468, 1914.
3. —— Atomic Structure of Minerals. London 1937.
4. C. G. DARWIN, Phil. Mag. *27*, 325 and 675, 1914.
5. A. H. COMPTON and S. K. ALLISON, X-rays in Theory and Experiments. Second edition. New York 1935.
6. R. W. G. WYKOFF, The Structure of Crystals. Chem. Cat. Co. New York 1931.
7. H. VAN BERGEN, Ann. d. Phys. (5) *39*, 553, 1941.
8. P. W. JAMES and G. W. BRINDLEY, Phil. Mag *12*, 104, 1931.
9. A. LARSSON, Phil. Mag. *3*, 1136, 1927.
10. M. SIEGBAHN, Spektroskopie der Röntgenstrahlen. Zweite Auflage. Berlin 1931.
11. J. R. BENOIT, Trav. et Mém. du Bur. int des Poids et Mes. *6*, 3, 1888.
12. G. BROGREN, Arkiv för Fysik *3*, 507, 1951.
13. —— Arkiv för Fysik *6*, 321, 1953.
14. S. K. ALLISON, Phys. Rev. *41*, 13 and 688, 1932.
15. L. G. PARRATT, Phys. Rev. *41*, 561, 1932.
16. K. V. MANNING, Rev. Sci. Inst. *5*, 316, 1934.
17. P. DEBYE, Ann. d. Phys. *43*, 49, 1914.
18. I. WALLER, Ann. d. Phys. *79*, 261, 1926.
19. —— Ann. d. Phys. *83*, 154. 1927.
20. —— Zs. f. Phys. *51*, 213, 1928.
21. R. W. JAMES, The Optical Principles of the Diffraction of X-rays. London 1948.
22. Internationale Tabellen zur Bestimmung von Kristallstrukturen. Bornträger. Berlin 1935.
23. W. KOSSEL, Ann. d. Phys. *26*, 533, 1936.
24. C. ZENER, Phys. Rev. *49*, 122, 1936.
25. C. W. BRINDLEY, Phil. Mag. *21*, 790, 1936.
26. —— Proc. Leeds Phil. Soc. *3*, 200, 1936.
27. L. G. PARRATT and F. MILLER jr., Phys. Rev. *49*, 280, 1936.

Tryckt den 7 maj 1953

Uppsala 1953. Almqvist & Wiksells Boktryckeri AB

ARKIV FÖR FYSIK Band 6 nr 47

Communicated 3 December 1952 by E. HULTHÉN

Preliminary analysis of the microwave spectrum of formic acid

By GUNNAR ERLANDSSON

With 3 figures in the text

The microwave spectrum of monomeric formic acid has been investigated previously by PIETENPOL, ROGERS and WILLIAMS (1) and further by ROGERS and WILLIAMS (2), who have also calculated the rotational constants of the molecule. A reinvestigation of this spectrum in the region 16.5–26.5 kMc/s has been undertaken here, resulting in an extended list of absorption frequencies. Three lines have been identified by means of their Stark-effect components. Of these lines only one, viz. the transition $0_{0.0}$–$1_{0.1}$ is in agreement with the constants given in (2). New values of the rotational constants have been calculated assuming the molecule to be a rigid rotator. The calculations show, however, that this approximation is not applicable to the higher J-values. A more detailed treatment of the centrifugal distortion appears to be much too laborious if it should be based on the present measurements and is therefore postponed untill some more transitions involving low J-values have been identified in other regions of the spectrum.

Experimental technique

A stark-effect modulation spectrometer has been used. The absorption cell consists of a 3 cm wave guide provided with a central steel band electrode. A 100 kc/s square wave modulation voltage having a maximum amplitude of about 500 volts has been employed. The square wave is normally zero-based, but for complete resolution of Stark-effect components a d.c. voltage of up to 3000 volts has been superimposed, giving a maximum field intensity of 5000 volts/cm.

The receiver consists of an amplifier tuned to 100 kc/s followed by a phase sensitive detector. The absorption lines may be alternatively presented on an oscilloscope screen or displayed by a Brown-recorder. In the latter case a slow motor drive is applied to the klystron tuning shaft.

Frequencies have been measured by means of a cavity wave-meter supposed to be accurate to ± 5 Mc/s.

Experimental results

The absorption frequencies are presented in Table I together with the corresponding values from (2) and (3). The table also gives the number of Stark-effect components for the resolved lines. The appearance of the Stark-effect patterns of the

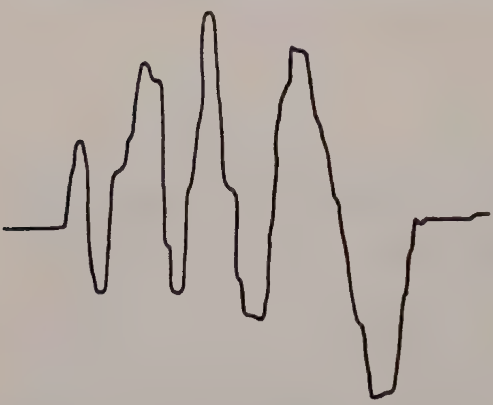

Fig. 1. Stark-effect components of the line at 24 569 Mc/s. D.c. voltage 3000 volts. Frequency increasing from left to right.

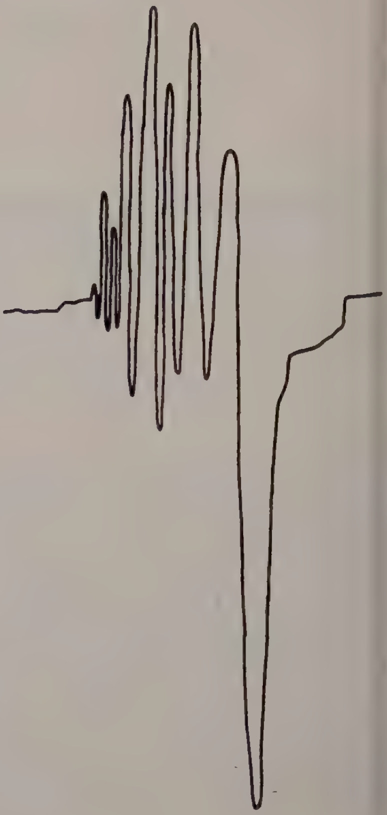

Fig. 2. Stark-effect components of the line at 20 298 Mc/s. D.c. voltage 3000 volts. Frequency increasing from left to right.

Table I

Frequency value found here Mc/s	Frequency according to (2) and (3)	Number of Stark components	Assignment	Intensity
16 989	—	—	—	S
17 282	—	—	—	S
20 294	20 297.9 (3)	8	$8_{2.7}$—$8_{2.6}$	S
22 326	22 326.42(2)	—	—	M
22 470	22 471.14(2)	1	$0_{0.0}$—$1_{0.1}$	S
23 206	23 203.41(2)	—	—	S
24 565	24 568.99(2)	4	$4_{1.4}$—$4_{1.3}$	S
24 595	—	—	—	W
25 218	—	—	—	S
26 342	—	—	—	M
—	27 817.12(2)	—	—	—
—	31 200 (2)	—	—	—

lines at 24 569 Mc/s and 20 298 Mc/s as displayed by the Brown-recorder is shown in Figs. 1 and 2. In both cases the spacing of the components is closest near the

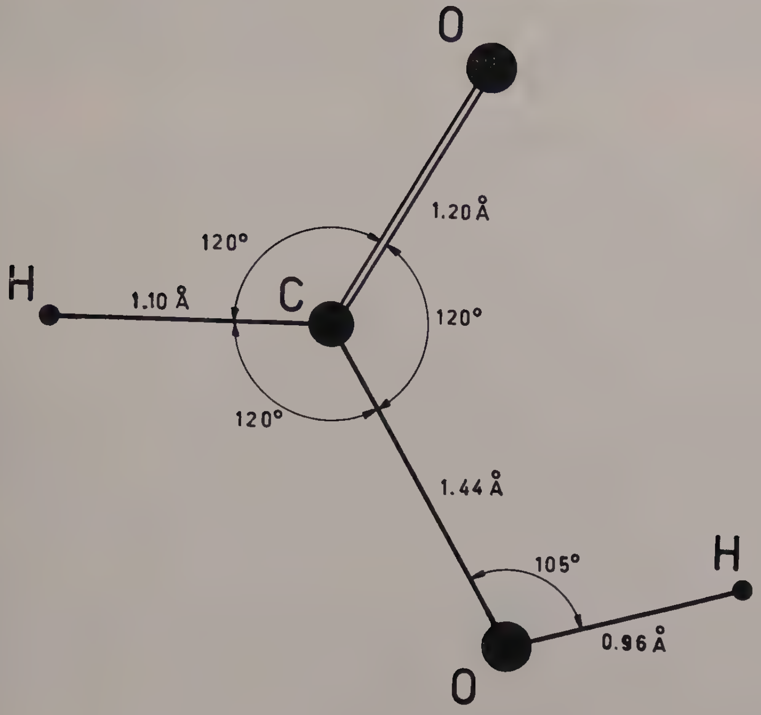

Fig. 3. Tentative model of formic acid molecule.

main line where also the intensity is smaller. From the formulas of Golden and Wilson (4) it is concluded that both of these lines have $\Delta J = 0$. The number of components then give $J = 4$ and $J = 8$ respectively.

Considerations regarding molecular structure

The structure formula of monomeric formic acid is generally written 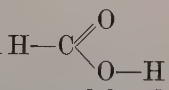 $H{-}C\genfrac{}{}{0pt}{}{\diagup\!\!\diagup O}{\diagdown O{-}H}$

If the molecule is supposed to be plane, and the interatomic distances and bond angles are given values ordinarily found for similar bonds in other molecules, the molecular structure will be such as shown in Fig. 3. For this model the rotational constants ($A = \frac{\hbar^2}{2\,c\,I_A}$ etc.) are found to be $A = 2.17$ cm^{-1}, $B = 0.394$ cm^{-1}, and $C = 0.332$ cm^{-1}. The direction of the b-axis (axis of intermediate moment of inertia) is found to be nearly parallel to the H–C bond.

The assumed molecular model may have components of the permanent electric dipole moment along the a- and b-axis but no component along the c-axis. According to Cross, Hainer and King (5) the allowed rotational transitions (in terms of the K_{-1}, K_1 notation) will then be those where only the index K_1 changes parity (a-transitions) or where both indexes change parity (b-transitions). Using the methods and energy level tables given by King, Hainer and Cross (6) the model is found to give a rotational spectrum similar to the one found experimentally. E.g. the transition $0_{0.0} - 1_{0.1} = B + C$ is found to give a line at 21.8 kMc/s. The model may therefore be supposed to give an approximate picture of the molecule.

Discussion of spectrum interpretation

Starting from the above model it is natural to interpret the line at 22471 Mc/s as arising from the transition $0_{0.0}$–$1_{0.1}$, which gives a value of $B + C = 0.74959$ cm^{-1} in agreement with the results of ROGERS and WILLIAMS (2). From the tables of (6) it is found that the only interpretation of the $J = 4$ line at 24569 Mc/s will be $4_{1.4}$–$4_{1.3}$. The $J = 8$ line at 20297 Mc/s must then be $8_{2.7}$–$8_{2.6}$.

The frequency of a Q-branch transition is given by $\frac{1}{2}(A - C)(E_\tau'' - E_\tau')$, where E_τ'' and E_τ' are functions only of the asymmetry parameter $\varkappa = \frac{2B - A - C}{A - C}$. The frequency ratio between two such lines is thus determined by $\varkappa$ alone. By means of successive approximations employing the continued fraction method of (6) the value of $\varkappa$ corresponding to the above assignements of the $J = 4$ and $J = 8$ lines has been calculated to $\varkappa = 0.88704$. The rotational constants are now easily calculated and the following values are obtained: $A = 1.78612$ cm^{-1}, $B = 0.41581$ cm^{-1} and $C = 0.33378$ cm^{-1}.

The above result is not quite satisfactory. E. g. the next Q-branch line to be expected within the investigated frequency region is found to be $13_{3.11}$–$13_{3.10}$ = 20112 Mc/s. The intensity of this line should be of the same order of magnitude as that of the others. No line is found, however, nearer than 3000 Mc/s away from this frequency.

It might be suspected that the assignments made are erroneous. A thorough investigation of other possibilities of interpretation has, however, given no better result. Is has therefore been concluded that the rigid rotor approximation is not applicable to the higher rotational levels. If the relation $I_A + I_B = I_C$ is supposed to be valid, new values of the rotational constants may be calculated from the $0_{0.0}$–$1_{1.1}$ and $4_{1.4}$–$4_{1.3}$ transitions. The result is

$$A = 1.6919 \text{ cm}^{-1} \quad B = 0.41581 \text{ cm}^{-1} \quad C = 0.33378 \text{ cm}^{-1}.$$

The values of B and C are to five figures the same as obtained above, whereas a smaller value of A is obtained.

Returning to the molecular model of Fig. 3 it may be found that a change in the $O = C - O$ angle by 1° alters the value of A sufficiently to explain the above discrepancies. The result may thus be considered reasonable. A more detailed treatment of centrifugal distortion would require calculation of five or six distortion constants. For this purpose an unambiguous identification of some more lines is necessary. Especially some transitions involving low J-values should be measured.

Conclusion

A satisfactory interpretation of the microwave spectrum of formic acid based on the rigid rotor approximation seems to be impossible. The spectrum is, however, compatible with the idea of a non rigid, planar molecular structure of the type shown in Fig. 3. From the observed low-J-transitions the rotational constants B

and C may be calculated to five significant figures. An approximate value of A may then be obtained from the relation $I_A + I_B = I_C$. The results seem to indicate that the $O=C-O$ angle should be smaller than 120° probably near 115°.

Table II

Rotational constants	Rogers and Williams (2)	Bauer and Badger (3)	Present results
A	2.7855	2.59	1.69
B	0.399901	0.396	0.41581
C	0.349696	0.329	0.33378

The values of the rotational constants found by different investigators are for comparison collected in Table II. It is found that the agreement is not very good. Especially the present value of A is considerably lower than the A-value found by BAUER and BADGER from infrared observations. It should be noted, however, that the infrared measurements involve a large number of rotational lines, whereas the microwave data refer to low-J-transitions only. It may be considered significant that the present results show an increase of A with increasing J. The B- and C-values according to BAUER and BADGER give for the transition $0_{0.0}$–$1_{0.1}$ the frequency 21800 Mc/s instead of 22471 Mc/s. The constants given by ROGERS and WILLIAMS are not compatible with the observed transition $4_{1.4}$–$4_{1.3}$.

To obtain more complete information about the molecule, it is desirable to extend the investigation to other frequency regions. Especially the region 40–50 kMc/s may be expected to give valuable information. The calculation of bond distances and angles will require the investigation of some isotopic molecules.

Acknowledgment.

I wish to express my thanks to Professor ERIK HULTHÉN for his interest in this work and for helpful discussions, to Dr. phil. BÖRGE BAK and Mag. Sci. JOHN ANDERSSON in Copenhagen for valuable collaboration and to Statens Naturvetenskapliga Forskningsråd for economical support.

Physical Department, University of Stockholm, December 1952.

REFERENCES

1. W. J. PIETENPOL, J. D. ROGERS and D. WILLIAMS, Phys. Rev. *78*, 480 (1950).
2. J. D. ROGERS and D. WILLIAMS, Phys. Rev. *83*, 210 (1951).
3. B. BAK and J. ANDERSON, private correspondence.
4. S. GOLDEN and E. B. WILSON jr. Journ. Chem. Phys. *16*, 669 (1948).
5. P. C. CROSS, R. M. HAINER and G. W. KING, Journ. Chem. Phys. *12*, 210 (1944).
6. G. W. KING, R. M. HAINER and P. C. CROSS, Journ. Chem. Phys. *11*, 27 (1943).
7. S. H. BAUER and R. M. BADGER, Journ. Chem. Phys. *5*, 852 (1937).

Tryckt den 11 maj 1953.

Uppsala 1953. Almqvist & Wiksells Boktryckeri AB

ARKIV FÖR FYSIK Band 6 nr 48

Communicated 10 September 1952 by G. Borelius and O. Klein

The influence of a cadmium sheet on the distribution of neutrons in graphite

By Nils Göran Sjöstrand

With 7 figures in the text

Introduction

The “cadmium difference method” is sometimes used in neutron physics to liminate the effect of fast neutrons. Measurements are made both without and vith a cadmium sheet between the neutron source and the detector. The diference between the two sets of measurements then corresponds to those neurons which are absorbed by the cadmium, i.e. to those having energies less han about 0.3 eV.

This method has recently been used at this laboratory for a determination f the diffusion length of thermal neutrons in graphite [1], and it became of nterest to study in some detail the influence of a flat cadmium plate on the eutron distribution in a rectangular graphite block. In the present paper a heoretical treatment of the problem is given, and experiments which were nade to check the theoretical results are described. Good agreement was found etween experiment and theory.

Theory

eneral

Fig. 1 is a schematic sketch of the system which will be considered: it contitutes a three-medium problem in a rectangular three-dimensional geometry.

In elementary diffusion theory the neutron density (n), for the stationary tate and in a region containing no sources, is given by the equation

$$\Delta n - \frac{n}{L^2} = 0$$

here L is the diffusion length. This equation is however not valid near sources r boundaries, or in regions of strong absorption, and it is therefore not suitable or the present investigation, which is concerned with a system including a rongly absorbing cadmium sheet.

Instead of the elementary equation we must use the Boltzmann diffusion quation, and attempt to solve it. The method which seems most suitable for ur problem is the “spherical harmonic method” [2, 3, 4], which can in prinple be used with any geometry.

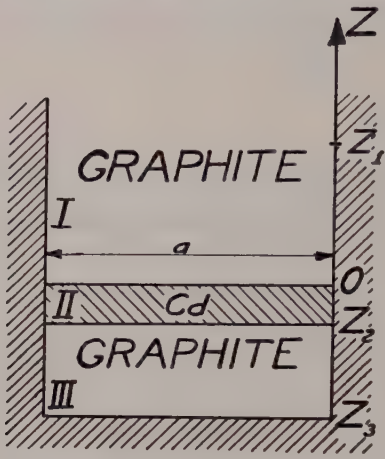

Fig. 1. The system treated theoretically. It consists of three square slabs of graphite, cadmium and graphite.

The Boltzmann equation

Assuming that the neutrons all have the same constant speed, and that al collisions are elastic and do not result in energy changes, the Boltzmann equation is

$$\frac{\partial N(\vec{r},\vec{\Omega},t)}{\partial t} = -V\vec{\Omega} \text{ grad } N(\vec{r},\vec{\Omega},t) - N(\vec{r},\vec{\Omega},t)\cdot V\sigma + \\ + V\sigma_s \int N(\vec{r'},\vec{\Omega'},t)\cdot F(\vec{\Omega}\cdot\vec{\Omega'})\,d\Omega' + S(\vec{r},\vec{\Omega},t$$

where

$N(\vec{r},\vec{\Omega},t)\,dr\,d\Omega$ = the number of neutrons in the volume element $dr = dx\,dy\,dz$ and having velocity vectors lying in the solid angle $d\Omega$ about $\vec{\Omega}$.

V = the speed of the neutrons.

σ = the total cross section per unit volume.

σ_s = the scattering cross section per unit volume.

$S(\vec{r},\vec{\Omega},t)\,dr\,d\Omega$ = the number of neutrons produced per unit time in the volume element dr and with their velocity vectors lying in the solid angle $d\Omega$.

$F(\vec{\Omega}\cdot\vec{\Omega'})$ = the relative probability of scattering through an angle having cosine $\mu_0 = \vec{\Omega}\cdot\vec{\Omega'}$ where $\vec{\Omega'}$ is a unit vector in the direction before collision, and $\vec{\Omega}$ a unit vector in the direction after collision. The function F is normalized as follows:

$$\int F(\vec{\Omega}\cdot\vec{\Omega'})\,d\Omega = \int F(\vec{\Omega}\cdot\vec{\Omega'})\,d\Omega' = 1$$

Developing the required function N in spherical harmonics, we get

$$N(\vec{r},\vec{\Omega},t) = \sum_{n=0}^{\infty} \frac{2n+1}{4\pi}\left\{A_n P_n(\mu) + 2\sum_{m=1}^{n} \frac{(n-m)!}{(n+m)!}\left(A_n^m \cos m\Phi + B_n^m \sin m\Phi\right) T_n^m(\mu)\right\}$$

where

$\mu = \cos\theta$, where θ is the angle between the velocity vector and the z-axis,

$$A_n(\vec{r},t) = \int N(\vec{r},\vec{\Omega},t)\, P_n(\mu)\, d\Omega$$

$$A_n^m(\vec{r},t) = \int N(\vec{r},\vec{\Omega},t)\, T_n^m(\mu) \cos m\Phi\, d\Omega$$

$$B_n^m(\vec{r},t) = \int N(\vec{r},\vec{\Omega},t)\, T_n^m(\mu) \sin m\Phi\, d\Omega$$

$$T_n^m(x) = (-1)^m (1-x^2)^{\frac{m}{2}} \frac{d^m}{dx^m} P_n(x)$$

(x is real, and $-1 \leq x \leq 1$).

$T_n^m(x)$ has the orthogonality properties

$$\int_{-1}^{1} T_n^m(x)\, T_k^m(x)\, dx = \frac{(n+m)!}{(n-m)!}\, \frac{2}{2n+1}\, \delta_{nk}$$

The scattering function F may be expanded in Legendre polynomials:

$$F(\mu_0) = \sum_{l=0}^{\infty} \frac{2l+1}{4\pi} F_l P_l(\mu_0) \text{ where } F_l = \int F(\mu_0) P_l(\mu_0)\, d\Omega$$

Substituting these series expansions in the Boltzmann equation, we get:

$$(1) \qquad \frac{\partial N}{\partial t} = -V\left(\frac{\partial N}{\partial x}\sin\theta\cos\Phi + \frac{\partial N}{\partial y}\sin\theta\sin\Phi + \frac{\partial N}{\partial z}\cos\theta\right) - NV\sigma + S +$$

$$+ V\sigma_s \sum_{n=0}^{\infty} \frac{2n+1}{4\pi} F_n \left\{ A_n P_n(\mu) + 2\sum_{m=1}^{n} \frac{(n-m)!}{(n+m)!} \left(A_n^m \cos m\Phi + B_n^m \sin m\Phi\right) T_n^m(\mu) \right\}$$

We next multiply equation (1) by $P_l(\mu)$ and integrate over $d\Omega$, which gives

$$\frac{\partial A_l}{\partial t} = -\frac{V}{2l+1}\left\{\frac{\partial A_{l-1}^1}{\partial x} - \frac{\partial A_{l+1}^1}{\partial x} + \frac{\partial B_{l-1}^1}{\partial y} - \frac{\partial B_{l+1}^1}{\partial y} + \right.$$

$$\left. + (l+1)\frac{\partial A_{l+1}}{\partial z} + l\frac{\partial A_{l-1}}{\partial z}\right\} - V b_l A_l + \int S P_l(\mu)\, d\Omega$$

where $b_l = \sigma - F_l \sigma_s$ and $l = 0, 1, 2, \ldots$

We then multiply equation (1) by $T_l^k(\mu) \cos k\Phi$ and integrate over $d\Omega$, getting

$$\frac{\partial A_l^k}{\partial t} = -\frac{V}{2l+1}\left\{\frac{l(l+1)}{2}\delta_{k1}\left(\frac{\partial A_{l+1}}{\partial x} - \frac{\partial A_{l-1}}{\partial x}\right) + \frac{(l-k+2)(l-k+1)}{2}\left(\frac{\partial A_{l+1}^{k-1}}{\partial x} - \right.\right.$$

$$\left. - \frac{\partial B_{l+1}^{k-1}}{\partial y}\right) - \frac{(l+k)(l+k-1)}{2}\left(\frac{\partial A_{l-1}^{k-1}}{\partial x} - \frac{\partial B_{l-1}^{k-1}}{\partial y}\right) + \tfrac{1}{2}\left(\frac{\partial A_{l-1}^{k+1}}{\partial x} + \frac{\partial B_{l-1}^{k+1}}{\partial y}\right) -$$

$$-\tfrac{1}{2}\left(\frac{\partial A_{l+1}^{k+1}}{\partial x}+\frac{\partial B_{l+1}^{k+1}}{\partial y}\right)+(l+k)\frac{\partial A_{l-1}^{k}}{\partial z}+(l-k+1)\frac{\partial A_{l+1}^{k}}{\partial z}\Big\}-$$

$$-V b_l A_l^k+\int S\, T_l^k(\mu)\cos k\Phi\cdot d\Omega$$

Finally, multiplying equation (1) by $T_l^k(\mu)\sin k\Phi$, and again integrating over $d\Omega$, we obtain

$$\frac{\partial B_l^k}{\partial t}=-\frac{V}{2l+1}\Big\{\frac{l(l+1)}{2}\delta_{k1}\left(\frac{\partial A_{l+1}}{\partial y}-\frac{\partial A_{l-1}}{\partial y}\right)+\frac{(l-k+2)(l-k+1)}{2}\left(\frac{\partial B_{l+1}^{k-1}}{\partial x}+\right.$$

$$\left.+\frac{\partial A_{l+1}^{k-1}}{\partial y}\right)-\frac{(l+k)(l+k-1)}{2}\left(\frac{\partial B_{l-1}^{k-1}}{\partial x}+\frac{\partial A_{l-1}^{k-1}}{\partial y}\right)+\tfrac{1}{2}\left(\frac{\partial B_{l-1}^{k+1}}{\partial x}-\frac{\partial A_{l-1}^{k+1}}{\partial y}\right)-$$

$$-\tfrac{1}{2}\left(\frac{\partial B_{l+1}^{k+1}}{\partial x}-\frac{\partial A_{l+1}^{k+1}}{\partial y}\right)+(l+k)\frac{\partial B_{l-1}^{k}}{\partial z}+(l-k+1)\frac{\partial B_{l+1}^{k}}{\partial z}\Big\}-$$

$$-V b_l B_l^k+\int S\, T_l^k(\mu)\sin k\Phi\, d\Omega$$

Instead of the Boltzmann equation we now have a system of differential equations. The more terms we take in the expansion of N the more differential equations we obtain: the accuracy of the calculation depends on the labour which can be expended on computation. It is found to be most convenient to take an even number of terms.

We shall now apply the above calculations to a rectangular three-media block on a square base. The system is assumed to be source-free, and in the stationary state. Defining the symbols as in Fig. 1, the boundary conditions are that the neutron density is zero at $x=0$, $x=a$, $y=0$, $y=a$, and at $z=z_3$. It is assumed that the neutron distribution is known at $z=z_1$.

The special case $n=0$ and 1

The simplest possible case is if only the terms for $n=0$ and $n=1$ are taken in the expansion for N. The following system of equations is then obtained:

$$-\frac{\partial A_1^1}{\partial x}-\frac{\partial B_1^1}{\partial y}+\frac{\partial A_1}{\partial z}+b_0 A_0=0$$

$$\frac{\partial A_0}{\partial z}+3\,b_1 A_1=0$$

$$-\frac{\partial A_0}{\partial x}+3\,b_1 A_1^1=0$$

$$-\frac{\partial A_0}{\partial y}+3\,b_1 B_1^1=0$$

Substituting for A_1, A_1^1 and B_1^1 in the first of the equations, we get:

$$\frac{\partial^2 A_0}{\partial x^2}+\frac{\partial^2 A_0}{\partial y^2}+\frac{\partial^2 A_0}{\partial z^2}-3\,b_0 b_1 A_0=0$$

which is simply the well-known elementary diffusion equation. By integrating the series expansion for N with respect to Ω one finds that A_0 is the total number of neutrons per unit volume. Furthermore $1/L^2=3\;b_0 b_1$.

With the boundary conditions assumed above, we may take as a particular solution:

$$A_0=(A\,e^{\alpha z}+B\,e^{-\alpha z})\,\sin\frac{m\pi x}{a}\cdot\sin\frac{n\pi y}{a}$$

where

$$\alpha^2=3\,b_0 b_1+\frac{\pi^2}{a^2}\,(m^2+n^2)$$

and m, n, are positive whole numbers. The general solution is the sum of such expressions over m and n: the neutron density is thus found as a double Fourier series with components of the type A_0 (compare [1]). The calculations will here only be carried through for *one* Fourier component. (For a medium of infinite extent in the x and y directions the solution would be $A_0=A\,e^{\alpha z}+B\,e^{-\alpha z}$, with $\alpha^2=3\,b_0 b_1$. In this case, as in that treated below, one gets the "plane" case, i.e. that for an infinite slab, by setting $m=n=0$ in the formulae for α).

We must now postulate a solution with undetermined coefficients for each of the three media, and then determine the coefficients by means of the conditions at the boundaries between the media. We assume:

I. $$M_0=(A\,e^{\alpha z}+B\,e^{-\alpha z})\,\sin\frac{m\pi x}{a}\cdot\sin\frac{n\pi y}{a}$$

$$M_1=-\frac{\alpha}{3\,b_1}\,(A\,e^{\alpha z}-B\,e^{-\alpha z})\,\sin\frac{m\pi x}{a}\cdot\sin\frac{n\pi y}{a}$$

II. $$N_0=(C\sinh\gamma z+D\cosh\gamma z)\,\sin\frac{m\pi x}{a}\cdot\sin\frac{n\pi y}{a}$$

$$N_1=-\frac{\gamma}{3\,c_1}\,(C\cosh\gamma z+D\sinh\gamma z)\,\sin\frac{m\pi x}{a}\cdot\sin\frac{n\pi y}{a}$$

III. $$K_0=E\sinh\alpha\,(z-z_3)\cdot\sin\frac{m\pi x}{a}\cdot\sin\frac{n\pi y}{a}$$

$$K_1=-\frac{\alpha}{3\,b_1}\,E\cosh\alpha\,(z-z_3)\cdot\sin\frac{m\pi x}{a}\cdot\sin\frac{n\pi y}{a}$$

In these equations M_0, N_0 and K_0 correspond to the original A_0, while M_1, N_1 and K_1 correspond to A_1. The symbols α, b_0 and b_1 refer to the graphite, and the corresponding symbols γ, c_0 and c_1 to the cadmium.

We have thus five unknown coefficients. By setting $M_0 = N_0$, $M_1 = N_1$, and $N_0 = K_0$, $N_1 = K_1$, at the boundaries between the media, we get four equations by means of which four of the unknowns may be expressed in terms of the fifth. The remaining unknown may be determined by Fourier analysis of the experimentally determined neutron distribution in the plane $z = z_1$.

Besides the boundary conditions used above there are also those corresponding to A_1^1 and B_1^1: these would however make the system of equations over-determined. This is a result of breaking off the series after only a finite number of terms.

The special case $n = 0, 1, 2, 3$

If one takes the terms for $n = 0, 1, 2, 3$, in the series expansion for N, one gets a system of 16 differential equations which is difficult to solve. We are however most interested in an exact calculation of the variation of neutron intensity in the z-direction. In the x and y directions the elementary theory, with appropriate corrections near the boundaries, should give a satisfactory result. We therefore take only the coefficients A_0, A_1, A_2, A_3, A_1^1 and B_1^1, and so we get the following system of equations:

$$-\frac{\partial A_1^1}{\partial x} - \frac{\partial B_1^1}{\partial y} + \frac{\partial A_1}{\partial z} + b_0 A_0 = 0$$

$$2\frac{\partial A_2}{\partial z} + \frac{\partial A_0}{\partial z} + 3 b_1 A_1 = 0$$

$$\frac{\partial A_2}{\partial x} - \frac{\partial A_0}{\partial x} + 3 b_1 A_1^1 = 0$$

$$\frac{\partial A_2}{\partial y} - \frac{\partial A_0}{\partial y} + 3 b_1 B_1^1 = 0$$

$$\frac{\partial A_1^1}{\partial x} + \frac{\partial B_1^1}{\partial y} + 3\frac{\partial A_3}{\partial z} + 2\frac{\partial A_1}{\partial z} + 5 b_2 A_2 = 0$$

$$3\frac{\partial A_2}{\partial z} + 7 b_3 A_3 = 0$$

It is reasonable to try:

$$A_0 = a_0 e^{\alpha z} \sin \frac{m \pi x}{a} \cdot \sin \frac{n \pi y}{a}$$

$$A_1 = a_1 e^{\alpha z} \sin \frac{m \pi x}{a} \cdot \sin \frac{n \pi y}{a}$$

$$A_2 = a_2 e^{\alpha z} \sin \frac{m \pi x}{a} \cdot \sin \frac{n \pi y}{a}$$

$$A_3 = a_3 e^{\alpha z} \sin \frac{m \pi x}{a} \cdot \sin \frac{n \pi y}{a}$$

$$A_1^1 = a_1^1 e^{\alpha z} \cos \frac{m \pi x}{a} \cdot \sin \frac{n \pi y}{a}$$

$$B_1^1 = b_1^1 e^{\alpha z} \sin \frac{m \pi x}{a} \cdot \cos \frac{n \pi y}{a}$$

By substitution we find:

$$a_2 = 7\, a_0 b_3 \cdot \frac{b_0 b_1 - \alpha^2}{\alpha^2 (14\, b_3 + 9\, b_1) - 35\, b_1 b_2 b_3}$$

$$a_1 = -\frac{\alpha}{3\, b_1} (2\, a_2 + a_0)$$

$$a_3 = -\frac{3\, \alpha}{7\, b_3} a_2$$

$$a_1^1 = \frac{m \pi}{3\, b_1 a} (a_0 - a_2)$$

$$b_1^1 = \frac{n \pi}{3\, b_1 a} (a_0 - a_2)$$

nd the condition

$$\alpha^4 - \alpha^2 (27\, b_0 b_1 + 28\, b_0 b_3 + 35\, b_2 b_3) + 105\, b_0 b_1 b_2 b_3 - \\ - \frac{\pi^2}{a^2} (m^2 + n^2) \left[\alpha^2 \left(9 + \frac{21\, b_3}{b_1} \right) - 35\, b_2 b_3 - 7\, b_0 b_3 \right] = 0 \qquad (2)$$

As a check, one may set $m = n = 0$, giving the plane case, or $b_2 = b_3 = 0$, vhich gives the special case $n = 0, 1$, described above.

We thus get the following expression for the Fourier component of order m, n:

I. $$M_0 = (A e^{\alpha z} + B e^{-\alpha z} + C e^{\beta z} + D e^{-\beta z}) \sin \frac{m \pi x}{a} \cdot \sin \frac{n \pi y}{a}$$

II. $$N_0 = (E \sinh \gamma z + F \cosh \gamma z + G \sinh \delta z + H \cosh \delta z) \cdot \sin \frac{m \pi x}{a} \cdot \sin \frac{n \pi y}{a}$$

II. $$K_0 = [I \sinh \alpha (z - z_3) + J \sinh \beta (z - z_3)] \sin \frac{m \pi x}{a} \cdot \sin \frac{n \pi y}{a}$$

nd corresponding expressions for M_1, M_2, M_3 etc. In these expressions $\pm \alpha$ nd $\pm \beta$ are the roots of equation (2), for graphite, and $\pm \gamma$ and $\pm \delta$ are the orresponding roots for cadmium. It is assumed that $|\alpha| < |\beta|$.

We have thus 10 unknowns. Continuity at the boundaries gives 8 equations, nd the two remaining equations are provided by the neutron distribution in he plane $z = z_1$, where one must assume an angular distribution. It is in fact he coefficient C which depends on the angular distribution, and C, which in ny case is only important in the region near $z = z_1$, is in our case negligible. Ve thus have 9 equations and 9 unknowns.

The special case $n=0, 1, 2, 3, 4, 5$

If, proceeding as above, we take only A_0, A_1, A_2, A_3, A_4, A_5, A_1^1 and B_1^1 we get the following system of equations:

$$-\frac{\partial A_1^1}{\partial x}-\frac{\partial B_1^1}{\partial y}+\frac{\partial A_1}{\partial z}+b_0 A_0=0$$

$$2\frac{\partial A_2}{\partial z}+\frac{\partial A_0}{\partial z}+3 b_1 A_1=0$$

$$\frac{\partial A_2}{\partial x}-\frac{\partial A_0}{\partial x}+3 b_1 A_1^1=0$$

$$\frac{\partial A_2}{\partial y}-\frac{\partial A_0}{\partial y}+3 b_1 B_1^1=0$$

$$\frac{\partial A_1^1}{\partial x}+\frac{\partial B_1^1}{\partial y}+3\frac{\partial A_3}{\partial z}+2\frac{\partial A_1}{\partial z}+5 b_2 A_2=0$$

$$4\frac{\partial A_4}{\partial z}+3\frac{\partial A_2}{\partial z}+7 b_3 A_3=0$$

$$5\frac{\partial A_5}{\partial z}+4\frac{\partial A_3}{\partial z}+9 b_4 A_4=0$$

$$5\frac{\partial A_4}{\partial z}+11 b_5 A_5=0$$

Making assumptions corresponding to those made in the previous case, we find:

$$a_2=-a_0\frac{\left(b_0-\frac{\alpha^2}{b_1}\right)\left(9 b_4-\frac{25\alpha^2}{11 b_5}-\frac{16\alpha^2}{7 b_3}\right)}{\left(5 b_2-\frac{2\alpha^2}{b_1}-\frac{9\alpha^2}{7 b_3}\right)\left(9 b_4-\frac{25\alpha^2}{11 b_5}-\frac{16\alpha^2}{7 b_3}\right)-\frac{144\alpha^4}{49 b_3^2}}$$

$$a_4=a_2\frac{\frac{12\alpha^2}{7 b_3}}{9 b_4-\frac{25\alpha^2}{11 b_5}-\frac{16\alpha^2}{7 b_3}}$$

$$a_1=-\frac{\alpha}{3 b_1}(2 a_2+a_0)$$

$$a_3=-\frac{\alpha}{7 b_3}(4 a_4+3 a_2)$$

$$a_5=-\frac{5\alpha a_4}{11 b_5}$$

$$a_1^1 = \frac{m\pi}{3\,b_1\,a}(a_0 - a_2)$$

$$b_1^1 = \frac{n\pi}{3\,b_1\,a}(a_0 - a_2)$$

The condition for the determination of α becomes:

$$\begin{aligned} 225\,\alpha^6 - \alpha^4 (&675\,b_0 b_1 + 700\,b_0 b_3 + 704\,b_0 b_5 + 875\,b_2 b_3 + 880\,b_2 b_5 + \\ &+ 891\,b_4 b_5) + \alpha^2 (2625\,b_0 b_1 b_2 b_3 + 2640\,b_0 b_1 b_2 b_5 + 2673\,b_0 b_1 b_4 b_5 + \\ &+ 2772\,b_0 b_3 b_4 b_5 + 3465\,b_2 b_3 b_4 b_5) - 10395\,b_0 b_1 b_2 b_3 b_4 b_5 - \\ &- \frac{\pi^2}{a^2}(m^2 + n^2)\left[\alpha^4 \left(225 + 525\frac{b_3}{b_1} + 528\frac{b_5}{b_1}\right) - \alpha^2 \left(175\,b_0 b_3 + 176\,b_0 b_5 + \right.\right. \\ &\left. + 875\,b_2 b_3 + 880\,b_2 b_5 + 891\,b_4 b_5 + 2079\frac{b_3}{b_1} b_4 b_5\right) + 693\,b_0 b_3 b_4 b_5 + \\ &\left. + 3465\,b_2 b_3 b_4 b_5\right] = 0 \end{aligned}$$

As before, a check can be made by setting $m = n = 0$, giving the corresponding equation for the plane case, and by setting $b_4 = b_5 = 0$ we get the equation found above for $n = 0,\ 1,\ 2,\ 3$.

Analogously to the previous case, the result is a system of equations having 15 unknowns. Continuity at the boundaries gives 12 equations, and the remaining three are provided by the neutron distribution in the plane $z = z_1$. One finds that in this special case two of the unknowns may be set equal to zero, and we thus arrive at 13 equations and 13 unknowns.

Numerical calculations

Numerical calculations have been made with the following assumptions:

$$a = 198.1 \text{ cm}$$

$$z_2 = -0.01 \text{ cm}$$

$$z_3 = -66.65 \text{ cm}$$

Graphite: $\sigma_a = 0.00485$ barns
$\sigma_s = 4.84$ barns
Density: 1.64 g/cm^3

Cd $\sigma_a = 2\,500,\ 2\,750$ and $3\,000$ barns
$\sigma_s = 6.5$ barns
Density: 8.64 g/cm^3

The absorption cross section of graphite has been chosen to fit the case with no cadmium sheet.

For the calculation of the scattering function F it has been assumed that the scattering is isotropic in the centre-of-mass system, and that the atoms are at rest before collision. With these assumptions one gets the following expressions for the F coefficients:

$$F_0 = 1$$

$$F_1 = \frac{2}{3A}$$

$$F_2 = \frac{5}{8} - \frac{3A^2}{8} + \frac{3}{16A}(A^2-1)^2 \cdot \log\frac{A+1}{A-1}$$

$$F_3 = 0$$

$$F_4 = \frac{1}{96}(81 - 190A^2 + 105A^4) + \frac{5}{64A}(1-A^2)^2(1-7A^2)\log\frac{A+1}{A-1}$$

$$F_5 = 0$$

where A is the mass of the scattering atoms. For large A, F_2 may be approximated by $1/5A^2$, and F_4 by $-1/63A^4$.

The amplitude of the "fundamental frequency", i.e. the Fourier component with $m = n = 1$, has been calculated for coordinates corresponding to the measuring planes used experimentally, which were at $z = \pm 16.2$ and $z = \pm 37.8$. The amplitude in the fourth plane has been set equal to 100. The results are given in Table 1.

Table 1

z	A_0 calculated using approximation								Measured experimentally
	A_0, A_1 with σ_{Cd}			A_0, A_1, A_2, A_3 with σ_{Cd}			A_0, A_1, A_2, A_3, A_4, A_5, with σ_{Cd}		
	2 500	2 750	3 000	2 500	2 750	3 000	2 750	3 000	
37.8	100	100	100	100	100	100	100	100	100
16.2	37.50	37.49	37.48	37.87	37.84	37.82	37.87	37.85	38.24
0	3.184	3.153	3.132	3.203	3.167	3.137	3.176	3.145	
− 0.01	0.7941	0.6470	0.5279	0.9959	0.8509	0.7303	0.8901	0.7685	
− 10	0.5752	0.4686	0.3824	1.0472	0.8880	0.7682	0.9067	0.7875	
− 16.2	0.4680	0.3813	0.3111	0.8525	0.7229	0.6254	0.7386	0.6416	0.751
− 37.8	0.2090	0.1703	0.1390	0.3810	0.3221	0.2795	0.3301	0.2867	0,380
− 66.65	0	0	0	0	0	0	0	0	

Experimental measurements

The influence of a 0.1 mm cadmium sheet on the neutron distribution in a rectangular mass of graphite has been measured using the same method as that described by CARLBOM [1]. The geometry of the arrangement is given in Fig. 2, which shows that two of the measuring planes are above, and two below the cadmium sheet. The neutron distribution in the fourth or uppermost plane gives a boundary condition which is used in the theoretical treatment, while the

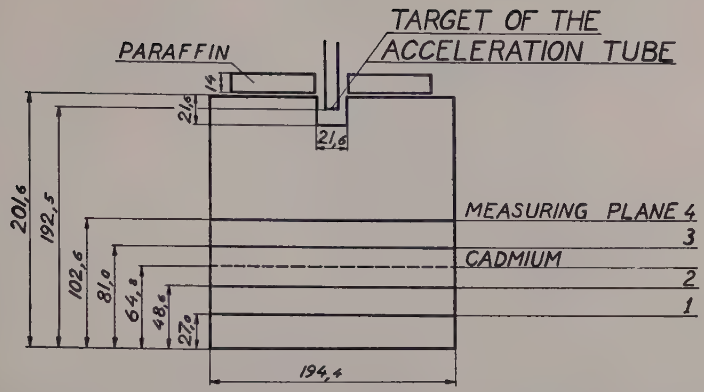

Fig. 2. The experimental arrangement. All dimensions are in centimeters. The graphite mass is shielded on the vertical sides and underneath with cadmium sheets not shown in the figure.

distributions in the three remaining planes are used for comparison between theory and experiment. With this arrangement one thus has one set of values above the cadmium sheet, and two in the more interesting region below it.

In setting numerical values to the symbols of Fig. 1 the dimensions of Fig. 2 have been taken, the values used for a and z_3 being corrected for edge effects in the usual way (see [1]).

The measurements were made at 36 different points in each measuring plane, Mn–Ni foils being used as detectors. The neutron source was a 200 kV neutron generator [5]. The activities were measured with Geiger counters. At the point of greatest neutron density in each plane the number of pulses above background in 64 minutes was roughly as follows:

Plane	With cadmium	Without cadmium
1	750	18 000
2	1 600	40 000
3	90 000	120 000
4	250 000	250 000

Since the background amounted in the same time to about 1 000 pulses, there is a relatively large statistical error on the measurements made in planes 1 and 2 when the cadmium sheet was included. Each measurement in these planes was therefore repeated at least three times.

All measurements of neutron density were made relatively to a monitor foil placed in the fourth plane, and, in order that densities found with and without the cadmium sheet should be comparable, measurements of the monitor foil activity were also made using a Ra Be neutron source, which was assumed to be constant. The ratio between the neutron densities at the monitor without and with the cadmium sheet was found to be

$$1.082 \pm 0.006$$

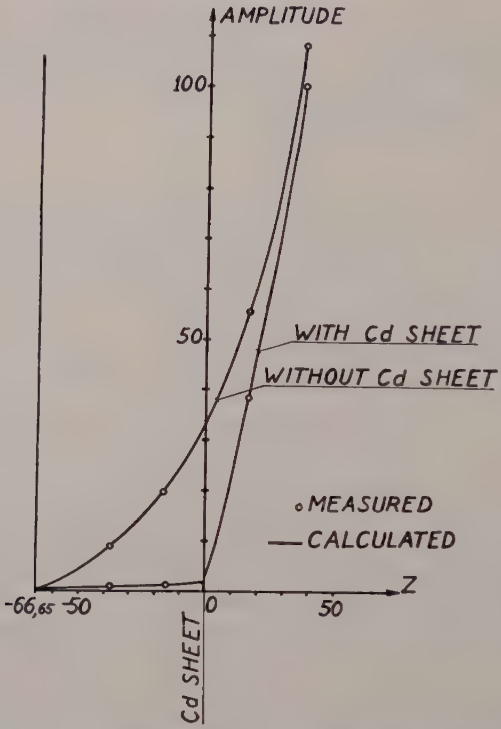

Fig. 3. The measured and calculated values for the amplitude of the fundamental frequency for the cases with and without the cadmium sheet in the graphite. Note the great difference even on the source side of the Cd sheet.

A Fourier analysis was made of the density values found, and the amplitude of the "fundamental" determined for each plane. The amplitude in plane 4, with the cadmium sheet, has been set equal to 100. The results are:

Plane	With cadmium	Without cadmium
4	100	108.2 ± 0.6
3	38.24 ± 0.13	55.54 ± 0.4
2	0.751 ± 0.006	19.51 ± 0.13
1	0.380 ± 0.005	8.73 ± 0.06

Discussion

Fig. 3 shows the measured and calculated values for the amplitude of the fundamental, with and without cadmium. The variations in the calculated values due to the different cross sections assumed for cadmium are so small that they would not be distinguishable on this figure. The influence of the cadmium sheet is very marked, even on the side nearest the source.

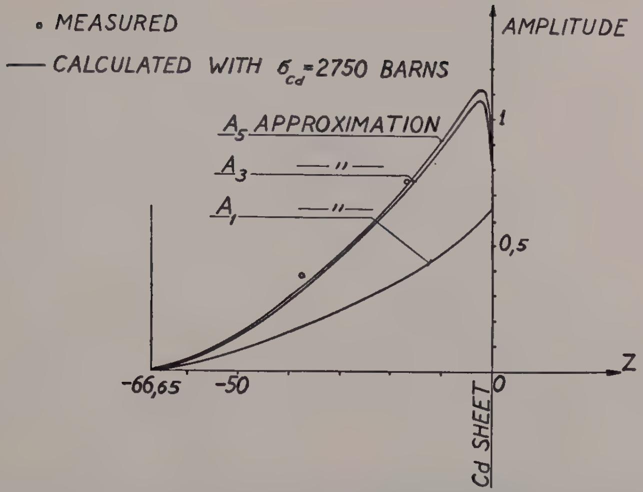

Fig. 4. The calculated values for the amplitude of the fundamental for the different approximations, taking $\sigma_{Cd}=2\,750$ barns. The figure shows plainly the great improvement when using the A_3 and higher approximation instead of the A_1 approximation.

Because of the nature of the neutron source it is difficult to calculate theoretically the ratio between the neutron densities without and with the cadmium sheet. An estimation made using the A_3 approximation and assuming the same neutron flux in both cases at the upper face of the graphite mass gave the value 1.10 for plane 4: this is reasonably close to the measured value $1.082 \pm \pm 0.006$.

Fig. 4 shows the calculated results for the region under the cadmium sheet, using the various approximations and taking $\sigma_{Cd} = 2\,750$ barns. The measured values for planes 1 and 2 are also included in the figure. It is clear that the A_3 approximation is a great improvement on the A_1 approximation, but the difference between the A_5 and A_3 approximations is very small, and there would be little advantage in attempting higher approximations. There is also a great difference between the A_1 and the higher approximations in the form of the curve near the cadmium sheet: the form of the higher approximations is much more as one would expect in the region near a strong absorber [8].

The effect of the cadmium cross section on the amplitude of the "fundamental" as calculated by the A_3 approximation is shown in Fig. 5. The value of the cross section which is in closest agreement with the experimental results can be estimated by interpolation, which is best done by plotting the amplitude of the fundamental in a given plane on a logarithmic scale against the cadmium cross section. This has been done for plane 2: the resulting curve (Fig. 6) is conveniently linear at high cross section values.

In this way the following values are found for the cadmium cross section:

	σ_{Cd} by approximation			
Plane	A_1	A_3	A_5	A_∞
1	$1\,800 \pm 30$	$2\,510 \pm 30$	$2\,540 \pm 30$	$2\,550 \pm 40$
2	$1\,950 \pm 20$	$2\,700 \pm 20$	$2\,730 \pm 20$	$2\,750 \pm 30$

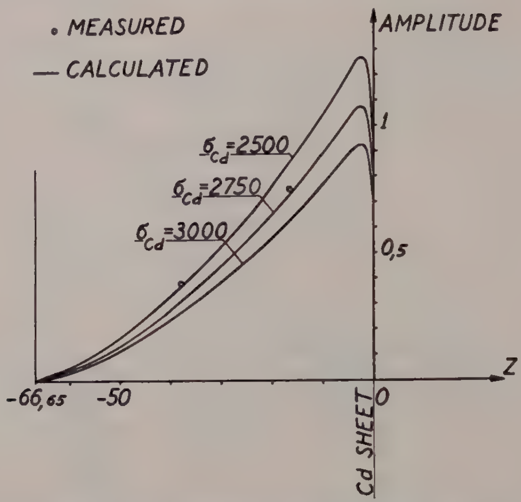

Fig. 5. The calculated values for the amplitude of the fundamental for different cross sections of Cd, using the A_3-approximation.

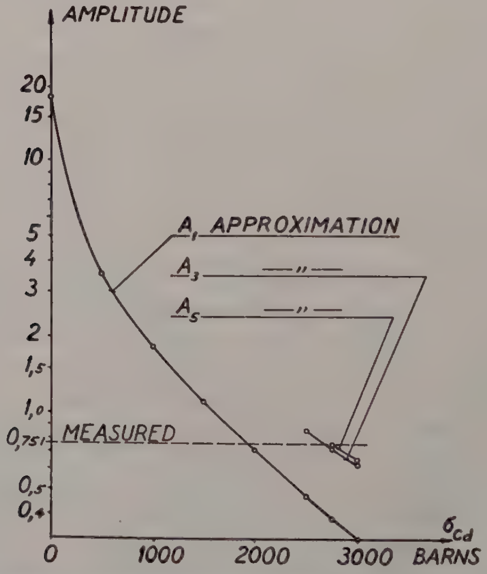

Fig. 6. The calculated amplitude of the fundamental in plane 2 as a function of the cross section, for different approximations. The measured value 0.751 gives the cross section values 1950, 2 700 and 2 730 for the different approximations.

The results for plane 3 have not been used, because their error is large compared to their dependency on the cross section.

An attempt has been made to find by extrapolation the value for the cross section which would result if an infinite number of terms were included in the

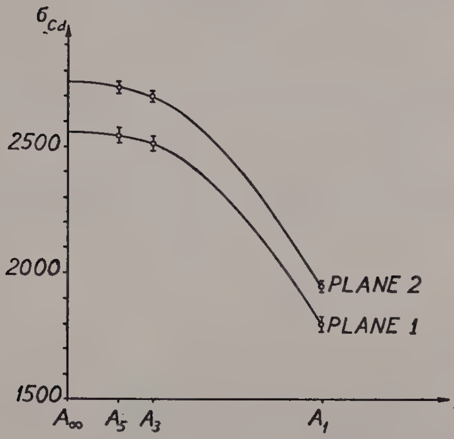

Fig. 7. The cross sections found for different approximations, plotted as functions of the inverse of the order of approximation. The extrapolated values indicate the value vhich would be found if an infinite number of terms were taken, i.e. the exact solution.

series expansion. This has been listed in the above table as A_∞. These values have been found by the use of Fig. 7, where the cross section is plotted as a function of the inverse of the order of the approximation. (The A_1, A_3, A_5 and A_∞ values thus correspond to the points 1, 0.33, 0.2 and 0). This extrapolation is of course very unreliable, but it nevertheless shows that the cross section for A_∞ cannot be much greater than that for A_5. Apart from the errors given in the table there is an uncertainty of at least 5 %, due to variations in the thickness of the cadmium plate. The values found may be compared with those given by Goldsmith *et al.* [6], which is about 2 900 barns for thermal neutrons having a Maxwellian distribution, and more recently by Hughes *et al.* [7], whose corresponding value is $3\,100 \pm 300$ barns.

The reason for the relatively large disagreement between the values for the cross section given above may be statistical error, but it may also be found in the assumptions which were made in the calculations. It was assumed that the neutrons were all of the same constant velocity, whereas in reality they have an unknown velocity distribution. Since cadmium only absorbs neutrons with an energy of less than about 0.3 eV, it is not unreasonable to suppose that those neutrons which have passed through the cadmium sheet have on the average a higher energy than those which have not done so. This would mean that the diffusion length for the neutrons below the cadmium would be longer than that of those above, and so the neutron density would fall off slower than the hyperbolic sine used in the calculation. The sense of the disagreement amongst the results for the cross section supports this argument.

It is of interest in this connection to note that K. E. Larsson [8] found an effect which can be explained in the same way, in his study of the neutron diffusion outside a cadmium sphere suspended in water (see his Fig. 8). The effect is greater in his case because of the higher energy of the primary neutrons.

Acknowledgements

I wish to express my thanks to Dr. S. EKLUND, director of the physical department, to Dr. N. SVARTHOLM and Mr. L. CARLBOM for valuable discussions, and to Mr. M. HÖIJERTZ and Mr. Å. FRANZON for help with the measurements and computations.

Aktiebolaget Atomenergi, Department of Physics, Stockholm.

REFERENCES

1. CARLBOM, L., Arkiv för fysik, in press.
2. MARK, J. C., NRC 1549.
3. ——, NRC 1588.
4. MARSHAK, R. E., BROOKS, H. & HURWITZ, H., Nucleonics *4*, No. 5 and 6 (1949).
5. SJÖSTRAND, N. G., Appl. Scient. Res. *B 2*, 227 (1951).
6. GOODMAN, C., *et al.* The Science and Engineering of Nuclear Power.
7. HUGHES, D. J., *et al.* AECU 2040.
8. LARSSON, K. E., Arkiv för fysik *2*: 7 (1950).

Tryckt den 7 maj 1953

Uppsala 1953. Almqvist & Wiksells Boktryckeri AB

ARKIV FÖR FYSIK Band 6 nr 49

Communicated 11 March 1953 by AXEL E. LINDH and GUNNAR HÄGG

A precision determination of the *K* excitation potential of some 3 *d* elements

By ÅKE NILSSON

With 41 figures in the text

Contents

Acknowledgements 514
Introduction 514

Chapter I. The X-ray tube 515
  A. The contamination of the target 515
  B. Construction 517

Chapter II. Spectrometer arrangements 526
  A. The concave crystal spectrometer 526
  B. The crystals and the crystal holder 527
  C. The Geiger counter 527
  D. The pumps and evacuation system 530
  E. The high voltage equipment 532

Chapter III. The intensity of the spectrometer 534

Chapter IV. Recordings with the spectrometer 535
  A. Adjustment 535
  B. Procedure 537

Chapter V. Measurements of the high voltage 540
  A. The potentiometer circuit 540
  B. The potentiometer resistances 540
  C. The *emf* of the Nife cell 542
  D. Voltage corrections applied 542
  E. The work function 544

Chapter VI. The K excitation curves 553
  A. Chromium 553
  B. Oxidation influence upon the curves 558
  C. Titanium 559
  D. Iron 563
  E. Cobalt 566
  F. Nickel 568
  G. Copper 569

Chapter VII. Comparison of excitation curves and absorption edges 575
  A. Electronic excitation 575
  B. The K absorption edge 577
  C. The resolution of the structure 579

Chapter VIII. Determination of h/e 581
A. Comparison between the two X-ray methods 581
B. The results 581
C. Error discussion 583

Chapter IX. The structure of the excitation curves and the electron theory of metals 584
A. Theoretical outline 584
B. Discussion of the structure 587

Summary 590
References 591

Acknowledgements

The following investigation was carried out at the Physical Laboratory of Uppsala University. After a period of preliminary work research was started in 1948. Some results were to hand as early as 1949–50, but since the apparatus was improved at a later stage, the majority of the results here published was obtained in the year 1952.

I should like to express my sincere gratitude to the head of the Physical Laboratory, Prof. AXEL E. LINDH, for the constant interest with which he has followed my investigations, for valuable suggestions and friendly encouragement.

For some years I have had the pleasure of co-operating with Prof. PER OHLIN and the present investigation is intimately connected with certain questions arising from his earlier work. I wish to thank him for criticism and advice and for the inspiration he has given me both as a teacher and a friend.

I wish to record my gratitude to all my fellow workers at the Physical Laboratory for good advice and interesting discussions. I am indebted to Mr. REGINALD STEDMAN, B.A., for the translation of the Swedish manuscript, and to Mr. JOHN ILIFFE, B.A., for assistance with the English text.

Finally I thank my family in Eslöv whose quiet support and patience have meant so much to me during the course of this investigation.

Uppsala, April, 1953.

Introduction

The present investigation deals with the determination of characteristic X-ray intensities as functions of the voltage of the X-ray tube, in order to find the excitation potentials of certain X-ray lines.

The excitation potential of an X-ray line is the lowest accelerating voltage of the X-ray tube for which the line in question appears. Characteristic radiation is emitted when excited atoms reorganise. The excitation of an energy level is therefore the primary atomic event, to which the measurements correspond.

An X-ray level may be excited by an electron or a photon of sufficient energy. The excitation potential and the frequency of the absorption edge are equivalent quantities, referring to the same amount of energy, eV and $h\nu$ respectively. This fact may be utilised for determination of the constant h/e.

The method of investigating the voltage dependence of X-ray intensities in order to find the position of atomic energy levels was early applied to the soft

X-ray region. [Cf. SIEGBAHN 1931, p. 434.] The radiation from the anticathode impinged directly on a metal surface, and the photo-current from this surface was determined as a function of the X-ray tube voltage. An investigation on these lines carried out by SKINNER [1932, 1933] introduced many of the problems recurring in the present investigation, such as target contamination and the work function correction.

A considerable improvement in technique is made possible by the construction of high intensity spectrometers with sensitive detectors such as the ionisation chamber, the Geiger counter and the photomultiplier. Use of monochromatic radiation greatly simplifies the problems involved. However, very few investigations of excitation potentials have been reported in the last two decades.

PARRATT [1936] made beautiful determinations of excitation potentials for satellite lines in the K spectrum, using a double crystal spectrometer and ionisation chamber.

Later, BEARDEN & SCHWARZ [1941], determined excitation potentials for Ni, Co, W and some other metals, and by numerical comparison with corresponding absorption edges, arrived at a figure for h/e.

The present research was undertaken in connection with precision determinations of h/e from the short wavelength limit of the continuous X-ray spectrum and investigations of the fine structure in the neighbourhood of this limit [OHLIN 1941, 1942, NILSSON & OHLIN 1946]. The original purpose was to endeavour to make a new determination of h/e, and at the same time to obtain data relevant to the problems associated with the work function correction. It was soon clear that a high degree of resolution could be achieved in determinations of excitation potential, and the unexpected detail richness of the curves obtained brought into the picture problems belonging to the sphere of solid state physics. The purity of the target — an essential factor in determinations of this kind — became one of the main experimental objects of attention.

Some questions of nomenclature may be made clear:

1) The curves obtained are consistently called excitation curves, as distinct from absorption curves, though the latter are also in a sense excitation curves. 2) The term "excitation potential" can be given a wider meaning than a single threshold value for a spectral line: it can refer to transitions to the bottom of each unoccupied energy band for which these transitions are connected with an abrupt increase in the recorded intensity. 3) By analogy with absorption curves, the word "edge" is also applied to the excitation curves, where there is no risk of misunderstanding.

Chapter I. The X-ray tube

A. The contamination of the target

One of the most troublesome problems in the present investigation was the contamination of the target while in operation. It is well known that a certain amount of vapourisation of the cathode cannot be avoided. Tungsten lines appear sooner or later in the spectrum from an X-ray tube with tungsten cathode. In order to minimise such difficulties, OHLIN constructed a tube with a large distance between the cathode and target for determinations of h/e. A magnetic lens was incorporated for the purpose of regulating the size and position of the focal spot. This tube was tested in connection with measurements of the Ohlin structure at the quantum limit of continuous spectra, and is described in the paper by NILSSON and OHLIN [1946]. The cathode used on that occasion was of unipotential oxide-coated type, which obviates the deterioration in the voltage resolution caused by the voltage drop across a tungsten cathode.

The first attempts to obtain excitation curves were made with this X-ray tube. Fairly reproducible curves were obtained with a powder anticathode; some K excitation curves were taken for calcium's Kα_1 line with calcium oxide as anticathode. But similar experiments with chromium and titanium were entirely unsuccessful. This proved to be due to the rapid formation of a contaminating layer on the focal spot. Organic molecules with abundant carbon from vacuum seals and pumps are distintegrated by the electron beam, leading to the deposition of a layer of free carbon on the target. Oxides and sulphides are also formed by oxygen and sulphur in the tube's residual gases. Since electrons accelerated by a voltage as low as that used here do not penetrate far in solids, the X-radiation is emitted from a very shallow surface layer. The characteristic radiation of the target metal is therefore increasingly repressed as the contaminating layer becomes thicker. With a powder anticathode, on the other hand, the target continually recovers from contamination as grains of the powder are loosened by the electron bombardment, exposing fresh surfaces of the powder. A powder anticathode, however, must be unsatisfactory for measurements where even small temporary variations of intensity may distort the results.

Instead of using a powder anticathode special precautions were taken to obtain an exceptionally clean vacuum, in order to eliminate contamination of the focal spot, at least during the time necessary for the determination of an excitation curve. This attempt was eventually successful, at first with red-hot anticathodes, and later even with cold. In metal X-ray tubes it is not possible to abolish all oxidation, as the degassing of the walls can never be perfect. In such tubes, under given vacuum conditions, there is for each element a maximum time for the determination of an excitation curve before oxide formation produces too large a distortion of the measurements. This maximum time was found to vary with different anticathodes from about ½ hr. for the easily oxidised elements to over 2 hrs. for metals such as chromium and nickel. A moderate increase in the target temperature effected a considerable reduction of oxidation, and it was in fact necessary to use higher target temperatures for cobalt and iron. (See the descriptions of the individual excitation curves in Chapter VI.)

The necessity for complete purity of the target surface is, as mentioned above, connected with the rapid absorption of an electron beam by solids. It is possible to estimate the retardation of the electrons quantitatively either by the Thomson-Whiddington law [see for instance TERRILL 1923], or with the help of an expression formulated by WILLIAMS [1930–31]. According to such calculations a carbon contamination of 100 Å retards a 10 kV electron beam by about 25 eV and a tungsten layer of the same thickness by about 200 eV. The 10 kV electron beam is totally absorbed by a metal target of the elements used in this investigation in a layer of, or less than, ½ micron.

The deposition of carbon on surfaces bombarded with electrons has been treated in detail in connection with the electron microscope [KÖNIG 1948 and references there].

Another important type of target contamination is the oxidation occurring during the evaporation from the metal furnace used. This oxidation is dependent on the degassing, on the degree of vacuum, and on the rate of evaporation. There is a greater risk of oxide contamination of the evaporated layer if evaporation is relatively slow [STAHL 1949, LEVINSTEIN 1949]. During the Cr Kα_1 measurements, an attempt was made to obtain excitation curves for chromium films, 100 Å thick, evaporated on to a Be layer. The excitation potentials for these films corresponded to the K absorption edge of Cr_2O_3. This result showed that the chromium layer was considerably oxidised.

The ordinary well known conditions for obtaining a pure vacuum must be strictly considered if the resolving power of the high voltage set employed is to be fully utilised. A summary of such important vacuum factors is given below: (1) The evacuating system should have a high pumping rate and low limiting vacuum. (2) Backstreaming of oil vapour from the diffusion pump or other parts of the apparatus must be effectively prevented. (3) Vacuum connections should be of large bore. Surfaces liable to appreciable rise in temperature under operating conditions should not be enclosed in spaces with narrow openings. (4) All parts of the apparatus exposed to higher temperatures under operating conditions should be effectively degassed beforehand, preferably at a temperature above the operational temperature. (5) Metal surfaces heated under operational conditions should not contain metals with high vapour pressures. Brass should be avoided in parts not effectively water-cooled, and likewise soft solders. (6) The inner surface of the X-ray tube should not include organic sealing substances liable to give off vapour at operating temperatures. All indispensable organic sealing substances should adjoin well-cooled surfaces, and should be isolated from the high vacuum space by long diffusion paths. Rubber seals and Glyptal laquer belong to this category. Picein seals should be totally avoided. (7) The effect of cathode evaporation or sputtering should be reduced to a minimum by having a large distance between the cathode and target, by screening non-emitting parts of the heater filament, and in the case of oxide cathodes, by applying a thin layer of oxide as well as careful formation and degassing. (8) A furnace for the renewal of the target surface with an evaporation film under vacuum should be mounted inside the X-ray tube. (9) The electron beam should be well concentrated, so that stray bombardment of badly cooled surfaces does not take place. (Good electron-optical symmetry and central beams.) (10) Provision should be made to deviate the electron beam from the anticathode after renewal of its surface, so that it is not under bombardment while other preparations are being made for intensity measurements.

B. Construction

The X-ray tube previously mentioned was reconstructed in complete conformity with these principles, and its final form is shown in Figs. 2–8. The parts liable to be bombarded with electrons were made of copper, and the other inner surfaces were of porcelain or brass. All vacuum seals were either rubber rings or Glyptal lacquer. The rubber rings were treated with warm potassium hydroxide solution [after YARWOOD]. Glyptal lacquer was dried in an oven at 120° C, after which its vapour pressure is comparable with that of brass [JNANANANDA].

The removable *target* was a cylinder of copper fitting tightly into the water-cooled copper holder, to which it was fastened by screws through the basal flange. Figs. 4 and 7. The target in Fig. 7 a was used for excitation curves at high temperatures. A molybdenum pin was screwed into the short copper base, its head being slotted to take the inset anticathode plate. The temperature of this plate depended on

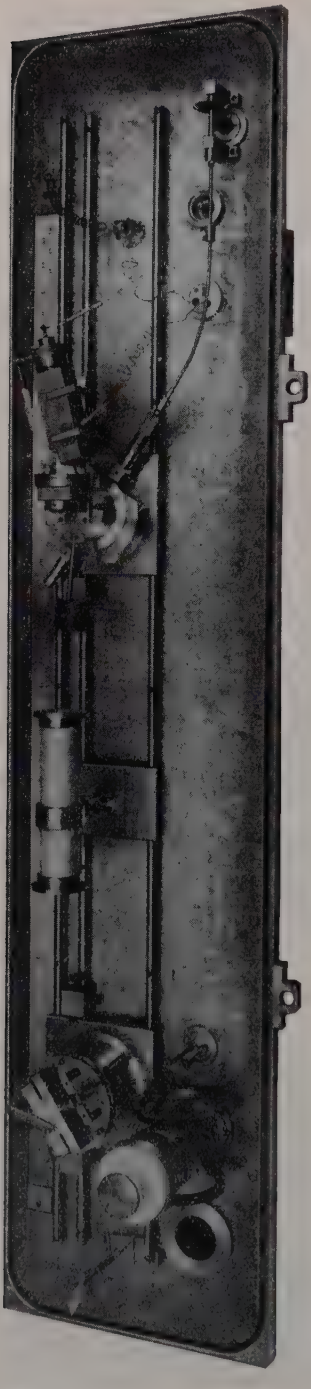

Fig. 1. View of the spectrometer table.

To the left the upper part of the X-ray tube, and the crystal holder; in the centre a screen against scattered radiation; to the right the slit and Geiger counter on their mounting, and a lamp to illuminate the micrometer scale.

the diameter of the pin and the intensity of bombardment, and could be regulated over a wide range. The principal type of target used is shown in Fig. 7 b. It was made of copper, and was used in conjunction with the metal evaporation furnace. The radiating surface was at an angle of 71.6° to the axis. There must be a certain temperature gradient in the copper cylinder, and a rough estimate gave the temperature at the focal spot as about 100° above room temperature with an emission current of 20 mA. For some metals it was desirable to increase the temperature some hundreds of degrees. Since the metals in question were all relatively poor conductors of heat, this higher temperature was obtained by using a plate of the metal, fitted tightly into the slot in the end of the copper cylinder.

The target was observable under bombardment through a window in the lid of the spectrometer, by means of two aluminium mirrors and a telescope. Incandescent temperatures were measured with an optical pyrometer, which was corrected for the reflections at the two aluminium mirrors. The aperture at S in Fig. 4 had to be kept open when the target was observed visually, and a pyrex-glass tube was then fitted over the copper cylinder to isolate the tube and spectrometer vacua from one another.

The evaporating furnace and its mounting are shown in Fig. 8. The mounting was attached to the cooling jacket, and bored with a hole of sufficient diameter to allow the electron beam to pass unobstructed through the centre when the X-ray tube was in normal operation. The furnace was made of molybdenum, which can be machined without difficulty. Tungsten would have been better with regard to its lower vapour pressure, but attempts to make a tungsten furnace had to be abandoned because of the metal's hardness and brittleness. The vapour pressure of molybdenum is sufficiently low at 1500° C not to affect evaporation of the target metal [LAW 1948]. (A provisional tungsten furnace was made for the evaporation of titanium,

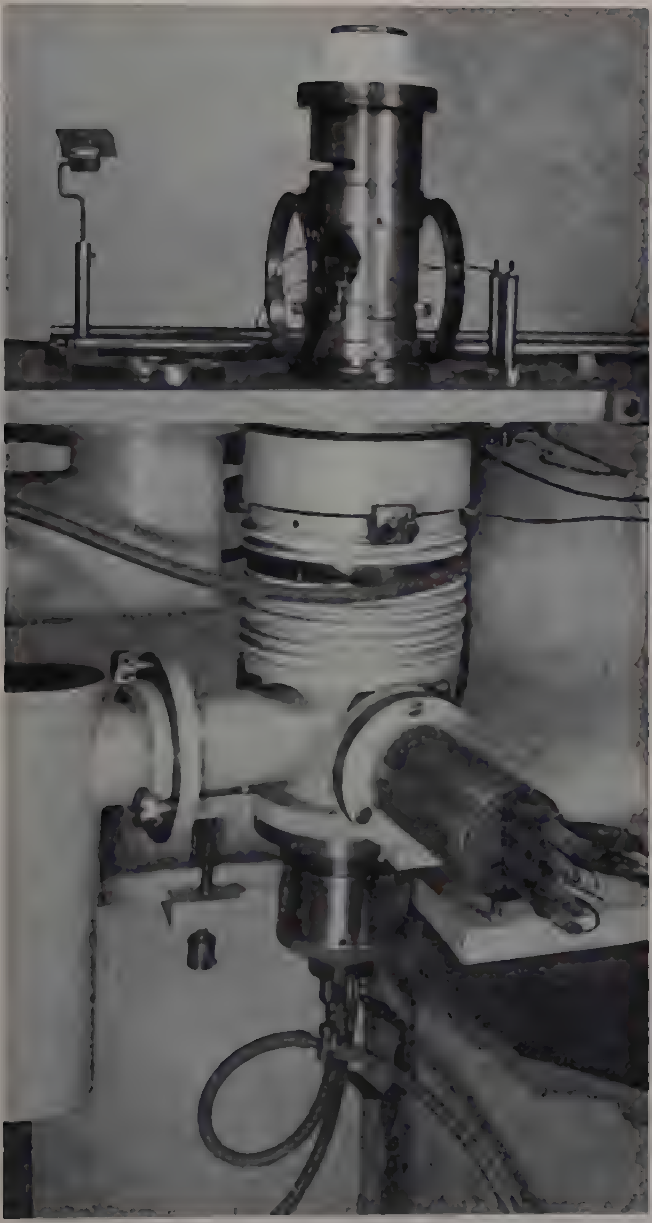

Fig. 2. View of the X-ray tube.

The radiation emerges from the horizontal slit near the top. Between this slit and the spectrometer table are the deflector coils and the circular opening through which the anticathode can be observed with the help of mirrrors when the tube is in operation. The iron case of the focusing coil is visible below the spectrometer table, the cathode and ionisation gauge lower down. To the left are the evacuation tubes to the spectrometer and X-ray tube, the latter fitted with a liquid-air trap.

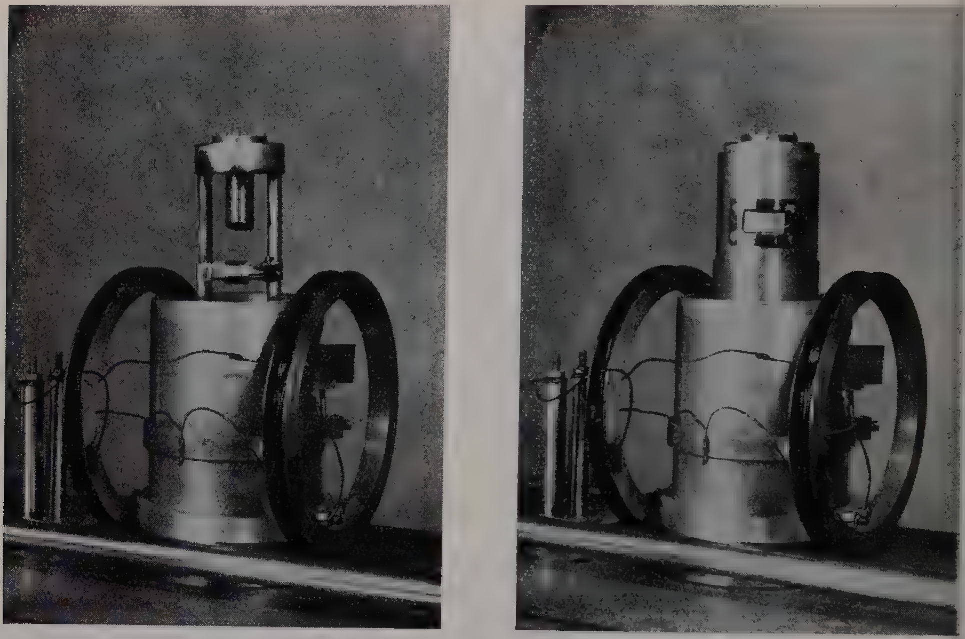

Fig. 3. The X-ray tube dismounted for changing of the target.

The earthed outer cover is removed in the right-hand figure, revealing the anticathode housing. This too is removed in the left-hand figure, showing the target and evaporation furnace.

which requires a temperature of 1800° C.) The furnace was heated by means of the electron beam, which was deflected from its normal central course for this purpose. The thick walls of the furnace ensured a uniform temperature distribution and a reproducible evaporation rate. At a given voltage, this rate could be determined in terms of the electron current. The furnace was calibrated in this respect by measuring the Kα_1 intensity of the evaporated element with copper or beryllium as target base. The intensity increases as evaporation proceeds until the layer deposited on the anticathode is so thick that the electrons penetrating the entire layer are retarded to such an extent that they can no longer emit the Kα_1 frequency, neither in the

---

Fig. 4. Section of the upper part of the X-ray tube.

A – porcelain insulator for centring the copper tube *E*.
B – exchangeable target. Fig. 7.
C – window covered with thin metal foil (Al or Ni).
D – evaporation furnace and mounting. Figs. 3 and 8.
E – anticathode housing of copper.
F – cooling tubes to the anticathode, in the figure turned 90° from their proper position.
G – coils for deflecting the electron beam.
H – spectrometer table.
I – focusing coil in soft iron case.
K – adjustment screw for the focusing coil.
L – brass plate supporting the anticathode system.
M – copper anode with a 6 mm aperture and an outer ring of evacuation holes. *L* and *M* are short-circuited.
N – water-cooling.
O – porcelain insulator.
P – inlet for cooling water to the anticathode.
Q – porcelain insulator.
R – grooves for rubber rings.
S – rotatable copper cylinder for closing the inner mirror window.
T – collar for the removable part of the outer cover.

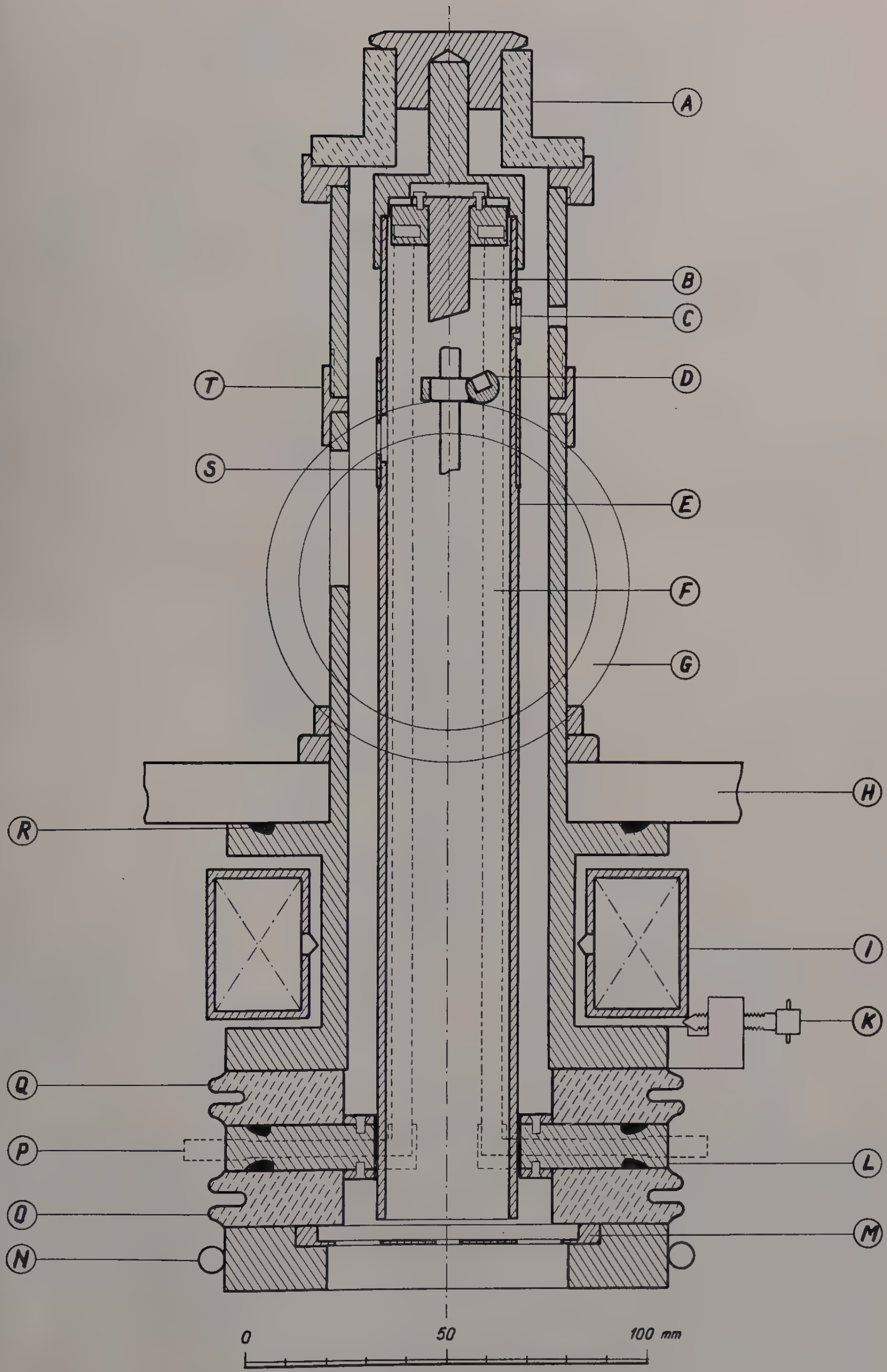
A
B
C
D
T
S
E
F
G
H
R
I
K
Q
P
L
O
M
N
0
50
100 mm

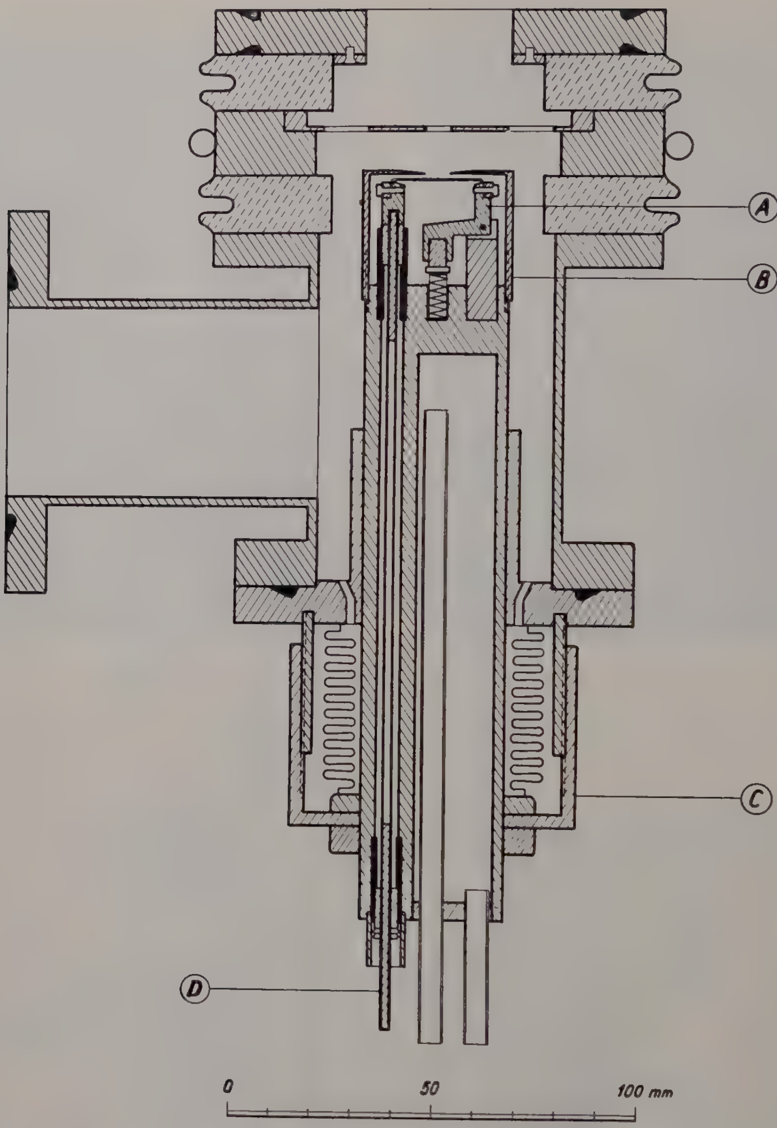

Fig. 5. Section of the lower part of the X-ray tube with the tungsten cathode.

A – pivoted cathode support, fitted with a spring to stretch the filament.

B – earthed cathode shield with 6 mm circular aperture.

C – threaded cylinder for adjusting the height of the cathode.

D – insulated steel rod, the outer end water-cooled when the tube is in operation.

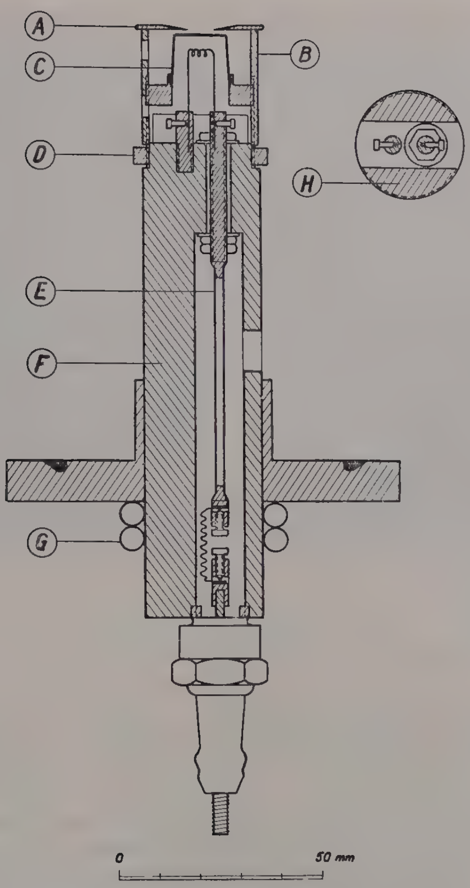

Fig. 6. Oxide-coated cathode.

A – nickel plate with 6 mm circular aperture, the height adjustable by means of the threaded brass cylinder *B*.
C – platinum cap for the oxide coating, with a flanged iron base adjustable vertically.
D – lock nut.
E – steel rod with insulating sheath. Longitudinal expansion is taken up by the free lower end, and thus does not move the insulated filament support.
F – solid copper rod.
G – water cooling.
H – filament base, horizontal section.

continuous spectrum nor in the characteristic. Evaporation rates giving this minimum layer in 2–5 minutes were preferred.

Special difficulties were encountered in evaporating nickel. Nickel readily forms an alloy with molybdenum, and its vapour pressure is then lowered considerably. The lowest melting point for a Mo-Ni alloy is a theoretical upper temperature limit for the evaporation furnace. But this temperature gave too low an evaporation rate. Attempts to separate the nickel from the molybdenum by graphite were unsuccessful because of carbide formation. The carbides formed a skin over the nickel surface [cf. SKINNER & JOHNSTON 1937]. Success was finally achieved by inserting a tungsten

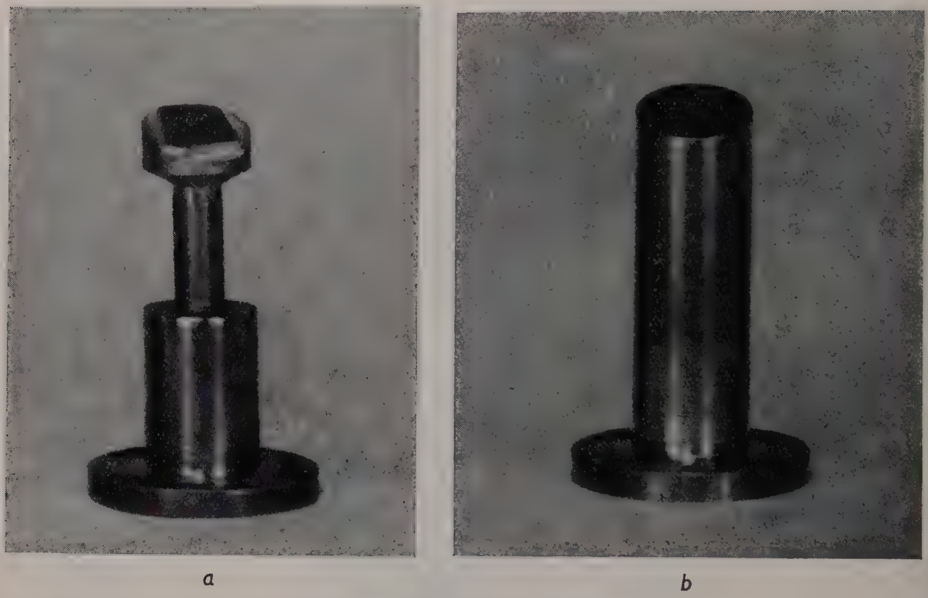

Fig. 7. Two types of target.

a. Molybdenum pin screwed into a copper base, with a wide slot for the target plate.
b. Solid copper target with a polished end surface to take the evaporation deposit.

crucible in place of the graphite, whereupon temperatures giving a good rate of evaporation were attained. A tungsten crucible with an evaporation plate is shown to the right of Fig. 8.

The experience gained with nickel was utilised in dealing with iron and cobalt. The evaporation temperature for these three elements was the melting point or just under (about 1500° C). Chromium and copper, neither of which wets a molybdenum surface, were both evaporated directly from the molybdenum furnace, at about 1100° C in each case. Titanium was evaporated just above its melting point (1720° C). The vapour pressures at the evaporation temperatures used were some hundredths of a mm Hg [LAW 1948].

Each time the spectrometer had been opened, the furnace had to be carefully degassed. This was performed at a temperature 100–200° lower than the evaporation temperature. The rate of evaporation is then decreased by about a power of ten. After degassing, a film three to four times the minimum thickness (see above) was evaporated on to the anticathode before the intensity measurements were commenced.

The cathode. Both oxide-coated cathodes and tungsten cathodes were used, the latter for the main determinations, the former to investigate the effect of the work function on the excitation potential.

The tungsten cathode is shown in Fig. 5. The filament was straight, with a free length of 22 mm and a diameter of 0.35 mm. It was kept taut by means of a spring arrangement, and was screened from the interelectrode electric field so that only a small central part emitted. The size of the emitting part could be estimated from the size of the focal spot, which was a comparatively sharp, enlarged image of the emitting wire. The length of the focal spot was about 6 mm, and the magnification

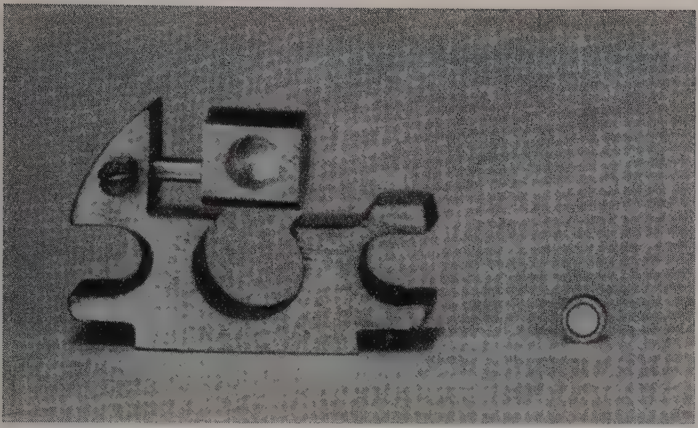

Fig. 8. Evaporation furnace of molybdenum with a copper mounting.

To the right a small wolfram crucible used when evaporationg iron, cobalt and nickel.

produced by the magnetic lens (I, Fig. 4) about 2, so the emitting length of the filament was about 3 mm, a seventh of the filament's total length. The heater voltage was 1.7–2.1 V, which means that the voltage drop across the emitting part of the wire must have been about 0.3 V. In view of this slight drop, the tungsten may be described as a cathode nearly unipotential.

The heater circuit is given in Fig. 13. The heater current was obtained from a lead accumulator, B6. Since this current was 10 A and the determination of a curve took several hours, the accumulator voltage fell slightly during the interval. A corresponding drop in emission was avoided by inserting the battery B5 (low internal resistance) in parallel with filament and the rheostat R7. The fixed resistor R8 was chosen so that a very small current was taken from B5. The B5 battery potential was thus kept constant, and consquently the heater current as well. The arrangement was convenient in operation, and variations in the electron emission did not exceed 0.1 %.

The construction of the oxide cathode is indicated in Fig. 6. The base metal used was originally nickel, but later platinum. The oxide-paste was obtained from *Schönander*, Stockholm, and contained roughly equal amounts of barium and strontium, with a slight addition of calcium. When degassing and formation were carried out carefully, emission was steady (though not to the same degree as with the tungsten cathode). The shortening of the oxide cathode's life due to the admission of air into the spectrometer was a serious disadvantage, however. The emission from the oxide cathode was very sensitive to variations in the residual gases, and was markedly affected by the degassing procedure prior to measurements. The oxide cathode is strictly unipotential, but this property is not balanced by the disadvantages mentioned. Yet another disadvantage is the fact that the work function for an oxide cathode is not known with the same exactitude as that for tungsten, about which more will be said in a later chapter.

The electron beam was employed for three purposes: it was used for degassing the X-ray tube, for heating the evaporation furnace, and for the production of X-rays. It was controlled by means of two electron lenses and a deflector coil.

The cathode and anode plate in combination can be described as an electrostatic acceleration lens. Centring should be precise, in order to avoid unnecessary spreading. Increasing the distance between the cathode and anode diminishes the angular aperture of the beam and increases the electron current to the anode. With the tungsten cathode a larger distance gave better focusing. At 20 mA emission, the current loss was about 1 mA with the distance actually used.

The encased coil I in Fig. 4 was a convergent electron-optical lens focusing an image of the emitting section of the cathode on the target when the current through it was correctly adjusted. A horizontal linear image could be obtained with the tungsten cathode. Magnetic lenses have a focal length proportional to V/i^2 — where V is the beam voltage and i the coil current — so a certain amount of blurring occurs when V varies. This effect must be taken into account when large voltage ranges are involved. When emission and voltage are constant, the X-ray intensity produced varies with i, and has a maximum for a particular value of i. This value of the coil current was taken as the operating current.

The deflector double-coil is shown in Figs 1–4. It was used to deflect the electron beam: (1) against the target housing for degassing, (2) against the furnace for evaporating metals, (3) from the normal focal position to protect a clean target, and (4) to broaden the focus, in order to even out the temperature and the radiating target surface. The latter effect was achieved by sending an alternating current through the coil, causing an oscillation of the beam. Such oscillation of the electron beam did not effect the X-ray intensity when the focus was central and the slit and crystal correctly adjusted.

Window C in Fig. 4, for X-rays, was covered with a thin metal foil. This was of 0.5 μ aluminium except when the heat from the furnace might have affected this metal. In such cases a 1–2 μ etched nickel foil was used.

Degassing was checked by two vacuum gauges — an ionisation instrument connected to the X-ray tube (Fig. 2) and a Pirani manometer between the mechanical pump and the booster pump. Both gauges were highly sensitive to degassing pressures. Degassing was satisfactory if neither gauge showed any pressure increase when the electron beam was swung over from the target to the target housing or the furnace.

Chapter II. Spectrometer arrangements

A. The concave crystal spectrometer

The high-vacuum spectrometer used for this investigation was constructed by OHLIN for the determination of Planck's constant from the short wavelength limit of the continuous X-ray spectra. This spectrometer was one employing a bent crystal [JOHANN 1931] and has already been described in detail [OHLIN, Diss. 1941]. Parts of the apparatus that have been used unaltered will therefore be described but briefly here. The changes necessitated by the special requirements of the present investigation apply chiefly to the previously described X-ray tube, the Geiger counter, and the vacuum system.

The body of the spectrometer was of wrought iron which has a very low porosity, imparting good vacuum properties to the walls of the chamber. The base was made from an I-section beam, and the lid from a segment of a boiler tube. Both were reinforced with welded flanges and plates. The ground, plane upper surface of the

I-beam was the spectrometer table. Holes were bored in it for evacuating, for the X-ray tube, and for mechanical attachments. Fig. 1. The spectrometer was made vacuum tight by means of rubber rings.

The main parts of the spectrometer were the X-ray tube, the crystal, and the detector, consisting of slit and Geiger counter.

The position of the X-ray tube was fixed, at a short distance from the crystal. The tube could be turned to give radiation in the desired direction.

The tables for crystal holder and for the detector could be moved longitudinally along steel rods and locked in any desired position. The crystal table was provided with a circular scale, and could be rotated to give the required angle of reflection. The slit and target were fixed at the same level above the spectrometer table, while the level of the crystal could be varied.

The slit consisted of two steel edges, one of which was adjustable. By means of a lever arrangement the slit could be turned to a position exactly parallel with the X-ray line investigated.

The slit, the Geiger counter, and a counterweight formed a single unit. It was possible to turn this unit about a vertical axis through the slit, and to move it in a straight line in a direction chosen. This was accomplished by a construction involving a cone and micrometer slide. Fig. 10. The slide was arranged to give a motion along the tangent to the Rowland circle for determining the position and intensity distribution of an X-ray line. Satisfactory reproducibility of the slide position had been obtained by a ball-bearing arrangement that rendered the motion almost frictionless. The position was adjusted by means of a micrometer screw, manipulated externally through a rotatable vacuum connection. The scale of the micrometer screw could be read through a window in the lid of the spectrometer.

B. The crystals and the crystal holder

The crystals were bent in steel holders with precision ground cylindrical surfaces of 1000 mm radius. The holders were so designed that stresses in the bending pieces were reduced to a minimum [HAGLUND 1941]. The dimension of the crystals were 15 × 25 × 0.5 mm.

The Ti $K\alpha_1$ line was recorded with quartz $10\bar{1}1$ [$d_1 = 3335.74$ X.U., BROGREN & FRISKOPP 1948], and the other lines with topaz 101 [$d_1 = 1352.86$ X.U., SILFVERBERG 1944]. Both crystals give high intensity in the first order reflection [INGELSTAM 1939].

The quartz crystal was supplied by *l'Optique Scientifique* and the topaz by *Steeg & Reuter*.

The opening of crystal holder was 2 × 12 mm for quartz and 1.5 × 12 mm for topaz. The entire reflecting surface of the crystal could be utilised. The radii of the crystal surfaces were within 1 % of that of the bending pieces.

Scattered radiation was screened by a knife-edge stop in front of the crystal.

C. The Geiger counter

The wavelengths of the X-ray lines investigated were between 1.5 and 2.7 Å. The usual Geiger counters with argon or krypton have low efficiency in this range. Xenon has the L_{III} absorption edge at 2.6 Å, and in the range immediately below

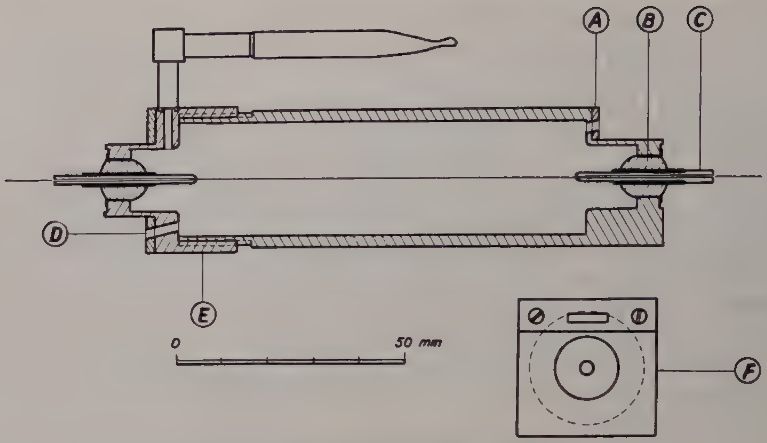

Fig 9. Section of the Geiger counter.

A – front window.	*D* – the rear window.
B – glass seal.	*E* – removable threaded end piece.
C – brass rod, drilled to take the central anode wire.	*F* – the counter seen from the front.

this value xenon's linear absorption coefficient is 4 or 5 times as large as krypton's and 6 to 8 times as large as argon's. Counters are seldom filled with xenon, however, partly because of the low mobility of xenon ions and partly because of the difficulties to get the counters to function. It is customary to increase the efficiency of the argon counters by raising the pressure, but this necessitates an undesirable increase in the starting potential.

Xenon-filled counters were used for the present investigation. The ionisation potentials of xenon and ethyl alcohol are too close for alcohol to be used as quenching agent [Brogren 1949]. But ethyl ether may be used. The ionisation potential of xenon is 12.08 V and of ethyl ether 9.72 V [Morrison & Nicholson 1952].

A diagram of the Geiger counter is given in Fig. 9. The X-ray beam passed through the tube diagonally in order to utilise the longest possible absorption path.

The ends of the anode wire in a Geiger counter are usually surrounded by tubular quartz insulators, which prevent a continuous discharge in the narrower parts of the tube. But such insulators give rise to insensitive volumes. Quartz tubes can be avoided if the anode is connected with end wires of a suitable larger diameter. In the Geiger counter used, the anode wire entered the tube through axial holes in brass rods of 2 mm diameter (C), soldered to commercial glass-metal seals. The ends of the brass envelope were bored with large diameter holes, barely allowing sufficient space for the two windows A and D. By this arrangement the brass sleeves could be drawn back towards the end of the main volume, without affecting the length of the plateau. The field achieved is such that no dead spaces occur, which is of great importance for the efficiency of the counter, since the greater part of the incident X-radiation is absorbed close to the window A.

The end piece E was removable to facilitate internal cleaning when refilling the tube. It was threaded on to the main section. The window D was provided for easy adjustment of the Geiger counter in the spectrometer.

The dimensions of the main volume were 25 × 90 mm. The radius of the end holes

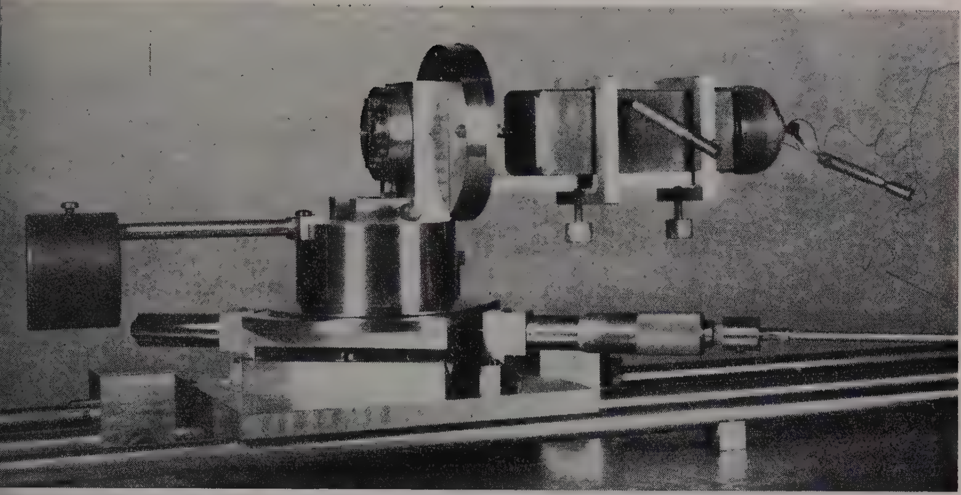

Fig. 10. The Geiger counter on its carriage.

The slit may be seen in front of the counter. The counter, slit and counterweight are mounted as a unit hich may be moved along the tangent to the Rowland circle by means of the micrometer screw visible ower down in the photograph.

vas 7 mm. The windows, 9 × 2 mm, were covered with 20 μ cellophane. The anode vas made of 0.15 mm molybdenum wire.

The counter was finally sealed with Glyptal lacquer, which was dried at 80° C since he cellophane windows did not tolerate higher temperatures. Special grooves were ut around the windows to prevent Glyptal lacquer coming into contact with the gas nside the tube. Since Glyptal absorbs ethyl ether to some extent, its presence would horten the life of the counter. The end piece E was also sealed with Glyptal lacquer, ainted around the outer end of the thread.

The counter was filled with xenon at 75–90 mm, and 10 mm ether. The $K\alpha_1$ lines nvestigated were absorbed 80 to 100 % (except Ti $K\alpha_1$ which lies on the wrong side f the L_{III} edge of xenon).

Fig. 11 shows an example of a plateau curve. The length of the plateau was about 50 V. It will be seen that the slope is very slight; it varied between 0.01 and 0.025 % er volt for four counters used. The slope of the plateau is principally due to spurious ounts and dead space. The small slope of the counters used indicates that these rawbacks were insignificant in the present case.

Since the components in the xenon-ether counter give heavier ions than those f an argon-ether tube, the dead-time of the former must be expected to be longer. he mean value of the dead-time measured on four occasions with newly filled tubes vas $(9.7 \pm 0.8)\ 10^{-4}$ seconds.

The life-time of the xenon-ether tube is comparable with that of the argon-alcohol ube, provided ether-absorbing substances are eliminated. When the counter died, t had to be taken apart for cleaning of the cathode and changing of the wire. Re-illing of uncleaned counters is not advisable, since the discharges lead to formation f heavy hydrocarbons which are deposited on the walls of the tube [cf. Farmer & rown 1948]. An interesting corroboration of this was given by a double-counter

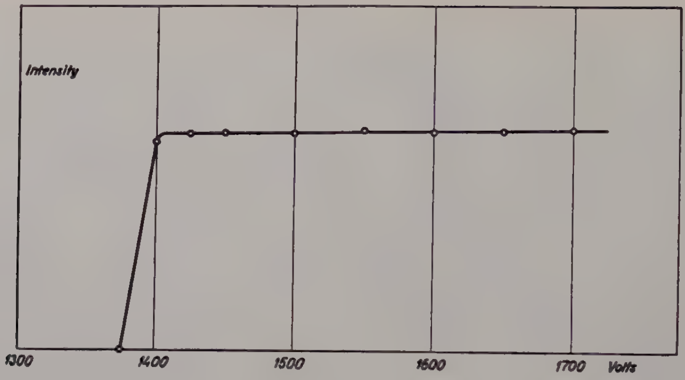

Fig. 11. The plateau curve of the Geiger counter filled with 75 mm xenon and 12 mm ethyl ether

used for the first determinations. The counter consisted of two single tubes coupled together with parallel anodes and with the gas in common. The incident radiation was perpendicular to the anode wires. When the tube subjected to the most intense radiation died, the other tube still had a perfectly good plateau, despite the fact that the gas mixture was common to them both.

A quenching circuit of Neher-Pickering type was used [Neher & Pickering 1938], and the pulses were recorded by a scale-of-64 and a Cenco mechanical high-impedance counter. The resolving time of the scaler was some microseconds. The scaler and the quenching circuit were supplied by the *Atomic Instrument Company* (Models 101-A and 203).

The mounting of the Geiger counter in the spectrometer is shown in Fig. 10.

D. The pumps and evacuation system

The high vacuum was obtained with a three-stage oil diffusion pump, preceded by a mechanical pump and booster diffusion pump. The high-vacuum pump contained octoil-S and the booster pump silicone oil (DC 703). The final vacuum was 10^{-6} mm Hg, the booster pump by itself giving 2.10^{-5} mm.

Both the diffusion pumps were kept constantly under vacuum. The spectrometer was evacuated to a few thousandths of a mm Hg by the mechanical pump, bypassing the diffusion pumps. The final pump was used only with high vacua (pressure less than 10^{-4} mm Hg).

Backstreaming of oil vapour from diffusion pumps is a well known fact [cf. Parratt & Jossem 1952]. It was absolutely essential that this phenomenon was completely prevented in the present investigation, to which end the system of traps shown in Fig. 12 was introduced. These traps lowered the pumping rate to some extent, but this was not inconvenient as the main factor determining the time of evacuation was the slow degassing of the spectrometer.

The final pump is G in Fig. 12. The water-cooled copper baffles at F were a sufficient barrier to oil vapour to prevent visible deposition of oil on the surface above them. The final obstruction to backstreaming oil vapour was the liquid air trap E, the lower end of which was surrounded by charcoal.

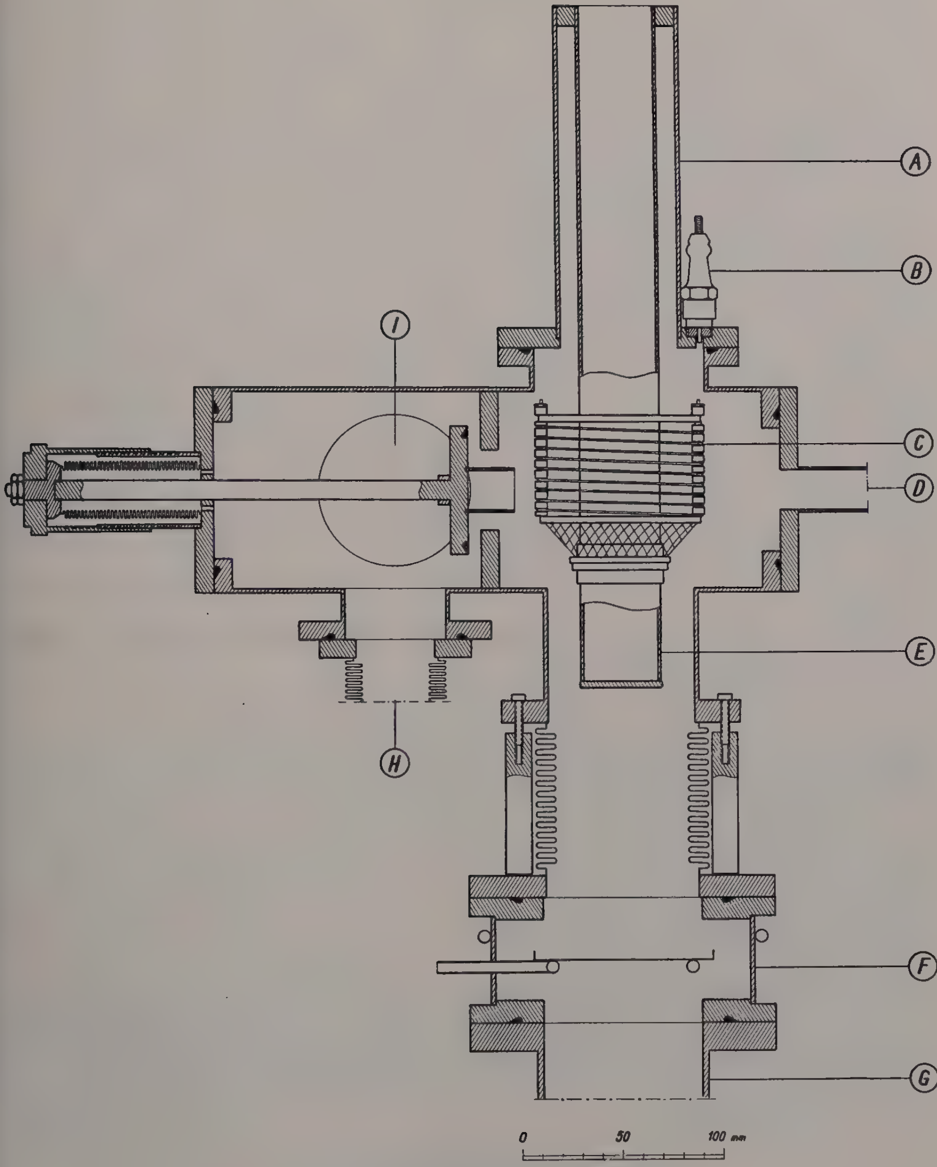

Fig. 12. Diagram of the high-vacuum system.

A – outer jacket of the liquid-air cooled charcoal trap. — A copper cooling cylinder is attached during the degassing of the charcoal.

B – sparking plug connection to the heating coil of the charcoal trap.

C – the charcoal trap. A heating coil of Kanthal[1] wire forms the outer wall, a wide-meshed metal net the bottom, while a sheet of mica insulates the charcoal from the nickel silver tube *E*.

D – connection to an ionisation gauge.

E – nickel silver liquid air trap.

F – top of the diffusion pump *G*, with water-cooled baffles for the condensation of oil vapour.

G – 3-stage oil diffusion pump (VMF-260, Distillation Products, Inc.).

H and *I* – connections to the X-ray tube and the spectrometer respectively.

---

[1] An alloy consisting of iron, chromium, aluminium and cobalt, manufactured by AB. Kanthal, Hallstahammar, Sweden.

Degassed charcoal is a powerful gas absorbent even at room temperature, and at the temperature of liquid oxygen it is an ideal pump with an almost infinite pumping rate.

The charcoal was degassed at no more than 200° C, as it was not desirable to heat nearby rubber joints to a higher temperature. The degassing was not found to be ineffective, however. The final pump was not in operation during degassing of the charcoal, because of the inferior vacuum conditions prevailing, and the booster pump with its more resistive oil pumped by itself.

The spectrometer and X-ray tube were evacuated simultaneously via the two connections I and H in Fig. 12. There was a second liquid air trap in the connection to the X-ray tube, to prevent organic vapours from the spectrometer from reaching the X-ray tube. The above system of traps provided a vacuum completely free from organic vapours. This was demonstrated by the fact that a water-cooled chromium target showed no colour change of the focal spot after a test run of ten hours.

The vacuum system also included two vacuum-meter tubes: one for the Pirani gauge, type *SER*, VM4, range 1–10^{-4} mm Hg, measuring the forevacuum, and one for the ionisation gauge, type *Standard* 4101–D, attached directly to the X-ray tube. The latter had been removed from its glass envelope and mounted in a brass chamber with a large opening into the X-ray tube (Fig. 2).

In making the preparations for an excitation curve, the apparatus was evacuated as follows: —

(1) The mechanical pump evacuated the spectrometer from atmospheric pressure down to the pump's limiting vacuum.

(2) The spectrometer was shut off from the rest of the vacuum system and left for 12–18 hrs., to remove occluded gases from its inner surfaces.

The booster pump was started, and the current through the heating coil of the charcoal trap switched on. The charcoal had to be kept at 200° for 6–10 hours.

(3) The degassed spectrometer was evacuated with the booster pump. The high-vacuum pump was started and the heating current of the charcoal trap switched off.

(4) When the ionisation gauge indicated 10^{-5} mm Hg, the charcoal trap was filled with liquid oxygen.

(5) After some hours of pumping with the high-vacuum pump, the X-ray tube was put into operation.

(6) The application of the cathode heating current and the anode voltage of the X-ray tube was accompanied by an increase in pressure, especially when the spectrometer had been opened prior to evacuation. When the degassing of the various parts of the X-ray tube was complete (see the description of the X-ray tube), the cooling trap of the X-ray tube was filled with liquid oxygen. The actual measurements then commenced.

E. The high voltage equipment

The circuit diagram of the high-voltage set is shown in Fig. 13. The primary voltage of the Greinacher rectifying circuit was stabilised with an a.c. voltage stabiliser (*Philips* GM 444), and was regulated with an autotransformer and rheostats. The high-voltage transformer delivered 10 kV with a primary voltage of 220.

The rectified voltage was filtered in a smoothing circuit according to OHLIN [1941]. A pulse in the rectified high-voltage passes via the condenser C3 to the triode

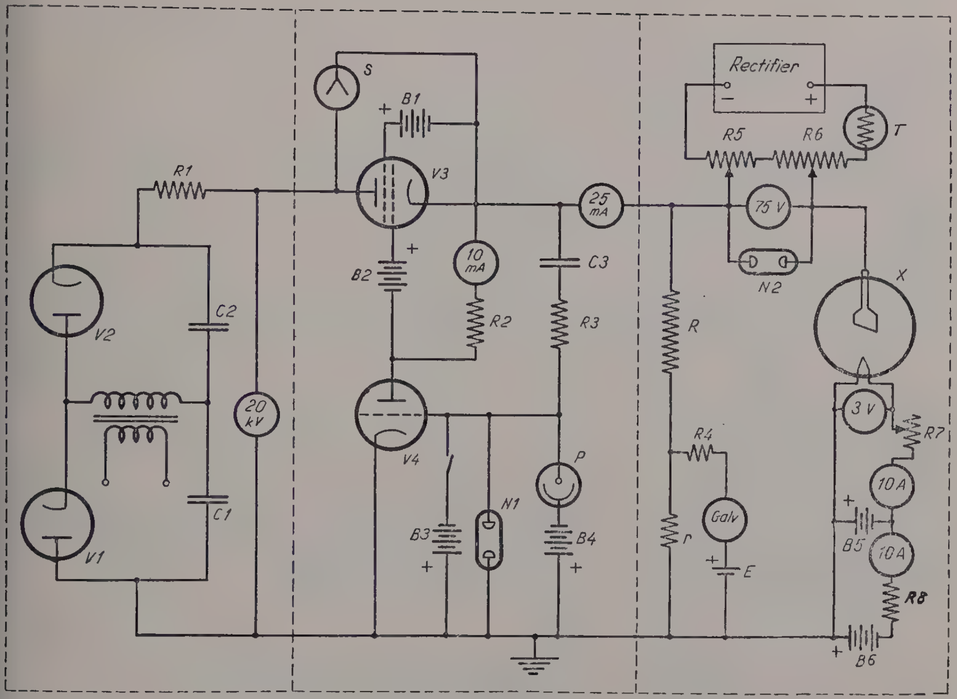

Fig. 13. Circuit diagram.

The section to the left is the Greinacher rectifying circuit, in the middle the smoothing circuit, and to the right the precision potentiometer, the rectifier for additional voltages, the filament heating circuit and the X-ray tube.

*V*1, *V*2 – Philips rectifier valves DA 7/700.
*V*3 – Philips amplifier valve 4650.
*V*4 – Marconi transmitting valve MT-4.
P – Cetron photocell 1 *V* AB.
T – Philips current regulator 1928.
*N*1, *N*2 – Philips neon lamps 4378.

*B*1, *B*2, *B*4 – dry batteries, 150–200 volts.
*B*3 – grid battery, 8–16 volts.
*B*5 – lead accumulator, 12V, 120 amp. hrs.
*B*6 – lead accumulator, 30V, 160 amp. hrs.

*R*1 – 50 kΩ.
*R*2 – 100 kΩ.
*R*3 – 0.5 MΩ.
*R*4 – 1 MΩ + 0.1 MΩ + 5 kΩ. disconnectible.
*R*5 – 10 Ω.
*R*6 – 2500 Ω.

*C*1, *C*2 – 2.3 μF.
*C*3 – 0.1 μF.
X – X-ray tube.
S – electrostatic voltmeter.

r – Wolff precision resistor box.
R – manganin-wire resistors:

Four Siemens-Halske prec. resistors of 1/2 MΩ, max. 10 mA.
Eight Siemens » » of 1/4 MΩ, max. 3 mA.
One Pye precision resistor of 1 MΩ, max. 2 mA.

E – Nife cell, 15 amp. hrs.
Galv – Moll galvanometer, Kipp & Zonen, type O (Period undamped 1.3 secs.).
Voltmeter, 0–75 *V* – Roller-Smith precision instument, type NPD.
Rectifier – rectifier circuit with high tension insulation, 600 V/200 mA (Schönander, Stockholm).

V4, where it is inverted and amplified, and reaches the grid of the pentode V3 with a phase and amplitude such that the original voltage pulse is compensated by the change in the anode voltage of the pentode.

Leakage in the condenser C3 is compensated by the photocell P, which acts as a counter-leak. This counter-leak was automatically controlled by the galvanometer in the potentiometer circuit, the photocell being illuminated by a band of light reflected from the galvanometer mirror. The galvanometer was adjusted so that this light band covered the border of the photocell in the zero position [VON FRIESEN 1935].

The following relation between variations in the input voltage (dV_1) and the output voltage (dV) may be derived from the value of the resistor R2 and data for the valves in the circuit [OHLIN 1941]: $dV = (dV_1/4000) - 6dI$, where I is the output current in amps. The ripple of the smoothed output was measured with a cathode ray oscillograph. It had the form of a somewhat distorted sine wave. The peak-to-peak voltage at $V = 6$ kV and $I = 0.02$ A was 0.08 V, approximately equal to the value obtained from the formula.

The variable additional voltage was obtained from a rectifying circuit floating at the basic high voltage. The primary voltage for this circuit was taken from the a.c. stabiliser mentioned above. The output voltage was regulated by means of a potentiometer coupling with coarse and fine adjustments. The smoothing section eliminated ripple entirely, within the limits of measurement.

Chapter III. The intensity of the spectrometer

The recorded intensity in the spectrometer depended on (1) the current density in focus, (2) the form of the focal spot, (3) the distance between target and crystal, (4) the reflection intensity of the crystal plane, (5) the size of the reflecting surface, (6) the slit width and (7) the efficiency of the detector.

The current density in focus. This was regulated by the cathode emission as the size of the focal spot was almost constant. A current of 20–25 mA was generally used. This value of the current was near the available maximum because of the short emitting section of the filament. With a wider diaphragm in front of the filament the available emission could have been increased but this would decrease the homogeneity of the electron beam.

The form of the focal spot. The focus of the X-ray tube should have such a form and position that the entire crystal opening is filled with radiation. The entering X-rays must strike the different parts of the crystal in such directions that reflection is possible according to the Bragg law. The beams capable of reflection have an intersection point (real or virtual) on the Rowland cricle. It is a wellknown condition for high intensity that the focal spot fills the entire extension between the two chords from the intersection point mentioned to the ends of the crystal opening. This condition is automatically fulfilled in the actual X-ray tube as the intensity is adjusted to the optimum value by regulation of the current in the magnetic focusing lens. The length of the focus was 6 mm (Chapter I). The height was determined by the oscillating motion of the electron beam. The alternating current in the deflection coils was regulated to give the focus a width on the target of 3 mm, corresponding to a vertical height of 1 mm. Thus the vertical projection of the focal spot had dimensions agreeing well with the projection of the crystal opening.

The distance between the target and crystal. Acc. to Johann the intensity will increase if the target is brought towards the crystal. At the same time a larger focal spot can be used, which is often advantageous. A tendency has therefore occurred to make the target-crystal distance short. In the actual case this distance was 10–15 cm.

Lately Brogren, however, has critizised this tendency on theoretical grounds and he has obtained preliminary experimental support for his ideas [to be published]. The opinion of Brogren is that the target should have a position near the above mentioned intersection point. A radiating surface element near this point would fill the entire crystal opening with radiation able to be reflected. If the surface element is moved towards the crystal only a very small angular width is reflected according to the diffraction theory of Darwin, Ewald and Prins [Compton and Allison 1935, Siegbahn 1931].

The reflection intensity of the crystal plane. See Ingelstam [1939].

The size of the reflecting surface. The bent crystals could be used without limiting the opening to prevent occurrence of "ghosts". Unfortunately the height of the crystal opening was small (1.5–2 mm) and could have been increased in order to gain intensity. The intensity gain with increased reflecting surface is obtained at the price of spectral resolution [cf. Sandström 1935]. An excitation curve, however, refers to a volt scale and to voltage resolution and spectral focusing defects only cause a decrease of the ratio of the characteristic intensity to the continuous background. This independence of the excitation curve in relation to focusing defects is founded on the following suppositions: (1) that the asymmetry of the spectral line is independent of the excitation voltage (and thus the excitation curve at the long wavelength side similar to that at the short wavelength side) and (2) that the continuous background has a constant slope. The first supposition is fulfilled as long as the voltage is not high enough to cause double ionization by direct electron impact. The second condition will be considered in Capter IV.

The slit width. The slit width was chosen equal to the width at half-maximum ntensity of the spectral lines. Because of the form of the spectral lines that is the optimal slit width. A smaller slit would only change the ratio between characteristic and continuous radiation to a negligible degree. In an artificial way this ratio could, however, be considerably increased by using target metal in the form of thin ayers on beryllium base. See Chapter VI (A).

The detector. The detector should have an efficiency of 100 %. This is almost realized with the present xenon-ether counters. See Chapter II (C).

Chapter IV. Recordings with the spectrometer

A. Adjustment

The electron beam was brought to bear on the centre of the target by means of the adjusting screws on the focusing lens. The tungsten cathode was turned to a position in which the elongated focal spot was put in the horizontal plane and at right angles to the target-crystal direction. Fluorescent material was applied to the target for this purpose.

The crystal was adjusted so that its cylindrical reflecting surface was parallel to the axis of rotation of the crystal table. The crystal was then moved horizontally

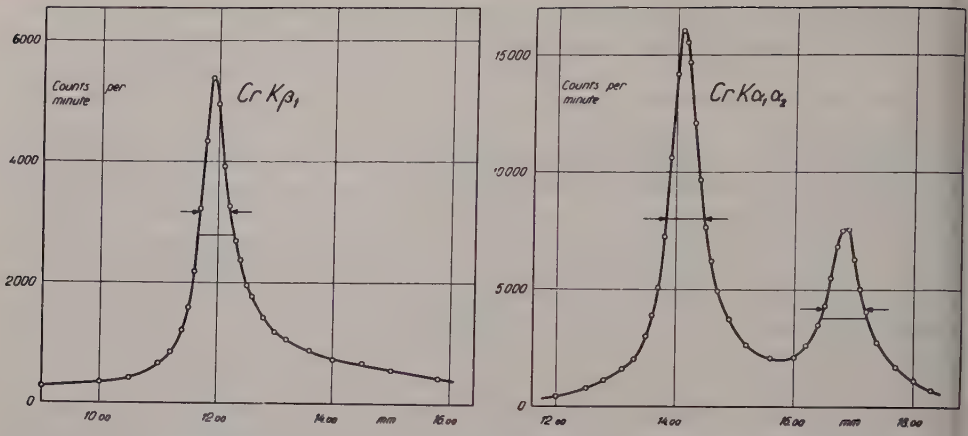

Fig. 14. The intensity distribution of the Cr lines, plotted against the readings of the micrometer screw.

until this axis coincided with the surface of the crystal. The end sections, if not as accurately bent as the rest, could be screened by the knife-edge so that sharp spectral lines were obtained. Further details regarding the adjustment of a concave crystal spectrometer may be obtained from the appropriate literature [e.g. SANDSTRÖM 1935].

The crystal was moved along the spectrometer track (Fig. 1) until the incident beam could fill the whole of the reflecting surface. The slit was adjusted on to the Rowland circle and arranged to be moved along the tangent. Then the slit opening was made parallel to the X-ray line. The latter adjustment was carried out with the aid of a photographic plate. The distances on the plate between the X-ray line and the opposite ends of the slit were measured with a comparator. The largest distance difference tolerated was 0.005 mm. This maximum allowance corresponds to between 1 and 4 % of the slit width used for the recordings of the excitation curves. The length of the slit was 8 mm.

The Geiger counter being mounted and its position adjusted, a profile curve of the X-ray line in question was plotted. The slit-width was about 0.02 mm during these

Table 1.

Element and X-ray line	Full width of the X-ray line at half maximum intensity		Slit width		
			Actual	Along the tangent	
	mm	volts	mm	mm	volts
Ti Kα_1	0.352	3.6	0.140	0.341	3.5
Cr Kα_1	0.640	2.2	0.540	0.640	2.2
Cr Kβ_1	0.628	3.1	0.400	0.520	2.6
Fe Kα_1	0.500	3.1	0.350	0.490	3.1
Co Kα_1	0.348	2.7	0.210	0.318	2.5
Ni Kα_1	0.292	2.8	0.170	0.278	2.6
Cu Kα_1	0.240	2.8	0.136	0.239	2.8

determinations. Fig. 14 shows the intensity distribution of the chromium lines considered, plotted against the reading of the micrometer screw.

The width and position of the slit were adjusted in accordance with the profile curve. Line breadths and slit-widths are given in Table 1. The half-maximum breadth in Fig. 14 is marked by a horizontal line, and the adjusted positions of the slit edges with arrows.

B. Procedure

The vacuum requirements and evacuation procedure have already been treated in the description of the evacuation system and X-ray tube. A check had to be made to ensure that degassing was complete before proceeding with measurements. When conditions in the X-ray tube had become stationary as regards temperature, heating current and emission, the Geiger counter was set in operation. The optimum focusing current and the invariability of the intensity with the oscillation current were tested before each series of determinations.

Before commencing with evaporation on to the target, the intensity of the X-ray beam was measured for the additional voltages $v = 0$ and 75 V. The potentiometer circuit was usually adjusted for an excitation potential in the v range between 15 and 25 V. The first series of determinations were made with an evaporated layer on a target base of a foreign metal (Be or Cu). Evaporation was performed in 5 minute stages, and the attainment of the thinnest layer functioning as a thick target was determined by measuring the intensity increase at 0 and 75 V between each evaporation period. Only one measurement was required with a target base of different atomic number, since the furnace conditions were completely reproducible. A layer four or five times as thick as the minimum layer was evaporated on to the target, to make quite sure of a pure target, and particular attention was paid to the vacuum gauges during the final stages of evaporation, to see that the pressure did not rise (cf. Chapter I.).

It was important to know for each element and temperature the longest bombardment time compatible with no appreciable oxidation of the target surface. This time was first estimated by visual examination of the target, and later, when signs of oxidation had been identified in sensitive parts of the excitation curves, with the help of these curves.

The maximum times thus determined for normal targets were not sufficiently long to permit uninterrupted measurements of the complete K excitation curve. The curve therefore had to be divided up into two, three or four sections, the target surface being renewed between the different sections. It was later possible to combine these sections to a complete curve. Since minor displacements might possibly occur between the different sections, the ends of these sections should overlap. The intensity at a certain voltage point was calculated from the time for 50 × 64 or 100 × 64 pulses, this time being converted to counts per minute with the dead-time of the Geiger counter taken as 3.0 secs. per 3200 counts. Between one and five such determinations were made for each voltage value. The total number of pulses per point depended on (1) the time available for the curve section concerned, (2) the risk of external electric disturbances, and (3) the statistical resolution required. The number of pulses given in Tables 20–22, and the standard deviation indicated in the figures, is an average value for the entire curve. The voltage interval between the points was 1, 1/2 or 1/4 volt, according to the circumstances. The cobalt curve of Fig. 34 provides a

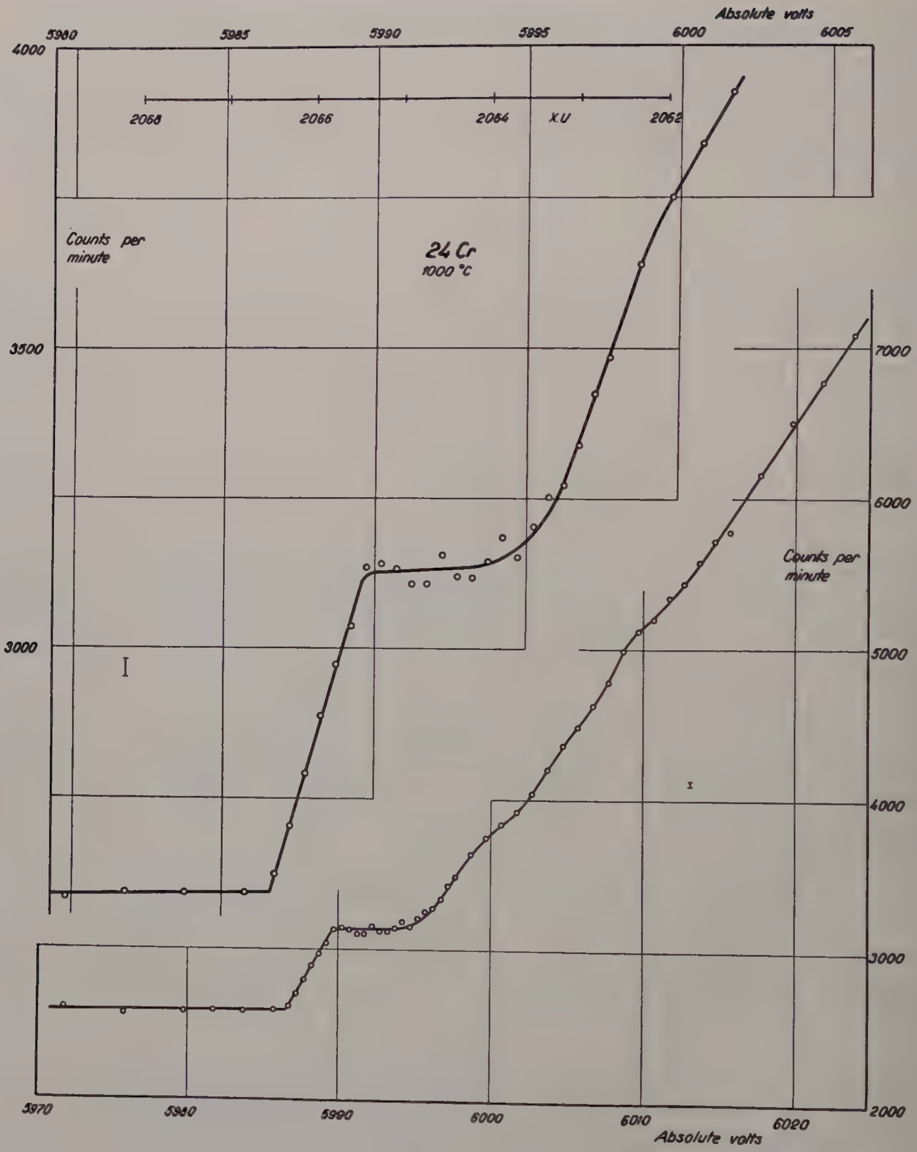

Fig. 15. Excitation curve of Cr Kα_1. Mean of Nos. 14 and 15, Table 7.

The upper curve shows an enlarged section of the lower one. The voltage scale includes the work function correction.

The separate X.U. scale in this and the following figures is calculated from the absolute-volt scale, with $h/e = 1.3793 \cdot 10^{-17}$ erg. sec/e.s.u.

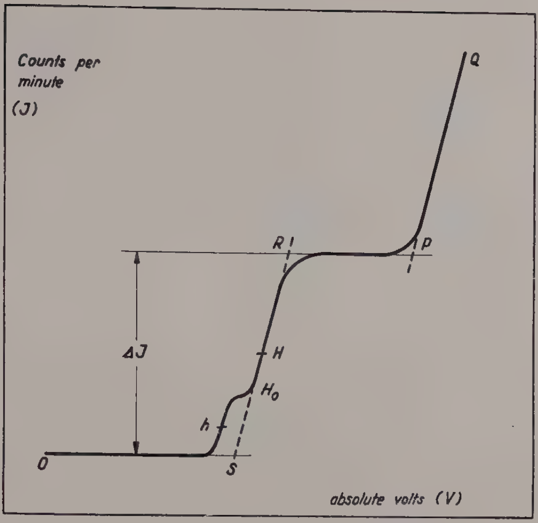

Fig. 16. The general appearance of the excitation curves, and the notation used.

diagrammatic illustration of the procedure in determining an excitation curve in two sections.

The occasional displacement in the intensity level which was mentioned above might conceivably be explained by (1) changes in the target or the window foil during evaporation, (2) slow change of the efficiency of the Geiger counter, or (3) gradually increasing contamination of the target. The effect of (2) was eliminated by taking series with decreasing voltages as well as with increasing voltages. A check was made on (3) by means of one or two "standard points" on horizontal parts of the curve, which were measured before and after a series of determinations. When displacement of a section was observed, the curve was regarded as suspect.

Fig. 15 shows a chromium curve taken at a temperature of 1000–1100° C. There is a clearly marked plateau before the definite increase in intensity.

The wavelength scale included with the curves is calculated from the relation $hc/\lambda = eV$, with $c = 299790$ km/sec. [Bearden & Watts 1951], $h/e = 1.3793.10^{-17}$ erg. sec./e.s.u. [Bearden & Watts 1951], and the conversion factor for kX units to Ångström units = 1.00202 [Bragg 1947].

An interesting structural detail was discovered at the foot of the excitation curve for normal target temperatures. Its disappearance at the higher temperatures may be due to insufficient resolution — but there are presumably other more fundamental causes as well (See Chapter VI). The essential features of the excitation curves are illustrated diagrammatically by Fig. 16. The voltages and intensities given in the tables refer to this model and the notation used there. The model is most appropriate for chromium and titanium; for other metals, the respective figures give an idea of how close the resemblance is.

The sections OS, RP and PQ have usually been drawn as straight lines. Strictly speaking, this is true only for the intensity in the section OS. Both RP and PQ probably have a fine structure which the number of pulses counted was too low to reveal. See Fig. 39, however.

Apart from the zero level of the Geiger counter (80 counts/min.), the background is due to the continuous radiation. The intensity distribution of this radiation from a thick target was investigated by KULENKAMPFF [1922]. He showed that when the voltage applied to the X-ray tube is constant, the continuous intensity is a linear function of the frequency (apart from an interval near the short wavelength limit). Estimation based on Kulenkampff's results shows that the background of the excitation curves for the elements considered increases about 0.1 % per volt.

The standard deviation (the square root of number of pulses per point) shown in the figures, refers to the intensity where it is drawn.

Chapter V. Measurement of the high voltage

A. The potentiometer circuit

This circuit is shown to the right in Fig. 13. The smoothed high voltage measured by the precision potentiometer is

$$V_{R+r} = E \cdot \frac{R+r}{r}.$$

The resistances R and r are described under Fig. 13. They had a low temperature coefficient (of the order of 10^{-5} deg.$^{-1}$), being made of manganin wire. The temperature coefficient of the Nife cell is about ten times as high, but at constant temperature its *emf* E is very stable, because of the low self-discharge of the alkali accumulator.

The resistances in the potentiometer circuit were measured with a Wolff precision bridge. The *emf* of the Nife cell was measured by comparison with a standard cell, using a Wolff potentiometer.

The laboratory temperature was kept constant with the aid of thermostats. The temperature variation of the Nife cell was not allowed to exceed 0.2° during a series of determinations.

The additional voltage v was measured with a Roller-Smith voltmeter, which was calibrated with a bridge against a standard cell.

Certain corrections ΔV had to be applied to the calculated voltage V_{R+r}. If the corrected voltage is denoted by V_0, the following expression is obtained for V, the voltage corresponding to the electron energy at the target:—

$$V = V_0 + v, \text{ where } V_0 = V_{R+r} + \Delta V.$$

The voltages are expressed in absolute volts, unless otherwise stated. The Wolff bridge was graduated in international ohms, so resistances are given in that unit.

B. The potentiometer resistances

The Wolff bridge had a guaranteed accuracy of 0.01 % at 20° C.

Readings were made for several consecutive bridge positions in the neighbourhood of the galvanometer zero. The same series was then measured with reversed bridge current, after which the resistance value was determined graphically.

Table 2. Measurements of the precision resistance R.

Date	R (int. ohm)	R_{mean}
13.3.48	3 968 620	
4.7.49	3 968 790	
16.3.50	3 968 520	
14.8.50	3 968 840	3 968 690
24.8.50	3 719 960	
27.2.51	3 719 690	3 719 820
13.4.51	4 964 780	
28.8.52	4 964 940	4 964 860
28.8.52	4 960 930	
23.10.52	4 960 790	4 960 860

Table 3. The potentiometer resistances.

	Nos.	r (int. ohm)	R (int. ohm)
Ti Kα_1	1–10	1 288.30	4 960 860
Cr Kα_1	1	845.78	3 968 690
	2– 6	840.78	3 968 690
	7– 8	870.78	3 968 690
	9–19	815.78	3 719 820
	20	1 083.33	4 964 860
	21–23	1 066.33	4 960 860
Cr Kβ_1	24	1 072.35	4 964 860
	25	1 082.34	4 964 860
Fe Kα_1	1–5	897.76	4 960 860
Co Kα_1	1–5	828.76	4 964 860
Ni Kα_1	1	767.78	4 964 860
	2–4	765.78	4 960 860
Cu Kα_1	1–5	713.79	4 964 860

The large resistance R was divided up into 1/2 MΩ sections for measurement. The 1000 : 10 ratio of the Wolff bridge was used for this measurement, whereas the 1000 : 1000 ratio was used for the resistance r. It was therefore necessary to determine the relationship between these two ratios. The 1000 : 10 ratio gave a higher value than the 1000 : 1000, the factor involved being 1.00018 ± 0.00004. Table 2 summarises the measurements of R. The values given have been corrected with the above factor. Table 3 gives details of the potentiometer resistances used for the various determinations.

Table 4 a.

Cell No.	LN 363 896	LN 363 923	L 215 790	Mean	
Date of certificate	13.5.47	13.5.47	30.7.47	Int. volts	Abs. volts
Certified int. volts	1.01896	1.01892	1.01826		
April 1948			1.01822	1.01822	1.01856
Nov. 1948	1.01821	1.01822	1.01823	1.01822	1.01856
April 1949	1.01823	1.01824	1.01824	1.01824	1.01858

Table 4 b.

Cell No.	L 265 648	L 265 694	M 163 417	M 164 214	Mean (abs. volts)
Date of certificate	23.8.50	23.8.50	31.7.50	1.9.50	
Certified abs. volts	1.01856	1.01857	1.01864	1.01858	
April 1951	1.01862	1.01857	1.01854	1.01850	1.01856
Nov. 1951	1.01866	1.01859	1.01855	1.01849	1.01857
March 1952	(1.01870)	1.01860	1.01856	1.01851	1.01856
June 1952	(1.01874)	1.01861	1.01856	1.01850	1.01856
Sept. 1952		1.01862	1.01855	1.01849	1.01855

Table 4 a and b. Comparison between the Pye 58946 cell and various new Weston elements at the Institute of Physics. The tables give the *emf* at 20° C of Pye 58946 in the same unit system as the corresponding certificate. In the mean column of Table a, the conversion factor between absolute and international volts is 1.00033. [DuMond & Cohen 1948.] LN = Leeds & Northrup Co. L = Cambridge Instrument Co. M = Muirhead and Co.

C. The *emf* of the Nife cell

The Nife cell was compared before and after each series of determinations with Weston cell L-215790, which served as secondary standard cell. The primary standard was the Pye 58946 cell, manufactured in 1936 and with a certified *emf* at 20° C of 1.0182 int. volts. This cell was frequently compared with new Weston cells; the results of the comparisons are given in Tables 4 a and b. The same cell was used by Ohlin in 1940 [cf. Ohlin 1941], and since then the *emf* has remained constant within the limits of measurement. A twin cell, Pye 58947, has remained equally invariable, the largest measured difference between the two being 2.10^{-5} V. The potential assigned to the Pye 58946 cell in all calculations was 1.01856 absolute volts.

The mean value of E for each series of determinations is given in the tables of the excitation potentials. It was not possible to avoid a slight increase in the temperature of the Nife cell, which meant a decrease in its *emf*, but the difference between the initial and final values was less than $5 \cdot 10^{-5}$ V, except in a few cases.

D. Voltage corrections applied

1. The cathode potential

The cathode potential was zero for the oxide cathode. Most of the determinations were made with the tungsten cathode, however. Only a short central section of the tungsten filament emitted electrons, and the mean potential v_c of this section was

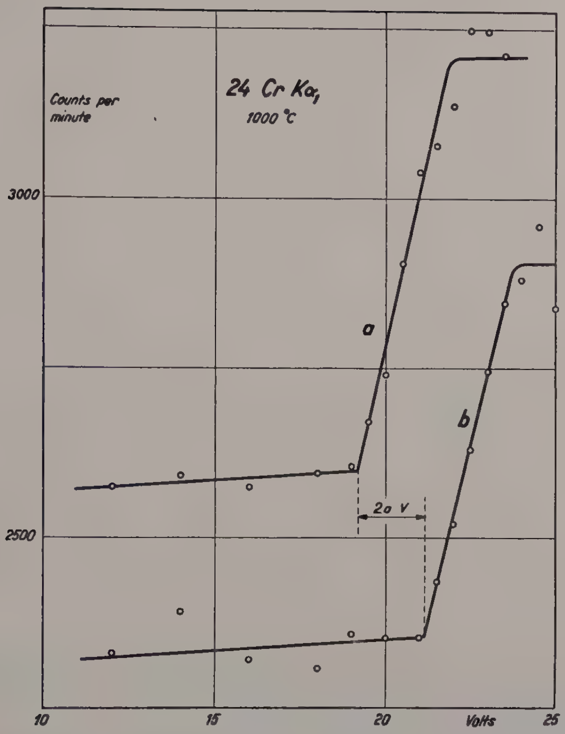

Fig. 17. Voltage displacement resulting from a change in the sign of the cathode potential. a – negative filament, b – positive filament.

Table 5. The potential v_c of the tungsten cathode.

	Ti	Cr	Cu
Point determined (Fig. 16)	h	S	S
Filament voltage v_f	1.99	1.71	1.76
v_f negative (v volts)	20.1	19.1	35.7
v_f positive (v volts)	22.3	21.1	37.8
Voltage displacement	2.2	2.0	2.1
Cathode potential v_c (v_f neg.)	−1.1	−1.0	-1.0_5

determined by reversing the potential of the unearthed end of the filament. The displacement of the curve due to this reversal should be $2v_c$. Table 5 and Fig. 17. The filament was normally negative with respect to earth.

2. The temperature effect of the manganin resistors

The current through the resistors R was of the order of 10^{-5} A during measurements with the Wolff bridge. But for the excitation determinations the current was 1–2 mA.

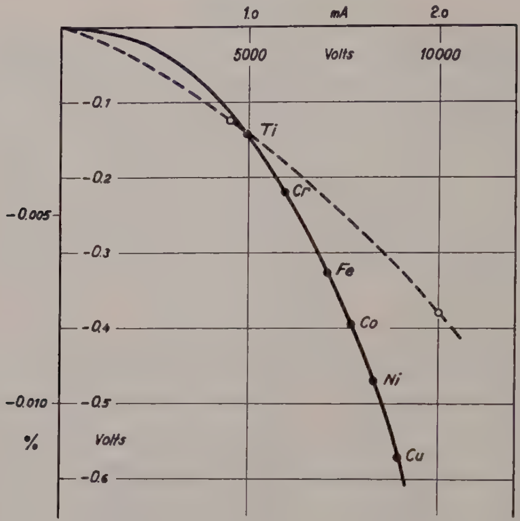

Fig. 18. Voltage corrections for the temperature effect in the resistance R (4 964 860 Ω). ○ – observed values of $\Delta R/R$. ● – voltage corrections (v_R).

The resistance correction for the consequent temperature change was determined in the following manner. Currents of 0.9 and 2.0 mA were sent through the resistors, and the resistance then measured several times at 5 min. intervals. Extrapolation to time zero gave the values of $\Delta R/R$ in Fig. 18. The corresponding voltage corrections are given by the unbroken line.

3. Mean thermal energy of the emitted electrons

When electrons leave the surface of the cathode, they have an initial thermal energy distribution which approximately obeys Maxwell's distribution law [see, for instance, HERRMANN & WAGENER 1943]. The mean energy in the direction normal to the emitting surface, v_M, is calculated from the formula $v_M = kT$, where k is Boltzmanns constant ($= 0.86 \cdot 10^{-4}$ eV/deg.) and T the absolute temperature. T may be taken as 2400° K for the tungsten cathode, and 1200° K for the oxide cathode. The corresponding values of v_M are 0.2 and 0.1 eV.

A summary of the corrections described above is given for Ti and Cr in Table 6 a.

E. The work function

1. Introduction

The work function of a metal signifies the energy required to lift an electron from the Fermi level in the conduction band to a point just outside the metal's surface. The work function is due to image forces and the electrostatic double layer at the surface.

If two metals at the same temperature are electrically connected, the number of electrons passing from one metal to the other in unit time, as well as their velocity

Table 6 a. Voltage corrections for Ti and Cr with the work function omitted.

	Nos.	Cathode	$\lvert v_c \rvert$	v_R	v_M	ΔV^*
Ti	1–4, 8–9	W	1.1	−0.1	0.2	+1.2
	5–7, 10	oxide	0	−0.1	0.1	0
Cr	4– 6	W	2.2	−0.4	0.2	+2.0
	13–18	W	1.0	−0.4	0.2	+0.8
	19	W	1.1	−0.4	0.2	+0.9
	20, 22–25	W	1.1	−0.2	0.2	+1.1
	21	W	1.2	−0.2	0.2	+1.2
	1–3, 7–12	oxide	0	−0.4	0.1	−0.3

Table 6 b. Voltage corrections for 22 Ti–29 Cu. Tungsten cathode. Work function included.

	Nos.	$\lvert v_c \rvert$	v_R	v_M	v_φ	ΔV
Ti	1–4, 8–9	1.1	−0.1	0.2	4.5	+5.7
Cr	22–25	1.1	−0.2	0.2	4.5	+5.6
	21	1.2	−0.2	0.2	4.5	+5.7
Fe	1–4	1.1	−0.3	0.2	4.5	+5.5
	5	1.0	−0.3	0.2	4.5	+5.4
Co	1–5	1.1	−0.4	0.2	4.5	+5.4
Ni	1–4	1.1	−0.5	0.2	4.5	+5.3
Cu	1, 4, 5	1.0	−0.6	0.2	4.5	+5.1
	2, 3	1.1	−0.6	0.2	4.5	+5.2

Table 6 a and b. The voltage corrections.

v_c = cathode potential. The filament voltage v_f was between -1.70 and -2.10 volts, with the exception of Nos. 4–6, Cr, where $v_f = -3.6$ volts.

v_R = voltage correction for the temperature effect in the resistance R (Fig. 18).

v_M = mean thermal energy of the emitted electrons.

v_φ = work function correction.

$\Delta V = |v_c| - |v_R| + v_M + v_\varphi$ = the total correction to be applied to V_{R+r}.

ΔV^* = the total correction to be applied to V_{R+r} with the work function correction omitted.

$V_{R+r} + \Delta V = V_0$.

$V_{R+r} + \Delta V^* = V_0^*$.

distribution, must be equal in opposite directions. This means that the Fermi levels of the two metals are shifted to the same potential. An external potential difference — the Volta potential — therefore arises, as may be confirmed experimentally.

If we suppose that the two metals are the cathode and anticathode of an X-ray tube, whose applied voltage we for the moment put equal to zero, it follows from what has been said above (1) that only electrons with thermal energy greater than the cathode's work function can leave its surface and reach the interelectrode vacuum, and (2) that if such an electron happens to reach the target, it delivers up the same maximum energy as if it had happened to return to the cathode — i.e. an energy equal to the cathode's work function.

But if the cathode and anticathode are now separated by an electromotive force, the energy corresponding to this force will be added to the work function energy. The total kinetic energy of an electron striking the target is therefore the sum of the potential difference between the Fermi levels and the cathode's work function. As the potential difference between the Fermi levels is the quantity measured by a voltmeter, the work function must be a further necessary correction.

OHLIN [1941], in his determination of h/e by an X-ray method, obtained results which cast doubt on the necessity for the work function correction. OHLIN determined the minimum anode-cathode voltage V which could produce X-radiation of wavelength λ. The relation $hc/\lambda = eV$ implies that for a constant wavelength, h/e should be proportional to the voltage V. OHLIN carried out his determinations in the range 3000–5000 V, where the work function would mean a correction of about 0.1 %. This correction is much larger than the obtained reproducibility (±0.02 %). When OHLIN corrected his voltage values V with the work function, a definite drift appeared in the results. Without the correction, the individual results had a normal statistical distribution about a mean. For this reason, and on account of the precision with which he had made all measurements, he drew the understandable conclusion that the theory was incorrect on this point, and rejected the correction.

OHLIN's results gave rise to a discussion which may be described as still unsettled [PANOFSKY, GREEN & DUMOND 1942, OHLIN 1942, DUMOND 1947 and 1948, DUMOND & COHEN 1948, BEARDEN & SCHWARZ 1950, BEARDEN, JOHNSON & WATTS 1951]. Two papers are of special interest:— OHLIN [1942 b] and BEARDEN, JOHNSON & WATTS [1951]. Both contain a comparison of voltage determinations for the high frequency limit of the continuous X-ray spectrum with oxide and tungsten cathodes. OHLIN found that the values obtained with tungsten target and tungsten filament closely agreed with those obtained with oxide cathodes and different target substances. BEARDEN, JOHNSON & WATTS, however, observed a difference of 3 V, corresponding to the difference in work function between the two cathodes used. This difference is 0.03 % of their total voltage (10 kV), and the probable error given is ±0.003 %.

2. Measurements and discussion

Since it is possible to determine h/e from measurements of excitation potentials, the problem of the work function correction also appears in the present investigation. The phenomena concerned are, however, different, involving different excitation processes, and consequently a rule for one may not be valid for the other. It was therefore necessary to make a new enquiry into the question of the work function correction in the case of K excitation, regardless of previously published

Table 7. Cr Kα_1. Temperature: 1 000°–1 100° C.

	No.	E_{mean}	V_{R+r}	V_0^*	S	H	R	P
Oxide-coated cathode	1	1.26660	5 944.6	5 944.3	5 985.6	5 987.0	5 988.3	5 994.9
	2	1.26017	5 949.6	5 949.3	5 985.2	5 986.7	5 988.1	5 993.9
	3	1.26016	5 949.5	5 949.2	5 985.1	5 986.6	5 988.1	5 993.9
				Mean, abs. volts	5 985.3	5 986.8	5 988.2	5 994.2
Tungsten cathode	4	1.25913	5 944.7	5 946.7	5 982.3	5 983.7	5 985.1	5 991.4
	5	1.25913	5 944.7	5 946.7	5 982.3	5 983.7	5 985.0	5 991.2
	6	1.25853	5 941.8	5 943.8	5 982.7	—	—	—
	13	1.30733	5 962.5	5 963.3	5 982.4	5 983.8	5 985.2	—
	14	1.30727	5 962.2	5 963.0	5 982.0	5 983.6	5 985.2	5 990.4
	15	1.30733	5 962.5	5 963.3	5 982.1	5 983.4	5 984.7	5 990.8
				Mean, abs. volts	5 982.3	5 983.6	5 985.0	5 991.0
				$V_{\text{oxide}} - V_W$	3.0	3.2	3.2	3.2

Anticathode: Chromium plate, supported on a molybdenum pin (Fig. 7 a).

The work function correction is omitted in this table.

Table 8. Cr Kα_1.

	No.	E_{mean}	V_{R+r}	V_0^*	S	H	R	P
Oxide-coated cathode	7	1.30969	5 970.4	5 970.1	5 985.8	5 987.5	5 989.1	5 995.5
	8	1.30965	5 970.2	5 969.9	5 985.9	5 987.4	5 988.9	5 995.3
	9	1.30707	5 961.3	5 961.0	5 985.5	5 986.8	5 988.0	5 994.2
	10	1.30716	5 961.7	5 961.4	5 985.8	5 987.2	5 988.5	5 995.2
	11	1.30727	5 962.2	5 961.9	5 985.8	5 987.2	5 988.7	5 995.1
	12	1.30731	5 962.4	5 962.1	5 985.8	5 987.3	5 988.7	5 995.4
				Mean, abs. volts	5 985.8	5 987.2	5 988.7	5 995.1
Tungsten cathode	16	1.30735	5 962.6	5 963.4	5 983.5	5 984.8	5 986.1	5 992.6
	17	1.30735	5 962.6	5 963.4	5 983.4	5 984.9	5 986.4	5 992.8
	18	1.30707	5 961.3	5 962.1	5 982.8	5 984.5	5 986.2	5 991.8
	19	1.30662	5 959.3	5 960.2	5 982.9	5 984.4	5 985.9	5 993.1
	20	1.29837	5 951.7	5 952.8	5 983.6	5 985.1	5 986.6	5 993.4
	21	1.28189	5 965.0	5 966.2	5 983.3	5 984.9	5 986.4	5 992.5
	22	1.28187	5 964.9	5 966.0	5 983.5	5 985.0	5 986.4	5 992.5
				Mean, abs. volts	5 983.3	5 984.8	5 986.3	5 992.7
				$V_{\text{oxide}} - V_W$	2.5	2.4	2.4	2.4

Anticathode: Nos. 7–12, 16–19. Chromium-electroplated copper.
Nos. 20–22, Chromium, evaporation deposit on copper.

The work function correction is omitted in this table.

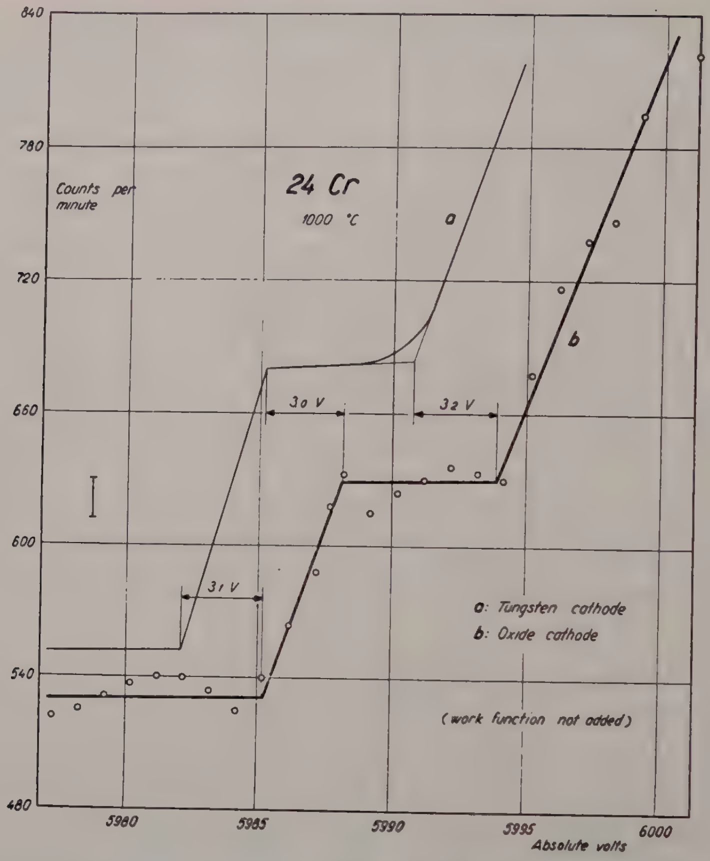

Fig. 19. Cr Kα_1 excitation curves, the work function correction omitted. Anticathode at red heat.

The intensity scale refers to the oxide cathode curve (No. 2, Table 7). The tungsten cathode curve is the one shown in Fig. 15.

measurements. One of the curves obtained was so near the quantum limit for the continuous radiation, that it was possible to make a direct comparison between the two types of curves.

The K excitation potential of chromium was determined in 1949–50 with both oxide cathode and tungsten cathode. The results of these determinations are given in Tables 7–8 and Figs. 19–20 (together with some later results). Similar determinations were made in 1952 for a titanium target. The results are given in Tables 12–13. A graphical summary of the results for both chromium and titanium is given in Fig. 21.

The chromium curves were obtained for both incandescent and cooled targets. The results for cooled targets require a considerably cleaner vacuum to be reproducible than do the targets at red-heat. The surface of a chromium target at red-heat may be said to renew itself, in view of the high vapour pressure of the metal at such temperatures.

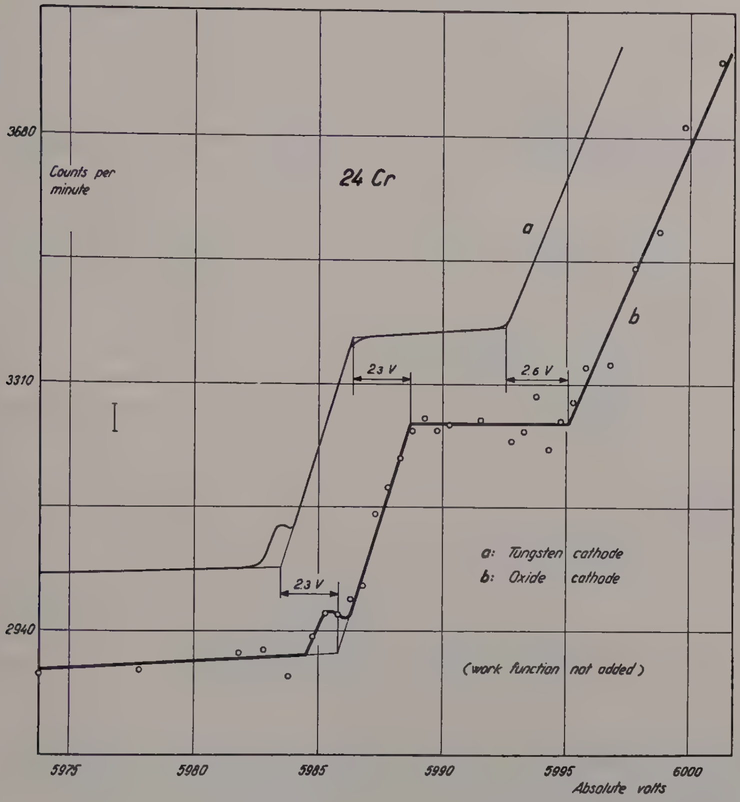

Fig. 20. Cr Kα_1 excitation curves, the work function correction omitted. Water-cooled anticathode.

The intensity scale refers to the oxide cathode curve (No. 11, Table 8). The tungsten cathode curve is the one shown in Fig. 22.

The coating of the oxide cathode was a mixture of barium, strontium and calcium oxides. Barium chloride, strontium nitrate and calcium chloride in the molecular proportions 5 : 5 : 1 were emulsified in a mixture of amyl acetate and Zapon lacquer, and applied to the cathode with a glass rod. The oxides were formed at 1000–1100° C, the subsequent operating temperature being 950–1000° C. The base metal was platinum, except for chromium curves Nos. 1–3 and 7–8, for which it was nickel.

The oxide layer of normal thickness was bright white in colour. It proved to be difficult to degas such layers sufficiently for water-cooled anticathodes not to be contaminated in operation, and thinner oxide films were therefore used with such anticathodes. For this purpose, the emulsion of the salts previously mentioned was further diluted with amyl acetate, and the layer applied to the cathode was so thin that the metal underneath was clearly discernible. The contamination of the target was reduced by this means, and reproducible curves obtained, even with cooled targets. As may be seen from Fig. 21, the voltage displacement for these cathodes was not quite regular, and curves for a cooled titanium target were therefore determined later with a normal oxide coating on the cathode. Rapid determination in combination

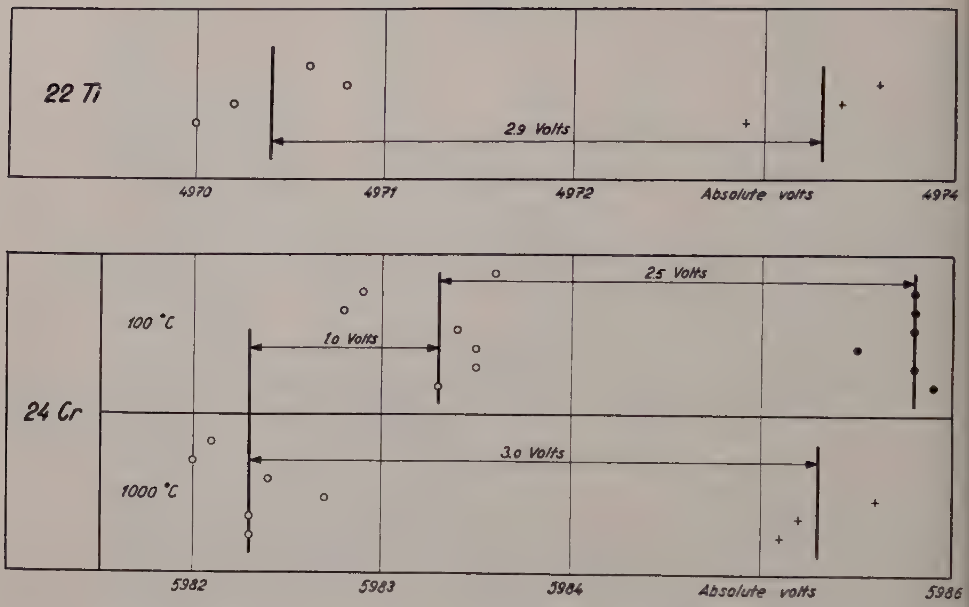

Fig. 21. The distribution of the determined potentials of 22 Ti, point *P*, and 24 Cr, point *S*, the work function correction being omitted.

○ – tungsten cathode. + – normal oxide cathode. ● – thin oxide films.

with titanium evaporation made this possible. (Chromium curves Nos. 1–19 were obtained without evaporation.) On account of the large structure at the foot of the primary edge S of the titanium curves, the excitation potential given for Ti in Fig. 21 refers to the secondary edge P.

Fig. 21 gives a good idea of the spread of the measured values due to random variations. When the same resistances *R* and *r* were used for the whole series of measurements, the spreading was mainly due to the error of the Wolff potentiometer (± 0.01 %), and of the galvanometer zero reading (± 0.3 V). Fig. 21 shows that the measured values lie within a range of 1 V, which is a measure of the reproducibility attainable. Voltage differences occurring when either the cathode or target were changed, without other alterations, may therefore be assigned a maximum uncertainty of ± 1 V. The values obtained with oxide and tungsten cathodes differ by a clear voltage margin. Fig. 21 and Tables 7, 8 and 13 show that the average values for the different targets were displaced 2.9–3.2 V with normal oxide cahtodes, and 2.4–2.5 V with the extremely thin oxide coatings.

Tungsten's work function is 4.5 V. An applied electrostatic field diminishes the work function by an amount which is proportional to the square root of the field intensity at the surface. This effect is only a matter of millivolts for the fields used here, however, and is therefore negligible. Thermoelectric potentials at the cathode can be estimated to be of the same order of magnitude.

The work function of an oxide cathode is more complicated. The definition is analogous to that given for a metal, i.e., the work function is the amount of energy required to transfer an electron from the Fermi level of the base metal to a point in the vacuum just outside the surface of the oxide layer. The work function depends on the composition of the oxide, on the base metal, on the thickness of the oxide layer, and on the activation of the cathode. During the activation a boundary layer of metal oxides is formed, an interface which plays an important part in the emissive properties of the cathode. The passage of a current gives rise to a potential drop across the interface and the oxide layer. For further details about oxide cathodes, reference may be made to relevant literature [HERRMANN & WAGENER 1943 and 1944, FRIEDENSTEIN et al. 1946–47, EISENSTEIN 1948].

The work functions for the individual oxides on a nickel base are given as 1.9 V (CaO), 1.4 V (SrO), and 1.1 V (BaO). The value given for extremely thin layers of SrO on a nickel base is 2.0 V, which is 0.6 V higher than that for the normal oxide layer [EISENSTEIN 1948]. LIEBOLD used a similar oxide mixture as in the present investigation, and obtained a value of 1.4 V for both nickel and platinum bases. HUBER gave 1.4–1.6 V for mixtures of SrO and BaO in different proportions on a nickel base. Regarding LIEBOLD's and HUBER's results, see FRIEDENSTEIN et al. [1946–47].

Electron and X-ray diffraction measurements have shown that the more volatile components of the oxide mixture disappear from the surface of the oxide layer. A BaO–SrO cathode coating was found to consist of SrO to a depth of 300–2000 atom layers [HUBER & WAGENER 1942], so it may be presumed that SrO predominated in the oxide coating used by the present author. There is thus good reason to assume that the work function for the oxide cathodes in question was 1.4 ± 0.2 V. The difference between this value and the work function of tungsten is 3.1 V, which agrees with the observed voltage displacements for Ti and Cr targets. Moreover, the voltage displacement between the normal oxide coating and extremely thin oxide coating is of the same magnitude and sign as the difference between the work function values for normal and thin SrO coatings.

The results obtained constitute a proof that a correction should be applied, depending on the cathode and of the same order of magnitude as the thermionic work function. The proper correction is a quantity called the calorimetric work function. The difference between the calorimetric and thermionic work function is negligible for our purpose. [Cf. PANOFSKY, GREEN & DUMOND 1942.]

3. Continuous and characteristic radiation

The electronic processes involved in the emission of brehmsstrahlung and in the excitation of X-ray levels may be different with regard to the work function correction. A decision can be reached by comparing the "electronic" energy difference between two energy levels in an atom with the spectroscopically determined difference. These differences should either be the same or differ by an amount equivalent to the work function of the cathode. If they are equal, it is shown that the work function should be treated in the same way in relation to continuous and characteristic radiation.

The curve in Fig. 25 enables us to make such a comparison. One level considered is the $M_{II,\,III}$ level of chromium, corresponding to the maximum intensity of the $K\beta_1$ line. The $K\beta_1$ line arises from the $(K–M_{II,\,III})$ transition, and its shape and position have been determined by BEARDEN & SHAW [1935]. The shape may be given in terms of the width at half-maximum and the asymmetry. BEARDEN & SHAW give the width as 3.0 V, and the asymmetry as 1.53 for the $(1+1)$ position of the

Table 9. Cr Kα_1, Kα_2 and Kβ_1.

	No.	E_{mean}	V_{R+r}	V_0	h	S	H	R	P
Cr Kα_1	21	1.28189	5 965.0	5 970.7	5 987.4	5 987.8	5 989.4	5 990.9	5 997.0
	22	1.28187	5 964.9	5 970.5	5 987.4	5 988.0	5 989.5	5 990.9	5 997.0
		Mean, abs. volts			5 987.4	5 987.9	5 989.4	5 990.9	5 997.0
Cr Kα_2	23	1.28187	5 964.9	5 970.5	—	5 988.1	5 989.6	5 991.0	5 996.7
Cr Kβ_1	24	1.28669	5 958.5	5 964.1	—	5 988.2	5 989.7	5 991.2	5 996.8

Anticathode: Nos. 21–23. Chromium, evaporation deposit on copper.
No. 24. Chromium, evaporation deposit on beryllium.

Cathode: Tungsten filament.

Table 10. The quantum limit (V_L) of the continuous spectrum at the Cr Kβ_1 line.

No.	E_{mean}	V_{R+r}	V_0^*	V_0	V_L^*	V_L	$(h/e)^* \cdot 10^{17}$	$h/e \cdot 10^{17}$
25 a	1.28669	5 903.5	5 904.6	5 909.1	5 941.1	5 945.6	1.3782	1.3792
25 b	1.28669	5 903.5	5 904.6	5 909.1	5 941.6	5 946.1	1.3783	1.3794
						Mean	1.3783	1.3793

Cr Kβ_1 = 2 080.60 X.U. [BEARDEN and SHAW 1935.]
λ_{slit} = 2 080.67 X.U. (Correction for asymmetry of Kβ_1. Fig. 14.)
Slit width = 2.6 volts.

Units in the table: voltages in absolute volts.
h/e in ergsec./e.s.u.

* signifies that the work function correction is omitted.

crystals in the double crystal spectrometer. The present author's corresponding values for the Kβ_1 line (Fig. 14) are 3.1 and 1.5, so there should be no risk of discrepancy in the position of the maximum intensity.

The other level considered corresponds to the main edge of the K absorption curve obtained by SANNER [1941]. Sanner measured the inflection point of the absorption edge. His results show that it occurs at 1/3 the height of the main edge.

The difference between the above-mentioned levels may be calculated from SANNER's K absorption edge (2065.95 ± 0.15) X.U., and BEARDEN & SHAW's Cr Kβ_1 value (2080.60 ± 0.05) X.U., using the expression $h/e \cdot (c/\lambda_K - c/\lambda_{\beta_1})$.

The energy difference obtained is (42.2 ± 0.6) eV (independent of inaccuracy in the h/e value, arising from uncertainty as to the necessity for the work function correction).

The same energy level difference can be calculated from electronic determinations as the energy between the K excitation potential and the short wavelength limit of the continuous spectrum for a wavelength corresponding to the peak of the Kβ_1 line. The excitation potential value must be commensurable with the inflection point of the K absorption edge, which means that the value taken should be 5989.2 abs. volts (Table 9). The quantum limit determined has to be corrected for the 0.2 V difference between the centre of the slit and the peak of the line: 5945.9 + 0.2 = 5946.1 abs. volts (Table 10). The required voltage difference is thus 43.1 V, with an approximate error of ± 1 V, which is in full agreement with the value obtained spectroscopically.

Since the $K\beta_1$ and $K\alpha_1$ lines have the same excitation potential, it is possible to obtain a more exact value from the $K\alpha_1$ determination (Table 11). The voltage difference obtained in this way is 42.7 V.

A new value for the Cr $M_{II,\,III}$ edge has recently been published [GYORGY & HARVEY 1952]. The voltage value for this edge is equal to the difference between the $M_{II,\,III}$ level and the Fermi level. This difference has a more exact definition than the difference calculated from the K absorption edge. As we shall see later, the Fermi level corresponds to the point h in Fig. 16. The voltage difference $h_{Cr} - V_L = 5987.4 - 5946.1 = 41.3$ V (Tables 9 and 10). The direct spectroscopic value is 41.6 ± 0.3 V.

4. Conclusions

We may thus conclude (1) that the nature of the cathode surface effects the energy of the electron, (2) that this effect coincides with the work function of the cathode within the limits of experimental error, and (3) that the maximum available kinetic energy of electrons is the same in determinations of the excitation potential as in determinations of the limit of continuous radiation.

The excitation potentials in the tables have been corrected for the work function of the cathode. A summary of all corrections applied is given for the greater part of the curves obtained with a tungsten cathode in Table 6 b. Where no correction has been made for the work function, the value is marked with an asterisk.

Chapter VI. The *K* excitation curves

A. Chromium

General properties

The chromium targets were of three types: (1) ground chromium plate 1 mm thick, (2) electrolytic deposits on a copper-nickel base, and (3) chromium films evaporated on to a copper base. Analytically pure chromium was used for (1) and (3), fused according to Goldschmidt.

Chromium melts at 1860° C, but the vapour pressure is high even in the solid state. The evaporation temperature was 1100–1200° C, and the molybdenum furnace was used.

Chromium is not readily oxidised under electron bombardment. The experience of the present author was quite different from that of GYORGY & HARVEY [1952] in this respect; — they evaporated chromium continuously on to the target when making determinations.

Chromium crystallises in body-centred cubic crystals, and is stable in this form up to more than 1600° C.

The K absorption edges for Cr and Cr_2O_3 have been determined by SANNER [1941]. The main edge of Cr_2O_3 is 10.5 V higher than the edge of the pure element.

Information about the physical and chemical properties of the metals concerned have been taken from ESPE & KNOLL [1936], VAN ARKEL [1939], LAW [1948] and SZABÓ & LAKATOS [1952].

Tables and Curves

The earlier K excitation curves were obtained without an evaporation furnace. Only Nos. 20–24 are with evaporation films. There was very seldom any trace of contamination in focus after the introduction of liquid-air traps.

Table 11. Summary of Cr $K\alpha_1$, tungsten cathode. Work function correction included.

Nos.	Anticathode temperature	S	H	R	P
4–15	1 000° C	5 986.8	5 988.1	5 989.5	5 995.5
16–20	100° C	5 987.7	5 989.2	5 990.7	5 997.2
21–22	100° C	5 987.9	5 989.4	5 990.9	5 997.0
Mean Nos. 16–22		5 987.8	5 989.3	5 990.8	5 997.1
$V_{100°} - V_{1000°}$		1.0	1.2	1.3	1.6

There is a better statistical resolution in Nos. 21–22 than in the earlier curves, and more attention has been paid to the h structure. The results are given in Table 9. A summary of the chromium determinations with tungsten cathode is given in Table 11. Voltage differences and intensity characteristics are given in Tables 20a and b, the latter including a comparison between the three lines determined in chromium's K spectrum.

Figs. 15, 22–26 and 30 show the different curves obtained for chromium. See also Figs. 17, 19 and 20.

100° C and 1 000° C

The curves for incandescent targets (1000–1100° C) differ from those for targets at about 100° C in the following respects: (1) the h structure is absent, (2) ΔI is larger, (3) the plateau RP is shorter (Table 20a), and (4) the curve as a whole is displaced towards lower energies. Compare Figs. 15, 17 and 19 with Figs. 20 and 22.

The reasons that the h structure disappears at higher temperatures may be purely experimental: too low a statistical resolution, and too large voltage intervals between the points plotted. But the broadening of the Fermi level as the temperature rises may also account for a smoothing out of the excitation curve near the excitation limit. According to SKINNER [1946], we may take the breadth of the Fermi level as $6kT$. This corresponds to the energy difference between the levels 5 % and 95 % occupied (cf. Chapter IX), and gives us widths of 0.19 V and 0.66 V at 100° C and 1000° C respectively. A structure 0.5 V wide is consequently smoothed out at the higher temperature.

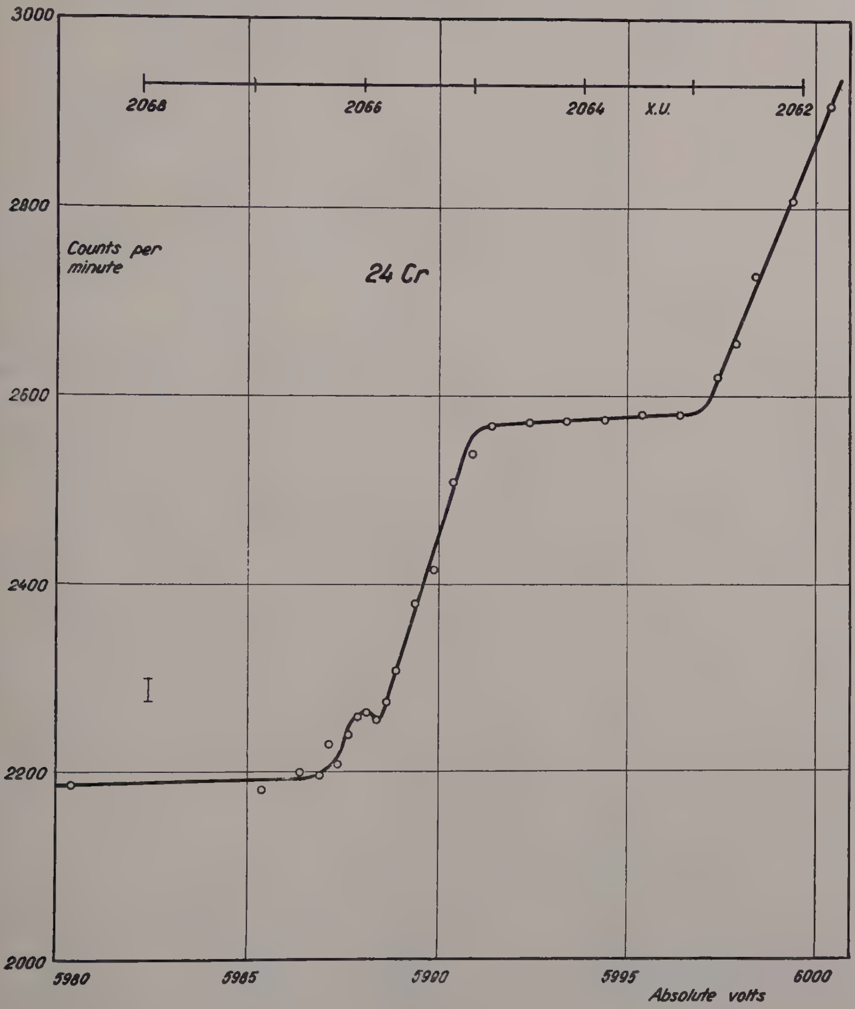

Fig. 22. Cr Kα_1. Evaporation deposit on copper. No. 22, Table 9.

Generally, a smoothing out of the structural details may be expected at higher temperatures, by analogy with what happens in the case of the absorption edges [HANAWALT 1931]. Where the excitation curve has been drawn with a sharp corner, this should be regarded as a more or less rough approximation.

The displacement towards lower energies at higher temperatures is clearly evident n Fig. 21 and Table 11. Displacements might be expected as a consequence of changes in the lattice constant — e.g. owing to thermal expansion, or transition to another crystal system. KURYLENKO [1939] observed a similar displacement with temperature of iron's K absorption edge. He made his measurements for a target at 960° C, thus above the transition temperature to γ-Fe. [See also CAUCHOIS 1952.]

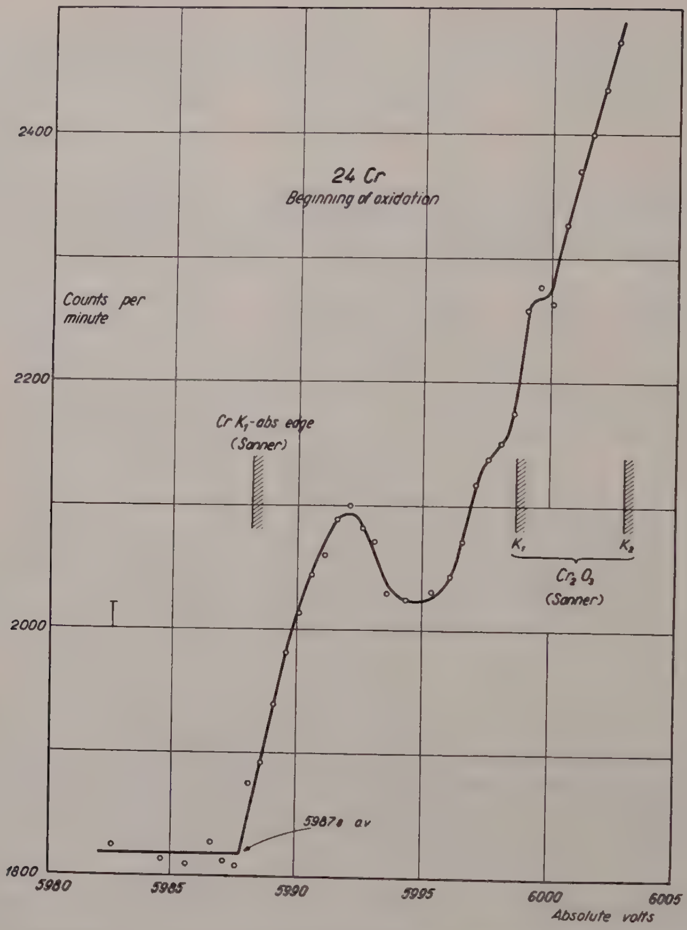

Fig. 23. Cr Kα_1 excitation curve with the chromium-plated copper anticathode slightly contaminated.

K α_1 and K α_2

Series Nos. 22 and 23 were obtained in immediate succession, and Fig. 24 shows their agreement as to position and shape. It will be seen from Table 20 b that ΔI for Kα_1 and Kα_2 are in the ratio 1 : 0.48.

K β_1

The intensity of the Cr Kβ_1 line is only about 20 % of that of the Kα_1 line. Near the excitation potential it scarcely rises above the continuous background. Figs. 25, 26 and Table 20 b.

With a thick target the slope of the background is so steep that the structure of the Kβ_1 curve disappears. However, the use of a thin target makes it possible to obtain a level background. The thin target was prepared by evaporating chromium on to a beryllium base. This method has been used previously for similar purposes [cf.

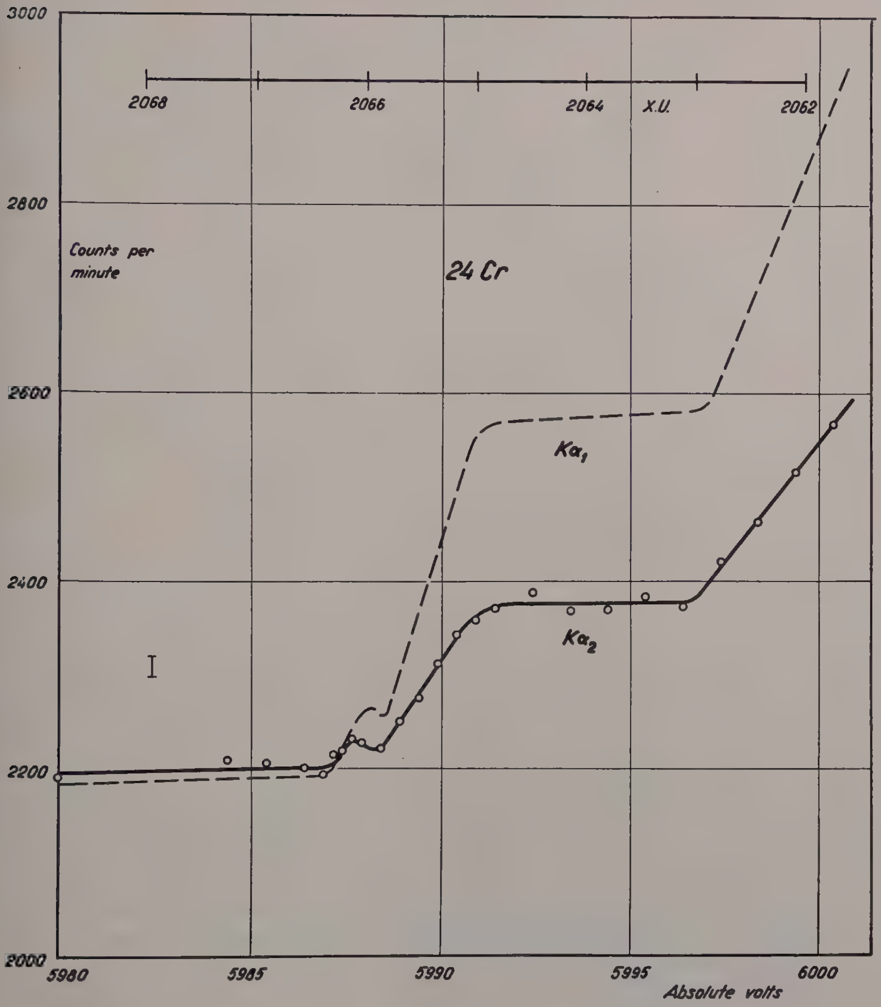

ig. 24. Cr Kα_2. Evaporation deposit on copper. No. 23, Table 9. The dotted line is the Kα_1 curve of Fig. 22.

OSTER & VAN ZUYLEN 1932]. An attempt was made to evaporate beryllium diectly on to a copper base, but the metal is very brittle, and showed a tendency to lake at thicknesses of about 1 micron. The target base finally used consisted of 0.2–0.3 icrons beryllium on copper, with 0.3 microns aluminium as an intermediate layer. his target was durable. Its continuous spectrum is shown in Fig. 25, curve (a). he thickness of the evaporated chromium layer was of the order of 500 Å.[1]

The continuous background with the thin Cr film had an intensity about 40% f the thick Cr target's, and levelled out just before the excitation potential of r Kβ_1 to an almost horizontal distribution.

---

[1] Docent E. INGELSTAM, Stockholm, determined the thickness interferometrically, and I ould like to take this opportunity of thanking him.

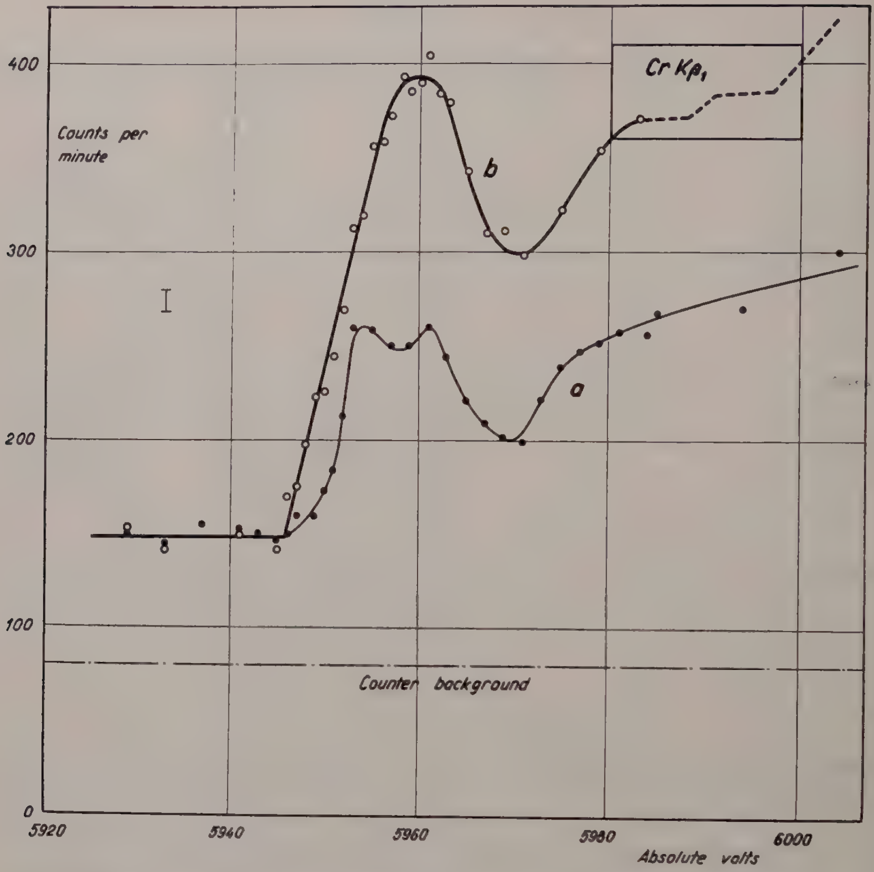

Fig. 25. The continuous X-ray spectrum at the Cr Kβ_1 excitation curve (dotted).

The rectangle in the upper right corner corresponds to the square marked in Fig. 26.
a. Isochromat for the pure beryllium anticathode.
b. Isochromat for the same beryllium anticathode with a thin evaporation deposit of chromium.

B. Oxidation influence upon the curves

Contamination of the focal spot because of oxidation could be detected in the excitation curves even when there was scarcely any visible discolouration of the target. Certain structural details were very sensitive to contamination. A broad intensity minimum appeared in the RP ridge of the titanium and chromium curves (Fig. 23). At the same time, changes occurred in the neighbourhood of the oxide absorption edges (the positions of these according to Sanner are indicated in Fig. 23). Nevertheless, the position of the main edge in the voltage scale did not change even when the focal spot was discoloured to such a degree that the oxidation depression of the *RP* ridge might touch the level of the background.

The elements 26 Fe to 29 Cu behaved otherwise. The immediate effect of the first signs of oxidation was a marked diminution of intensity just above *R*, with a simul-

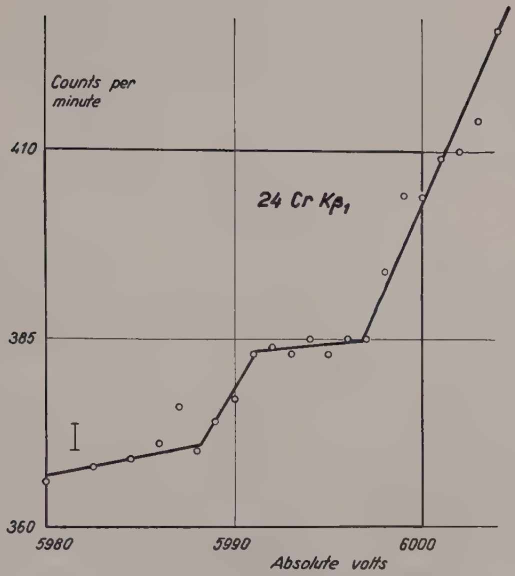

Fig. 26. Cr $K\beta_1$. Thin evaporation deposit on beryllium. The curve corresponds to the mean of six series of readings. No. 24, Table 9.

taneous appearance of intensity peaks near *P*. Fig. 37 shows two copper curves, one (a) for slight oxidation, the other (b) with so extensive oxidation of the focal spot that the pure copper radiation is completely suppressed. The displacement of curve (a) relative to curve (b) is about 3 V, which agrees with the difference between the K absorption curves for Cu and CuO given by BARNES [1933].

Whereas the *RP* ridge of chromium and copper tends to sink, the opposite effect is observed with Fe-Cu, apart from the depression at *R*. The difference seems to be connected with the position of the oxide edge. It is the region immediately below the oxide edge that is most markedly affected by the diminution of intensity, the metal's main edge remaining intact until oxidation is well advanced.

C. Titanium

General properties

The titanium target was prepared by evaporation of the metal on to a copper base. Analytically pure titanium was evaporated from a tungsten furnace. This provisional furnace was of 2 mm tungsten plate with small depressions ground into the surface to hold grains of titanium. Titanium melts at 1720° C, and evaporation took place just above the melting-point. There was considerable risk of alloying if the furnace was overheated. It is quite likely that the evaporated film contained some oxide, as it was not possible to degas the X-ray tube effectively for such a high furnace temperature.

Titanium crystallises in the hexagonal system, and the transition to the body-centred cubic form does not occur until 880° C.

The main K absorption edge for TiO_2 is 12,3 V above the corresponding edge for the pure element [SANNER 1941].

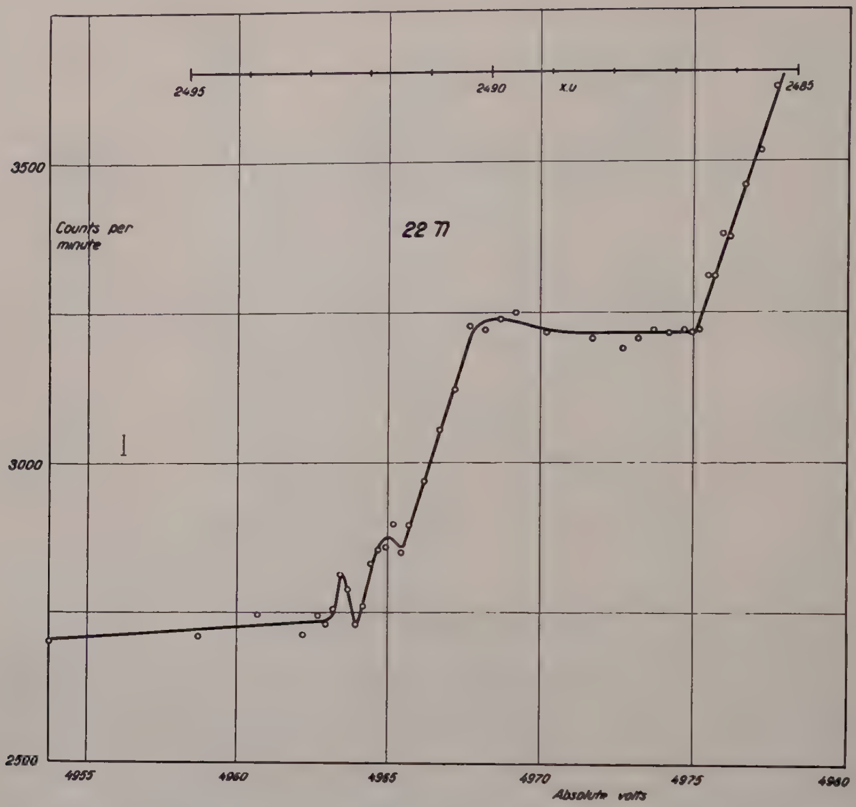

Fig. 27. Ti Kα_1. Evaporation deposit on copper. Nos. 1–3, Table 12.

Table 12. Ti Kα_1.

No.	E_{mean}	V_{R+r}	V_0	h	S	H	R	P
1	1.28206	4 938.1	4 943.8	4 963.3	4 964.5	4 966.0	4 967.5	—
2	1.28206	4 938.1	4 943.8	—	4 964.7	4 966.3	4 967.9	—
3	1.28206	4 938.1	4 943.8	—	4 964.7	4 966.2	4 967.7	4 975.1
4	1.28205	4 938.1	4 943.8	4 963.6	4 964.8	4 966.4	4 967.9	4 975.3
8	1.28201	4 937.9	4 943.6	4 963.7	4 964.8	4 966.1	4 967.3	4 974.7
9	1.28199	4 937.8	4 943.5	—	4 964.8	4 966.4	4 967.9	4 974.5
Mean, abs. volts				4 963.5	4 964.7	4 966.2	4 967.7	4 974.9
Mean without v_φ-correction				4 959.0	4 960.2	4 961.7	4 963.2	4 970.4

Anticathode: Titanium, evaporation deposit on copper (except no. 4, where a thin Ti layer was evaporated on to a beryllium target).

Cathode: Tungsten filament.

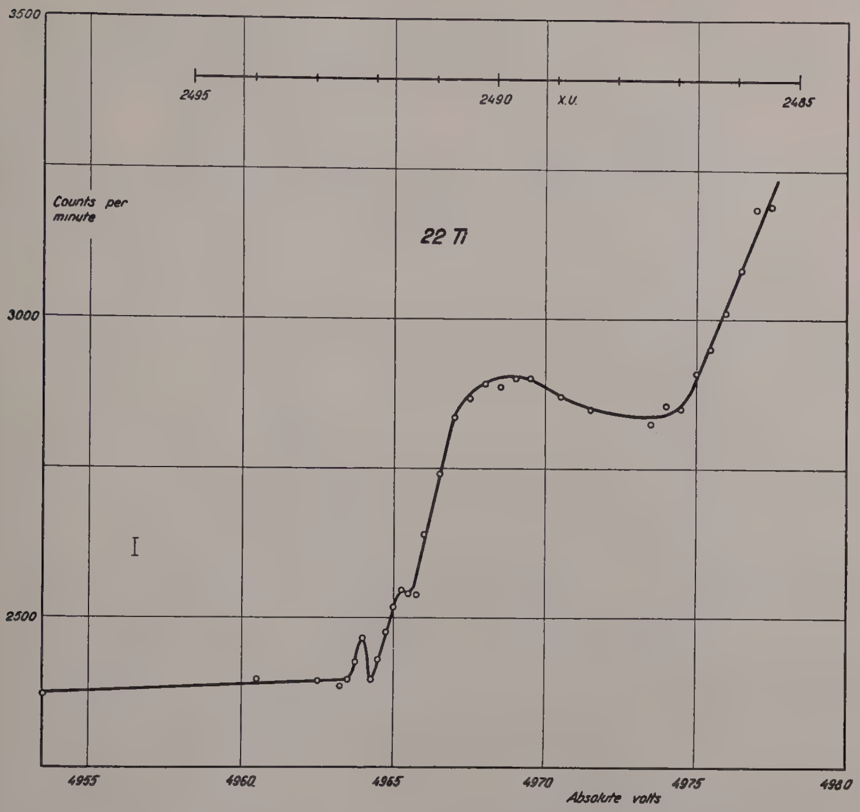

Fig. 28. Ti Kα_1. Evaporation deposit on copper. No. 8, Table 12.

Table 13. Ti Kα_1.

No.	E_{mean}	V_{R+r}	V_0^*	S	R	P
5	1.28204	4 938.0	4 938.0	4 963.4	4 966.7	4 972.9
6	1.28204	4 938.0	4 938.0	4 961.8	4 965.7	4 973.4
7	1.28204	4 938.0	4 938.0	—	—	4 973.6
10	1.28198	4 937.8	4 937.8	4 964.0	—	—
Mean, abs. volts (oxide cathode)				4 963.1	4 966.2	4 973.3
Mean, abs. volts (W-cathode, tab. 12)				4 960.2	4 963.2	4 970.4
$V_{\text{oxide}} - V_W$				2,9	3.0	2.9

Anticathode: Titanium, evaporation deposit on copper.
Cathode: Oxide-coated cathode (Nos. 5–7, 10).

The work function correction is omitted in this table.

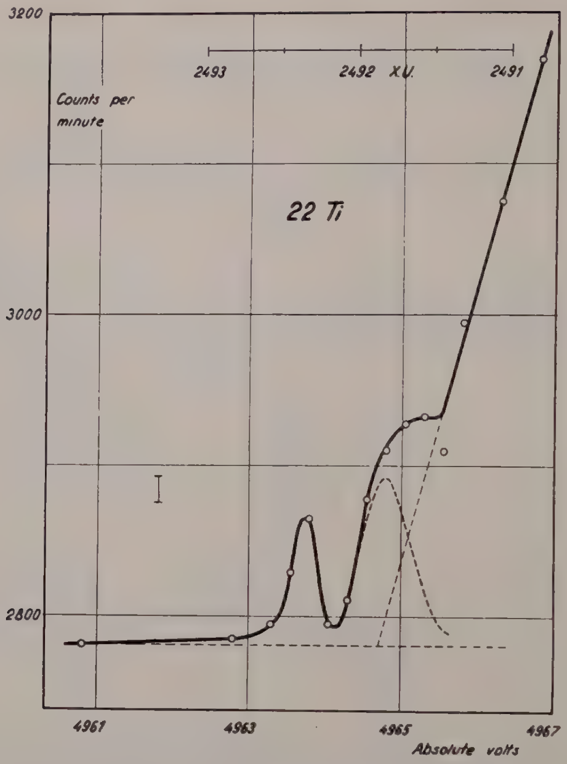

Fig. 29. The fine structure of the Ti Kα_1 excitation curve. Mean of three series of readings.

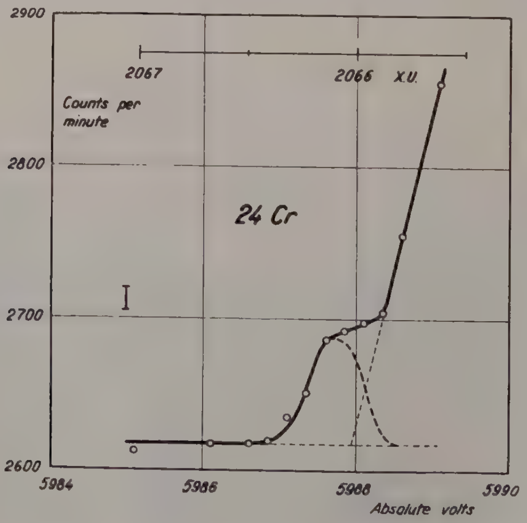

Fig. 30. The fine structure of the Cr Kα_1 excitation curve. Mean of four series of readings.

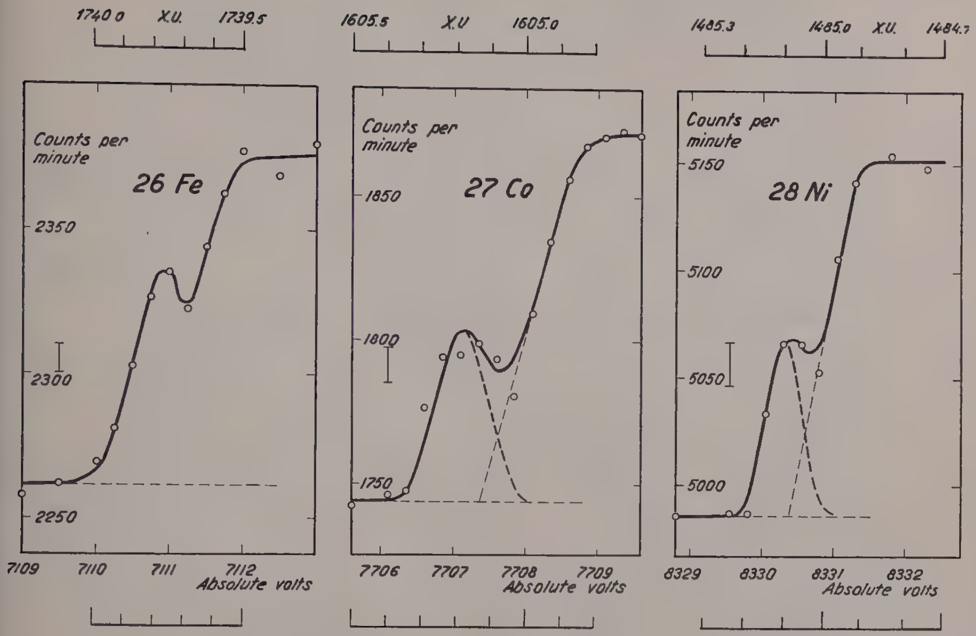

Fig. 31. The main edge and the fine structure of the Kα_1 excitation curves for Fe, Co and Ni.

The Fe curve is the mean of Nos. 2–5, Table 14, the Co curve of Nos. 4–5, Table 15, and the Ni curve of six series of readings, No. 4, Table 16.

Tables and curves

The excitation potentials from curves obtained with tungsten cathodes are given in Table 12. Voltage differences and intensity characteristics are given in Table 21. Figs. 27–29 show excitation curves. These exhibit considerable resemblances to the chromium curves. The *RP* plateau is horizontal for entirely uncontaminated targets. In contrast to the other metals, the *h* structure has a double peak, which may be due to oxidation. This explanation is supported by (1) the risk of oxidation during evaporation, and (2) the conspicuous similarity of the *h* structure of titanium and the type of oxide influence shown in Fig. 37 for Cu. Against the oxide explanation are (1) the absence of an absorption edge in this region, and (2) the "purity" of the curve in other respects.

D. Iron

General properties

The iron targets were prepared by evaporation either on to a solid copper base or on to a 1 mm iron plate inset in the copper hase. The temperature of the target was regulated by the emission, which was lowered to a value at which incandescence ceased.

The material evaporated was a piece (diam. = 2.5 mm) of spectroscopically pure iron in the tungsten crucible (Fig. 8).

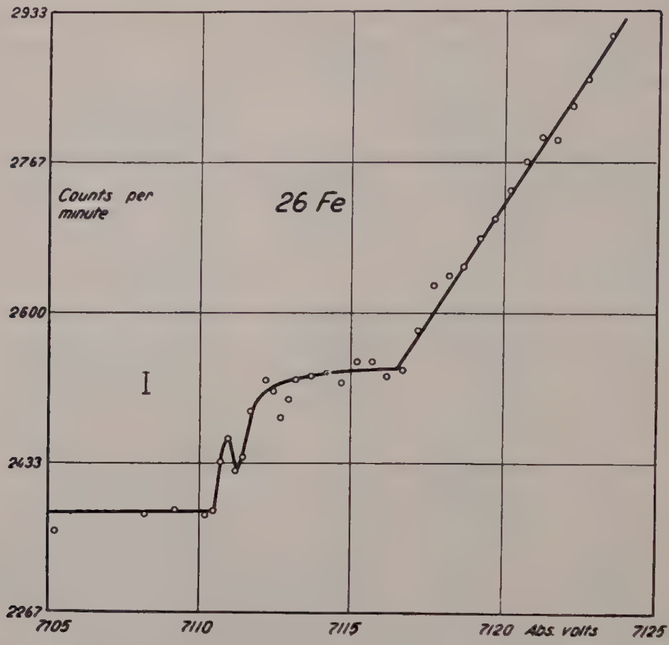

Fig. 32. Fe Kα_1. Evaporation deposit on 1 mm iron plate. No. 3, Table 14.

Table 14. Fe Kα_1.

No.	E_{mean}	V_{R+r}	V_0	h	S	H	H_0	R	P
1	1.28247	7 088.0	7 093.5	7 110.6	—	—	7 112.2	—	7 116.4
2	1.28245	7 087.9	7 093.4	7 110.8	(7 111.2)	(7 111.7)	7 111.8	(7 112.2)	7 116.6
3	1.28244	7 087.8	7 093.3	7 110.6	7 111.0	7 111.5	7 111.5	7 112.0	7 116.6
4	1.28233	7 087.2	7 092.7	7 110.4	(7 110.7)	(7 111.3)	7 111.6	(7 111.9)	7 116.2
5	1.28232	7 087.2	7 092.6	7 110.2	(7 110.4)	(7 111.0)	7 111.0	(7 111.6)	7 116.8
Mean, abs. volt (Nos. 2–5)				7 110.5	7 110.9	7 111.4	7 111.5	7 111.9	7 116.6

Anticathode: No. 1. Iron, evaporation deposit on copper.
Nos. 2–5. Iron, evaporation deposit on 1 mm iron plate.
Cathode: Tungsten filament.

The brackets indicate uncertainty in identifying the point in question. These voltages have been assigned a weight of $^1/_2$ in the calculation of the mean.

Iron melts at 1539° C, and evaporation took place just below the melting-point. There was no observable tendency to alloy with the tungsten.

Iron crystallises at normal temperatures in body-centred cubic crystals (α-Fe), and transformation to the paramagnetic form begins at 769° C without alteration of the crystal system. Iron adopts a face-centred cubic modification (γ-Fe) in the range 900–1400° C. Above 1400° C the stable form is again body-centred cubic.

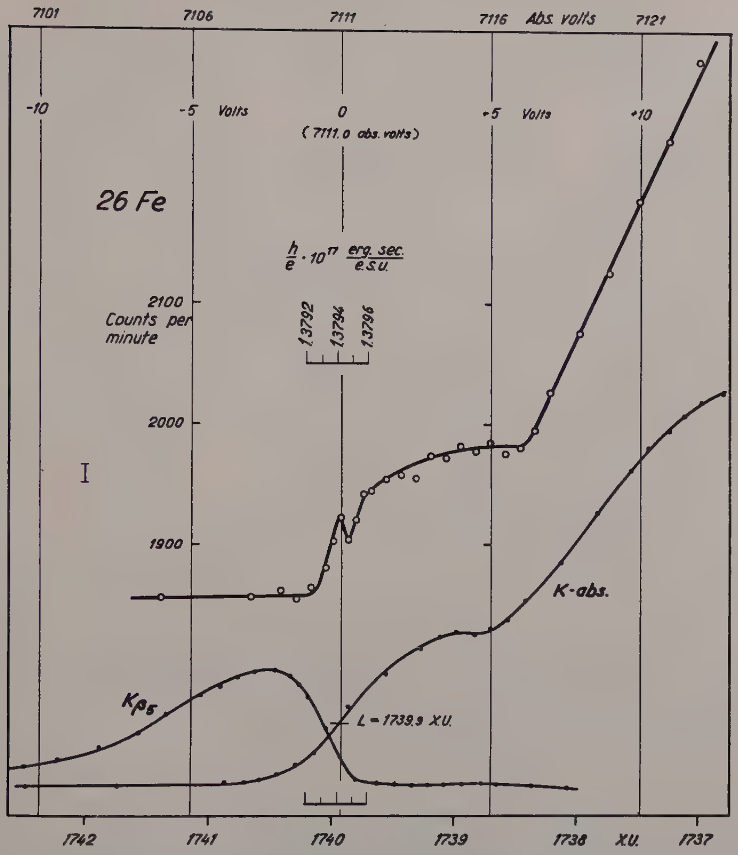

Fig. 33. Kα_1 excitation curve for Fe (No. 5, Table 14), and the K absorption edge for comparison.

(Fe target: — evaporation deposit on 1 mm iron plate.)

The excitation curve is moved + 0.4 V in order to bring the main edge into coincidence with the mean values in Table 14.

The K absorption edge and the Kβ_5 line in Figs. 33, 35, 36 and 38 are taken from Beeman and Friedman [1939], being redrawn with the same voltage dispersion as the corresponding excitation curve. The absolute-volt scale belongs to the excitation curve, and the wave-length scale to the absorption edge and the Kβ_5 line.

According to Sanner [1941], the main K absorption edge for FeO is 9.2 V higher than the corresponding edge for the pure element, and that for Fe_2O_3 12.1 V higher. Barnes [1933] observed, however, structural details in the Fe_2O_3 curve extending as far as to the main edge for the pure element.

Tables and curves

The excitation potentials are given in Table 14, and the voltage differences and intensity characteristics in Table 22. Figs. 31–33 show the excitation curves.

Uninterrupted determinations could not last more than about 20 mins. with cooled targets, owing to the rapid oxidation. Series of two or three times this duration could

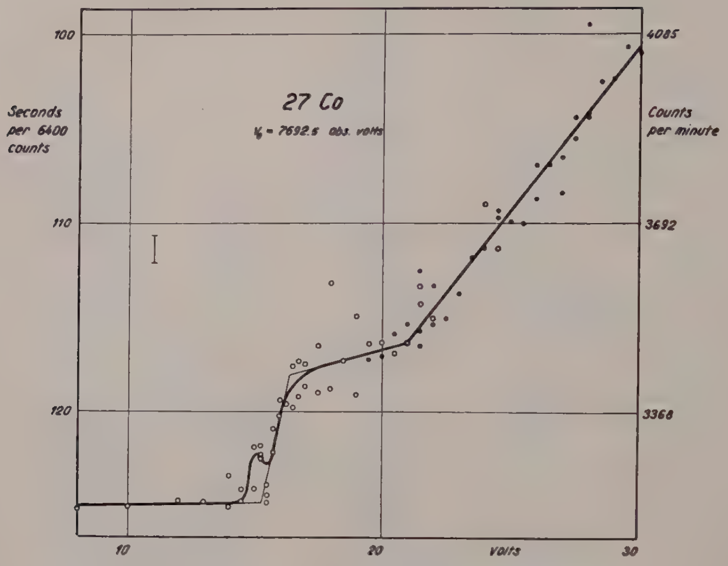

Fig. 34. Co $K\alpha_1$. Evaporation deposit on 1 mm cobalt plate, No. 1, Table 15. Original series of readings.

The horizontal axis gives the additional voltages as read form the Roller-Smith voltmeter. The curve was taken from right to left, and the different kinds of points marked indicate different cobalt evaporations. The voltages have to be corrected for a small drift in the Roller-Smith scale (here −0.1 V), and the intensity values for the dead time of the Geiger counter.

be obtained with the 1 mm iron plates (at about 500° C). This temperature is lower than the Curie temperature, where displacements of the excitation potential may be expected. The means in the table refer to the film evaporated on to the iron-plate target, while control determinations were made with an iron deposit on copper.

The *h* structure of iron is farther up on the main edge than in the case of Cr and Ti, but it is not really higher in counts/min. (32 c/m for Fe and 27 c/m for Cr, with the background reduced to 1000 c/m). For iron, the *RP* plateau represents only 6 % of the background, whereas it is 18 % for chromium and 22 % for titanium (Tables 20–22).

The identification of the points *S* and *R* is uncertain, as Figs. 32–33 indicate, so a new point, H_0, has been introduced. In determining this point, the curve is drawn as in Fig. 16, and H_0 is identified as the intersection point of the line *RS* and a horizontal line through the plateau of the *h* structure.

E. Cobalt

General properties

The targets were prepared by evaporation of spectroscopically pure cobalt from a tungsten crucible on to a 1 mm thick cobalt plate. (Cf. Fe.) Two curves were obtained with thin layers of cobalt on beryllium (Nos. 4, 5, Table 15), the Be layer on a cobalt plate for one of them and on copper target for the other. (Cf. Cr $K\beta_1$.)

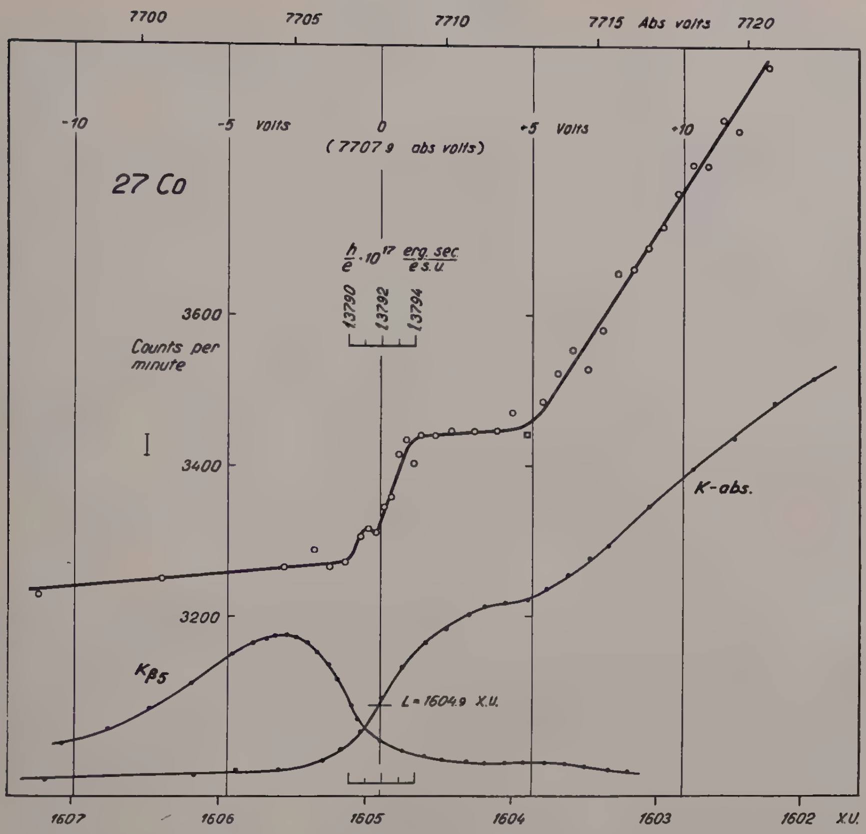

Fig. 35. Kα_1 excitation curve for Co (No. 3, Table 15), and the K absorption edge for comparison. (Co target: — evaporation deposit on 1 mm cobalt plate.)

Cobalt melts at 1495° C, and evaporation took place just below the melting-point. There were no observable signs of alloying with tungsten.

Cobalt crystallises in hexagonal crystals at normal temperatures (α-Co). The transition to the cubic modification (β-Co) occurs at a temperature between 450 and 800° C, depending on the size of the crystallites. Evaporation gives a fine-grained layer [LEVINSTEIN 1949], which retards the α-β transition. Both α- and β-cobalt are ferromagnetic; the Curie temperature is 1120° C.

According to BARNES [1933], the foot of the K absorption edge of Cr_2O_3 is only 1 V above that of the pure element.

Tables and curves

The excitation potentials are given in Table 15, voltage differences and intensity characteristics in Table 22. The excitation curves are shown in Figs. 31, 34 and 35.

The rapidity of oxidation under electron bombardment was about the same for cobalt as for iron.

Table 15. Co Kα_1.

No.	E_{mean}	V_{R+r}	V_0	h	S	H	H_0	R	P
1	1.28296	7 687.1	7 692.5	7 707.2	7 707.7	7 708.3	7 708.0	7 708.8	7 713.3
2	1.28266	7 685.3	7 690.7	7 706.7	7 707.2	7 708.2	7 707.8	7 709.2	7 713.6
3	1.28265	7 685.3	7 690.7	7 707.0	7 707.4	7 708.1	7 707.7	7 708.8	7 712.8
Mean, abs. volts				7 707.0	7 707.4	7 708.2	7 707.8	7 708.9	7 713.2
4	1.28264	7 685.2	7 690.6	7 706.6	7 707.4	7 708.1	7 707.9	7 708.7	7 713.5
5	1.28258	7 684.8	7 690.2	7 706.6	7 707.5	7 708.2	7 708.0	7 708.9	—
Mean, abs. volts				7 706.6	7 707.5	7 708.2	7 708.0	7 708.8	7 713.5
Mean, Nos. 1–5, abs. volts				7 706.8	7 707.4	7 708.2	7 707.9	7 708.9	7 713.3

Anticathode: Nos. 1–3. Cobalt, evaporation deposit on 1 mm cobalt plate. Below red heat or just faintly glowing.
No. 4. Cobalt, evaporation deposit on Be–Co plate. Thin Co layer.
No. 5. Cobalt, evaporation deposit on copper. Thin Co layer.

Cathode: Tungsten filament.

The continuous background was repressed when thin cobalt films were used. There was no discernible voltage displacement for these films, nor for the different target temperatures.

It will be seen from Table 22 that there is a striking resemblance in shape between the Fe and Co curves.

F. Nickel

General properties

The targets are described in Table 16. Evaporation was performed with analytically pure nickel from a tungsten crucible (cf. Fe).

Nickel melts at 1453° C. The evaporation temperature chosen was just below the melting-point. Very slight overheating melted the nickel, which immediately formed an alloy with the tungsten of the crucible, making evaporation impossible.

Nickel crystallises in face-centred cubic crystals. The Curie point is about 380° C.

Nickel is resistant to oxidation under electron bombardment. A cooled target was tested for 10 hrs. continuous operation, and there was scarcely any visible contamination.

The foot of the K absorption edge for Ni_2O_3 is 5–6 V above the corresponding point for the pure element [BARNES 1933].

Tables and curves

The excitation potentials are given in Table 16, voltage differences and intensity characteristics in Table 22. An excitation curve is shown in Fig. 36.

Series Nos. 1–4 were all determined below the Curie point. With incandescent targets there was a displacement of about 1 V upwards. Similar observations regarding the L_{III} absorption were made by CAUCHOIS [1952].

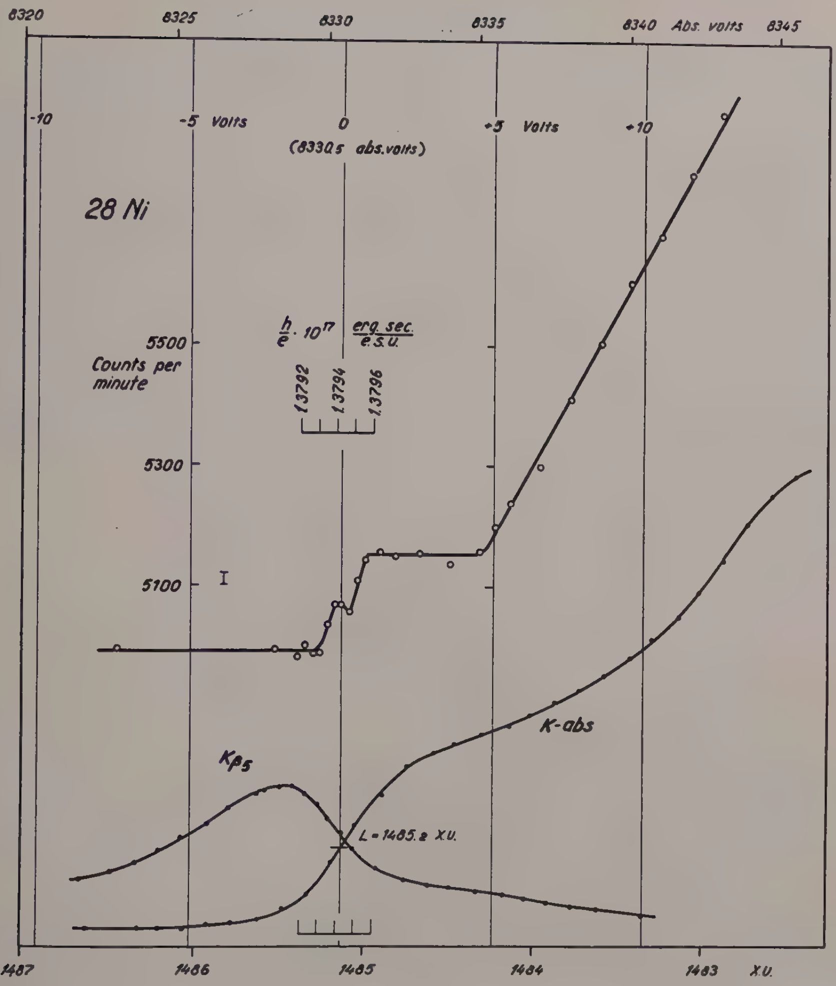

Fig. 36. Kα_1 excitation curve for Ni (No. 4, Table 16), and the K absorption edge for comparison. (Ni target: — evaporation deposit on copper.)

In nickel, the *h* structure has sunk in height and width. The height for chromium, iron and cobalt was about 30 counts/min. (I_{OS} = 1000 c/m), but is only half as great in the case of nickel (16 c/m). The *RP* plateau for nickel is also only half the height of iron's and cobalt's (Table 22).

G. Copper

General properties

The targets were prepared by the evaporation of electrolytic copper on to a copper base. A molybdenum furnace was used for the evaporation. Molten copper does not wet molybdenum, and the molten metal in the furnace gathered in a globule at the bottom.

Table 16. Ni Kα_1.

No.	E_{mean}	V_{R+r}	V_0	h	S	H	H_0	R	P
1	1.28468	8 308.7	8 314.0	8 330.3	8 331.1	8 331.6	8 331.5	8 332.1	8 335.9
2	1.28226	8 308.0	8 313.3	(8 330.0)		—	—	—	8 335.2
3	1.28225	8 307.9	8 313.2	8 329.4	8 329.8	8 330.3	8 330.1	8 330.8	—
4	1.28224	8 307.9	8 313.2	8 330.0	8 330.4	8 330.9	8 330.8	8 331.3	8 335.2
Mean (weighted), abs. volts				8 329.8	8 330.3	8 330.8	8 330.6	8 331.2	8 335.3

Anticathode: No. 1. Nickel-electroplated copper.
Nos. 2, 4. Nickel, evaporation deposit on copper.
No. 3. Nickel, evaporation deposit on a nickel plate (below red heat).
Cathode: Tungsten filament.

The weights assigned to the different series of readings are proportional to the number of counts per point. See Table 22.

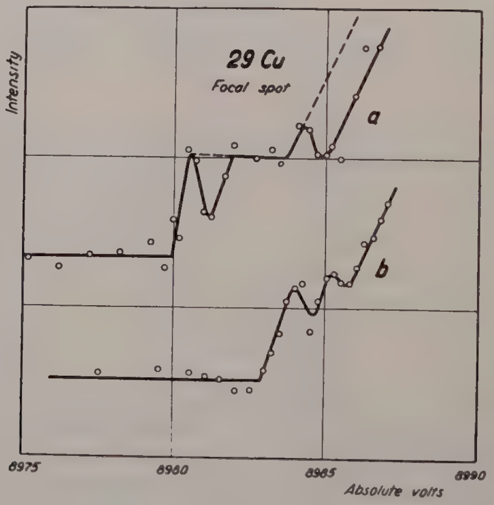

Fig. 37. Cu Kα_1 excitation curves.

a. Sligthly contaminated Cu target. The pure Cu curve is indicated by the dotted line.
b. Heavy contamination. The electron-bombarded Cu surface was left for some days in vacuum and further determination then carried out.

Copper melts at 1083° C. The evaporation temperature was above the melting-point.

Copper crystallises in face-centred cubic crystals.

The foot of the main K absorption edge of CuO is about 3 V above the corresponding point for the pure element [BARNES 1933].

Tables and curves

The excitation potentials are given in Table 17, voltage differences and intensity characteristics in Table 22. Excitation curves are shown in Fig. 38.

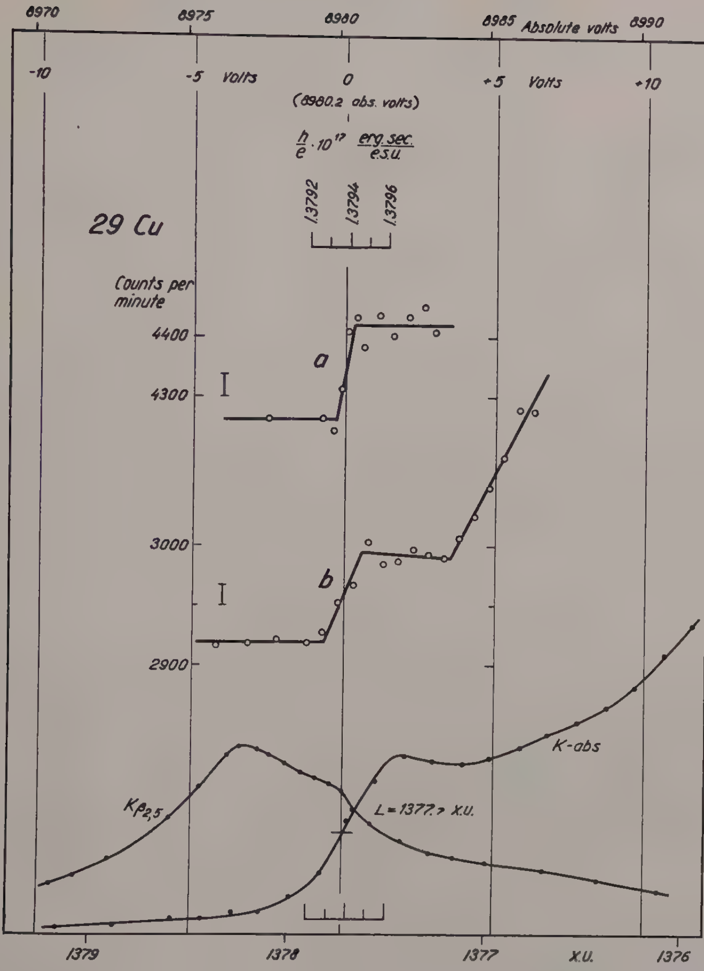

Fig. 38. Kα_1 excitation curves for Cu, and the K absorption edge for comparison.

Curve *a* corresponds to No. 5 and curve *b* to the mean of Nos. 1–3, Table 17, The anticathode was evaporated Cu on a copper base. The additional voltage was advanced in steps of $\frac{1}{2}$ V, except near the main edge of curve *a*, where the steps were $\frac{1}{4}$ V.

The excitation curves are slightly displaced in the voltage scale, to bring the main edge into coincidence with the means in Table 17: — curve *a* −0.3 V, curve *b* + 0.3 V.

The period of uninterrupted determinations was short (20–40 mins.), owing to the risk of target oxidation.

The *h* structure has completely disappeared in the copper curves. The *RP* plateau has the same low height as for nickel, and showed a tendency to negative slope in some series of determinations.

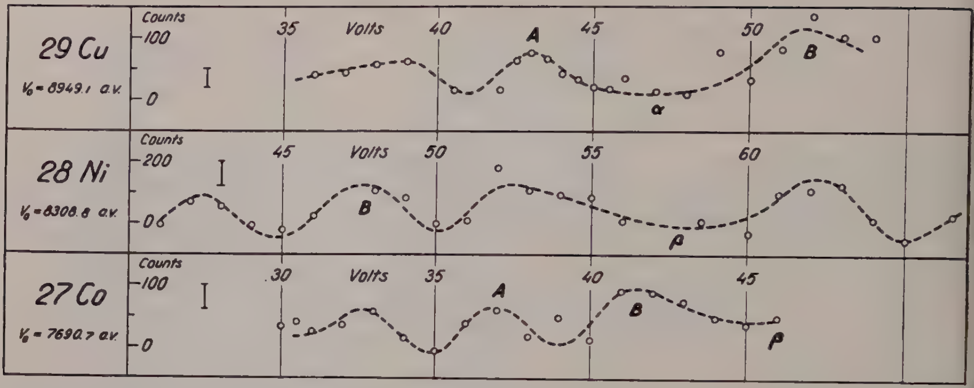

Fig. 39. The fine structure of the excitation curves for Co, Ni and Cu some tens of volts above the excitation potential.

The figure shows the intensity difference between the points determined and a straight line in the general direction of the excitation curve in the voltage range in question.

Table 17. Cu Kα_1.

No.	E_{mean}	V_{R+r}	V_0	S	H	R	P
1	1.28568	8 944.0	8 949.1	8 979.3	8 979.9	8 980.5	8 983.5
2	1.28545	8 942.4	8 947.6	8 978.5	8 978.9	8 979.3	8 982.6
3	1.28546	8 942.5	8 947.7	8 979.9	8 980.5	8 981.0	8 984.3
4	1.28505	8 939.6	8 944.7	8 980.6	8 981.0	8 981.4	8 984.6
5	1.28505	8 939.6	8 944.7	8 980.2	8 980.5	8 980.8	—
		Mean, abs. volts		8 979.7	8 980.2	8 980.6	8 983.8

Anticathode: Copper, evaporation deposit on copper.

Cathode: Tungsten filament.

Table 18. Summary in absolute volts.

	h	S	H	H_0	R	P
22 Ti	4 963.5	4 964.7	4 966.2	—	4 967.7	4 974.9
24 Cr	5 987.4	5 987.9	5 989.4	—	5 990.9	5 997.0
26 Fe	7 110.5	7 110.9	7 111.4	7 111.5	7 111.9	7 116.6
27 Co	7 706.8	7 707.4	7 708.2	7 707.9	7 708.9	7 713.3
28 Ni	8 329.8	8 330.3	8 330.8	8 330.6	8 331.2	8 335.3
29 Cu	—	8 979.7	8 980.2	—	8 980.6	8 983.8

For notation, see Fig. 16.

Table 19. Summary in int. volts.

	h	S	H	H_0	R	P
22 Ti	4 961.9	4 963.1	4 964.6	—	4 966.1	4 973.3
24 Cr	5 985.4	5 985.9	5 987.4	—	5 988.9	5 995.0
26 Fe	7 108.1	7 108.5	7 109.0	7 109.1	7 109.5	7 114.2
27 Co	7 704.2	7 704.8	7 705.6	7 705.3	7 706.3	7 710.7
28 Ni	8 327.0	8 327.5	8 328.0	8 327.8	8 328.4	8 332.5
29 Cu	—	8 976.7	8 977.2	—	8 977.6	8 980.8

Table 20 a. Voltage differences and intensity characteristics of the excitation curves for Cr Kα_1.

Nos.	counts/point	SR	RP	SP	ΔI	$\left(\frac{\Delta I}{\Delta V}\right)_{SR}$	$\left(\frac{\Delta I}{\Delta V}\right)_{PQ}$	Anticathode
			volts		counts	counts/volt		
1– 3	1 600	2.9	6.0	8.9	217	75	57	Chromium plate (Fig. 7 a) Temp. = 1 000° C
4– 5	2 560	2.8	6.2	9.0	229	82	45	
14–15	6 400	2.9	5.7	8.6	224	77	55	
	Mean	2.9	5.9	8.8	223	78	52	
7–12	6 400	2.9	6.4	9.3	(110)	(38)	(30)	Chromium-electroplated copper
16–19	6 400	3.0	6.4	9.4	(135)	(45)	(38)	
	Mean	3.0	6.4	9.4	—	—	—	
20	3 200	3.0	6.8	9.8	181	60	49	Evaporation deposit on copper
21	19 200	3.1	6.1	9.2	193	62	69	
22	9 600	2.9	6.1	9.0	168	58	44	
	Mean	3.0	6.3	9.3	181	60	54	

The intensities correspond to a continuous background (I_{OS}) of 1 000 counts per minute. For notation, see Fig. 16. In the intensity columns of the Tabs. 20–22 the word "counts" stands for counts per minute.

Table 20 b. Voltage differences and intensity characteristics of the excitation curves for Cr Kα_1, Cr Kα_2 and Cr Kβ_1.

Nos.	counts/point	SR	RP	SP	ΔI	$\left(\frac{\Delta I}{\Delta V}\right)_{SR}$	$\left(\frac{\Delta I}{\Delta V}\right)_{PQ}$	Line
			volts		counts	counts/volt		
22	9 600	2.9	6.1	9.0	168	58	44	Cr Kα_1
23	9 600	2.9	5.7	8.6	80	28	24	Cr Kα_2
24	9 600	3.0	5.6	8.6	(34)	(11)	(15)	Cr Kβ_1

Table 21. Voltage differences and intensity characteristics of the excitation curves for Ti Kα_1.

Nos.	counts/point	SR	RP	SP	ΔI	$\left(\frac{\Delta I}{\Delta V}\right)_{SR}$	$\left(\frac{\Delta I}{\Delta V}\right)_{PQ}$
		volts			counts	counts/volts	
3	8 000	3.0	7.4	10.4	170	57	56
4	6 400	3.1	7.4	10.5	(301)	(97)	(66)
8–9	8 000	2.8	7.0	9.8	212	76	54
5–7, 10	6 400	3.1	7.1	10.2	263	85	65
	Mean	3.0	7.2	10.2	215	73	58

The anticathode of No. 4 was a thin Ti layer on a beryllium target and is not included in the intensity means. (I_{OS} = 1 000 counts per minute.)

Table 22. Voltage differences and intensity characteristics of the excitation curves for 26 Fe–29 Cu.

	No.	counts/point	SR	RP	SP	hP	ΔI	$\left(\frac{\Delta I}{\Delta V}\right)_{PQ}$
							counts	counts/volt
Fe	1	8 000	—	—	—	5.8	62	31
	2	16 000	1.0	4.4	5.4	5.8	49	24
	3	12 000	1.0	4.6	5.6	6.0	65	22
	4	19 200	1.2	4.3	5.5	5.8	63	30
	5	12 000	1.2	5.2	6.4	6.6	62	28
		Mean	1.1	4.6	5.7	6.0	60	27
Co	1	12 800	1.1	4.5	5.6	6.1	63	21
	2	25 600	2.0	4.4	6.4	6.9	67	24
	3	16 000	1.4	4.0	5.4	5.8	54	19
	4	6 400	1.3	4.8	6.1	6.9	(68)	(16)
	5	12 800	1.4	—	—	—	(84)	—
		Mean	1.4	4.4	5.8	6.4	61	21
Ni	1	6 400	1.0	3.8	4.8	5.6	33	29
	2	12 800	—	—	—	5.2	33	17
	3	32 000	1.0	—	—	—	31	—
	4	64 000 (OR) 25 600 (RQ)	0.9	3.9	4.8	5.2	33	18
		Mean	1.0	3.8	4.8	5.3	33	21
Cu	1	12 800	1.2	3.0	4.2		25	16
	2	6 400	0.8	3.3	4.1		30	21
	3	12 800	1.1	3.3	4.4		32	17
	4	6 400	0.8	3.2	4.0		37	17
	5	12 800	0.6	—	—		37	—
		Mean	0.9	3.2	4.1		32	18

Nos. 4 and 5, cobalt, refer to thin Co layers and are omitted in the intensity means. (I_{OS} = 1 000 counts per minute.) For notation, see Fig. 16.

Chapter VII. Comparison of excitation curves and absorption edges

A. Electronic excitation

1. The K excitation curves

An excitation curve refers to the intensity of a single wavelength, and is therefore an isochromat. The photons associated with each point of the curve may be ascribed to two groups of electrons, both of which are spread over a certain energy band. The two groups correspond to the continuous and the characteristic radiation. Continuous radiation of wavelength λ may be emitted from any electron with kinetic energy in the interval eV to hc/λ, where λ is the wavelength of the line investigated and eV the maximum kinetic energy of the electrons striking the target. This energy band has here a breadth of 400–900 electron-volts. The characteristic radiation may be excited by electrons with energies between eV and eV_K, where V_K is the K excitation potential, — that is, within an interval small compared with that for the continuous radiation. The energy distribution within the intervals depends on the nature of the retardation mechanism exerted on the incident electrons by the target.

The continuous radiation forms a linear background of constant slope. The electrons which give rise to the K radiation are such a small proportion of the total, that the linearity established by Kulenkampff cannot be disturbed.

A knowledge of the electron energy distribution in the interval eV to eV_K is essential for the interpretation of the excitation curves. If the energy losses may be arbitrarily small, the existence of a horizontal section must be due to the occurrence of a forbidden energy band above the conduction band. A negative slope would be inexplicable [cf. DuMond 1947]. According to the electron theory of metals, no such forbidden band exists, as the unoccupied energy bands overlap. Hence the only way to explain the horizontal part of the curve is to assume the electron beam monochromatic. The negative slope discernible in Figs. 23, 37 may then be explained as a consequence of decreased level density due to the occurrence of oxide in the metal of the target.

2. The elementary process involved in the retardation of electrons by solids

The small energy losses of 5–8 kV electrons on passing through thin foils of various materials were determined experimentally by Ruthemann [1941, 1942, 1948] and Lang [1948] with a magnetic spectrometer of the semicircular type. Similar measurements at 25–40 kV were carried out by Möllenstedt [1949], using an electrostatic lens as velocity analyser. The foils used were a few hundred Ångström units thick. The energy distribution of the retarded electrons was given by Ruthemann and Lang in the form of photometer curves of the spectroscopic material. A maximum at zero energy decrement shows that some electrons passed through the foil without loss of energy. The retarded electrons are divided into a continuous band and one or a few strongly marked maxima. Where several maxima occur, they are equidistant. The existence of such maxima indicates that the electrons give up energy in discrete amounts at some kind of elementary retardation process. The continuous region may be interpreted as a statistical combination of several elementary processes. The zero maximum and the first retardation maximum in the distribution curve are well separated. The distance between them is 19–20 V for copper and 22–24 V for nickel. The discrete energy loss for beryllium, 19.0 V, is nearly equal to the voltage difference between the short wavelength limit and the intensity minimum of the Ohlin structure in Fig. 25 [cf. NIJBOER 1946].

The investigations mentioned show that above the excitation potential, in a region corresponding to the discrete energy loss in the elementary process, the K radiation arises from a monochromatic electron beam, since each loss of energy renders the electron incapable of exciting a K level. This accords with the conclusions drawn in the preceding paragraph from the appearance of the excitation curves. The magnitude of the discrete energy decrement spans the whole structure around the RP plateau of the excitation curves.

The ratio of the area under the zero maximum to the total integrated area of the distribution curve shows that the non-retarded electrons are only a small fraction of the total number. From the foil thickness used we see that K quanta by direct electron impact at voltages near the excitation potential of a thick target are emitted from a surface layer some hundreds of Ångström thick. (Cf. Chapter I, A.)

3. Kα_1 emission from electron impacts

Let:

Φ_K = the cross section per atom for K excitation by electron impact.
n = the number of atoms per cm^3.
x = depth below the target surface.
$m(x)$ = the number of electrons per cm^2 and sec., penetrating the layer x to $(x+\delta x)$ with energy $\geq eV_K$.
ω = the product of the K fluorescence yield and the ratio between the Kα_1 intensity and the total K emission.
V_K = the K excitation potential.
ε = the discrete energy decrement of electron retardation.
V = the maximum kinetic energy of the incident electrons.
C = an apparatus constant.

Then we have the following expression for the Kα_1 intensity δI per cm^2 of the layer x to $(x+\delta x)$, where δx is so small that the change in $m(x)$ may be neglected:

$$\delta I = \Phi_K \cdot n \delta x \cdot m(x) \cdot \omega C.$$

The radiation per cm^2 from a thick target is obtained by summation over all the emitting layers:

$$I = \Phi_K \cdot \omega C n \cdot \sum m(x) \delta x.$$

In accordance with the preceding section, the Σ-expression may be regarded as constant in the range V_K to $(V_K+\varepsilon)$. In this range the excitation curve therefore is a measure of the probability of K excitation.

If the voltage $V_K+\varepsilon$ is exceeded, a further term enters into the intensity expression, corresponding to excitation from electrons with energy $V-\varepsilon$.

K excitation may also occur indirectly by photo-absorption of bremsstrahlung quanta. Such fluorescence radiation cannot be neglected at higher values of V/V_K [STODDARD 1934 and 1935]. This contribution to the Kα_1 intensity is proportional to $(V-V_K)$ in the neighbourhood of the excitation potential. However, the

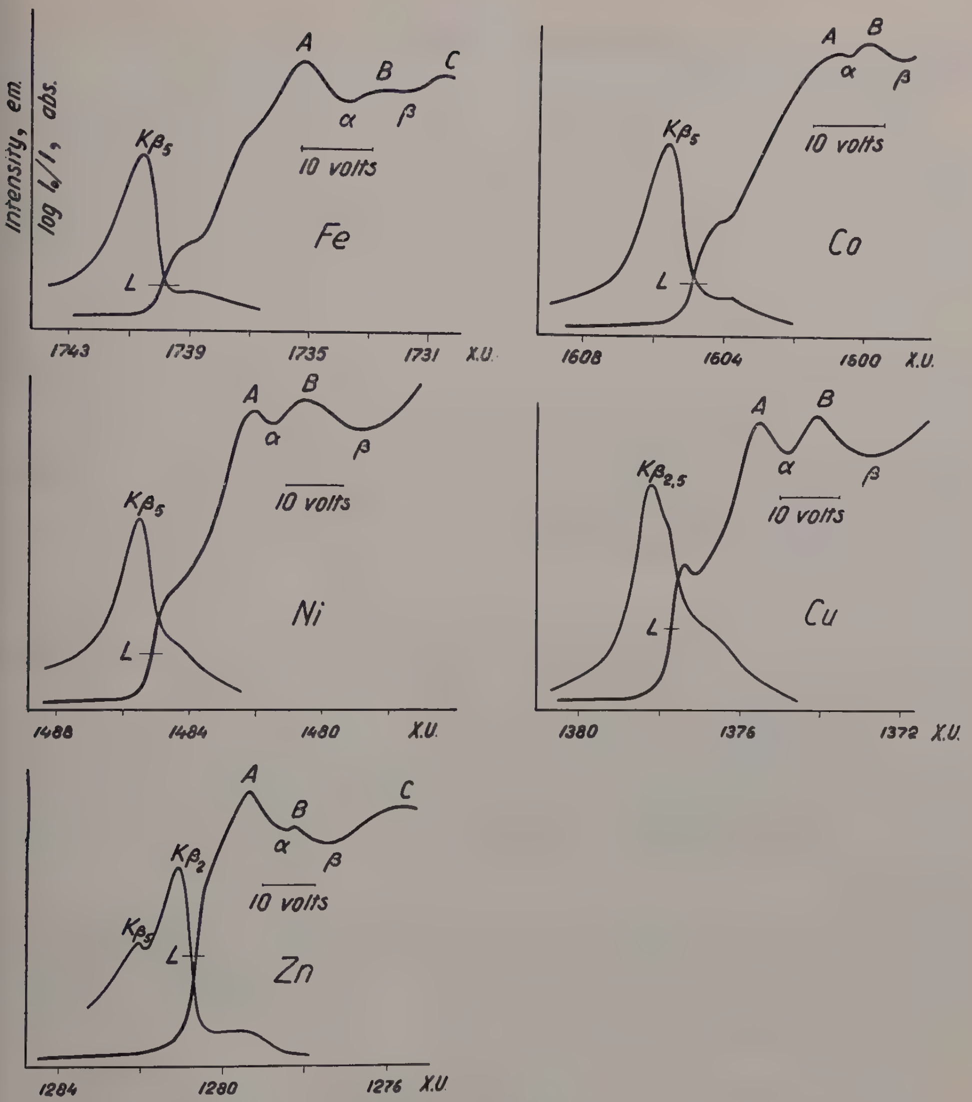

Fig. 40. X-ray absorption and emission curves for 26 Fe–30 Zn.

(After BEEMAN and FRIEDMAN 1939).

constant intensity on the RP plateau of the excitation curves indicates that the fluorescence radiation in this region is unimportant compared with the direct impact radiation.

B. The K absorption edge

The absorption edges in Figs. 33, 35, 36 and 38 are given with the same voltage dispersion as the excitation curves. Their relative positions are such that the vertical zero line cuts both edges in corresponding points, — "corresponding points" here signifying points in the respective curves which represent the same energy value. The ordinate axis of the absorption curves is log I_0/I.

The absorption edges have been taken from BEEMAN & FRIEDMAN [1939]. Their curves were obtained with a double crystal spectrometer and GM counter. As may be seen from Fig. 40, the dispersion and resolution are sufficiently high for the double edges to be clearly apparent. The $K\beta_5$ emission bands from Fig. 40 have been inserted in Figs. 33, 35, 36 and 38 with a somewhat reduced scale of intensity.

The absorption coefficient may be expressed as a sum of terms

$$\mu = \tau_K + \tau_L + \cdots + \sigma$$

where τ refers to the photoelectric absorption at the different X-ray levels, and σ to the scattering, with and without change of wavelength. Within a small region near the K absorption edge all the terms may be regarded as constant, apart from τ_K. This term is zero on the long wavelength side of the edge; on the short wavelength side for the 3d elements it is about 10 times as large as the sum of the other terms. Each term in the expression for μ is proportional to the cross section of the corresponding process. If the cross section per atom for K excitation is called Θ_K, — the coefficient μ in the neighbourhood of the absorption edge may be expressed in the following way:

$$\mu = n\Theta_K + \text{const.}$$

But μ is proportional to log I_0/I, so the absorption edges given in this scale are a direct expression for the cross section of the radiative K excitation.

What has been said in this and the preceding sections suggests that there is within limits an analogy between the two types of curve. They both represent K excitation cross sections, the absorption edges generally and the excitation curves in a region near the excitation potential. It will be seen from the figures that no considerable difference appears until higher energies are reached. Then the excitation curve continues to move upwards, while the absorption curve gradually assumes a constant value.

According to the electron theory of metals the cross section for K excitation is proportional to the density $N(E)$ of the unoccupied levels above the Fermi surface, and to the transition probability $p(E)$. [JONES, MOTT & SKINNER 1934, JONES & MOTT 1937]. E is here the energy relative to the bottom of the conduction band. Expressing this in symbols, we have

$$\Phi_K(E) = A \cdot N(E) \cdot p(E)$$
$$\Theta_K(E) = B \cdot N(E) \cdot p(E)$$
$$\text{and } \Phi_K = \Theta_K \cdot A/B.$$

It seems justifiable to consider A/B constant [cf. GRAF SODEN 1934], and full agreement may therefore be expected in the neighbourhood of the main edge between the two types of curves, not only as regards position but also in their shapes.

The existence of a retarded exciting electron in one of the excitation events can disturb the identity of the level density function $N(E)$ for the two cases. As this electron, however, must occupy a level in or above the Fermi surface and thus belong to the lattice, rather than to a single atom, the possible fine structure created is probably too small to be recorded with the present method.

C. The resolution of the structure

1. The voltage resolution

A comparison between the absorption edge and the excitation curves reveals a considerable difference in the resolution of the structure.

The resolution of the excitation curves depends only on the voltage and current circuits connected to the X-ray tube. The continuous background depends on the slit-width and focusing defects, that is true, but since it varies linearly, it has no effect on the resolution of the excitation curves. The main factors limiting the resolving power are the inhomogeneity of the electron beam and the ripples in the target voltage.

The size of the ripples is determined by the smoothing circuit used. The peak-to-peak voltage was measured as 0.08 V at 6 kV and 0.28 V at 10 kV. It seems correct to employ the double r.m.s. values, 0.06 and 0.2 V, when estimating the resolution.

The inhomogeneity of the electron beam is due to (1) uncertainty in the work function of the cathode arising from patch effects, (2) the thermal distribution of the electron velocities, and (3) the voltage drop across the cathode filament. The resolving power theoretically possible is determined by (1) and (2). The patch effects may be disregarded for a tungsten cathode. The uncertainty arising from the thermal distribution is about 0.2 V [Klemperer].

The voltage drop across the cathode introduces a maximum uncertainty of 0.3 V (cf. Chapter I). As the emission is mainly concentrated to the centre of the filament, we may ascribe a half-maximum width to this distribution. It can be taken as 0.2 V.

It is difficult to know how to combine the three main dispersive elements. Arithmetical addition certainly gives values which are too high. For the voltage dispersion of the electron beam we choose a quadratic addition and obtain the value 0.3 V, which we add arithmetically to double the r.m.s. value for the ripples. The total voltage dispersion is then 0.3–0.5 V and the resolving power, V/dV, about 20000.

This resolving power is twice as large as that attained by Beeman and Friedman for the absorption edges. They used calcite crystals, and obtained in the $(1+1)$ position for Cu Kα_1, a half-maximum width of 39,5″ (= 2.9 volts). In the $(1-1)$ position the width was 10.3″ (= 0.8 V). This value corresponds to a resolving power somewhat greater than 10000.

2. The width of the *K* level

The predominant limiting factor in the resolution of structural details in the excitation and absorption curves is the energy width of the X-ray levels. This is greater the deeper the atomic level. From the resolution point of view, it is therefore advantageous to select transitions from one of the outer X-ray levels for the investigation of the level density in the conduction band. The existence of a detailed structure in the K excitation curves was therefore surprising. It indicated that the width of the K level of the 3d elements is smaller than the widths hitherto calculated from the spectral lines. The half-maximum width of an emission line is the sum of the widths of the initial and final levels between which the transition takes place. Hence it is possible to derive the width of all energy levels in an atom from the widths of the emission lines, if the width of one level is known.

RICHTMYER, BARNES & RAMBERG [1934] described a method of estimating the level widths on the basis of quantum mechanical radiation theory. Assuming the density distribution N(E) constant, the absorption edge has the form of an arctangent curve. The point of inflection of this curve corresponds to the Fermi surface, and the width of the X-ray level is obtainable from the energy difference in the absorption spectrum between 1/4 and 3/4 of the maximum value of the absorption coefficient. BEEMAN and FRIEDMAN used this method to determine the width of the K energy levels of some investigated elements. Point L in Fig. 40 indicates the position of the point of inflection of the appropriate arctangent curve. The wavelength given for the absorption edge refers to this point. The widths of the K levels for Fe, Co, Ni and Cu were determined to be 1.3 V, 1.9 V, 1.5 V and 1.8 V respectively. The value for copper is remarkably small compared with the value for the ferromagnetic metals. This difference can be explained by the occurrence of the *h* structure in the curves for Fe to Ni, and its absence in the Cu edge. The assumption of constant N(E) therefore applies strictly only to Cu. The arctangent curve is too flat for the other elements, leading to the higher values of the level widths.

BEARDEN & SHAW [1935] give the width of Cu $K\alpha_1$ as 2.7 V, from which the width of the L_{III} level is calculated to be 1.4 V. This value is suspiciously high, because the L_{III} level should be narrower than the K level. The fault could lie in an overestimation of the width of the $K\alpha_1$ line.

BROGREN has recently shown that the customary corrections applied to the measurement of line widths with double crystal spectrometer are probably too small [BROGREN, to be published]. This correction is usually obtained by subtracting the square of the half-maximum width of the rocking curve from the square of the width of the emission line. Measurements of the Cu $K\alpha_1$ width with different crystals and crystal planes have shown that the line widths corrected in this way are dependent on the resolving power of the crystal plane. If a linear subtraction is adopted, however, a line width independent of the resolving power is obtained. Such a correction is permissible, if the true line shape and the shape of the rocking curve are of the classical dispersion form [PARRATT 1934]. BROGREN obtained in this way values for the half-maximum width of Cu $K\alpha_1$ which lie between the limits 0.42 and 0.45 X.U. The average value gives a voltage width of 2.2 V. The width of the L_{III} level obtained from this value is 0.9 V, an acceptable figure in relation to a K level width of 1.3 V. [Cf. CAUCHOIS 1953, p. 180.] A similar correction applied to Fe $K\alpha_1$ gives a half-maximum width of 1.4 V, which must correspond to a K level width for Fe of about 1 volt. The K level width of 0.58 V for argon according to PARRATT [1939] agrees with these calculations.

The acceptance of the smaller line and level widths explains the high structure resolution in the excitation curves. The level width (b) and the voltage dispersion (w) are not additive. SKINNER [1946] gives a sum of the type $(b+\beta w)$, where the fraction β is equal to 1/3 when b and w are "roughly equal". A combination af w and b according to this formula shows that the resolution of the structure details is mainly limited by the finite width of the K level.

Chapter VIII. Determination of h/e

A. Comparison between the two X-ray methods

The X-ray determinations of h/e refer to the formula $eV = hc/\lambda$. Two methods can be used, one connected with the quantum limit of the continuous spectrum and the other with the excitation potential of characteristic X-ray lines.

The quantum limit method endeavours to find the smallest voltage of the X-ray tube that enables the electrons to produce continuous quanta of a frequency corresponding to the detector position, adjusted by means of a well defined emission line. The method with excitation potential involves a comparison between electronic and radiative excitation of convenient energy levels and is thus referred to wavelength data for absorption edges.

The determination of the wavelength to be put in the formula above involves two types of error, (1) error in the wavelength used as reference and (2) error in the adjustment of the spectrometer. In the latter group we include the focusing defects of the crystal. As regards the quantum limit method, error (1) is negligible to error (2). For the concave crystal spectrometer OHLIN [1941] calculated a mean square value, which amounted to 0.01 %, whereas the wavelength error of the reference line was taken to 0.001 %. For the excitation potential method, error (2) is zero and the inaccuracy is entirely caused by error (1).

The inaccuracy in the voltage determination is identical for the two methods. The apparent advantage of the excitation method is, however, counterbalanced by a further important source of error, not existing in the quantum limit method: the error in the identification of corresponding points. For the identification we can start with a definite point in the excitation curve and try to find the corresponding point in the absorption edge. In such a case an identification error will appear in the wavelength determination. We can also enter the opposite way and introduce an identification error in the excitation potential.

B. The results

The determination of h/e in the present investigation is based on Figs. 33, 35, 36 and 38. The excitation curves shown in these figures have main edges which correspond to the mean values in the respective tables to within very small margins of error (0.1 – 0.2 V). The point L on the absorption curves is the point to which BEEMAN & FRIEDMAN's wavelength values refer. The inaccuracy in the wavelength determination is given to 0.02 X.U. The vertical zero line through L intersects the excitation curve in a point chosen as the point corresponding to L.

A scale with values of h/e is incorporated in the figures. This scale is calculated from the L value given and is fixed in relation to the volt scale and excitation curve. For different choices on this curve of voltage points corresponding to the wavelength point L, it indicates the resulting h/e value.

Copper and nickel give the most reliable determinations, and have been grouped by themselves. Copper has no h structure, so the corresponding points are easily fixed. The curve for nickel has a high degree of symmetry, which facilitates the determination of the point corresponding to L. Iron and cobalt give less accurate values, as will be seen from Fig. 33 and 35.

Table 23. Calculation of h/e from the excitation potentials.

X-ray line	λ_{abs} (X.U.)	V_{exc} (abs. volt)	$h/e \cdot 10^{17}$ $\frac{\text{erg} \cdot \text{sec.}}{\text{e.s.u.}}$	Weight	Mean
Fe $K\alpha_1$	1 739.9	7 111.0	1.3794	1	1.3793 ± 0.0006
Co $K\alpha_1$	1 604.9	7 707.9	1.3792	1	
Ni $K\alpha_1$	1 485.2	8 330.5	1.3794	2	1.3794 ± 0.0006
Cu $K\alpha_1$	1 377.7	8 980.2	1.3794	2	
				Mean	1.3794 ± 0.0006

Table 24. Comparison of various recent values of h/e.

	Year	Method	$h/e \cdot 10^{17}$	Stated error	Notes
OHLIN	1941	Quantum limit	1.3799	± 0.0008	3–5 kV
SCHWARZ & BEARDEN	1941	Excitation potential	1.3795	0.0010	Ni & Co $K\alpha_1$, $WL\alpha_1$
PANOFSKY, GREEN & DUMOND	1942	Quantum limit	1.3786	0.0002	20 kV
BEARDEN & SCHWARZ	1950	Quantum limit	1.37926	0.00008*	8–10 & 20 kV Oxide cathode
BEARDEN, JOHNSON & WATTS	1951	Quantum limit	1.37928	0.00004*	6, 10 kV
NILSSON	1952	Excitation potential	1.3794	0.0006	Fe–Cu $K\alpha_1$

The OHLIN value given is recalculated from his original figures and corrected for the work function of the cathode.

Probable errors are indicated with an asterisk, the other ones are conservative maximum errors.

As identification error we may choose a fraction of the total main edge in the excitation curve. It is improbable that L falls outside a range 2/3 of the distance hR (See Fig. 16) in the iron and cobalt curves and for nickel and copper we can no doubt choose the smaller ranges $\frac{1}{2}hR$ and $\frac{1}{2}SR$ respectively. This introduces an identification error of ± 0.01 % for the former elements and ± 0.005 % for the latter. Table 23 summarises the values of h/e obtained.

For chromium and titanium there exist no measurements of the K absorption edge with a resolution and accuracy as high as in BEEMAN & FRIEDMAN's curves. As the h structure is small compared with the entire height of the main edge for these elements they are more convenient for h/e determination than the ferromagnetic group.

The K level determination of h/e may be compared with the quantum limit value $(1.3793 \pm 0.0006)10^{-17}$ erg · sec./e.s.u., given in Table 10. As previously mentioned, the value of c used in the calculation was $2.99790 \cdot 10^{10}$ cm/sec., and of the conversion factor for kX units to Ångström, 1.00202.

In Table 10 a h/e value is also computed neglecting the work function correction. It is a remarkable fact that this value, $1.3783 \cdot 10^{-17}$ erg · sec./e.s.u., well agrees with OHLIN's values of h/e [1941] if these are recalculated with the constants used in this investigation and with applied correction for the temperature effect in the resistors R. These recalculated OHLIN values are kept within the small range (1.3782 – 1.3784) 10^{-17} erg · sec./e.s.u.

Table 24 gives a summary of X-ray determinations of h/e from OHLIN and onwards. OHLIN's value was the first to bridge the gap between the X-ray values and those determined from the formula for the Rydberg constant [OHLIN 1942 b]. His recalculated value in Table 24 is corrected for the work function of the cathode.

SCHWARZ & BEARDEN's value from excitation potential determinations [1941] is averaged by the author, who has also corrected it according to a note in the paper of BEARDEN & SCHWARZ [1950, Tab. II]. All the h/e values agree perfectly well with the value $1.3793 \cdot 10^{-17}$ erg · sec./e.s.u. computed from the Rydberg constant.

C. Error discussion

The use of the method of least squares for computing the so-called probable errors requires great statistical material. In the present investigation we prefer to perform a conservative maximum error estimation. In the calculation of the accuracy of the high voltage seven systematic errors are introduced. As all the errors probably do not act in the same direction we may add them by computing the square root of the sum of the squares. The accidental error, taken as the average deviation of the mean, is then added arithmetically.

A survey of the estimates of the relative errors is given below. The maximum errors are introduced in Table 23.

1. Errors in the determination of the voltage

a) The standard cells (Tab. 4)	8×10^{-5}
b) The Wolff precision potentiometer	10×10^{-5}
c) The resistors R (Chapter V, B)	10×10^{-5}
d) The resistors r (Chapter V, B)	10×10^{-5}
e) The correction factor for the bridge ratios (Chapter V, B)	5×10^{-5}
f) Zero point drift of the galvanometer	7×10^{-5}
g) Contact potentials and thermo-*emf* (arbitrary estimation)	10×10^{-5}
The square root of the sum of squares	23×10^{-5}
Average deviation from the mean (calc. for the S and P voltages)	5×10^{-5}
Sum:	$\pm 28 \times 10^{-5}$

2. Errors in the calculation of h/e

The excitation potential method.

a) Error in the wavelength determination [BEEMAN & FRIEDMAN 1939]	3×10^{-5}
b) Error in the voltage determination	28×10^{-5}
c) Error in the factor c^2 [acc. to BERGSTRAND, see BEARDEN & WATTS 1951]	2×10^{-5}
d) Error in the conversion factor kX to Å [BRAGG 1947]	3×10^{-5}
e) Identification error (Chapter VIII, B)	5×10^{-5}
Sum:	$\pm 41 \times 10^{-5}$

This sum refers to copper and nickel. For iron and cobolt the sum increases to 46×10^{-5} owing to the higher identification error.

The quantum limit method.

The identification error will be excluded, and the error in the wavelength determination changed to 10×10^{-5} in order to cover the errors due to the adjustment of the spectrometer [see OHLIN 1941]. The relative maximum error will then amount to 43×10^{-5}.

Chapter IX. The structure of the excitation curves and the electron theory of metals

A. Theoretical outline

1. The energy bands

According to the Sommerfeld theory of metals the energy states of the valence electrons form a continuum with a level density $N(E)$ proportional to the square root of the energy E. At the temperature of absolute zero the electrons occupy entirely the lowest states up to a discrete limit $E_{\max}$, above which the energy levels are completely empty. At finite temperatures electrons in the neighbourhood of the limit $E_{\max}$ (the Fermi level) are to a certain degree thermally excited. Generally, the density of occupied states will be expressed with the Fermi distribution function $f(E, T)$. Thus the number of electrons having energies between E and $E + dE$ is

$$2f(E, T) \cdot N(E)\,dE = \frac{2\,N(E)\,dE}{1 + e^{\Delta E/kT}},$$

where for ordinary temperatures approximately $\Delta E = E - E_{\max}$. The sharp jump in the density of occupied levels at zero temperature will be diffused over an energy range of the order of size kT (Cf. Chapter VI, A).

For the majority of metals the Sommerfeld theory gives only a very rough approximation and it has been necessary to develop the theory with more accurate assumptions to get satisfying descriptions of the properties of real metals.

The Sommerfeld theory assumes a constant potential distribution over the entire volume of the specimen. In a real metal the potential is a periodic function, varying with the period of the lattice. An advanced metal theory must take this into consideration. The complexity of the problem prevents an exact treatment, but approximation methods have been developed for various important cases.

One of these, the "nearly free electron" method, assumes the periodic variations of the potential function small compared with the kinetic energies of the electrons. Owing to the lattice field the electron wave will suffer Bragg reflections for certain energies and directions. As a consequence of that the continuum of energy states in the free electron theory is divided into allowed and forbidden bands, corresponding to separate zones (Brillouin zones) in the momentum space.

A theory along these lines applied to the fine structure of the absorption edges in X-ray spectra has been worked out by KRONIG [1931, 1932]. In an investigation of the K absorption edge of different iron compounds COSTER & KIESTRA [1950] have shown that the Kronig theory is valid for energies about 175 eV above the Fermi level, in agreement with the assumption of small potential variations in relation to the kinetic energies of the electrons. Below 70 eV the absorption coefficient was mainly a property of the atom in question.

An approximate treatment, relevant to the case of small electron energies, is the method of "tight binding", which, contrary to the Brillouin theory, assumes the electrons strongly bound to the respective atoms. The influence from the surrounding atoms is introduced as a perturbation of the atomic field. As atoms are brought together from far apart, the discrete atomic energy levels will according to this treatment be broadened into energy bands with continually increasing widths. If the atomic distances are decreased to crystal lattice dimensions, higher energy bands with states of different symmetry overlap and form so-called hybridized states. For most metals the overlapping occurs already at the energy band, containing the conduction electrons.

A third approximation method, intermediate to the two other ones, the "cellular method", is worked out by WIGNER, SEITZ and SLATER. The majority of the existing numerical calculations for real metals are performed by this method.

For a detailed treatment of the different aspects of the electron theory of metals the reader is referred to MOTT & JONES 1936, CAUCHOIS 1948, RAYNOR 1952 and MOTT 1952.

2. Electronic transitions from X-ray levels

At the excitation of an X-ray level, with which case we are concerned here, an electron is raised from the discrete deeper level to one of the unfilled energy bands above the Fermi limit. As mentioned above these bands usually overlap and the energy states are hybridized. An exact theoretical treatment will be very complicated. For the special case of transition in which an X-ray level is involved, however, a simplified model can be used. According to JONES, MOTT and SKINNER [1934, JONES & MOTT 1937] the wave function for an energy state can, in the neighbourhood of the nucleus, be developed in a series of terms, each referring to a single symmetry $s, p, d, \ldots$ In the case of X-ray transitions we are therefore allowed to (1) regard the level densities $N(E)$ as a superposition of separate level densities with pure symmetry:

$$N(E) = N_s(E) + N_p(E) + N_d(E) + \cdots$$

and (2) apply the atomic selection rules to electronic transitions to or from the conduction band.

The selection rules for dipole radiation require a change in the l quantum number with $\Delta l = \pm 1$. This means that transitions to or from the K level can occur only to or from energy states with p character. Quadrupole radiation, with possible transitions for $\Delta l = 0$ or ± 2, could be taken into consideration, but the probability of such transitions is so small in relation to that of dipole transitions that they may be neglected.

Thus we can consider, according to Chapter VII, the partial absorption coefficient $\tau_K(E)$ proportional to the product of the density of unoccupied levels and the transition probability in the following way:

$$\tau_K(E) \propto N_p(E) \cdot p_{s \to p}(E).$$

The transition probability $p_{s \to p}(E)$ will be approximately constant in a small range. The absorption coefficient $\tau_K(E)$, the excitation cross section Φ_K and the radiated intensity $I_{K\alpha_1}$ (with the limitations metioned in Chapter VII), are therefore proportional to the density of energy states with p character:

$$I_{K\alpha_1}(E) \propto N_p(E).$$

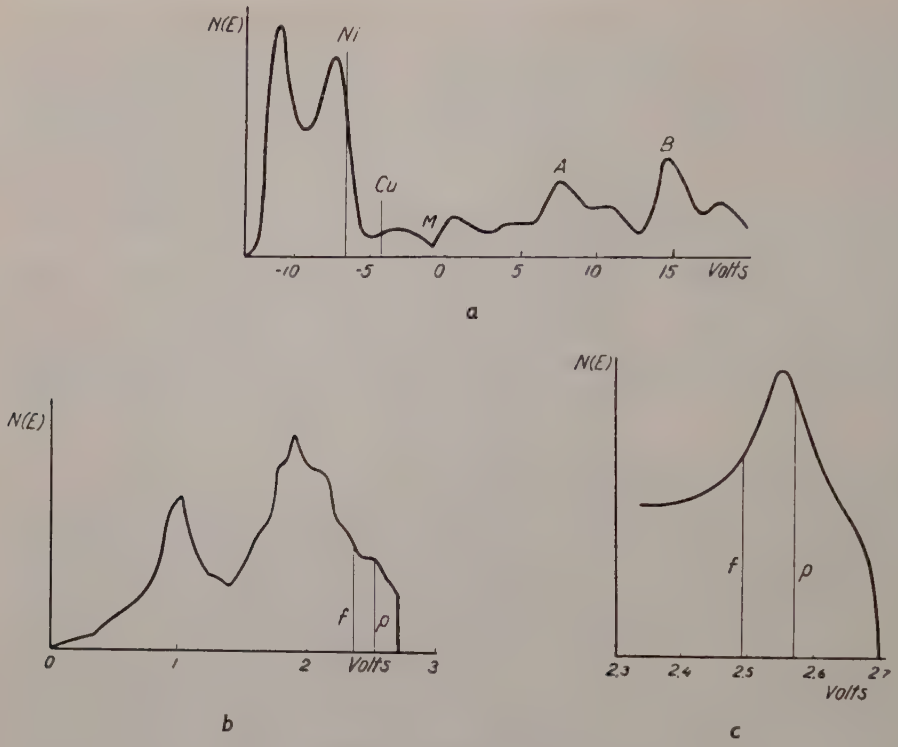

Fig. 41. Density of states as a function of energy.

a. Filled and unfilled energy bands of copper. After RUDBERG and SLATER 1936.

b. The 3d band of nickel. After FLETCHER and WOLFARTH 1951.

c. The higher energy maximum of the 3d band of nickel. FLETCHER 1952.

As a consequence of the theoretical considerations of JONES, MOTT and SKINNER we make use of the expressions "3d band", "4s band" and "4p band", according to the main symmetry, and identify these bands in the excitation curves. It must however be remembered that such a notation is mainly formal and that its correspondence to real properties is strongly limited.

3. The 3d elements

The 3d elements have the argon shell $1s^2\ 2s^2\ 2p^6\ 3s^2\ 3p^6$ completely filled. From the X-ray spectroscopy we know that the next higher states, 3d, 4s and 4p, are, because of the crystal formation, broadened into wide overlapping energy bands. The different energy levels around the Fermi limit must therefore exist in hybrid (spd) states. The investigated element with the lowest atomic number, 22 Ti, has 4 electrons outside the argon shell. These partly fill the 4s and partly the 3d band. The number of 4s electrons per atom is for the 3d elements nearly constant and as we proceed to higher atomic numbers the added electrons fall in the 3d band, which at 29 Cu contains 10 electrons, the maximum number for this band.

For a few of the 3d elements and the neighbouring metals the energy levels are calculated with some of the approximation methods mentioned in section A, 1.

The most extensive treatment has been applied to the band structure of copper and nickel. The cellular approximation method is applied to copper by KRUTTER and SLATER [KRUTTER 1935, SLATER 1936, RUDBERG & SLATER 1936]. The density curve for copper according to RUDBERG & SLATER is shown in Fig. 41 a. The states are occupied by electrons to the level marked Cu. The 3d band with its 10 electrons per atom has a remarkably high level density. It overlaps the 4s band which extends with low density from about the bottom of the 3d band to the trough M in the figure. The 3d band is split in two peaks, the lower containing two and the higher three sub-bands. According to Krutter the lower energy peak has no p admixture. [Cf. BEEMAN & FRIEDMAN 1939.] From the point M and above, the bands are mainly of p symmetry. Two sharp density maxima, A and B, occur.

The theoretical results for copper are extrapolated to nickel. The nickel bands contain one electron less than copper and the Fermi level is shifted to the level marked Ni in Fig. 41 a.

Recently FLETCHER and WOHLFARTH [1951] have recalculated the density of states for the 3d electrons in nickel with the method of tight binding. The general appearance of the resulting density curve is, as shown in Fig. 41 b, similar to the one calculated by RUDBERG & SLATER. An important difference exists, however. The tight binding method gives a total width of the 3d band of 2.7 volts, which is less than half the energy width according to RUDBERG & SLATER. The paramagnetic form of nickel is filled with electrons of both spins to the level marked p in the figure. For the ferromagnetic form the electrons of one spin fill the entire band, while the ones with the opposite spin have the upper limit marked f, thus having an empty range of 0.2 eV, which according to the improved calculations by FLETCHER [1952] includes the peak of the higher energy maximum (Fig. 41 c).

B. Discussion of the structure

1. The copper and nickel curves

The copper excitation curve (Fig. 38) and the corresponding absorption curve of BEEMAN & FRIEDMAN are similar in the main tracks. As is seen in Fig. 41 a the Fermi level lies in the 4s band, the p admixture of which determines the height ΔI of the RP ridge in the excitation curve. This ridge has a horizontal or slightly negative slope and is terminated by a sudden intensity increase at P, indicating the beginning of the 4p band with a high p level concentration. From P onwards the intensity curve rises almost linearly.

The SR edge is very sharp as is seen in Fig. 38 a, where the resolution is higher than in the curve b, because of the smaller intervals in the additional voltages v. The width SR of the edge corresponds to the breadth of the K level according to the discussion in Chapter VII, C. The Fermi limit is represented by the point H.

CAUCHOIS [1953] has measured copper's L_{III} absorption and found a second sharp increase in absorption about 3.5 eV from the main edge. This distance is in good agreement with the distance of 3.6 volts in the excitation curve between the points H and P, corresponding to the first and second intensity increase. In remarks on the work of CAUCHOIS, MOTT [1953] calls attention to the occurrence of s states of high density at the bottom of the 4p band (second Brillouin zone) but according to the sharp intensity increase in the excitation curve for about the same energy level the symmetry cannot be entirely of s character. The uncorrected width of the L_{III} edge is given by CAUCHOIS to be 1.2 volt, slightly greater than the *SR* width for copper in Tab. 22.

Apart from the *h* structure the nickel excitation curve is very similar to the copper curve. The $N_p(E)$ function for copper and nickel is drawn in the reference MOTT 1953, where for the bottom of the 4s band a density distribution proportional to $E^{3/2}$ is suggested on account of the earlier paper by JONES, MOTT & SKINNER [1934]. The distribution function reaches a maximum a few volts from the 4p band and has then a negative slope. For copper the Fermi limit lies near the maximum of the distribution function, while for nickel it lies at a more levelled range with low densities. The change in slope should be noticed in the excitation curve of nickel but is screened by the existence of the *h* structure, which, as we shall see later, can be interpreted as transitions to the empty part of the 3d band. This, according to FLETCHER, has a width of 0.2 volts for ferromagnetic nickel, but in our case we must reckon with a blurring effect because of the width of the K level. A reconstruction of the 3d contribution to the intensity could therefore give an estimate of this width. Such an attempt is made in Fig. 31 with the rough approximation of a straight line for the 4s edge. The value obtained is 0.6 V (the same size as for the copper edge measured with the smaller voltage intervals).

Fig. 39 shows the fine structure higher up on the *PQ* part of the excitation curves for copper, nickel and cobalt. The letters in the figure indicate the position of the points similarly marked in the absorption curves of BEEMAN & FRIEDMAN and in the theoretical curve in Fig. 41a according to RUDBERG & SLATER. For copper a numerical comparison is performed in Tab. 25 between the positions of the points $L(=H)$, $M(=P)$, *A* and *B* in the experimental and theoretical curves. It is seen that these are in good agreement.

In the case of nickel and cobalt some maxima are to be found, in the excitation curves, which do not correspond to similar structures in the absorption edges. It is interesting to note that the beginning of the extra Ni maximum above the maximum *B* has a voltage distance from the sharp intensity increase at *P* equal to the discrete energy loss measured for Ni by LANG (See Chapter VII).

2. General remarks

The h structure

The assumption that the *h* structure (See Figs. 29–31) corresponds to a transition into the empty 3d band is supported by several observations:

(1) The *h* structure decreases in width and height from Ti to Ni and disappears entirely at copper. Such a behavior corresponds to the decrease of the unfilled upper

Table 25. Comparison of the calculated and observed structure of the copper curves.

Structure	Theory	Exc. curve	BEEMAN and FRIEDMAN
H–P (*L–M*)	3.4	3.6	4.0
P–A (*M–A*)	8.3	8.2	10.7
A–B	7.2	8.7	9.4

part of the 3d band. The measured *h* dimensions are about the same for the elements Cr, Fe and Co. (The cobalt curve in Fig. 31 is measured with a thin cobalt target and has a somewhat larger *h* structure than the curves with thick targets. See Figs. 34 and 35.) Titanium definitely gives, however, a wider and higher *h* structure and nickel a smaller and lower one than the intermediate elements.

(2) If the interpretation of the *h* structure as arising from the 3d band is correct, the Fermi level should correspond to the point *h* (Fig. 16). A calculation on such assumptions for the $M_{II, III}$ level has been made for nickel and chromium and the result compared with directly measured values (Tab. 26). The agreement between calculated and experimental values supports the 3d interpretation, especially in the case of chromium, where a choice could possibly be made between the points *h* and *H* as representing the Fermi level and where the distance between these points is large enough not to be overbridged by the inaccuracy in the voltage measurements.

In Tab. 26 the L_{III} and $M_{II, III}$ levels have been calculated for all the investigated elements from the determined voltage value of *h* (for copper *H*) and the precision measured emission lines $K\alpha_1$ and $K\beta_1$. Available earlier measurements of emission bands and absorption edges show generally good agreement with the calculated values. (The calculations were made with $h/e = 1.3793 \cdot 10^{-17}$ erg. sec./e.s.u.).

(3) As we can see from the Figs. 33, 35 and 36 the $K\beta_5$ edge and the inflection point *L*, corresponding to the Fermi level calculated by Beeman & Friedman, coincide for Ni but not for Co and Fe. The discrepancy is of the same order of magnitude as the width of the *h* structure. The absorption edges constitute a mean of the unresolved (3d, 4s) structure; the $K\beta_5$ edge, however, corresponds entirely to the 3d limit.

(4) The long wavelength side of the $K\beta_2\beta_5$ emission band of Zn (Fig. 40) shows a similar picture as the main edge of the excitation curves for Fe, Co and Ni. This emission band is a poorly resolved doublet, for which the lower energy maximum is identified as the ($K - M_{IV, V}$) transition and the higher energy maximum is ascribed to transitions from p states intermingled with the s states in the 4s band. A similar appearance can be expected for the edge in the excitation curves when the 3d band contains empty states as in the case of all the 3d elements.

Table 26. L_{III} and $M_{II, III}$ edges (in absolute volts), calculated from the K excitation potentials and compared with experimental data. (Wavelengths of $K\alpha_1$ and $K\beta_1$ from Landolt-Börnstein, Zahlenwerte und Funktionen, 6. Auflage, 1950.)

	L_{III} edge		$M_{II, III}$ edge	
	Calc.	Exp.	Calc.	Exp.
22 Ti ($h = 4\,963.5$)	453.1	(452.6) (em.)[1]	32.2	
24 Cr ($h = 5\,987.4$)	573.3	(572.0) (em.)[1]	41.0	41.6 ± 0.3 (em.)[6]
26 Fe ($h = 7\,110.5$)	707.4	(705.7) (em.)[1]	53.3	
27 Co ($h = 7\,706.8$)	777.2	(776.3) (em.)[1]	58.1	
28 Ni ($h = 8\,329.8$)	852.4	852 (em.)[2]	66.0	65.8 ± 0.1 (abs.)[4]
29 Cu ($H = 8\,980.2$)	933.3	933 (abs.)[2] 932.4 (abs.)[3]	75.8	74.7 ± 0.5 (abs.)[5] 74.7 ± 0.3 (em.)[6]

[1] Tyrén 1937. (These figures refer to the maximum of the $L\alpha$ emission band.)
[2] Cauchois 1953. [3] Sørum 1946. [4] Skinner and Johnston 1937. [5] Johnston 1939.
[6] Gyorgy and Harvey 1952.

Alternative explanations of the origin of the *h* structure could be taken into consideration: (1) Oxide influence of the type shown in Fig. 37, (2) creation of exciton levels [see however CAUCHOIS & MOTT 1949, MOTT 1949] and (3) fine structure due to the screening of the residual positive charge according to FRIEDEL [for references, see MOTT 1953]. These alternative explanations are however not free from objections and can hardly counterbalance the four favourable arguments given above.

The 4s band.

The 4s plateau arises to a height of about 20 % of the continuous background for the elements chromium and titanium. As is seen from Figs. 22 and 27 the *RP* ridge is very well marked. The intensity rises apparently linearly both at the primary and the secondary edges. Tabs. 20–21 show that the slope of *SR* is slightly steeper than the slope of *PQ*. According to this observation the density of states with p character at the bottom of the 4s bands must be somewhat higher than at the bottom of the 4p band.

The width of the primary edge for Cr and Ti, 3.0 V, is larger than the dispersion of the voltage due to the K level width and limited apparatus resolution, and must be ascribed to a continuous increase in the p character admixture. At the bottom of the first zone the density of p states should be proportional to $E^{3/2}$ according to JONES & MOTT [1937]. If this is the case here, it cannot be seen from the excitation curves because of the fine structure at the foot. From emission bands, expected to vary with $E^{3/2}$, it can easily be seen that if the lowest part of the band is cut off, the rest has an approximately linear appearance. Compare, for instance, the emission bands in the reference SKINNER 1938, p. 271.

In comparison with Ti and Cr the elements Fe to Cu have a remarkably lower 4s plateau, indicating a fall of the p admixture in the 4s band as the atomic number increases. In the same direction the length of the plateau decreases, partly because of change in the relative position of the Fermi level with added electrons and partly because of the general shrinking of entire structure. Data for length and height of the 4s plateau are given in Tab. 22.

The 4p band.

Here we can expect a strong intensity increase because of the favourable symmetry of the dominating states. From Fig. 15 it can be seen that the steep slope of the intensity curve is definite. Fine structure occurs but is difficult to measure. An attempt has been made in the earlier considered Fig. 39. The most evident variations refer to the lattice influence on the excited electrons. Towards higher voltages the excitation mechanism will be more and more complicated and a detailed analysis difficult. Retarded electrons will soon be able to excite the K level and the fluorescence excitation by continuous quanta will be increasingly important.

Summary

1. A concave crystal spectrometer is used to determine the intensity function of K emission lines in the neighbourhood of the excitation potential for some 3d elements.

2. A method has been worked out to obtain pure targets under vacuum conditions and to suppress the contamination velocity in order to get reproducible intensity measurements of the characteristic radiation. The X-ray tube is reconstructed and equipped according to this method.

3. A Geiger counter is constructed with high efficiency in the wavelength region 1.5–2.6 Å.

4. The intensity function is recorded and the K excitation potential determined for the following lines:

a) the Kα_1, Kα_2 and Kβ_1 lines of chromium and

b) the Kα_1 line of titanium, iron, cobalt, nickel and copper.

5. The intensity function is recorded for Cr Kα_1 at a target temperature of 1000° C.

6. An isochromat is recorded, containing the quantum limit of the continuous spectrum and the excitation curve for the Cr Kβ_1 line.

7. A proof is given for the necessity of work function correction in the determination of the excitation potential.

8. A summary in absolute and international volts is given in Tabs. 18 and 19 of the excitation potentials measured. Voltage differences and intensity characteristics for the structure of the excitation curves are given in Tabs. 20–22.

9. The electronic and radiative excitation is discussed. A comparison of the absorption edges and excitation curves is given in Figs. 33, 35, 36 and 38.

10. A value of h/e is obtained from the K excitation potentials and the K absorption edges for the elements 26 Fe to 29 Cu. The result is $(1.3794 \pm 0.0006) \cdot 10^{-17}$ erg · sec./e.s.u.

11. L_{III} and $M_{II,III}$ edges are calculated for the 3d elements investigated.

12. An attempt is made to explain the structure of the intensity curves from the band theory of metals.

REFERENCES

van Arkel, A. E., Reine Metalle. Berlin 1939.
Barnes, A. H., Phys. Rev. *44*, 141 (1933).
Bearden, J. A., Johnson, F. T., Watts, H. M., Phys. Rev. *81*, 70 (1951).
Bearden, J. A., and Schwarz, G., Phys. Rev. *59*, 934 (1941).
—— Phys. Rev. *79*, 674 (1950).
Bearden, J. A., and Shaw, C. H., Phys. Rev. *48*, 18 (1935).
Bearden, J. A., and Watts, H. M., Phys. Rev. *81*, 73 (1951).
Beeman, W. W., and Friedmann, H., Phys. Rev. *56*, 392 (1939).
Bragg, W. L., Phys. Rev. *72*, 437 (1947).
Brogren, G., Nova Acta Reg. Soc. Scient. Upsaliensis, Ser. IV, Vol. 14, No. 4 (1949).
Brogren, G., and Friskopp, K. G., Arkiv f. Mat. Astr. o. Fysik *36 B*, No. 4 (1948).
Cauchois, Y., Les spectres de rayons X et la structure électronique de la matière. Paris 1948.
—— Phil. Mag. *43*, 375 (1952).
—— Phil. Mag. *44*, 173 (1953).
Cauchois, Y., and Mott, N. F., Phil. Mag. *40*, 260 (1949).
Compton, A. H., and Allison, S. K., X-rays in theory and experiment. New York 1935.
Coster, D., and Kiestra, S., Phil. Mag. *41*, 144 (1950).
Coster, D., and van Zuylen, J., Nature *129*, 942 (1932).
DuMond, J. W. M., Phys. Rev. *72*, 276 (1947).
—— Phys. Rev. *74*, 1883 (1948).
DuMond, J. W. M., and Cohen, E. R., Rev. Mod. Phys. *20*, 82 (1948).
Eisenstein, A. S., Oxide coated cathodes. Advances in Electronics I. New York 1948.
Espe, W., and Knoll, M., Werkstoffkunde der Hochvakuumtechnik. Berlin 1936.
Farmer, E. C., and Brown, S. C., Phys. Rev. *74*, 902 (1948).
Fletcher, G. C., Proc. Phys. Soc. *A 65*, 192 (1952).
Fletcher, G. C., and Wohlfarth, E. P., Phil. Mag. *42*, 106 (1951).
Friedenstein, H., Martin, S. L., and Munday, G. L., Rep. Progr. Phys. *11*, 298 (1946–47).
v. Friesen, S., Uppsala Universitets Årsskrift, No. 14 (1935).
Graf Soden, D., Ann. Physik *19*, 409 (1934).
Gyorgy, E. M., and Harvey, G. G., Phys. Rev. *87*, 861 (1952).
Haglund, Ph., Arkiv f. Mat., Astr. o. Fysik *28 A*, No. 8 (1941).
Hanawalt, J. D., Z. Physik *70*, 293 (1931).

HERRMANN, G., and WAGENER, S., Die Oxydkathode. Leipzig 1943 (I) and 1944 (II).
HUBER, H., and WAGENER, S., Z techn. Physik *23*, 1 (1942).
INGELSTAM, E., Arkiv f. Mat., Astr. o. Fysik *27 B*, No. 4 (1939).
JNANANANDA, S., High Vacua. New York 1947.
JOHANN, H. H., Z. Physik *69*, 185 (1931).
JOHNSTON, J. E., Proc. Camb. Phil. Soc. *35*, 108 (1939).
JONES, H., and MOTT, N. F., Proc. Roy. Soc. *A 162*, 49 (1937).
JONES, H., MOTT, N. F., and SKINNER, H. W. G., Phys. Rev. *45*, 379 (1934).
KLEMPERER, O., Einführung in die Elektronik. Berlin 1933.
KRUTTER, H. M., Phys. Rev. *48*, 664 (1935).
KRONIG, R. DE L., Z. Physik *70*, 317 (1931) and *75*, 191 (1932).
KULENKAMPFF, H., Ann. Physik *69*, 548 (1922).
KURYLENKO, C., Thèse. Paris 1939.
KÖNIG, H., Naturwiss. *35*, 261 (1948).
LANG, W., Optik *3*, 233 (1948).
LAW, R. R., R. S. I. *19*, 920 (1948).
LEVINSTEIN, H., J. App. Phys. *20*, 306 (1949).
MORRISON, J. D., and NICHOLSON, A. J. C., J. Chem. Phys. *20*, 1021 (1952).
MOTT, N. F., Proc. Phys. Soc. *A 62*, 416 (1949).
—— Progr. in Met. Phys. *3*, 76 (1952).
—— Phil. Mag. *44*, 187 (1953).
MOTT, N. F., and JONES, H., The theory of the properties of metals and alloys. Oxford 1936.
MÖLLENSTEDT, G., Optik *5*, 499 (1949).
NEHER, H. V., and PICKERING, W. H., Phys. Rev. *53*, 316 (1938).
NIJBOER, B. R. A., Physica *12*, 461 (1946).
NILSSON, Å., and OHLIN, P., Arkiv f. Mat., Astr. o. Fysik *33 A*, No. 23 (1946).
OHLIN, P., Diss. Uppsala Universitets Årsskrift (1941).
—— Arkiv f. Mat., Astr. o. Fysik *29 A*, No. 3 (1942).
—— Arkiv f. Mat., Astr. o. Fysik *29 B*, No. 4 (1942).
PANOFSKY, W. K. H., GREEN, A. E. S., and DUMOND, J. W. M.. Phys. Rev. *62*, 214 (1942).
PARRATT, L. G., Phys. Rev. *46*, 749 (1934).
—— Phys. Rev. *49*, 132 and 502 (1936).
—— Phys. Rev. *56*, 295 (1939).
PARRATT, L. G., and JOSSEM, E. L., R. S. I. *23*, 188 (1952).
PIORE, E. R., HARVEY, G. G., GYORGY, E. M., and KINGSTON, R. H., R. S. I. *23*, 8 (1952).
RAYNOR, G. V., Rep. Progr. Phys. *15*, 173 (1952).
RICHTMYER, F. K., BARNES, S. W., RAMBERG, E., Phys. Rev. *46*, 843 (1934).
RUDBERG, E., and SLATER, J. C., Phys. Rev. *50*, 150 (1936).
RUTHEMANN, G., Naturwiss. *29*, 648 (1941) and *30*, 145 (1942).
—— Ann. Physik (6) *2*, 113 (1948).
SANDSTRÖM, A. E., Nova Acta Reg. Soc. Scient. Upsaliensis, Ser. IV, Vol. 9, No. 11 (1935).
SANNER, V. H., Diss. Uppsala 1941.
SIEGBAHN, M., Spektroskopie der Röntgenstrahlen. Berlin 1931.
SILFVERBERG, L., Arkiv f. Mat., Astr. o. Fysik *31 B*, No. 10 (1944).
SKINNER, H. W. B., Proc. Roy. Soc. *A 135*, 84 (1932) and *A 140*, 277 (1933).
—— Rep. Progr. Phys. *5*, 257 (1938).
—— Phil. Trans. Roy. Soc. *A 239*, 95 (1946).
SKINNER, H. W. B., and JOHNSTON, J. E., Proc. Roy. Soc. *161*, 420 (1937).
SLATER, J. C., Phys. Rev. *49*, 537 (1936).
STAHL, H. A., J. App. Phys. *20*, 1 and 8 (1949).
STODDARD, K. B., Phys. Rev. *46*, 837 (1934) and *48*, 43 (1935).
SZABÓ, Z. G., and LAKATOS, B., Naturwiss. *39*, 486 (1952).
SØRUM, H., K. Norske Vidensk. Selsk. Forh. *19*, No. 13 (1946).
TERRILL, H. M., Phys. Rev. *22*, 101 (1923).
TYRÉN, F., Arkiv f. Mat., Astr. o. Fysik *25 A*, No. 32 (1937).
WILLIAMS, E. J., Proc. Roy. Soc. *A 130*, 310 (1930–31).
YARWOOD, J., High Vacuum Technique. New York 1946.

Tryckt den 5 maj 1953

Uppsala 1953. Almqvist & Wiksells Boktryckeri AB